Contributions à la détection directe des ondes gravitationnelles avec Virgo

Eric Chassande-Mottin

Université Paris Denis Diderot

Mémoire d'Habilitation à Diriger des Recherches

présenté par

Éric Chassande-Mottin

Contributions à la détection directe des ondes gravitationnelles avec Virgo

Caractérisation du détecteur, analyse de données et astrophysique multi-messager

Soutenue le 2 juillet 2014
devant le jury composé de MM.

Jean-Luc Atteia	—	**Examinateur**
Pierre Binetruy	—	**Rapporteur**
Damir Buskulic	—	**Examinateur**
Yannick Giraud-Héraut	—	**Président**
Cédric Richard	—	**Rapporteur**
Andrea Vicerè	—	**Rapporteur**

La guardia del nulla, Cicogna & Ricard, Copyright Casa Editrice Universo, 1987

Table des matières

Préface

Lorsque Patrick Flandrin, mon directeur de thèse suite à un échange avec Thibault Damour (voir le fax restitué à la page suivante) me parle de Virgo en 1996 et me propose de travailler sur la détection directe des ondes gravitationnelles et les difficiles problèmes d'analyse du signal qui y sont associés, j'étais loin de penser que cela aurait un tel impact sur ma carrière professionnelle. Cela représentait un terrain de jeu fascinant pour le jeune doctorant que j'étais.

Je n'avais pas non plus anticipé la diversité de problématiques impliquées, qui couvrent un large éventail de disciplines allant de la physique fondamentale (avec la Relativité Générale naturellement), l'astrophysique (formation, évolution et population des objets compacts), la physique expérimentale et instrumentale (optique, mécanique, contrôle, etc) à l'analyse des données (représentation/caractérisation, statistique, algorithmique, etc).

Cela explique l'interdisciplinarité de mes travaux et se reflète dans la structure de ce mémoire d'Habilitation à Diriger des Recherches. Outre l'introduction faite au Chapitre 1, les trois volets qui le composent suivent chronologiquement les thèmes que j'ai abordés et que j'ai développés dans trois cadres différents.

Le Chapitre 2 présente ma participation à la mise en service de l'instrument, et plus spécifiquement à l'analyse et la caractérisation du bruit instrumental, lors de ma présence sur le site Virgo à Cascina en Italie.

Le Chapitre 3 décrit les développements théoriques et méthodologiques faits en grande partie à l'Observatoire de la Côte d'Azur à Nice portant sur la détection temps-fréquence et non-paramétrique de signaux chirps ainsi qu'à la mise en application de ces méthodes pour la recherche d'ondes gravitationnelles transitoires.

Le Chapitre 4 expose des résultats obtenus à l'APC à Paris qui concernent des études et analyses combinant les ondes gravitationnelles et d'autres messagers astrophysiques, à savoir les neutrinos de haute énergie (en collaboration avec le télescope à neutrino ANTARES) et le rayonnement électromagnétique (contreparties optiques recherchées par les télescopes robotisés).

Thibault DAMOUR
INSTITUT
DES HAUTES ÉTUDES SCIENTIFIQUES
35, ROUTE DE CHARTRES
91440 BURES-SUR-YVETTE - FRANCE
☎ (1) 69.07.48.53
e-mail : damour@ihes.fr

7/2/94

Patrick FLANDRIN
ENS Lyon.
46 allée d'Italie
69364 Lyon Cedex 07

Cher Collègue,

les chirps d'ondes gravitationnelles venant des phases finales de rapprochement de systèmes binaires d'étoiles à neutron ont la forme

$$h(t) = A\, f(t)^{2/3} \cos\left[2\pi \int_{t_i}^{t} f(t')\,dt' + \varphi\right]$$

avec $\frac{df}{dt} = B\, f^{11/3} + \cdots \equiv f^2 \times \left(\frac{f}{f_0}\right)^{5/3} \left[1 + \cdots\right]$

($+\cdots$: corrections ; $[1+\cdots]$: corrections en puissances de $(f/f_0)^{2/3}$)

la fréquence caractéristique f_0 est grande par rapport à la fréquence instantanée $f(t)$ du signal, sauf à la fin quand les deux étoiles sont très proches.

En intégrant l'equation differentielle pour $f(t)$ (en négligeant les corrections relatives $\mathcal{O}\left((f/f_0)^{2/3}\right)$ on a

$$h(t) = A'(t_* - t)^{-\frac{1}{4}} \cos\left[-B'(t_* - t)^{5/8} + \varphi'\right]$$

chirp dépendant de 4 constantes A', B', t_*, φ'

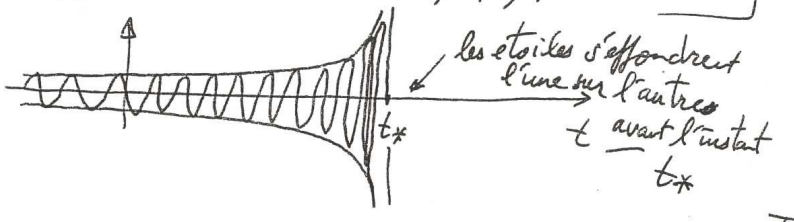

TSVP

Chapitre 1

Introduction aux ondes gravitationnelles

La théorie de la Relativité Générale d'Einstein réunit le temps et l'espace dans une seule entité, l'espace-temps qu'elle décrit comme un objet dynamique et déformable. La structure de l'espace-temps et sa dynamique résultent de son interaction avec la matière qu'il contient. Cette théorie décrit la gravitation comme émanant de la géométrie de l'espace-temps (de sa courbure plus précisément). Elle prédit l'existence de solutions radiatives aux équations d'Einstein qui gouvernent l'évolution de la géométrie de l'espace-temps. Ces solutions sont appelées *ondes gravitationnelles*.

Nous donnons ici une introduction aux ondes gravitationnelles et à leur phénoménologie. Nous passons en revue les sources astrophysiques d'ondes gravitationnelles potentiellement accessibles aux détecteurs qui nous intéressent ici.

1.1 Brefs rappels théoriques

Formellement, l'espace-temps relativiste est une variété à quatre dimensions (une de temps d'indice 0, et trois d'espace) munie d'un produit scalaire défini par le tenseur métrique g de signature $(-,+,+,+)$. Dans un certain système de coordonnées (x^α), on peut déterminer le carré de la distance entre deux points infiniment proches par [73]

$$ds^2 = g_{\mu\nu} dx^\mu dx^\nu, \tag{1.1}$$

où l'on utilise la convention de sommation d'Einstein sur les indices μ et $\nu = 0, 1, 2, 3$.

Dans la théorie de la Relativité Générale, la gravitation n'est pas une propriété des corps eux-mêmes, mais de l'espace. Elle émane de la courbure associée à la métrique g de l'espace-temps. Celle-ci est déterminée à partir de la distribution de masse-énergie grâce à l'équation d'Einstein (exprimées ici sans constante cosmologique)

$$G_{\mu\nu} = \frac{8\pi G}{c^4} T_{\mu\nu}, \tag{1.2}$$

où c est la vitesse de la lumière et G est la constante de gravitation universelle. Le tenseur d'Einstein $G_{\mu\nu}$ est directement relié à la métrique par le biais du tenseur de Ricci qui est lui-même une contraction du tenseur de courbure. Le tenseur d'énergie-impulsion $T_{\mu\nu}$ caractérise la distribution de masse et d'énergie.

L'équation d'Einstein peut être linéarisée dans l'approximation du champ faible où la métrique résulte d'une petite perturbation $h_{\mu\nu} \ll 1$ de la métrique de Minkowski $\eta_{\mu\nu} = \mathrm{diag}(-1, 1, 1, 1)$ de l'espace-temps plat de la Relativité restreinte

$$g_{\mu\nu} = \eta_{\mu\nu} + h_{\mu\nu}. \tag{1.3}$$

Dans le vide ($T_{\mu\nu} = 0$), on obtient alors en jauge de Lorenz l'équation d'onde suivante

$$\left(\nabla^2 - \frac{1}{c^2}\frac{\partial^2}{\partial t^2}\right)\bar{h}_{\mu\nu} = 0, \tag{1.4}$$

où $\bar{h}_{\mu\nu} = h_{\mu\nu} - \bar{h}/2\,\eta_{\mu\nu}$ est la perturbation métrique à trace renversée et $\bar{h} = \eta^{\mu\nu}h_{\mu\nu}$ la trace du tenseur h par rapport à η

L'adjonction de la jauge TT (transverse sans trace) détermine les degrés de liberté laissés libres par la jauge de Lorenz. Sous cette jauge, $h_{\mu\nu}$ coïncide avec $\bar{h}_{\mu\nu}$ et respecte donc la même équation. En choisissant arbitrairement la direction de propagation suivant z, les solutions de cette équation d'onde sont

$$h_{\mu\nu} = h_+(t - z/c)\varepsilon^+_{\mu\nu} + h_\times(t - z/c)\varepsilon^\times_{\mu\nu} \tag{1.5}$$

avec $h_\alpha(t) = a_\alpha \exp i\omega t$ pour $\alpha = +, \times$ et

$$\varepsilon^+_{\mu\nu} = \begin{bmatrix} 0 & 0 & 0 & 0 \\ 0 & 1 & 0 & 0 \\ 0 & 0 & -1 & 0 \\ 0 & 0 & 0 & 0 \end{bmatrix} \qquad \varepsilon^\times_{\mu\nu} = \begin{bmatrix} 0 & 0 & 0 & 0 \\ 0 & 0 & 1 & 0 \\ 0 & 1 & 0 & 0 \\ 0 & 0 & 0 & 0 \end{bmatrix}. \tag{1.6}$$

Ceci démontre l'existence de solutions ondulatoires aux équations d'Einstein, que l'on appellera *ondes gravitationnelles* (OG). Ces ondes se propagent à la vitesse de la lumière et possèdent deux modes de polarisation indépendants, notés + et ×.

1.2 Phénoménologie des ondes gravitationnelles

1.2.1 Effet des ondes gravitationnelles sur la matière

Les équations (1.5) et (1.6) montrent que les OG modulent à la fréquence ω la distance entre deux objets proches situés dans le plan transverse à la direction de propagation. La figure 1.1 montre la déformation subie par un anneau de masses ponctuelles soumises à la gravitation uniquement. On y voit l'effet causé par les polarisations + et × d'une OG se propageant perpendiculairement au plan de la figure.

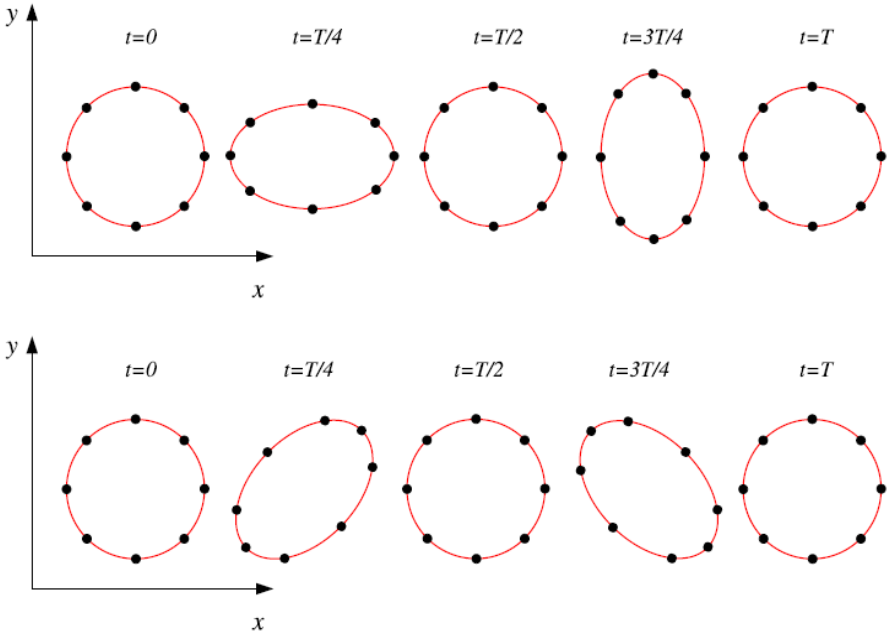

FIGURE 1.1 – **Déformation d'un anneau de masses ponctuelles causée par une OG** incidente se propageant suivant la direction normale au plan de l'anneau. Polarisations + (haut) et × (bas)

1.2.2 Production des ondes gravitationnelles

Les ondes électromagnétiques sont produites par les charges accélérées. Similairement, les OG sont produites par les masses accélérées. Le premier terme qui peut varier dans le développement multi-polaire de la distribution de masse de la source est le quadrupôle ; le monopôle et le dipôle restant constants à cause de la conservation de la masse et de la quantité de mouvement. Ceci est une différence majeure avec les ondes électromagnétiques, qui sont dominées par le dipôle. L'émission des OG est donc associée aux variations du moment quadrupolaire défini par

$$Q_{ij}(t) = \frac{1}{c^2}\int T_{00}(t,x)x_i x_j d^3x \tag{1.7}$$

où T_{00} est la composante temporelle du tenseur d'énergie-impulsion qui correspond à la densité d'énergie de la matière. Clairement, un système à symétrie sphérique n'émet pas d'OG puisque son quadrupôle ne varie pas. La formule dite "du quadrupôle" obtenue en champ lointain et dans l'approximation d'une source lentement variable ($v \ll c$) relie l'amplitude de l'émission gravitationnelle aux variations du quadrupôle défini dans l'Éq. (1.7) :

$$h_{ij} = \frac{2}{r}\frac{G}{c^4}\frac{\partial^2}{\partial t^2}Q_{ij}(t - r/c). \tag{1.8}$$

Les OG sont une *radiation* puisque la décroissance de leur amplitude est inversement proportionnelle à la distance r de l'observateur à la source.

Le facteur $G/c^4 \approx 8.3 \times 10^{-45}$ s^2/m/kg est très petit. Pour engendrer des OG d'amplitude détectable, il doit être compensé par de larges variations de Q.

On peut estimer l'ordre de grandeur de ces variations par $\ddot{Q} \sim (mv^2)_{\rm nonsph}$, de l'ordre donc de l'énergie cinétique associée à la partie non-sphérique de la source. Si l'on note R le rayon caractéristique de la source, ϵ le degré d'asymétrie de la distribution de masse et τ l'échelle de temps caractéristique d'évolution de la source, on obtient alors $\ddot{Q} \approx \epsilon m R^2/\tau^2$. L'application de cette estimation à des systèmes à l'échelle humaine donne de très faibles et insuffisantes valeurs de $\ddot{Q}$. Les OG d'amplitude détectables ne peuvent pas être produites en laboratoire.

Leur production demande des sources relativistes de grande masse et compacité qui sont donc nécessairement d'origine astrophysique. Considérons un système formé de deux objets compacts comme une binaire d'étoiles à neutrons, exemple que nous discuterons plus spécifiquement en Sec. 1.3. En utilisant la troisième loi de Kepler, l'estimation proposée ci-dessus devient $\ddot{Q} \sim m(\Omega R)^2 \sim m^{5/3}\Omega^{2/3}$ avec $m = 1.4M_\odot$, la masse typique d'une étoile à neutrons. Si la binaire est située dans l'amas de la Vierge à $r = 10$ Mpc et s'approche du point de coalescence avec la fréquence orbitale $\Omega/(2\pi) \sim 100$ Hz, on obtient $h \sim 10^{-21}$. Ceci correspond à la limite de détection des détecteurs terrestres de première génération (voir en Chapitre 2).

1.2.3 Énergie rayonnée par émission gravitationnelle

Il est intéressant de calculer le flux énergétique transporté par les OG afin de le comparer à celui d'autres processus physiques. En champ lointain, où l'espace-temps

peut être considéré plat, il est donné par [99]

$$F_{GW} = \frac{c^3}{16\pi G}\langle \dot{h}_+^2(t) + \dot{h}_\times^2(t)\rangle \tag{1.9}$$

où $\dot{x}$ désigne la dérivée temporelle et $\langle\cdot\rangle$, un opérateur de moyenne qui opère sur plusieurs périodes. Cette moyenne provient de l'impossibilité, dans la théorie de la Relativité Générale, de définir localement l'énergie du champ gravitationnel.

Le flux énergétique d'une onde polarisée linéairement d'amplitude h et de fréquence angulaire ω s'écrit

$$F_{GW} = \frac{c^3}{32\pi G}\omega^2 h^2. \tag{1.10}$$

En considérant une fréquence $\omega/(2\pi) = 100$ Hz et une amplitude $h = 10^{-21}$, on obtient un flux de 3.3 mW/m^2 soit 3.3 erg/s/cm^2. Ceci représente une quantité appréciable d'énergie pour les standards astrophysiques. Elle est, par exemple, huit ordres de grandeur plus grande que la luminosité du pulsar du Crabe dans la bande autour de 10 keV, qui est pourtant l'une des sources X les plus lumineuses. Si l'on considère une onde gravitationnelle comme une "déformation" de l'espace-temps, on peut ainsi dire, par analogie avec la théorie de l'élasticité, que l'espace-temps est un milieu très rigide puisqu'une grande quantité d'énergie donne une petite déformation.

L'énergie rayonnée s'obtient à partir du flux mesuré par le détecteur grâce à l'expression

$$E_{GW} = D_L^2 \int d\Omega \int_T F_{GW}(t)dt \tag{1.11}$$

où D_L est la distance de luminosité de la source et T la durée d'émission.

1.2.4 Preuve indirecte d'existence

En 1974, les radioastronomes Russel Hulse et Joseph Taylor découvrent et observent le pulsar binaire PSR1913+16 [82] (voir Figure 1.2) qui est composé de deux étoiles à neutrons dont l'une est un pulsar. Le nombre d'impulsions reçues par unité de temps variant selon que le pulsar s'approche ou s'éloigne de l'observateur, l'observation des temps d'arrivée des impulsions permet de déduire le mouvement orbital de la binaire avec une grande précision. Hulse et Taylor ont ainsi montré que la période orbitale de la binaire décroît (de 40 secondes sur 30 années), mettant ainsi en évidence que ce système perd de l'énergie. La mesure est en remarquable accord ($\sim 0.2\%$) [133] avec la prédiction obtenue à partir de la Relativité Générale en considérant que cette perte d'énergie est due à l'émission d'OG, fournissant ainsi une preuve indirecte de l'existence de celles-ci. Depuis la découverte de PSR1913+16, d'autres binaires de pulsars ont été découvertes comme PSR B1534+12, PSR J0737-3039A/B [95] et PSR J1141-6545 [68]. Toutes les nouvelles binaires présentent le type de décroissance orbitale que PSR1913+16. Ces observations donnent des indications fortes de l'existence des OG, telle que prédite par la Relativité Générale. Bien que cela soit improbable, on ne peut pas exclure que la décroissance de la période orbitale observée soit dû à un autre effet que l'émission gravitationnelle.

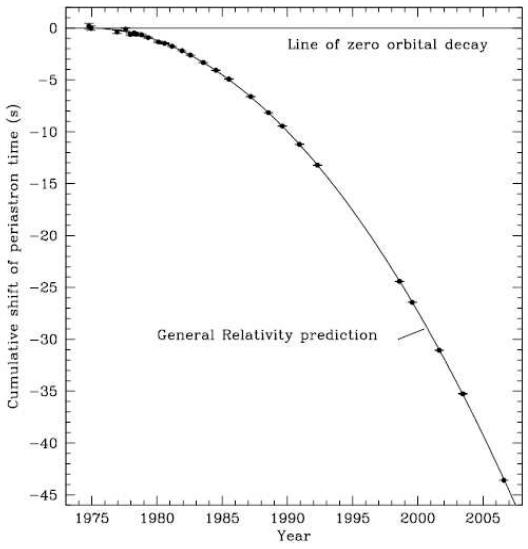

FIGURE 1.2 – **Décalage cumulé du passage au périastre de PSR 1913+16 sur la période de 1975 à 2007**. La courbe continue montrent la prédiction obtenue par la Relativité Générale. Les observations sont indiquées par des points avec des barres d'erreur. Crédit : [133].

Ceci motive la construction de détecteurs capable de *mesurer les ondes gravitationnelles in situ*. Nous aborderons ce sujet au Chapitre 2.

1.3 Sources astrophysiques d'onde gravitationnelle

La nomenclature habituellement utilisée divise les sources d'onde gravitationnelles en deux grandes familles : les sources *permanentes* et les sources *transitoires*.

Les sources permanentes comprennent les *sources périodiques* et les *fonds stochastiques*. Les sources périodiques sont associées à des étoiles à neutrons isolées possédant un certain degré d'asymétrie (ellipticité) pouvant être due à de l'accrétion de matière environnante ou à l'influence d'intenses champs magnétiques internes. Un tel système émet une OG monochromatique au double de la fréquence orbitale. Les fonds stochastiques d'OG peuvent être d'origine astrophysique ou cosmologique. Ces signaux résultent de la superposition incohérente d'une multitude de sources irrésolues. Dans le premier cas, il s'agit de sources astrophysiques proches situées dans la Galaxie ou son environnement proche. Dans le deuxième cas, il s'agit des fluctuations quantiques primordiales lors des premiers instants de l'Univers tels qu'ils sont décrits par les modèles cosmologiques actuels. La détection du signal provenant de ces sources requiert des méthodes spécifiques exploitant la permanence du signal. Nous ne les abordons pas ici et renvoyons le lecteur aux revues récentes sur ce sujet [119, 121].

Dans ce qui suit, nous nous concentrons sur les sources transitoires observables par les détecteurs qui nous intéressent et que nous présenterons au prochain chapitre. Nous décrivons les deux principaux processus astrophysiques vraisemblablement associés à une production importante d'OG : la coalescence de deux objets compacts et l'effondrement gravitationnel.

1.3.1 Binaires coalescentes

Une grande partie des étoiles sont en système binaire. Si chaque étoile de la binaire conduit à la formation d'un objet compact (étoile à neutrons ou trou noir), ce système finira par coalescer tout comme la binaire d'Hulse et Taylor présentée plus haut après avoir converti une quantité considérable d'énergie potentielle en OG.

Globalement, la signature en OG consiste en un signal quasi-périodique illustré en Fig. 1.3. Pendant la phase spirallante où les deux objets sont distants l'un de l'autre, la dynamique du système (et ainsi son émission gravitationnelle) peut être prédite avec une bonne précision par un développement post-newtonien [38,43,121]. Au premier ordre (newtonien), l'amplitude $A(t)$ et la phase $\varphi(t)$ du signal suivent une loi de puissance

$$h_+(t) = A(t)\frac{1+\cos^2\epsilon}{2}\cos 2\varphi(t) \tag{1.12}$$

$$h_\times(t) = A(t)\cos\epsilon\sin 2\varphi(t) \tag{1.13}$$

où $A(t) = 5^{1/4}\mathcal{M}^{5/4}(t_c-t)^{-1/4}$ et $\varphi(t) = -5^{5/8}\mathcal{M}^{-5/8}(t_c-t)^{5/8}$ avec la *chirp mass* $\mathcal{M} = \nu^{3/5}M$ définie en fonction de rapport de masse symétrique $\nu = m_1m_2/M^2$ et de la masse totale $M = m_1+m_2$, et en ayant fixé $c = G = 1$. L'angle ϵ désigne l'inclinaison du plan orbital.

Ces méthodes d'approximation cessent d'être valides lorsque les deux objets s'approchent de leur fusion. On doit alors recourir à des simulations numériques. À la dernière orbite stable (*last stable orbit*, LSO) qui correspond à la fréquence d'émission [121],

$$f_{LSO} = 220\text{Hz}\left(\frac{20M_\odot}{M}\right), \tag{1.14}$$

les deux objets plongent l'un sur l'autre.

Le processus se conclut par la formation d'un trou noir déformé qui irradie son asymétrie sous forme d'OG caractérisée par une sinusoïde amortie à la fréquence du mode quasi normal dominant obtenu pour $l = m = 2$ (*quasi normal mode*, QNR) [69]

$$f_{QNR} = 1430\text{Hz}\left(\frac{20M_\odot}{M}\right). \tag{1.15}$$

Pour les détecteurs de type Virgo décrits en Sec. 2.1, la fréquence du signal OG des binaires d'étoiles à neutrons ($M = 2.8M_\odot$) traverse la bande d'observation de la coupure basse (quelques dizaines de Hertz) à la coupure haute (autour de quelques kiloHertz). Le rapport signal-à-bruit est dominé par la partie spirallante.

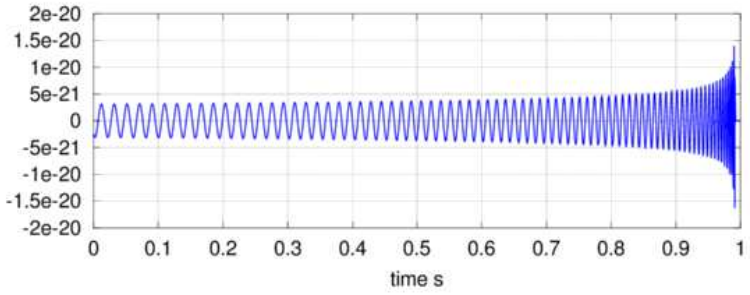

FIGURE 1.3 – **Exemple de la signature en OG de la coalescence de deux étoiles à neutrons**

La courbe d'évolution de la fréquence se translate vers les basses fréquences au fur et à mesure que la masse de la binaire augmente. Ainsi la part de la phase de fusion dans le rapport signal-à-bruit croît avec la masse jusqu'à ce que la fréquence du mode quasi normal dominant atteigne la coupure basse de la bande d'observation, ce qui correspond à $M \sim 500 M_\odot$. Les binaires de masse supérieure ne sont plus observables par les détecteurs tels que Virgo.

Durant la coalescence, une binaire de masse stellaire émet typiquement de l'ordre d'un pourcent de sa masse en OG [30]. Comme indiqué plus haut, cela se traduit par une OG d'amplitude $h \sim 10^{-21}$ pour un système situé à 10 Mpc. Cela correspond à la limite de détectabilité des détecteurs dits "initiaux", cf Sec. 2.1. Nous donnerons dans le prochain chapitre une évaluation plus précise de l'observabilité des systèmes binaires par les détecteurs d'OG.

Outre la confirmation des observations indirectes décrites en Sec. 1.2.4, l'observation en OG directe des binaires compactes coalescentes permet de tester la gravité en champ fort [97]. En effet, dans les secondes qui précèdent leur coalescence, ces systèmes entrent dans le régime dynamique non-linéaire associé à des vitesses relativistes $v/c \sim 0.5$ pour un facteur de compacité orbitale $\Xi \sim GM/(Rc^2) \sim 0.2$ où R est le rayon orbital de la binaire. Ce domaine n'a été exploré par aucune expérience jusqu'à maintenant. (En comparaison, le pulsar double J0737-3039 [95] mentionné plus haut $v/c \sim 10^{-3}$ et $\Xi \sim \times 10^{-6}$.)

1.3.2 Effondrement gravitationnel de cœur stellaire

S'il présente un certain degré de non-axisymétrie, l'effondrement gravitationnel de cœur stellaire ou supernova gravitationnelle donne lieu à une émission OG transitoire substantielle. Les simulations numériques nécessaires à la compréhension de ce processus sont particulièrement difficiles à réaliser. L'équation d'Einstein doit être résolue dans un cadre multidimensionnel en y intégrant plusieurs autres ingrédients comme la magnéto-hydrodynamique, le transport des neutrinos et les interactions nucléaires [107]. Jusqu'ici aucune simulation ne réunit tous les ingrédients requis. Les estimations actuelles indiquent que la quantité d'énergie gravitationnelle rayonnée est de l'ordre de $10^{-7} M_\odot$

pour une fréquence d'émission autour du kiloHertz.

D'autres scénarios plus spéculatifs conduisent à une émission d'OG significativement accrue. Ceux-ci font intervenir des étoiles massives entraînées par l'accrétion dans un fort mouvement de rotation. Dans ce cas, des instabilités dynamiques peuvent se développer [59, 65] conduisant à l'émission de $10^{-2} M_\odot$ en OG autour de quelques centaines de Hz, qualitativement comparable au cas des binaires coalescentes. Ces scénarios sont évoqués pour expliquer les sursauts gamma longs.

Comme pour les binaires, nous verrons dans le prochain chapitre en Sec. 2.3 comment ces niveaux d'émission se traduisent en terme d'observabilité par les détecteurs d'OG.

Chapitre 2

Détection directe des ondes gravitationnelles par interférométrie laser

La détection directe des OG est importante pour deux raisons. Elle autorise des tests fondamentaux de la gravitation [121], qu'elle soit décrite par la théorie de la Relativité Générale ou par une théorie alternative, par l'observation des OG elles-mêmes (test de la vitesse des OG et de leur polarisation) ou à travers les signaux reçus des objets relativistes ainsi observés. L'observation des binaires compactes coalescentes permet le test de la gravité en champ fort (cf Sec. 1.3.1), et par là même, de la structure post-Newtonienne de la théorie d'Einstein. La détermination à partir des signaux OG de la masse et du spin du trou noir produit après la coalescence d'un binaire de trous noirs permet également de tester le second principe de la thermodynamique des trous noirs ainsi que la conjecture de censure cosmique énoncée par Penrose.

Au delà des tests de physique fondamentale, la détection directe des OG est un nouveau mode d'observation de l'Univers en général, et des objets compacts en particulier. À ce titre, on peut anticiper l'importance de liens futurs avec l'astrophysique des hautes énergies, point que nous développerons au Chapitre 4.

La détection directe des OG a d'abord été tentée via l'observation du faible effet mécanique exercé par celles-ci sur des objets massifs possédant une extension spatiale. L'effet de marée causé sur un tel objet excite ses modes propres de vibrations longitudinales. Il s'agit ainsi de détecter une amplitude anormale de vibration d'un objet isolé des perturbations extérieures. Ce principe a été mis en application en couplant une barre de métal à un accéléromètre (en fait, un transducteur piézo-électrique) permettant de mesurer les vibrations de la barre. Plusieurs spécimens de ce dispositif communément appelé "barre de Weber" ont fonctionné depuis les années 90 atteignant une sensibilité de $\sim 10^{-21}/\mathrm{Hz}^{1/2}$ dans une bande de fréquence étroite autour du kiloHertz [28]. Les recherches d'OG impulsives dans les données de ces détecteurs n'ont révélé aucun événement convaincant. Elles ont permis de fixer une limite supérieure sur l'amplitude quadratique moyenne des OGs de ce type à $h_{\mathrm{rss}} \sim 10^{-19}/\mathrm{Hz}^{1/2}$ (voir la définition en

FIGURE 2.1 – **Localisation géographique des détecteurs interférométriques actuels et futurs**. Cette carte du monde montre la localisation des quatre sites où sont installés les détecteurs de première génération (LIGO Handford and Livingston, Virgo et GEO). Elle indique également les six sites de seconde génération (incluant en plus LIGO India et KAGRA au Japon). Le site du détecteur LIGO India doit encore être déterminé.

Éq. (2.2)), avec un taux de fausse alarme d'un événement par siècle (soit 3×10^{-10} s) [28].

Grâce aux travaux pionniers de Forward, Weiss et Drever, un nouveau concept d'instrument s'est développé dans les années 70 utilisant l'interférométrie laser. Ce chapitre donne une présentation générale des détecteurs interférométriques basés sur ce principe et qui ont supplanté les barres de Weber. Une première génération de ce type d'instruments a fonctionné durant la dernière décennie. Il s'agit de cinq instruments de grande envergure (voir Fig. 2.1). Laser Interferometer Gravitational-Wave Observatory (LIGO) [13] opère trois instruments kilométriques aux États-Unis situé à Livingston en Louisiane et à Hanford dans l'État de Washington (ce dernier site héberge deux interféromètres dans la même enceinte à vide). Le projet franco-italien Virgo [16] a un instrument de même classe situé à Cascina près de Pise en Italie. Nous y consacrons une section spécifique de ce chapitre. Enfin, GEO [74] est un détecteur anglo-allemand aux dimensions plus modestes (600 mètres) situé près d'Hannovre en Allemagne.

Ce chapitre se concentre sur cette première génération de détecteurs dits "initiaux" par contraste aux détecteurs de seconde génération dit "avancés" que l'on évoquera brièvement en Sec. 2.5.

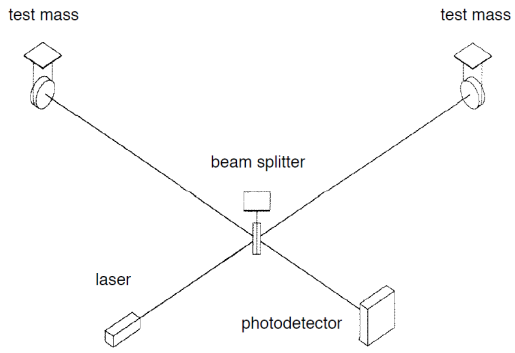

FIGURE 2.2 – **Schéma de principe d'un interféromètre de Michelson**

2.1 Principe de détection

Malgré des différences majeures dans les technologies utilisées, tous les instruments cités plus haut mesurent les OG selon le même principe. La déformation qu'une OG incidente exerce sur l'espace-temps modifie la longueur différentielle $\delta\ell$ du chemin optique suivi par deux faisceaux laser se propageant dans deux directions orthogonales sur une distance L délimitée par des masses test soumises uniquement à la gravité. Similairement à l'expérience de Michelson-Morley, on mesure alors l'interférence entre les deux faisceaux (voir Fig. 2.2). Celle-ci est directement reliée à la différence de phase accumulée par les deux faisceaux avant leur recombinaison et ainsi à la différence de longueur de leur chemin optique. La mesure de la puissance lumineuse de la frange d'interférence permet ainsi celle de $\delta\ell$ avec une grande précision. La réponse du détecteur $h \equiv \delta\ell/L$ (quantité sans dimension) est directement reliée aux amplitudes h_+ et $h_\times$ des deux polarisations de l'OG.

La précision de la mesure est limitée par deux bruits fondamentaux dans la bande utile entre quelques dizaines de Hertz et le kiloHertz : l'agitation brownienne des atomes constituant les optiques (bruit thermique) et la nature quantique de la lumière (bruit de photons). Avec la première génération de détecteurs, la sensibilité atteint $h(f) \sim 5 \times 10^{-23}/\mathrm{Hz}^{1/2}$ à 100 Hz (voir Fig. 2.3) et $h \sim 10^{-21}$, une fois intégré sur la bande d'observation.

La réponse du détecteur résulte d'un mélange linéaire $h = F_+ h_+ + F_\times h_\times$ des deux polarisations de l'OG. Les facteurs du diagramme d'antenne F_+ et $F_\times$ caractérisent le couplage de chacune des polarisations avec le détecteur. Le couplage quadratique moyen $\mathcal{F} = (F_+^2 + F_\times^2)^{1/2} \leq 1$ est maximum pour les ondes en incidence normale au plan du détecteur et il est minimum (et exactement zéro) pour celles qui proviennent d'une des quatre directions "aveugles" associées aux deux bissectrices des bras du détecteur. Les détecteurs sont des antennes non-directionnelles puisque $\mathcal{F} \gtrsim 1/2$ pour plus de la moitié du ciel (voir la Fig. 2.4).

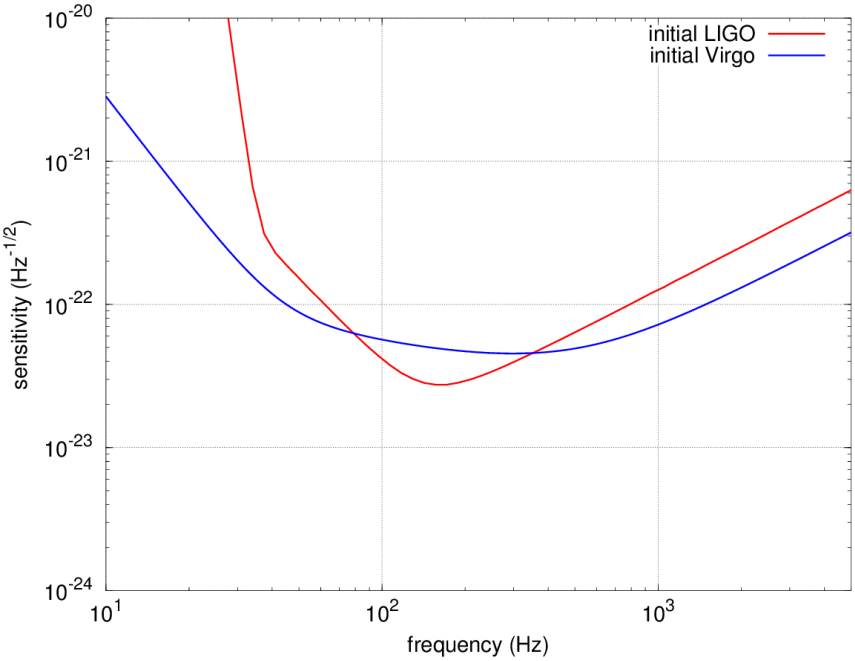

FIGURE 2.3 – **Sensibilités théoriques des détecteurs initiaux LIGO et Virgo**. Elles sont exprimées en amplitude et correspondent donc à la racine carrée de la densité spectrale de puissance, d'où l'unité $1/\mathrm{Hz}^{1/2}$ pour une quantité sans dimension telle que h.

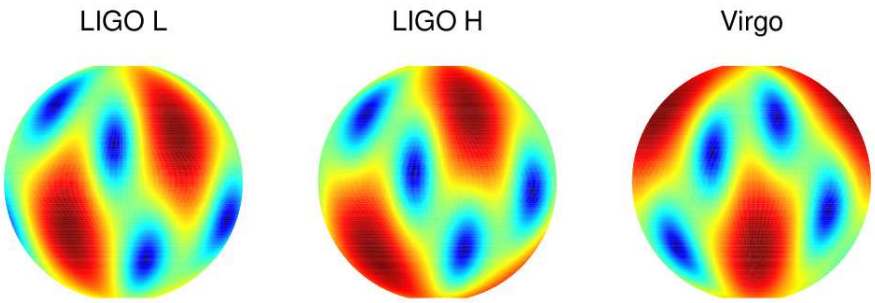

FIGURE 2.4 – **Diagrammes d'antenne de LIGO et Virgo en projection sphérique**.

FIGURE 2.5 – **Vue aérienne du détecteur Virgo**.

2.2 Le détecteur Virgo

Le détecteur Virgo est un projet franco-italien piloté par le Centre National de la Recherche Scientifique CNRS en France et l'Istituto Nazionale di Fisica Nucleare en Italie. Le projet a été initialement proposé en 1989 et le site localisé à Cascina près de Pise Italie (voir Fig. 2.5) a été inauguré en 2003.

Nous allons dans cette section au delà des principes généraux énoncés dans la précédente section et présentons le détecteur Virgo dans les grandes lignes en insistant sur ses spécificités.

2.2.1 Description de l'instrument

Virgo est un interféromètre aux bras de trois kilomètres. La Figure 2.6 présente le schéma optique original de l'instrument qui n'inclut donc pas les améliorations faites par la suite. À ce schéma correspond la sensibilité théorique en Fig. 2.3.

Cette sensibilité présentée en Fig. 2.3 est limitée à basse fréquence ($f \lesssim 10$ Hz) par le bruit sismique issu de l'activité géologique et anthropique. Aux fréquences intermédiaires ($10\text{ Hz} \lesssim f \lesssim O(100)$ Hz), la sensibilité est limitée par le bruit thermique provenant des fluctuations des atomes qui composent les miroirs et les fils des suspensions sismiques. Aux plus hautes fréquences ($f \gtrsim 1$ kHz), la sensibilité est limitée par le bruit poissonien de comptage des photons effectué à la lecture de l'interférence.

Super-atténuateur Afin d'assurer que les masses test (les optiques de l'interféromètre) soient des masses d'épreuve soumises seulement à la gravité), il est nécessaire de les suspendre. Ceci est réalisé par un système d'isolation qui permet aussi l'extension de la bande de détection aux basses fréquences en atténuant le bruit sismique. Les optiques

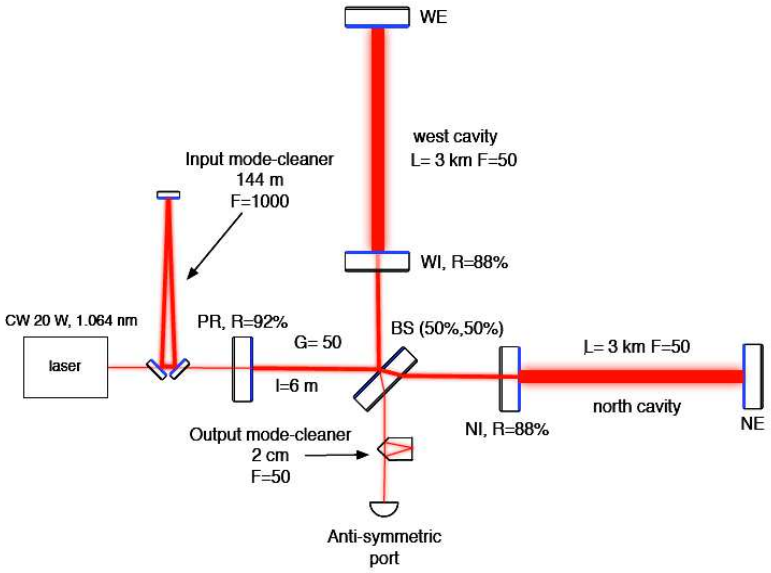

FIGURE 2.6 – **Schéma optique de Virgo**.

de l'interféromètre sont suspendues à une chaîne de sept pendules passifs appelée *super-atténuateur* sismique, chaque élément réalisant une atténuation en $1/f^2$ au dessus de la fréquence de résonance du filtre. Grâce au super-atténuateur, Virgo est aujourd'hui le détecteur le plus sensible en dessous de 50 Hz.

Cavités optiques résonantes Pour les ondes électromagnétiques, le couplage à l'antenne est maximum quand la longueur de l'antenne est égale à la moitié de la longueur d'onde. Une relation similaire existe pour les détecteurs interférométriques présentés ici. Pour une onde à la fréquence de 200 Hz, la longueur optimale (des bras de l'interféromètre) est de l'ordre du 1000 km, ce qui est irréalisable. La solution est de replier le chemin optique en accordéon. Comme il est indiqué dans le schéma optique en Fig. 2.6, ceci est réalisé par des cavités de Fabry-Perot constituées d'un miroir semi-réfléchissant en entrée de bras et d'un miroir de fin de bras. La lumière fait de multiples allers et retours à l'intérieur de ces cavités. La longueur de la cavité doit être contrôlée avec précision afin que le champ électromagnétique sortant se combine en phase avec le champ entrant. Le nombre équivalent d'aller-retour est proportionnel à la finesse de la cavité (qui est ~ 50 pour Virgo). La finesse est limitée par les pertes optiques et la réduction de la bande passante du détecteur qui est inversement proportionnelle à la finesse.

Recyclage de la puissance lumineuse La source lumineuse est un laser Nd :Yag (de longueur d'onde 1064 nm) de puissance 20 W, stabilisé en fréquence. Le bruit de photons évolue comme la racine carrée de la puissance lumineuse dans l'interféromètre. De forte puissances laser sont donc nécessaires afin d'arriver aux spécifications de sensibilité. La

puissance du laser étant insuffisante, on “recycle” la lumière disponible.

Lorsque l'interféromètre est placé sur la frange noire, la lumière est donc presqu'entièrement réfléchie vers la source. Un miroir semi-réfléchissant placé entre le laser et la séparatrice (voir Fig. 2.6) recycle cette lumière et amplifie ainsi la puissance lumineuse entrant dans l'interféromètre. Comme pour les cavités des bras, le recyclage doit être réalisé en phase entre champs sortant et entrant et forme ainsi une nouvelle cavité de Fabry-Perot composite avec le reste de l'interféromètre.

2.2.2 Mise en fonction de l'interféromètre

Le démarrage de l'interféromètre s'est déroulé en deux temps. Mon entrée au CNRS coïncide avec la première phase de mise en fonction de la partie centrale qui commence à la livraison des bâtiments principaux et à l'installation de l'enceinte à vide dans ceux-ci ; la construction du tunnel et du tube formant les bras se poursuivent en parallèle. Durant cette période de 2000 à 2003, je travaille en permanence sur le site Virgo à Cascina et contribue aux travaux d'installation (connexion du laser d'injection au système d'acquisition de données incombant au groupe ILGA de l'observatoire de Côte d'Azur auquel j'étais affilié) et aux premières études de caractérisation de l'instrument. Ceci m'amène à expérimenter un certain nombre de méthodes d'analyse de données qui seront ensuite réutilisées pour la deuxième phase de 2003 à 2007 qui regarde l'interféromètre complet avec ses bras kilométriques après leur livraison courant 2003. Au fur et à mesure de l'intégration et de la mise au point des composants de l'interféromètre, la sensibilité s'améliore comme on le constate en Figure 2.7 qui en montre l'évolution sur la période 2003 à 2007. Cette période de mise au point est jalonnée par une série de prise de données “commissioning” (C$\star$) et “science” (VSR$\star$). Contrairement aux détecteurs de physique des particules où les différentes parties (faisceau, calorimètres, etc) sont indépendantes les unes des autres, les composants d'un détecteur d'OG sont couplés ce qui rend la phase de mise au point particulièrement délicate.

J'ai contribué des outils de pré-analyse et de caractérisation utiles aux équipes d'expérimentateurs afin de réduire le cycle d'identification et de résolution des problèmes. S'il est difficile de dresser un inventaire précis des développements effectués, on peut citer quelques exemples d'outils que j'ai initiés, qui ont été ensuite repris et automatisés et dont certains fonctionnent encore aujourd'hui.

Suivi de la non-stationarité à long terme Thomas Cokelaer (alors doctorant à l'observatoire de la Côte d'Azur) et moi-même avons proposé et implémenté l'idée d'un calcul de spectre glissant permettant une vision globale et instantanée de l'évolution de celui-ci sur une durée d'un à plusieurs jours (qui correspond à la durée d'une prise de données), mettant ainsi en évidence les non-stationnarités lentes (dizaines de minutes à quelques heures). Dans l'exemple présenté en Fig. 2.8, quatre périodes de dysfonctionnements sont clairement identifiables, ce qui permet de focaliser les investigations à ces instants.

Notre idée a été ensuite reprise par Didier Verkindt (LAPP) qui en a automatisé le calcul, l'a systématisé à un ensemble de canaux et intégré le résultat au tableau de

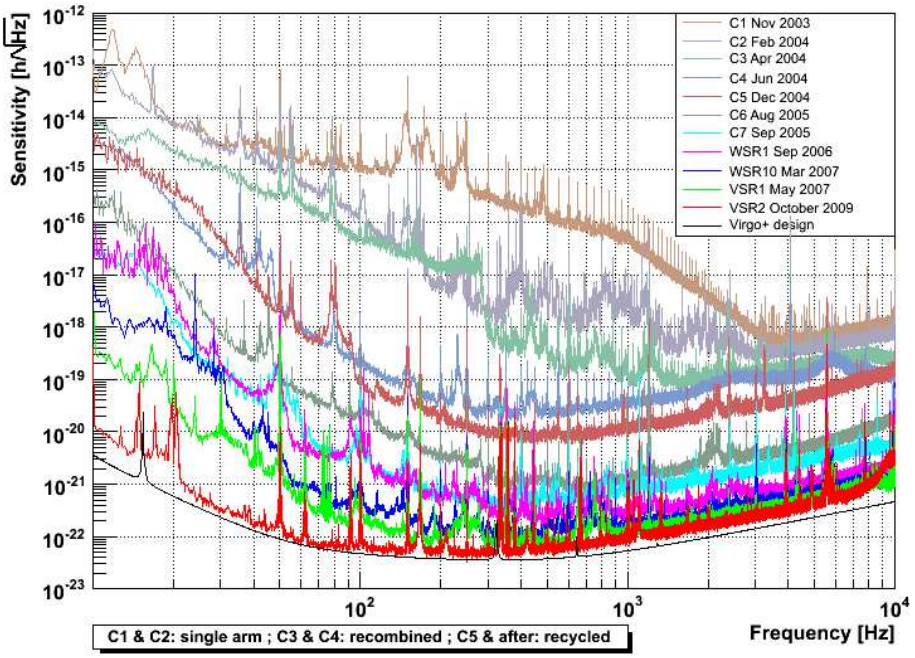

FIGURE 2.7 – **Progression de la sensibilité de Virgo pendant la période de mise en fonction** de 2003 à 2007

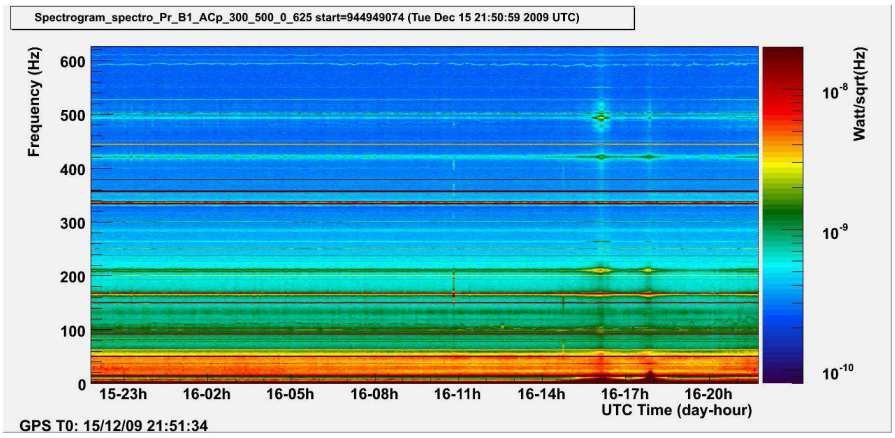

FIGURE 2.8 – **Exemple de spectrogramme de la photodiode B1 mesurant le signal de sortie de l'interféromètre**

contrôle de l'interféromètre disponible en ligne, voir https://wwwcascina.virgo.infn.it/MonitoringWeb/Spectro. Cet outil a été largement utilisé durant la mise au point de l'instrument.

Détection d'anomalies - Glitch J'ai également développé un algorithme de détection de transitoires instrumentaux ou environnementaux `outlierMoni`. Le projet consistait à mettre en œuvre un algorithme simple permettant une analyse en ligne d'un grand nombre de canaux. Cet algorithme repose sur la recherche de points aberrants (*outliers*) dans la série temporelle obtenue par blanchiment spectral. Une analyse systématique des transitoires intrumentaux des prises de données C6 et C7 a été réalisée par ce biais. `outlierMoni` a fonctionné de 2006 jusqu'en 2012. L'algorithme de blanchiment adaptatif développé pour cet algorithme a été le premier à fonctionner en ligne sur les données de frange noire. Ce résultat a été couplé avec le calcul de spectrogramme évoqué précédemment (voir les illustrations en Fig. 2.9).

Identification et archivage des lignes fréquentielles Certains bruits sont des lignes fréquentielles parasites qu'il faut supprimer lorsqu'elles affectent la sensibilité des recherches d'OG continues. On peut tirer des informations importantes sur le fonctionnement de l'interféromètre à partir d'un catalogue qui les répertorie. Avec Thomas Cokelaer et Irene Fiori (à l'époque, post-doctorant à l'Université de Pise) nous avons développé un algorithme de détection robuste des lignes [17] couplé à une base de données (voir https://tds.ego-gw.it/linesdb) permettant de répertorier ces lignes et leur origine physique, et d'archiver leur date d'apparition et/ou disparition. Cet algorithme et la base de données ont fonctionné plusieurs années avant de servir de modèle pour les versions ultérieures utilisées actuellement [3].

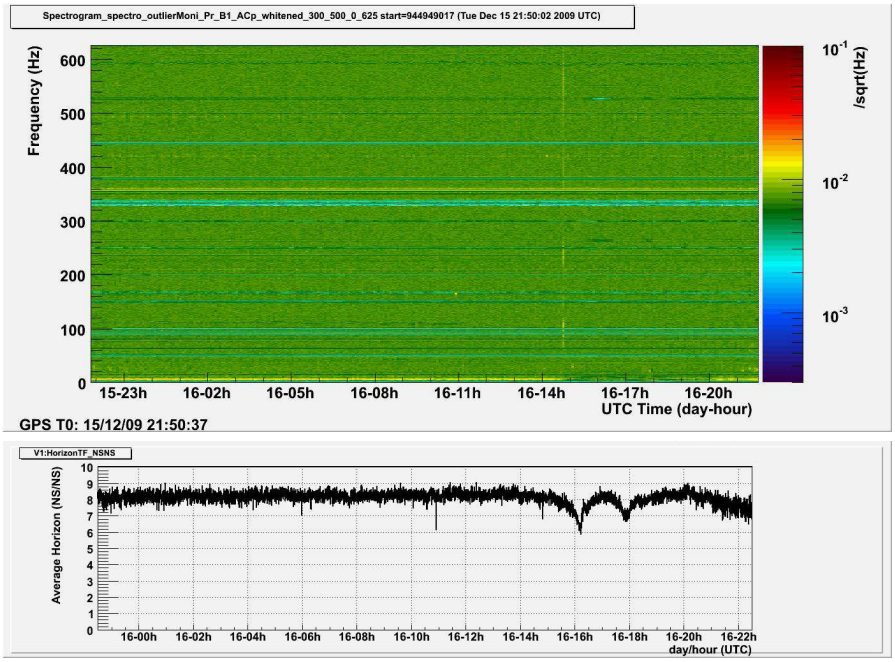

FIGURE 2.9 – **Exemple de spectrogramme courant sur une journée du signal de la photodiode B1 en sortie de l'interféromètre après blanchiment par l'algorithme `outlierMoni` décrit en Sec. 2.2.2.** On note le transitoire apparaissant clairement après t=14h (haut) qui coïncide avec une perte de sensibilité comme l'indique l'évolution de l'horizon pour une binaire d'étoiles à neutrons (bas). Voir Sec. 2.3 pour une définition de l'horizon.

2.3 Portée astrophysique des détecteurs interférométriques

La détectabilité d'un signal est caractérisée par son rapport signal-sur-bruit ρ conventionnellement défini dans le contexte de la recherche des OG par

$$\rho^2 \equiv \int_{-\infty}^{+\infty} \frac{|H(f)|^2}{S(f)} df \tag{2.1}$$

où $H(f)$ est la transformée de Fourier de la réponse du détecteur $h(t) = F_+ h_+(t) + F_\times h_\times(t)$ et $S(f)$ est la densité spectrale de puissance (bilatérale) du bruit instrumental et correspond au carré de la sensibilité introduite en Sec. 2.1.

Le rapport signal-sur-bruit dépendant linéairement de l'amplitude des ondes gravitationnelles, il décroît comme celle-ci en proportion inverse la distance à la source. Il dépend également de l'angle d'incidence de l'onde par rapport au plan du détecteur ainsi que de l'angle d'inclinaison de la source si son motif d'émission n'est pas isotrope. Lorsque le couplage est maximal, on dit que la source est optimalement située et orientée.

On définit l'*horizon* [12] par la distance d'une source optimalement située et orientée qui donne un rapport signal-sur-bruit $\rho = 8$. Pour les sources polarisées circulairement (les binaires coalescentes, par exemple), l'horizon est plus grand que la distance moyenne calculée sur une distribution uniforme de directions du ciel et d'orientations pour la source d'un facteur 2.26 [12].

Le rapport signal-à-bruit et l'horizon sont des indicateurs de la portée astrophysique des détecteurs d'OG que nous détaillons ici pour les sources gravitationnelles transitoires présentées en Sec. 1.3. Du point de vue de l'analyse des données, il est habituel de diviser ces sources en deux sous-familles dont nous verrons au Chapitre 3 qu'elles correspondent à deux approches de recherche distinctes. La première comprend les binaires compactes coalescentes introduites en Sec. 1.3.1. Au lieu d'un scénario astrophysique précis, la seconde s'appuie sur une caractérisation générique du signal (en statistique, on dirait "non-paramétrique"). On considère les *transitoires gravitationnels* associés à une émission d'énergie gravitationnelle de courte de durée (inférieure à quelques secondes) sans modèle précis pour la forme d'onde. Les effondrements de cœur stellaire présentés en Sec. 1.3.2 en font partie.

2.3.1 Binaires compactes coalescentes

En combinant les prédictions astrophysiques issus des développements post-newtoniens de la dynamique des binaires coalescentes [38, 43] à la sensibilité du détecteur, on peut en déterminer l'horizon via l'Éq. (2.1).

Grâce à la sensibilité théorique en Fig. 2.3, le réseau LIGO-Virgo peut observer les binaires d'étoiles à neutrons (possédant chacune une masse de 1.4 $M_\odot$) jusqu'à une distance de $\sim$ 33 Mpc, les binaires de trous noirs (10 $M_\odot$ chacun) jusqu'à 160 Mpc [6].

Bien que les systèmes binaires d'étoiles soient répandus, seule une petite fraction conduit à la formation d'une binaire d'objets compacts suffisamment liés pour que leur coalescence puisse être observée aujourd'hui. Une revue des prédictions des modèles de population [6] donne un taux "réaliste" d'occurrence d'une coalescence de deux étoiles à

neutrons tous les 10 000 ans par galaxie de taille équivalente à la Voie Lactée. Dans le volume d'Univers délimité par les horizons donnés plus haut, ceci se traduit par un nombre de coalescences détectables égal à ~ 0.02 événements par an, rendant leur observation improbable par les détecteurs initiaux. Nous verrons que ce nombre est bien supérieur pour les détecteurs avancés. De larges barres d'erreurs sont cependant associées à ces estimations qui reflètent la faiblesse des contraintes d'observation à disposition sur ces systèmes astrophysiques. Les taux peuvent être 10 fois plus petits ou plus grands selon que l'on se place dans un scénario pessimiste ou optimiste.

2.3.2 Transitoires gravitationnels

On peut caractériser l'amplitude d'un transitoire gravitationnel indépendamment de tout *a priori* astrophysique par le biais de la déformation quadratique moyenne exercée sur l'espace-temps au détecteur, soit

$$h_{\rm rss}^2 = \int h_+^2(t) + h_\times^2(t) dt. \tag{2.2}$$

Pour les sources monochromatiques à la fréquence f_0 et sous hypothèse d'émission isotrope, il est possible de relier cette quantité au rapport signal-sur-bruit défini en Éq. (2.1)

$$\rho^2 \approx \mathcal{F}^2 \frac{h_{\rm rss}^2}{S(f_0)}, \tag{2.3}$$

avec $\mathcal{F}^2 = F_+^2 + F_\times^2$ et à la quantité d'énergie émise par la source en combinant avec les Éqs. (1.9) et (1.11)

$$E_{GW} = \frac{\pi^2 c^3}{G} D_L^2 f_0^2 h_{\rm rss}^2. \tag{2.4}$$

On peut également déduire une expression similaire en fonction du rapport signal-sur-bruit

$$E_{GW} = 2\frac{\pi^2 c^3}{G} D_L^2 f_0^2 S(f_0) \rho^2. \tag{2.5}$$

On peut vérifier [125] que la validité de celle-ci ne se restreint pas au seul cas d'émission isotrope mais s'étend à tous les cas physiques réalistes (polarisations linéaire ou elliptique).

Si l'on considère les modèles de supernova gravitationnelle décrit en Sec. 1.3.2, on obtient les distances de détectabilité suivantes. L'horizon (à $\rho = 8$) d'une source émettant $E_{GW} = 10^{-7} M_\odot$ à une fréquence $f_0 = 1$ kHz où la sensibilité de Virgo est $S^{1/2}(f_0) \approx 10^{-22}/\mathrm{Hz}^{1/2}$ est $D_L \sim 2.3$ kpc (c'est-à-dire dans la Galaxie). Tandis qu'une source émettant $E_{GW} = 10^{-2} M_\odot$ à $f_0 = 50$ Hz où $S^{1/2}(f_0) \approx 8 \times 10^{-23}/\mathrm{Hz}^{1/2}$, on obtient $D_L \sim 11.3$ Mpc.

2.4 Réseau mondial des détecteurs interférométriques

En 2007, les détecteurs LIGO et Virgo ont conclut un accord de collaboration, d'échange et d'analyse conjointe des données. Ils ont conduit ensemble une série de prises de données totalisant un temps d'observation cumulé d'environ un an (voir Fig. 2.10). Ces prises de données sont coordonnées de façon à maximiser le temps d'observation commun à Virgo et LIGO tout en maintenant au moins un détecteur en opération (mode "astro-watch") en cas d'un événement galactique remarquable. La meilleure sensibilité obtenue par ces détecteurs présentée en Fig. 2.10 est très proche de la sensibilité théorique. Pour les binaires d'étoiles à neutrons (de masses identiques et égales à 1.4 $M_\odot$), l'horizon moyen [12] atteint durant la dernière prise de données (S6–VSR2/3) est 44.1 ± 4.7 Mpc, 36.6 ± 6.9 Mpc et 18.8 ± 3.9 Mpc pour LIGO H, LIGO L et Virgo respectivement. Pour les binaires de trous noirs (de masses identiques et égales à 10 $M_\odot$), celui-ci devient 175 ± 62 Mpc, 155 ± 60 Mpc et 72 ± 19 Mpc pour les mêmes détecteurs pris dans le même ordre.

Des recherches sur un ensemble de sources ont été effectuées sur ces données collectées donnant lieu à près de 35 publications. Aucune OG n'a été détectée. Ce résultat de non-détection a permis d'établir des limites astrophysiques sur les populations de sources, modèles d'émission, etc. Nous aborderons certains de ces résultats dans la suite de ce document. Pour une revue complète, voir par exemple [37, 119], et pour les sources transitoires [49] et Sec. C.1.

2.5 Perspectives et détecteurs avancés

La première génération de détecteurs "initiaux" a été décommissionnée. Elle est en cours de remplacement par une seconde génération de détecteurs "avancés" utilisant une nouvelle instrumentation installée dans la même infrastructure (enceinte à vide, bâtiments). Cette nouvelle instrumentation doit permettre une amélioration de la sensibilité d'un facteur ~ 10 comme indiqué en Fig. 2.11. Plus précisément, à la sensibilité théorique, l'horizon de détection est ~ 440 Mpc pour les binaires d'étoiles à neutrons ($2 \times 1.4 M_\odot$) et ~ 2.2 Gpc pour les binaires de trous noirs ($2 \times 10 M_\odot$) [4, 6].

L'amplitude des OG allant comme l'inverse de la distance, ceci correspond à un facteur 1000 en terme de volume observable et donc de sources détectables. Les détecteurs avancés peuvent potentiellement observer des dizaines voire centaines de sources. En utilisant les modèles de population décrits en Sec. 2.3.1, on prédit 40 événements par an (prédiction connue à facteur $\sim$ 10 près selon que l'on se place dans un scénario "pessimiste" ou "optimiste"). Ces détecteurs devraient donc réaliser la première détection directe des OGs.

L'installation des détecteurs LIGO [79] a été accomplie début 2014 et la première prise de données scientifiques devrait avoir lieu courant 2015. Le projet initial d'installer deux détecteurs jumeaux à Handford a été revu récemment suite à la proposition de déplacer l'un des deux détecteurs en Inde. Si cette proposition se concrétise, ce troisième détecteur LIGO India serait alors opérationnel à partir de 2020. Le calendrier d'Advan-

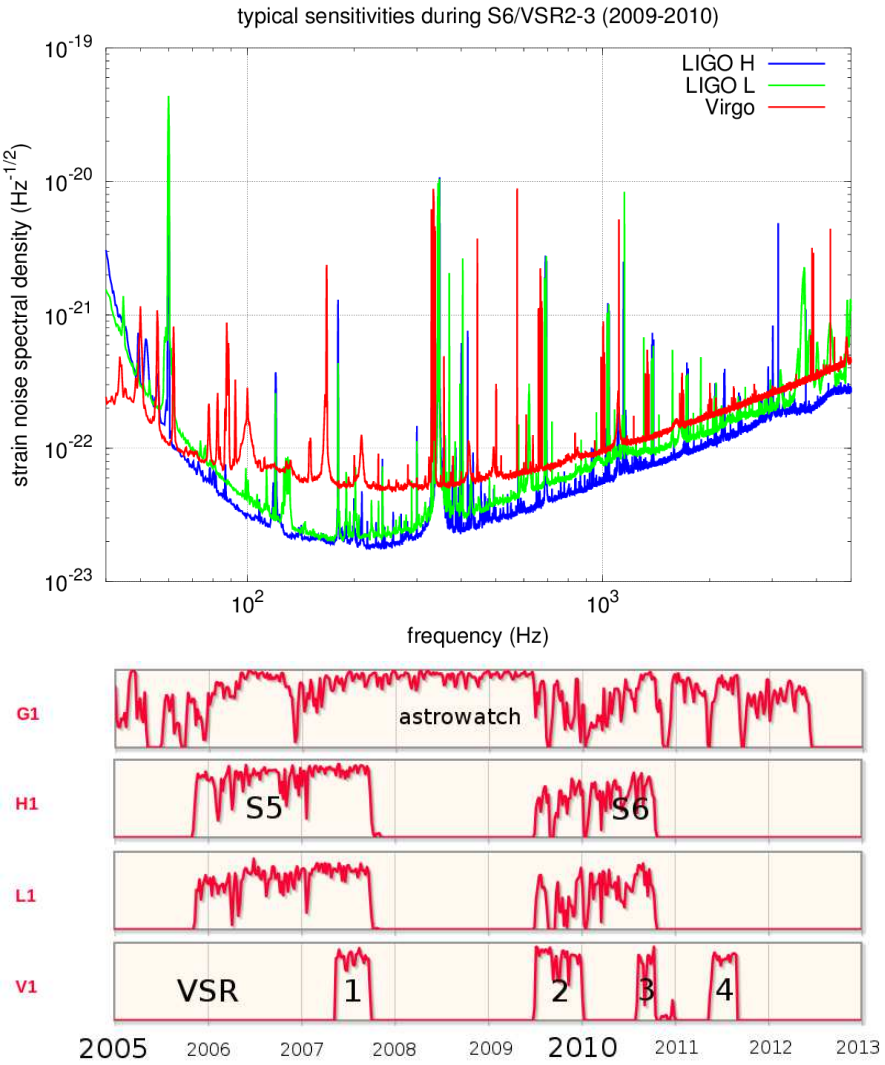

FIGURE 2.10 – **(haut) Sensibilité atteinte par LIGO et Virgo durant leur dernière collecte de données scientifiques S6/VSR2–3. (bas) Progression des prises de données collectées par LIGO (H1 et L1), Virgo (V1) et GEO (G1) jusqu'ici.** Source : [1, 12].

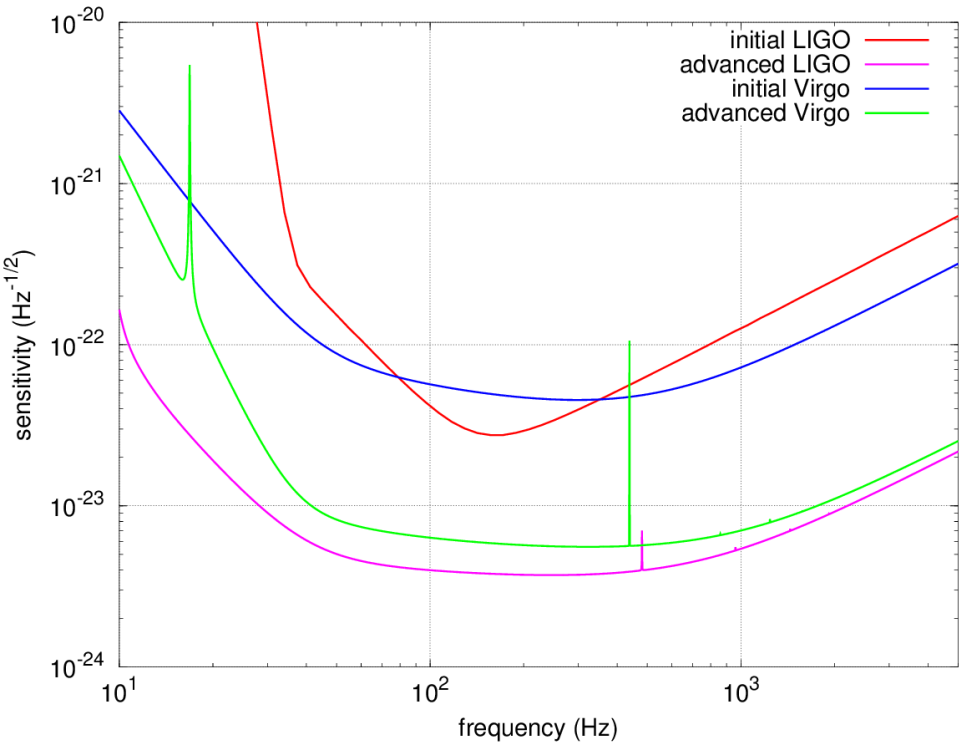

FIGURE 2.11 – **Sensibilités théoriques des détecteurs de seconde génération advanced LIGO et advanced Virgo detectors comparées à celles des détecteurs initiaux**.

ced Virgo est d'avoir un détecteur opérationnel en 2015 et de commencer la collecte des données aussi vite que possible [15]. GEO prévoit un programme d'amélioration "GEO-HF" [98] qui vise à accroître la sensibilité à haute fréquence grâce à un laser de plus grande puissance et à l'utilisation de "lumière comprimée". Cet ensemble sera complété par le détecteur japonais KAGRA [123] installé sous terre dans la mine de Kamioka (où les perturbations sismiques sont bien plus faibles qu'à la surface) et fonctionnant à température cryogénique pour réduire le bruit thermique. Un détecteur initial fonctionnant à température ambiante devrait cependant entrer en fonction en 2015, alors que le détecteur complet devrait prendre ses premières données en 2018.

À plus long terme, une troisième génération de détecteurs est actuellement à l'étude. Elle vise un nouveau facteur 10 d'amélioration de la sensibilité (un facteur 100 par rapport aux détecteurs initiaux). L'étude de l'Einstein Telescope financée par le programme européen FP7 ont aboutit à un premier concept consistant en un interféromètre cryogénique souterrain aux bras de 10 km [14]. Un tel instrument qui pourrait entrer en fonction à l'horizon 2030, permettrait d'explorer les populations de sources jusqu'à des distances cosmologiques. L'horizon des binaires d'étoiles à neutrons s'étend jusqu'à $z \sim 2$, tandis que celui des binaires de trous noirs de masses intermédiaires $M \sim 10^2 - 10^4 M_\odot$ atteint $z \sim 15$ [14]. Ce détecteur offre également des perspectives intéressantes en terme d'astrophysique multimessager [52].

L'ESA a annoncé récemment avoir sélectionner les OG comme la thématique phare de sa troisième grande mission du programme *Cosmic Vision*. L'observatoire spatial eLISA est actuellement le concept le plus abouti [22] et le candidat principal pour cette mission. L'envoi d'un détecteur dans l'espace permet de s'affranchir du bruit d'origine sismique qui limite la sensibilité sur Terre. eLISA donne accès aux fréquences autour du milliHertz où l'on peut observer les binaires compactes les plus massives de l'Univers, composées trous noirs supermassifs $M \sim 10^4 - 10^8 M_\odot$ et formées lors de fusion des galaxies.

Chapitre 3

Contributions à la recherche des transitoires gravitationnels

Dans les problèmes de détection, la quantité d'information disponible *a priori* joue une rôle majeur. Nous avons vu en Sec. 1.3 que l'on peut prédire la signature en OG de la coalescence d'une binaire d'étoiles à neutrons et/ou trous noirs avec une bonne précision. Cette information peut être utilisée afin de distinguer le vrai signal gravitationnel du bruit instrumental ou environnemental. Ainsi que l'a montré la théorie statistique de la décision développée dans les années 40 avec les premiers radars [129,130], la technique de *filtrage adapté* permet la recherche optimale d'un signal connu dans un bruit gaussien. Le filtrage adapté, qui consiste à corréler les données avec la forme d'onde espérée est la méthode suivie pour la détection des binaires compactes coalescentes.

La production d'OG est associée à des régimes dynamiques relativistes. Dans le régime en champ fort où la non-linéarité de la théorie ne peut plus être négligée, il n'est pas toujours possible d'obtenir une prédiction précise pour l'OG émise. Ceci rend nécessaire des "méthodes agnostiques" de détection, robustes aux incertitudes de modélisation. Les méthodes de *détection d'excès d'énergie* consistent à identifier des excursions dans une carte temps-fréquence des observations. Cette carte est obtenue en projetant les données sur un dictionnaire de formes d'onde élémentaires qui effectuent un pavage du plan temps-fréquence. Plusieurs types de dictionnaires ont été testés comme les cosinus locaux [25], les ondelettes de Morlet [56], les ondelettes de Meyer [92]. Ces dictionnaires temps-fréquence sont composés de formes d'onde "génériques" principalement motivées par des arguments mathématiques ou algorithmiques. Des dictionnaires pilotés par des modèles ou des simulations astrophysiques ont été également proposés [42, 46, 80, 120]. La multiplicité des options conduit à la multiplicité des chaînes d'analyse disponibles et utilisées pour la recherche de transitoires gravitationnels.

Les deux méthodes mentionnées ci-dessus sont appliquées séparément par deux groupes de travail ("CBC" et "burst") dans la collaboration LIGO Virgo. Nous proposons ici une stratégie hybride établissant un pont entre les deux approches afin de réaliser la détection robuste non-paramétrique de signaux quasi-périodiques ou "chirps" gravitationnels.

Quasi-périodicité des transitoires gravitationnels Les systèmes astrophysiques détectables par Virgo ou LIGO font intervenir des objets compacts en rotation. Indépendamment des détails du modèle qui décrit ces systèmes (si un tel modèle est disponible !), nous arguons ici que les OG qu'ils émettent sont quasi-périodiques.

L'émission gravitationnelle est activée par la dynamique de la distribution de masse de la source qui en détermine la forme. Nous avons vu que la formule du quadrupôle permet de relier l'émission gravitationnelle à la dérivée seconde du moment quadrupolaire. Lorsque le mouvement du système est orbital ou rotationnel, le moment quadrupolaire est quasi-périodique, et par conséquent l'OG émise aussi.

Si l'on considère que l'émission gravitationnelle est dominée par le quadrupôle [1], on peut montrer que la polarisation de l'onde est préférentiellement elliptique [110] et on peut alors décrire l'onde gravitationnelle émise par

$$h_+(t) = A\frac{1+\cos^2\epsilon}{2}\,\cos(\varphi(t-t_0)+\theta)\,, \tag{3.1}$$

$$h_\times(t) = A\cos\epsilon\,\sin(\varphi(t-t_0)+\theta), \tag{3.2}$$

où θ est la phase du signal à une date fiducielle t_0 et ϵ représente l'inclinaison de la source (angle entre le moment orbital ou l'axe de rotation du système et la ligne de visée).

Nous considérons d'abord le cas simplifié où l'amplitude A est constante. Il s'agit clairement d'une simplification excessive, une modulation en amplitude étant probable. Nous aborderons le cas d'une amplitude variable en fin de ce chapitre.

Nous supposerons que l'évolution de la phase du signal $\varphi(\cdot)$ est une fonction inconnue ce qui nous permet de décrire notre méconnaissance de la nature physique de la source ou d'éventuels écarts aux modèles (post-newtoniens dans le cas des binaires coalescentes, par exemple). Afin qu'elle soit possible physiquement, nous imposons que la phase $\varphi(\cdot)$ et ses trois premières dérivées soient continues et telles que

$$\left|\frac{df}{dt}\right| \leq \dot{F} \qquad\qquad \left|\frac{d^2f}{dt^2}\right| \leq \ddot{F}, \tag{3.3}$$

où on note la fréquence instantanée $f(t) \equiv (2\pi)^{-1}d\phi/dt$ et $\dot{F}$ et $\ddot{F}$ désignent des limites supérieures fixées *a priori*.

Nous considérons ici le problème de la détection d'un "chirp" gravitationnel tel que le décrivent les Éqs. (3.1), (3.2) et (3.3). On peut qualifier ce problème d'intermédiaire aux deux approches habituellement considérées (filtre adapté pour les binaires compactes coalescentes et détection d'excès d'énergie pour les transitoires gravitationnels).

Ce problème demande l'utilisation de nouveaux outils. En effet, les techniques de filtrage adapté utilisées pour les binaires sont inapplicables car elles requièrent une connaissance précise de la phase $\varphi(\cdot)$. Les techniques de détection d'excès d'énergie n'exploitent pas l'information de structure du signal "chirp".

1. La validité de cette hypothèse est plus vaste que le seul domaine de validité de la formule du quadrupôle. Cela a, par exemple, été vérifié grâce à des simulations pour les binaires coalescentes de trous noirs [34].

On se propose ici de modifier ces dernières afin qu'elles prennent cette information en compte. Nous avons considéré deux approches complémentaires, l'une portant sur l'adéquation du dictionnaire temps-fréquence aux signaux de type "chirp" (voir en Sec. 3.1) et l'autre portant sur l'extraction d'un agrégat significatif dans la décomposition faite à partir du dictionnaire, voir en Sec. 3.2, 3.3 et 3.4.

En Sec. 3.1, nous introduisons un dictionnaire composé d'ondelettes modulées en fréquence ou *chirplets* [53, 102] pouvant suivre les variations locales de fréquence du signal. Ce dictionnaire s'affranchit donc de l'hypothèse de stationnarité locale habituellement invoquée et qui conduit au choix d'ondelettes localement stationnaires (à fréquence instantanée constante, telle que l'ondelette de Morlet) ce qui induit des pertes de performance dues à la désadaptation entre les ondelettes sélectionnées et le signal.

En Sec. 3.2 et 3.4, nous présentons une méthode d'extraction des composantes du "chirp". Ces signaux sont décrits comme une succession de paquets d'onde inter-connectés entre eux, analogue à une chaîne markovienne d'états. On peut rassembler l'ensemble de ces chaînes dans un graphe. L'extraction du chirp se ramène alors au problème d'optimisation combinatoire de recherche de chemin optimal dans le graphe [48, 55, 110] (voir en annexe C.2 et C.3).

Les travaux présentés ici prolongent les développements entrepris pendant ma thèse [50, 51] et ceux de multiples autres contributeurs [24, 44, 83, 104] à ce problème de la détection temps-fréquence de chirps.

3.1 Des ondelettes aux chirplets

Les chirplets sont définies par

$$\psi(\tau) \equiv w(\tau - t) \exp 2\pi i \phi(\tau - t), \tag{3.4}$$

où t définit le centre temporel de la chirplet. L'enveloppe $w(\cdot) \in C^\infty(\mathbb{R})$ est une fonction positive, symétrique, unimodale et de norme unité, $\int w^2 = 1$. Nous nous intéresserons dans un premier temps spécifiquement au cas où $w(\cdot)$ est une enveloppe gaussienne

$$w(\tau) = A \exp\left(-\frac{(2\pi f)^2}{Q^2}\tau^2\right), \tag{3.5}$$

avec $A = (8\pi f^2/Q^2)^{1/4}$ afin d'assurer la normalisation. Q est analogue à un facteur de qualité sans dimension.

La phase $\phi(\cdot)$ est quadratique

$$\phi(\tau) \equiv \theta + b\tau + a\tau^2, \tag{3.6}$$

si bien que sa fréquence instantanée varie linéairement en fonction du temps

$$f(\tau) = f + d\tau \tag{3.7}$$

où $f = b/(2\pi)$ désigne la fréquence centrale de la chirplet.

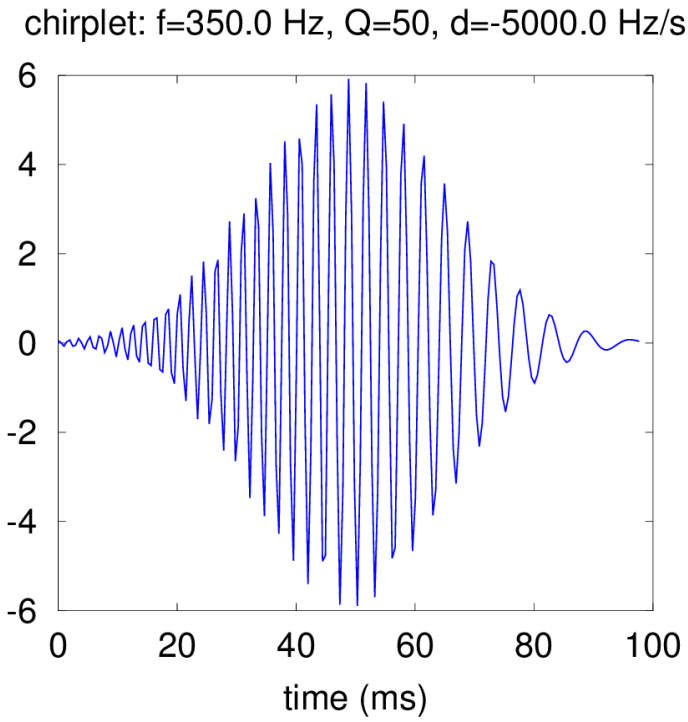

FIGURE 3.1 – **Exemple d'une chirplet à enveloppe gaussienne**

Un paramètre important de la chirplet est son taux de modulation (ou chirp rate) $d = a/\pi$ qui caractérise la pente de l'évolution de la fréquence. Pour une enveloppe gaussienne et $d = 0$, on retrouve l'ondelette de Morlet ou de Gabor. Une chirplet à enveloppe gaussienne est donc caractérisée par quatre paramètres que nous regrouperons dans un seul descripteur $\boldsymbol{p} \equiv \{t, f, Q, d\}$. En Fig. 3.1, on voit un exemple de chirplet à enveloppe gaussienne.

3.1.1 Transformée en chirplets

La *transformée en chirplets* T s'obtient en corrélant les données avec les chirplets définies dans la précédente section. Dans le domaine fréquentiel, cela donne

$$T[x;\boldsymbol{p}] = \left| \int X(\xi)\Psi^*(\xi;\boldsymbol{p})d\xi \right|^2, \tag{3.8}$$

où $X(\cdot)$ et $\Psi(\cdot;\boldsymbol{p})$ désignent la transformée de Fourier des données $x(\cdot)$ et la chirplet $\psi(\cdot)$ de descripteur $\boldsymbol{p}$ resp.

La transformée de Fourier de la chirplet à enveloppe gaussienne s'écrit

$$\Psi(\xi;\boldsymbol{p}) = \mathcal{A}\exp\left(-\frac{\tilde{Q}^2}{4}\frac{(\xi-f)^2}{f^2}\right), \tag{3.9}$$

où $\mathcal{A} = [(\tilde{Q}^4/Q^2)/(2\pi f^2)]^{1/4}$ est écrit en fonction du facteur de qualité généralisé $\tilde{Q} = Q\sqrt{z}/|z|$ où on note $z = 1 + id\Delta_t^2$ et [2] $\Delta_t = Q/\left(2\sqrt{\pi}f\right)$ est la durée de la chirplet.

3.1.2 Métrique et dictionnaire de chirplets

Par la variation des paramètres de la chirplet, on décrit un espace continu. Dans cet espace, nous devons choisir un ensemble fini de chirplets qui seront utilisées pour analyser les données. Nous adoptons ici la méthode proposée dans [57, 109] qui consiste à échantillonner l'espace considéré par une grille régulière pour la *métrique* déduite de la *désadaptation* $T\left[\psi(\boldsymbol{p}'); \boldsymbol{p}\right]$ entre deux nœuds $\boldsymbol{p}$ et $\boldsymbol{p}' = \boldsymbol{p} + \delta\boldsymbol{p}$ voisins de la grille. La métrique résulte du développement au second ordre de la désadaptation $\mu_{\boldsymbol{p}}(\delta\boldsymbol{p}) \equiv 1 - T\left[\psi(\boldsymbol{p} + \delta\boldsymbol{p}); \boldsymbol{p}\right] \approx \delta s^2$ lorsque $\delta\boldsymbol{p} \to \boldsymbol{0}$ et conduit à [3] :

$$\delta s^2 = \frac{Q^4 d^2 + 16\pi^2 f^4}{4Q^2 f^2}\delta t^2 + \frac{2 + Q^2}{4f^2}\delta f^2 + \frac{\delta Q^2}{2Q^2} + \frac{Q^4}{128\pi^2 f^4}\delta d^2 - \frac{Q^2 d}{2f^2}\delta t\delta f - \frac{\delta f \delta Q}{Qf}. \quad (3.10)$$

On note plusieurs différences comparé au cas des ondelettes de Morlet ($d = 0$). Le long de l'axe temporel et aux basses fréquences $f \lesssim Q\sqrt{d}$, le pas d'échantillonnage $\delta t \propto f/(Qd)$ est inférieur à celui des ondelettes de Morlet, $\delta t \propto Q/f$. On note aussi le pas d'échantillonnage $\delta d \propto (f/Q)^2$. Il y a donc beaucoup de chirplets aux basses fréquences et aux grandes valeurs de Q.

En négligeant les termes diagonaux, l'espace des chirplets équipé de la métrique ci-dessus peut alors être discrétisé par une grille régulière. On note $\delta s = \mu^{1/2}$ la distance maximale entre une chirplet arbitraire et le nœud de la grille le plus proche et $\mu_{\max}^{1/2}$ la valeur maximale que peut prendre cette quantité. La longueur des arêtes d'un cube étant égale à la moitié de sa diagonale dans un espace à quatre dimensions, on doit donc avoir $\ell \leq \sqrt{\mu_{\max}}$ où ℓ est le pas de la grille. Il en résulte une procédure de discrétisation qui procède de proche en proche où les voisins d'un nœud $\boldsymbol{p}_n$ se déduisent par $\mu_{\boldsymbol{p}_n}(\boldsymbol{p}_n - \boldsymbol{p}_{n+1}) \leq \mu_{\max}$. Dans ce qui suit, on fixe la désadaptation maximale à $\mu_{\max} = 20\%$. La Figure 3.2 montre un exemple de famille de chirplets obtenue à partir de cette procédure.

On peut estimer le nombre de chirplets nécessaire pour couvrir l'ensemble de l'espace à partir de son volume. Si l'on fait ce calcul à temps t fixé, celui-ci s'écrit $V = \int |\boldsymbol{\mu}^\star|^{1/2} d^3\boldsymbol{p}^\star$ où $\delta s^2 = |\boldsymbol{\mu}^\star|$ désigne la métrique en Éq. (3.10) réduite aux trois coordonnées restantes $\boldsymbol{p}^\star = \{f, Q, d\}$. On obtient

$$\mathcal{N} \equiv V/\ell^3 \propto f_{\min}^{-2} Q_{\max}^3 d_{\max}, \quad (3.11)$$

où l'on considère que, pour chaque paramètre, la limite inférieure (*min*) est beaucoup plus petite que la limite supérieure (*max*). La Figure 3.3 compare le résultat de cette estimation au nombre de chirplets obtenues par l'application de la procédure de discrétisation.

2. Par définition, $\Delta_t^2 \equiv 4\pi \int (\tau - t)^2 \psi^2(\tau) d\tau$.

3. Ce calcul suppose que le bruit instrumental est à spectre presque plat dans la bande fréquentielle couverte par la chirplet. Pour les chirplets couvrant une grande gamme fréquentielle, cette approximation peut conduire à un écart significatif.

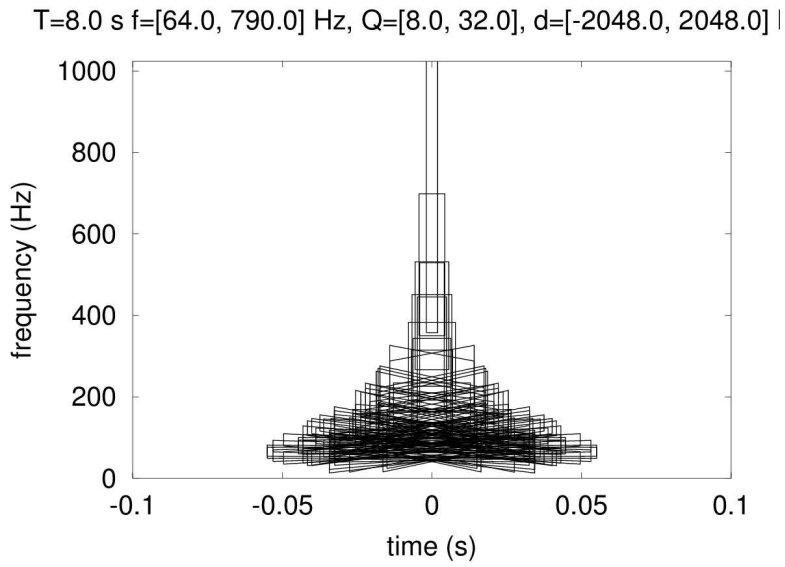

FIGURE 3.2 – **Exemple d'un dictionnaire de chirplets obtenu à partir de la procédure présentée en Sec. 3.1.2.** Dans ce graphe, chaque boîte temps-fréquence est associée à une chirplet. La pente des bords inférieur et supérieur des boîtes obliques est égale à d.

Il est important de noter que ces calculs et simulations sont effectués en considérant que l'on dispose d'une bande fréquentielle infinie. En réalité, les données sont échantillonnées et on est limité à la bande de Nyquist. Les chirplets dont le contenu fréquentiel dépasse cette limite doivent être éliminées afin d'éviter tout repliement spectral. La Fig. 3.3 inclut également le nombre de chirplets compatibles avec les limites fixées par l'échantillonnage. Ce nombre est près d'un facteur 10 plus grand que celui des ondelettes de Morlet pour les mêmes limites de l'espace de paramètres ce qui donne une indication du coût de calcul de la transformée en chirplets, celui-ci étant approximativement proportionnel au cardinal du dictionnaire. Ce nombre accru de chirplets comparé aux ondelettes indique qu'on explore avec les chirplets un espace signal significativement plus grand.

La transformée en chirplets a été implémentée (on consultera les détails de l'implémentation [53]) et intégrée à la chaîne d'analyse "Omega" [56] qui est l'une des chaînes d'analyse utilisées par la collaboration LIGO/Virgo.

3.1.3 Performances

Dans cette section, nous présentons une comparaison des performances des chaînes d'analyse basées sur les chirplets et sur les ondelettes de Morlet.

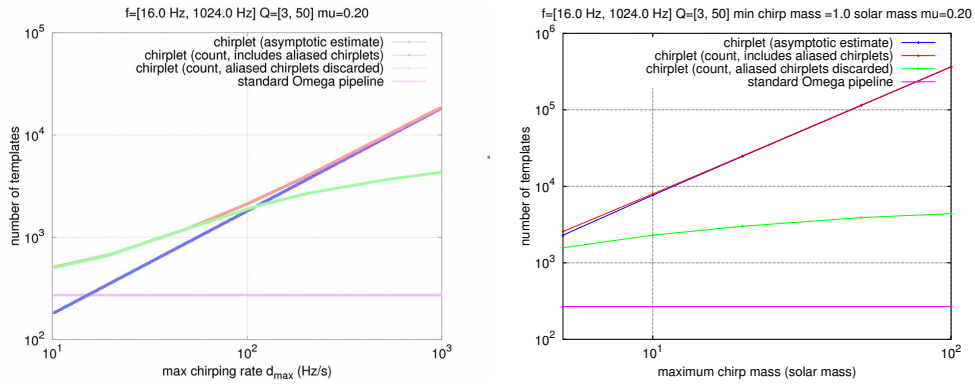

FIGURE 3.3 – **Taille du dictionnaire de chirplets** dans les deux cas suivants : (*gauche*) limites uniformes $\pm d_{\max}$ sur le taux de modulation ; (*droit*) limites dépendant de la fréquence $CM_{\min}^{5/3} f^{11/3} \lesssim d \lesssim CM_{\max}^{5/3} f^{11/3}$ correspondant à un modèle newtonien du signal de coalescence de binaire compacte. La taille du dictionnaire d'ondelettes est indiqué pour comparaison.

Jeu de données test On utilise deux mois de bruit gaussien coloré selon le spectre des trois détecteurs LIGO, soit deux interféromètres H1 et H2 à Handford, WA et un seul L1 à Livingstone, LA.

Statistique de décision On utilise ici une statistique de décision simplifiée basée sur la chirplet du dictionnaire dont la corrélation avec les données est la plus significative et dépasse un certain seuil. Cette opération est réalisée séparément pour chacun des trois flux de données. On définit un événement lorsqu'on fait une détection en coïncidence (avec une incertitude de ± 10 ms) dans les trois flux de données analysés. La moyenne géométrique des rapports signal-sur-bruit (cf. la définition en Éq. (2.1)) observés dans les trois détecteurs fournit une caractérisation globale de l'événement.

Estimation du fond La détection est établie à partir de la signification statistique de l'événement qui s'obtient en évaluant la p-valeur d'un événement similaire du fond, de même statistique. On estime le fond par le biais d'une analyse à décalage temporel. Ceci consiste à répéter un grand nombre de fois l'analyse en décalant les instants sélectionnés dans les données du détecteur L1 par un délai non-physique très supérieur à celui attendu pour les ondes gravitationnelles (soit $\sim$10 ms au maximum entre H et L). L'histogramme obtenu à partir du grand nombre d'événements ainsi produits caractérise le bruit de fond de l'analyse d'où l'on tire la p-valeur. Pour les deux chaînes d'analyse testées (ondelettes et chirplets), on choisit le même seuil de détection, soit une p-valeur inférieure à 5×10^{-2}, équivalent à un taux de fausse alarme égal à 10^{-8} Hz.

Signaux astrophysiques Afin d'en déterminer les performances, on applique les chaînes d'analyse à un jeu de données auquel on ajoute des modèles de signaux astrophysiques.

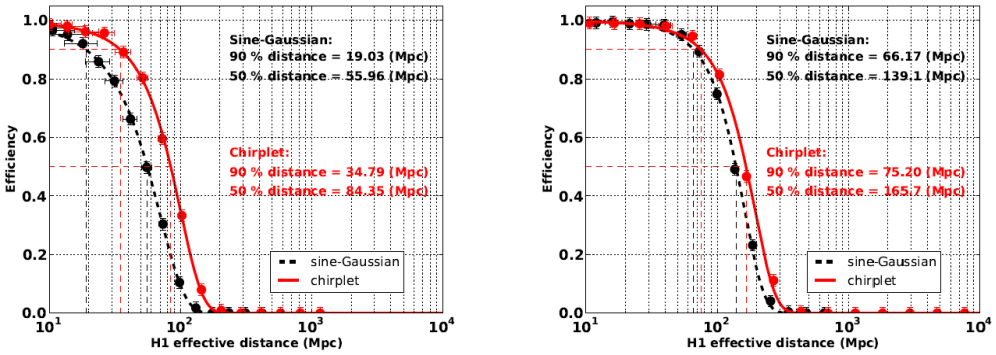

(a) Efficiency curves for set 4-35 $M_\odot$.

(b) Efficiency curves for set 35-80 $M_\odot$.

FIGURE 3.4 – **Comparaison des efficacités de détection d'un signal chirp provenant d'une binaire de trous noirs** par l'utilisation d'ondelette (courbe noire) et chirplet (courbe rouge) et pour les binaires de masse totale dans la gamme 4–35 $M_\odot$ (gauche) et 35–80 $M_\odot$ (droite).

Nous utilisons ici les signaux chirp de coalescences de binaire de trous noirs. Les masses des trous noirs sont choisies uniformément entre 2 et 40 $M_\odot$. On divise les binaires en deux familles sur la base de masse totale, de 4-35 $M_\odot$ et de 35-80 $M_\odot$.

Efficacité et portée On estime alors la probabilité de détection (ou efficacité) en fonction de la distance à laquelle a été placée la binaire. On évalue à l'aide d'un ajustement les distances correspondant à des efficacités de 50 % et 90 %. Les résultats sont présentés en Fig. 3.4 pour une évaluation globale sur chaque gamme de masse et en Fig. 3.5 pour une évaluation plus détaillée montrant la distance de détectabilité par bin de masse. L'utilisation des chirplets permet une amélioration de plus de 50 % de la portée comparé aux ondelettes (nommées "sine-Gaussian" dans ces figures). Comme on pouvait s'y attendre, l'amélioration est plus marquée pour la gamme basse de masse (4-35 $M_\odot$) puisqu'elle est associée aux signaux chirp présentant une variation de fréquence plus marquée.

3.2 Chaînes de chirplets

Les bons résultats présentés dans la précédente section démontre le potentiel des chirplets. Il s'appuie cependant sur la corrélation avec une seule chirplet du dictionnaire. Il est improbable qu'un signal gravitationnel authentique corrèle avec un unique élément du dictionnaire. Des algorithmes d'agrégation sont nécessaires afin de récolter au mieux l'énergie du signal dispersée sur plusieurs éléments [55, 91, 127].

La méthode d'agrégation à adopter est évidemment intimement liée au signal que l'on cherche à détecter. Jusqu'ici, les méthodes utilisées pour la détection des transitoires gravitationnels recherchent des agrégats connexes sans imposer de morphologie particulière.

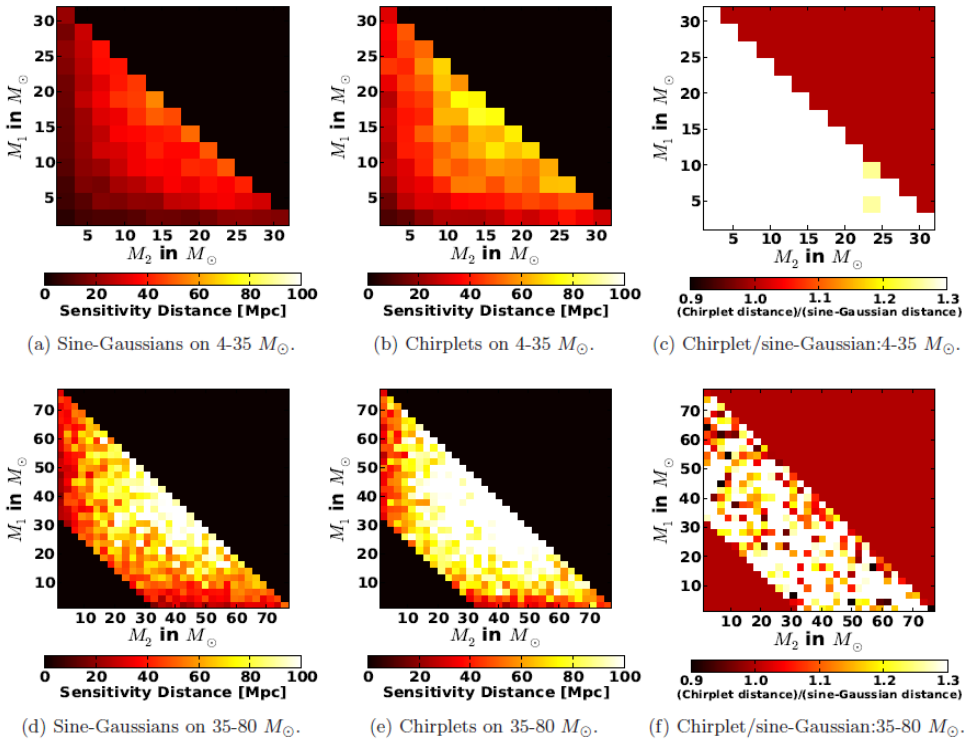

(a) Sine-Gaussians on 4-35 $M_\odot$. (b) Chirplets on 4-35 $M_\odot$. (c) Chirplet/sine-Gaussian:4-35 $M_\odot$.

(d) Sine-Gaussians on 35-80 $M_\odot$. (e) Chirplets on 35-80 $M_\odot$. (f) Chirplet/sine-Gaussian:35-80 $M_\odot$.

FIGURE 3.5 – **Distance de détectabilité d'une binaire de trous noirs** de masse totale dans la gamme 4–35 $M_\odot$ (haut) et 35–80 $M_\odot$ (bas) via l'utilisation d'ondelettes (ou sine-Gaussian) en (a) et (d) ou de chirplets en (b) et (e). La comparaison des deux approches est montrée en (c) et (f).

Intuitivement, il est naturel de penser un signal chirp comme une suite de chirplets. À cause de la continuité de phase et de fréquence du signal chirp, les chirplets dans la suite sont nécessairement liées les unes aux autres. C'est cette idée qui nous amène à proposer la méthode d'agrégation proposée ici qui effectue la recherche de *chaînes de chirplets*.

Avant d'aborder cette question, il nous faut d'abord caractériser la géométrie de l'espace signal qui nous intéresse, c'est-à-dire la variété décrite par l'ensemble des signaux chirps.

3.2.1 Statistique de détection des signaux chirps en bruit gaussien

Si on considère un *chirp* $s(t) = A(t)\cos\varphi(t)$ de durée T, d'amplitude $A(t) \equiv A\,a(t) > 0$ et de phase $\varphi(t) \equiv \phi(t) + \theta$ qui sont connues à un facteur d'échelle $A > 0$ et une phase $\theta \in (-\pi/2, \pi/2]$ près. On suppose que les signaux sont discrétisés et on a donc $s_k = s(t_s k) = A\,a_k \cos(\phi_k + \theta)$ avec $k = 0, \ldots, N-1$ et $N = T f_s$.

On désire effectuer la détection de ce signal dans un bruit gaussien de variance unité. On note le rapport signal-à-bruit $\rho^2 = \sum_k s_k^2 \approx A^2 \sum_k a_k^2$, expression qui est cohérente avec la définition en Éq. (2.1).

La statistique optimale est le *filtre adapté à détection d'enveloppe* qui s'exprime par [55]

$$\ell(x; a, \phi) = \frac{n_s x_c^2 - 2 n_x x_c x_s + n_c x_s^2}{n_c n_s - n_x^2}, \tag{3.12}$$

où $x_c \equiv \sum_k x_k\, a_k \cos\phi_k$ et $x_s \equiv \sum_k x_k\, a_k \sin\phi_k$ désignent la corrélation des données avec les formes d'ondes en quadrature du patron d'onde, et $n_c \equiv \sum_k a_k^2 \cos^2\phi_k$, $n_x \equiv \sum_k a_k^2 \cos\phi_k \sin\phi_k$ et $n_s \equiv \sum_k a_k^2 \sin^2\phi_k$ servent à la normalisation de la statistique.

Pour des variations suffisantes de la phase $\varphi(t)$, on a [55]

$$\ell(x; a, \phi) \approx \left| \sum_k x_k a_k \exp i\phi_k \right|^2 \tag{3.13}$$

où l'amplitude est de norme unité, $\sum_k a_k^2 = 1$. Pour les signaux d'enveloppe constante, on a donc $a_k = 1/\sqrt{N}$.

3.2.2 Géométrie de la variété des chirps

En s'inspirant de l'approche proposée dans [108] pour les binaires coalescences, on peut écrire la métrique naturelle pour les signaux chirp à partir de la statistique optimale obtenue dans la section précédente [47]. Pour simplifier les notations, on concatène l'amplitude et la phase du chirp dans un unique vecteur c de taille $2N$ tel que $c_k = a_k$ et $c_{N+k} = \phi_k$ pour $k = 0, \ldots, N-1$.

Considérons deux signaux chirp de paramètres c^* et c. On mesure la similarité entre ces deux signaux par

$$\mathcal{L}(c; c^*) \equiv \frac{\ell(s; c) - \ell(s; c^*)}{\ell(s; c)}. \tag{3.14}$$

On vérifie que $\mathcal{L} \geq 0$ et que $\mathcal{L}(c;c) = 0$. Par un développement de Taylor pour des petites variations de $c^* - c$, on obtient la métrique suivante

$$\mathcal{L}(c;c^*) \approx \frac{1}{N} \sum_k a_k^2 \left[(\alpha_k - \overline{\alpha})^2 + (\Delta_k - \overline{\Delta})^2 \right], \tag{3.15}$$

où $\overline{\alpha} = 1/N \sum_k a_k^2 \alpha_k$ et $\overline{\Delta} = 1/N \sum_k a_k^2 \Delta_k$. Ceci met en évidence le lien explicite entre la métrique et des différences de phase $\Delta_k = \phi_k^* - \phi_k$ et d'amplitude $\alpha_k = (a_k^* - a_k)/a_k$ (ce dernier s'apparente plutôt à un écart logarithmique).

Tous ces développements se généralisent (par le biais d'une approximation de phase stationnaire) au cas d'un bruit coloré de densité spectrale $\Gamma(f)$ en remplaçant a_k par $a_k/\sqrt{f_s \Gamma(f_k)}$ où $f_k = f(t_s k)$.

Dans le cas de signaux d'amplitude constante que nous traitons immédiatement, on obtient

$$\mathcal{L}(\phi,\phi^*) \approx \frac{1}{N} \sum_{k=0}^{N-1} \left(\Delta_k - \overline{\Delta} \right)^2, \tag{3.16}$$

où $\overline{\Delta} = 1/N \sum_{k=0}^{N-1} \Delta_k$.

On reconnaît ici l'estimateur empirique de la variance appliqué à la différence de phase Δ_k. Deux signaux chirps sont identiques si et seulement si ils ont la même phase à une constante additive près.

3.2.3 Agrégation par chaînage

De par les hypothèses formulées en Sec. 3, l'amplitude et la phase du signal chirp recherché est inconnue. Si l'on suit une approche fréquentiste et les principes du *test du rapport de vraisemblance généralisé* [129], on doit alors considérer

$$\ell_{\max}(x) = \max_{c \in \mathcal{C}} \ell(x;c), \tag{3.17}$$

où $\mathcal{C}$ désigne l'ensemble des phases et amplitudes physiquement admissibles.

Ce problème de maximisation est non-linéaire et non-convexe ce qui le rend très difficile à résoudre sous cette forme. Cette difficulté peut être cependant contournée en discrétisant la variété continue $\mathcal{C}$ en une famille discrète $\tilde{\mathcal{C}}$ grâce à laquelle la maximisation peut être effectuée numériquement.

On propose ici de construire les éléments de $\tilde{\mathcal{C}}$ par le biais d'un graphe connectant des signaux élémentaires provenant du dictionnaire de chirplets. Les conditions d'admissibilité peuvent se traduire dans des règles autorisant ou interdisant la connexion de deux chirplets. Il s'agit alors de trouver un sous-graphe ou *chaîne de chirplets* associé au maximum en Éq. (3.17). Ceci se rapporte à un problème d'optimisation combinatoire.

Chirplets sur une grille temps-fréquence

Les contraintes d'admissibilité nous conduisent à modifier le dictionnaire de chirplets proposé précédemment en Sec. 3.1.2. Afin d'assurer la continuité des chaînes de chirplets

par construction, on définit celles-ci à partir d'une grille temps-fréquence $\{t_n = n\delta_t, f_m = m\delta_f\}$ avec $n = 0 \dots N_t$ et $m = 0 \dots N_f$ et où les pas temporel et fréquentiel de la grille sont $\delta_t = T/N_t$ et $\delta_f = f_s/(2N_f)$. Les chirplets du dictionnaire possèdent ainsi une fréquence instantanée variant linéairement entre deux nœuds successifs de la grille (t_n, f_{m_n}) et $(t_{n+1}, f_{m_{n+1}})$ (voir en Fig. 3.6). Leur phase définie en Éq. (3.6) s'écrit donc

$$\phi_k = \phi(t_s k) \equiv \theta_{n-1} + v_n t_{n,k} + u_n t_{n,k}^2, \tag{3.18}$$

avec $u_n = (f_{m_{n+1}} - f_{m_n})/(2\delta_t)$, $v_n = f_{m_n}$ et où $t_{n,k} = t_s k - t_n$ mesure le temps par rapport au début de la chirplet.

Si la continuité en fréquence du signal associé à une chaîne de chirplets est assurée par construction, celle de la phase impose que

$$\theta_{n-1} = \pi\delta_t(f_{m_n} + f_{m_{n-1}}) + \theta_{n-2}\,, \tag{3.19}$$

avec $\theta_{-1} \equiv 0$.

De plus, les conditions de régularité des dérivées de la fréquence amènent à requérir que (i) $|m_{n+1} - m_n| \leq N_r'$ and (ii) $|m_{n+1} - 2m_n + m_{n-1}| \leq N_r''$ où N_r' et N_r'' sont deux paramètres dont on déterminera la valeur en fonction des bornes supérieures sur les dérivées première et seconde de la fréquence.

On considère dans un premier temps des chirplets d'amplitude constante ($w(t) = $ cste en Éq. (3.4)) ce qui assure la continuité en amplitude de la chaîne. On examinera le cas à amplitude variable en Sec. 3.3.1.

En conclusion, la fréquence instantanée d'une chaîne de chirplets peut être représentée par une ligne brisée dans le plan temps-fréquence. Les lignes brisées peuvent être de bonnes approximations des courbes continues à condition que les morceaux de lignes qui les composent soient suffisamment petits par rapport aux variations de la courbe. Nous allons montré qu'il en est de même pour les chaînes de chirplets en tant qu'approximations des signaux chirps.

Borne minimax d'approximation des chirps par des chaînes de chirplets

La construction des chaînes de chirplets dans la section précédente laisse les quatre paramètres libres N_t, N_f, N_r' et N_r''. Les valeurs de ces paramètres peuvent être ajustées afin de contrôler l'erreur d'approximation maximale (au sens de la métrique introduite en Sec. 3.2.2) entre un signal chirp quelconque et la chaîne de chirplets la plus proche. C'est ce qu'établit le théorème ci-dessous dont la démonstration détaillée peut être trouvée dans [55].

Soit un signal chirp arbitraire de phase ϕ respectant les conditions de régularité en Éq. (3.3). Si l'on a

$$N_r'' \geq \frac{4}{3}\left(\frac{N''}{N_t}\right)^2 \frac{N_f}{2N} + 2 \qquad\qquad N_r' \geq 4\frac{N'}{N_t}\frac{N_f}{2N} + 1, \tag{3.20}$$

où $N' \equiv \dot{F}T^2$ et $N'' \equiv \sqrt{3\ddot{F}T^3}$, il existe une chaîne de chirplets de phase ϕ^* telle que

$$\mathcal{L}(\phi, \phi^*) \leq \mu', \tag{3.21}$$

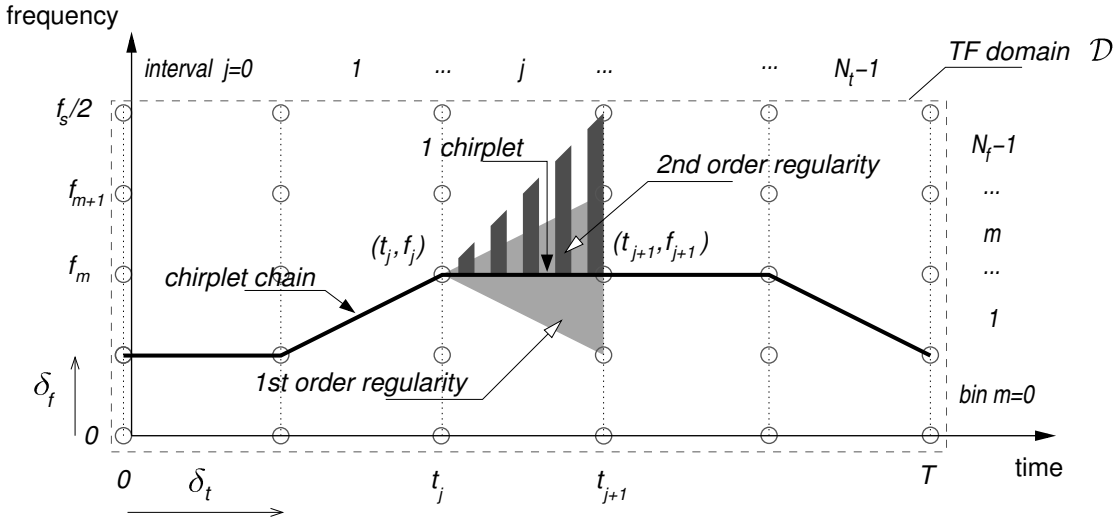

FIGURE 3.6 – **Chaîne de chirplets -** Le domaine temps-fréquence représenté sur ce diagramme est divisé en N_t intervalles temporels et N_f intervalles fréquentiels. La fréquence instantanée d'une chirplet varie linéairement entre deux nœuds consécutifs de cette grille. On obtient un modèle non-paramétrique des signaux chirp en formant des chaînes de chirplets. La pente de la variation en fréquence est limitée (région triangulaire en gris clair – ici, $N_r' = 1$) ainsi que la différence des pentes de deux chirplets consécutives dans la chaîne (région triangulaire indiquée par des rayures gris foncé – ici, $N_r'' = 1$).

où $\mathcal{L}$ est la métrique obtenue en Éq. (3.16) et $\mu' = \pi^2 T^2 (3\ddot{F}\delta_t^2/4 + \delta_f)^2/12$ est la perte maximum de rapport signal à bruit (exprimé ici en énergie) dû à la désadaptation de phase. Si l'on exprime cette perte en rapport signal à bruit en amplitude, on a $\mu = 1 - \sqrt{1-\mu'} \approx \mu'/2$ pour $\mu' \ll 1$. En fonction des paramètres libres dans le schéma de construction des chaînes de chirplet, on a

$$\mu = \frac{\pi^2}{96}\left[\frac{1}{2}\left(\frac{N''}{N_t}\right)^2 + \frac{1}{2}\left(\frac{2N}{N_f}\right)\right]^2. \tag{3.22}$$

On peut ainsi imposer que cette perte soit arbitrairement petite en choisissant N_t and N_f de manière adéquate.

Deux types d'erreurs contribuent indépendemment à l'erreur d'approximation finale. La première est de nature géométrique et est liée au fait que sur les parties linéaires, les lignes brisées (i.e., chaînes de chirplets) ne suivent pas parfaitement les lignes courbes (i.e., signaux chirp). La seconde est une erreur de quantisation associée à l'utilisation du grille discrétisée qui interdit aux jonctions des lignes brisées de correspondre exactement aux points de la ligne courbe si ceux-ci se situent entre deux nœuds de la grille. La première erreur peut être réduite en réduisant le pas temporel de la grille et la deuxième par le pas fréquentiel. Quand $N_t = N''$ et $N_f = 2N$, la perte maximale de rapport signal-à-bruit est de l'ordre de $\sim \pi^2/96 \approx 10\%$ et les deux types d'erreur contribuent à parts égales.

Nature combinatoire du problème

Grâce au résultat de la section précédente, nous concluons que la maximisation en Éq. (3.17) peut se faire sur l'ensemble (discret) des chaînes de chirplets plutôt que sur l'ensemble (continu) des signaux chirp avec une perte maîtrisée en rapport signal-à-bruit.

Ceci permet de recourir à des méthodes numériques. On voit que la recherche de la "meilleure" chaîne de chirplets (qui réalise la maximisation en Éq. (3.17)) est un problème d'optimisation combinatoire. Ceci apparaît lorsqu'on dénombre les chaînes de chirplets. En effet, si l'on néglige les coupures aux bords ($f = 0$ et $f = f_s/2$), le nombre de chaînes de chirplets est égal à

$$\log N_{cc} \lesssim \log(2N_r' N_f) + (N_t - 1)\log(2N_r'' + 1). \tag{3.23}$$

et la croissance exponentielle en fonction de N_t indique la nature combinatoire de ce dénombrement. De ce fait, il est clair que l'on doit renoncer à une méthode exhaustive testant toutes les chaînes pour réaliser la maximisation en Éq. (3.17).

Par ailleurs, la minimisation de N_{cc} pour une perte maximale en rapport signal-à-bruit μ fixée peut constituer un critère objectif pour déterminer les valeurs des paramètres laissés libres qui s'expriment alors comme suit

$$N_t = 0.52\,\mu^{-1/4}\,N'', \qquad\qquad N_f = 0.78\,\mu^{-1/2}\,N. \tag{3.24}$$

3.2.4 Recherche de la meilleure chaîne de chirplets

Dans cette section, nous proposons une solution praticable s'appuyant sur les méthodes d'optimisation dans les graphes. Cette solution passe par une reformulation du problème dans le plan temps-fréquence.

Formulation temps-fréquence via la distribution de Wigner-ville discrète

Dans [54], nous proposons de définir la *distribution de Wigner-Ville discrète* (WVD) par

$$w_x(n,m) \equiv \sum_{k=-k_n}^{k_n} x_{p_{n,k}} x^*_{q_{n,k}}\, e^{-2\pi i m k/(2N)}, \tag{3.25}$$

avec $k_n \equiv \min\{2n, 2N-1-2n\}$, $p_{n,k} \equiv \lfloor n+k/2 \rfloor$ and $q_{n,k} \equiv \lfloor n-k/2 \rfloor$ où $\lfloor\cdot\rfloor$ est la partie entière.

La WVD réalise une distribution de l'énergie du signal dans le plan temps-fréquence discrétisé selon $t_n = t_s n$ et $f_m = f_s m/(2N)$ pour $0 \le m \le N$ et $f_m = f_s(N-m)/(2N)$ pour $N+1 \le m \le 2N-1$. Cette nouvelle WVD résout un défaut fondamental des définitions existant jusqu'alors. Elle est en effet à la fois unitaire et relativement immune au repliement spectral. Son unitarité implique qu'elle satisfait la formule de Moyal [54]

$$\left|\sum_{k=0}^{N-1} x_k\, y_k^*\right|^2 = \frac{1}{2N} \sum_{n=0}^{N-1} \sum_{m=0}^{2N-1} w_x(n,m)\, w_y(n,m), \tag{3.26}$$

qui permet de reformuler le module carré d'un produit scalaire de deux séries temporelles x et y en un produit scalaire de leur distributions temps-fréquence.

Si la chaîne de chirplets est suffisamment oscillante, on peut approcher la statistique ℓ par (voir [55] pour la démonstration complète)

$$\hat{\ell}(x;\phi) = \frac{1}{N}\left|\sum_{k=0}^{N-1} x_k \exp(i\phi_k)\right|^2. \tag{3.27}$$

Par application de Éq. (3.26), on obtient

$$\hat{\ell}(x;\phi) = \frac{1}{2N^2} \sum_{n=0}^{N-1} \sum_{m=0}^{2N-1} w_x(n,m) w_e(n,m) \tag{3.28}$$

où w_e est la WVD de la forme d'onde associée à la chaîne de chirplet $e_k \equiv \exp i\phi_k$.

Intégrale de chemin temps-fréquence

Il est bien connu [70] que la distribution de Wigner-Ville (définie en temps et fréquence continus) d'un signal chirp linéaire (i.e., dont la fréquence varie linéairement en fonction du temps) est une distribution de Dirac le long d'une ligne temps-fréquence correspondant à la fréquence instantanée du signal.

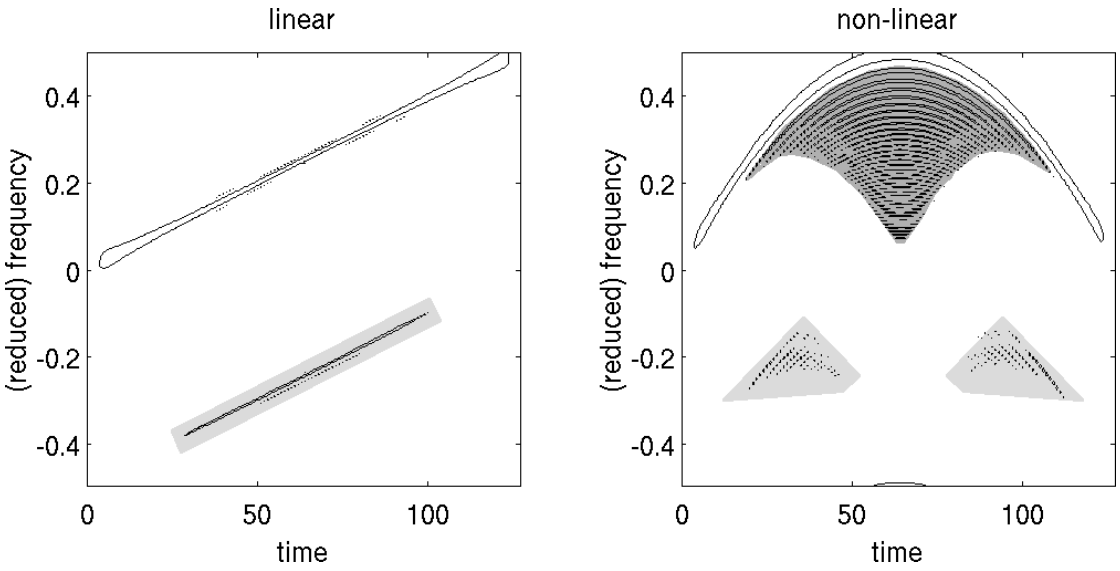

FIGURE 3.7 – **Distribution de Wigner-Ville discrète (WVD) de deux signaux chirps** - *gauche* : la WVD d'un chirp linéaire est presque Dirac le long de ligne de fréquence instantanée. La WVD est affecté par le repliement spectral aux fréquences négatives (zone grisée) Le modèle heuristique en Éq. (3.29) néglige ce terme. *droite* : la WVD d'un chirp non-linéaire (ici, parabolique) présente en plus des artefacts dus au repliement (régions gris clair) des termes d'interférences (régions gris foncé).

Nous allons exploiter cette propriété et postuler qu'elle reste approximativement vraie pour la distribution discrète introduite en Éq. (3.25) et pour les signaux chirps présentant une variation non-linéaire de leur fréquence. On considère donc que

$$w_e(n, m) \approx 2N\, \delta(m - m(n)), \tag{3.29}$$

où $m(n) = [2T\, f(t_n)]$ et $[\cdot]$ désigne l'entier le plus proche.

Nous avons vérifié cette approximation, comme par exemple dans l'illustration en Fig. 3.7 où l'on constate que la relative immunité de la WVD utilisée ici au repliement spectral inhérent aux distributions temps-fréquence quadratiques discrètes est un ingrédient clé.

En insérant l'Éq. (3.29) dans l'Éq. (3.28), on peut alors $\tilde{\ell}$ comme une intégrale de chemin dans le plan temps-fréquence :

$$\tilde{\ell}(x; \phi) = \frac{1}{N} \sum_{n=0}^{N-1} w_x(n, m(n)). \tag{3.30}$$

L'approximation aboutissant à ce résultat revient à négliger les termes d'interférence. Ceci est justifié par la nature oscillante des interférences (avec des valeurs positives et négatives) qui conduit à une contribution négligeable à l'intégrale ci-dessus.

Utilisation de la programmation dynamique

Grâce à l'approximation réalisée dans la précédente section, la maximisation en Éq. (3.17) revient à trouver le chemin temps-fréquence d'intégrale maximum ou le chemin le plus "long" si l'on assimile l'intégrale de chemin en Éq. (3.30) au calcul d'une longueur. Il existe des méthodes efficaces pour la recherche de chemins optimaux [36]. Ces méthodes requièrent des propriétés structurelles pour la fonction objectif, en particulier l'additivité. Grâce à sa linéarité, ceci est vérifié pour $\tilde{\ell}$ en Éq. (3.30) qui peut ainsi se décomposer comme une somme sur les chirplets dans la chaîne

$$\tilde{\ell}(x;\phi) = \frac{1}{N}\sum_{j=0}^{N_t-1}\sum_{n\in\mathcal{T}_j} w_x(n, m(n)) \tag{3.31}$$

en notant $\mathcal{T}_j$, le support temporel de la $j^{\text{ième}}$ chirplet.

Notons que les statistiques ℓ en Éq. (3.12) ou pour $\hat{\ell}$ en Éq. (3.27) ne sont pas additives.

Grâce à cette propriété, le problème de maximisation peut être décomposé en une série récursive de sous-problèmes, que l'on peut résoudre rapidement (en un temps polynomial). Dans le cas présent, la décomposition naturelle est celle de la division de la chaîne en N_t chirplets. Le *principe d'optimalité* de la programmation dynamique est appliqué récursivement à chaque chirplet de gauche à droite. Pour une chirplet donnée dans la Fig. 3.8, on détermine pour toutes celles qui y sont connectées vers la gauche (♢, ♡ et ♣). On suppose que l'on a, pour chacune de ces chirplets, la "longueur" (l'intégrale de chemin temps-fréquence) du chemin optimal arrivant jusqu'ici. Le principe d'optimalité consiste à sélectionner le chemin de plus grande longueur (l'intégrale la plus grande) parmi celles-ci. À la fin de la récursion, lorsqu'on arrive aux chirplets de la dernière colonne tout à fait à droite, on sélectionne la chirplet associée au chemin le plus long qui est ainsi le *maximum global*. Cette procédure permet ainsi d'élaguer l'arbre combinatoire et aboutit à un résultat en un coût polynomial évalué en nombre d'opérations à

$$C \propto 5NN_f \log_2 N_f + [N + (2N_r'' + 1)N_t](2N_r' + 1)N_f. \tag{3.32}$$

Ce coût est compatible avec la capacité de calcul typiquement disponible. Par exemple en considérant des blocs de $T = 0.5s$ et les paramètres suivants $N_t = 512$, $N_f = 1024$, $N_r' = 9$ et $N_r'' = 3$ (cf prochaine section), on estime le coût à 142 millions d'opération à virgule flottantes par bloc. Si l'on autorise un recouvrement de 10% entre les blocs successifs, un calcul en temps réel peut être effectué avec 2.8 Gflops, ce qui est bien en deçà des capacités de calcul actuelles.

3.2.5 Applications

Dans cette section, nous évaluons la méthode proposée.

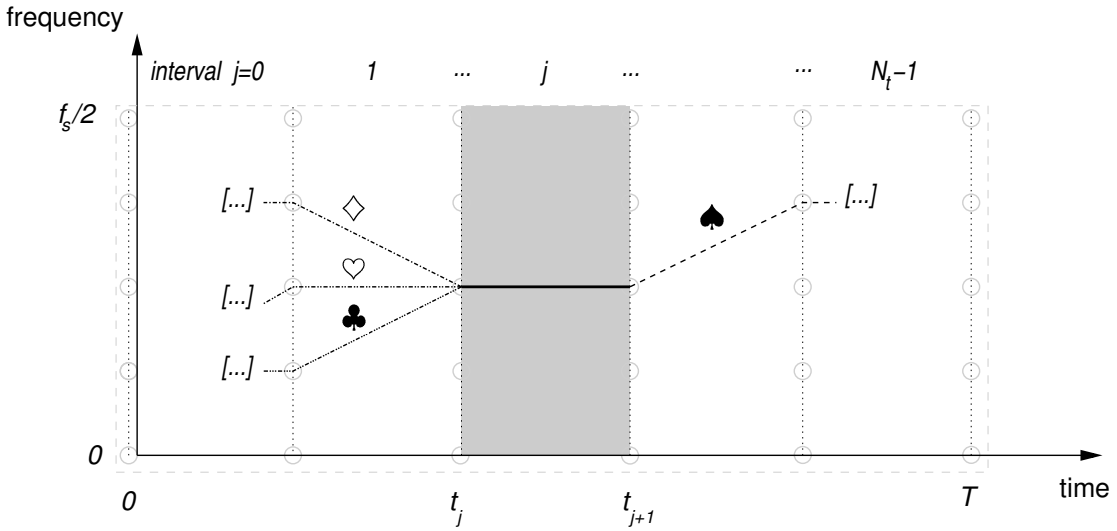

FIGURE 3.8 – **Principe d'optimalité de la programmation dynamique**

Sélection des paramètres

On s'inspire du modèle newtonien des binaires coalescentes pour déterminer la variabilité en fréquence des signaux chirp. L'évolution fréquentielle pour ce modèle est (voir Éq. (1.12))

$$f(t) = f_0 \left(1 - \frac{t - t_0}{T}\right)^{-3/8} \quad \text{for } t < t_0 + T, \tag{3.33}$$

où t_0 est le temps de passage à la fréquence f_0 et T désigne la durée totale du signal qui s'exprime pour les binaires d'objets de masse identique

$$T \sim 0.5\,\mathrm{s} \left(\frac{f_0}{20}\right)^{-8/3} M_{80}^{-5/3} \tag{3.34}$$

où on note $M_{80} = M/(80M_\odot)$. Pour une fréquence d'échantillonnage $f_s = 2048$ Hz, on obtient

$$N = f_s T \sim 1068\, M_{80}^{-5/3} \tag{3.35}$$

On utilise pour $\dot{F}$ et $\ddot{F}$ les valeurs des dérivées première et seconde de la fréquence à la dernière orbite stable (voir Éq. (1.14))

$$\dot{F} \sim 520\,\mathrm{Hz/s}\, M_{80}^{-2} \qquad \ddot{F} \sim 18\,\mathrm{kHz/s^2}\, M_{80}^{-3} \tag{3.36}$$

et on en déduit

$$N' \sim 180\, M_{80}^{-16/3} \qquad N'' \sim 106\, M_{80}^{-4} \tag{3.37}$$

En appliquant Éq. (3.24) pour $\mu = 10\%$, on obtient

$$N_t \sim 645\, M_{80}^{-4} \qquad N_f \sim 6566\, M_{80}^{-5/3} \tag{3.38}$$

et ainsi on a

$$N'_r \sim 9\, M_{80}^{-4/3} \qquad\qquad N''_r \sim 4. \tag{3.39}$$

Évaluation des performances à l'aide de signaux chirp aléatoires

Nous appliquons la méthode à la recherche de signaux chirp dont l'évolution fréquentielle est une marche aléatoire dans le plan temps-fréquence afin d'en tester la robustesse. Il est clair que les méthodes de filtrage adapté ne sont pas applicables dans ce cadre puisqu'on ne dispose pas de la forme d'onde a priori.

On utilise les paramètres de recherche ($N_t = 512$, $N_f = 1024$, $N'_r = 9$ and $N''_r = 3$) définis dans la section précédente inspiré du modèle newtonien de la coalescence d'un binaire de trous noirs afin de se placer dans une gamme de valeurs physiquement réalistes.

On tire au hasard des chaînes de chirplets compatibles avec ces caractéristiques. La Figure 3.9 présente un exemple d'un tel signal dans un bruit blanc gaussien avec un rapport signal-sur-bruit $\rho = 20$. On présente également le résultat de la recherche de la meilleure chaîne de chirplets. En Fig. 3.10, on montre la courbe COR (Caractéristiques Opérationnelles de Réception) pour un rapport signal-sur-bruit $\rho = 12$ ainsi que celle du filtre adapté réalisé par un observateur clairvoyant qui possède toute l'information sur le signal (son évolution de phase, en particulier) et pour lequel on a ajusté le rapport signal-sur-bruit pour que les deux courbes se superposent. Le facteur d'ajustement est ~ 2.6 ce qui est donc le prix de la robustesse de la méthode.

3.3 Extensions

Nous présentons ici des extensions à la version initiale de la recherche de la meilleure de chaîne de chirplets introduites dans la section précédente.

3.3.1 Inclusion de la modulation d'amplitude

Nous proposons d'abord l'extension au cas de signaux chirp d'amplitude variable, $s(t) = A(t) \exp i\varphi(t)$ présentée dans [48].

Pour cela, nous continuons à considérer des chirplets d'amplitude constante mais nous leur accordons individuellement un facteur d'amplitude a_l. Une chaîne de chirplets décrit ainsi un signal d'amplitude constante par morceaux. On discrétise les facteurs d'amplitude sur une échelle logarithmique à N_a niveaux, $a_l = 2^{-l/2}/\sqrt{b}$ pour $0 \leq l < N_a - 1$ avec $b = N/N_t$, le support d'une chirplet en nombre d'échantillons et $a_{N_a-1} = 0$. La normalisation du patron d'onde de référence dans la statistique en Éq. (3.13) impose celle de la séquence des facteurs d'amplitude de la chaîne, qui implique

$$b \sum_{j=0}^{N_t-1} a_{l_j}^2 = 1. \tag{3.40}$$

Cette condition de normalisation introduit une connexion entre le support de la chaîne (i.e., le nombre de facteurs d'amplitude pouvant prendre une valeur non nulle)

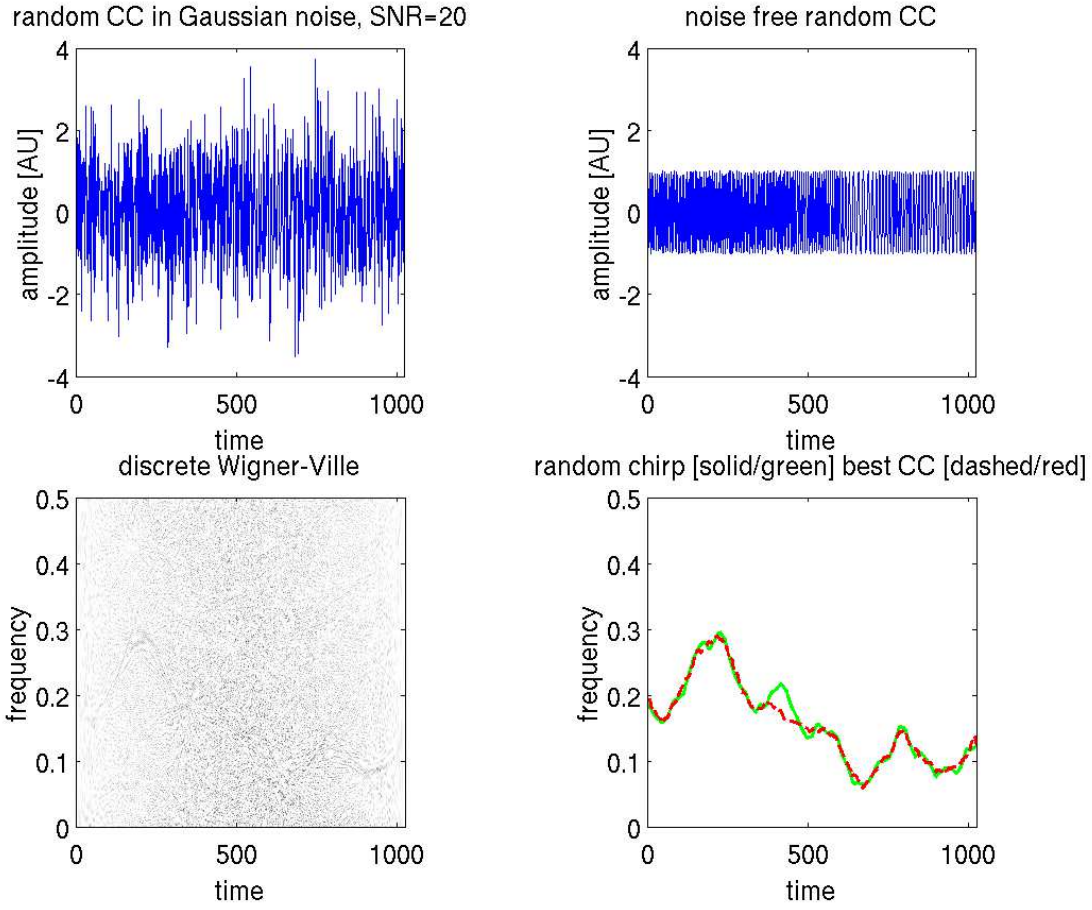

FIGURE 3.9 – **Chaîne aléatoire de chirplets dans un bruit blanc gaussien** - *en haut à gauche* : représentation temporelle du signal bruité *en haut à droite* : idem pour le signal seul en bas à gauche : WVD du signal bruité *en bas à droite* : fréquence du signal en vert et celle de la meilleure chaîne de chirplets en rouge. On remarque que, grâce à l'optimisation globale réalisée ici l'algorithme peut localement perdre la trace du signal à cause d'une fluctuation du bruit et la reprendre par la suite.

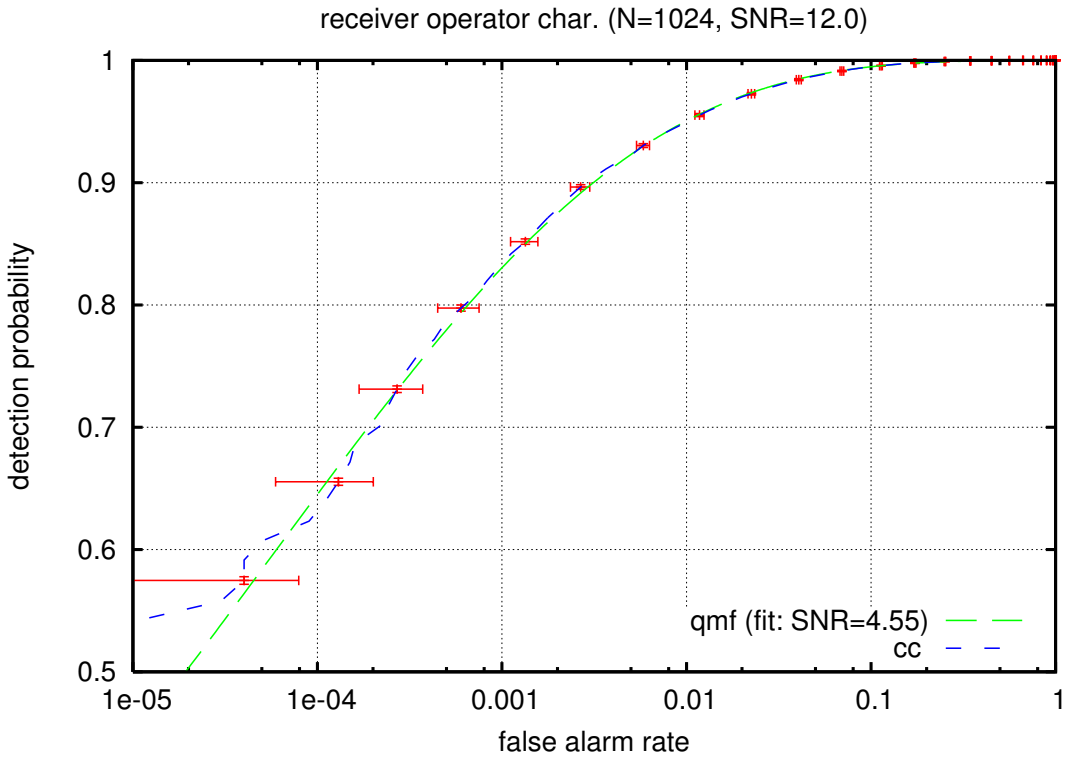

FIGURE 3.10 – **Probabilité de détection en fonction de la probabilité de fausse alarme pour la recherche de la meilleure chaîne de chirplets** (bleu, obtenue pour $\rho = 12$) comparée celle du filtre adapté réalisé par un observateur clairvoyant qui possède toute l'information sur le signal (son évolution de phase en particulier) avec un rapport signal-sur-bruit réduit à $\rho_c = 4.55$ afin que les deux courbes s'ajustent.

et l'amplitude maximale. Par exemple, si l'une des chirplets est d'amplitude maximale, soit $l = 0$ et $a_0 = 1/\sqrt{b}$, toutes les amplitudes des autres chirplets dans la chaîne doivent être nulles. Inversement, le nombre de niveaux N_a détermine le nombre maximum de facteurs d'amplitude non nuls. En fixant $N_a \geq \log_2(N_t) + 2$, on peut obtenir des chaînes de chirplets au support couvrant l'intégralité du segment temporel de base.

Similairement à la fréquence, on fixe le degré de régularité de l'enveloppe de la chaîne en imposant que la différence de l'indice d'amplitude entre deux chirplets consécutives n'excède pas $\pm N_s'$ (paramètre donné *a priori*).

Comme précédemment, on effectue la formulation temps-fréquence de la statistique (3.13) via la formule de Moyal. On remplace ensuite la WVD de la chaîne de chirplets par un modèle géométrique simplifié. Dans le cas précédent (chirps à amplitude constante), celle-ci était remplacée par une ligne brisée qui suit la fréquence instantanée. Dans le cas présent, la modulation d'amplitude se traduit par un élargissement du spectre inversement proportionnel au support temporel du signal. Ceci motive le modèle heuristique suivant : on approche la WVD de la chaîne par une bande de largeur fréquentielle $\mathcal{F}$ qui dépend du temps. La connexion entre amplitude et support temporel établie par l'Éq. (3.40) suggère de fixer la largeur de bande de la $j^{\text{ième}}$ chirplet $\mathcal{F}_j = \{m \text{ tel que } m \leq 2Na_{l_j}\}$ [48]. On obtient alors l'approximation suivante pour la statistique de détection

$$\tilde{\ell}(x; c) = \sum_{j=0}^{N_t-1} \sum_{n \in \mathcal{T}_j} \sum_{m - m_j(n) \in \mathcal{F}_j} a_{l_j} w_x(n, m), \tag{3.41}$$

Au lieu d'une intégrale de chemin (1D) comme précédemment en Éq. (3.31), nous calculons maintenant une intégrale de bande (2D) dont la largeur est couplée à l'amplitude.

Cette fonction objectif étant additive, sa maximisation peut être réalisée par une méthode similaire à celle employée jusqu'ici. Une différence importante réside cependant dans la contrainte de normalisation en Éq. (3.40). Celle-ci n'étant pas satisfaite par construction, elle doit être imposée durant l'optimisation. Le problème à résoudre peut être rapproché de la famille des problèmes d'optimisation sous contrainte de *rendu de monnaie* ou de *sac à dos* [112]. L'algorithme de programmation dynamique permet également de résoudre ce type de problème en temps polynomial. Notons que le coût de calcul est significativement plus grand que précédemment à cause de la complexité accrue du modèle.

La Figure 3.11 montre le résultat de l'application de cette méthode à l'estimation couplée de l'amplitude et la fréquence d'un signal chirp choisi aléatoirement. Bien que le support temporel estimé du signal est légèrement tronqué, sa partie centrale est bien identifiée.

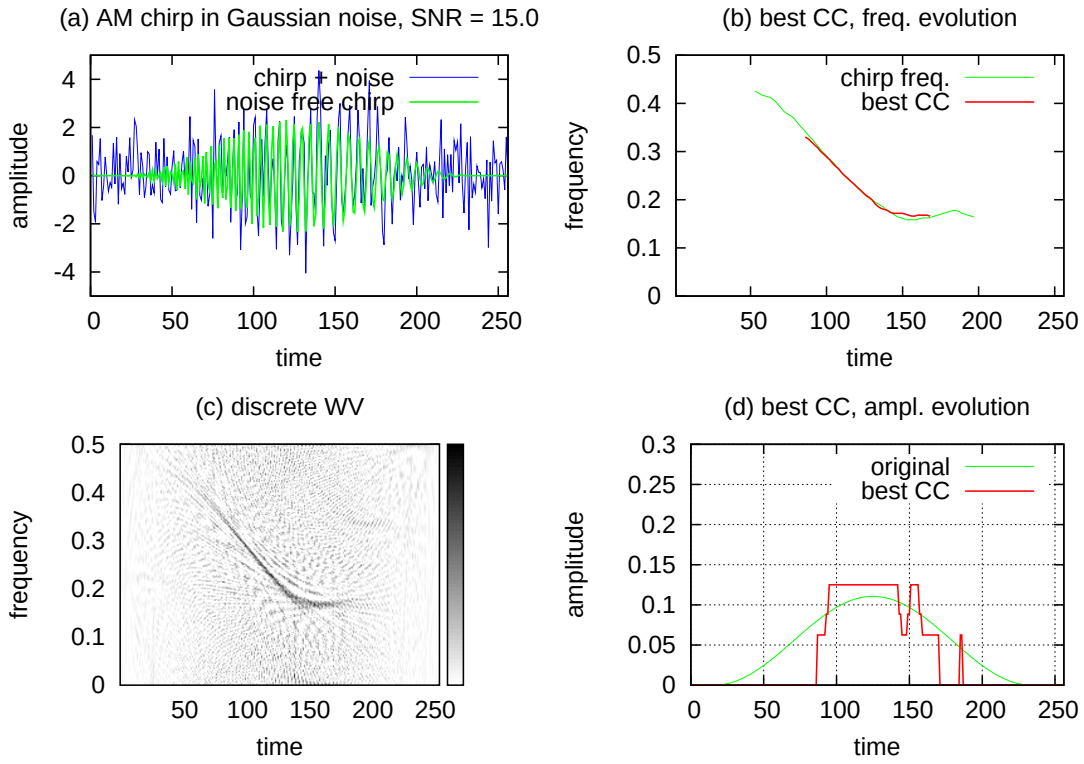

FIGURE 3.11 – **Chaîne aléatoire de chirplets à modulation d'amplitude (fenêtre de Hanning)**. (a) représentation temporelle du signal bruité et (c) sa WVD. Le rapport signal-à-bruit est fixé à $\rho = 12$. (b) et (d) comparent la fréquence et l'amplitude (mise à la norme unité) du signal chirp (vert) à l'estimation obtenue à partir de la meilleure chaîne de chirplets et la méthode décrite en Sec. 3.3.1.

3.3.2 Analyse multi-détecteur cohérente

Principe de l'analyse cohérente

En introduction à ce chapitre, nous avons décrit les principales méthodes d'analyse de séries temporelles provenant d'un unique détecteur. On peut espérer obtenir un gain de sensibilité par l'analyse conjointe des données de plusieurs détecteurs recevant la même OG.

Chaque détecteur reçoit un mélange linéaire des deux polarisations de l'onde incidente (cf. Sec. 2.2.1). Les cœfficients du mélange dépendent de l'alignement et de l'orientation respectifs du détecteur et de l'onde. Les détecteurs formant un réseau qui n'est ni plan ni régulier (en espacement et alignement), ils couplent différemment à une OG incidente. De plus, la vitesse de propagation des OG étant finie, l'onde atteint les détecteurs à des instants différents.

Pour une OG donnée, les réponses reçues ont une amplitude, une phase et un temps d'arrivée déterminés. Ceci est exploité par les techniques d'*analyse cohérente* afin d'améliorer la sensibilité de la recherche. Celles-ci s'apparentent aux méthodes de *formation de voie* [130,131] utilisées par exemple, pour les réseaux phasés d'antennes radio servant pour les radars ou en radioastronomie.

Le principe de base de l'analyse cohérente consiste à aligner les différentes réponses en temps et en phase en compensant le déphasage et le délai temporel associés à une incidence donnée. Les séries temporelles obtenues sont ensuite combinées par addition. La somme est ainsi constructive pour les OG provenant de la direction considérée, ce qui maximise le rapport signal-sur-bruit. La réponse combinée peut ensuite être analysée par des méthodes inspirées de celles que nous avons évoqué plus haut, à savoir les détecteurs d'excès d'énergie [75,93] et le filtrage adapté [78,111].

L'analyse cohérente est intrinsèquement directionnelle (chaque réponse combinée est associée à une direction donnée). La répétition de l'analyse en chaque point d'une grille céleste permet d'obtenir la distribution sur le ciel de la probabilité *a posteriori* à partir de laquelle on peut obtenir la position la plus vraisemblable de la source.

Analyse cohérente avec les chaînes de chirplets

Dans [110, 115], nous avons proposé une extension multi-détecteur cohérente à la recherche de la meilleure chaîne de chirplets. Nous décrivons ici les principales étapes conduisant à l'obtention de cet algorithme.

Le passage d'une OG produit une réponse qui s'exprime comme la combinaison linéaire de ses polarisations, que l'on écrit sous forme complexe par

$$s(t) = \mathrm{Re}[F^* h(t-\tau)], \tag{3.42}$$

où $F = F_+ + iF_\times$ désigne le facteur du diagramme d'antenne, $h = h_+ + ih_\times$ suit le modèle introduit en Éqs. (3.1) et (3.2), et τ désigne le délai de propagation de l'onde (plane) entre le détecteur et le centre de la Terre choisi comme référence.

Grâce à un développement en fonctions de Gel'fand [111] du diagramme d'antenne, les termes liés à l'angle de polarisation de l'onde ψ et à l'inclinaison ϵ du plan orbital peuvent être factorisés comme suit

$$F = t_+(\psi, \epsilon)\, d(\phi, \theta; \mathcal{D}) + t_-(\psi, \epsilon)\, d^*(\phi, \theta; \mathcal{D}), \tag{3.43}$$

où les coordonnées θ et ϕ de la source sur la sphère céleste sont inconnues et doivent être estimées. Les caractéristiques de position et d'orientation $\mathcal{D}$ du détecteur sont, elles, connues. Les variables $t_\pm$ et d s'exprime en fonction des fonctions de Gel'fand de rang 2.

On échantillonne les données reçues par les N_d détecteurs composant le réseau et on les rassemble dans un unique vecteur $\boldsymbol{s} = [\boldsymbol{s}_1 \boldsymbol{s}_2 \dots \boldsymbol{s}_{N_d}]$. Celui-ci prend alors la forme d'un modèle linéaire

$$\boldsymbol{s} = \boldsymbol{\Pi p} \tag{3.44}$$

où l'on a isolé dans le vecteur $\boldsymbol{p} \in \mathbb{C}^4$, les paramètres A, θ, ϵ et ψ intervenant par l'intermédiaire des $t_\pm$.

L'*espace signal* décrit par $\boldsymbol{\Pi}$ est le produit direct de l'*espace des OG* engendré par le vecteur $\boldsymbol{d}$ qui rassemble les facteurs de diagramme d'antenne de tous les détecteurs et son conjugué et de l'*espace chirp* engendré par le modèle temporel du signal $\exp i\varphi(kt_s)$, $k = 0 \dots N-1$ et son conjugué.

Sous hypothèse de gaussianité et d'indépendance du bruit de chaque détecteur, la log-vraisemblance du problème global de détection à partir des données du réseau s'écrit

$$\Lambda(\boldsymbol{x}) = -\left\|\boldsymbol{x} - \boldsymbol{\Pi p}\right\|_{\boldsymbol{R}^{-1}} + \left\|\boldsymbol{x}\right\|_{\boldsymbol{R}^{-1}}, \tag{3.45}$$

où la construction du vecteur des observations $\boldsymbol{x}$ est calquée sur celle de $\boldsymbol{s}$. L'hypothèse d'indépendance du bruit entre détecteurs implique que la matrice de corrélation globale du bruit $\boldsymbol{R}$ est diagonale par blocs.

Grâce à cette formulation, la maximisation de la vraisemblance s'effectue simplement et donne

$$\hat{\boldsymbol{p}} = \boldsymbol{\Pi}^{\#} \tilde{\boldsymbol{x}}, \tag{3.46}$$

où l'on note $\tilde{\boldsymbol{\Pi}} = \boldsymbol{R}^{-1/2}\boldsymbol{\Pi}$. $\boldsymbol{A}^{\#}$ est la pseudo-inverse de $\boldsymbol{A}$ qui s'exprime simplement au moyen de la décomposition en valeurs singulières de $\boldsymbol{A} = \boldsymbol{U_A \Sigma_A V_A^H}$ comme $\boldsymbol{A}^{\#} = \boldsymbol{V_A \Sigma_A^{-1} U_A^H}$, où l'exposant $\cdot^H$ désigne la transposée hermitienne.

En combinant (3.46) et (3.45), on obtient la statistique optimale de détection

$$\hat{\Lambda}(\boldsymbol{x}) \equiv \left\|\boldsymbol{U}_{\tilde{\Pi}}^H \tilde{\boldsymbol{x}}\right\|^2. \tag{3.47}$$

La matrice $\boldsymbol{U}_{\tilde{\Pi}}$ est de rang 2 et identifie les deux directions principales de l'espace des OG auxquelles sont associées, par projection, deux séries temporelles que l'on appelle "flux synthétiques". La formulation de la statistique dans le plan temps-fréquence permet de la réécrire comme une intégrale de chemin comme en l'Éq. (3.30) mais opérant cette fois sur la somme des WVD des deux flux synthétiques. La maximisation de la statistique peut alors être réalisée de la même manière que précédemment par la programmation dynamique (voir en Sec. 3.2.4). Cela doit être réalisé sur un ensemble de directions

discrétisant la sphère céleste. On sélectionne ensuite la direction associée au maximum de vraisemblance.

La Figure 3.12 illustre la capacité de cette méthode à effectuer l'estimation jointe du signal et de la position spatiale de la source.

Dans certaines parties du ciel, la matrice $\boldsymbol{U}_{\tilde{\Pi}}$ est dégénérée et prend un rang unité : pour ces directions du ciel, le réseau ne reçoit qu'une seule polarisation. Cela est vrai lorsque la matrice de Gram associée aux vecteurs $\boldsymbol{d}$ et $\boldsymbol{d}^*$ engendrant l'espace des OG est mal conditionnée. Nous proposons un schéma de régularisation de la statistique dans les parties dégénérées du ciel [110].

Chaînes de chirplets pour les binaires spirallantes à rapport de masse extrême

Nous avons appliqué les chaînes de chirplets au problème de la détection des binaires spirallantes à rapport de masse extrême (extreme-mass ratio inspirals, EMRI), un des objectifs scientifiques de l'observatoire gravitationnel spatial européen eLISA. Les EMRI sont des systèmes binaires formés d'un trou noir super-massif (des millions de masses solaires) et d'un objet beaucoup plus petit (une étoile à neutrons ou un trou noir de masse solaire). L'orbite suivie par le petit objet autour du trou noir central est affectée par d'extrêmes effets relativistes (effet Lense-Thirring et précession du périhélie) lors de son passage dans le voisinage du trou noir. Ces effets combinés à la grande asymétrie du système conduisent à une émission gravitationnelle quasi-périodique à l'évolution complexe et comportant de multiples harmoniques. On peut espérer observer quelques-uns de ces systèmes avec eLISA durant la durée de la mission. Les techniques de filtrage adapté sont ici inapplicables car elles nécessiteraient la mise en œuvre d'une énorme banque de filtres dépassant de plusieurs ordres de grandeur les limites calculatoires actuelles. Dans [116], nous adaptons le schéma de base des chaînes de chirplets à ce problème et proposons d'intégrer le long d'un "peigne" temps-fréquence plutôt qu'un chemin afin de collecter l'énergie portée par les harmoniques du signal. Une ensemble de simulations permet de valider cette preuve de concept.

3.4 Bilan et perspectives

Nous avons conclu ces travaux préparatoires courant 2006 avec l'idée de développer, à partir des codes prototypes, un logiciel pouvant réaliser l'analyse complète des données expérimentales et fonctionner sur un super-ordinateur. Le cadre de la collaboration avec LIGO signé en 2007 a changé la donne. Il devenait difficile d'être compétitifs face aux chaînes d'analyse développées par les équipes de LIGO qui avaient déjà accumulé l'expérience de quatre prises de données scientifiques depuis 2002. Nous avons dû adapté notre stratégie initiale d'écriture d'une chaîne d'analyse à part entière au profit de l'intégration de nos idées aux chaînes existantes. Les méthodes de graphes d'ondelettes que nous présentons maintenant suit cette logique.

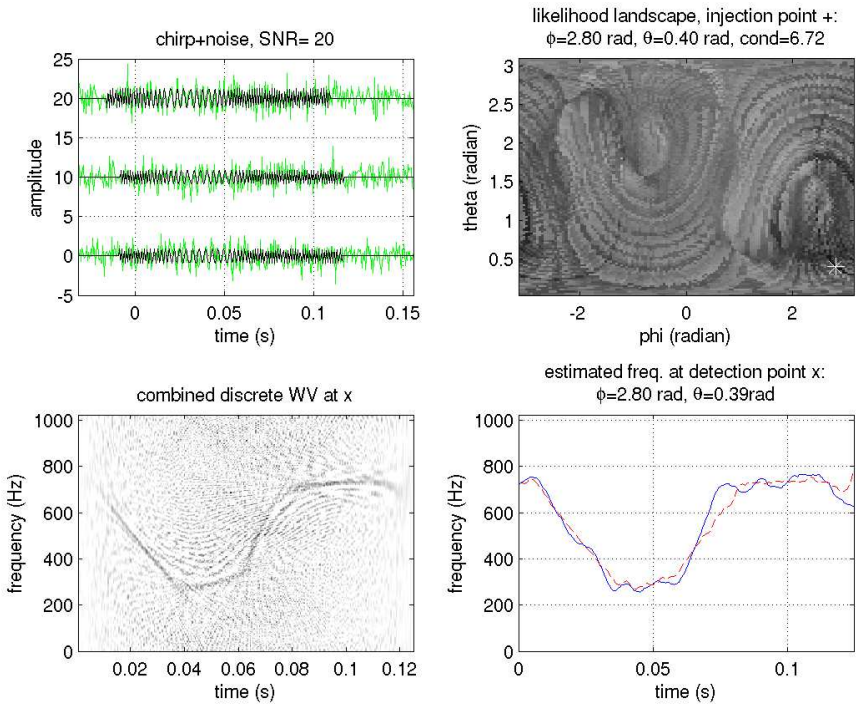

FIGURE 3.12 – **Détection et estimation cohérente d'une chaîne de chirplets aléatoire avec un réseau de trois détecteurs d'OG**. Le diagramme (a) présente les données des trois détecteurs où l'on a mis en évidence le signal OG simulé émis par une source de coordonnées célestes $\phi = 2.8$ rad et $\theta = 0.4$ rad. (b) Paysage de vraisemblance produit par la méthode d'analyse cohérente présentée en Sec. 3.3.2. La source est indiquée par un "+" et le maximum de vraisemblance par un "×". (c) Distribution WVD combinée des deux flux synthétiques obtenus au point de détection. (d) Comparaison de la fréquence vraie du signal chirp (ligne continue bleue) et de son estimation (ligne pointillée/rouge).

Graphe d'ondelettes pour coherent WaveBurst Nous proposons d'intégrer ces développements à la chaîne d'analyse *coherent WaveBurst* (cWB) [92]. cWB a été appliquée avec succès à multiples reprises pour la recherche de transitoires OG de courte durée[4], voir e.g. [8]. Grâce un certain nombre d'astuces algorithmiques, cWB conduit efficacement une recherche pleinement cohérente, qu'elle peut réaliser en ligne avec une latence de quelques minutes. L'idée est d'étendre les capacités de cWB à des signaux de type chirps de plus longue durée.

Dans sa version standard, cWB calcule, pour chaque détecteur, un ensemble de transformées temps-fréquence de Wilson [64,105] obtenues avec des ondelettes de Meyer d'échelles différentes. La totalité de ces transformées fournit une représentation (redondante) des données en fonction de trois variables : le temps, la fréquence et l'échelle. Ces transformées sont combinées en cohérence, puis on identifie des agrégats de grands cœfficients dans le résultat de cette combinaison. Aucune contrainte n'est imposée sur ces agrégats qui peuvent ainsi prendre des formes arbitraires.

Nous proposons de remplacer ce schéma d'agrégation par un nouveau qui s'inspire des chaînes de chirplets. On se concentre dans un premier temps sur les signaux chirps provenant des coalescences de binaires compactes. Pour une gamme de masses pour les composantes de la binaire, on établit des liens entre les cœfficients en ondelettes successifs présentant un couplage maximum avec le signal OG associé. La collection de tous les liens obtenus pour toutes les binaires considérées forme un graphe. L'idée est de faire la recherche de chemins optimaux dans ce graphe par les méthodes d'optimisation discutées plus haut.

De premiers résultats prometteurs ont été obtenus suite au récent stage d'Hugo Magaldi (élève-ingénieur de l'Ecole Centrale) encadré avec Eric Le Bigot. La figure 3.13 montre en particulier le graphe construit avec la décomposition habituellement calculée par cWB et une gamme réaliste de masse pour les binaires de référence. On voit que la procédure sélectionne ~ 2500 cœfficients en ondelettes, soit une petite fraction du cube de données calculées par cWB, et créé un graphe assez peu connecté (9 connexions au maximum). La recherche de chemins optimaux dans ce graphe est en cours d'implémentation et sera incluse dans les prochains mois à cWB.

Généralité et applicabilité des idées Dans la dernière partie de ce chapitre, nous nous intéressons à la détection de signaux composites dont les parties n'émergent pas significativement du bruit si elles sont prises isolément mais elles deviennent significatives lorsqu'on les agrègent. La méthode utilise un graphe dont les connexions portent l'information de structure (le modèle) et les nœuds celle de l'adéquation des composantes du signal aux données (les observations). Le jeu consiste alors à identifier l'agrégat dans ce graphe qui possède certaines propriétés d'optimalité i.e., celui qui maximise un facteur de mérite obtenu en sommant les termes d'adéquation aux données. La généralité de ces idées font de ces méthodes un outil flexible et adaptable qui peut être appliqué à de nombreux autres problèmes et contextes.

4. Nous nous intéresserons de nouveau à cWB au chapitre suivant en Sec. 4.1.3.

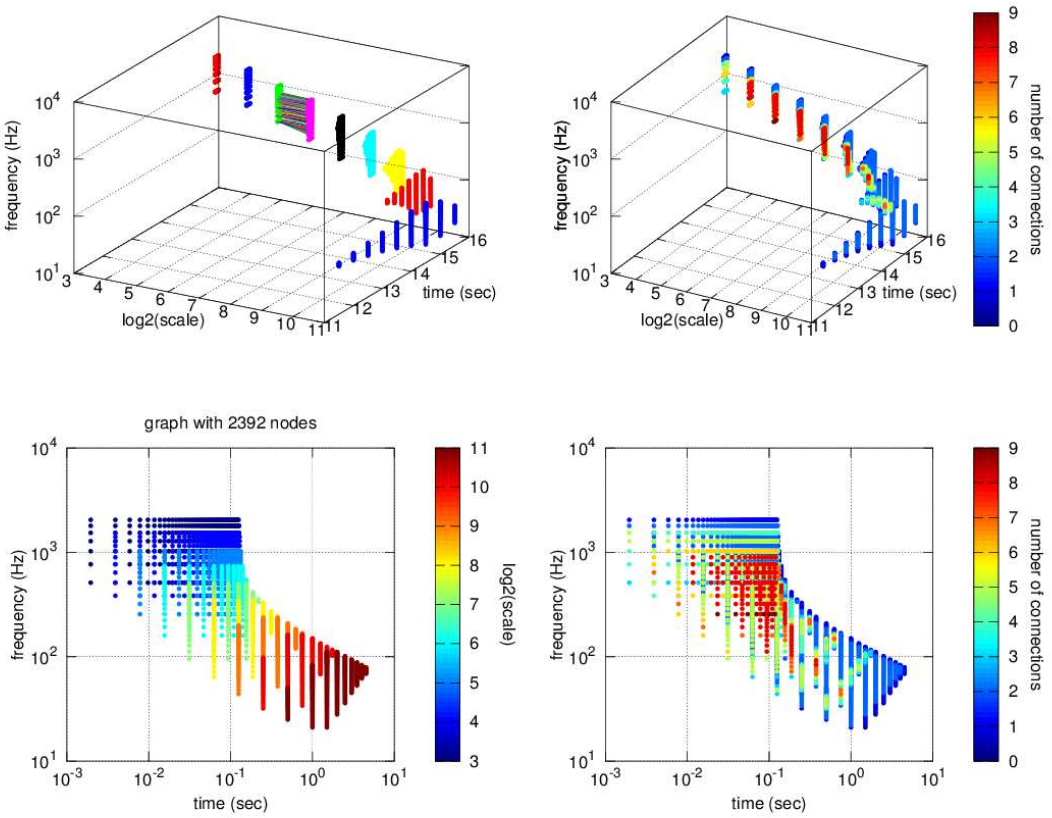

FIGURE 3.13 – **Graphe d'ondelettes pour les chirps newtoniens de binaires compactes coalescentes**. On considère ici les binaires d'objets de masses égales dans la gamme $[1.4M_\odot - 25M_\odot]$. (droite) Cœfficients en ondelettes sélectionnés à chaque échelle. (gauche) Connectivité du graphe.

Chapitre 4

Vers une astrophysique multi-messager avec les ondes gravitationnelles

Les sources d'OG transitoires sont associées à des phénomènes cosmiques violents (coalescences ou effondrement gravitationnel). Il est probable que ces phénomènes soient aussi à l'origine de rayonnement électromagnétique et/ou de rayons cosmiques de haute énergie (particules chargées et neutrinos). L'observation d'une contrepartie électromagnétique ou neutrino à un événement gravitationnel aurait un impact important puisqu'elle viendrait confirmer l'origine astrophysique de cet événement.

À l'instar de l'astrophysique multi longueur d'onde, l'*astrophysique multi-messager* réalisée en combinant des signaux électromagnétique, OG et neutrino permet une vision et une compréhension plus complète des processus ainsi observés. En effet, chaque messager porte des renseignements complémentaires sur la source. Les OG sont liées à la dynamique de la distribution de masse ; le rayonnement électromagnétique résulte des processus micro-physique ayant lieu en surface des objets astrophysiques ou dans la matière qui y en est éjectée tandis que les neutrinos signent des phénomènes d'interaction et désintégration de particules.

De telles observations combinées peuvent potentiellement lever le voile sur des questions importantes comme par exemple, celle de l'origine des sursauts gamma pour laquelle nous ne disposons aujourd'hui que des présomptions.

Suite à mon arrivée au laboratoire AstroParticule et Cosmologie, j'ai contribué au développement d'une astrophysique multi-messager avec les ondes gravitationnelles à travers les deux projets qui sont décrits dans ce chapitre. Le premier présenté en Sec. 4.1 consiste en la recherche conjointe d'OG et de neutrinos de haute énergie. Le second présenté en Sec. 4.2 concerne le suivi électromagnétique d'événements candidats OG à l'aide de télescopes robotisés et s'accompagne de la recherche du transitoire optique associé.

4.1 Ondes gravitationnelles et neutrinos de haute énergie

Ce travail a été effectué en collaboration avec le groupe ANTARES, l'équipe de coherent WaveBurst, notamment Francesco Salemi (Albert-Einstein-Institute, Hanovre Allemagne) et Gabriele Vedovato (Laboratori Nazionali di Legnaro, Padoue Italie) et le groupe de Szabolcs Márka (Columbia University, NYC US). Il est associé à la thèse de doctorat de Boutayeb Bouhou que j'ai dirigée avec Antoine Kouchner. Il a donné lieu à de multiples publications dont un article [18] (voir en annexe C.4) signé par les collaborations LIGO, Virgo et ANTARES.

De 2009 à 2014, j'ai assuré le rôle de co-ordinateur du groupe de travail GWHEN où s'est déroulé ces activités.

4.1.1 Contexte et motivations

Le neutrino est une particule élémentaire de spin demi-entier. Il est produit lors de désintégrations radioactives (par exemple, la désintégration bêta) et dans certaines réactions nucléaires. Grâce à sa neutralité et sa faible masse, le neutrino interagit faiblement avec les autres particules et champs. Ceci lui permet de s'échapper des environnements denses tels que l'intérieur des étoiles ou d'objets astrophysiques plus compacts. La détection de neutrinos en provenance de sources astrophysiques reçoit un grand intérêt depuis plusieurs dizaines d'années. L'astronomie neutrino est étroitement liée à la physique des rayons cosmiques. L'observation de neutrinos cosmiques de haute énergie (au delà du TeV) fournirait des indications importantes sur leur origine. De nouveaux détecteurs tels que ceux que nous décrivons en Sec. 4.1.2 permettent l'émergence d'une nouvelle astronomie utilisant les neutrinos de haute énergie (NHE).

Nous nous intéressons ici à l'éventuelle observation en coïncidence de NHE et OG. Nous commençons ici par discuter des possibles sources astrophysiques communes. Nous verrons que beaucoup des scénarios évoqués sont directement reliés à ceux qui sont proposés pour expliquer les sursauts gamma [27].

Sources jointes d'ondes gravitationnelles et neutrinos de haute énergies

Nous extrayons ici de la liste des sources d'OG présentées en Sec. 1.3, celles qui conduisent possiblement à l'émission de NHE. Nous prêtons une attention particulière à celles qui, pour des raisons d'opacité ou de limitations d'observation, pourraient ne pas laisser de trace dans les observations électromagnétiques.

Supernova gravitationnelle associée à un jet faiblement relativiste

Une connexion a pu être établie entre supernovas gravitationnelles et sursauts gamma longs [132]. Le modèle de la "boule de feu", communément invoqué pour expliquer les sursauts gamma, fait intervenir un jet relativiste de plasma. Les observations gamma proviennent du rayonnement synchrotron émis par des électrons accélérés lors de collisions entre inhomogénéités dans le jet.

Les observations gamma sont généralement en accord avec l'émission de jets ultra-relativistes de facteur de Lorentz $\Gamma \gtrsim 100$. Il est possible qu'une fraction importante des supernovas gravitationnelles soit associée à des jets moins extrêmes, avec $\Gamma \sim 2-3$. Cette hypothèse est étayée par l'observation, pour certaines supernovas, d'une rémanence radio en l'absence d'un sursaut gamma [113]. Les jets faiblement relativistes peuvent ne pas être suffisamment puissants pour percer l'enveloppe de l'étoile [26]. C'est l'hypothèse à la base du modèle de "sursaut gamma étranglé" ("choked GRB"). Si le jet n'émerge pas, cela atténue ou supprime le sursaut gamma ainsi que les rémanences associées (radio, infrarouge, optique ou X).

Le modèle du sursaut étranglé pourrait expliquer certains sursauts longs de luminosité nettement plus faible. Les sursauts sous-lumineux sont situés à des distances bien inférieures que les sursauts standard (SN 1998bw à des décalages vers le rouge $z = 0.0085$ soit 40 Mpc, SN 2003lw à $z = 0.105$, et SN 2006aj à $z = 0.033$). S'il s'agit effectivement d'une population distincte, sa densité est alors d'un ordre de grandeur plus grande que celle des sursauts longs conventionnels.

Si des protons p sont accélérés dans le jet de la même manière que les électrons, les interactions pp et $p\gamma$ produisent des kaons et des pions qui produisent ensuite des neutrinos en se désintégrant [26, 118]. On estime que 20% de l'énergie des protons est ainsi convertie en neutrinos. Une source située à 10 Mpc qui accélère un jet d'énergie cinétique 3×10^{51} erg à un facteur de Lorentz de 3, conduit à ~ 30 événements dans un détecteur actuel couvrant un volume de l'ordre du km^3 [26].

Nous avons déjà discuté de l'émission OG associée à l'effondrement d'étoile massive en Sec. 1.3.2. Nous mentionnons ici deux modèles extrêmes possiblement accessibles aux observations actuelles.

En présence d'une grande vitesse de rotation, des instabilités de mode barre peuvent se développer donnant lieu à une émission OG accrue. Dans [72], la puissance ainsi émise est estimée à $P_{max} = 10^{53}$ erg/s à $f = 1$ kHz. Si la barre reste stable pendant ~ 100 cycles de révolution, ceci conduit à une énergie émise de l'ordre de $10^{-2} M_\odot$.

Une rotation extrême peut entraîner la formation de fragments ($< 1 M_\odot$) ce qui conduit alors à une émission OG similaire à celle d'une binaire [65]. Si l'on considère que $\sim 1\%$ de la masse au repos est émise sous forme d'OG pendant la coalescence, nous obtenons ici aussi une énergie rayonnée de l'ordre de $\sim 10^{-2} M_\odot$ mais, cette fois, autour du pic de sensibilité de LIGO et Virgo, à des fréquences autour de la centaine de Hertz.

En conclusion, les supernovas gravitationnelles associées un jet faiblement relativistes sont des sources prometteuses d'OG et NHE. Elles sont possiblement issues d'une grande population locale et leur opacité les masque potentiellement des observations électromagnétiques.

Autres sources

Les sursauts courts sont probablement associés aux coalescences de binaires compactes (étoiles à neutrons et trous noirs) [132]. Sous l'hypothèse d'une charge baryonique dans le jet, cela devrait en principe donné lieu à une émission NHE. On ne dispose

cependant pas d'estimation du niveau d'émission. L'émission OG est, par contre, bien connue (voir en Sec. 1.3.1).

Parmi les autres sources d'émission jointe OG et NHE, on peut citer les répéteurs gamma doux (SGR). Selon le modèle actuellement préféré du "magnetar", ces objets seraient des étoiles à neutrons fortement magnétisées $B \gtrsim 10^{15}$ G. La soudaine libération de grande quantité d'énergie suite à la reconfiguration du champ magnétique interne de l'étoile conduit à la rupture de la croûte rigide et à l'éjection de particules qui donnent lieu à l'émission X et γ observée [88] et en présence de baryons, possiblement aussi à celle de NHE. L'impulsion causée par la rupture de la croûte peut également entraîner l'excitation des modes fondamentaux de l'étoile qui sont amortis par émission gravitationnelle [60,84].

Parmi les sources plus exotiques, on peut évoquer les cordes cosmiques. Les cordes cosmiques sont des défauts topologiques formés lors de transitions de phase de grande unification dans l'univers primordial. La désintégration des boucles issues de reconnections de cordes cosmiques conduit à l'émission d'OG ainsi que celle de particules (des neutrinos, en particulier) jusqu'à l'échelle de Planck [63].

Délai entre les émissions gravitationnelle et neutrino

Les scénarios astrophysiques évoqués dans les précédentes sections sont étroitement liés aux sursauts gamma. C'est pourquoi nous choisissons d'utiliser les sursauts gamma pour caractériser le délai entre émissions OG et NHE. Grâce à une étude statistique d'un catalogue rassemblant des sursauts observés par BATSE, Swift et le Fermi LAT [31] nous avons déterminé une borne supérieure à ce délai, $\Delta t_{\mathrm{GWHEN}} = [-500s, +500s]$. Cette borne englobe une vaste gamme de modèles d'émission OG et NHE pour les sursauts (voir Fig. 4.1). La fenêtre de coïncidence entre observation OG et NHE qui est utilisée ici découle de cette étude.

4.1.2 Télescopes à neutrinos de hautes énergies

À cause de la très petite section efficace du neutrino et la décroissance rapide en loi de puissance des spectres astrophysiques aux hautes énergies, l'astronomie NHE requiert l'instrumentation de très grands volumes ($\sim$ km^3) de matériau cible. Les détecteurs actuels utilisent l'eau (de mer ou des lacs) et la glace des calottes polaires. Les NHE sont détectés indirectement par la lumière Cherenkov émise par les muons secondaires produits lors de l'interaction à courant chargé du neutrino avec un noyau dans l'environnement du détecteur lorsque ceux-ci pénètrent la cible (eau ou glace) transparente. On profite alors du fait que la trace du muon peut s'étendre sur plusieurs kilomètres, ce qui augmente d'autant le volume effectif du détecteur. Les télescopes à neutrinos basés sur ce principe sont des matrices tridimensionnelles de photo-multiplicateurs assemblés sur des câbles verticaux eux-mêmes répartis sur une grille quadrillant régulièrement la surface terrestre. La connaissance du temps de passage et de l'amplitude des impulsions lumineuses reçues par les photo-multiplicateurs permet de reconstruire la trajectoire du muon et ainsi celle du neutrino incident.

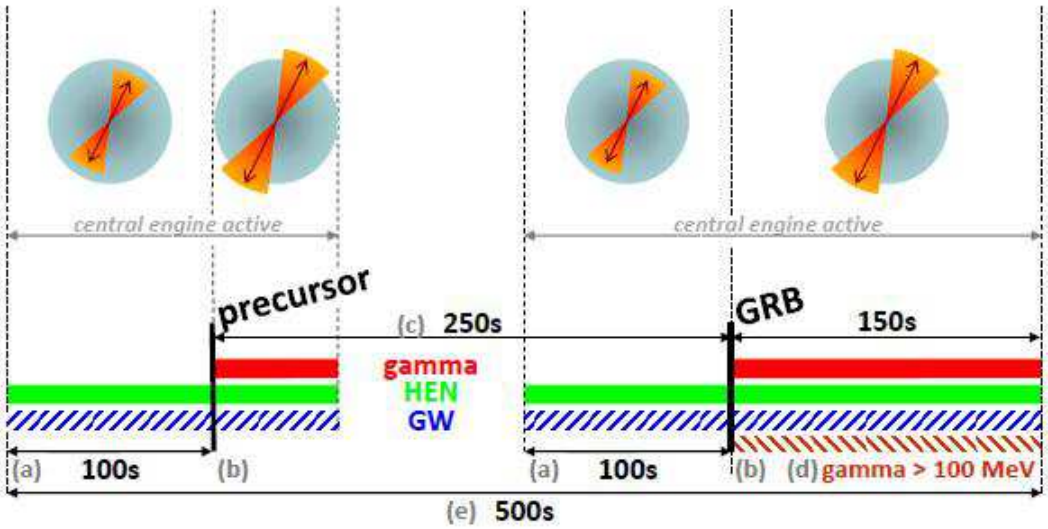

FIGURE 4.1 – **Description des phases d'émissions EM, OG et NHE associées aux sursauts**. Durant les périodes entre (a) et (b) (indiquées ici pour le sursaut et son éventuel précurseur, typiquement distants (c) de 250 sec), le jet progresse vers les couches externes de l'étoile jusqu'à en percer l'enveloppe. Il y a alors une émission γ qui s'étend sur la période (d). Les émission OG et NHE sont associées aux phases d'activités du cœur de la source et s'étend donc sur toute la durée (e) soit 500 sec. La fenêtre [-500s ; 500s] englobe donc tous les cas de figure. (Adapté de [31])

Ces détecteurs doivent faire face à un fond de muons provenant des gerbes atmosphériques dues à l'interaction des rayons cosmiques avec l'atmosphère. C'est pour cette raison qu'ils sont installés à de grandes profondeurs sur le fond de la mer ou des lacs profonds, ou encore sur la base du glacier antarctique. Ces détecteurs sont également optimisés pour détecter les muons montants produits par des neutrinos ayant traversé la Terre. La matière au dessus (l'eau ou la glace) et en dessous (la Terre) du détecteur agit comme un bouclier réduisant le fond des muons atmosphériques.

Comme les détecteurs d'OG, les télescopes à neutrinos ont un champ de vue très large qui correspond à 2π sr aux énergies 100 GeV $\leq E_\nu \leq$ 100 TeV.

Trois télescopes à neutrinos sont en fonction dans le monde actuellement. Le plus avancé est IceCube [77]. Il a récemment atteint sa configuration finale avec 86 lignes qui instrumentent 1 km^3 de glace au Pôle Sud à des profondeurs entre 1500 m et 2500 m. ANTARES [19] est déployé à des profondeurs entre 2000 m et 2500 m dans la Mer Méditerranée près de Toulon (France). Il opère dans sa configuration complète (12 lignes) depuis mi 2008. Le consortium européen KM3NeT (auquel les équipes d'ANTARES appartiennent) ambitionne la construction d'un détecteur à l'échelle du km^3 en Méditerranée [89].

Des revues récentes sont consacrées à l'astronomie avec les NHE pour plus de détails [23, 58].

4.1.3 Recherches jointes d'ondes gravitationnelles et de neutrinos de haute énergie

Fin 2007, LIGO et Virgo ont conclu une première prise de données conjointe. Durant cette période, ANTARES opérait dans une configuration incomplète avec cinq lignes uniquement. Afin d'arriver à un résultat rapidement, des outils d'analyse existant ont été réutilisés. Les candidats neutrinos (une centaine) proviennent d'une sélection déjà faite pour une recherche de sources ponctuelles. La recherche d'OG en coïncidence avec ces candidats neutrinos a été réalisée grâce à la chaîne d'analyse conçue pour le suivi des sursauts gamma. Cette première recherche a donné lieu à une publication [18] (voir en annexe C.4) et plusieurs présentations dans les conférences internationales.

Durant 2009-2010, LIGO et Virgo ont conduit une seconde prise de données conjointe. Durant cette période, ANTARES opérait dans sa configuration finale avec douze lignes. La sélection des candidats neutrinos utilise un nouvel algorithme de reconstruction qui, par rapport à la précédente analyse, améliore l'efficacité de sélection ainsi que la précision angulaire de reconstruction. Un nouvel algorithme de recherche d'OG a été développé en se basant sur la chaîne d'analyse cohérent WaveBurst (cf. Sec. 3.4) habituellement utilisée pour les recherches plein-ciel. Cette chaîne d'analyse est beaucoup plus rapide que la précédente et permet d'effectuer, en un temps plus court, la recherche d'OG associée à un plus grand nombre de candidats neutrino (un millier) sur une bande fréquentielle plus large (allant jusqu'à 2 kHz plutôt que 500 Hz pour la première recherche) englobant ainsi la signature des supernovas gravitationnelles, la source prévalente ici.

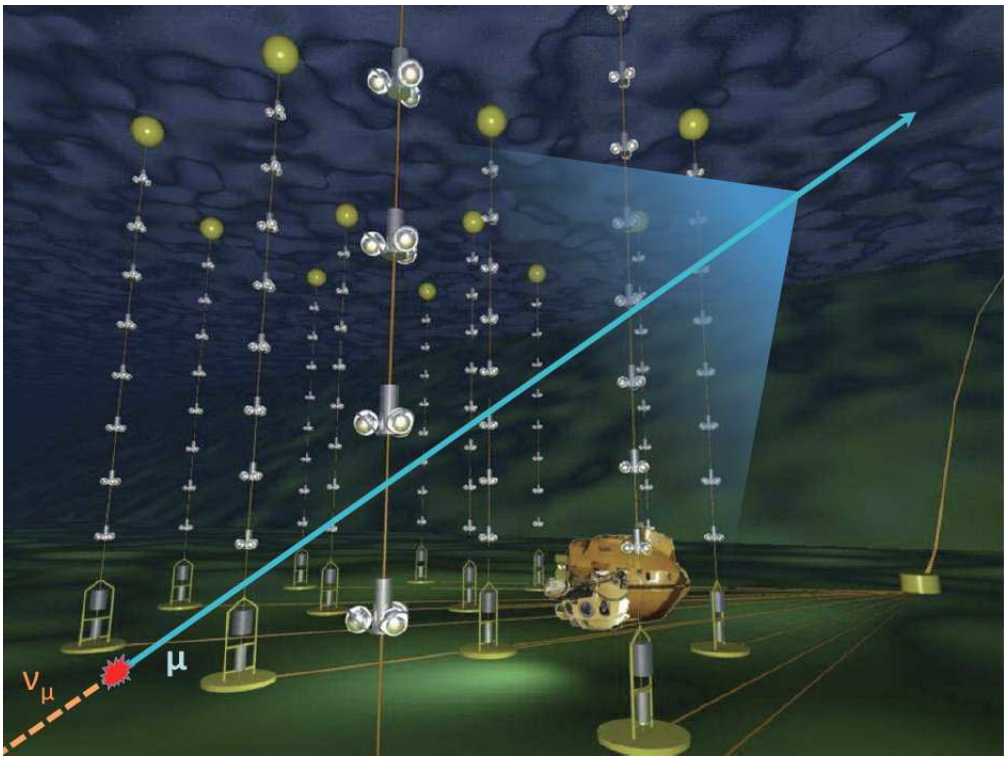

FIGURE 4.2 – **Vue schématique du détecteur ANTARES** avec une illustration du principe de détection : un neutrino ν_μ montant interagit avec la roche environnante et produit un muon qui traverse le détecteur en émettant un cône de lumière Cherenkov qui est détecté par la matrice de capteurs optiques. ANTARES est constitué de 12 lignes instrumentées qui sont ancrées au fond marin à 2475 m de profondeur. Il se situe à 40 km au large de Toulon (France).

Première recherche conjointe d'ondes gravitationnelles et neutrinos de haute énergie avec les données de 2007

Le premier jeu de données concerne la période allant du 27 janvier au 30 septembre 2007 avec ANTARES 5L et LIGO S5, et inclus Virgo VSR1 à partir de 18 mai. La stratégie choisie pour ce jeu de données est une recherche d'OG coïncidente événement par événement calquée sur celle qui est utilisée pour les sursauts gamma.

Sélection des candidats neutrinos Un total de 216 candidats ont été reconstruits par la méthode BBFit [20] dont 18 avec les données de trois lignes et plus, et 198 de deux lignes uniquement. Dans ce dernier cas, le problème de reconstruction est dégénéré sous les hypothèses de BBfit ce qui donne deux solutions symétriques dans le plan azimutal. L'erreur angulaire de reconstruction de la direction d'arrivée dépend de l'énergie et de la direction de l'événement. La distribution de cette erreur a été calculée par intervalle de déclinaison et d'énergie puis ajustée dans chaque intervalle par une loi log-normale. L'erreur angulaire est définie par le quantile à 90 % de cette loi. Elle est typiquement égale à 12°.

Suivi OG des candidats neutrinos En utilisant la fenêtre de coïncidence décrite en Sec. 4.1.1, on identifie 158 candidats NHE (14 avec 3 lignes et plus, 144 avec deux) sont coïncidents avec les données de deux détecteurs d'OG ou plus. Pour chacun de ces candidats, le suivi OG est réalisé par X-Pipeline [126], une chaîne d'analyse initialement conçue pour une recherche similaire en association avec les sursauts gamma.

X-pipeline réalise une détection d'excès d'énergie dans une représentation temps-fréquence obtenue via la transformée de Fourier à court-terme des données combinées de manière cohérente (voir Sec. 3.3.2). On sélectionne un segment "on-source" de durée ±496 s compatible avec le délai OG–NHE maximal calculé en Sec. 4.1.1 et un segment "off-source" (±1.5 heures autour du temps du NHE). Ce dernier segment est utilisé pour l'optimisation de la statistique, des paramètre d'analyse et des coupures afin de maximiser l'efficacité de détection événement par événement. Il est également utilisé pour l'estimation empirique du fond d'analyse calculé en répétant celle-ci quelques milliers de fois sur le grand volume de données de substitution obtenu par l'application de délais temporels non-physiques aux données réelles d'un ou plusieurs détecteurs. De ce fond, on déduit la p-valeur d'un événement OG et ainsi sa signification statistique.

Deux types d'analyse ont été conduites : l'une limitée à 500 Hz est appliquée à tous les neutrinos sans exception et l'autre étendue à 2 kHz est appliquée uniquement aux NHE reconstruits avec 3 lignes et plus pour des raisons de coût de calcul. Aucun candidat OG n'a été observé.

Post-traitement et interprétation astrophysique La sensibilité de la recherche OG est déterminée par une simulation de Monte-Carlo consistant à répéter l'analyse sur le segment "on-source" après l'ajout de signaux OG simulés (injection). L'efficacité évaluée en Fig. 4.3 est obtenue en fixant le seuil de détection au niveau de l'événement de

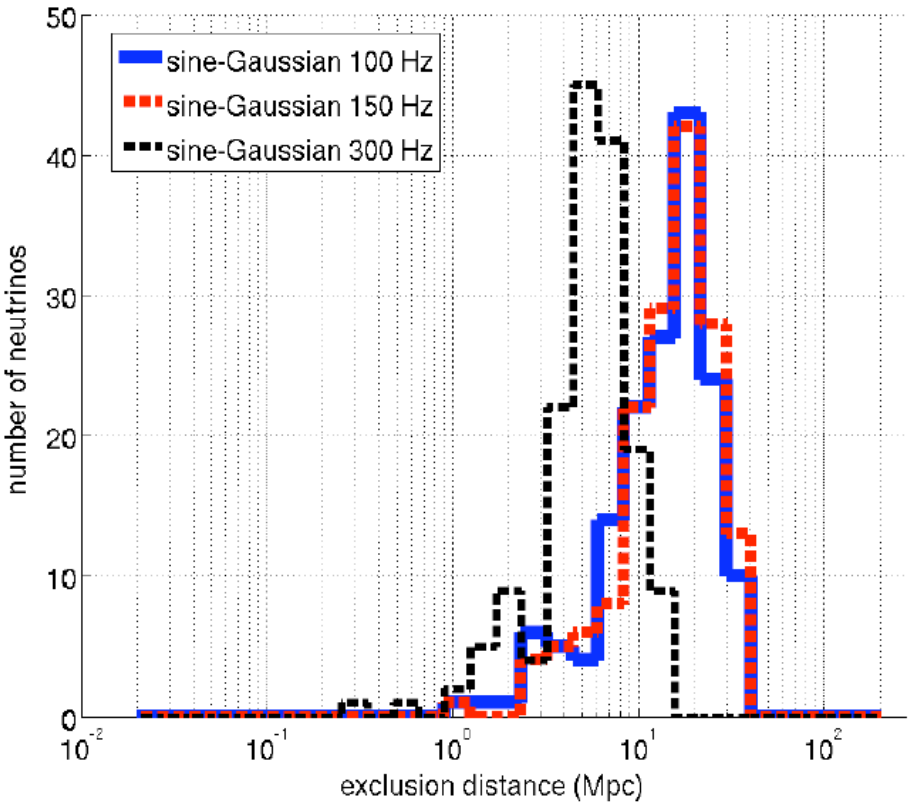

FIGURE 4.3 – **Distribution des distances d'exclusion** calculées pour chaque NHE pour un modèle d'émission transitoire monochromatique (fréquence allant de 100 à 300 Hz) et une énergie émise égale à $E_{GW} = 10^{-2} M_{\odot}$.

plus grande amplitude détecté dans le segment "on-source". À partir de ce résultat calculé pour chaque NHE, nous définissons une distance d'exclusion $D_{90\%}$ comme la distance où l'efficacité atteint 90 %. Fig. 4.3 donne la distribution des distances d'exclusion obtenue en injectant des ondelettes de Morlet (sine-Gaussian) polarisées circulairement et normalisées pour avoir une énergie émise $E_{GW} = 10^{-2} M_{\odot}$ (cf. Éq. (1.11) en Sec. 1.2.3). Ceci correspond à une limite optimiste de l'émission OG lors d'un effondrement de cœur stellaire d'étoile massive en rotation. La distance d'exclusion est typiquement $D_{90\%} \sim 20$ Mpc à 150 Hz. Notons que l'on peut déduire cette distance pour des sources plus ou moins puissantes en utilisant la relation $D_{90\%} \propto E_{GW}^{1/2}$.

La possibilité d'une accumulation de signaux faibles a été aussi examinée par l'utilisation d'un test binômial. Sous hypothèse nulle, la distribution de p-valeurs des événements OG détectés pour l'ensemble des NHE est uniforme entre 0 et 1. Le test binômial compare cette distribution de référence à celle des p-valeurs mesurées et détermine s'il y a un écart significatif dû à une ou plusieurs de ces p-valeurs. Fig. 4.4 présente le résultat

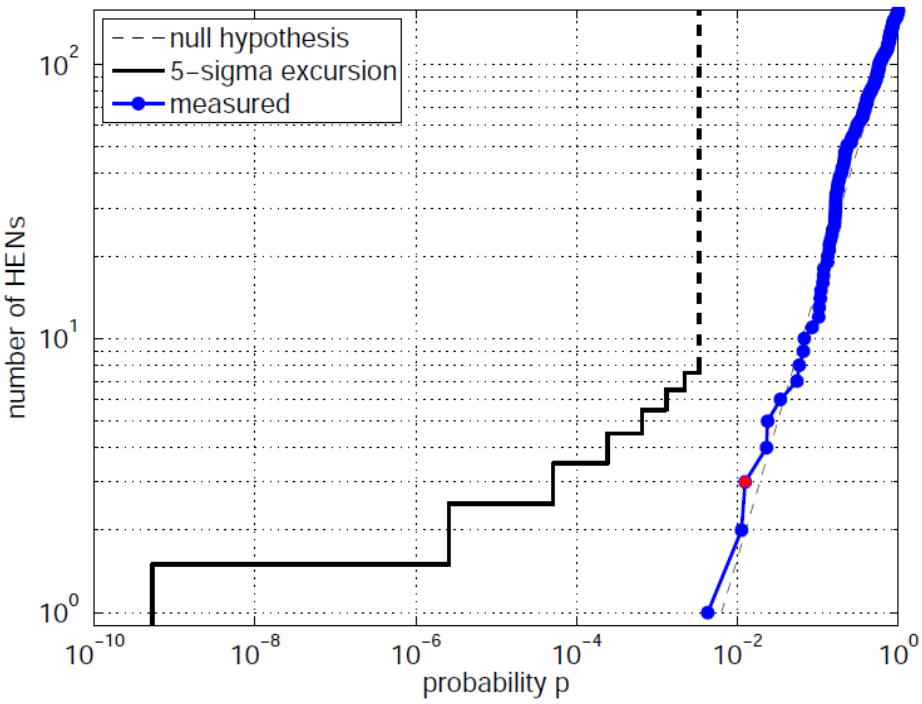

FIGURE 4.4 – **Test binômial permettant de vérifier une éventuelle accumulation de signaux faibles associés à un sous-ensemble de candidats NHE**

de ce test qui est négatif avec une signification post-trial de l'écart le plus important de 66 %.

Cette recherche n'ayant révélé aucune détection, la limite à 90 % de niveau de confiance sur le taux de coïncidence OG–NHE détectable est $2.3/T_{obs}$ où la durée d'observation est $T_{obs} \approx 90$ jours. Ceci peut être traduit en une limite sur la densité de source (par unité de volume et de temps)

$$\rho_{\mathrm{GWHEN}} \leq \frac{2.3\mathcal{F}_b}{VT_{obs}} \tag{4.1}$$

où $\mathcal{F}_b$ désigne le facteur de collimation de la source ($\mathcal{F}_b \approx 300$ pour une ouverture angulaire de 5°) et V est le volume d'univers observé.

Le volume d'univers est contraint à la fois par la sensibilité des observations NHE et OG. Si l'on considère une source NHE qui suit les prédictions de [76] pour les sursauts longs, on obtient un horizon à 50 % d'efficacité $d_{50\%} \sim 12$ Mpc pour ANTARES 5 lignes. En se plaçant dans un modèle optimiste d'émission OG avec $E_{GW} = 10^{-2} M_\odot$ et le cas le plus favorable (émission aux fréquences voisines de 150 Hz), l'horizon OG est plus grand et s'étend à ~ 20 Mpc. On en déduit $\rho^{LGRB}_{\mathrm{GWHEN}} \lesssim \mathcal{F}_b E_{0.01}^{-3/2} \times 10^{-3}$ Mpc^{-3} yr^{-1}. Cette limite se situe bien au dessus des limites actuelles sur la densité des sursauts longs ($\sim 10^{-8}$ Mpc^{-3} yr^{-1}) mais approche celles des supernova Ib/c ($\sim 10^{-5}$ Mpc^{-3} yr^{-1}).

Développements méthodologiques et application au jeu de données 2009-2010

La deuxième prise de données concerne la période du 7 juillet 2009 au 20 octobre 2010, (soit 266 jours d'observation) avec ANTARES 12 L (configuration complète) ce qui coïncide avec LIGO S6 Virgo VSR2/3.

Un nouveau schéma d'analyse a été développé pour ces données. La reconstruction des candidats NHE utilise l'algorithme Aafit [2] utilisant une méthode au maximum de vraisemblance. Nous avons adapté la chaîne d'analyse `coherent WaveBurst` (cf. Sec. 3.4) afin qu'elle puisse effectuer une analyse déclenchée des données OG. Grâce à son efficacité numérique, cette nouvelle procédure nous permet d'effectuer plus rapidement la recherche d'OG associées à un plus grand nombre de candidats neutrino sur une bande fréquentielle élargie. Enfin, la sélection initiale des candidats NHE résulte de l'optimisation du pouvoir de découverte de la recherche conjointe, ce que nous détaillons dans la section suivante.

Principe d'optimisation jointe des coupures À probabilité de fausse alarme fixée, les efficacités des coupures NHE et OG varient en sens opposé. En effet, si l'on relâche les coupures NHE, on améliore l'efficacité de la sélection. On augmente aussi le nombre de candidats NHE ce qui entraîne l'augmentation du volume de données OG à analyser et ainsi celle de la probabilité d'une fausse détection accidentelle. Pour maintenir cette probabilité constante, on est alors contraint de renforcer les coupures OG ce qui diminue l'efficacité OG. Nous proposons une méthode d'optimisation qui trouve un compromis à ce problème.

L'approche est de maximiser le pouvoir de découverte de la recherche que nous quantifions par le nombre de sources OG et NHE détectables $\mathcal{N}_{\mathrm{GWHEN}}$. On considère une population isotrope de sources transitoires identiques émettant une énergie E_{GW} en OG et une fluence φ_ν en NHE. Soit R sa densité par unité de temps et de volume. On a alors

$$\mathcal{N}_{\mathrm{GWHEN}}(\mathrm{cuts}) = \iint dt d^3\Omega\, \mathcal{R}(r,t)\epsilon_\nu(\mathrm{cuts})\epsilon_{GW}(\mathrm{cuts}; E_{GW}, r) \tag{4.2}$$

où $\mathcal{R}(r,t) = R\mathcal{P}(N_\nu > 0|\varphi_\nu/(4\pi r^2))$ est la densité des sources détectables. Des propriétés de la statistique de Poisson, nous déduisons $\mathcal{P}(N_\nu > 0|\varphi_\nu/(4\pi r^2)) \propto 1/r^2$ dans la limite des faibles flux.

Les coupures "cuts" font référence au seuil appliqué sur le paramètre de qualité de la reconstruction de la trace du muon Λ et sur le paramètre ρ de l'analyse OG qui est proportionnel au rapport signal-sur-bruit. On obtient

$$\mathcal{N}_{\mathrm{GWHEN}}(\Lambda, \rho_{threshold}) \propto \int_0^\infty 4\pi r^2 dr\, \frac{1}{r^2}\epsilon_\nu(\Lambda)\epsilon_{GW}(\rho_{threshold}; E_{GW}, r) \tag{4.3}$$

où nous avons éliminé les termes constants comme ceux qui résultent de l'intégrale en temps.

La forme typique suivie par $\epsilon_{GW}(\rho_{threshold}; E_{GW}, r)$ en fonction de r pour un seuil et une énergie E_{GW} donnés présente une transition franche (en moins d'une décade) entre

100% et 0% (voir e.g., Figures 3 et 4 de [8]). Cette courbe peut donc être raisonnablement bien approchée par un échelon à la transition $D(\rho_{threshold})$ correspond à l'horizon OG.

Éq. (4.3) peut donc être ré-écrit comme

$$\mathcal{N}_{\mathrm{GWHEN}}(\Lambda, \rho_{threshold}) \propto \epsilon_\nu(\Lambda) \int_0^{D(\rho_{threshold})} dr. \tag{4.4}$$

Pour des sources rayonnant en OG une énergie donnée, le paramètre $\rho_{threshold}$ qui définit la plus petite amplitude OG détectable est inversement proportionnel à $D(\rho_{threshold})$. Nous obtenons ainsi

$$\mathcal{N}_{\mathrm{GWHEN}}(\Lambda, \rho_{threshold}) \propto \epsilon_\nu(\Lambda)/\rho_{threshold}, \tag{4.5}$$

qui donne une expression simple du facteur de mérite en fonction des coupures à optimiser.

Mise en œuvre de l'optimisation jointe des coupures On détermine le point de fonctionnement de l'optimisation en fixant la probabilité de coïncidence fortuite (en temps et direction) entre événements du fond OG et NHE à FAP$= 4.7 \times 10^{-3}$ ce qui correspond une excursion de "2σ".

L'efficacité ϵ_ν et le nombre N de candidat NHE sont obtenues en fonction de Λ par une simulation de Monte-Carlo ajustée pour reproduire les caractéristiques des données d'ANTARES.

Pour chaque valeur de N dans une gamme prédéfinie, on calcule le taux de fausse alarme par

$$\mathrm{FAR}_{GW} = \frac{\mathrm{FAP}}{N\Delta T}, \tag{4.6}$$

où ΔT est la durée de la fenêtre de coïncidence (cf. Sec. 4.1.1).

Cette valeur cible est comparée au fond empirique d'une recherche dirigée utilisant N neutrinos. On estime ce fond à partir de celui qui a été calculé pour la recherche pleinciel [8] en appliquant une correction par le facteur $\sim (\Omega_{GW}^{1/2} + \Omega_{HEN}^{1/2})^2/(4\pi)$ où Ω_{GW} et Ω_{HEN} sont les angles solides sous les boîtes d'erreur OG et NHE respectivement. Notons que Ω_{HEN} dépend de Λ, et donc de N. On a évalué que, pour le réseau LIGO H, LIGO L et Virgo, Ω_{GW} couvre en moyenne 425 degrés carré et est faiblement dépendant de ρ. Nous avons déterminé de manière heuristique qu'un facteur supplémentaire $\sim N/10^4 + .5$ est nécessaire pour obtenir un bon accord avec le fond observé expérimentalement.

La valeur de $\rho_{threshold}$ correspond au point où ce fond empirique est $\leq \mathrm{FAR}_{GW}$. On en déduit alors le facteur de mérite par l'Éq. (4.5) et son maximum indique l'ajustement optimal des coupures.

Le fond OG a évolué au cours de la prise de données 2009-2010 selon la configuration des détecteurs utilisés. On montre [40] que la procédure d'optimisation se généralise aisément à cette situation.

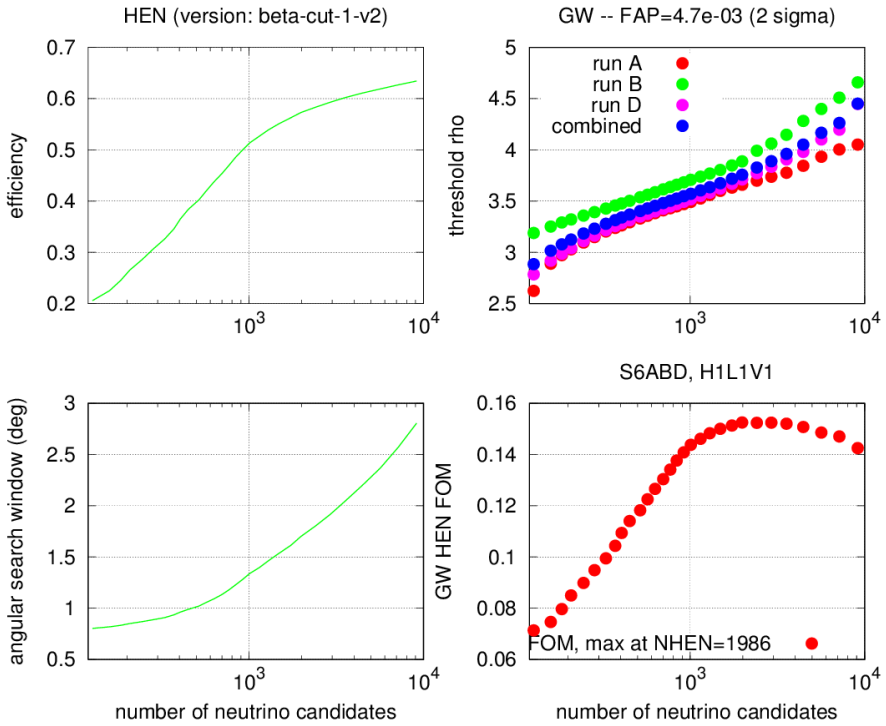

FIGURE 4.5 – **Application de la procédure d'optimisation conjointe des coupures.** (haut–gauche) Efficacité ϵ_ν des coupures NHE. (bas–gauche) Rayon de la fonction d'étalement du point mesurant l'erreur angulaire sur la reconstruction de la direction du muon incident, soit $\Omega_{HEN}^{1/2}/\sqrt{\pi}$. (haut-droite) Seuil de sélection OG assurant une probabilité de coïncidence fortuite FAP$= 4.7 \times 10^{-3}$ calculés pour les périodes A,B et D de S6 VSR2/3 où trois détecteurs OG sont disponibles. (bas-droite) Facteur de mérite défini en Éq. (4.5). Le point de coupure optimal est obtenu pour $N = 1986$.

Sélection des candidats neutrinos Fig. 4.5 présente le résultat de l'application de la procédure d'optimisation. Le point optimal correspond à la coupure $\Lambda > -5.44$ (avec la coupure auxiliaire $\beta < 1°$), soit la sélection de 1986 candidats NHE (plus d'un facteur 10 par rapport à la première recherche). L'erreur angulaire pour cette coupure est d'environ 1.6° et l'efficacité est d'environ 57 %. C'est significativement mieux que la première recherche. Il a été également évalué [40] que la surface effective est 50 % plus grande au dessous du TeV (20 % au dessus).

Suivi OG des candidats neutrinos Parmi les près de 2000 candidats NHE sélectionnés, 775 (soit 40 %) sont en coïncidence avec les données de deux ou trois interféromètres (on requiert la disponibilité d'un segment d'au moins 300 sec autour du temps d'arrivée du neutrino), suivant la répartition suivante : 303 en association avec trois détecteurs et 472 avec seulement deux.

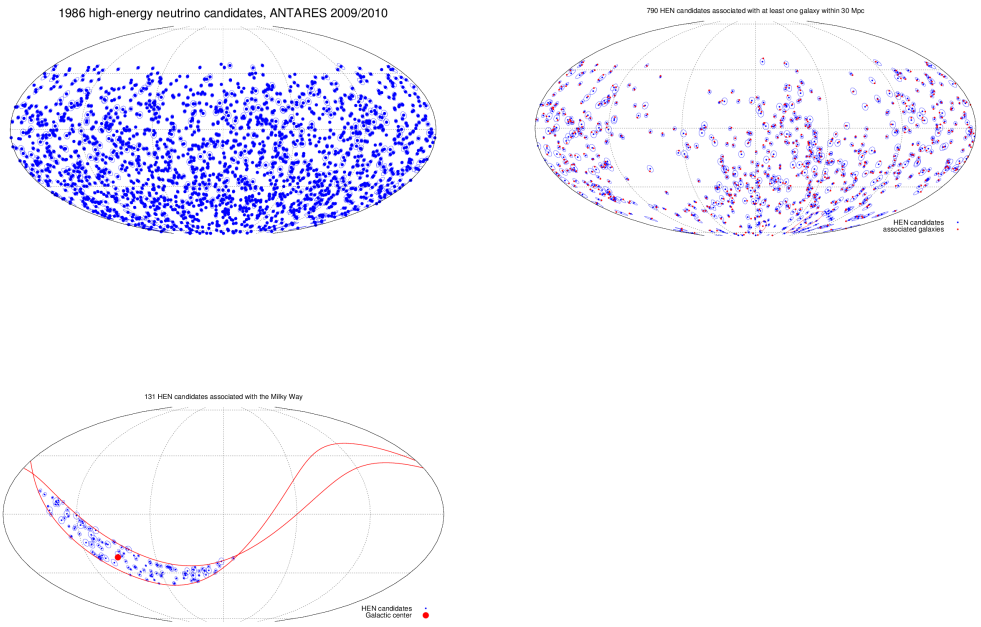

FIGURE 4.6 – **Candidats NHE sélectionnés par la procédure d'optimisation.** (haut–gauche) Cartes de tous les candidats. (haut–droite) Sous-ensemble associé à des galaxies proches. (bas–droite) Sous-ensemble associé au plan galactique.

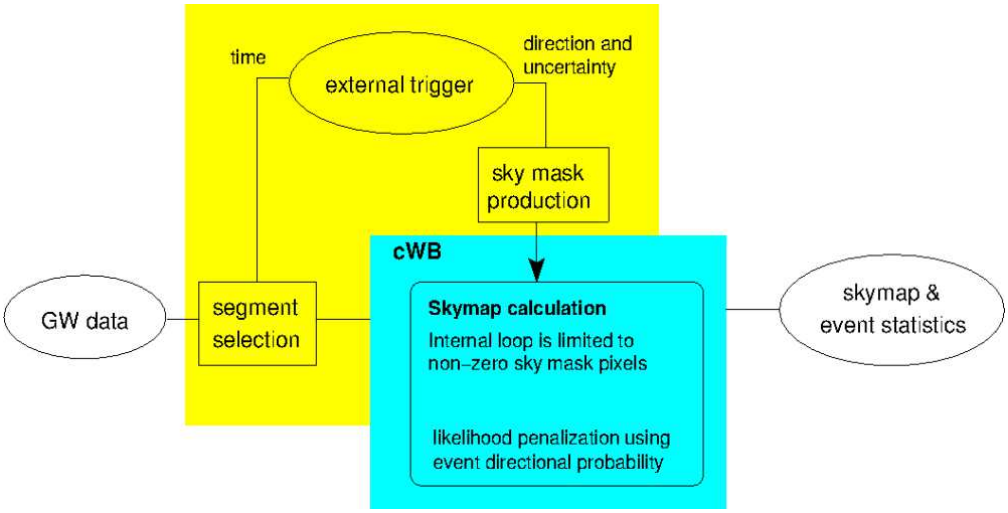

FIGURE 4.7 – **Schéma fonctionnel de la chaîne d'analyse** `skymask-cWB` présentée en Sec. 4.1.3

Nous avons effectué le suivi de chacun de ces candidats NHE dans les données de LIGO et Virgo à l'aide de la chaîne d'analyse "skymask coherent Wave-Burst" (s-cWB) développée pour l'occasion (voir Fig. 4.7 pour un schéma fonctionnel) en collaboration avec Francesco Salemi (Albert-Einstein-Institute, Hanovre Allemagne) et Gabriele Vedovato (Laboratori Nazionali di Legnaro, Padoue Italie). Celle-ci est une adaptation de coherent WaveBurst présentée en Sec. 3.4 qui reconstruit les événements OG uniquement dans une région du ciel spécifiée a priori par un masque. Ce masque directionnel est directement calculé à partir de la direction du candidat NHE et de son erreur angulaire. Pour chacun des événements OG ainsi détectés, s-cWB renvoie les même statistiques cohérentes que cWB à savoir, l'amplitude ρ, le cœfficient de corrélation net_{cc} et le déséquilibre énergétique net_{ED}. Si ces deux dernières permettent de distinguer les transitoires instrumentaux du vraie OG, la sélection finale et le calcul de la signification statistique s'effectue à l'aide de ρ.

Outre l'application du masque, une deuxième différence entre s-cWB et cWB standard est la méthode d'estimation empirique du fond. En effet, en plus de l'estimation par application de décalages temporels ("time-lags"), s-cWB permet de calculer le fond par l'échange de masque ou "skymask mixing" (i.e., un segment associé à un certain neutrino est analysé avec les masques d'autres neutrinos pointant dans d'autres régions du ciel). "Time-lags" et "skymask mixing" peuvent être éventuellement combinés. Le "skymask mixing" étant bien plus économe en calcul, ceci permet d'augmenter considérablement le nombre de réalisations de la Monte-Carlo utilisées pour l'évaluation du fond et ce à faible coût. Nous avons cependant observé que cela est limité par la corrélation de la statistique entre différentes régions du ciel (surtout pour le cas à deux détecteurs) qui empêche d'obtenir des réalisations du fond raisonnablement décorrélées les unes des autres. Pour les résultats présentés en Fig. 4.8, nous avons utilisé 201 décalages temporels

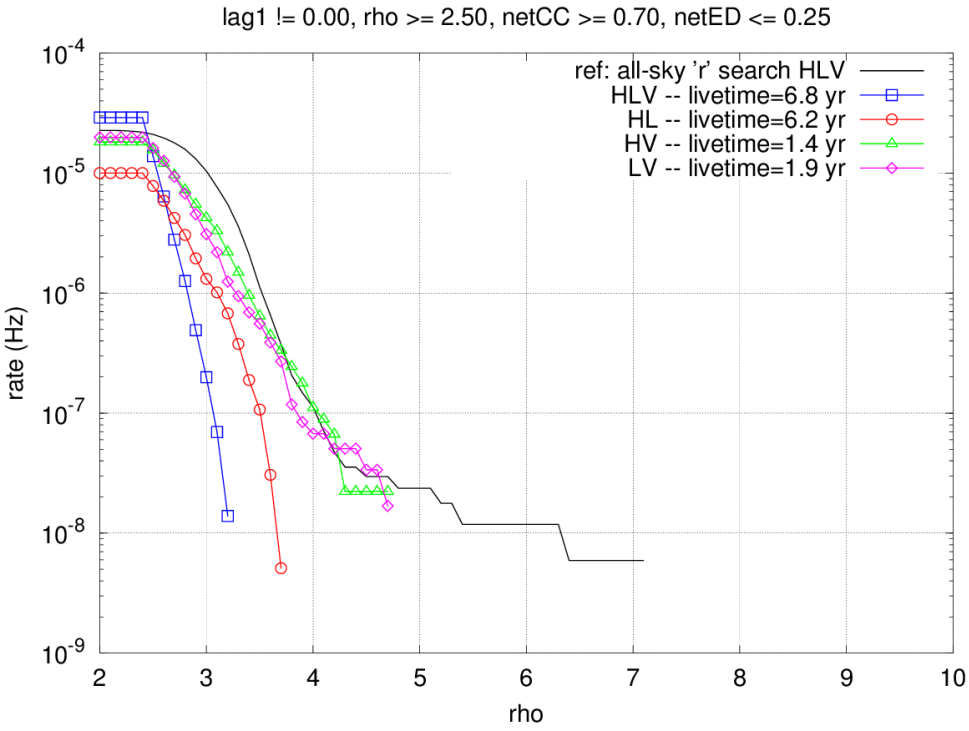

FIGURE 4.8 – **Fond de l'analyse obtenue pour la partie LIGO S6D/Virgo VSR3 et estimé par 201 décalages temporels et 10 mélanges de masque.**

et 10 mélanges de masque, soit 2010 réalisations.

Comme pour la première recherche, nous avons évalué les performances de cette nouvelle chaîne d'analyse en effectuant l'injection d'OG simulées. L'efficacité est montrée en Fig. 4.9. L'analyse finale incluant le post-traitement est en cours sous la coordination de Bruny Baret du groupe ANTARES de l'APC. La revue de l'analyse est sur le point de débuter. Pour cette raison, le résultat n'est pas connu. En cas de non détection, nous estimons que cette recherche permettrait d'améliorer d'un facteur ~ 7 les limites supérieures établies par l'analyse précédente (données 2007).

4.2 Suivi électromagnétique et recherche de transitoires optiques

Une variété de processus astrophysiques sont possiblement associés à une émission d'OG *et* électromagnétiques (EM). Ceci motive la réalisation de systèmes d'alertes produites à partir des données OG et envoyés à un ensemble de télescopes en charge d'effectuer une observation de suivi. Un tel système a fonctionné pour la première fois lors de la dernière prise de données conjointe de Virgo et LIGO (août 2009 – octobre 2010).

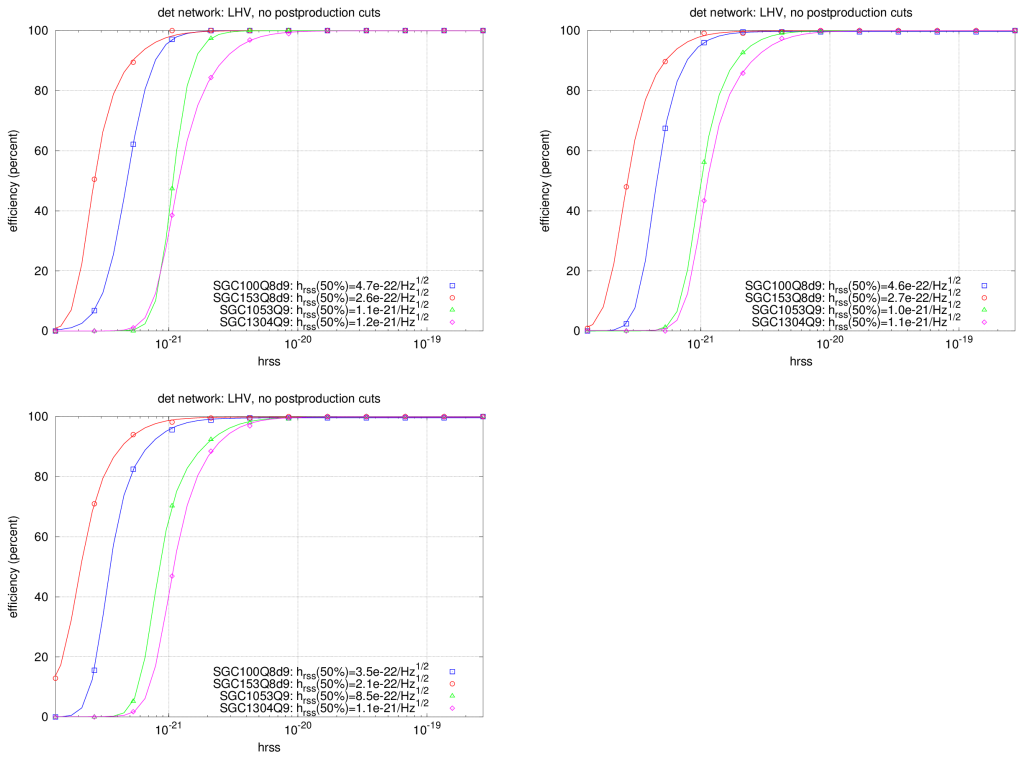

FIGURE 4.9 – **Courbes d'efficacité obtenues le réseau à trois détecteurs** (LIGO H & L et Virgo) pour les différentes parties de la prise de données où les trois instruments sont en fonction (A, B et D).

J'ai été parmi les principaux contributeurs de ce projet, en assurant le rôle de liaison avec les télescopes TAROT et Zadko. Mes contacts étaient Alain Klotz (Professeur à l'IRAP, Toulouse) et Myrtille Laas-Bourez (à l'époque, post-doctorante à l'UWA). J'ai coordonné un groupe de travail du PCHE sur ce sujet pendant trois ans. J'ai participé à la mise en place de l'accord de collaboration, du système de communication d'alertes et de son protocole et j'ai effectué le suivi des prises de données. J'ai réalisé l'analyse des images recueillies par TAROT, Zadko et QUEST en collaboration avec Marica Branchesi (post-doctorante, Univ. Urbino).

Ce projet a donné lieu à plusieurs publications au nom des collaborations LIGO et Virgo dont deux auxquelles je suis directement impliqué [5, 10] (voir en annexe C.5).

4.2.1 Sources jointes d'ondes gravitationnelles et électromagnétiques

Sursauts gamma Les sursauts gamma sont des sources très prometteuses d'émission OG et EM. Les sursauts gamma sont traditionnellement divisés en deux classes [132], les sursauts courts et longs que l'on associe à des progéniteurs différents. Les sursauts longs sont associés aux "collapsars", c'est-à-dire à l'effondrement gravitationnel du cœur d'une étoile massive, tandis que les coalescences de binaires compactes comprenant au moins une étoile à neutrons sont les candidats les plus probables des sursauts courts au vu des observations actuelles [71]. Comme décrit en Sec. 1.3, tous ces systèmes astrophysiques sont des sources potentielles d'OG.

L'émission prompte X et gamma, qui dure quelques fractions à quelques dizaines de secondes, provient de jets relativistes de plasma. Une rémanence est ensuite observée dans une vaste de gamme de longueurs d'onde s'étendant des fréquences radio aux X. La rémanence dure de l'ordre de la minute jusqu'à plusieurs jours. Pour le spectre optique qui nous intéresse ici, la luminosité de la rémanence décroît avec le temps selon une loi de puissance d'exposant ~ 1 à 1.5. À distance égale les rémanences des sursauts courts sont bien moins lumineuses que celles des sursauts longs [86, 87]. La Table 4.1 résume les modèles de rémanences considérés ici.

Il y a de fortes indications que l'émission prompte et, dans une moindre mesure, la remanence soient collimatées [132]. Les sursauts gamma sont observés dans l'axe du jet, dont l'ouverture est de $\sim 10^\circ$ pour les sursauts longs et est un peu plus large pour les sursauts courts. S'il n'y a pas encore eu de sursauts observés hors axe, des modèles [128] prédisent des courbes de lumière évidemment moins brillantes et plus lentes, avec un pic de luminosité atteint après des semaines ou des mois.

Kilonovas La fusion de deux étoiles à neutrons ou d'une étoile à neutrons avec un trou noir peut donner lieu à un transitoire du type supernova, comme décrit dans [96]. Selon ce modèle, des éléments radioactifs lourds sont formés par capture neutronique dans la matière éjectée lors de la fusion. La désintégration des isotopes ainsi produits libère de l'énergie qui chauffe l'éjection. L'émission thermique devient visible lorsque la densité permet aux photons de s'échapper, et peut être observé comme un transitoire optique globalement isotrope que certains auteurs dénomme "kilonova". Les modèles

TABLE 4.1 – **Modèles de courbe de lumière de transitoires optiques associés aux rémanences des sursauts courts ou longs et au kilonova**

Source	Modèle de courbe de lumière	Normalisation
Sursaut court	$L \propto t^{-1.1}$	23-31 mag à 1 jour et $z = 1$
Sursaut long	$L \propto t^{-1.1}$	16-24 mag à 1 jour $z = 1$
Kilonova	$L = (1.2 \times 10^{42}) t^{0.43}$ erg s^{-1} pour $t < 0.7$ jour	
	$L = (1.2 \times 10^{42}) t^{0.43}$ erg s^{-1} pour $t > 0.7$ jour	

prédisent une courbe de lumière atteignant son maximum un jour après la fusion [101,114] typiquement. Certains paramètres du modèle (comme la quantité de matière éjectée) sont mal connus et implique une incertitude sur les échelles de temps, de luminosité et les caractéristiques spectrales de ces phénomènes. La Table 4.1 résume les modèles de kilonova considérés ici.

Supernova à effondrement de cœur Parmi les sources d'OG citées en Sec. 1.3, les supernovas gravitationnelles font naturellement partie de celles qui sont associées à une contrepartie optique. Cette dernière s'étend sur une durée bien plus longue [66] (plusieurs jours ou plusieurs semaines) que les cas discutés précédemment.

LIGO et Virgo ont un horizon essentiellement limité à la Galaxie pour ce type de source. La détection d'une supernova galactique étant un phénomène d'une telle brillance qu'il ne demande pas d'observation spécifique, la stratégie observationnelle s'est concentrée sur le suivi de transitoires courts associés aux phénomènes extra-galactiques mentionnés plus haut.

Impact potentiel de l'observation d'une contrepartie EM à une OG Si la signature OG permet l'identification de la source et que l'on conclut que celle-ci est une binaire compacte coalescente, l'observation d'une contrepartie EM permet d'améliorer l'estimation des paramètres de la binaire et de lever certaines dégénérescences. Par exemple, la mesure précise de la position de la source via la contrepartie, ou celle de sa distance à travers celle de la galaxie hôte peut aider à casser la dégénérescence entre la distance de la source et son inclinaison (qui sont parfois même couplées à la position de la source).

L'association de la signature d'une binaire à un sursaut court donne une indication forte sur les progéniteurs de ces sursauts. Le rapport du nombre de binaires observées via les OG avec et sans contrepartie fournit une indication sur le facteur de collimation du jet donnant naissance aux sursauts [39]. De plus, un petit ensemble de telles observations combinées peut permettre la mesure de paramètres cosmologiques [62, 122]. En effet, la distance de luminosité s'obtient à partir du signal OG, et le décalage vers le rouge à

partir de celui du spectre de la galaxie hôte. Pris ensemble, ces mesures fournissent une estimation de la constante de Hubble dans l'univers local.

Les observations conjointes OG/EM permettent de tester l'hypothèse (faite jusqu'ici) de validité de la Relativité Générale aux grandes échelles par la vérification de la vitesse de propagation des OG et de leur polarisation [135].

Dans le cas d'un transitoire OG ne provenant pas de la fusion d'une binaire, la combinaison des observations OG et EM est également très utile. En effet, la distance de la source estimée à l'aide des données EM permet de fixer l'ordre de grandeur de l'énergie libérée sous forme d'OG. Dans le cas d'une association avec un sursaut long ou d'une supernova, il serait alors possible de contraindre ou potentiellement distinguer parmi les différents modèles de progéniteur.

4.2.2 Système d'alertes pour le suivi électromagnétique

Premier programme de suivi électromagnétique

Un premier programme de suivi électromagnétique a eu lieu courant 2009-2010 alors que LIGO et Virgo effectuaient une prise de données concomitante. Ce programme est divisé en deux grandes phases allant de décembre 2009 à janvier 2010, puis de septembre à octobre 2010.

Durant la première phase (hiver 2009), un total de huit événements OG ont été sélectionnés puis transmis aux télescopes QUEST et TAROT qui participaient à l'opération. De ces huit alertes OG, quatre ont été suivies.

Durant la deuxième phase (automne 2010), six alertes ont été transmises et quatre d'entre elles ont été suivies d'observation (voir la Table 4.2).

Deux alertes méritent d'être détaillées. L'équipe d'astreinte validant chacune des alertes avant leur transmission a immédiatement remarqué la spécificité de l'événement du 16 septembre 2010 (et notamment sa grande signification statistique). Par la suite, cet événement s'est avéré être une "injection aveugle" (c'est-à-dire un signal OG simulé ajouté secrètement aux données afin de tester la chaîne de traitement et de décision de bout en bout). Notons également l'événement du 26 septembre qui est l'événement le plus significatif au dessus de 200 Hz pour les périodes où les trois détecteurs LIGO et Virgo ont fonctionné en coïncidence. On dénombre 1 événement de ce type dans le fond de l'analyse tous les 44 jours. La durée d'observation cumulée par les trois détecteurs en coïncidence pendant cette prise de données étant de 52.2 jours, un tel événement est finalement assez probable.

Sélection des événements

Durant les deux phases du programme, les données ont été analysées par un ensemble de chaînes d'analyse capables de fournir un résultat avec une faible latence [9,10] : Omega (Ω) Pipeline et coherent WaveBurst (cWB) que nous avons mentionnés au Chapitre 3 ainsi que Multi-Band Template Analysis (MBTA) [32].

Les événements détectés par ces chaînes d'analyse ayant une signification statistique suffisante (soit un taux de fausse alarme équivalent à 0.25/jour) sont soumis à une équipe d'opérateurs qui effectue un ensemble de vérifications afin de valider la qualité de l'événement puis le transmettre sous forme d'alerte.

Ces alertes comportent l'information sur la position estimée de la source du candidat OG extraite de la carte des probabilités *a posteriori* obtenue à partir des probabilités calculées sur une grille du ciel avec un pas de 0.4 degré. Au premier ordre, l'erreur angulaire sur la position estimée est $\propto 1/(\rho f)$ en fonction du rapport signal-sur-bruit ρ et de la fréquence typique du signal f [4]. La boîte d'erreur peut être caractérisée plus finement par la *région de recherche* qui est la région du ciel où la probabilité *a posteriori* est plus grande que celle obtenue à la vraie position de la source. La figure 4.10 présente le résultat de simulations de Monte Carlo. On y montre l'angle solide en degré carré de la région de recherche en fonction de l'amplitude de l'OG mesurée par $h_{\rm rss}$ (qui est proportionnel à ρ, cf. Éq. 2.2) pour deux modèles de signaux (sinusoïdes à enveloppe gaussienne de fréquences différentes). Pour les événements détectables d'amplitude $h_{\rm rss} \sim 10^{-21}/{\rm Hz}^{1/2}$, cet angle solide est typiquement de 50 degrés carré ce qui est pratiquement un ordre de grandeur plus grand que le champ de vue des télescopes utilisés pour le suivi. Il est donc nécessaire de faire une mosaïque d'image pour couvrir l'intégralité de la boîte d'erreur ou bien de se satisfaire d'une couverture partielle en acceptant de perdre une fraction des contreparties.

La distribution des sources d'OG suit celle des étoiles. Les sources d'OG sont situées dans les galaxies ou dans leur environnement proche. Il y a $\sim$ 16 000 galaxies à une distance de 50 Mpc [134] et celles-ci occupent moins de 1 % du ciel. Dans une région de 50 degré carré, on dénombre typiquement une vingtaine de galaxies, mais à cause de l'anisotropie de l'univers local, ce nombre peut aller jusqu'à une centaine. On peut donc améliorer la probabilité de réussir le pointé i.e, d'observer dans la direction effective de la source et réduire substantiellement les observations à réaliser en ciblant les galaxies proches. Pour ce faire on calcule la statistique suivant qui combine l'information portée par la carte *a posteriori* avec celle d'un catalogue de galaxies proches [134]. Chaque pixel de la carte est pondéré par un poids défini par [106]

$$P \propto L\left(\frac{M}{D}\right), \tag{4.7}$$

où L est la probabilité *a posteriori* du pixel obtenue par l'analyse des données OG seules, D est la distance de la galaxie et M est la luminosité de ou des galaxies contenues dans le pixel. On utilise la luminosité en lumière bleue qui est un indicateur du taux de formation d'étoiles. Les alertes contiennent les coordonnées des champs qui couvre une somme des P maximale. Grâce à cette méthode, il est possible d'obtenir une fraction raisonnable de pointés réussis avec des télescopes grand champ comme l'illustre la figure 4.11.

Ces alertes sont transmises par des canaux dédiés, en particulier un système de "socket" inspiré du protocole GCN que j'ai mis en place.

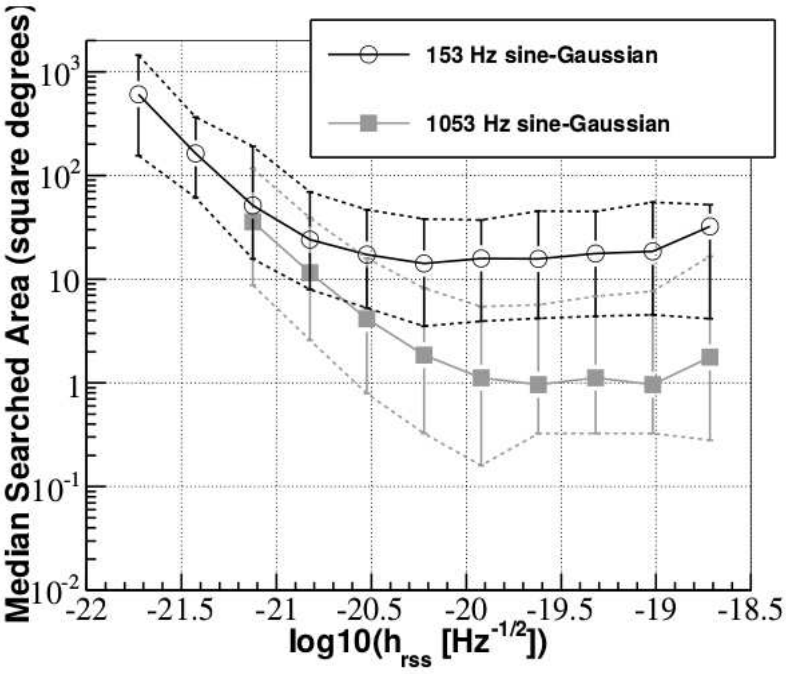

FIGURE 4.10 – **Boîte d'erreur angulaire de reconstruction de la direction de la source OG**. Valeur médiane de l'angle solide de la région de recherche en fonction de l'amplitude de OG pour deux modèles de signaux (sinusoïdes à enveloppe gaussienne autour de 100 Hz et du kiloHertz). Pour les événements détectables $h_{\rm rss} \sim 10^{-21}/{\rm Hz}^{1/2}$, l'incertitude angulaire est typiquement de 50 degrés carré.

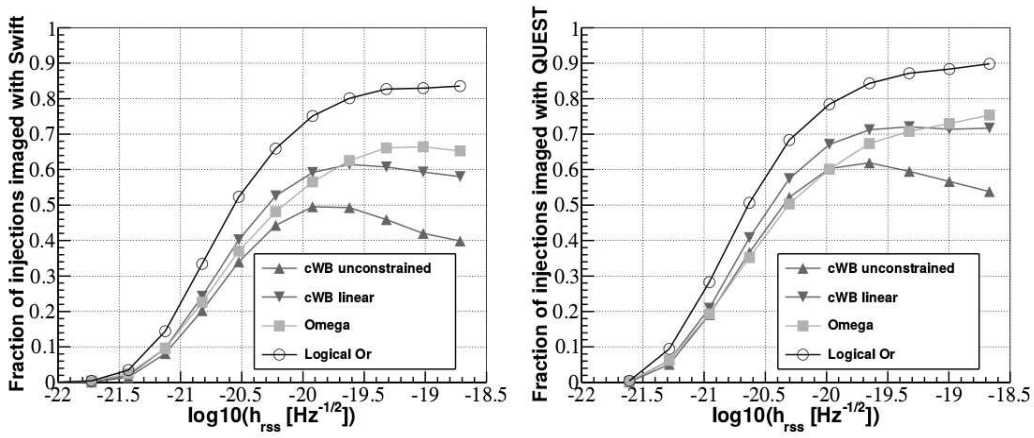

FIGURE 4.11 – **Fraction de pointés réussis après pondération par le catalogue de galaxies proches** pour l'observatoire Swift et pour l'instrument Quest. On considère le pointé réussi lorsque la vraie source se situe dans le ou l'un des champs observés. Pour Swift, la stratégie d'observation consiste en cinq pointés centrés sur les cinq galaxies qui possèdent la statistique pondérée P la plus grande, chaque pointé correspondant à un champ de vue de 23 arcmin de côté. Le champ de vue et la stratégie suivie pour le télescope Zadko sont semblables à Swift. Pour Quest, on réalise un seul pointé de 9 degrés carré.

TABLE 4.2 – **Evénements OG durant la deuxième phase (automne 2010) du programme de suivi EM**

ID	Date	UTC	Pipeline	Taux FA (jour^{-1})	Suivi
G19377	Sep 16, 2010	06 :42 :23	cWB (unmodeled)	< 0.01	ROTSE : 117 images, TAROT : 20, Zadko : 129, et SkyMapper : 21. "Injection aveugle"
G20190	Sep 19, 2010	12 :02 :25	MBTA	0.16	ROTSE : 257 images, QUEST : 23, Zadko : 159, et TAROT : 3
G21852	Sep 26, 2010	20 :24 :32	cWB (linear)	0.02	ROTSE : 130 images, PTF : 149, CAT 3 DQ
G23004	Oct 3, 2010	16 :48 :23	Ω	0.21	ROTSE : 153 images, QUEST : 40, Liverpool - RATCam : 22, Liverpool - SkyCamZ : 121, et POTS : 444

TABLE 4.3 – **Caractéristiques des instruments impliqués dans le programme de suivi.** La colonne "mosaïque" indique le nombre maximum de champs observés par événement.

Nom	Site	Champ (deg^2)	Ouverture (m)	Expo. (s)	Mag. limite	Mosaïque
Palomar Transient Factory	1	7.3	1.2	60	20.5	10
Pi of the Sky	1	400	0.072	10	11.5	1
QUEST	1	9.4	1	60	20.5	3
ROTSE III	4	3.4	0.45	20	17.5	1
SkyMapper	1	5.7	1.35	110	21.5	8
TAROT	2	3.4	0.25	180	17.5	1
Zadko Telescope	1	0.15	1	120	20.5	5
Liverpool Telescope - RATCam	1	0.0058	2	300	21	1
Liverpool Telescope - SkyCamZ	1	1	0.2	10	18	1

Télescopes partenaires

Durant la première phase (hiver 2009), les alertes ont été transmises aux télescopes TAROT [94] et QUEST [29].

Durant la deuxième phase (automne 2010), le réseau de télescopes partenaires (voir aussi la Table 4.3) inclut également Palomar Transient Factory [117], Pi of the Sky (POTS) [100], ROTSE III [21], SkyMapper [90], Zadko Telescope [61], et Liverpool Telescope [124].

4.2.3 Détection des transitoires optiques dans les observations de TAROT, Zadko et QUEST

La détection de transitoires optiques consiste essentiellement en la recherche dans une séquence d'image astronomique d'une source ponctuelle qui diminue en intensité avec le temps. Deux caractéristiques rendent spécifiques la recherche de contrepartie aux OGs. D'abord, il y a une grande incertitude sur la variation de la courbe de lumière. Nous

avons ciblé les transitoires de durée courte (quelques jours au plus) en cohérence avec les modèles de rémanences de sursauts et les kilonovas présentés en Table 4.1. Ensuite, la mauvaise localisation de la position de la source OG implique l'observation de grandes régions du ciel, bien plus grandes que celles qui sont fournies par *Swift* (arc-minute, typiquement), par exemple, pour la recherche de la rémanence des sursauts.

Nous avons implémenté des chaînes d'analyse dédiées qui s'inspirent par certains aspects des procédures que nous employons pour les données OG. Ces chaînes d'analyse s'appuient, en particulier, sur des simulations de Monte-Carlo pour l'estimation de la signification statistique des candidats, ce qui à notre connaissance, est une approche originale dans ce domaine.

Cette section est dédiée aux développements effectués en collaboration avec Marica Branchesi, Univ. Urbino Italie dans ce domaine pour les observations de TAROT, Zadko Telescope, et QUEST. Contrairement aux autres approches considérées dans le cadre du programme de suivi, cette chaîne d'analyse n'utilise pas la technique de soustraction optimale d'image mais elle s'appuie sur l'utilisation de catalogues de sources extraits pour chaque image.

Chaîne d'analyse

La procédure consiste en trois étapes principales (après correction du dark, flat et du niveau du fond céleste) : calibration photométrique, détection des sources et reconstruction de leur courbe de lumière et sélection des transitoires.

TAROT, Zadko Telescope et QUEST ont conduit leurs observations au filtre clair. La calibration du point zéro en magnitude est effectuée en corrélant la liste des sources avec le catalogue USNO-A2.0 [103] fournissant ainsi des magnitudes rouge équivalentes (système photométrique Vega). Pour QUEST, la calibration et l'analyse sont effectuées indépendamment sur les 112 images CCD ce qui permet de tenir compte des variations de réponse, qualité et sensibilité des capteurs.

La liste de sources ponctuelles dans chaque image est extraite par `SExtractor` [35]. Ces listes sont corrélées spatialement avec le catalogue de référence USNO-A2.0 avec le logiciel `match` [67]. Le rayon angulaire de corrélation est fixé à 10 arcsec pour TAROT, 2 arcsec pour Zadko et 3 arcsec pour QUEST. Ces valeurs tiennent compte des incertitudes de position des observations et du catalogue USNO-A2.0. Les sources qui coïncident en position et luminosité avec les objets du catalogue de référence sont exclues. Les sources des listes ainsi obtenues pour chaque image sont appariées afin de former une liste d'objets astrophysiques associés à une courbe de lumière.

Deux types d'analyse sont ensuite conduites. L'analyse "on-source" est restreinte aux objets dans le voisinage des galaxies proches (distantes de 50 Mpc) ou des amas globulaires. Le voisinage est une région circulaire de rayon égal à cinq fois le demi-axe de la galaxie soit $\sim$ 20 kpc ce qui correspond au décalage typique observé entre les sursauts courts et le centre de la galaxie la plus proche. [33]. L'analyse "whole-field" couvre l'intégralité du champ de vue et est limitée aux objets les plus brillants. Les grandes variations de sensibilité de QUEST ont empêché la réalisation de cette analyse.

Des coupures sont ensuite appliquées afin de rejeter les fausses associations et les faux candidats tels que les rayons cosmiques, les astéroïdes, le bruit CCD, les satellites, les étoiles variables ... Ces coupures portent sur le nombre d'images consécutives où l'objet apparaît, la magnitude initiale et la variabilité de la courbe de lumière. La variabilité est caractérisée par l'exposant β de déclin de la courbe de lumière après ajustement par une loi de puissance $\mathcal{L} \propto t^{-\beta}$, soit une variation linéaire de magnitude $m = 2.5\beta \log_{10}(t) + C$. Les coupures sont effectivement réalisées sur l'indice 2.5β. Les objets présentant un indice plus grand que 0.5 sont sélectionnés, ce qui englobe tous les modèles en Table 4.1.

Estimation du fond Le fond de cette analyse est estimé en appliquant celle-ci répétitivement (100 fois) sur de multiples séries d'images obtenues par des permutations aléatoires des vraies observations. Les images collectées durant les premières nuits sont exclues des premières places et systématiquement renvoyées en fin de classement. Ainsi, tout transitoire astrophysique réel possédant une courbe de lumière en loi de puissance perd cette propriété dans la série permutée tandis que les artefacts de courte durée (rayons cosmiques, etc.) sont globalement conservés. Cette procédure permet donc une évaluation du fond dû au bruit d'observation, mais elle ne permet pas d'évaluer le fond astrophysique. Une estimation de ce dernier nécessiterait l'analyse d'un grand volume d'images provenant d'un relevé décorrélé des données OG, ce dont nous ne disposons pas. Un exemple est montré en Fig. 4.12. Nous avons estimé que, pour une coupure à 0.5 sur l'indice de variabilité de la courbe de lumière, le nombre de fausses détections est inférieure à 1 par degré carré pour les objets de magnitude initiale 14.5 (ou plus brillant) pour TAROT et 15.5 pour Zadko.

Ajustement des coupures Pour les images de TAROT et Zadko, les coupures sont ajustées pour qu'on obtienne une probabilité de fausse alarme de 10% pour chaque analyse ("on-source" et "whole-field"). Pour une moitié des analyses "on-source" effectuées la coupure nominale sur l'indice de variabilité (< 0.5) suffit. Pour le reste, une coupure supplémentaire sur la magnitude initiale (12–13 mag) doit être utilisée. Pour les analyses "whole-field", une coupure sur la magnitude initiale a été appliquée à 14 mag pour TAROT/G19377 et à 10 mag pour Zadko/G19377 et G20190. L'observation de l'objet sur les trois premières images a été également requise pour TAROT/G20190. Des observations supplémentaires effectuées plusieurs mois après les alertes ont permis la réjection d'une fraction supplémentaire du fond en sélectionnant les objets absents de ces images de référence. L'ajustement des coupures pour QUEST suit globalement la même procédure et aboutit aux coupures suivantes : variation de la magnitude supérieure à 0.5 entre la première et deuxième nuit d'observation, magnitude initiale inférieure à 17.5 pour G20190, et 18.5 pour G23004 (renforcé à 15 pour huit galaxies).

Résultats

Dans cette section, nous résumons les résultats obtenus lors du programme de suivi pour les événements observés par TAROT, Zadko et QUEST. Pour une vue globale des

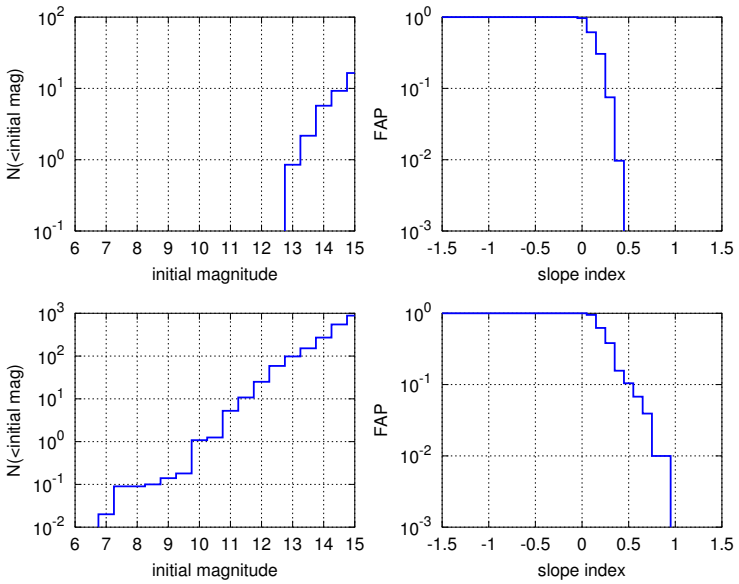

FIGURE 4.12 – **Exemple de fond calculé par la procédure présentée en Sec. 4.2.3 avec les observations collectées par TAROT** suite à l'alerte G19377 pour l'analyse "on-source" (haut) et l'analyse "whole-field" (bas). (gauche) Distribution cumulative du nombre de événements de fond détectés (après 100 permutations) en fonction d'une coupure sur leur magnitude initiale. (droite) Probabilité de fausse alarme en fonction de la coupure sur l'indice de variabilité (une coupure sur la magnitude initiale à 14 est utilisé pour l'analyse "whole-field"). Comme attendu, on constate que le fond de l'analyse "on-source" est considérablement réduit comparé à celui de l'analyse "whole-field".

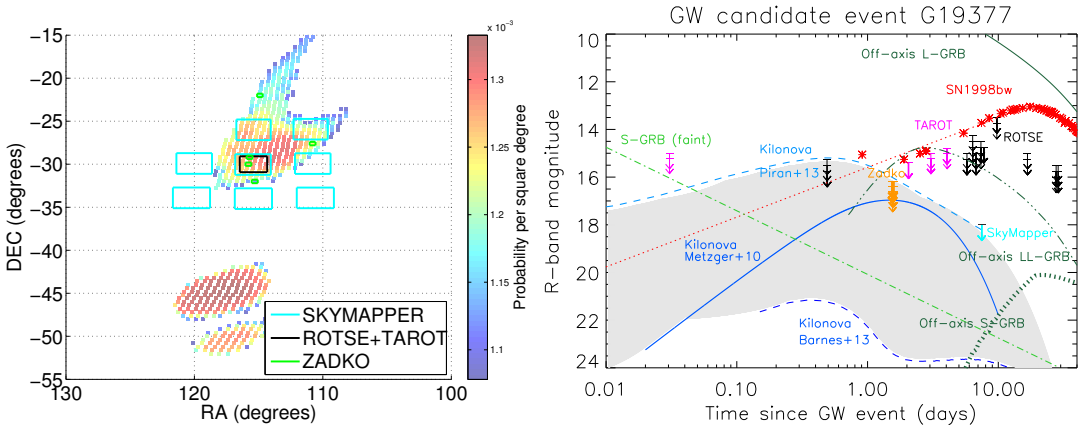

FIGURE 4.13 – **Résultats pour G19377, injection aveugle** : (gauche) boîte d'erreur OG donnant la probabilité par degré carré (avant la pondération par le catalogue de galaxies proches) associée à chaque direction du ciel ainsi que les champs observés (sélectionnés après pondération). (droite) chronologie et magnitude limite des observations (l'origine des temps est l'instant de l'événement OG). Les courbes de lumière pour plusieurs modèles de sources placées à 30 Mpc sont également présentées (voir aussi Sec. 4.2.3).

résultats obtenus, voir [5].

G19377 Comme signalé précédemment, l'événement G19377 est un signal simulé ajouté aux données OG afin de tester la procédure d'analyse. Fig. 4.13 montre un résumé des observations faites en réponse à cette alerte ainsi que leur sensibilité.

TAROT a pris des images à partir de T +43 min (c'est-à-dire moins de 15 minutes après l'alerte !) puis il a répété les observations à T +2 j , T +3 j et T +4 j. Les observations ont une magnitude limite de 15.1. L'analyse "on-source" a été effectué sur les deux galaxies à $\sim$ 24 Mpc (PGC 078144 et PGC 078133) présentes dans le champ et n'a détecté aucun transitoire. L'analyse "whole-field" a identifié un candidat avec un indice de 0.6. Une analyse plus approfondie a montré que ce candidat résulte d'un artefact de l'identification des points source particulièrement difficile dans cette région peuplée du ciel.

Le télescope Zadko a observé les régions autour des cinq galaxies les plus probables dans la boîte d'erreur OG : NGC 2380, ESO 560-004, ESO 429-012, PGC 078133 et PGC 07814, les deux derniers étant en commun avec TAROT. Les observations ont commencé à T +1 j12.6h et ont été répétées 5 mois plus tard. La magnitude limite moyenne est de 16.5 mag. Aucune contrepartie électromagnétique n'a été identifiée.

Cet événement a également été observé par le télescope ROTSE-IIIc à partir de T +$\sim$12h 30 et SkyMapper, 7 jours après l'alerte. Aucun transitoire plausible n'a été découvert dans ces observations.

G20190 Fig. 4.14 montre un résumé des observations faites en réponse à cette alerte ainsi que leur sensibilité.

Le télescope TAROT a recueilli environ trois images en association avec G20190. En raison de la pleine lune, la magnitude limite de ces observations est de 14.6 mag. Neuf mois plus tard, 18 images de référence (magnitude limite : 17 mag) ont été prises par TAROT dans la même région du ciel. Aucune contrepartie avec une probabilité de fausse alarme de moins de 10 % a été identifié par l'analyse "on-source". L'analyse "whole-field" a donné quatre candidats. Ces candidats ont été ensuite associés à une mauvaise reconstruction causés par la présence de motif de saturation de la CCD pour certaines étoiles très brillantes dans le champ.

Le télescope Zadko a pointé vers deux amas globulaires NGC 7078 et NGC 7089 ainsi que trois galaxies NGC 7177, UGC 11868 et NGC 7241. Ces deux dernières galaxies ont été observées à T +50 min puis à T +1j et T+4 j avec le reste des cibles. Les observations ont été répétées onze mois plus tard pour référence. La magnitude limite est de 16.4 et 17.3 mag resp. pour les observations initiales et de référence. L'analyse "on-source" a détecté trois candidats transitoires associés à NGC 7078 et 15 associés avec le centre de NGC 7089 qui ont tous été exclu par la suite. La grande densité de la région centrale des amas globulaires pose un problème de séparation des sources ponctuelles. C'est probablement une des limites de l'approche considérée ici. Aucun transitoire n'a été identifié pour les analyses restantes.

Les observations de QUEST ont débuté à T +12h 3m. Chaque champ a été observé deux fois en 15 minutes (observation par paires d'images tramées pour combler les lacunes entre les rangées de capteurs CCD). La séquence d'observation a été répétée à T +1.5 j. Dix galaxies distantes d'au plus 30 Mpc sont dans le champ. Trois de ces galaxies n'ont pas été analysés en raison de la mauvaise qualité de l'image ou des problèmes d'étalonnage. La magnitude limite est 17.6 mag (limitée par la pleine lune). Un candidat a été identifié en association avec UGC 11916. Une analyse plus approfondie du candidat a montré qu'il s'agissait d'un artefact.

Cette alerte a également été observée par les quatre télescopes ROTSE-III à partir de T+34h38m. Aucun candidat n'a passé la procédure de validation.

Performances de la recherche

Pour mesurer l'efficacité de détection, des transitoires optiques simulés sont ajoutés à chaque séquence d'images, qui ont été ensuite analysées de la même manière et avec les mêmes coupures que les données brutes. Les transitoires simulés reproduisent les courbes de lumière observées pour les rémanences de sursauts ou bien ils proviennent de modèles de kilonovas (voir Table 4.1). Les rémanences des sursauts ainsi simulées couvrent la gamme des luminosités effectivement observées. Leur magnitude est calculée pour chaque instant d'observation en fonction de la distance de la source fictive.

Pour chaque jeu d'image collectées par TAROT et Zadko, une centaine de transitoires ont été ajoutés pour chaque type de source et chaque distance. Pour produire une source ponctuelle réaliste, nous avons utilisé des étoiles de référence prises dans le voisinage du point d'injection qui sont ainsi représentatives de la fonction d'étale-

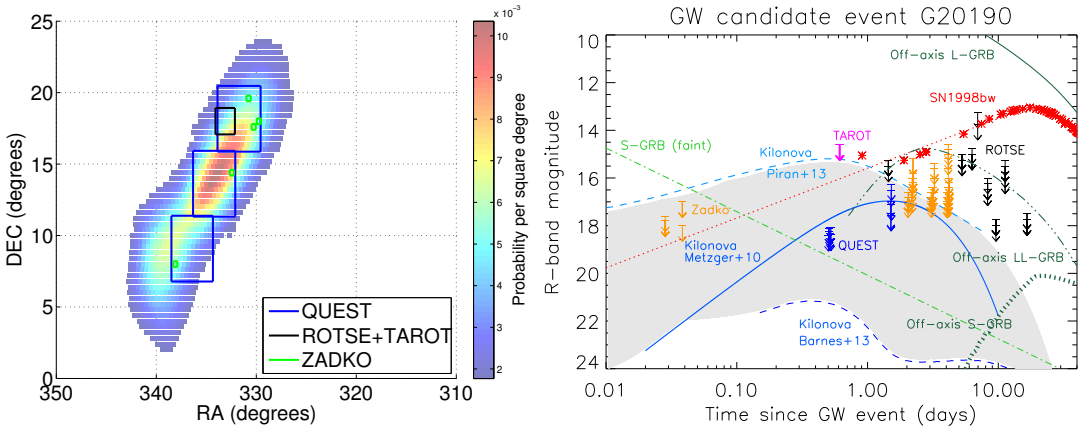

FIGURE 4.14 – **Résultat pour G20190. Voir Fig. 4.13 pour une explication.**

ment dans cette région. Les résultats sont présentés en Fig. 4.15. Les rémanences de sursauts longs de sursauts courts et les kilonovas sont détectées avec une efficacité de 50 % dans les images de TAROT à des distances de 400 Mpc/18 Mpc/6.5 Mpc respectivement pour l'alerte G19377 355 Mpc/16 Mpc/13 Mpc pour G20190. Pour Zadko, on obtient 195 Mpc/8 Mpc/4 Mpc pour G19377, et 505 Mpc/ 25 Mpc 13 Mpc pour G20190. Ainsi qu'il est attendu, la profondeur des observations, la rapidité de pointé du télescope et la densité des étoiles dans le champ influent considérablement sur la performance. Notons que les horizons obtenus pour les sursauts courts sont comparables avec celui des détecteurs LIGO et Virgo pour les binaires coalescentes.

4.2.4 Discussion

L'accomplissement du premier programme de suivi EM décrit dans ce chapitre est une réalisation cruciale car nous démontrons ainsi pour la première fois qu'il est possible de coupler les observations OG avec celles de l'astronomie conventionnelle. Nous réalisons cet exercice de bout en bout, analyse des données électromagnétiques incluse. Cela nous a permis de tirer des leçons utiles à la préparation des stratégies d'observation avec les détecteurs de deuxième génération, leçons qui nous ont guidé pour la définition du prochain programme de suivi, voir http://www.ligo.org/science/GWEMalerts.php.

La mise en opération des chaînes d'analyse en ligne, la caractérisation de la boîte d'erreur OG et l'utilisation de catalogue de galaxies pour l'amélioration du pointé ont été des développements particulièrement importants.

La connaissance de la boîte d'erreur OG était approximative et consistait en des ordres de grandeur et des lois d'échelle avant les simulations de Monte-Carlo effectuées en préparation au programme de suivi. Ses caractéristiques sont maintenant bien mieux cernées. Cela a notamment influencé le développement de nouveaux concepts de télescopes grand champ dédiés au suivi des OG comme par exemple BlackGEM, GOTO, TOROS, etc. Ces études montrent aussi l'impact important d'un quatrième détecteur en

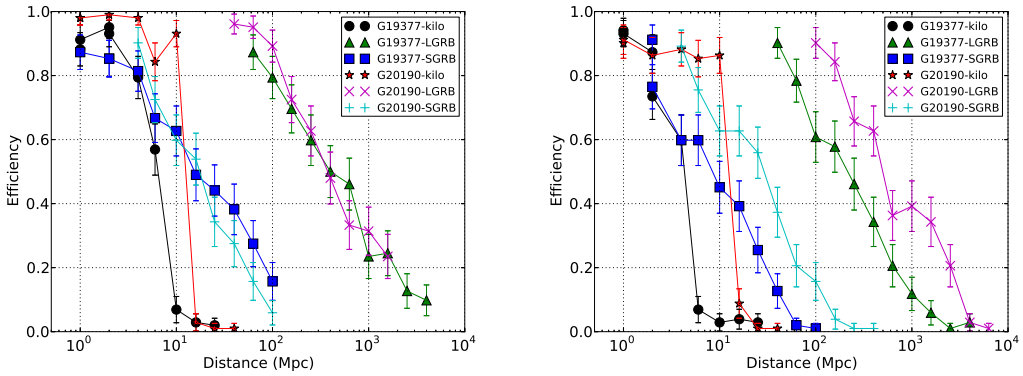

FIGURE 4.15 – **Efficacité de détection de transitoires optiques** dans les données de TAROT (gauche) et Zadko (droite). Cette efficacité est obtenue avec l'analyse "on-source" et n'incluent les pertes dues à la restriction des observations à une petite partie de la région du ciel possible pour la source.

Asie (LIGO-India ou KAGRA au Japon) qui permettrait de réduire d'un ordre de grandeur l'incertitude angulaire de position [4]. Avec des valeurs typiques autour du degré, la couverture de la boîte d'erreur deviendrait ainsi accessible à la majorité des télescopes robotiques grand champ.

La restriction des observations aux galaxies proches dans la boîte d'erreur permet d'améliorer la qualité du pointé et de réduire significativement la zone du ciel à imager. Des observations sont en cours afin de complèter les catalogues existants jusqu'à l'horizon des détecteurs avancés, soit $\sim$ 200 Mpc (ils sont actuellement complets jusqu'à $\sim$ 40 Mpc).

Concernant l'analyse des images astronomiques, nous insistons sur l'importance de l'estimation empirique de la signification statistique et de la sensibilité de la recherche utilisées dans les recherches présentées ici. Ces pratiques, empruntées au schéma d'analyse des données OG, ne sont pas courantes dans ce domaine, e.g., la recherche de remanences des sursauts gamma. La grande signification statistique des sursauts observés et la boîte d'erreur réduite qui leur est attachée ne demandent pas de traitement statistique fin des observations de suivi. La situation sera très différente avec les événements OG marginalement significatifs (par ex., à 3 sigmas) et des boîtes d'erreur de plusieurs dizaines de degrés carrés. Il sera alors utile et nécessaire d'estimer la signification jointe des coïncidences observées.

Si l'imagerie grand champ réalisée par les petits télescopes est essentielle à une première localisation de la contrepartie optique, elle ne permet pas une caractérisation suffisante des candidats. N'ayant pas eu de candidat suffisamment convaincant durant cette première expérience, nous n'ayons pas expérimenté de suivi approfondi par de grands instruments offrant des observations photométriques et spectrométriques précises. Il est clair que cela sera nécessaire afin de réduire le nombre de faux positifs à un niveau

acceptable.

Bien que les tests préliminaires effectués avec LOFAR n'aient pas abouti lors de cette première campagne, les radiotélescopes phasés restent très attractifs grâce à leur grand champ et la grande flexibilité de leur mode d'observation. Le ciel transitoire aux basses fréquences radio est cependant mal connu et les prochains relevés de LOFAR seront essentiels pour conclure sur l'intérêt d'un tel mode de suivi.

Avec les futurs grands relevés du ciel comme le Large Synoptic Survey Telescope (LSST) [85] ou le Square Kilometer Array (SKA) [45], l'astrophysique des objets transitoires va prendre de l'ampleur dans les années qui viennent. Les grands volumes d'observation à venir offrent des perspectives passionnantes pour les recherches combinant observations OG et EM.

Perspectives

Avec l'imminente entrée en fonction des détecteurs avancés, la prochaine décennie sera une période charnière et particulièrement riche pour l'astronomie gravitationnelle. Le plan arrêté par LIGO et Virgo [4] jalonne les dix prochaines années par des prises de données scientifiques. La première aura lieu courant 2015 avec une sensibilité modérément (un facteur 2 environ) supérieure à la meilleure sensibilité obtenue jusqu'ici. D'autres prises de données s'échelonnent ensuite jusqu'à 2022 avec une sensibilité qui va croissant. On estime que, lorsqu'ils seront arrivés à la sensibilité cible, les détecteurs avancés pourront réalistiquement faire l'observation de dizaines de ces systèmes par an [7] voire de centaines pour les prédictions les plus optimistes.

Si ces scénarios sont confirmés, il est cependant difficile de prédire quand la première détection interviendra. Pour la période 2014–2018, les pistes que je considère pour les prochaines années sont dans la continuité de mes activités actuelles. À court terme, elles se concentrent sur la préparation de l'analyse de données des détecteurs avancés (en se concentrant sur le domaine des OG transitoires) afin de maximiser les chances de détection (Cf. Chap. 3). À moyen terme, il s'agit de contribuer à une meilleure interprétation des sources astrophysiques à l'origine des OG détectées par Virgo et LIGO. Ceci passe par l'obtention d'observations (électromagnétiques) complémentaires faites en collaboration avec des équipes d'astronomes (Cf. Chap. 4).

Analyse des données d'Advanced Virgo et LIGO

Graphes d'ondelettes pour la recherche de signaux chirps Nous avons déjà évoqué en Sec. 3.4 les développements de graphes d'ondelettes permettant la recherche pleinement cohérente des signaux chirps provenant des binaires compactes coalescentes. L'idée est d'assembler et tester une première version de ce nouvel algorithme courant 2014. Ce projet fait l'objet d'une proposition de thèse.

Accélération GPU de coherent WaveBurst Afin de déclarer une détection à cinq sigmas, il faut estimer le fond de l'analyse jusqu'à des p-valeurs $\sim 3 \times 10^{-7}$. Pour aller à ce niveau de précision, l'estimation empirique (time-lag analysis) du fond de l'analyse doit être itérée de l'ordre du million de fois. Pour que cette partie de l'analyse puisse être réalisée en un temps raisonnable, un soin particulier doit être apporté à l'optimisation du calcul et du logiciel d'analyse. Nous proposons d'explorer l'accélération GPU des parties les plus demandeuses de la chaîne d'analyse coherent WaveBurst. Ce travail s'effectuera

en collaboration avec un groupe d'informaticiens de l'Université Tsinghua (Chine), spécialistes des GPU. L'objectif est de gagner un facteur 10 sur le temps d'execution.

Recherches dirigées d'ondes gravitationnelles La chaîne d'analyse développée dans le cadre de la collaboration avec ANTARES [41] pourrait être généralisée à des recherches d'OG transitoires dirigées par des signaux astrophysiques autres que les neutrinos de haute énergie. La bande de fréquence analysée pour le suivi des sursauts gamma [11] est actuellement limitée à 500 Hz. Grâce à l'efficacité numérique de la nouvelle méthode, elle peut être étendue au delà du kHz et ainsi couvrir les modèles d'émission proposés pour les effondrements de cœur stellaire. Ceci serait particulièrement important pour le suivi des sursauts longs qui sont actuellement associés à l'effondrement d'étoile massive (modèle du collapsar).

Il en est de même pour la méthode d'optimisation qui s'appuie sur un principe général, qui pourrait être appliqué à d'autres cas comme les sursauts gamma ou les transitoires X. En effet, les seuls sursauts annoncés publiquement sont ceux qui sont sélectionnés avec un seuil de détection élevé. On pourrait envisager d'abaisser ce seuil afin de sélectionner des sursauts moins significatifs et moins lumineux. Ceci pourrait donner accès à l'hypothétique population locale de sursauts sous-lumineux [81] évoquée dans la littérature mais dont l'existence reste encore à confirmer. Le seuil de sélection des observations gamma ne peut être baissé sans en contrepartie augmenter celui appliqué aux ondes gravitationnelles afin de maintenir constante la probabilité de fausse alarme. La procédure d'optimisation que nous avons développée permettrait de comprendre à quel niveau il est utile de fixer les seuils afin de maximiser le nombre de sources détectables à taux de fausse alarme donné.

Suivi électromagnétique des événements de LIGO et Virgo L'observation d'une contrepartie électromagnétique à une OG transitoire peut avoir un impact décisif car elle peut permettre d'établir l'origine astrophysique de l'événement. L'observation conjointe d'un signal gravitationnel et électromagnétique pourrait apporter des éléments de réponse cruciaux à deux questions importantes [119, 121] : la question de l'origine des sursauts gamma, et celle de la mesure des paramètres cosmologiques par les binaires coalescentes comme "chandelle standard".

Depuis mi 2013, je coordonne la mise en place du programme de suivi électromagnétique pour les détecteurs LIGO et Virgo avancés et l'écriture des règles de collaboration qui seront appliquées durant les prochaines années. Suite à un appel publié courant 2013 auquel 60 groupes réunissant près de 400 chercheurs ont répondu, nous avons lancé une série de consultations (incluant deux réunions à Amsterdam et à Chicago, que j'ai co-organisées) avec la communauté des astronomes afin d'élaborer un cadre de collaboration acceptable pour tous.

Ce travail m'a permis de tisser des liens avec les communautés française et internationale des astronomes possédant une expertise dans ce domaine. Il s'agit pour l'instant d'une prise de contact afin de définir une stratégie et un programme de travail commun.

Ceci m'a amené à m'investir dans différents groupes de travail. Je suis co-Investigateur

de la mission X/gamma sino-française SVOM. Le segment sol de cette mission comprend un réseau de télescopes robotiques (GFT) pour le suivi optique et proche infrarouge des sursauts. Ce réseau inclut un instrument d'un mètre en construction à l'Observatoire de San Pedro Mártir au Mexique sous l'égide d'une équipe de l'IRAP. Ce télescope, qui sera vraisemblablement opérationnel bien avant le lancement du satellite, pourrait être utilisé pour le suivi électromagnétique des événements LIGO/Virgo. Je poursuis également la collaboration initiée avec l'équipe du télescope robotisé TAROT. Récemment, j'ai aussi intégré le groupe de travail sur la LOFAR Super Station/NenuFAR (Nançay) et désire initier une évaluation des capacités de cet instrument pour le suivi des OG.

Bibliographie

[1] LIGO open science center, 2012. https://losc.ligo.org/timeline.

[2] H. Aart. *Track reconstruction and point source searches with ANTARES*. PhD thesis, Université d'Amsterdam, 2004.

[3] J. Aasi et al. The characterization of Virgo data and its impact on gravitational-wave searches. *Class. Quantum Grav.*, 29 :155002, 2012.

[4] J. Aasi et al. Prospects for Localization of Gravitational Wave Transients by the Advanced LIGO and Advanced Virgo Observatories, 2013. arXiv :1304.0670. LIGO-P1200087, VIR-0288A-12.

[5] J. Aasi et al. First Searches for Optical Counterparts to Gravitational-wave Candidate Events. *ApJS*, 211(7), 2014.

[6] J. Abadie et al. Predictions for the rates of compact binary coalescences observable by ground-based gravitational-wave detectors. *Class. Quantum Grav.*, 27(17) :173001–+, 2010.

[7] J. Abadie et al. Predictions for the rates of compact binary coalescences observable by ground-based gravitational-wave detectors. *Class. Quantum Grav.*, 27(17) :173001–+, 2010.

[8] J. Abadie et al. All-sky search for gravitational-wave bursts in the second joint ligo-virgo run. *Phys. Rev. D*, 85 :122007, 2012.

[9] J. Abadie et al. First low-latency LIGO+Virgo search for binary inspirals and their electromagnetic counterparts. *A&A*, 541 :A155, 2012.

[10] J. Abadie et al. Implementation and testing of the first prompt search for gravitational wave transients with electromagnetic counterparts. *A&A*, 539(A124), 2012.

[11] J. Abadie et al. Search for gravitational waves associated with gamma-ray bursts during LIGO science run 6 and Virgo science runs 2 and 3. *ApJ*, 760 :12, 2012.

[12] J. Abadie et al. Sensitivity achieved by the LIGO and Virgo gravitational wave detectors during LIGO's sixth and Virgo's second and third science runs. 2012.

[13] B. P. Abbott et al. LIGO : The Laser Interferometer Gravitational-Wave Observatory. *Rept. Prog. Phys.*, 72 :076901, 2009.

[14] M. Abernathy et al. Einstein gravitational-wave telescope. Technical Report ET-0106C-10, ET Science Team, 2011.

[15] T. Accadia et al. Advanced Virgo technical design report. Technical Report VIR-0128A-12, Virgo Collaboration, 2012. https://tds.ego-gw.it/ql/?c=8940.

[16] T. Accadia et al. Virgo : a laser interferometer to detect gravitational waves. *JINST*, 7 :P03012, 2012.

[17] F. Acernese et al. A simple line detection algorithm applied to virgo data. *Class. Quantum Grav.*, 22(18) :S1189, 2005.

[18] S. Adrian-Martinez et al. A First Search for coincident Gravitational Waves and High Energy Neutrinos using LIGO, Virgo and ANTARES data from 2007. *JCAP*, 1306, 2013.

[19] M. Ageron et al. ANTARES : the first undersea neutrino telescope. *Nucl. Instrum. Meth.*, A656 :11–38, 2011.

[20] J. A. Aguilar et al. A fast algorithm for muon track reconstruction and its application to the {ANTARES} neutrino telescope. *Astroparticle Physics*, 34(9) :652 – 662, 2011.

[21] C W Akerlof et al. The ROTSE-III robotic telescope system. *PASP*, 115(803) :132–140, 2003.

[22] P. Amaro-Seoane et al. Doing science with eLISA : Astrophysics and cosmology in the millihertz regime. Technical report, eLISA Science Team, 2012. arXiv :1201.3621.

[23] L. A. Anchordoqui and T. Montaruli. In Search for Extraterrestrial High Energy Neutrinos. *Ann. Rev. Nucl. Part. Sci.*, 60 :129–162, 2010.

[24] W. Anderson and R. Balasubramanian. Time-frequency detection of gravitational waves. *Phys. Rev. D*, D60 :102001, 1999. gr-qc/9905023.

[25] W. G. Anderson et al. Excess power statistic for detection of burst sources of gravitational radiation. *Phys. Rev. D*, 63 :042003, 2001.

[26] S. Ando and J. F. Beacom. Revealing the Supernova Gamma-Ray Burst Connection with TeV Neutrinos. *Phys. Rev. Lett.*, 95(6) :061103, 2005.

[27] S. Ando et al. Multimessenger astronomy with gravitational waves and high-energy neutrinos. *Rev. Mod. Phys.*, 85(4) :1401–1420, 2013.

[28] P. Astone et al. IGEC2 : A 17-month search for gravitational wave bursts in 2005-2007. *Phys. Rev. D*, D82 :022003, 2010.

[29] C. Baltay et al. The QUEST large area CCD camera. *PASP*, 119 :1278–1294, 2007.

[30] E. Barausse, V. Morozova, and L. Rezzolla. On the mass radiated by coalescing black-hole binaries. *ApJ*, 758 :63, 2012.

[31] B. Baret et al. Bounding the time delay between high-energy neutrinos and gravitational-wave transients from gamma-ray bursts. *Astroparticle Physics*, 35 :1–7, 2011.

[32] F. Beauville et al. Detailed comparison of LIGO and Virgo inspiral pipelines in preparation for a joint search. *Class. Quantum Grav.*, 25(4) :045001, 2008.

[33] E. Berger. A short GRB no-host problem ? Investigating large progenitor offsets for short GRBs with optical afterglows. *ApJ*, 722 :1946, 2010.

[34] Emanuele Berti et al. Inspiral, merger and ringdown of unequal mass black hole binaries : A multipolar analysis. *Phys. Rev. D*, 76 :064034, 2007.

[35] E. Bertin and S. Arnouts. Sextractor : Software for source extraction. *A&AS*, 117 :393, 1996.

[36] D. P. Bertsekas. *Dynamic Programming and Optimal Control*, volume 1. Athena Scientific, 2nd edition, 2000.

[37] M.-A. Bizouard and M.-A. Papa. Searching for gravitational waves with the ligo and virgo interferometers. *C. R. A. S.*, 14(4) :352–365, 2013.

[38] L. Blanchet. Gravitational radiation from post-Newtonian sources and inspiralling compact binaries. *Living Rev. Rel.*, 5 :3, 2002.

[39] J. S. Bloom et al. Astro2010 decadal survey whitepaper : Coordinated science in the gravitational and electromagnetic skies, 2009. arXiv :0902.1527v1.

[40] B Bouhou. *Recherche conjointe d'ondes gravitationnelles et de neutrinos cosmiques de haute énergie avec les détecteurs Virgo LIGO et ANTARES*. PhD thesis, Université Pierre et Marie Curie, 2013.

[41] B Bouhou, B Baret, E Chassande-Mottin, A Kouchner, F Salemi, and G Vedovato. Triggered searches for gravitational-wave transients associated with high-energy neutrinos using coherent WaveBurst. 12th Grav. Wave Physics and Astronomy Workshop, GWPAW12 (Hannover, Germany), 2012.

[42] P R Brady and S Ray-Majumder. Incorporating information from source simulations into searches for gravitational-wave bursts. *Class. Quantum Grav.*, 21 :S1839–S1848, 2004.

[43] A. Buonanno, G. B. Cook, and F. Pretorius. Inspiral, merger and ring-down of equal-mass black-hole binaries. *Phys. Rev. D*, 75 :124018, 2007.

[44] E. J. Candès, P. R. Charlton, and H. Helgason. Detecting Highly Oscillatory Signals by Chirplet Path Pursuit. *Appl. Comp. Harm. Anal.*, 24 :14–40, 2008.

[45] C. L. Carilli and S. Rawlings. Science with the Square Kilometer Array : Motivation, key science projects, standards and assumptions. *New Astron. Rev.*, 48(11-12) :979, 2004.

[46] E. Chassande-Mottin. A Learning approach to the detection of gravitational wave transients. *Phys. Rev. D*, D67 :102001, 2003.

[47] É. Chassande-Mottin. Géométrie des ensembles de chirps et détection des ondes gravitationnelles. In *Actes du 20ème Colloque GRETSI*, pages 261–264, Louvain-la-Neuve (Belgique), 2005. Presses universitaires de Louvain.

[48] É. Chassande-Mottin. Chains of chirplets for the detection of gravitational wave chirps. In *Wavelets XII, Proceedings of SPIE*, pages 6707–12–39, San Diego (US), 2007.

[49] E. Chassande-Mottin. Data analysis challenges in transient gravitational wave astronomy. In *AIP Conf. Proc. : Acoustic and Radio EeV Neutrino Detection Activities, ARENA'12*, volume 1535, page 252, Erlangen (Germany), 2012.

[50] E. Chassande-Mottin and P. Flandrin. On the time-frequency detection of chirps and its application to gravitational waves. In *Proceedings of the 2nd Grav. Wave Data Anal. Workshop*, pages 47–52, Orsay (France), 1997.

[51] E. Chassande-Mottin and P. Flandrin. On the time-frequency detection of chirps. *Appl. Comp. Harm. Anal.*, 6(9) :252–281, 1999.

[52] E Chassande-Mottin, M Hendry, P Sutton, and S Màrka. Multimessenger astronomy with the Einstein Telescope. *Gen. Relat. Gravit.*, 43 :437–464, 2011.

[53] E. Chassande-Mottin, M Miele, S Mohapatra, and L Cadonati. Detection of gravitational-wave bursts with chirplet-like template families. *Class. Quantum Grav.*, 27 :194017, 2010.

[54] E. Chassande-Mottin and A. Pai. Discrete time and frequency Wigner-Ville distribution : Moyal's formula and aliasing. *IEEE Signal Proc. Lett.*, 12(7) :508–511, 2005.

[55] E. Chassande-Mottin and A. Pai. Best chirplet chain : Near-optimal detection of gravitational wave chirps. *Phys. Rev. D*, D73 :042003, 2006.

[56] S. Chatterji et al. Multiresolution techniques for the detection of gravitational-wave bursts. *Class. Quantum Grav.*, 21 :S1809–S1818, 2004.

[57] S. K. Chatterji. *The search for gravitational-wave bursts in data from the second LIGO science run.* PhD thesis, MIT Dept. of Physics, 2005.

[58] T. Chiarusi and M. Spurio. High-energy astrophysics with neutrino telescopes. *EPJ C*, 65(3-4) :649–701, 2010.

[59] L. F. Chris and C. B. N. Kimberly. Gravitational waves from gravitational collapse. *Living Rev. Rel.*, 14(1), 2011.

[60] A. Corsi and B. J. Owen. Maximum gravitational-wave energy emissible in magnetar flares. *Phys. Rev. D*, 83 :104014, 2011.

[61] D Coward et al. The Zadko Telescope : A southern hemisphere telescope for optical transient searches, multi-messenger astronomy and education. *Publications of the Astronomical Society of Australia*, 27 :331, 2010.

[62] N Dalal, D Holz, S Hughes, and B Jain. Short GRB and binary black hole standard sirens as a probe of dark energy. *Phys. Rev. D*, 74 :063006, 2006.

[63] T. Damour and A. Vilenkin. Gravitational wave bursts from cosmic strings. *Phys. Rev. Lett.*, 85 :3761–3764, 2000.

[64] I. Daubechies. *Ten Lectures on Wavelets.* Number 61. SIAM, 1992.

[65] M. B. Davies et al. Gamma-ray bursts, supernova kicks, and gravitational radiation,. *ApJ*, 579(L63), 2002.

[66] J. B. Doggett and D. Branch. A comparative study of supernova light curves. *AJ*, 90 :2303–2311, 1985.

[67] T. F. Droege et al. TASS Mark IV Photometric Survey of the Northern Sky. *PASP*, 118 :1666, 2006.

[68] G. Esposito-Farèse. Binary-pulsar tests of strong-field gravity and gravitational radiation damping. In *Proceedings of the Tenth Marcel Grossmann Meeting*, volume 647, Rio de Janiero (Brazil), 2005.

[69] Eanna E. Flanagan and Scott A. Hughes. Measuring gravitational waves from binary black hole coalescences : 1. Signal-to-noise for inspiral, merger, and ringdown. *Phys. Rev. D*, 57 :4535–4565, 1998.

[70] P. Flandrin. *Time-frequency/Time-scale Analysis*. Academic Press, 1999.

[71] W.-f. Fong and E. Berger. The Locations of Short Gamma-ray Bursts as Evidence for Compact Object Binary Progenitors, 2013. arXiv :1307.0819.

[72] C. Fryer and K. New. Gravitational waves from gravitational collapse. *Living Rev. Rel.*, 14(1), 2011.

[73] É Gourgoulhon. Introduction à la relativité générale, 2014. Notes de cours de Master 2.

[74] H. Grote for the LIGO Scientific Collaboration. The GEO 600 status. *Class. Quantum Grav.*, 27 :084003, 2010.

[75] Y. Guersel and M. Tinto. Near optimal solution to the inverse problem for gravitational wave bursts. *Phys. Rev. D*, 40 :3884–3938, 1989.

[76] D. Guetta et al. Neutrinos from individual gamma-ray bursts in the BATSE catalog. *Astroparticle Physics*, 20(429), 2004.

[77] F. Halzen and S. R. Klein. IceCube : An Instrument for Neutrino Astronomy. *Rev. Sci. Instrum.*, 81 :081101, 2010.

[78] I. Harry and S. Fairhurst. A coherent triggered search for single spin compact binary coalescences in gravitational wave data. *Class. Quantum Grav.*, 28 :134008, 2011.

[79] G. M. Harry for the LIGO Scientific Collaboration. Advanced ligo : the next generation of gravitational-wave detectors. *Class. Quantum Grav.*, 27(084006), 2010.

[80] I S Heng. Supernova waveform catalogue decompositon : A Principal Component Analysis approach. *Class. Quantum Grav.*, 26 :105005, 2009.

[81] J. Hjorth and J. S. Bloom. The gamma-ray burst – supernova connection. In C. Kouveliotou et al., editors, *Gamma-Ray Bursts*, pages 169–190. Cambridge University Press, Cambridge, UK, 2011.

[82] R. A. Hulse and J. H. Taylor. Discovery of a pulsar in a binary system. *ApJ*, 195 :L51–L53, 1975.

[83] J.M. Innocent and B. Torrésani. Wavelet transform and binary coalescence detection. In *Mathematics of Gravitation*, volume 41, pages 179–208, Warsaw, Poland, 1997. Banach Center Publications.

[84] K. Ioka. Magnetic deformation of magnetars for the giant flares of the soft gamma-ray repeaters. *MNRAS*, 327 :639–662, 2001.

[85] Z. Ivezic et al. LSST : From science drivers to reference design and anticipated data products, 2011. Internal report. arXiv :0805.2366v2.

[86] D. A. Kann et al. The Afterglows of Swift-era Gamma-ray Bursts. I. Comparing pre-Swift and Swift-era Long/Soft (Type II) GRB Optical Afterglows. *ApJ*, 720 :1513–1558, 2010.

[87] D. A. Kann et al. The Afterglows of Swift-era Gamma-Ray Bursts. II. Type I GRB versus Type II GRB Optical Afterglows. *ApJ*, 734 :96–+, 2011.

[88] V. M. Kaspi. Grand Unification in Neutron Stars. *Proc. Natl. Acad. Sci.*, 107 :7147–7152, 2010.

[89] U. F. Katz. Underwater neutrino detection in the Mediterranean Sea : From present to future. *Nucl. Phys. Proc. Suppl.*, 221 :130–135, 2011.

[90] S C Keller et al. The SkyMapper telescope and the Southern Sky Survey. *Publications of the Astronomical Society of Australia*, 24(1) :1–12, 2007.

[91] R Khan and S Chatterji. Enhancing the capabilities of LIGO time-frequency plane searches through clustering. *Class. Quantum Grav.*, 26 :155009, 2009.

[92] S. Klimenko et al. Performance of the WaveBurst algorithm on LIGO data. *Class. Quantum Grav.*, 21 :S1685–S1694, 2004.

[93] S. Klimenko et al. Coherent method for detection of gravitational wave bursts. *Class. Quantum Grav.*, 25 :114029, 2008.

[94] A Klotz, M Boer, J L Atteia, and B Gendre. Early optical observations of gamma-ray bursts by the TAROT telescopes : Period 2001-2008. *AJ*, 137 :4100, 2009.

[95] M. Kramer et al. Tests of general relativity from timing the double pulsar. *Science*, 314 :97–102, 2006.

[96] L. Li and B. Paczyński. Transient events from neutron star mergers. *ApJ*, 507 :L59, 1998.

[97] T. Li et al. Towards a generic test of the strong field dynamics of general relativity using compact binary coalescence. *Phys. Rev. D*, 85 :082003, 2012.

[98] H. Lück et al. The upgrade of GEO 600. *J. Phys. Conf. Ser.*, 228(012012), 2010.

[99] M. Maggiore. *Gravitational Waves – Volume 1 : Theory and Experiments*. Oxford University Press, 2008.

[100] K Malek et al. General overview of the "Pi of the Sky" system. *Proc. SPIE*, 7502 :75020D, 2009.

[101] B D. Metzger et al. Electromagnetic counterparts of compact object mergers powered by the radioactive decay of r-process nuclei. *MNRAS*, 406 :2650–2662, 2010.

[102] S. Mohapatra, Z. Nemtzow, E. Chassande-Mottin, and L. Cadonati. Performance of a Chirplet-based analysis for gravitational waves from binary black hole mergers. In *JPCS : 9th Amaldi Conference*, volume 363, page 012031, Cardiff (UK), 2012.

[103] D. Monet et al. *The USNO-A2.0 Catalogue*. U.S. Naval Observatory, Washington DC, 1998.

[104] M. Morvidone and B. Torrésani. Time-scale approach for chirp detection. *Int. J. Wavelets. Multi.*, 1 :19–49, 2003.

[105] V. Necula et al. Transient analysis with fast wilson-daubechies time-frequency transform. *J. Phys. Conf. Ser.*, 363 :012032, 2012.

[106] L. Nuttall and P. J. Sutton. Identifying the host galaxy of gravitational wave signals. *Phys. Rev. D*, 82 :102002, 2010.

[107] C. D. Ott. The Gravitational Wave Signature of Core-Collapse Supernovae. *Class. Quantum Grav.*, 26 :063001, 2009.

[108] B. J. Owen. Search templates for gravitational waves from inspiraling binaries : Choice of template spacing. *Phys. Rev. D*, 53 :6749, 1996.

[109] B. J. Owen and B. S. Sathyaprakash. Matched filtering of gravitational waves from inspiraling compact binaries : Computational cost and template placement. *Phys. Rev. D*, 60 :022002, 1999.

[110] A. Pai, E. Chassande-Mottin, and O. Rabaste. Best network chirplet chain : Near-optimal coherent detection of unmodeled gravitational wave chirps with a network of detectors. *Phys. Rev. D*, 77(062005) :1–21, 2008.

[111] A. Pai, S. Dhurandhar, and S. Bose. A Data analysis strategy for detecting gravitational wave signals from inspiraling compact binaries with a network of laser interferometric detectors. *Phys. Rev. D*, D64 :042004, 2001.

[112] C. Papadimitriou and K. Steiglitz. *Combinatorial optimization : Algorithms and complexity*. Dover, New York, 1998.

[113] Z. Paragi et al. A mildly relativistic radio jet from the otherwise normal Type Ic Supernova 2007gr. *Nature*, 463 :516–518, 2010.

[114] T. Piran, E. Nakar, and S. Rosswog. The electromagnetic signals of compact binary mergers. *MNRAS*, 430 :2121–2136, 2013.

[115] O Rabaste, É. Chassande-Mottin, and A. Pai. Goniométrie pour les chirps gravitationnels. In *Actes du 21ème Colloque GRETSI*, pages 741–744, Troyes (France), 2007.

[116] O Rabaste, A. Petiteau, and É. Chassande-Mottin. Détection de chirps multi-composantes et application aux ondes gravitationnelles des binaires à rapport de masses extrême. In *Actes du 22ème Colloque GRETSI*, Dijon (France), 2009.

[117] A Rau et al. Exploring the optical transient sky with the Palomar Transient Factory. *PASP*, 121(886) :1334–1351, 2009.

[118] S. Razzaque, P. Meszaros, and E. Waxman. High energy neutrinos from a slow jet model of core collapse supernovae. *Mod. Phys. Lett.*, A20 :2351–2368, 2005.

[119] K. Riles. Gravitational Waves : Sources, Detectors and Searches. *Prog. Part. Nucl. Phys.*, 68 :1–54, 2013.

[120] C Rover et al. Bayesian reconstruction of gravitational wave burst signals from simulations of rotating stellar core collapse and bounce. *Phys. Rev. D*, 80 :102004, 2009.

[121] B. S. Sathyaprakash and B. F. Schutz. Physics, astrophysics and cosmology with gravitational waves. *Living Rev. Rel.*, 12(2), 2009.

[122] B. F. Schutz. Determining the Hubble constant from gravitational wave observations. *Nature*, 323 :310–311, 1986.

[123] K. Somiya for the KAGRA Collaboration. Detector configuration of KAGRA, the Japanese cryogenic gravitational-wave detector. *Class. Quantum Grav.*, 29(124007), 2012.

[124] I. A. Steele et al. The Liverpool Telescope : performance and first results. In J. M. Oschmann, Jr., editor, *Society of Photo-Optical Instrumentation Engineers (SPIE) Conference Series*, volume 5489, pages 679–692, 2004.

[125] P. J. Sutton. A Rule of Thumb for the Detectability of Gravitational-Wave Bursts. arXiv :1304.0210, 2013.

[126] P. J. Sutton et al. X-pipeline : an analysis package for autonomous gravitational-wave burst searches. *New J. Phys.*, 12(5) :053034, 2010.

[127] J. Sylvestre. Time-frequency detection algorithm for gravitational wave bursts. *Phys. Rev. D*, 66 :102004, 2002.

[128] H. J. van Eerten and A. I. MacFadyen. Synthetic Off-axis Light Curves for Low-energy Gamma-Ray Bursts. *ApJ Lett.*, 733 :L37, 2011.

[129] H. L. Van Trees. *Detection, estimation and modulation theory – Part I.* Wiley, New-York, 1968.

[130] H. L. Van Trees. *Optimum array processing.* Wiley, New York, US, 2002.

[131] B. D. Van Veen and K. M. Buckley. Beamforming : A versatile approach to spatial filtering. *IEEE ASSP Mag.*, 5(2) :4–24, 1988.

[132] G. Vedrenne and J.-L. Atteia. *Gamma-Ray Bursts : The brightest explosions in the Universe.* Springer, 2009.

[133] J. M. Weisberg, D. J. Nice, and J. H. Taylor. Timing measurements of the relativistic binary pulsar PSR B1913+16. *ApJ*, 722 :1030–1034, 2010.

[134] D. J. White, E. J. Daw, and V. S. Dhillon. A list of galaxies for gravitational wave searches. *Class. Quantum Grav.*, 28 :085016, 2011.

[135] C. M. Will. The confrontation between general relativity and experiment. *Living Rev. Rel.*, 9, 2005.

Éric Chassande-Mottin

42, av. Edison 75013 Paris
France
T +33 1 5727 6036
E ecm@apc.univ-paris7.fr
W http://www.apc.univ-paris7.fr/~ecm
44 ans, 1 enfant

Fonction actuelle

AstroParticule et Cosmologie (Paris), Chargé de Recherche du CNRS. **2006–**

Carrière et formation

ARTEMIS, Observatoire de la Côte d'Azur (Nice), Chargé de Recherche du CNRS. **2000–2006**

Albert Einstein Institute – Max-Planck-Institut für Gravitationsphysik (Golm, Allemagne), Post-doctorant. **1998–2000**

Laboratoire du Physique – École Normale Supérieure (Lyon), *Méthodes de réallocation dans le plan temps-fréquence pour l'analyse et le traitement des signaux non stationnaire*, Thèse de Doctorat de l'Université de Cergy-Pontoise effectuée sous la direction de Patrick Flandrin et soutenue le 28 septembre 1998, Mention très honorable avec les félicitations du jury. **1995–1998**

École Nationale Supérieure de l'Électronique et de ses Applications, ENSEA (Cergy-Pontoise), Élève Ingénieur, DEA Traitement du Signal et des Images. **1992–1995**

Participation aux projets

Co-I de la mission SVOM. **2013–**

Membre de la Collaboration Virgo. **2000–**

Expertise et rayonnement scientifique

- 72 articles dans des journaux à comité de lecture
- 92 communications dans des conférences
- 9 contributions à des ouvrages collectifs
- 2 présentations invitées dans les conférences internationales
- Organisation de 2 ateliers scientifiques et une école d'été. Participation au comité scientifique de 5 conférences et ateliers scientifiques internationaux
- Expertise pour les revues Classical and Quantum Gravity, Physical Review D, IEEE Transactions on Signal Processing, Applied and Computional Harmonic Analysis, Signal Processing et pour la conférence EUSIPCO
- Membre du jury de 3 thèses, dont 1 à l'étranger
- Membre de 2 commissions de spécialistes (recrutement de Maître de Conférences)

Encadrement

Boutayeb Bouhou (doctorant co-encadré à 50 % avec Antoine Kouchner, APC), Recherche conjointe d'ondes gravitationnelles et de neutrinos cosmiques de haute énergie avec les détecteurs Virgo-LIGO et ANTARES. **2009–2012**
Thèse de doctorat soutenue le 19 décembre 2012

Olivier Rabaste (post-doctorant, boursier Virgo-EGO Scientific Forum). **2006–2008**
Olivier Rabaste est maintenant Ingénieur de Recherche à l'ONERA

Archana Pai (post-doctorante, bourse Henri Poincaré). **2002–2003**
Archana Pai est maintenant Assistant Professor à l'IISER-TVM Thiruvananthapuram, Inde
À cette liste, s'ajoute une dizaine de stagiaires au niveau licence et master, français et étrangers.

Enseignement et diffusion du savoir

- Interventions aux écoles d'été suivantes : IVème Ecole de Physique des Astroparticules (école internationale), 2013. Co-organisateur et intervenant. VESF School on Gravitational Waves (école internationale), éditions 2009, 2010, 2011 et 2013. Cargèse School on Gravitational Waves (école internationale), 2011. IIIème École de Physique des Astroparticules (école nationale), 2011. Réseau européen ISAPP (International School on AstroParticle Physics), 2010
- Chargé de cours et TD. Cours de statistiques communs aux écoles doctorales STEP'UP et Phenix, 2014
- Séminaire du magistère de Physique de l'Université Paris Denis Diderot, 2012

Contrats

Responsable du groupe de travail "Astrophysique multi-messager" financé par le GdR PCHE, (Budget total $\sim$ 20k€). **2009–2011**

European Gravitational Observatory – VESF Post-Doctoral Fellowship program, *Network detection of gravitational wave chirps*, (Allocation $\sim$ 90 k€). **2006–2008**

Programme interdisciplinaire Astroparticule, IN2P3, *Groupe de travail "Méthodes temps-fréquence pour les ondes gravitationnelles"*, (Allocation $\sim$ 30 k€). **2001–2002**

Responsabilités

Co-responsable du comité en charge du programme de suivi électromagnétique des événements LIGO Virgo pour les détecteurs avancés. **2013–**

Co-responsable du groupe GWHEN (Onde gravitationnelle et neutrino de haute énergie – une dizaine de chercheurs et étudiants) de la collaboration LIGO/Virgo. **2010–**

Responsable adjoint du groupe de Science des données et Astrophysique numérique (ex-ADAMIS) de l'APC. **2008–**

Membre du conseil de laboratoire. **2008–2009**

Autres activités scientifiques

- Vulgarisation scientifique : animation à la Fête de la Science, 2008. Contribution à l'ouvrage collectif *Passeport pour les deux infinis*, 2010 et ré-édition en 2013.

Production scientifique (1995–2013)

1 Publications dans les revues avec comité de lecture

[1] Ando (S.) et al. – Multimessenger astronomy with gravitational waves and high-energy neutrinos. *Rev. Mod. Phys.*, vol. 85, n° 4, 2013, pp. 1401–1420.

[2] Auger (F.), Chassande-Mottin (E.) et Flandrin (P.). – On phase-magnitude relationships in the short-time fourier transform. *IEEE Signal Proc. Lett.*, vol. 19, 2012, pp. 267–270.

[3] Baret (B.) et al. – Multimessenger science reach and analysis method for common sources of gravitational waves and high-energy neutrinos. *Phys. Rev. D*, vol. 85, 2012, p. 103004.

[4] Baret (B.) et al. – Bounding the time delay between high-energy neutrinos and gravitational-wave transients from gamma-ray bursts. *Astroparticle Physics*, vol. 35, 2011, pp. 1–7.

[5] Chassande-Mottin (E.), Hendry (M.), Sutton (P.) et Màrka (S.). – Multimessenger astronomy with the Einstein Telescope. *Gen. Relat. Gravit.*, vol. 43, 2011, pp. 437–464.

[6] Pai (A.), Chassande-Mottin (E.) et Rabaste (O.). – Best network chirplet chain : Near-optimal coherent detection of unmodeled gravitational wave chirps with a network of detectors. *Phys. Rev. D*, vol. 77, n° 062005, 2008, pp. 1–21. – gr-qc/0708.3493.

[7] Chassande-Mottin (E.) et Pai (A.). – Best chirplet chain : near-optimal detection of gravitational wave chirps. *Phys. Rev. D*, vol. 73, n° 042003, 2006, pp. 1–25. – gr-qc/0512137.

[8] Chassande-Mottin (E.) et Pai (A.). – Discrete time and frequency Wigner-Ville distribution : Moyal's formula and aliasing. *IEEE Signal Proc. Lett.*, vol. 12, n° 7, 2005, pp. 508–511.

[9] Chassande-Mottin (E.). – Learning approach to the detection of gravitational wave transients. *Phys. Rev. D*, vol. 67, n° 102001, 2003, pp. 1–13. – gr-qc/0210008.

[10] Chassande-Mottin (E.) et Dhurandhar (S.). – Adaptive filtering techniques for gravitational wave interferometric data : Removing long-term sinusoidal disturbances and oscillatory transients. *Phys. Rev. D*, vol. 63, n° 042004, 2001, pp. 1–15. – gr-qc/0003099.

[11] Chassande-Mottin (E.) et Flandrin (P.). – On the time-frequency detection of chirps. *Appl. Comp. Harm. Anal.*, vol. 6, n° 9, 1999, pp. 252–281.

[12] Chassande-Mottin (E.), Auger (F.) et Flandrin (P.). – On the statistics of spectrogram reassignment. *Multidim. Syst. Sign. Process.*, vol. 9, n° 4, 1998, pp. 355–362.

[13] Chassande-Mottin (E.), Daubechies (I.), Auger (F.) et Flandrin (P.). – Differential reassignment. *IEEE Signal Proc. Lett.*, vol. 4, n° 10, 1997, pp. 293–294.

Publications en tant que co-auteur de la Collaboration Virgo

[14] Aasi (J.) et al. – Search for long-lived gravitational-wave transients coincident with long gamma-ray bursts. *Physical Review D*, vol. 88, n° 122004, 2013.

[15] Aasi (J.) et al. – A directed search for continuous Gravitational Waves from the Galactic Center. *Physical Review D*, vol. 88, 2013, p. 102002 [13 pages].

[16] Accadia (T.) et al. – Central heating radius of curvature correction (CHRoCC) for use in large scale gravitational wave interferometers. *Classical and Quantum Gravity*, vol. 30, 2013, p. 055017.

[17] Aasi (J.) et al. – Einstein@Home all-sky search for periodic gravitational waves in LIGO S5 data. *Physical Review D*, vol. 87, 2013, p. 042001.

[18] Aasi (J.) et al. – Search for Gravitational Waves from Binary Black Hole Inspiral, Merger and Ringdown in LIGO-Virgo Data from 2009-2010. *Physical Review D*, vol. 87, 2013, p. 022002.

[19] Aasi (J.) et al. – Parameter estimation for compact binary coalescence signals with the first generation gravitational-wave detector network. *Physical Review D*, vol. 88, 2013, p. 062001.

[20] Adrián-Martínez (S.) et al. – A First Search for coincident Gravitational Waves and High Energy Neutrinos using LIGO, Virgo and ANTARES data from 2007. *Journal of Cosmology and Astroparticle Physics*, vol. 06, 2013, p. 008.

[21] Evans (P.A.) et al. – Swift Follow-up Observations of Candidate Gravitational-wave Transient Events. *Astrophysical Journal Supplement*, vol. 203, 2012, p. 28.

[22] Accadia (T.) et al. – The NoEMi (Noise Frequency Event Miner) framework. *Journal of Physics : Conference Series*, vol. 363, 2012, p. 012037.

[23] Abadie (J.) et al. – First low-latency LIGO+Virgo search for binary inspirals and their electromagnetic counterparts. *Astronomy and Astrophysics*, vol. 541, 2012, p. A155.

[24] Aasi (J.) et al. – The characterization of Virgo data and its impact on gravitational-wave searches. *Classical and Quantum Gravity*, vol. 29, 2012, p. 155002.

[25] Abadie (J.) et al. – Upper limits on a stochastic gravitational-wave background using LIGO and Virgo interferometers at 600-1000 Hz. *Physical Review D*, vol. 85, 2012, p. 122001.

[26] Abadie (J.) et al. – Search for gravitational waves associated with gamma-ray bursts during LIGO science run 6 and Virgo science runs 2 and 3. *Astrophysical Journal*, vol. 760, 2012, p. 12 (18 p.).

[27] Abadie (J.-P.) et al. – Search for Gravitational Waves from Low Mass Compact Binary Coalescence in LIGO's Sixth Science Run and Virgo's Science Runs 2 and 3. *Physical Review D*, vol. 85, 2012, p. 082002.

[28] Abadie (J.) et al. – All-sky search for gravitational-wave bursts in the second joint LIGO-Virgo run. *Physical Review D*, vol. 85, 2012, p. 122007.

[29] Abadie (J.) et al. – Search for Gravitational Waves from Intermediate Mass Binary Black Holes. *Physical Review D*, vol. 85, 2012, p. 102004.

[30] Abadie (J.) et al. – Implementation and testing of the first prompt search for electromagnetic counterparts to gravitational wave transients. *Astronomy and Astrophysics*, vol. 539, 2012, p. A124.

[31] Abadie (J.) et al. – All-sky Search for Periodic Gravitational Waves in the Full S5 LIGO Data. *Physical Review D*, vol. 85, 2012, p. 022001.

[32] Accadia (T.) et al. – Virgo : a laser interferometer to detect gravitational waves. *Journal of Instrumentation*, vol. 7, 2012, p. P03012.

[33] Accadia (T.) et al. – Characterization of the Virgo Seismic Environment. *Classical and Quantum Gravity*, vol. 29, 2012, p. 025005.

[34] Abadie (J.) et al. – Directional limits on persistent gravitational waves using LIGO S5 science data. *Physical Review Letters*, vol. 107, 2011, p. 271102.

[35] Abadie (J.) et al. – Beating the spin-down limit on gravitational wave emission from the Vela pulsar. *Astrophysical Journal*, vol. 737, 2011, p. 93.

[36] Abadie (J.) et al. – Search for Gravitational Wave Bursts from Six Magnetars. *Astrophysical Journal Letters*, vol. 734, 2011, p. L35.

[37] Abadie (J.) et al. – Search for gravitational waves from binary black hole inspiral, merger and ringdown. *Physical Review D*, vol. 83, 2011, p. 122005.

[38] Accadia (T.) et al. – A state observer for the Virgo inverted pendulum. *Review of Scientific Instruments*, vol. 82, 2011, p. 094502.

[39] Accadia (T.) et al. – The seismic Superattenuators of the Virgo gravitational waves interferometer. *Journal of Low Frequency Noise Vibration and Active Control*, vol. 30, 2011, pp. 63–79.

[40] Accadia (T.) et al. – Status of the Virgo project. *Classical and Quantum Gravity*, vol. 28, 2011, p. 114002.

[41] Accadia (T.) et al. – Corrigendum to Calibration and sensitivity of the Virgo detector during its second science run. *Classical and Quantum Gravity*, vol. 28, 2011, p. 079501.

[42] Accadia (T.) et al. – Calibration and sensitivity of the Virgo detector during its second science run. *Classical and Quantum Gravity*, vol. 28, 2011, p. 025005.

[43] Accadia (T.) et al. – Performance of the Virgo interferometer longitudinal control system during the second science run. *Astroparticle Physics*, vol. 34, 2011, pp. 521–527.

[44] Accadia (T.) et al. – Automatic Alignment system during the second science run of the Virgo interferometer. *Astroparticle Physics*, vol. 34, 2011, pp. 327–332.

[45] Abadie (J.) et al. – Search for gravitational waves from compact binary coalescence in LIGO and Virgo data from S5 and VSR1. *Physical Review D*, vol. 82, 2010, p. 102001.

[46] Abadie (J.) et al. – All-sky search for gravitational-wave bursts in the first joint LIGO-GEO-Virgo run. *Physical Review D*, vol. 81, 2010, p. 102001.

[47] Abadie (J.) et al. – Search for gravitational-wave inspiral signals associated with short Gamma-Ray Bursts during LIGO's fifth and Virgo's first science run. *Astrophysical Journal*, vol. 715, 2010, pp. 1453–1461.

[48] Abadie (J.) et al. – Predictions for the Rates of Compact Binary Coalescences Observable by Ground-based Gravitational-wave Detectors. *Classical and Quantum Gravity*, vol. 27, 2010, p. 173001.

[49] Abbott (B.P.) et al. – Search for gravitational-wave bursts associated with gamma-ray bursts using data from LIGO Science Run 5 and Virgo Science Run 1. *Astrophysical Journal*, vol. 715, 2010, pp. 1438–1452.

[50] Abbott (B.P.) et al. – Searches for gravitational waves from known pulsars with science run 5 LIGO data. *Astrophysical Journal*, vol. 713, 2010, pp. 671–685.

[51] Accadia (T.) et al. – In-vacuum Faraday isolation remote tuning. *Applied Optics*, vol. 49, 2010, pp. 4780–4790.

[52] Acernese (F.) et al. – Automatic Alignment for the first science run of the Virgo interferometer. *Astroparticle Physics*, vol. 33, 2010, pp. 131–139.

[53] Acernese (F.) et al. – Measurements of Superattenuator seismic isolation by Virgo interferometer. *Astroparticle Physics*, vol. 33, 2010, pp. 182–189.

[54] Acernese (F.) et al. – Performances of the Virgo interferometer longitudinal control system. *Astroparticle Physics*, vol. 33, 2010, pp. 75–80.

[55] Abbott (B.P.) et al. – An upper limit on the stochastic gravitational-wave background of cosmological origin. *Nature*, vol. 460, 7258, 2009, pp. 990–994.

[56] Acernese (F.) et al. – Laser with an in-loop relative frequency stability of 1.0×10^{-21} on a 100-ms time scale for gravitational-wave detection. *Physical Review A*, vol. 79, 2009, p. 053824.

[57] Acernese (F.) et al. – Gravitational wave burst search in the Virgo C7 data. *Classical and Quantum Gravity*, vol. 26, 2009, p. 085009.

[58] Abbott (B.) et al. – Astrophysically Triggered Searches for Gravitational Waves : Status and Prospects. *Classical and Quantum Gravity*, vol. 25, 2008, p. 114051.

[59] Acernese (F.) et al. – In-vacuum optical isolation changes by heating in a Faraday isolator. *Applied Optics*, vol. 47, 2008, pp. 5853–5861.

[60] Acernese (F.) et al. – First joint gravitational waves search by the Auriga-Explorer-Nautilus-Virgo collaboration. *Classical and Quantum Gravity*, vol. 25, 2008, p. 205007.

[61] Acernese (F.) et al. – Lock acquisition of the Virgo gravitational wave detector. *Astroparticle Physics*, vol. 30, 2008, pp. 29–38.

[62] Acernese (F.) et al. – The Virgo 3 km interferometer for gravitational wave detection. *Journal of Optics A : Pure and Applied Optics*, vol. 10, 2008, p. 064009.

[63] Acernese (F.) et al. – Search for gravitational waves associated with GRB 050915a using the Virgo detector. *Classical and Quantum Gravity*, vol. 25, 2008, p. 225001.

[64] Acernese (F.) et al. – Status of coalescing binaries search activities in Virgo. *Classical and Quantum Gravity*, vol. 24, 2007, pp. 5767–5775.

[65] Acernese (F.) et al. – The Virgo interferometric gravitational antenna. *Optics and Lasers in Engineering*, vol. 45, 2007, pp. 478–487.

[66] Acernese (F.) et al. – Measurement of the optical parameters of the Virgo interferometer. *Applied Optics*, vol. 46, 2007, pp. 3466–3484.

[67] Acernese (F.) et al. – Length Sensing and Control in the Virgo Gravitational Wave Interferometer. *IEEE Transactions on Instrumentation and Measurement*, vol. 55, 2006, pp. 1985–1995.

[68] Braccini (S.) et al. – Measurement of the seismic attenuation performance of the VIRGO Superattenuator. *Astroparticle Physics*, vol. 23, 2005, pp. 557–565.

[69] Acernese (F.) et al. – Lock acquisition of the central interferometer of the Virgo gravitational wave detector. *Astroparticle Physics*, vol. 21, 2004, pp. 465–477.

[70] Acernese (F.) et al. – The commissioning of the central interferometer of the Virgo gravitational wave detector. *Astroparticle Physics*, vol. 21, 2004, pp. 1–22.

[71] Acernese (F.) et al. – A local control system for the test masses of the Virgo gravitational wave detector. *Astroparticle Physics*, vol. 20, 2004, pp. 617–628.

[72] Acernese (F.) et al. – First locking of the VIRGO central area interferometer with suspension hierarchical control. *Astroparticle Physics*, vol. 20, 2004, pp. 629–640.

[73] Acernese (F.) et al. – Search for inspiralling binary events in the Virgo engineering run data. *Classical and Quantum Gravity*, vol. 21, 2004, pp. S709–S716.

2 Publications dans des actes de colloques avec comité de lecture

[74] Mohapatra (S.), Nemtzow (Z.), Chassande-Mottin (E.) et Cadonati (L.). – Performance of a Chirplet-based analysis for gravitational waves from binary black hole mergers. *J. Phys. Conf. Ser.*, vol. 363, 2012, p. 012031. – Proc. of the 9th Amaldi Conference, Cardiff UK.

[75] Chassande-Mottin (E.). – Data analysis challenges in transient gravitational wave astronomy. *In : AIP Conf. Proc. : Acoustic and Radio EeV Neutrino Detection Activities, ARENA'12*, p. 252. – Erlangen (Germany), 2012.

[76] Auger (F.), Chassande-Mottin (E.) et Flandrin (P.). – Making reassignment adjustable : The Levenberg-Marquardt approach. *In : IEEE Int. Conf. on Acoust., Speech and Signal Proc. ICASSP-12*. – Kyoto (Japan), 2012.

[77] Flandrin (P.), Chassande-Mottin (E.) et Auger (F.). – Uncertainty and spectrogram geometry. *In : 20th European Signal Processing Conf. EUSIPCO-12*. – Bucharest (Romania), 2012.

[78] Auger (F.), Chassande-Mottin (E.) et Flandrin (P.). – Réallocation de Levenberg-Marquardt. *In : 23e Colloque GRETSI - Traitement du Signal et des Images*. – Bordeaux (France), 2011.

[79] Chassande-Mottin (E). – Joint searches for gravitational waves and high-energy neutrinos. *J. Phys. Conf. Ser.*, vol. 243, n° 012002, 2010. – Proc. of the 14th Grav. Wave Data Anal. Workshop (Rome, Italy).

[80] Chassande-Mottin (E.), Miele (M.), Mohapatra (S.) et Cadonati (L.). – Detection of gravitational-wave bursts with chirplet-like template families. *Class. Quantum Grav.*, vol. 27, 2010, p. 194017.

[81] Van Elewyck (V.) et al. – Joint Searches Between Gravitational-Wave Interferometers and High-Energy Neutrino Telescopes :. Science Reach and Analysis Strategies. *Int. J. Mod. Phys. D*, vol. 18, 2009, pp. 1655–1659.

[82] Rabaste (O.), Petiteau (A.) et Chassande-Mottin (É.). – Détection de chirps multi-composantes et application aux ondes gravitationnelles des binaires à rapport de masses extrême. *In : Actes du 22ème Colloque GRETSI*. – Dijon (France), 2009.

[83] Rabaste (O.) et Chassande-Mottin (É.). – Echantillonnage minimal de la sphère céleste adapté au réseau d'antennes gravitationnelles terrestres. *In : Actes du 22ème Colloque GRETSI*. – Dijon (France), 2009.

[84] Chassande-Mottin (É.). – Chains of chirplets for the detection of gravitational wave chirps. *In : Wavelets XII, Proceedings of SPIE*, pp. 6707–12–39. – San Diego (US), 2007.

[85] Rabaste (O.), Chassande-Mottin (É.) et Pai (A.). – Goniométrie pour les chirps gravitationnels. *In : Actes du 21ème Colloque GRETSI*, pp. 741–744. – Troyes (France), 2007.

[86] Chassande-Mottin (É.). – Géométrie des ensembles de chirps et détection des ondes gravitationnelles. *In : Actes du 20ème Colloque GRETSI*. pp. 261–264. – Louvain-la-Neuve (Belgique), 2005.

[87] Chassande-Mottin (E.). – Testing normality of gravitational wave data with a low cost recursive estimate of the kurtosis. *In : Proc. of PSIP'2003*, pp. 157–160. – Grenoble (France), 2003. gr-qc/0212010.

[88] Chassande-Mottin (E.), Auger (F.) et Flandrin (P.). – Estimating singularities with reassigned distributions. *In : Proc. of the 5th Int. Conf. on Sig. Proc.* – Beijing (China), 2000.

[89] Chassande-Mottin (E.) et Flandrin (P.). – Reassigned scalograms and singularities. *In : Proc. of the 3rd European Congress of Mathematics*, pp. 583–590. – Barcelona (Spain), 2000.

[90] Chassande-Mottin (E.) et Dhurandhar (S. V.). – Adaptive filtering techniques for interferometric data preparation : removal of long-term sinusoidal signals and oscillatory transients. *Int. J. Mod. Phys. D*, vol. 9, n° 3, 2000, pp. 275–279. – Proc. of the 4th Grav. Wave Data Anal. Workshop.

[91] Chassande-Mottin (E.) et Flandrin (P.). – On the stationary phase approximation of chirp spectra. *In : Proc. of the IEEE Int. Symp. on Time-Frequency and Time-Scale Analysis*, pp. 117–120. – Pittsburgh (US), 1998.

[92] Chassande-Mottin (E.), Auger (F.), Daubechies (I.) et Flandrin (P.). – Partition du plan temps-fréquence et réallocation. *In : Proc. 16ème Colloque GRETSI*, pp. 1447–1450. – Grenoble (France), 1997.

[93] Gonçalvès (P.), Chassande-Mottin (E.) et Flandrin (P.). – Time-frequency methods in time-series data analysis. *In : Proc. of the 2nd Workshop on Grav. Wave Data Analysis*, éd. par Davier (M.) et Hello (P.), pp. 35–46. – Gif-sur-Yvette, France, Editions Frontières, 1997.

[94] Chassande-Mottin (E.) et Flandrin (P.). – On the time-frequency detection of chirps and its application to gravitational waves. *In : Proc. of the 2nd Grav. Wave Data Anal. Workshop*, éd. par Davier (M.) et Hello (P.). pp. 47–52. – Gif-sur-Yvette, France, 1997.

[95] Chassande-Mottin (E.), Auger (F.) et Flandrin (P.). – Supervised time-frequency reassignment. *In : Proc. of the IEEE Int. Symp. on Time-Frequency and Time-Scale Analysis*, pp. 517–520. – Paris (France), 1996.

[96] Abry (P.), Chassande-Mottin (E.) et Flandrin (P.). – Algorithmes rapides pour la décomposition en ondelette continue. Application à l'implantation de la réallocation du scalogramme. *In : Proc. 15ème Colloque GRETSI*, pp. 313–316. – Juan-Les-Pins (France), 1995.

[97] Flandrin (P.) et Chassande-Mottin (E.). – Sur la réallocation des scalogrammes. *In : Proc. 15ème Colloque GRETSI*, pp. 309–312. – Juan-Les-Pins (France), 1995.

[98] Flandrin (P.), Chassande-Mottin (E.) et Abry (P.). – Reassigned scalograms and their fast algorithms. *In : Proc. SPIE – Wavelet Appl. in Signal and Image Proc.*, pp. 152–158. – San Diego (US), 1995.

Publications en tant que co-auteur de la Collaboration Virgo

[99] Accadia (T.) et al. – Noise monitor tools and their application to Virgo data. *In : Journal of Physics : Conference Series*, p. 122024. – Cardiff, 2012.

[100] Degallaix (J.) et al. – Advanced Virgo Status. *In : Astronomical Society of the Pacific Conference Series*, p. 151. – Paris, 2012.

[101] Accadia (T.) et al. – The Virgo interferometer for gravitational wave detection. *In : International Journal of Modern Physics D*, pp. 2075–2079. – Shanghai, 2011.

[102] Accadia (T.) et al. – Tools for noise characterization in Virgo. *In : Journal of Physics : Conference Series*, p. 012004. – Rome, 2010.

[103] Accadia (T.) et al. – Noise from scattered light in Virgo's second science run data. *In : Classical and Quantum Gravity*, p. 194011. – Rome, 2010.

[104] Accadia (T.) et al. – Commissioning status of the Virgo interferometer. *In : Classical and Quantum Gravity*, p. 0824002. – New York, 2010.

[105] Accadia (T.) et al. – Status and perspectives of the Virgo gravitational wave detector. *In : Journal of Physics Conference Series*, p. 012074. – Rome, 2010.

[106] Accadia (T.) et al. – Virgo calibration and reconstruction of the gravitational wave strain h(t) during VSR1. *In : Journal of Physics : Conference Series*, p. 012015. – New York, 2010.

[107] Buskulic (D.) et al. – Very low latency search for low mass compact binary coalescences in the LIGO S6 and Virgo VSR2 data. *In : Classical and Quantum Gravity*, p. 194013. – Rome, 2010.

[108] Chassande-Mottin (E.). – Joint searches for gravitational waves and high-energy neutrinos. *In : Journal of Physics : Conference Series*, p. 012002. – Rome, 2010.

[109] Punturo (M.) et al. – The third generation of gravitational wave observatories and their science reach. *In : Classical and Quantum Gravity*, p. 084007. – New York, 2010.

[110] Acernese (F.) et al. – Cleaning the Virgo sampled data for the search of periodic sources of gravitational waves. *In : Classical and Quantum Gravity*, p. 204002. – San Juan, 2009.

[111] Acernese (F.) et al. – Noise studies during the first Virgo science run and after. *In : Classical and Quantum Gravity*, p. 184003. – Cambridge, 2008.

[112] Acernese (F.) et al. – Virgo status. *In : Classical and Quantum Gravity*, p. 184001. – Cambridge, 2008.

[113] Acernese (F.) et al. – VIRGO : a large interferometer for gravitational wave detection started its first scientific run. *In : Journal of Physics : Conference Series*, p. 032007. – Sendai, 2008.

[114] Acernese (F.) et al. – Status of Virgo. *In : Classical and Quantum Gravity*, p. 114045. – Sydney, 2008.

[115] Acernese (F.) et al. – The real-time distributed control of the Virgo Interferometric Detector of Gravitational Waves. *In : IEEE Transactions on Nuclear Science*, pp. 302–310. – Chania, 2008.

[116] Acernese (F.) et al. – Interferometric detectors of gravitational waves on Earth : the next generations. *In : Journal of Physics : Conference Series*, p. 062016. – Manchester, 2008.

[117] Acernese (F.) et al. – Data Acquisition System of the Virgo Gravitational Waves Interferometric Detector. *In : IEEE Transactions on Nuclear Science*, pp. 225–232. – Batavia, 2008.

[118] Bignotto (M.) et al. – A Cross-correlation method to search for gravitational wave bursts with AURIGA and Virgo. *In : Classical and Quantum Gravity*, p. 114046. – Sydney, 2008.

[119] Tournefier (E.) et al. – The status of Virgo. *In : Journal of Physics : Conference Series*, p. 062025. – Manchester, 2008.

[120] Acernese (F.) et al. – The status of VIRGO. *In : Proceedings of ICALEPCS 2007 Conference*, p. TOAB05. – Knoxville, 2007.

[121] Acernese (F.) et al. – Status of Virgo. *In : Proceedings of the 42nd Rencontres de Moriond*. – La Thuile, 2007.

[122] Acernese (F.) et al. – LIGO and VIRGO : large interferometers searching for gravitational waves. *In : Proceedings of ICHEP 2006*. – Moscou, 2007.

[123] Acernese (F.) et al. – Status of coalescing binaries search activities in Virgo. *In : Proceedings of the 42nd Rencontres de Moriond*. – La Thuile, 2007.

[124] Acernese (F.) et al. – The Automatic Alignment System of the Virgo Interferometer. *In : 2007 Gravitational Waves and Experimental Gravity*, pp. 153–158. – La Thuile, 2007.

[125] Acernese (F.) et al. – All-sky gravitational wave burst search in the Virgo C7 run data. *In : 2007 Gravitational Waves and Experimental Gravity*, pp. 115–118. – La Thuile, 2007.

[126] Acernese (F.) et al. – Future Virgo Upgrades. *In : Proceedings of the 42nd Rencontres de Moriond*. – La Thuile, 2007.

[127] Acernese (F.) et al. – Data quality and detector characterization for Burst Search in Virgo data. *In : 2007 Gravitational Waves and Experimental Gravity*, pp. 111–114. – La Thuile, 2007.

[128] Acernese (F.) et al. – Status of Virgo detector. *In : Classical and Quantum Gravity*, pp. S381–S388. – Potsdam, 2007.

[129] Acernese (F.) et al. – Gravitational waves by gamma-ray bursts and the Virgo detector : the case of GRB 050915a. *In : Classical and Quantum Gravity*, pp. S671–S679. – Potsdam, 2007.

[130] Acernese (F.) et al. – Improving the timing precision for inspiral signals found by interferometric gravitational wave detectors. *In : Classical and Quantum Gravity*, pp. S617–S625. – Potsdam, 2007.

[131] Acernese (F.) et al. – Coincidence analysis between periodic source candidates in C6 and C7 Virgo data. *In : Classical and Quantum Gravity*, pp. S491–S499. – Potsdam, 2007.

[132] Acernese (F.) et al. – Analysis of noise lines in the Virgo C7 data. *In : Classical and Quantum Gravity*, pp. S433–S443. – Potsdam, 2007.

[133] Acernese (F.) et al. – Data quality studies for burst analysis of Virgo data acquired during Weekly Science Runs. *In : Classical and Quantum Gravity*, pp. S415–S422. – Potsdam, 2007.

[134] Acernese (F.) et al. – Noise budget and noise hunting in VIRGO. *In : 2007 Gravitational Waves and Experimental Gravity*, pp. 147–152. – La Thuile, 2007.

[135] Acernese (F.) et al. – Normal/independent noise in VIRGO data. *In : Classical and Quantum Gravity*, pp. S829–S836. – Brownsville, 2006.

[136] Acernese (F.) et al. – The Virgo status. *In : Classical and Quantum Gravity*, pp. S635–S642. – Brownsville, 2006.

[137] Acernese (F.) et al. – Status of Virgo. *In : Journal of Physics Conference Series*, pp. 32–35. – Zaragoza, 2006.

[138] Acernese (F.) et al. – Testing Virgo burst detection tools on commissioning run data. *In : Classical and Quantum Gravity*, pp. S197–S205. – Okinawa, 2006.

[139] Acernese (F.) et al. – The status of coalescing binaries search code in Virgo, and the analysis of C5 data. *In : Classical and Quantum Gravity*, pp. S187–S196. – Okinawa, 2006.

[140] Acernese (F.) et al. – The Virgo automatic alignment system. *In : Classical and Quantum Gravity*, pp. S91–S101. – Okinawa, 2006.

[141] Acernese (F.) et al. – The variable finesse locking technique. *In : Classical and Quantum Gravity*, pp. S85–S89. – Okinawa, 2006.

[142] Acernese (F.) et al. – The status of VIRGO. *In : Classical and Quantum Gravity*, pp. S63–S69. – Okinawa, 2006.

[143] Acernese (F.) et al. – Virgo upgrade investigations. *In : Journal of Physics Conference Series*, pp. 223–229. – Okinawa, 2006.

[144] Acernese (F.) et al. – A parallel in-time analysis system for Virgo. *In : Journal of Physics Conference Series*, pp. 35–43. – Okinawa, 2006.

[145] Acernese (F.) et al. – A first study of environmental noise coupling to the Virgo interferometer. *In : Classical and Quantum Gravity*, pp. S1069–S1077. – Annecy, 2005.

[146] Acernese (F.) et al. – Virgo status and commissioning results. *In : Classical and Quantum Gravity*, pp. S185–S191. – Noordwijk, 2005.

[147] Acernese (F.) et al. – The Virgo detector. *In : IFAE 2005 : XVII Incontri di Fisica delle Alte Energie ; 17th Italian Meeting on High Energy Physics*, pp. 307–310. – Catania, 2005.

[148] Acernese (F.) et al. – A simple line detection algorithm applied to Virgo data. *In : Classical and Quantum Gravity*, pp. S1189–S1196. – Annecy, 2005.

[149] Acernese (F.) et al. – Testing the detection pipelines for inspirals with Virgo commissioning run C4 data. *In : Classical and Quantum Gravity*, pp. S1139–S1148. – Annecy, 2005.

[150] Acernese (F.) et al. – NAP : a tool for noise data analysis. Application to Virgo engineering runs. *In : Classical and Quantum Gravity*, pp. S1041–S1049. – Annecy, 2005.

[151] Acernese (F.) et al. – Virgo and the worldwide search for gravitational waves. *In : General Relativity and Gravitational Physics*, pp. 92–100. – Vietri sul Mare, 2005.

[152] Acernese (F.) et al. – Status of VIRGO. *In : Classical and Quantum Gravity*, pp. S869–S880. – Annecy, 2005.

[153] Tournefier (E.) et al. – The status of VIRGO. *In : HEP2005 International Europhysics Conference on High Energy Physics*, p. PoS(HEP2005)029. – Lisboa, 2005.

[154] Acernese (F.) et al. – Status of VIRGO. *In : Gravitational Wave and Particle Astrophysics Detectors*. – Glasgow, 2004.

[155] Acernese (F.) et al. – Properties of seismic noise at the Virgo site. *In : Classical and Quantum Gravity*, pp. S433–S440. – Tirrenia, Pise, 2004.

[156] Acernese (F.) et al. – The last-stage suspension of the mirrors for the gravitational wave antenna Virgo. *In : Classical and Quantum Gravity*, pp. S425–S432. – Tirrenia, Pise, 2004.

[157] Acernese (F.) et al. – Results of the Virgo central interferometer commissioning. *In : Classical and Quantum Gravity*, pp. S395–S402. – Tirrenia, Pise, 2004.

[158] Acernese (F.) et al. – Status of VIRGO. *In : Classical and Quantum Gravity*, pp. S385–S394. – Tirrenia, Pise, 2004.

[159] Beauville (F.) et al. – The VIRGO large mirrors : a challenge for low loss coatings. *In : Classical and Quantum Gravity*, pp. S935–S945. – Tirrenia, Pise, 2004.

[160] Yvert (M.) et al. – A first test of a sine-Hough method for the detection of pulsars in binary systems using the E4 Virgo engineering run data. *In : Classical and Quantum Gravity*, pp. S717–S727. – Tirrenia (Pisa), 2004.

[161] Acernese (F.) et al. – Data analysis methods for non-Gaussian, nonstationary and nonlinera features and their application to VIRGO. *In : Classical and Quantum Gravity*, pp. 915–924. – Kyoto, 2003.

[162] Acernese (F.) et al. – Search for non-Gaussian events in the data of the VIRGO E4 engineering run. *In : Classical and Quantum Gravity*, pp. 623–632. – Kyoto, 2003.

[163] Acernese (F.) et al. – The Virgo data acquisition system. *In : Proceedings Conference Real Time 2003*. – Montreal, 2003.

[164] Flaminio (R.) et al. – The gravitational wave detector VIRGO. *In : Nanobeam 2002*, pp. 7–13. – Lausanne, 2003.

3 Contributions à des ouvrages de synthèse

[165] Auger (F.), Flandrin (P.) et Chassande-Mottin (E.). – Time-frequency reassignment. *In : Time-frequency signal analysis and processing*, éd. par Boashash (B.). – Elsevier, 2nd édition, 2014.

[166] Auger (F.) et Chassande-Mottin (E.). – Quadratic time-frequency analysis (I) : Cohen's class. *In : Time-frequency analysis : concepts and methods*, éd. par Hlawatsch (F.) et Auger (F.), pp. 131–164. – London and Hoboken, ISTE and Wiley, 2008.

[167] Chassande-Mottin (E.), Auger (F.) et Flandrin (P.). – Reassignment. *In : Time-frequency analysis : concepts and methods*, éd. par Hlawatsch (F.) et Auger (F.), pp. 249–278. – London and Hoboken, ISTE and Wiley, 2008.

[168] Auger (F.) et Chassande-Mottin (E.). – Analyse temps-fréquence quadratique (I) : la classe de Cohen. *In : Traité IC2 – Temps-fréquence : concepts et outils*, éd. par Hlawatsch (F.) et Auger (F.), pp. 139–172. – Paris, Hermès Science, Lavoisier, 2005.

[169] Chassande-Mottin (E.), Auger (F.) et Flandrin (P.). – La réallocation. *In : Traité IC2 – Temps-fréquence : concepts et outils*, éd. par Hlawatsch (F.) et Auger (F.), pp. 259–288. – Paris, Hermès Science, Lavoisier, 2005.

[170] Chassande-Mottin (E.) et Flandrin (P.). – Détection temps-fréquence et réallocation. *In : Traité IC2 – Décision dans le plan temps-fréquence*, éd. par Martin (N.) et Doncarli (C.), pp. 103–126. – Paris, Hermès, 2004.

[171] Auger (F.), Flandrin (P.) et Chassande-Mottin (E.). – Time-frequency reassignment. *In : Time-frequency signal analysis and processing*, éd. par Boashash (B.). – Elsevier, 2003.

[172] Chassande-Mottin (E.), Auger (F.) et Flandrin (P.). – Time-frequency/time-scale reassignment. *In : Wavelets and Signal Processing*, éd. par Debnath (L.). – Birkhäuser, 2003.

[173] Flandrin (P.), Auger (F.) et Chassande-Mottin (E.). – Time-frequency reassignment from principles to algorithms. *In : Applications in Time-Frequency Signal Processing*, éd. par Papandreou-Suppappola (A.), pp. 179–203. – CRC Press, 2002.

Data analysis challenges in transient gravitational-wave astronomy

Éric Chassande-Mottin for the LIGO Scientific Collaboration and the Virgo Collaboration

APC, Univ Paris Diderot, CNRS/IN2P3, CEA/Irfu, Obs de Paris, Sorbonne Paris Cité, France

Abstract. Gravitational waves are radiative solutions of space-time dynamics predicted by Einstein's theory of General Relativity. A world-wide array of large-scale and highly sensitive interferometric detectors constantly scrutinizes the geometry of the local space-time with the hope to detect deviations that would signal an impinging gravitational wave from a remote astrophysical source. Finding the rare and weak signature of gravitational waves buried in non-stationary and non-Gaussian instrument noise is a particularly challenging problem. We will give an overview of the data analysis techniques and associated observational results obtained so far by Virgo (in Europe) and LIGO (in the US), along with the prospects offered by the upcoming advanced versions of those detectors.

Keywords: Gravitational waves, Data analysis
PACS: 95.85.Sz, 04.80.Nn, 95.55.Ym

Einstein's theory of General Relativity introduces the concept of a deformable and evolving space-time. The dynamics of space-time is prescribed by the Einstein equation. In linearized gravity which assumes small deformations in a nearly flat space-time, this equation reduces to the wave equation which therefore evidences the existence of radiative solutions. The latter are referred to as *gravitational waves* (GW) and can be phenomenologically seen as propagating disturbances of space-time itself. The theory also predicts that GW are transverse waves, that they nominally propagate at the speed of light and possess two independent polarizations [1, 2].

GW have never been directly detected, i.e. through the measurement of their effect on a man-made instrument. Strong evidence of their existence has been provided by the observation of the famous Hulse-Taylor pulsar binary (PSR B1913+16) [3]. The decay rate of the binary orbital period is in remarkable agreement with the predicted evolution obtained under the assumption that this system radiates energy away in the form of GW.

The direct search for GW made notable progress with the advent of dedicated instruments based on high-precision laser interferometry such as LIGO and Virgo (see [4, 5] for a detailed review). With the ongoing installation of a new and improved generation of those instruments, the first discovery is expected within the decade.

While electromagnetic waves are produced by accelerated charges, GW are produced by accelerated masses. Very large masses and relativistic velocities are necessary to generate GW at a detectable level. For this reason, the current projects aiming at detecting GW target potential astrophysical sources involving very dense and compact objects such as neutron stars or black holes. Very energetic astrophysical events such as the coalescence of neutron star and/or black hole binaries, or stellar core collapses are expected to be the source of intense and short-duration bursts of GW [4].

Because of the limited rate of occurrence of such events, searching for such transient GW in the LIGO and Virgo data essentially consists in searching for rare and weak signals at the detectability limit. This article reports the state-of-the-art of the search for GW transient signals with a focus on the related data analysis challenges. Searches for long-lived signals such as periodic GWs from rotating neutron stars and stochastic GW backgrounds are beyond the scope of this paper. We first give some introductory material with a general presentation of the detectors in Sec. 1 and a review of the relevant astrophysical sources in Sec. 2. Sec. 3 gives an overview of the major problems faced when searching for transient GW along with the data analysis methods deployed to address them.

1. INTERFEROMETRIC GW DETECTORS

The first generation of interferometric GW detectors comprises five large-scale instruments in total (see Fig. 1). The US-based Laser Interferometer Gravitational-Wave Observatory (LIGO) [6] includes three kilometric-scale instruments located in Livingston, Louisiana (labelled L1) and Hanford, Washington (the latter hosting two interferometers in the same vacuum enclosure with labels H1 and H2). The French-Italian project Virgo [7] has one instrument of the same class

5th International Workshop on Acoustic and Radio EeV Neutrino Detection Activities
AIP Conf. Proc. 1535, 252-259 (2013); doi: 10.1063/1.4807558

FIGURE 1. Geographic location of the current and future GW interferometric detectors. This world map displays the location of the four sites of the first generation detectors (LIGO H and L, Virgo and GEO), and six sites of the second generation (complemented by LIGO I and KAGRA). The future detector LIGO India is still pending approval and its exact location is yet to be determined. Credits: [9]

located in Cascina near Pisa, Italy (labelled V1). This set of kilometer-scale instruments is complemented by a detector with more modest dimensions (several hundreds of meters): GEO [8] (labelled G1), a German-British detector in operation near Hanover, Germany.

Despite major differences in the technologies in use, all those instruments measure gravitational waves through the same principle. They all sense the strain that a passing GW exerts on space-time by monitoring the differential length $\delta\ell$ of the optical path followed by two laser beams propagating along orthogonal directions over a distance L. This is performed by letting the two beams interfere similarly to the Michelson-Morley experiment. The interference is closely related to the difference in the phase accumulated by the two beams before they combine and hence to the difference in their optical paths. The measurement of the interference light power allows that of $\delta\ell$ with high accuracy. Measurement noises (mainly the thermal noise due to the Brownian agitation of the atoms constitutive of the optics and the shot noise due to the quantum nature of light) can be reduced to reach the level of $h \equiv \delta\ell/L \sim 10^{-21}$, where the detector response h is directly connected to the amplitude h_+ and $h_\times$ of the two GW polarizations[1]. The best sensitivity is achieved in a frequency band ranging from $\sim$ 100 Hz to 1 kHz approximately (see Fig. 2 – bottom).

The detector response is a linear mixture $h = F_+ h_+ + F_\times h_\times$ of the two GW polarizations. The antenna pattern factors F_+ and $F_\times$ characterize the way the wave polarizations couple to the detector. The coupling $\mathscr{F} = (F_+^2 + F_\times^2)^{1/2} \leq 1$ is maximum for waves impinging perpendicularly to the detector plane and is minimum (and exactly zero) for waves from the four "blind" directions associated to the two bisectors of the detector arms. GW detectors are non-directional instruments as $\mathscr{F} \gtrsim 1/2$ for more than half of the sky.

[1] These quantities measure the strain or fractional length change that a GW exerts on space-time and are therefore dimensionless

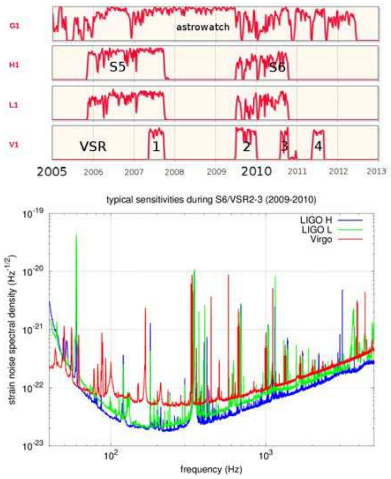

FIGURE 2. (top) Time line of the data takings completed so far. Credits: [10] **(bottom) Sensitivity achieved by LIGO and Virgo during their last science data taking S6/VSR2–3** [11].

The first generation detectors have conducted a series of science data takings reaching an integrated observation time of about 2 years (see Fig. 2 – top). The data takings are coordinated in order to maximize the observation time with the three most sensitive detectors operating while always maintaining at least one detector in "astro-watch" mode in case of an outstanding galactic event.

The first generation of detectors has now been decommissioned and it is currently being replaced by a second generation of "advanced" detectors. Thanks to major upgrades in their infrastructure and instrumentation, a ten-fold increase in sensitivity is expected with the advanced detectors as indicated in Fig. 3. The GW amplitude decaying inversely with the distance, this corresponds to a factor of thousand in the observable volume and hence in the number of detectable sources. Advanced detectors are likely to detect several tens and possible several hundreds of sources as we will see in the next Section.

The installation of the advanced LIGO detectors [12] should be completed by the end of 2013 and a first sci-

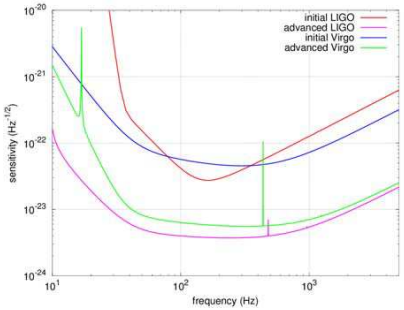

FIGURE 3. Projected sensitivities for the advanced LIGO and advanced Virgo detectors compared with the design sensitivity of their initial version.

ence run is likely to take place in 2015. The original plan was to install two four-kilometer detectors at Hanford site, but there is now a proposal (still to be approved by U.S. and Indian institutions) to move one of those detectors to a new observatory in India. If this plan materializes, the third detector at the Indian site would start operation around 2020. Advanced Virgo plans to have a robustly operating detector in 2015 and to begin collecting science data as soon as possible after that [13]. GEO foresees a program of upgrades "GEO-HF" [14] which focuses on improving the detector sensitivity at high-frequencies thanks to a larger laser power and the use of "squeezed light". The network of advanced detectors will be completed by the Japanese KAGRA detector [15] which has the specificity of being installed underground in the Kamioka mine (where the seismic motion is much lower than at the surface) and to operate at cryogenic temperatures to reduce thermal noise. An initial three-kilometer room-temperature interferometer is expected to be operational by 2015, with the full cryogenic interferometer ready to start taking data by 2018.

2. ASTROPHYSICAL SOURCES OF GW TRANSIENTS

Phenomenologically, GW emission arises from relativistic bulk motion. At lowest order, GW can be related to variations in the quadrupolar moment of the mass distribution [1]. Therefore, GW sources have to present some degree of non-axisymmetry. In this section, we review the astrophysical scenarios giving rise to GW emission. The coalescence of neutron-star and/or black-hole binaries similar to the Hulse-Taylor binary mentioned previously is often considered the most promising one.

The last minutes before the system merges give rise to the emission of an intense burst of GW. Post-Newtonian expansions of the binary dynamics [16, 17] are used to predict the gravitational waveforms radiated during the inspiral phase which precedes the merger. The GW signature consists in a *chirp* signal whose frequency sweeps towards high values according to a power law at first order . A substantial amount of energy is radiated in the following phase when the two bodies merge into a black hole. In this highly relativistic phase, the perturbative treatment of binary dynamics is not valid anymore and one has to resort to numerical simulations. The process is concluded by the ring-down phase during which the resulting distorted black hole radiates away its asymmetry down to equilibrium. During the whole coalescence process, a stellar-mass binary with equal masses radiates away of order of a percent of its rest mass[4].

Although binary systems are fairly common, only a small fraction eventually forms a compact binary that is sufficiently tight to coalesce in less than Hubble time. A survey of population estimates [18] gives a "realistic" rate of one neutron-star–neutron-star coalescence[2] per 10,000 years per galaxy equivalent in size to the Milky Way. GW detectors can ideally observe those binary systems up to a distance of $\sim$ 30 Mpc and $\sim$ 440 Mpc for initial and advanced detectors resp. [18]. Converted into a rate of *detectable* coalescences, this leads to ~ 0.02 events per year with the first generation of (initial) detectors and to ~ 40 events for the second generation (advanced). Large error bars are attached to those estimates reflecting the weakness of the observational constraints we have about those systems. The above stated rates can then be 10 times smaller or larger in the "pessimistic" or "optimistic" scenarios respectively. The "realistic" rates presented above are corroborated by the ones derived assuming that compact binary mergers are the progenitors of short-hard gamma-ray bursts (GRB) [18].

Gravitational stellar-core collapse is another potential source of GW if some degree of non-axisymmetry is exhibited during this process. The simulations required to make reliable predictions of the emission levels are very challenging as they have to incorporate many physical ingredients including relativistic magneto-hydrodynamics and a detailed treatment of neutrino transport and nuclear interactions [19]. The current realistic estimate of the amount of radiated GW energy is of order $10^{-7}M_{\odot}$ and corresponds approximately [20] to a distance reach of order $\sim$ 10 kpc with the initial detectors, $\sim$ 100 kpc with the advanced detectors. The detectable sources are therefore located in the Galaxy.

[2] Similar rates are obtained for the other types of systems mixing neutron stars and/or black-holes.

Another potential source of GW bursts are "neutron-star quakes" [21] during which the vibrational normal modes of a neutron star are excited and damped by GW emission. Star quakes may origin from the disruption of the star crust due to the sudden rearrangement of the magnetic field of a highly-magnetized neutron star (magnetar). Cosmic string cusps may be also listed among the potential GW burst sources [22].

3. SEARCHES FOR GW TRANSIENT SIGNALS

3.1. Time-series analysis

In detection problems, the availability of *a priori* information plays a major rôle. We have seen in Sec. 2 that the GW signature from coalescing binaries of neutron stars and/or black holes have a specific time evolution which can be predicted with good accuracy. This morphological information helps to distinguish a real GW signal from the instrumental or environmental noise. The search for known signals is efficiently performed by *matched filtering techniques* [23] which cross-correlates the data with the expected "template" waveforms obtained from the source model.

Because of the highly-relativistic dynamics associated with the production of GW, some of the expected GW waveforms are difficult to predict with accuracy. This calls for detection methods that are robust to the model uncertainties. *Excess power methods* essentially consist in searching for a broad family of GW waveforms by scanning a time-frequency map for transient excursions. The time-frequency map is obtained by projecting the data onto a dictionary of elementary waveforms that tiles the time-frequency plane. Several types of dictionary have been tested including local cosines [24], sine-Gaussian wavelets [25], orthogonal wavelet packet bases [26] or chirplets [27]. Real GW signals are unlikely to correlate exactly with one element in the dictionary, but with several of them. Clustering algorithms are generally applied to harvest the signal energy scattered over several elements [28, 29, 30].

The time-frequency dictionaries mentioned above are composed of "generic" elementary waveforms mainly motivated by mathematical or algorithmic arguments. Astrophysically motivated dictionaries can be obtained by extracting the relevant information from catalogs of GW signals developed through numerical simulations [31, 32, 33, 34].

3.2. Multi-detector analysis

We described the basic ideas employed to analyze the data stream from individual detectors. A gain in sensitivity is expected from the availability of a joint observation by multiple detectors. This section discusses several aspects related to the combined analysis of multiple detector data.

3.2.1. Coherent analysis of multiple data streams

We already mentioned that the detector receives a mixture of both GW polarizations which depends on the relative orientation and alignment of the detector and wave. Since the detectors are not co-planar and co-aligned, they couple differently to the incoming wave resulting in observed responses with different initial phases and amplitudes. Because of its finite speed, a GW reaches the detectors at different times. All those differences can be exploited using *coherent analysis techniques* to improve the overall sensitivity. Those techniques consist in compensating the phase shift and delay of the various responses to align them in time and phase assuming a given direction-of-arrival. The resulting data streams are combined so that the sum operates constructively for GW signals from the selected direction. The data stream which results from the coherent combination maximizes the signal-to-noise ratio (SNR). The combined stream can then be analyzed using methods inspired by the single detector case, i.e., excess power methods for the unmodelled GW bursts [35, 36] and matched filtering techniques [37, 38] for inspiralling binaries. The coherent analysis being directional (each coherently combined stream is associated to a given direction), the outcome is a probability (pseudo-)distribution over the sky usually referred to *sky map* from which the most likely location of the source can be extracted.

3.2.2. Mitigation of non-Gaussian/non-stationary noise

The noise of the real instruments is far from the ideal properties of stationarity and Gaussianity we expect from the main fundamental (thermal and quantum) noises. The tails of the noise distribution is dominated by a non-Gaussian and non-stationary component consisting in a large number of transient noise excursions commonly called *glitches*. Glitches are produced by a variety of environmental and instrumental processes, such as upconversion of seismic noise or saturations in feedback control systems. Since glitches occasionally occur nearly simultaneously in separate detectors by chance, they can mimic a gravitational-wave signal.

The population of glitches is difficult to model. The size and the large complexity of GW detectors makes this modelling even more difficult. GW detectors being instruments extended over kilometers, it is hard to completely isolate them from the outside world and the surrounding anthropic activity. Therefore, the accurate modelling of the non-Gaussian/non-stationary noise background is for now out-of-reach. It has to be mitigated and this can be done at least partially by using multiple data.

It is possible to calculate combinations of the data from multiple detectors where the GW signals from all detectors interfere destructively in the sum. The GW signal thus cancels, but not background glitches. The energy in these "null" stream(s) may be used to reject or down-weight events not consistent with a gravitational wave [39, 36]. The success of such tests depend critically on having several independent detectors of comparable sensitivity.

3.2.3. Use of multiple detector data for background estimation

We explained earlier that the accurate modelling of non-Gaussian non-stationary noise is out-of-reach. The remaining part of the glitches that cannot be identified by the coherent techniques described in the previous section constitutes the dominating background noise in burst searches. This background has to be estimated. However, GW signals cannot be turned off: the detectors cannot be shielded from them. Therefore, we don't have "noise-only" data at our disposal for background estimation.

Nevertheless, the background can be estimated thanks to the availability of multiple data streams by time shifting one detector's data. The time shift is chosen to be much longer than the time-of-flight between detectors (~ 30 ms) and coherence time scale of the detector noise ($\sim$ seconds). The time-shifted (or "time-slide") analysis leaves only triggers due to accidental coincidences of instrumental glitches. The contribution from real GW signals is practically erased. By repeating the analysis many times with different time shifts, we get an accurate estimate of the rate of background events. For sufficiently large time shifts, each trial can be considered independent of the other. However, the number of time slides cannot be increased indefinitely as a significant correlation between time slides will occur above a certain level [40].

The p-value measuring the significance of a GW event can be computed by computing the fraction of louder background events from the time-slide analysis.

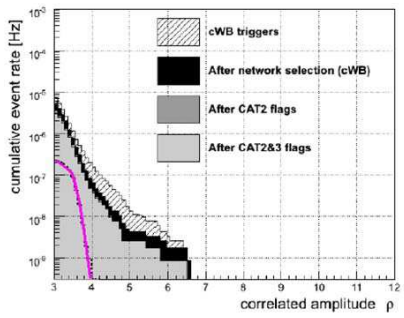

FIGURE 4. Examples of background distributions for the coherent Wave-Burst algorithm [36] for a three-detector network (LIGO-H and L and Virgo) during S6-VSR2/3 data taking. This distribution is given as a function of the correlated amplitude ρ homogeneous to the signal-to-noise ratio. **Hatch area**: background *before* any glitch rejection scheme is applied. **Black area**: *after* the "null-stream" glitch rejection (see Sec. 3.2.2). **Gray area**: *after* data-quality flags (see Sec. 3.3). CAT2 and 3 refers to the different categories of the data-quality flags whose description goes beyond the scope of this article. **Bold curve**: expectation if noise is stationary and Gaussian. Credits: [41].

3.3. Data quality

Besides the gravitational-wave channel $h(t)$, hundreds of auxiliary channels including microphones, seismometers, magnetometers, etc. are recorded at any given time during science data takings. Those channels can be used to get an image of the operational and environmental status of the detector. The observed correlation between the GW channel with the auxiliary channels can help determine the origin of noise artifacts and how the original disturbance couples into the detector [41]. A significant number of noise sources are identified *a posteriori* after the science data taking is done. Those noise sources cannot be mitigated by fixing the instrument. Instead, this leads to the development of a data-quality flag which, when "raised", indicates that the data are improper, and any event occurring at that time should be *vetoed*. This provides also an important resource for background glitch rejection. Data-quality flags with a large ($\gg 1$) efficiency (percentage of glitches vetoed by the flag) over dead-time (fraction of science time rejected by the flag) ratio are of particular interest [41]. About 200 data-quality flags are used in GW burst searches. Figure 4 shows the background improvement after vetoing.

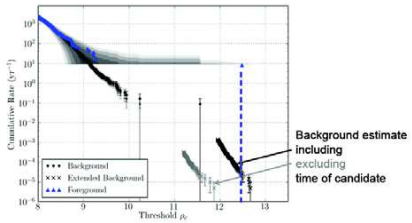

FIGURE 5. Cumulative event rate associated to the search for compact binary coalescences. The "candidate" at $\rho_c \approx 12.5$ is a simulated signal inserted as part of a "blind injection challenge exercise" (see text). Credits: [42]

3.4. Results

LIGO and Virgo conducted two joint science runs, labelled S5 for LIGO and VSR1 for Virgo for the first run, S6 and VSR2/3 for the second. A total of $T = 635$ days of observing time have been analyzed [43, 44]. No GW detection has been claimed yet. Upper limits (at 50% confidence level) on the GW strain obtained from an all-sky all-time GW burst search have been set. It is slightly below $h_{rss} < 5 \times 10^{-22}$ Hz$^{-1/2}$ for frequency at about 200 Hz, where the bound is on the root-sum-square (rss) amplitude $h^2_{rss} \equiv \int dt\, h^2_+(t) + h^2_\times(t)$ of the two GW polarizations at Earth. While the exact result depends on the assumed GW model (here, a generic sine Gaussian waveform characterized by its central frequency), it remains comparable for waveforms with a similar spectrum.

This upper limit placed on a local quantity (h_{rss} at Earth) can be translated into astrophysical constraints: for instance, upper limits on the radiated energy E_{GW} by generic sources of linearly polarized GW located at distance d. Averaging over the source inclination, the above strain limit corresponds to $E_{GW} = 2 \times 10^{-8} M_\odot c^2$ for galactic sources at distance $d = 10$ kpc, and $E_{GW} = 5 \times 10^{-2} M_\odot c^2$ for source in the Virgo cluster with $d = 15$ Mpc. Those estimates are comparable to the expected GW-radiated energy from core collapses and mergers of stellar-mass compact objects respectively.

The same data, when searched specifically for inspiralling binaries of neutron stars, leads to an upper limit on the rate of such astrophysical events of $\mathscr{R}_{90\%} = 1.3 \times 10^{-4}$yr^{-1}Mpc^{-3} [45, 42] which is still two orders of magnitude larger than the rate estimate obtained from population models [18]. Fig. 5 shows the cumulative rate of events detected by the matched-filtering procedure outlined in Sec. 3.1 in coincidence in the H1 and L1 detectors during four months of S6/VSR2-3 data taking. This distribution is displayed as a function of the ranking statistic ρ_c which combines the signal-to-noise ratios measured at both detectors. The distribution of candidate events (triangle) is superimposed to a background estimate (black dots) with error bars (in gray). The last triangle on the right-hand side of the plot at $\rho_c \approx 12.5$ is a candidate event detected with a false alarm rate of 1 in 7,000 years [42]. It was known in advance that a small number of fake GW signals might be added "blindly" to the data. The exact time and characteristics of these signals were only known by a small group of people sworn to silence until the eventual "opening of the envelope". The envelope was *not* empty and contained the detected event code-named GW100916 [46]. Thanks to this exercise, it was possible to test the entire decision-making chain up through the preparation of a publication.

4. ONLINE ANALYSIS AND RAPID ELECTROMAGNETIC FOLLOW-UP

Sources of GW are likely sources of other kinds of emissions, such as electromagnetic waves or jets of high-energy particles. The possible connection between compact binary coalescences and GRB is an example [47]. This motivates cross-correlating GW with other types of observations in the electromagnetic or neutrino spectra see e.g., [48, 49] for recent results. We will briefly report here on rapid follow-up observations seeking electromagnetic counterparts to GW candidate events. A low-latency analysis pipeline was operated for the first time during the last data taking [50]. It allows to generate alerts "on the fly" within 20 minutes of the associated GW candidate event. Major changes were required with respect to the original off-line pipelines. The most probable direction of the source along with an error box were communicated to a dozen of partner observatories [50] including radio telescopes, wide-field optical telescopes and the X/gamma-ray satellite Swift. This has led to follow-up observations which have been scanned for transient excursions. This exercise has been extremely useful and will help to prepare the exciting future of multi-messenger astronomy with the advanced detectors [51, 9].

ACKNOWLEDGMENTS

The authors gratefully acknowledge the support of the United States National Science Foundation for the construction and operation of the LIGO Laboratory, the Science and Technology Facilities Council of the United Kingdom, the Max-Planck-Society, and the State of Niedersachsen/Germany for support of the construction and operation of the GEO600 detector, and the Italian Istituto Nazionale di Fisica Nucleare and the French Cen-

tre National de la Recherche Scientifique for the construction and operation of the Virgo detector. The authors also gratefully acknowledge the support of the research by these agencies and by the Australian Research Council, the International Science Linkages program of the Commonwealth of Australia, the Council of Scientific and Industrial Research of India, the Istituto Nazionale di Fisica Nucleare of Italy, the Spanish Ministerio de Economía y Competitividad, the Conselleria d'Economia Hisenda i Innovació of the Govern de les Illes Balears, the Foundation for Fundamental Research on Matter supported by the Netherlands Organisation for Scientific Research, the Polish Ministry of Science and Higher Education, the FOCUS Programme of Foundation for Polish Science, the Royal Society, the Scottish Funding Council, the Scottish Universities Physics Alliance, The National Aeronautics and Space Administration, the National Research Foundation of Korea, Industry Canada and the Province of Ontario through the Ministry of Economic Development and Innovation, the National Science and Engineering Research Council Canada, the Carnegie Trust, the Leverhulme Trust, the David and Lucile Packard Foundation, the Research Corporation, and the Alfred P. Sloan Foundation. This paper has been assigned LIGO Document Number LIGO-P1200135 and Virgo TDS number VIR-0379C-12.

REFERENCES

1. K. Thorne, "Gravitational Radiation," in *300 Years of Gravitation*, edited by S. W. Hawking, and W. Israel, Cambridge University Press, 1987.
2. M. Maggiore, *Gravitational Waves – Volume 1: Theory and Experiments*, Oxford University Press, 2008.
3. J. M. Weisberg, D. J. Nice, and J. H. Taylor, *ApJ* **722**, 1030–1034 (2010), arXiv:1011.0718.
4. B. S. Sathyaprakash, and B. F. Schutz, *Living Rev. Rel.* **12** (2009).
5. K. Riles, Gravitational waves: Sources, detectors and searches (2012), to appear in Progress in Particle and Nuclear Physics, arXiv:1209.0667.
6. B. P. Abbott, et al., *Rept. Prog. Phys.* **72**, 076901 (2009), arXiv:0711.3041.
7. T. Accadia, et al., *JINST* **7**, P03012 (2012).
8. H. Grote for the LIGO Scientific Collaboration, *Class. Quantum Grav.* **27**, 084003 (2010).
9. P. S. Shawhan for the LIGO Scientific Collaboration and Virgo Collaboration, Rapid alerts for following up gravitational wave event candidates (2012), arXiv:1206.6163.
10. LIGO open science center (2012), https://losc.ligo.org/timeline.
11. J. Abadie, et al., Sensitivity achieved by the LIGO and Virgo gravitational wave detectors during LIGO's sixth and Virgo's second and third science runs (2012), arXiv:1203.2674.
12. G. M. Harry for the LIGO Scientific Collaboration, *Class. Quantum Grav.* **27** (2010).
13. T. Accadia, et al., Advanced Virgo technical design report, Tech. Rep. VIR-0128A-12, Virgo Collaboration (2012), https://tds.ego-gw.it/ql/?c=8940.
14. H. Lück, et al., *J. Phys. Conf. Ser.* **228** (2010).
15. K. Somiya for the KAGRA Collaboration, *Class. Quantum Grav.* **29** (2012).
16. L. Blanchet, *Living Rev. Rel.* **5**, 3 (2002), gr-qc/0202016.
17. A. Buonanno, G. B. Cook, and F. Pretorius, *Phys. Rev. D* **D75**, 124018 (2007), gr-qc/0610122.
18. J. Abadie, et al., *Class. Quantum Grav.* **27**, 173001–+ (2010).
19. C. D. Ott, *Class. Quantum Grav.* **26**, 063001 (2009).
20. P. Sutton, A rule of thumb for the detectability of gravitational-wave bursts (2010), https://dcc.ligo.org/cgi-bin/DocDB/ShowDocument?docid=P1000041.
21. N. Chamel, and P. Haensel, *Living Reviews in Relativity* **11** (2008), http://www.livingreviews.org/lrr-2008-10.
22. X. Siemens, et al., *Phys. Rev. D* **D73**, 105001 (2006), gr-qc/0603115.
23. B. F. Schutz, *The detection of Gravitational Waves*, Cambridge University Press, Cambridge, England, 1991, chap. Data processing, analysis and storage for interferometric antennas, pp. 406–452, D. Blair, ed.
24. W. G. Anderson, et al., *Phys. Rev. D* **63**, 042003 (2001).
25. S. Chatterji, et al., *Class. Quantum Grav.* **21**, S1809–S1818 (2004), gr-qc/0412119.
26. S. Klimenko, et al., *Class. Quantum Grav.* **21**, S1685–S1694 (2004), gr-qc/0407025.
27. E. Chassande-Mottin, et al., *Class. Quantum Grav.* **27**, 194017 (2010), arXiv:1005.2876.
28. J. Sylvestre, *Phys. Rev. D* **66**, 102004 (2002).
29. R. Khan, and S. Chatterji, *Class. Quantum Grav.* **26**, 155009 (2009), arXiv:0901.3762.
30. E. Chassande-Mottin, and A. Pai, *Phys. Rev. D* **D73**, 042003 (2006), gr-qc/0512137.
31. I. S. Heng, *Class. Quantum Grav.* **26**, 105005 (2009), arXiv:0810.5707.
32. C. Rover, et al., *Phys. Rev. D* **D80**, 102004 (2009), arXiv:0909.1093.
33. P. R. Brady, and S. Ray-Majumder, *Class. Quantum Grav.* **21**, S1839–S1848 (2004), gr-qc/0405036.
34. E. Chassande-Mottin, *Phys. Rev. D* **D67**, 102001 (2003), gr-qc/0210008.
35. Y. Guersel, and M. Tinto, *Phys. Rev. D* **40**, 3884–3938 (1989).
36. S. Klimenko, et al., *Class. Quantum Grav.* **25**, 114029 (2008), arXiv:0802.3232.
37. I. Harry, and S. Fairhurst, *Class. Quantum Grav.* **28**, 134008 (2011), 1101.1459.
38. A. Pai, S. Dhurandhar, and S. Bose, *Phys. Rev. D* **D64**, 042004 (2001), gr-qc/0009078.
39. S. Chatterji, et al., *Phys. Rev. D* **74**, 082005 (2006).
40. M. Was, et al., *Class. Quantum Grav.* **27**, 015005 (2010), arXiv:0906.2120.
41. J. Aasi, et al., *Class. Quantum Grav.* **29**, 155002 (2012), arXiv:1203.5613.
42. J. Abadie, et al., *Phys. Rev. D* **85**, 082002 (2012).
43. J. Abadie, et al., *Phys. Rev. D* **81**, 102001 (2010).
44. J. Abadie, et al., *Phys. Rev. D* **85**, 122007 (2012).
45. J. Abadie, et al., *Phys. Rev. D* **82**, 102001 (2010).
46. GW100916 blind injection data release (2011), http://www.ligo.org/science/GW100916.
47. A. Corsi, "Gravitational waves and gamma-ray bursts," in *Proceedings of the International Astronomical Union*, Cambridge University Press, 2011, vol. 7, pp. 142–149.
48. J. Abadie, et al., Search for gravitational waves associated with gamma-ray bursts during LIGO science run 6 and Virgo science runs 2 and 3 (2012), to appear in ApJ, arXiv:1205.2216.
49. S. Adrian-Martinez, et al., A First Search for coincident Gravitational Waves and High Energy Neutrinos using LIGO, Virgo and ANTARES data from 2007 (2012), arXiv:1205.3018.
50. J. Abadie, et al., *A&A* **539** (2012).
51. LSC and Virgo policy on releasing gravitational wave triggers to the public in the advanced detectors era (2012), https://dcc.ligo.org/cgi-bin/DocDB/ShowDocument?docid=M1200055.

Downloaded 03 Jun 2013 to 134.158.186.247. This article is copyrighted as indicated in the abstract. Reuse of AIP content is subject to the terms at: http://proceedings.aip.org/about/rights_permissions

Best chirplet chain: Near-optimal detection of gravitational wave chirps

Éric Chassande-Mottin[1,*] and Archana Pai[2,†]

[1]*CNRS, Observatoire de la Côte d'Azur, ARTEMIS, BP 4229 06304 Nice Cedex 4 FRANCE*

[2]*INFN, Sezione Roma 1–P.le Aldo Moro, 2 00185 Roma ITALIA*

(Received 22 December 2005; published 27 February 2006)

The list of putative sources of gravitational waves possibly detected by the ongoing worldwide network of large scale interferometers has been continuously growing in the last years. For some of them, the detection is made difficult by the lack of a complete information about the expected signal. We concentrate on the case where the expected gravitational wave (GW) is a quasiperiodic frequency modulated signal i.e., a chirp. In this article, we address the question of detecting an *a priori* unknown GW chirp. We introduce a general chirp model and claim that it includes all physically realistic GW chirps. We produce a finite grid of template waveforms which samples the resulting set of possible chirps. If we follow the classical approach (used for the detection of inspiralling binary chirps, for instance), we would build a bank of quadrature matched filters comparing the data to each of the templates of this grid. The detection would then be achieved by thresholding the output, the maximum giving the individual which best fits the data. In the present case, this exhaustive search is not tractable because of the very large number of templates in the grid. We show that the exhaustive search can be reformulated (using approximations) as a pattern search in the time-frequency plane. This motivates an approximate but feasible alternative solution which is clearly linked to the optimal one. The time-frequency representation and pattern search algorithm are fully determined by the reformulation. This contrasts with the other time-frequency based methods presented in the literature for the same problem, where these choices are justified by "*ad hoc*" arguments. In particular, the time-frequency representation has to be *unitary*. Finally, we assess the performance, robustness and computational cost of the proposed method with several benchmarks using simulated data.

DOI: 10.1103/PhysRevD.73.042003 PACS numbers: 04.80.Nn, 07.05.Kf, 95.55.Ym

I. INTRODUCTION

The worldwide network [1] of large scale interferometric gravitational wave (GW) detectors have started to take data. The network includes the detectors GEO600, LIGO and TAMA. It will be completed soon by the upcoming Virgo. The overall sensitivity of these detectors is continuously improving. Interesting upper limits for the amplitude of GWs are being set and the first detection is hopefully not too far.

A large variety of astrophysical sources are expected to emit GWs in the observational frequency bandwidth of these detectors. From the data analysis viewpoint, the detection methodology for these sources depends on the availability of a reliable and complete model of the GW.

Generally speaking, the oscillations of the GWs are related to the orbital, rotational bulk motion of the constituents of the emitting system. Since the system loses energy by radiation, or because of some other physical process involved, its orbital period, and consequently the GW frequency can vary with time. In such case, the emitted GW is a frequency modulated signal i.e., a *chirp*. A detailed knowledge of the dynamics of the system is required to describe precisely the characteristics of the GW chirps, in particular the phase evolution. This may not be always possible as described in the following examples.

The GW emitted by a coalescing binary of compact objects can be divided into three phases (inspiral, merger and ringing). Although the GW can be obtained accurately in the inspiral phase when the bodies are well separated [2] (using post-Newtonian expansions) and in the ringing phase after they have merged [3] (using perturbative methods), the in-between merger phase still defeats both the numerical and analytical efforts [4] for modeling its highly nonlinear regime. For large mass binaries, the merger phase contributes to a dominant fraction of the signal-to-noise ratio (SNR) [5]. In this case, the search method has to accommodate the significant lack of signal information.

Kerr black holes accreting matter from a surrounding magnetized torus are putative sources of the long gamma-ray bursts (GRBs) [6]. It is claimed that, the black hole spin energy is radiated away through GWs along with the GRB. The precise shape of the emitted waveform would need accurate hydrodynamical numerical simulations.

A third example is the GW emitted in the form of the quasinormal modes [7] by a newly born hot neutron star (during the cooling phase which follows the core collapse). Here, the characteristics of the GW depend on the equation of state of the proto-neutron star and various physical processes (like neutrino diffusion, thermalization and cooling) which are currently not known with accuracy.

All these three examples are expected to emit GW as an *unmodeled chirp*, the phase information being not (perfectly) known. Its typical duration in the detector bandwidth is of the order of a few seconds.

While matched filtering is a well-known and efficient detection technique when a precise waveform model is available, the lack of waveform information prevents us from using the same approach. It is thus natural to advocate for *exploratory searches* (based on partial information or "good sense" models) as opposed to *targeted* ones (relying on a precise model).

Various strategies [8–14] have been designed following this viewpoint, for the detection of transients of short duration (tenth to hundredth of milliseconds) or GW *burst*. Such transients are typically from supernovae core collapses. The notion of a varying frequency is not adequate for such a small number of cycles. It is thus not meaningful to describe such transients as chirps. Their detection is a different issue than the one considered here.

Here, we are interested in exploratory search specifically for unmodeled chirps. In the past, this question has already been investigated yielding a detection method, the Signal Track Search (STS) [13]. The STS relies on the observation that, in a time-frequency (TF) representation, a chirp appears as a filiform pattern and this discriminatory signature can be searched for. A satisfactory implementation of this phenomenological argument calls for a proper TF representation (TFR) and pattern search algorithm. The STS results from "*ad hoc*" choices for the above mentioned points.

In this paper, we propose a new method for the detection of unmodeled chirps. It is based on the same general principles (pattern search in a TFR) as the STS. Its originality resides in the clear link we establish between the method (i.e., the choices of TFR and pattern search) and an optimality criterion.

The paper is organized as follows. We state the detection problem in Sec. II. We introduce the general chirp model referred to as *smooth chirp* and we assume that most physically realistic GW chirps can be described by this model. The phase of a smooth chirp is an arbitrary continuous and differentiable function with bounded first and second derivatives. In Sec. III, we derive the optimal statistic for detecting a given smooth chirp in noise, which is usually referred to as *quadrature matched filtering*. The idea is then to apply this statistic for any smooth chirp, and select the maximum which is associated to the individual that best fits the data. This maximization has to be done numerically. To do so, the set of smooth chirps being a continuous set, has to be discretized. In Sec. IV, we show that grids of templates can be constructed for smooth chirps using chains of small chirps, we call *chirplet chains* (CC). We further prove that the grid is *tight* i.e., any smooth chirp can be closely approximated by a chirplet chain. The maximization of the statistic over the set of smooth chirp can be reliably replaced by a maximization over the set of CCs. However, the number of CCs being very large, the computation of the quadrature matched filter for all CCs is not tractable. In Sec. V, we propose a feasible (TF based) procedure for finding the best CC. We show that the quadrature matched filter can be reformulated approximately as a path integral computed in the TF representation given by the discrete Wigner-Ville (WV) distribution. As a result, the maximization of the statistic over the CCs amounts to obtaining the TF path of largest integral. We demonstrate that this kind of problem can be solved efficiently with dynamic programming. We detail our path search algorithm and we evaluate its computational cost. Finally, we compare the resulting algorithm with other methods in Sec. VI. Receiver operating characteristics obtained in several realistic situations demonstrate the superiority of the proposed approach.

II. SMOOTH CHIRPS IN GAUSSIAN NOISE

We introduce a general chirp model which we refer to as *smooth chirp*,

$$s(t) = A\cos(\phi(t) + \varphi_0) \quad \text{for } t_0 \le t \le t_0 + T, \tag{1}$$

and $s(t) = 0$ outside this interval.

A smooth chirp is characterized by the amplitude A, the initial phase φ_0 and a *smooth* phase evolution $\phi(t)$ (without loss of generality, we assume $\phi(t) = 0$ at the arrival time $t = t_0$). We define the term *smooth* as follows. A phase $\phi(t)$ is smooth if this function and its first three derivatives are continuous and we have

$$\left|\frac{df}{dt}\right| \le \dot{F} \qquad \left|\frac{d^2 f}{dt^2}\right| \le \ddot{F}, \tag{2}$$

for all t and where $f(t) \equiv (2\pi)^{-1} d\phi/dt$ is the instantaneous frequency. The chirping rate limits $\dot{F}$ and $\ddot{F}$ are chosen based on the allowed upper bounds obtained from general astrophysical arguments on the GW source of interest. The chirp model thus includes four parameters $\mathbf{p} \equiv \{A, \varphi_0, t_0, \phi(\cdot)\}$ which are not known *a priori* and need to be determined from the data.

Let the signal be correctly sampled at the Nyquist rate $f_s \equiv 1/t_s$ and let us assume that we acquire the data x_k by blocks of N samples. The GW signal is denoted by $s_k \equiv s(kt_s)$ for $k = 0, \cdots, N-1$ with the duration $T = t_s N$. The noise n_k is assumed to be additive white and Gaussian with zero mean and unit variance. Since the noise of GW detectors is colored, this noise model implies that a whitening procedure has been already applied to the data. (Therefore, the signal s_k in Eq. (3) is a "whitened" version of the actual GW signal).

In this initial work, we restrict the smooth chirp model to have a constant envelope, although GW chirps are generally amplitude modulated. The constant envelope thus limits the descriptive power of the model. However, we

*Electronic address: ecm@obs-nice.fr

†Electronic address: Archana.Pai@aei.mpg.de

Present affiliation: Max Planck Institut für Gravitationsphysik (AEI), Am Mühlenberg 1, D-14476 Potsdam, Germany

argue that the model is still reasonable for many cases[1] and that the phase information plays a major role for detection of chirps. We leave the problem of detecting amplitude modulated chirps for subsequent work.

III. OPTIMAL DETECTION OF A SMOOTH CHIRP

For each block of N data samples, the signal detection problem is to decide which statistical hypothesis suits best to the data among the following two:

$$(H_0) \quad x_k = n_k \qquad \text{noise only} \tag{3a}$$

$$(H_1) \quad x_k = s_k + n_k \qquad \text{signal + noise} \tag{3b}$$

In practice, this requires thresholding a functional of the data, commonly referred to as *statistic*. If the statistic crosses the threshold, H_1 is chosen as opposed to H_0 and *vice versa*.

Because of the presence of random noise, this decision may not be always the right one. There are two types of errors associated to this: false alarms (decide H_1 while H_0 is present) and false dismissals (the opposite). The probabilities of occurrence of these two errors fully quantify the performance of a given statistic. This information can be used to rank the large number of possible statistics and to identify the best one. This is the approach followed by the Neyman-Pearson (NP) criterion [15]: the NP-optimal statistic minimizes one error probability, while keeping the other fixed to a given value. To be precise, in the present case, it minimizes the false dismissal probability for a fixed false alarm probability.

It can be shown that the likelihood ratio (LR) defined by $\lambda \equiv \mathbb{P}(\{x_k\}|H_1)/\mathbb{P}(\{x_k\}|H_0)$ is NP-optimal [15]. For the detection problem described in Eq. (3), the LR can be easily obtained if we assume that the chirp parameters $\mathbf{p}$ are known in advance. When the parameters are not known *a priori* (which is the situation here), the ideal would be to have a statistic which is NP-optimal for all values of the parameters. This statistic is usually referred to as *uniformly most powerful*. However, it is not guaranteed that such statistic always exists, and even if it does, it is generally difficult to obtain.

A sensible solution consists in getting some kind of estimates for the unknown parameters and then use the LR assuming that the estimated value is the actual value. If we use *maximum likelihood* (ML) estimators of the unknown parameters, the resulting statistic is referred to as *generalized likelihood ratio test* (GLRT) [15] (or maximum likelihood test in the statistical community).

[1]It is important to stress here that the model applies to the whitened chirp. For inspiralling binary chirps crossing the entire detector bandwidth, the envelope of whitened chirp is flatter than the original GW signal. For the other cases, this fact depends on the location of the chirp within the detector band.

The GLRT can be shown to be uniformly most powerful in certain cases [15]. For our problem, up to our knowledge, this is an open question. Strictly speaking, it is thus not correct to qualify the GLRT as ''optimal'' (as is often done in the literature on GW data analysis). Nevertheless, we continue this misuse of language since the GLRT has proven to perform reasonably well and no better alternative appears to be available.

In the following subsections, we give the derivation of the GLRT statistic. We proceed with the maximization of likelihood ratio with respect to the parameters. Following [16], we note that out of the four parameters, A, φ_0 and t_0 are *extrinsic* parameters (known as kinematical or dynamical parameters) whereas $\phi(\cdot)$ is an *intrinsic* parameter (which determines the shape of the chirp waveform). On the basis of this distinction, the maximization over the extrinsic parameters can be treated in a simple manner whereas the computation of the ML estimate of the intrinsic parameter requires a more sophisticated numerical treatment.

A. Maximize the likelihood ratio: A and φ_0

In this subsection, we maximize the LR with respect to A and φ_0. In case of Gaussian noise, it is more convenient to use the log-likelihood ratio (LLR) which is expressed by

$$\Lambda(x;\mathbf{p}) \equiv \ln\lambda = \sum_{k=0}^{N-1} x_k s_k - \frac{1}{2}\sum_{k=0}^{N-1} s_k^2. \tag{4}$$

We introduce $\bar{s}_k \equiv \cos(\phi_k + \varphi_0)$ (such that $s_k = A\bar{s}_k$) with the norm $\mathcal{N} \equiv \sum_{k=0}^{N-1} \bar{s}_k^2$.

The maximization of the LLR $\Lambda(x;\mathbf{p})$ over A is straightforward and gives the expression of the ML estimate of the amplitude, namely $\hat{A} = \sum_{k=0}^{N-1} x_k\bar{s}_k/\mathcal{N}$. Inserting this expression into Eq. (4), we obtain

$$\Lambda(x;\{\hat{A},\varphi_0,t_0,\phi(\cdot)\}) = \frac{1}{2\mathcal{N}}\left(\sum_{k=0}^{N-1} x_k\bar{s}_k\right)^2. \tag{5}$$

The analytical maximization of the LLR over φ_0 deserves a little more attention. The same calculation has been performed for the detection of chirps from inspiralling binaries [17,18] but it is based on the assumption that $\mathcal{N}$ is independent of φ_0 which is not valid in the context of arbitrary chirps. In Appendix A, we detail this calculation and discuss the validity of this assumption.

We express the resulting statistic $\ell(x;t_0,\phi) \equiv \Lambda(x;\{\hat{A},\hat{\varphi}_0,t_0,\phi(\cdot)\})$ using the following notations for the cross-correlation of the data with the two quadrature waveforms,

$$x_c \equiv \sum_{k=0}^{N-1} x_k\cos\phi_k \qquad x_s \equiv \sum_{k=0}^{N-1} x_k\sin\phi_k, \tag{6}$$

and for the norms and cross-products of $\cos\phi_k$ and $\sin\phi_k$,

$$n_c \equiv \sum_{k=0}^{N-1}\cos^2\phi_k \qquad n_s \equiv \sum_{k=0}^{N-1}\sin^2\phi_k, \tag{7a}$$

$$n_x \equiv \sum_{k=0}^{N-1}\cos\phi_k\sin\phi_k. \tag{7b}$$

We distinguish two cases. In the degenerate case where the two quadrature waveforms are linearly dependent (ϕ_k is a constant), $\mathcal{O} \equiv n_c n_s - n_x^2$ vanishes and we have

$$\ell(x;t_0,\phi) = (x_c^2 + x_s^2)/(2N). \tag{8}$$

Otherwise $\mathcal{O} > 0$, the optimal statistic is

$$\ell(x;t_0,\phi) = (n_s x_c^2 - 2n_x x_c x_s + n_c x_s^2)/(2\mathcal{O}), \tag{9}$$

and is commonly referred to as *quadrature matched filtering*, (see Appendix A).

B. Maximize the likelihood ratio: ϕ and t_0

The statistic ℓ results from a quadratic combining of the cross-correlations defined in Eq. (6). It can be seen as a ''generalized dot-product'' and can be related to a ''distance'' measuring the discrepancy between the data and *template* waveforms (or, in short, templates) defined by the phase ϕ [see Eq. (A8)]. Maximizing ℓ over ϕ is equivalent to minimizing this distance.

The expression in Eq. (9) is for a given known phase ϕ. If the phase is unknown but belongs to the set of smooth chirps, then we need to minimize the distance within this feasible set. In other words, we need to find that smooth chirp which best fits the data i.e., find

$$\ell_{\max}(x;t_0) = \max_{\text{all smooth chirps}}\{\ell(x;t_0,\phi)\}. \tag{10}$$

This maximization is difficult to tackle analytically and has to be done numerically. The set of smooth chirps is a continuous set and hence not easy to manipulate numerically without discretizing it. For this purpose, we introduce *chirplet chains*, which we discuss in the next section.

As described earlier, we process the data stream blockwise. We compute the statistic independently for each block. The maximization over t_0 is obtained by comparing $\ell_{\max}$ for neighboring blocks and selecting the maximum. The ML estimate of t_0 is then given by the starting time of the corresponding block. The period separating two successive starting times thus defines the resolution of the estimate. If required, this resolution can be improved by increasing the overlap between two neighboring blocks.

We now concentrate on the maximization of $\ell(x;t_0,\phi)$ over ϕ in a given block. In the following, we remove t_0 from the arguments of ℓ to keep the notations simple.

IV. CHIRPLET CHAINS: A TIGHT TEMPLATE GRID FOR SMOOTH CHIRPS

In this section, we show that chirplet chains (CCs) can be used to construct template grids for smooth chirps. CCs are based on the simple geometrical observation: broken lines give good approximations of smooth curves. CCs are signals whose (instantaneous) frequency is a broken line. We verify that they are good approximation of the frequency curve of an arbitrary smooth chirp. We obtain the conditions ensuring that, for any smooth chirp, there always exists a sufficiently close CC. If these conditions are satisfied, the set of the CCs forms a tight template grid which can be used to search for an unknown smooth chirp. Finally, we examine the implementation of such grid for the toy (but realistic) model given by the inspiralling binary chirp.

A. Chirplet chains: piecewise linear frequency

All smooth chirps in Eq. (1) are supported in the TF domain $\mathcal{D}$, a rectangle of width T and of height equal to the Nyquist bandwidth $f_s/2$, as illustrated in Fig. 1. Let $\{(t_j = j\delta_t, f_m = m\delta_f); j = 0,\cdots,N_t, m = 0,\cdots,N_f\}$ be a regular TF grid led on $\mathcal{D}$ by splitting the time axis into N_t intervals of size $\delta_t \equiv T/N_t$, and the frequency axis into N_f bins of size $\delta_f \equiv f_s/(2N_f)$.

In the following, the subscripts j and m designate the index of the time interval and the frequency bin of the grid, respectively. The index $k \in \{0,\cdots,N-1\}$ denotes the time index of a sample.

A *chirplet* is a short piece of signal whose frequency varies linearly between two successive nodes of the grid. In the time interval j, we denote the time and frequency coordinates of the chirplet extreme points by (j,m_j) and $(j+1,m_{j+1})$. In the TF plane, it is thus represented by a line joining the grid nodes (t_j,f_{m_j}) and $(t_{j+1},f_{m_{j+1}})$ (see Fig. 1). Concretely, this means that the phase $\phi_k = \phi(t_s k)$ of a chirplet is a quadratic function of time, as follows, for $t_j \le kt_s < t_{j+1}$

$$\phi_k \equiv a_j t_{j,k}^2 + b_j t_{j,k} + \theta_{j-1}, \tag{11}$$

where $a_j = \pi(f_{m_{j+1}} - f_{m_j})/\delta_t$, $b_j = 2\pi f_{m_j}$ and $t_{j,k} = t_s k - t_j$.

We build the chirplet chain (CC) by enforcing chaining rules. The frequency and phase of this chain are continuous. Clearly, the continuity of the frequency is ensured by construction, while the phase continuity requires that

$$\theta_{j-1} = \pi\delta_t(f_{m_j} + f_{m_{j-1}}) + \theta_{j-2}, \tag{12}$$

for $j \ge 1$, and fixing $\theta_{-1} = 0$. We also require that the slope of the chirplet frequency as well as the difference between the slopes of the frequencies of two consecutive chirplets are bounded absolutely. These bounds are given by the two parameters N_r' and N_r'' respectively such that

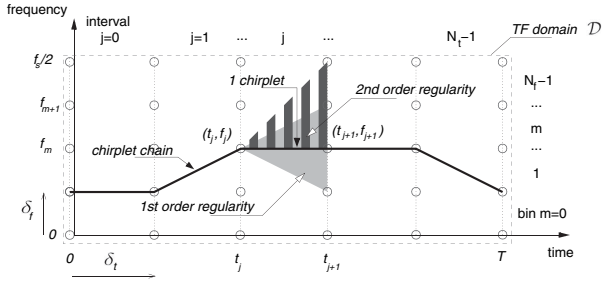

FIG. 1. Chirplet chains—The TF domain of interest $\mathcal{D}$ is tiled by a regular TF grid of N_t time intervals and N_f frequency bins. A chirplet is a short piece of signal whose frequency varies linearly between two successive nodes of the grid. It is thus represented by a line joining the grid nodes. The slope of the chirplet frequency is limited (triangular region in light gray, here $N_r' = 1$). We chain the chirplets, imposing the continuity of the chain and limiting the difference between the slopes of two consecutive chirplets (triangular region with dark gray stripes, here $N_r'' = 1$). Admissible chirplets in time interval j belong to the intersection of these two regions associated to the regularity constraints. Clearly, a chirplet chain is represented by a broken line in the TF plane.

(i) $|m_{j+1} - m_j| \le N_r'$ and
(ii) $|m_{j+1} - 2m_j + m_{j-1}| \le N_r''$.

Clearly, a CC is represented by a broken line in $\mathcal{D}$. The two parameters N_r' and N_r'' control the regularity of this line. Consistently, we will refer to (i) and (ii) as *regularity constraints*.

The instantaneous frequency of a smooth chirp is associated to a smooth curve in $\mathcal{D}$. In the same manner that broken lines are good approximations of smooth curves, CCs are good approximations of smooth chirps. Since CCs form a finite discrete set, they sample[2] the set of smooth chirps. In other words, they form a *template grid* of this set.

It is important to know whether this template grid is sufficiently tight i.e., whether for any smooth chirp, there always exists a sufficiently close CC. The template grid tightness is controlled by the choice of the four parameters defining the set of CCs, namely, the TF grid parameters N_t, N_f and the regularity parameters N_r' and N_r''. The first and preliminary step to address the tightness question is to define a distance measuring the "similarity" (or ambiguity) between two different chirps.

B. Distance in the set of smooth chirps

We follow the approach suggested in [18] and assume that we "receive" a chirp whose phase ϕ is different than the template phase ϕ^*. We set $x_k \triangleq s_k = A\cos(\phi_k + \theta)$, and consider

$$\mathcal{L}(\phi, \phi^*) \equiv \frac{\ell(s;\phi) - \ell(s;\phi^*)}{\ell(s;\phi)}. \tag{13}$$

[2]Strictly speaking, CCs do not *sample* the set of smooth chirps since they do not belong to this set (the second derivative of their frequency is not defined at the boundaries of the grid time intervals and it is thus not bounded).

Clearly, $\mathcal{L}$ measures the reduction factor of the "detection peak" due to the mismatch between the chirp present in the data and the chosen template. It is a relative measurement done with respect to the ideal case where the template matches exactly the considered chirp. In this sense, it can be interpreted as a SNR loss.

Since $\mathcal{L} \ge 0$ and equals 0 when $\phi = \phi^*$, it can be interpreted as a *distance* between the chirps. Note that $\mathcal{L}$ does not depend upon A. It depends only on the phases ϕ and ϕ^*, but this dependency is difficult to perceive intuitively from its definition in Eq. (13).

An approximated but much simpler expression can be obtained when the chirp and the template are close by Taylor expanding $\mathcal{L}$ for small $\Delta_k \equiv \phi_k^* - \phi_k$ and retaining the leading terms. The approximation is detailed in Appendix B and leads to the following expression

$$\mathcal{L}(\phi, \phi^*) \approx \frac{1}{N}\sum_{k=0}^{N-1}(\Delta_k - \Delta)^2, \tag{14}$$

with $\Delta = 1/N\sum_{k=0}^{N-1}\Delta_k$.

Interestingly, we recognize in this expression the empirical estimate of the variance of the phase difference Δ_k. With this definition of the distance, two chirps are "identical" (their distance measured by $\mathcal{L}$ is zero) if and only if they have the same phase evolution up to an additive offset.

C. Is the CC grid tight?

In this section, we address the grid tightness problem and find the regularity and TF grid parameters which yield a tight template grid of CCs. We proceed as follows: we first consider an arbitrary smooth chirp of phase ϕ. Then we construct a CC "geometrically" close to this chirp. We check if this CC is admissible i.e., if it satisfies the regularity constraints. This imposes two conditions on the parameters. Finally, we check whether it is *effectively* close to the chirp (as measured by the distance). This yields the loss due to the approximation of the chirp by a CC in the worst case. For tight CC grid, this loss (homogeneous to a SNR loss) has to be small which imposes one more condition on the parameters.

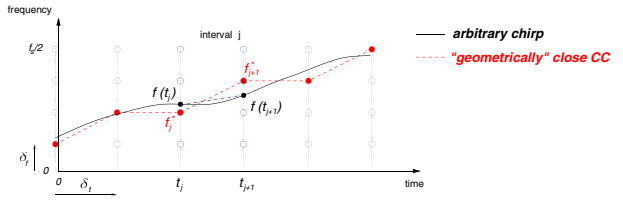

FIG. 2 (color online). Smooth chirp (solid curve) and its geometrically close CC (dotted broken line).

1. Geometrically close CC

Let $\phi(t)$ and $f(t)$ be the phase and frequency of an arbitrary smooth chirp. The frequency evolution appears as a smooth curve in the TF plane.

We construct a CC geometrically close to this chirp as follows: for each $j = 0, \cdots, N_t$, we choose the node (t_j, f_j^*) of the jth column of the TF grid defined in Sec. IVA which is nearest to the point $(t_j, f(t_j))$. We draw the broken line which joins these nodes (see Fig. 2). The associated CC is the geometrically close CC to the chirp under consideration and we denote its phase ϕ^*.

2. Admissibility of the geometrically close CC

For given chirping rate limits $\dot{F}$ and $\ddot{F}$, the geometrically close CC may or may not satisfy the regularity constraints. This depends on the regularity and TF grid parameters. Below, we investigate this question.

a. 1st order regularity—Let us consider the chirplet of the interval j, we have

$$|f_{j+1}^* - f_j^*| \le |f_{j+1}^* - f(t_{j+1})| + |f(t_{j+1}) - f(t_j)| + |f_j^* - f(t_j)|. \tag{15}$$

Using the mean value theorem[3] (see e.g., [19]), we get $|f(t) - f(s)| \le \dot{F}|t - s|$ from which we deduce a bound on $|f(t_{j+1}) - f(t_j)|$. By construction, we have $|f_j^* - f(t_j)| \le \delta_f/2$ and this leads to

$$|f_{j+1}^* - f_j^*| \le \delta_f + \dot{F}\delta_t. \tag{16}$$

Thus, the geometrically close CC satisfies the regularity constraint (i) mentioned in Sec. IVA if

$$N_r' \ge \dot{F}\delta_t/\delta_f + 1. \tag{17}$$

We rewrite this condition in the following form

$$N_r' \ge 4\frac{N'}{N_t}\frac{N_f}{2N} + 1, \tag{18}$$

where $N' \equiv \dot{F}T^2$ is an adimensional quantity which depends only on the fundamental characteristics of the smooth chirp model.

b. 2nd order regularity—We consider two successive chirplets in intervals $j-1$ and j. Using a similar method, the difference of their slopes can be bounded by

$$|f_{j+1}^* - 2f_j^* + f_{j-1}^*| \le |f(t_{j+1}) - 2f(t_j) + f(t_{j-1})| + 2\delta_f. \tag{19}$$

Two consecutive applications of the mean value theorem to a function $f(\cdot)$ which satisfies Eq. (2) for all $s \in [r, t]$ with $0 \le r < t \le T$ yield the following result

$$|f(t) - 2f(s) + f(r)| \le \ddot{F}((t-s)2 + (r-s)2)/2 + \dot{F}|t - 2s + r|. \tag{20}$$

Using $r = t_{j-1}$, $s = t_j$ and $t = t_{j+1}$, we get

$$|f_{j+1}^* - 2f_j^* + f_{j-1}^*| \le \ddot{F}\delta_t^2 + 2\delta_f. \tag{21}$$

Therefore, the geometrically close CC satisfies the regularity constraint (ii) mentioned in Sec. IVA if

$$N_r'' \ge \ddot{F}\delta_t^2/\delta_f + 2. \tag{22}$$

We rewrite the above condition as

$$N_r'' \ge \frac{4}{3}\left(\frac{N''}{N_t}\right)^2\frac{N_f}{2N} + 2, \tag{23}$$

where $N'' \equiv \sqrt{3\ddot{F}T^3}$ is an adimensional quantity which depends only on the fundamental characteristics of the smooth chirp model, and thus from the astrophysical input. It is related to the maximum overall curvature of the chirp

[3]Let the function $g(\cdot)$ be continuous in the open interval (a, b) and differentiable in the closed interval $[a, b]$. The mean value theorem states that there exists c in (a, b) such that $g(b) - g(a) = \dot{g}(c)(b - a)$ where $\dot{g}(\cdot)$ is the derivative of $g(\cdot)$. Consequently, we have $|g(b) - g(a)| \le \dot{G}|b - a|$ with $\dot{G} = \sup_{x\in(a,b)}(\dot{g}(x))$.

frequency or more precisely to the largest number $\ddot{F}T^3$ of Fourier bins that the chirp frequency can sweep, the linear trend being removed.

3. Is the geometrically close CC effectively close?

We obtain a worst case estimate of the distance between the smooth chirp and its geometrically close CC by bounding the variations of their phase difference. We begin with bounding the frequency discrepancy.

The starting point is the following lemma (inspired from [20], p. 23) obtained from the application of the mean value theorem and some algebraic manipulations. If $f(\cdot)$ satisfies Eq. (2) for all $s \in [r, t)$ then

$$\left| f(s) - \left[f(r) + \frac{s-r}{t-r}(f(t) - f(r)) \right] \right| \leq \ddot{F}(t-r)^2. \tag{24}$$

However, this upper bound can be slightly improved: the term $(t-r)^2$ overestimates the more precise bound $g(s) \equiv \min\{(t-s)(t-(s+r)/2), (s-r)((s+t)/2-r)\}$. [Note that $g(t) = 0$ and $g(r) = 0$ as expected.] In the worst case, we have $s = (t+r)/2$ and $g(s) = 3/8(t-r)^2$ as opposed to $(t-r)^2$. We include this gain in the following.

We apply the lemma in Eq. (24) with $t = t_{j+1}$ and $r = t_j$. The term inside the square brackets in the left hand side of Eq. (24) is equal to the frequency at time s of the chirplet obtained by joining $f(t_{j-1})$ to $f(t_j)$ (see the dot-dash line in Fig. 2). We denote this frequency $\tilde{f}(s)$, and then obtain

$$|f(s) - \tilde{f}(s)| \leq 3\ddot{F}\delta_t^2/8. \tag{25}$$

Since $|f(s) - f^*(s)| \leq |f(s) - \tilde{f}(s)| + |\tilde{f}(s) - f^*(s)|$ and $|\tilde{f}(s) - f^*(s)| \leq \delta_f/2$, we have

$$|f(s) - f^*(s)| \leq 3\ddot{F}\delta_t^2/8 + \delta_f/2 \equiv \Delta_f. \tag{26}$$

By definition $\phi(t) - \phi(r) = 2\pi \int_r^t f(s)ds$. Integrating both sides of the above inequality between two successive points $r = t_s(k-1)$ and $t = t_s k$ for $k \in \{1, \cdots, N-1\}$, we get

$$|\Delta_k - \Delta_{k-1}| \leq 2\pi\Delta_f t_s, \tag{27}$$

which constrains the variations of the phase difference $\Delta_k = \phi^* - \phi_k^*$.

We prove in Appendix C that the approximated distance $\mathcal{L}(\phi, \phi^*)$ as shown in Eq. (14) is maximum under this constraint, when $\Delta_k = \pm 2\pi\Delta_f t_s k$. In this case, the maximum is $\mathcal{L}(\phi, \phi^*) = (\pi\Delta_f T)^2/3 \equiv \mu'$.

We can finally state the following *tight template grid* theorem: for all smooth chirps of phase ϕ, there exists a CC of phase ϕ^* such that

$$\mathcal{L}(\phi, \phi^*) \leq \mu', \tag{28}$$

where $\mu' = \pi^2 T^2 (3\ddot{F}\delta_t^2/4 + \delta_f)^2/12$ is the maximum (i.e., in the worst case) *energy* SNR loss due to the mismatch between the smooth chirp and the chosen template given by a close CC. The corresponding maximum *amplitude* SNR loss is $\mu = 1 - \sqrt{1-\mu'} \approx \mu'/2$ for small μ'. Note that the *amplitude* SNR loss is linked to the *minimal match MM* defined in [18] by the relation $MM = 1 - \mu$. We express the maximum SNR loss μ in terms of the CC parameters as

$$\mu = \frac{\pi^2}{96}\left[\frac{1}{2}\left(\frac{N''}{N_t}\right)^2 + \frac{1}{2}\left(\frac{2N}{N_f}\right)\right]^2. \tag{29}$$

In principle, this loss can be made arbitrarily small by choosing N_t and N_f adequately. Therefore, *the grid of CC can sample the set of smooth chirps tightly.*

It is evident that two types of losses contribute to μ. The first one is related to the *geometrical error* due to the fact that the model is a broken line: within the time intervals of the TF grid, the model is a straight line which cannot perfectly follow the curvature of the smooth chirp frequency. The finer the grid along the time axis, the smaller the time interval, the better the line fits the smooth chirp frequency, thus reducing this error. The other is related to the *quantization error* as we require the node of the best broken line to belong to the TF grid: there is a difference between the best broken line we can possibly draw and the closest (quantized) one with vertices belonging to the grid. The finer the grid along the frequency axis, the closer the quantized line from the original, thus reducing this error.

When $N_t = N''$ and $N_f = 2N$, the maximum SNR loss is of order $\sim\pi^2/96 \approx 10\%$ and the two types of errors contribute equally. The same maximum SNR loss can be achieved with other choices for N_t and N_f. In the next section, we propose a criterion to solve this indetermination.

D. Smallest tight CC grid

As elaborated in the previous section, the tight template grid theorem gives the condition on the TF grid parameters N_t and N_f which ensures that the template set (the CCs) covers all the feasible set (the smooth chirps) with a given accuracy specified by the maximum SNR loss. The same accuracy can be achieved with several pairs of parameters, leading to a parameter indetermination.

For a small maximum SNR loss, the maximization of the LLR in Eq. (10) performed over the set of smooth chirps can be safely replaced by a maximization over the set of CCs, i.e.,

$$\ell_{\max}(x) \simeq \max_{\text{all CCs}}\{\ell(x;\phi)\}. \tag{30}$$

The statistic $\ell_{\max}$ in Eq. (30) results from the CC which maximizes the statistic or in other words, from the waveform of the template set which best fits the data. Generally speaking, when the data is noise *only*, the larger the number of (reasonably different) waveforms in the template set, the larger the risk that one of the waveforms fits the noise and consequently, the larger the false alarm rate.

The TF grid parameters N_t and N_f influence very differently the number of CCs. The above argument suggests to select the parameters which minimize the numbers of CCs, for a given specified maximum SNR loss. We refer to the *smallest tight CC grid* as the set of CCs which results from this constrained optimization.

Let us first estimate the number of CCs. According to the regularity conditions, each of the number $N_c \sim N_f(2N_r' + 1)$ of possible chirplets in a given time interval can be chained to (at most) $2N_r'' + 1$ chirplets in the next time interval. Counting CCs is then a combinatorial problem. We have N_c chirplets in the first time interval, and $2N_r'' + 1$ possible choices for the $N_t - 1$ successive time intervals. Neglecting what happens at the lower and upper boundaries of the frequency axis (i.e., near DC and Nyquist), we obtain an upper-bound on (the logarithm of) the number N_{cc} of CCs as

$$\ln N_{cc} \lesssim \ln(2N_t'N_f) + (N_t - 1)\ln(2N_r'' + 1). \tag{31}$$

In practice, we have $N_t \gg 1$. The second term largely dominates the right-hand side and the first term can be neglected. We thus have $\ln N_{cc} \sim N_t \ln(2N_r'' + 1)$.

At this point, it is convenient to introduce $u \equiv N''/N_t$ and $v \equiv 2N/N_f$ and express the *smallest tight CC grid* problem with these variables. From the regularity constraints, we have $N_r'' = 4u^2/(3v) + 2$. We want to minimize the number of CCs

$$\ln N_{cc} \propto g(u, v) \equiv \frac{1}{u}\ln\left(\frac{8}{3}\frac{u^2}{v} + 5\right), \tag{32}$$

subject to a given maximum SNR loss i.e., $u^2 + v = C \equiv 8\sqrt{6\mu}/\pi$.

Combining the derivatives of the objective $dg = \partial_u g du + \partial_v g dv$ and of the constraint $dv = -2udu$, we obtain the equation giving the admissible point where the derivative dg/du vanishes, viz.

$$\frac{\ln y}{y-5} + \frac{7}{4y} - \frac{3}{4} = 0 \tag{33}$$

where we defined $y \equiv 8u^2/(3v) + 5$. This equation can be solved numerically and gives $y \approx 8.95$. Let $\alpha \equiv u^2/v = 3(y-5)/8$ be the ratio between the two errors contributing to μ. We obtain the smallest tight template grid when this ratio is $\alpha \sim 1.48$. For a required μ, we get the parameters of the resulting grid as follows. Using the constraint, we have $u = \sqrt{C\alpha/(1+\alpha)}$ and $v = C/(1+\alpha)$, from which we obtain the parameters,

$$N_t = 0.52\mu^{-1/4}N'', \qquad N_f = 0.78\mu^{-1/2}N. \tag{34}$$

Interestingly, this also implies that $N_r'' = 4\alpha/3 + 2 \approx 4$ is a constant (i.e., does not depend on μ). The last parameter N_r' is directly determined by substituting Eqs. (34) in (18).

The parameters of the smallest tight template grid may not be always suitable in practice (see the later discussion on the implementation and numerical contingencies in Sec. V B 5) but they give interesting indications.

At this point, it is useful to see with an example if the proposed model and template grid sound tractable in a realistic case.

E. Toy model and CC parameters

We use the inspiralling binary chirps as a toy model to check whether the various parameters have reasonable order of magnitudes in this physically realistic situation. We consider the Newtonian approximation of the chirp whose frequency evolution is given by [17]

$$f(t) = f_0\left(1 - \frac{t-t_0}{T}\right)^{-3/8} \quad \text{for } t < t_0 + T, \tag{35}$$

where t_0 denotes the arrival time. In practice, the arrival time corresponds to the time at which the chirp enters the detector's bandwidth i.e., when its frequency reaches the low frequency (seismic) cutoff (denoted f_0) of the interferometric detectors. T defines the chirp duration, i.e. the time taken by the chirp from the arrival time until the binary coalescence.

The chirp duration can thus be estimated by

$$T \sim 1.3\text{s}\left(\frac{f_0}{20}\right)^{-8/3}\left(\frac{M}{50M_\odot}\right)^{-5/3}, \tag{36}$$

where M is the total mass (objects of equal masses).

In this calculation, we assume the seismic cutoff frequency[4] of 20 Hz.

We fix $\dot{F}$ and $\ddot{F}$ to the corresponding values of the first and second derivatives of the chirp frequency, pertaining to the last stable circular orbit (LSCO[5]) viz.,

$$f_{\text{LSCO}} \sim 88.4\ \text{Hz}\left(\frac{M}{50M_\odot}\right)^{-1}, \tag{37}$$

$$\dot{F} \sim 1.33\ \text{kHz/s}\left(\frac{M}{50M_\odot}\right)^{-2}, \tag{38}$$

$$\ddot{F} \sim 74\ \text{kHz/s}^2\left(\frac{M}{50M_\odot}\right)^{-3}. \tag{39}$$

We note that T, f_{LSCO}, $\dot{F}$ and $\ddot{F}$ decrease with an increasing mass. When M increases, the chirp is thus shorter, less steep and curved, and it reaches only the lower part of the

[4] This is the seismic cutoff frequency targeted by the detector Virgo.

[5] For nonrotating stars, the LSCO is when the objects are at the distance $r = 6\ \text{GM}/\text{c}^2$.

frequency band. From the above equations, we deduce that

$$N' \sim 2.2\times 10^3\left(\frac{M}{50M_\odot}\right)^{-16/3}, \qquad N'' \sim 698\left(\frac{M}{50M_\odot}\right)^{-4}. \tag{40}$$

The sampling frequency f_s is fixed by the width of the observational band of the GW detector, namely $f_s = 2048$ Hz. We thus have

$$N = f_s T \sim 2662\left(\frac{M}{50M_\odot}\right)^{-5/3}. \tag{41}$$

Following Sec. IV D and fixing $\mu = 10\%$, the smallest tight CC grid has the following parameters for the TF grid

$$N_t \sim 645\left(\frac{M}{50M_\odot}\right)^{-4}, \tag{42}$$

$$N_f \sim 6566\left(\frac{M}{50M_\odot}\right)^{-5/3}, \tag{43}$$

and for the regularity, we have

$$N_r' \sim 17\left(\frac{M}{50M_\odot}\right)^{-4/3}, \qquad N_r'' \sim 4. \tag{44}$$

The orders of magnitude for the various parameters appear to be reasonable. Since these parameters do not increase with M, the template grid defined with the above values remains acceptable and tight for higher masses $M \geq 50M_\odot$.

V. FIND THE BEST CHIRPLET CHAIN

In Sec. IV, we have shown that the SNR loss due to the use of a CC instead of the *ideal* template can be made small with an appropriate choice of parameters i.e., by making the CC grid tight. In other words, the problem of detecting a smooth chirp is equivalent to the one of detecting a CC as stated by Eq. (30). The maximization over the set of CCs—involved in the latter case—has the great advantage that it can be resolved numerically.

A. The exhaustive search is not feasible

Since CCs are in finite number, an obvious maximization procedure is to try them all and select the one which gives the maximum. To understand whether this solution is tractable, we need to know how many CCs are there. We consider that the search parameters N_t, N_f, N_r' and N_r'' are known and can be obtained from the physical and grid tightness requirements as discussed earlier.

We already presented an estimate of the number of CCs in Eq. (31) and saw that it grows exponentially with the number of time intervals of the TF grid. This estimate computed for the toy model example presented in the previous section gives $\log_{10} N_{cc} \approx 1400$. Clearly, this number is too large for an exhaustive search (i.e., computing ℓ for all possible CCs) to be carried out in real-time on existing computers. Generally speaking, since the number of CCs increases exponentially with N_t, the cost of an exhaustive search scales exponentially with N_t and thus with the problem size N.

In the next section, we propose an algorithm which gives a good estimate for the optimal CC instead of the exact solution of the maximization problem described in Eq. (30). However, as opposed to the exhaustive search, the computational cost of this algorithm scales as a polynomial of the problem size N.

B. Near-optimal search

The maximization of $\ell(x;\phi)$ in Eq. (30) is a combinatorial maximization problem. The existence of an efficient solving algorithm for such problem is related to the structural properties of the "objective" function to be maximized, that is, ℓ in the present case. In this section, we show that ℓ can be reasonably approximated by a path integral computed over a time-frequency representation (TFR) of the data. The structure of the approximated statistic allows us to perform its maximization efficiently with dynamic programming. The approximation goes through two stages with an intermediate step for the reformulation of the statistic in the TF plane.

1. Approximation 1: for a CC, cosine and sine are almost orthogonal

As shown in Eq. (A8), the statistic ℓ can be expressed as

$$\ell(x;\phi) = \frac{1}{2}\left[\left(\sum_{k=0}^{N-1} x_k \tilde{c}_k\right)^2 + \left(\sum_{k=0}^{N-1} x_k \tilde{s}_k\right)^2\right], \tag{45}$$

where the templates $\tilde{c}_k$ and $\tilde{s}_k$ are the orthonormalized counterparts of the waveforms in quadrature $\cos\phi_k$ and $\sin\phi_k$ obtained from the Gram-Schmidt procedure as given below

$$\tilde{c}_k = \frac{\cos\phi_k}{\sqrt{n_c}} \qquad \tilde{s}_k = \frac{n_c \sin\phi_k - n_x \cos\phi_k}{\sqrt{n_c \mathcal{O}}}. \tag{46}$$

Let $\{\cos\phi_k\}$ and $\{\sin\phi_k\}$ be the vectors in $\mathbb{R}^N$ associated to the quadrature waveforms. As it appears in the above expressions, these vectors are generally not orthonormal. Their deviation from orthonormality can be quantified with two parameters, defined by

$$\delta \equiv \frac{n_c - n_s}{n_c + n_s}, \qquad \epsilon \equiv \frac{2n_x}{n_c + n_s}, \tag{47}$$

which are related to their vector lengths n_c, n_s and their scalar product n_x. The parameter δ measures the relative difference in the vector lengths while ϵ measures the angle between them. The vectors are orthonormal if and only if both δ and ϵ are zero.

Intuitively, if the quadrature waveforms oscillate sufficiently, they should be close to orthonormality and δ and ϵ are expected to be small. This intuition is examined in detail in Appendix D, in which we exploit the fact that ϕ is not arbitrary but it is the phase of a CC. We show that if ϕ is the phase of a CC whose node frequencies are in the bandwidth $f_l \leq f_{m_j} \leq f_s/2 - f_l$ for all j with

$$f_l \approx 2.5\delta_f \sqrt{N'}\left(\frac{N_f}{N}\right)^{3/2}\left(\frac{0.1}{\eta}\right)^{1/2}, \tag{48}$$

then $|\delta| \leq \eta$ and $|\epsilon| \leq \eta$.

In the following, we assume that this condition is satisfied. This imposes the CC frequency not to approach arbitrarily close to the DC nor to the Nyquist frequencies. Since the amplitude of the instrumental noise of GW interferometers diverges rapidly when going close to DC, it is not expected to detect GWs at low frequencies. Therefore the reduction of the bandwidth in the low frequency region should not be a problem as long as f_l remains small. We will check later with examples that the reduction of the useful bandwidth is indeed sufficiently small.

Using Eqs. (46) and (47), we can write $\tilde{c}_k$ and $\tilde{s}_k$ in terms of δ and ϵ as

$$\tilde{c}_k = \left(\frac{2}{N(1+\delta)}\right)^{1/2} \cos\phi_k, \tag{49}$$

$$\tilde{s}_k = \left(\frac{2}{N(1+\delta)}\right)^{1/2} \frac{(1+\delta)\sin\phi_k - \epsilon\cos\phi_k}{\sqrt{1-(\delta^2+\epsilon^2)}}, \tag{50}$$

noting that $n_c = N(1+\delta)/2$, $n_s = N(1-\delta)/2$ and $n_x = N\epsilon/2$.

Inserting this expression in Eq. (45) and taking the limit for small δ and ϵ, we find that $\ell(x;\phi) \to \hat{\ell}(x;\phi) \equiv (x_c^2 + x_s^2)/N$, the reminder $R(\delta,\epsilon) \equiv \hat{\ell}(x;\phi) - \ell(x;\phi)$ being given by

$$R(\delta,\epsilon) = \frac{1}{N}\,\frac{\delta(x_c^2 - x_s^2) + 2\epsilon x_c x_s - (\delta^2+\epsilon^2)(x_c^2+x_s^2)}{1-(\delta^2+\epsilon^2)}. \tag{51}$$

Considering that we have $\delta^2 + \epsilon^2 \leq \eta^2$ (see Appendix D) and

$$\frac{|x_c^2 - x_s^2|}{x_c^2 + x_s^2} \leq 1, \qquad \frac{|2x_c x_s|}{x_c^2 + x_s^2} \leq 1, \tag{52}$$

the relative error can be bounded as

$$\frac{|R(\delta,\epsilon)|}{\hat{\ell}(x;\phi)} \leq \frac{2\eta - \eta^2}{1-\eta^2} \approx 2\eta, \tag{53}$$

for small η.

Provided a good choice of η (and checking the consequences on f_l), this approximation error can be made small. We can safely replace ℓ by $\hat{\ell}$ which we express as the following complex sum :

$$\hat{\ell}(x;\phi) = \frac{1}{N}\left|\sum_{k=0}^{N-1} x_k \exp(i\phi_k)\right|^2. \tag{54}$$

2. Go to time-frequency: Moyal

The expression of $\hat{\ell}$ in Eq. (54) computes the canonical Hermitian scalar product between the data and a complex template waveform. While Parseval's formula allows an equivalent formulation of this scalar product in the frequency domain, *Moyal's formula* does the same in the TF domain, provided the use of a unitary TFR. One such TFR is the *discrete Wigner-Ville* (WV) distribution defined in [21] and given by

$$w_x(n,m) \equiv \sum_{k=-k_n}^{k_n} x_{p_{n,k}} x^*_{q_{n,k}} e^{-2\pi i m k/(2N)}, \tag{55}$$

with $k_n \equiv \min\{2n, 2N-1-2n\}$, $p_{n,k} \equiv \lfloor n + k/2 \rfloor$ and $q_{n,k} \equiv \lfloor n - k/2 \rfloor$ where $\lfloor\cdot\rfloor$ gives the integer part. The arguments of w_x are the time index n and the frequency index m which correspond in physical units, to the time $t_n = t_s n$ and the frequency is $f_m = f_s m/(2N)$ for $0 \leq m \leq N$ and $f_m = f_s(N-m)/(2N)$ for $N+1 \leq m \leq 2N-1$. Thus, the frequency axis gets sampled at twice the usual rate (as performed by the FFT). The WV distribution is associated with a particular sampling of the TF plane. As discussed later in Sec. V B 5, this leads to some restrictions on the TF grid used for defining CCs.

Let $\{x_k\}$ and $\{y_k\}$ be two time series. Moyal's formula states that [21]

$$\left|\sum_{k=0}^{N-1} x_k y_k^*\right|^2 = \frac{1}{2N}\sum_{n=0}^{N-1}\sum_{m=0}^{2N-1} w_x(n,m) w_y(n,m). \tag{56}$$

Using Eqs. (54) and (56), we rewrite $\hat{\ell}$ as the inner-product of two TFRs, namely, the WV of the data w_x and the *template WV* w_e which is the WV of complex template waveform $e_k \equiv \exp i\phi_k$,

$$\hat{\ell}(x;\phi) = \frac{1}{2N^2}\sum_{n=0}^{N-1}\sum_{m=0}^{2N-1} w_x(n,m) w_e(n,m). \tag{57}$$

Qualitatively, we expect that the TFR of a chirp signal have large values essentially in the vicinity of a curve corresponding to their instantaneous frequency and vanishes elsewhere. The template WV w_e being the TFR of a chirp, it shares these characteristics. In the following section, we make use of this feature to simplify the statistic.

3. Approximation 2: the WV of a CC is almost Dirac

With continuous time and frequency variables, it is well-known that ([22], p. 130 and also 217) the WV of a *linear chirp* (i.e., a chirp whose frequency is a linear function of time) is a Dirac distribution along the TF line associated to the chirp frequency.

We assume that this remains reasonably true for discrete time and frequency and when the chirp is nonlinear (and, in particular, when it is a CC). More precisely, we consider that we have

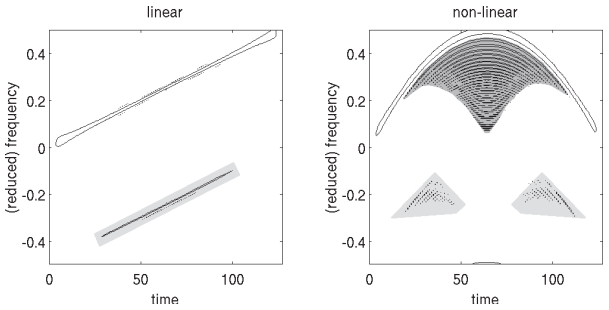

FIG. 3. Discrete Wigner-Ville of two chirp signals—The signals are normalized to unit ℓ_2 norm and we show the contour at the level 1/8. Left: when the chirp frequency is a linear function of time, its WV is almost Dirac along the corresponding TF line in the TF half plane associated to positive frequencies. For the negative frequencies, the WV distribution exhibits *aliasing terms* (we highlight them by a background in light gray) which we neglect in the simplified model in Eq. (58). Right: when the chirp frequency is not linear (here, it is a parabolic chirp), *interference terms* appear (evidenced by a dark gray background). Their contribution are also disregarded in the simplified model. Note that the WV of the nonlinear chirp chosen for this illustration do present aliasing terms (with a light gray background), but they have a smaller amplitude than in the linear case.

$$w_e(n, m) \approx 2N\delta(m - m_n), \tag{58}$$

where $m_n = [2Tf_n]$ where $[\cdot]$ denotes the nearest integer.

Here, f_n is the instantaneous frequency of the (possibly nonlinear) chirp. Equation (58) dissembles two approximations which we explain now.

For discrete time and frequency, the discrete WV of a linear chirp can be calculated analytically [21]. For the positive frequencies i.e., for $0 \le m \le N$, the model in Eq. (58) is an acceptable approximation of the exact result, as illustrated in Fig. 3. However, there is a significant difference in the negative frequencies i.e., for $N + 1 \le m \le 2N - 1$. In this region, the discrete WV exhibits *aliasing terms* (clearly seen in the left panel of Fig. 3) which are closely related to the unitarity property of the WV. In [21], the aliasing terms are shown to be oscillating terms (switching signs) with smaller amplitude than the preponderant terms modeled by Eq. (58). We can then expect their contribution to the summation in Eq. (57) to be negligible.

It is well known [22] that *interference terms* appear when computing (both continuous and discrete) WVs of nonlinear chirps. They can be related to the quadratic nature of this distribution (see [22] for a detailed analysis of the nature and geometry of these interferences). Interference terms change sign rapidly (see Fig. 3, right panel) and can be neglected for the same argument invoked for aliasing terms.

Inserting Eq. (58) into Eq. (57), we get the following approximation of $\hat{\ell}$:

$$\tilde{\ell}(x; \phi) = \frac{1}{N} \sum_{n=0}^{N-1} w_x(n, m_n). \tag{59}$$

We see that this statistic results from the integral of the WV of the data along the TF path determined by the CC frequency f_n. In other words, this integral is the area under this TF path. We refer to this quantity as the *path length*.[6]

With this approximation, the maximization of the statistic in Eq. (30) amounts to finding the path giving the largest integral, or the longest path. Efficient methods exist for longest path problems [23]. These methods exploit the structural properties of path length (or integral) measurement, in particular, *additivity*. The length of this entire path can be measured by splitting the path and summing the length of its constituent parts. Thanks to this property, the maximization problem can be decomposed into a recursive series of small problems, each of them being solvable in polynomial time. This is the main principle of *dynamic programming* (DP), which we describe in the next section.

We remind the reader that, contrarily to the new statistic $\tilde{\ell}$, the exact statistic ℓ is not additive. DP *cannot* be applied to maximize ℓ.

4. Maximization with dynamic programming

DP is a classical method [23] for solving combinatorial optimization problems. As explained in the previous section, the idea is to decompose the problem into smaller ones that can easily be solved. In our context, the natural decomposition is given by the tiling of the time axis into chirplet intervals i.e., $t_j \le t_s n < t_{j+1}$ or equivalently $jb \le n \le (j + 1)b - 1$ where $b \equiv \delta_t/t_s$ is the number of

[6] If we see the WV as a Lebesgue measure (although this is an misuse of language since the WV can take negative values), the integral in Eq. (59) effectively defines a path length.

samples in an interval. The overall path integral is equal to the sum of the integrals computed in each chirplet interval marked with a superscript index as follows

$$\tilde{\ell}(x; \phi) = \sum_{j=0}^{N_t-1} \tilde{\ell}^j(x; \phi) \tag{60}$$

$$\text{with } \tilde{\ell}^j(x; \phi) \equiv \frac{1}{N} \sum_{n=jb}^{(j+1)b-1} w_x(n, m_n^j), \tag{61}$$

where $m_n^j = [2Nf_n^j]$ and the frequency f_n^j follows the line joining the grid points (t_j, f_{m_j}) and $(t_{j+1}, f_{m_{j+1}})$. We also denote with a subscript index j, the path integral up to interval j, viz.

$$\tilde{\ell}_j(x; \phi) = \sum_{j'=0}^{j} \tilde{\ell}^{j'}(x; \phi). \tag{62}$$

DP relies on the *principle of optimality*. We elaborate this principle with the help of Fig. 4. We consider the chirplet in time interval j. In a chain passing through this chirplet, the regularity constraints limit the choice of preceding chirplets in the time interval $j - 1$. We suppose that there are only three such chirplets; namely α, β and γ.

Now, consider the time interval $j - 1$. We assume that we know the chain passing through the chirplet z (z being either α, β or γ) and giving the largest path integral summed up to the interval $j - 1$. We denote this quantity by $\tilde{\ell}_{j-1}^{(z)}$. (In this discussion, the chirplet and its associated CC are designated by the same label).

We compute the path integral contribution in jth interval for the considered chirplet, and add the result to $\tilde{\ell}_{j-1}^{(z)}$ to obtain $\tilde{\ell}_j^{(z)}$ for all the three paths $z = \alpha, \beta$ and γ.

We mark with $(\star)$ the optimal chain associated to the *global* maximum of $\tilde{\ell}$ (i.e., summing from interval 0 to $N_t - 1$) which we denote $\tilde{\ell}^{(\star)}$. We further assume that this optimal chain $(\star)$ follows (α) up to interval $j - 1$, continues following the considered chirplet in interval j and proceeds to the last interval $j = N_t - 1$ with some chain (δ), hence $\tilde{\ell}^{(\star)} = \tilde{\ell}_j^{(\alpha)} + \tilde{\ell}^{(\delta)}$ where $\tilde{\ell}^{(\delta)}$ denotes the contribution of the chain (δ).

The principle of optimality states that the optimal chain $(\star)$ has the largest path integral $\tilde{\ell}_{j-1}^{(\star)}$ at interval $j - 1$ as compared to *all* the other chains passing by the same chirplet in interval j. In particular, this means that $\tilde{\ell}_{j-1}^{(\star)} = \tilde{\ell}_{j-1}^{(\alpha)}$ is larger that $\tilde{\ell}_{j-1}^{(\beta)}$ and $\tilde{\ell}_{j-1}^{(\gamma)}$.

Proof by contradiction: Let us assume that $\tilde{\ell}_{j-1}^{(\beta)} > \tilde{\ell}_{j-1}^{(\alpha)}$. We construct the chain $(\triangle)$ formed by (β), the considered chirplet in interval j and the chain (δ). This CC is admissible. By construction, its path integral $\tilde{\ell}^{(\triangle)} = \tilde{\ell}_j^{(\beta)} + \tilde{\ell}^{(\delta)}$ is larger than $\tilde{\ell}^{(\star)}$. Therefore, the chain $(\star)$ is not optimal which contradicts our hypothesis—QED.

We apply this principle recursively starting from interval $j = 0$ and incrementing. For each chirplet interval and for all N_c chirplets of interval j, we keep only the CC maximizing the path integral up to this point and we discard the others. This procedure "prunes the combinatorial tree" and avoids to consider useless candidates before going to the next interval.

When the recursion reaches the last interval $N_t - 1$, we end up with a number N_c of CCs ending with a different last chirplet and having the maximum path integral among all chains with the same last chirplet. Finally, within these "short-listed" candidates, we select the chain with the largest $\tilde{\ell}$ which is the *global maximum*.

5. Numerical contingencies and computational cost

To summarize, we started with the initial problem in Eq. (30) of finding the CC with the largest statistic. We rephrased this problem (using approximations) into a *longest path* problem in the TF plane. Here, *path* refers to the TF curve followed by the frequency of the CC, and the *length* is given by the integral of the WV of the data along the path. The maximization of the path length over the set

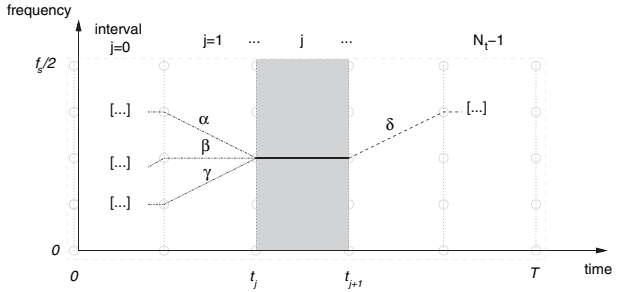

FIG. 4. Principle of optimality of DP

of CCs can be performed efficiently using DP. The resulting algorithm is tractable numerically as shown by the estimate obtained in the second part of this section.

The definition of the CCs does not comprehend the fact that we only have access to discretized versions of the data and of their associated TF domain, denoted $\mathcal{D}$ in Sec. IV A. We begin this section by a discussion on these aspects.

a. Discretization issues—On one hand, the definition of the set of CCs relies on a TF grid sampling the *continuous* TF domain $\mathcal{D}$. Theoretically, this grid can be refined arbitrarily. On the other hand, the search operates effectively using the *discretized* version of $\mathcal{D}$, resulting from the sampling associated to the WV. This fixes a maximum TF resolution which cannot be surpassed.

It is useless to increase the resolution of the TF grid used for defining CCs beyond the one defined by WV. The WV divides the time axis into N intervals and the frequency axis into N bins.[7] Consequently, we have the following limitations, $N_t \leq N$ and $N_f \leq N$. Furthermore, in order to have time intervals (resp. frequency bins) of equal size , the TF grid parameters N_t (resp. N_f) must be divisors of N.

All these requirements limit the choice of N_t and N_f. It may happen that the parameters of smallest tight CC grid are not suitable because of that. Note that in the case we consider, we are generally led to adopt the finest resolution for the frequency axis i.e., $N_f = N$.

b. Estimate of the computational cost—

We estimate the computational cost by counting the floating point operations for all the primary subparts in the course of the procedure. The computation of the WV of the data involves N FFTs with time base $2N_f$ [21], such that the cost of this part is about $5NN_f \log_2 N_f$ (assuming a standard implementation with RADIX-2).

The number of operations required by DP is better estimated by grouping them by types, rather than by a sequential assessment. The path integral $\tilde{\ell}_j$ in Eq. (61) is computed (with b additions) only once for each N_c chirplets of all N_t intervals, with a corresponding cost equal to $N_c N$.

For each of the N_c chirplets in each interval, the algorithm selects among the (at most) $2N_r'' + 1$ possibly connected paths. This procedure is repeated $N_t - 1$ times, and thus requires $\sim N_t N_c (2N_r'' + 1)$ operations.

Knowing that the number of chirplets is $N_c \approx (2N_r' + 1)N_f$, the overall cost C thus scales with

$$C \propto 5NN_f \log_2 N_f + [N + (2N_r'' + 1)N_t](2N_r' + 1)N_f, \quad (63)$$

which is a polynomial of the problem size.

[7]It is possible to modify slightly the definition of WV in Eq. (55) to get a finer sampling of the frequency axis and keep unitarity. We reserve this possibility for later investigations.

VI. APPLICATIONS

In this section, the proposed method is evaluated with several numerical tests and compared with two other TF based algorithms for the detection of unmodeled chirps, namely, the Signal Track Search (STS) [12] and Time-Frequency Clusters (TFC) [14]. The simulation code[8] of these tests uses the implementation of these algorithms provided by [24]. We first give a brief presentation of STS and TFC.

A. Existing algorithms

1. Signal Track Search

We have seen earlier that the TFR of a chirp signal can be essentially described in the TF plane as a regular alignment of large values forming ''ridges'' along the instantaneous frequency evolution. The STS uses this observation as a heuristic basis: detecting chirps amounts to finding ridges in a TFR.

In practice, the algorithm extracts the ridges from the WV distribution[9] of the data. Because of the presence of noise, image processing techniques are required to get a good ridge extraction. The authors chose an algorithm which is normally used for road extraction from aerial images. This algorithm is based on the fact that a ridge is a locus of points having a maximum curvature (as measured by the second derivative) in the transverse direction and a small gradient along the longitudinal direction. A hysteresis thresholding procedure is applied over the second derivative of the WV (smoothed by a low pass filter) to detect TF points which suffice the above condition, and to grow iteratively chains of TF points from these ridge precursors. In [12], the ridge length (number of TF points in a ridge) is then employed as the detection statistic. However, we do not use this definition here, but we rather consider the one given by the largest path integral computed along the detected ridges. We observed that this variation outperforms the original definition of STS.

2. TFClusters

TFClusters is initially thought to detect short oscillatory transients (and not specifically chirps). The TFR of such transient is sparse i.e., the TF contents is essentially described by few components of large amplitude. The basic idea of TFClusters is that, for reasonable SNR, the amplitude of the transient components is larger than the noise.

This motivates the thresholding of the TFR of the data, given by the spectrogram (modulus square of short-time Fourier transform), to retain the TF points with the largest values. A clustering algorithm is used to group the selected points. ''Significant'' clusters are chosen whose cardinals are greater than a threshold. ''Insignificant'' clusters are merged iteratively if they are sufficiently close to eventually form significant clusters. The statistic is then chosen to be the maximum sum of the TF powers over the clusters in the resulting list of significant clusters.

[8]Freely distributed scripts are available at http://www.obs-nice.fr/ecm for reproducing all the illustrations presented here.

[9]In [12], the authors use the standard definition of the discrete WV originally proposed by Claasen-Mecklenbräuker (see [21] for a definition and a detailed discussion). This definition differs from the one presented in Sec. V B 3. In particular, it does not satisfy unitarity.

3. Discussion

It is important to stress a major difference between STS and TFClusters and the proposed method. By construction, the formers work well provided that the signal ''stands above'' the noise somewhere in the TF plane. If we define a local SNR in the TF plane (by computing at a given TF point, the squared difference of the mean values of the TFR under the hypotheses H_0 and H_1 divided by its variance under H_0), then this is equivalent to say that the *local* SNR has to be large at least for some TF points. However, just like the standard matched filtering, a detection with the best CC algorithm requires the *global* SNR (obtained by summing the local SNRs for all TF points) to be large. Clearly, this is a less stringent condition.

TF path integration is a central ingredient of the best CC search. This idea is also used for other methods developed for the detection of other GW sources. For instance, for inspiralling binaries, we can cite [25,26] and for the periodic GW sources, the Hough transform [27] and the stack slide searches [28].

Several distinctions must be stressed. First, the TF representation we use here (discrete WV) satisfies a specific and crucial property, namely, unitarity. This allows us to link the final statistic to the quadratic matched filtering. TF representations based on short-time Fourier or wavelet bases used by the above methods are not unitary. Second, the other methods require a precise model of the TF path (relying on the astrophysical source modeling) as opposed to our method.

For the problem addressed here i.e., the detection of unmodeled chirps, we have shown that CCs can be treated as an effective finite template grid. We could then imagine to apply one of the above methods and integrate along the entire set of TF paths associated to CCs. This is however computationally impossible because of the too large number of CCs, as already discussed in Sec. V A.

B. Newtonian chirps: illustrations and benchmark

For the illustration of the best CC search, we use the Newtonian chirp signal introduced in Sec. IV E. We recall that the frequency of such chirp is a power law given by Eq. (35). Normally, the Newtonian chirp also includes a prescribed evolution of the chirp amplitude. However, for simplicity and better match with our initial model, we decide not to take this into account and keep the chirp envelope to a constant.

The Newtonian chirp is completely defined by the total mass M of the binary (if we assume that the objects have equal masses) and its initial frequency f_0. Figure 5 presents an example of a typical Newtonian chirp signal, where we set $M = 7.3 M_\odot$ and $f_0 = 96$ Hz. The chirp duration is $T = 0.5$ s. We fix the sampling frequency to $f_s = 2048$ Hz (therefore, the number of samples is $N = T f_s = 1024$). A white Gaussian noise of unit variance is added to the signal.

Within the GW literature, it is customary to define the SNR through matched filtering (assuming the initial phase is known *a priori*). We follow this definition which gives in the present case,

$$\rho^2 \equiv \sum_{k=0}^{N-1} s_k^2 \approx A^2 N/2. \quad (64)$$

We note that, with this definition we have $\rho^2 = 2\ell(s;\phi)$ (the factor of 2 accounts for the unknown initial phase).

We choose to scale the chirp amplitude to a SNR $\rho = 20$.

We apply the best CC search to this signal with the following search parameters. We arbitrarily fix the chirping rate limits to be $\dot{F} = 8192$ Hz/s and $\ddot{F} = 917.5$ kHz/s^2. These values are quite smaller than the ones expected at the LSCO (see Sec. IV E) but the time instant when these limits are reached is close (few tenths of milliseconds before) to the LSCO. In Fig. 5, the time instants when the chirp (the solid line on the right panel) reaches the chirping rate limits (with dotted vertical lines) and when the binary system reaches LSCO (with dashed-dotted horizontal line) are indicated. We fix the frequency axis sampling to the finest accessible resolution i.e., $N_f = N = 1024$. Similarly, we choose the smallest possible chirplet size with $N_t = N/2$. The rest of the parameters are derived from the regularity constraints. In this respect, it is useful to calculate the adimensional characteristics of the problem i.e., $N' = 2048$ and $N'' = 586.6$. The resulting parameters are $N_r' = 9$ and $N_r'' = 3$, which gives a maximum SNR loss $\mu \approx .28$.

We recall that the best CC search relies on the approximation of the optimal statistic by a complex sum presented in Sec. V B 1. The parameter η controls the relative precision of this approximation. From the results of Sec. V B 1 and the above general chirp specifications, the approximation holds with a precision $\eta = 0.14$ in a frequency bandwidth $[f_l, f_s/2 - f_l]$ with $f_l = 96$ Hz which coincides (at least for the low frequencies, which are most important) with the frequency support of the present chirp.

Figure 5 presents the result of the best CC search with the above choice of parameters. The best CC closely matches the actual instantaneous frequency in the region where the regularity constraints are satisfied.

An example is obviously not sufficient to evaluate the method thoroughly. Receiver operating characteristics (ROC) gives a systematic assessment of the performance. The ROC of a given statistic l is the diagram giving the

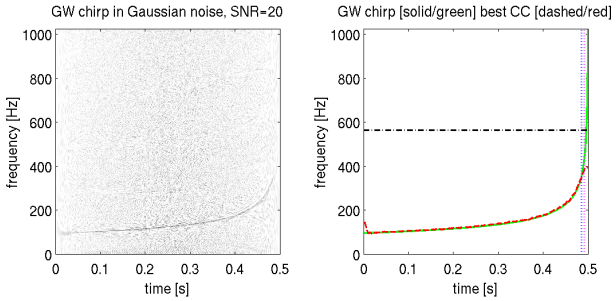

FIG. 5 (color online). Newtonian chirp in white Gaussian noise—Left: WV distribution of the signal. Only positive contributions are displayed (negative ones are set to zero) with a gray-scaled color map going from white (minimum i.e, zero) to black (maximum). Right: the best CC in dashed/red closely matches the actual instantaneous frequency in solid/green in the region where the regularity constraints are satisfied. We indicate the instant when the chirp reaches the chirping rate limits with the dotted vertical lines and the frequency at LSCO with dashed-dotted horizontal line.

detection probability $P_d(l_0) \equiv \mathbb{P}(l \geq l_0|H_1)$ versus the false alarm probability $P_{fa}(l_0) \equiv \mathbb{P}(l \geq l_0|H_0)$ at a given SNR and for all thresholds l_0.

For this exercise, due to computing limitations, we prefer short signals with a small number of samples N. We choose a Newtonian chirp with total mass $M = 11M_\odot$ and initial frequency $f_0 = 96$ Hz which has a short duration $T \sim 250$ ms. Choosing the sampling frequency $f_s = 1024$ Hz, we have $N = 256$ samples. White Gaussian noise is added to the signal and the amplitude is scaled such that the SNR is $\rho = 10$.

We fix the chirping rate limits to $\dot{F} = 8.192$ kHz/s and $\ddot{F} = 1.05$ MHz/s^2. Like the above example, these limits are reached at a time instant close to the LSCO. We choose the finest TF grid parameters $N_t = 128$ and $N_f = 256$, and the regularity parameters $N_r' = 9$, $N_r'' = 4$. The resulting CC grid is tight with $\mu \approx 0.4$.

Concerning STS[10] and TFClusters,[11] we set their free parameters empirically using the recommendations available in the references, without a precise fine-tuning. Figure 6 displays a single trial and Fig. 7 presents the ROCs of the three methods presented previously. We see that the best CC search outperforms the two others as expected.

Here, we wish to add few remarks regarding the comparison between the best CC search and STS. The improvement in the ROC of the best CC with respect to STS has two origins. First, the use of a unitary discrete WV instead of the standard WV helps in increasing the detection probability by few percent. The unitarity preserves the power in TF plane and hence improves the efficiency. Second, the major part of the improvement comes from the TF pattern search procedure. As explained in Sec. VI A, the use of a global search criterion instead of a local one is a crucial ingredient.

It is interesting to compare these ROCs with what could optimally achieve an imaginary observer which knows in advance the targeted chirp. Since this *clairvoyant* observer knows the chirp phase exactly, he can apply the optimal statistic i.e., the quadrature matched filter obtained in Appendix A. The ROCs of the quadrature matched filter can be obtained analytically (under Gaussian noise hypotheses). The false alarm and detection probabilities are given, respectively, by [29]:

$$P_{fa}(l_0) = \exp(-l_0), \tag{65}$$

$$P_d(l_0) = 1 - \exp(-\rho_c^2/2) \sum_{n=0}^{+\infty} \frac{(\rho_c^2/2)^n}{n!} I_{l_0}(n+1) \tag{66}$$

where $I_y(x) \equiv 1/\Gamma(x) \int_0^y e^{-u} u^{x-1} du$ is the incomplete Gamma function.

This ROC depends only on one parameter, namely, the SNR ρ_c. The ROC curve of the clairvoyant statistic with $\rho_c = \rho$ provides an absolute upper bound on the detection probability. Obviously, having in hand all the information makes a very large difference with respect to the case where we only know that the incoming GW is a smooth chirp. The detection probability of the clairvoyant statistic is very close to 1 over the entire range of values chosen for the false alarm rate. This is why we do not show this curve. It is more interesting to compare the performances of the various methods with the ones of the clairvoyant observer for SNRs $\rho_c < \rho$. More precisely, we adjust ρ_c in such a way that the resulting curve matches reasonably well the ROC of the best CC search in the region of interest i.e., for false alarm probabilities in the range 10^{-5} to 10^{-4}. Since the SNR is inversely proportional to the distance of the GW source, the ratio of the actual SNR to the best-fit value ρ/ρ_c gives the reduction factor of the sight distance with respect to the ideal (and nonaccessible) situation where we have at our disposal all the information about the chirp we want to detect. We include the fitted clairvoyant ROC in Fig. 7. The ratio in the sight distance can be estimated $\sim 10/6.15 \approx 1.6$.

[10]Following the notations of [12], the size of the Gaussian kernel of the presmoothing filter is fixed to $\sigma = 2$. The low and high thresholds of the hysteresis are set to $3.3/\text{pixel}^2$ and $10/\text{pixel}^2$ resp.

[11]The TFR is given by the short-time Fourier transform computed over nonoverlapping blocks of 16 samples (i.e., intervals of ≈ 7.8 ms). The frequency axis is tiled into 32 bins (i.e., a resolution of 32 Hz). We use the nominal values given in [14] for the rest of the parameters namely $p = 0.1$, $\sigma = 5$, $\delta = [0, 0, 0, 0, 0, 0, 2, 3, 4, 4]$ and $\alpha = 0.25$.

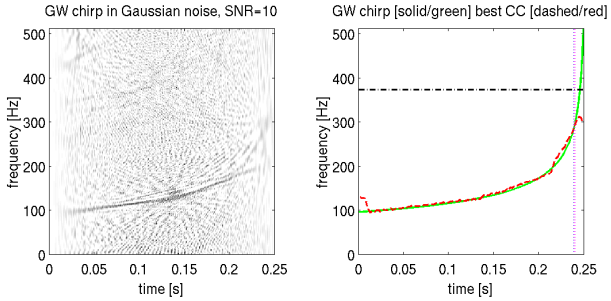

FIG. 6 (color online). Newtonian chirp in white Gaussian noise—Left: WV distribution of the signal (displayed similarly as in Fig. 5). Right: actual chirp frequency in solid/green and best CC in dashed/red. We indicate where the chirp reaches the chirping rate limits with dotted vertical lines and the frequency at LSCO with dashed-dotted horizontal line.

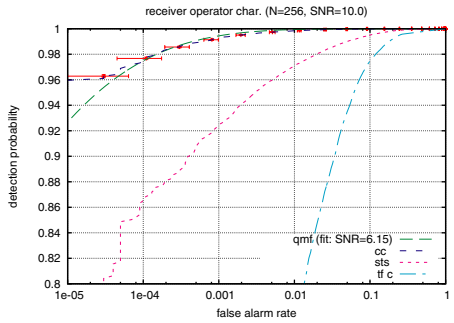

FIG. 7 (color online). Newtonian chirp in white Gaussian noise—Comparison of ROCs of the best CC search (dashed/blue, with error bars in solid/red) with STS (dotted/magenta) and TFC (dashed-dotted/cyan). The computation of each ROCs is perfomed over 2×10^5 trials (half for the false alarm probability and half for the detection probability). The diagram also includes the ROC of the clairvoyant quadrature matched filter (bold dashed/green) shown here with the SNR $\rho_c = 6.15$ adjusted to reasonably fit the ROC of the best CC search.

C. Random CCs and robustness

While benchmarks based on Newtonian chirps are satisfactory for a comparison of several detection methods in a nominal situation, they do not provide a test for the robustness i.e., a measurement of the ability to detect reliably a large class of different chirps.

In this section, we present ROC curves computed using *random CCs*. Random CCs are generated by chaining chirplets which are randomly chosen in a range specified by regularity constraints. Therefore, the frequency of a random CC follows a kind of random walk in the TF plane. We generate a new random CC for each trial made to estimate the detection probability.

The detection of random CCs is obviously much more difficult than the detection of a single chirp. It is an effective test of the method robustness. No classical approaches (e.g., based on banks of quadrature matched filters as for inspiralling binary chirps) can be applied successfully in this case.

We assume the same general characteristics of the Newtonian chirp used in the first example in the previous section, namely $T = 0.5$ s, $f_s = 2048$ Hz, thus $N = 1024$ samples, $\dot{F} = 8192$ Hz/s and $\ddot{F} = 917.5$ kHz/s^2. We already computed satisfactory search parameters for this setup. Therefore, they remain unchanged ($N_t = 512$, $N_f = 1024$, $N_r' = 9$ and $N_r'' = 3$). The random CCs are generated on the same basis, but with a time interval slightly larger, the regularity parameters being increased accordingly i.e., $N_t = 64$, $N_f = 1024$, $N_r' = 65$ and $N_r'' = 57$. We use an additive white Gaussian noise.

Figure 8 presents an example of such signal (with SNR $\rho = 20$) and the result of the application of the best CC search. Figure 9 displays the ROC curve of the best CC

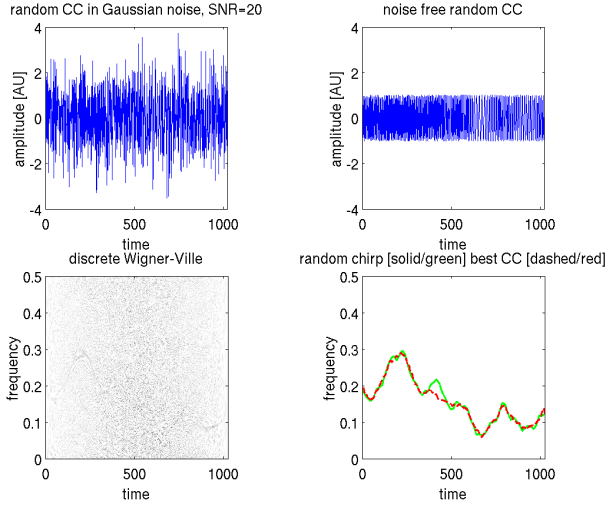

FIG. 8 (color online). Random CC in white Gaussian noise—In these plots, we arbitrarily set $f_s = 1$. Top left: example of a random CC in white Gaussian noise. Top right: noise free random CC. Bottom left: WV distribution of the signal (displayed similarly as in Fig. 5). Bottom right: actual chirp frequency in solid/green and best CC in dashed/red. It is worthwhile to note that, although the best CC can lose track for some time because of noise fluctuations, it is able to recover the exact TF path.

search (with SNR $\rho = 12$) along with the one of the clairvoyant quadrature matched filter adjusted to an adequate SNR. We estimate a loss in the sight distance with respect to the clairvoyant case to be a factor of $\sim$2.6. Best CC search "sees" to distances comparable to (in the sense, with a reduction factor less than 1 order of magnitude) what classical methods achieve in other GW detection problems.

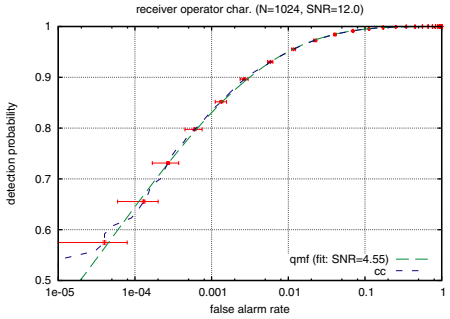

FIG. 9 (color online). Random CC in white Gaussian noise—This diagram displays the ROC of the best CC search (dashed/blue, obtained from 2×10^5 trials) compared with the analytical ROC of the clairvoyant matched filter (bold dashed/green) with the SNR $\rho_c = 4.55$, adjusted to produce a reasonable fit.

The computational cost of this search as estimated by Eq. (63) is about 1.42×10^8 of floating points operations for one block of duration $T = 0.5$ s. Assuming 10% overlap between successive blocks, real-time processing can be achieved with a computing power of 2.8 Gflops which is less than what a single standard workstation can handle today.

VII. CONCLUDING REMARKS

Smooth chirps define a general model of "nearly physical" GW chirps. Chirplet chains—chains of linear chirplets—allow the design of tight template grids for the detection of smooth chirps. The optimal detection requires these grids to be searched thoroughly to find the template which best matches with the data. Although the shear large number of templates prevents the use of an exhaustive search, near-optimal detection can be performed with the time-frequency based procedure presented here. Its originality lies in the clear link established between the optimal statistic and the proposed search algorithm. In particular, it justifies the choice of a specific time-frequency representation (the unitary discrete WV) and pattern search algorithm (TF path integral and dynamic programming). We have evaluated that best CC search is computationally tractable for detection of typical GW chirps.

It is important to emphasize several features which makes the proposed method attractive in practice. First, the free parameters (the chirp duration T and the chirping rate limits $\dot{F}$ and $\ddot{F}$) are few and directly related to physical characteristics. Second, the principle "*He who can do more can do less*" applies here: smooth chirps is a very general class of chirps. This model, and thus the search algorithm can be easily modified and adapted to incorporate additional astrophysical information. For instance, it is easy to search only chirps with an increasing (or decreasing) frequency. One may also want a more stringent constraint on the chirping rate at low frequencies than at high frequencies. The inclusion in the algorithm of a dependency of the chirping rate limit upon the frequency is straightforward. This leaves the possibility of a compromise between efficiency (since the restriction of the set of admissible waveforms due to additional constraints reduces the false alarm rate) and robustness, depending on the quantity and reliability of the information available on a specific GW source. Third and finally, it is simple to restrict the search to chirps starting and/or finishing at given time-frequency location. This feature could be used for partially known chirps whose waveforms is known only on a part of the total duration. Those signals could be detected with a hybrid approach combining a standard matched filtering where the waveform model is available, and best CC search for the rest.

ACKNOWLEDGMENTS

This work has benefited from many discussions and exchanges of ideas. For this reason, we would like to thank Sanjeev Dhurandhar, Patrick Flandrin, Jérôme Idier, Ekatherina Karatsuba and Bruno Torresani. We gratefully acknowledge ICTP (Trieste, Italy), Observatoire de la Côte d'Azur (France) and EGO (Cascina, Italy) for their support and hospitality.

APPENDIX A: MAXIMIZING LLR $\Lambda(\cdot)$ OVER THE INITIAL PHASE φ_0

In this appendix, we maximize the statistic $\Lambda(x; \{\hat{A}, \varphi_0, t_0, \phi(\cdot)\})$ over the initial phase φ_0. We recall that

$$\Lambda(x; \{\hat{A}, \varphi_0, t_0, \phi(\cdot)\}) = \frac{1}{2\mathcal{N}} \left(\sum_{k=0}^{N-1} x_k \bar{s}_k \right)^2, \qquad \text{(A1)}$$

where $\mathcal{N} \equiv \sum_{k=0}^{N-1} \bar{s}_k^2$ is the norm of $\bar{s}_k = \cos(\phi_k + \varphi_0)$. To keep the notations simple, we do not mention all parameters explicitly in this appendix and set $\Lambda(x; \varphi_0) = \Lambda(x; \{\hat{A}, \varphi_0, t_0, \phi(\cdot)\})$.

In the literature concerning the detection of inspiralling binaries of compact objects [17,18], this maximization is usually performed assuming that $\mathcal{N}$ is independent of φ_0. This assumption is correct when the two quadratures $\cos\phi_k$ and $\sin\phi_k$, viewed as vectors of $\mathbb{R}^N$, are orthonormal (i.e., orthogonal and of same norms). In this case, we have $n_c = n_s = N/2$ and $n_x = 0$ where n_c, n_s and n_x are the norms and cross-products of the quadratures as defined in Eqs. (7). Inserting this into

$$\mathcal{N} = n_c \cos^2\varphi_0 - n_x \sin(2\varphi_0) + n_s \sin^2\varphi_0, \qquad \text{(A2)}$$

we conclude that $\mathcal{N} = N/2$ is a constant.

However, for general phase evolution, the quadrature waveforms are not necessarily orthonormal. This is approximately true when the chirp oscillates sufficiently rapidly during many cycles (e.g., for inspiralling binaries of small mass). Since we are considering chirps with an arbitrary phase and of relatively short duration, such assumption is not realistic and we opt for the general case keeping the dependency of $\mathcal{N}$ upon φ_0.

Expanding $\bar{s}_k$ in terms of two quadratures and rewriting Eq. (A1), we get

$$\Lambda(x; \varphi_0) = \frac{(x_c \cos\varphi_0 - x_s \sin\varphi_0)^2}{2(n_c \cos^2\varphi_0 - n_x \sin(2\varphi_0) + n_s \sin^2\varphi_0)}, \qquad \text{(A3)}$$

where x_c and x_s are the cross-correlation of the data with $\cos\phi_k$ and $\sin\phi_k$ as defined in Eq. (6).

To proceed with the maximization, we first examine the special case where the quadratic waveforms are linearly dependent i.e., $\cos\phi_k \propto \sin\phi_k$ for all k. This implies that we are in the degenerate case where $\phi_k = \varphi_0$ is constant. Introducing the two angles $\varphi = \arg(x_c + i x_s)$ and $\eta = \arg(\sqrt{n_c} + i\sqrt{n_s})$, we can rewrite Eq. (A3) as

$$\Lambda(x; \varphi_0) = \frac{1}{2} \frac{x_c^2 + x_s^2}{n_c + n_s} \frac{\cos^2(\varphi + \varphi_0)}{\cos^2(\eta + \varphi_0)}. \qquad \text{(A4)}$$

The proportionality of the quadrature waveforms implies that $\sqrt{n_c} x_s \pm \sqrt{n_s} x_c = 0$ which gives $\sin(\eta - \varphi) = 0$, and hence $\eta = \varphi + \pi\mathbb{Z}$. We conclude that $\Lambda(x; \varphi_0)$ remains constant for all φ_0 and is equal to the statistic given by

$$\ell(x; t_0, \phi) = \frac{x_c^2 + x_s^2}{2N}. \qquad \text{(A5)}$$

In the non degenerate case, we compute the derivative of the statistic as given in Eq. (A3) with respect to φ_0. Its numerator turns out to be a second order polynomial of $\tan\varphi_0$. The root associated to the local maximum is

$$\hat{\varphi}_0 = \tan^{-1}\left(\frac{x_s n_c - x_c n_x}{n_x x_s - n_s x_c} \right) \qquad \text{(A6)}$$

which gives the ML estimator of the initial phase.

Inserting this expression in Eq. (A3) yields

$$\ell(x; t_0, \phi) \equiv \Lambda(x; \hat{\varphi}_0) = \frac{n_s x_c^2 - 2n_x x_c x_s + n_c x_s^2}{2\mathcal{O}}, \quad \text{(A7)}$$

where $\mathcal{O} \equiv n_c n_s - n_x^2 > 0$.

We can reexpress this statistic as

$$\ell(x; t_0, \phi) = \frac{1}{2}\left[\left(\sum_{k=0}^{N-1} x_k \tilde{c}_k\right)^2 + \left(\sum_{k=0}^{N-1} x_k \tilde{s}_k\right)^2\right], \quad \text{(A8)}$$

where $\tilde{c}_k$ and $\tilde{s}_k$ are the orthonormalized counterparts of the waveforms in quadrature $\cos\phi_k$ and $\sin\phi_k$ obtained from the Gram-Schmidt procedure as given below

$$\tilde{c}_k = \frac{\cos\phi_k}{\sqrt{n_c}}, \qquad \tilde{s}_k = \frac{n_c \sin\phi_k - n_x \cos\phi_k}{\sqrt{n_c \mathcal{O}}}, \quad \text{(A9)}$$

and referred to as templates of phase ϕ.

In practice, this orthonormalization is indeed performed for the detection of inspiralling binaries (see [30], p. 3046) and is justified with heuristic arguments. The derivation shows that it results directly from the maximization of the LLR.

APPENDIX B: TAYLOR APPROXIMATION OF THE DISTANCE BETWEEN CHIRPS

In this appendix, we detail the approximation of the statistic $\ell(s; \phi^*)$ with $s_k = A\cos(\phi_k + \varphi_0)$ and assuming that the template phase ϕ^* is close to the phase ϕ of the signal s present in the data. We start from the following Taylor expansion of $\ell(s; \phi^*)$ for small $\Delta_k \equiv \phi_k^* - \phi_k$

$$\ell(s; \phi*) = \ell(s; \phi) + \sum_{k=0}^{N-1} \partial_k \ell|_{\phi^*=\phi} \Delta_k + \frac{1}{2}\sum_{k,l=0}^{N-1} \partial_{kl}^2 \ell|_{\phi^*=\phi} \Delta_k \Delta_l + \cdots, \quad \text{(B1)}$$

where the partial derivatives $\partial_k \equiv \partial/\partial\phi_k^*$ and $\partial_{kl}^2 \equiv \partial^2/\partial\phi_k^*\partial\phi_l^*$ are taken with respect to the samples of the template phase ϕ^*. Next, we examine this expansion term by term and obtain analytical expressions as a function of the phase samples $\{\phi_k\}$ and $\{\phi_k^*\}$.

1. First derivative: local extremum

From Eq. (9), we write the statistic ℓ as the ratio $\ell = n/d$. The numerator is $n = n_s x_c^2 - 2n_x x_c x_s + n_c x_s^2$ and the denominator is $d = 2(n_c n_s - n_x^2)$. We thus have $\partial_k \ell = (\partial_k n - \ell\,\partial_k d)/d$.

We get the following general expressions of the derivative of the numerator[12]

$$\partial_k n = \partial_k n_s x_c^2 + n_s 2x_c \partial_k x_c - 2(\partial_k n_x x_c x_s + n_x \partial_k x_c x_s + n_x x_c \partial_k x_s) + \partial_k n_c x_s^2 + n_c 2x_s \partial_k x_s, \quad \text{(B2)}$$

and of the denominator

$$\partial_k d = 2(\partial_k n_c n_s + n_c \partial_k n_s - 2n_x \partial_k n_x). \quad \text{(B3)}$$

We insert $s_k = A\cos(\phi_k + \varphi_0)$ and work out each of their component term. At the match (when $\phi^* = \phi$), we get

$$\partial_k n_s|_{\phi^*=\phi} = \sin 2\phi_k, \qquad \partial_k n_x|_{\phi^*=\phi} = \cos 2\phi_k, \quad \text{(B4)}$$

$$\partial_k n_c|_{\phi^*=\phi} = -\sin 2\phi_k = -\partial_k n_s|_{\phi^*=\phi}, \quad \text{(B5)}$$

$$\partial_k x_s|_{\phi^*=\phi} = A\cos\phi_k \cos(\phi_k + \varphi_0), \quad \text{(B6)}$$

$$\partial_k x_c|_{\phi^*=\phi} = -A\sin\phi_k \cos(\phi_k + \varphi_0). \quad \text{(B7)}$$

Combining all the above expressions, the derivative $\partial_k n$ can be factorized, yielding

$$\partial_k n|_{\phi^*=\phi} = \ell(s; \phi)\partial_k d|_{\phi^*=\phi}, \quad \text{(B8)}$$

where $\partial_k d|_{\phi^*=\phi} = 2(n_c - n_s)\sin 2\phi_k - 4n_x \cos 2\phi_k$ and $\ell(s; \phi) = A^2(n_c \cos^2\varphi_0 - n_x \sin 2\varphi_0 + n_s \sin^2\varphi_0)/2$. In conclusion, the first derivative $\partial_k \ell|_{\phi^*=\phi} = 0$ vanishes at $\phi^* = \phi$ which is thus a local extremum.

Using the parameters $\epsilon = 2n_x/N$ and $\delta = (n_c - n_s)/N$ as defined later in Sec. V B (and also discussed in Appendix D), the statistic and the denominator at the match can be expressed as functions of δ and ϵ as

$$\ell(s; \phi) = \frac{A^2 N}{4}(1 + \delta\cos 2\varphi_0 - \epsilon \sin 2\varphi_0) \quad \text{(B9)}$$

$$d|_{\phi^*=\phi} = \frac{N^2}{2}(1 - \delta^2 - \epsilon^2). \quad \text{(B10)}$$

2. Second derivative and distance

We show in the previous subsection that the first derivative at the match $\partial_k \ell|_{\phi^*=\phi}$ vanishes. Consequently, the second derivative at the match can be expressed simply in terms of the second derivatives of the numerator and denominator at the match, namely

$$\partial_{kl}^2 \ell|_{\phi^*=\phi} = \left[\frac{\partial_{kl}^2 n - \ell(s; \phi^*)\partial_{kl}^2 d}{d}\right]_{\phi^*=\phi}. \quad \text{(B11)}$$

We obtain the following general expressions for the second derivatives of the denominator

$$\partial_{kl}^2 d = 2[\partial_{kl}^2 n_c n_s + \partial_k n_c \partial_l n_s + \partial_l n_c \partial_k n_s + n_c \partial_{kl}^2 n_s - 2(\partial_k n_x \partial_l n_x + n_x \partial_{kl}^2 n_x)]. \quad \text{(B12)}$$

[12]Here, we adopt the precedence rule $\partial_k ab = (\partial_k a)b$.

and of the numerator

$$\partial_{kl}^2 n = \partial_{kl}^2 n_s x_c^2 + 2(\partial_k n_s x_c \partial_l x_c + \partial_l n_s x_c \partial_k x_c + n_s \partial_k x_c \partial_l x_c + n_s x_c \partial_{kl}^2 x_c) - 2(\partial_{kl}^2 n_x x_c x_s + \partial_k n_x \partial_l x_c x_s + \partial_k n_x x_c \partial_l x_s + \partial_l n_x \partial_k x_c x_s + \partial_l n_x x_c \partial_k x_s + n_x \partial_k x_c \partial_l x_s + n_x \partial_l x_c \partial_k x_s + n_x x_s \partial_{kl}^2 x_c + n_x x_c \partial_{kl}^2 x_s) + \partial_{kl}^2 n_c x_s^2 + 2(\partial_k n_c x_s \partial_l x_s + \partial_l n_c x_s \partial_k x_s + n_c \partial_k x_s \partial_l x_s + n_c x_s \partial_{kl}^2 x_s), \quad \text{(B13)}$$

Similarly to the first derivative, we insert the expression of the signal $s_k = A\cos(\phi_k + \varphi_0)$ and evaluate each of the component terms of the above expressions. We have to distinguish two cases i.e., the nondiagonal cross terms of the Hessian matrix when $k \neq l$ and the diagonal ones when $k = l$.

a. Cross terms, $k \neq l$

When $k \neq l$, the above Eqs. (B12) and (B13) are significantly simplified because all the second order cross derivatives are zeros (namely $\partial_{kl}^2 n_c = \partial_{kl}^2 n_x = \partial_{kl}^2 n_s = 0$ and $\partial_{kl}^2 x_c = \partial_{kl}^2 x_s = 0$). We get

$$\partial_{kl}^2 d|_{\phi^*=\phi} = -4\cos 2(\phi_k - \phi_l), \quad \text{(B14)}$$

and combined with Eq. (B9),

$$[\partial_{kl}^2 - \ell(s; \phi^*)\partial_{kl}^2 d]_{\phi^*=\phi} = \frac{A^2 N}{4}[1 + \cos 2(\phi_k - \phi_l) - \cos 2(\phi_k + \varphi_0) - \cos 2(\phi_l + \varphi_0) + \epsilon(\sin 2(\phi_k + \phi_l + \varphi_0) - \sin 2\phi_k - \sin 2\phi_l - \sin 2\varphi_0) + \delta(\cos 2(\phi_k + \phi_l + \varphi_0) - \cos 2\phi_k - \cos 2\phi_l + \cos 2\varphi_0)]. \quad \text{(B15)}$$

In Appendix D, we discuss the range of values taken by ϵ and δ depending on the phase ϕ. We show that these parameters are small $\epsilon, \delta \ll 1$ if the phase ϕ is a CC whose frequency does not come close to DC nor the Nyquist frequency. We assume that this remains true in the more general case, when ϕ is the phase of a smooth chirp. We retain the leading term (of order 0 in ϵ and δ) and get the following approximation

$$\partial_{kl}^2 \ell|_{\phi^*=\phi} \equiv X_{kl} = \frac{A^2}{2N}((1 - \hat{c}_k)(1 - \hat{c}_l) + \hat{s}_k \hat{s}_l) \quad \text{(B16)}$$

where $\hat{c}_k = \cos 2(\phi_k + \varphi_0)$ and $\hat{s}_k = \sin 2(\phi_k + \varphi_0)$.

b. Autoterms, $k = l$

We consider the case where $k = l$. Now, the second order derivatives do not vanish. In fact, we have

$$\partial_k^2 n_c|_{\phi^*=\phi} = -2\cos 2\phi_k, \qquad \partial_k^2 n_x|_{\phi^*=\phi} = -2\sin 2\phi_k, \quad \text{(B17)}$$

$$\partial_k^2 n_s|_{\phi^*=\phi} = 2\cos 2\phi_k, \quad \text{(B18)}$$

$$\partial_k^2 x_c|_{\phi^*=\phi} = -A/2(\cos(2\phi_k + \varphi_0) + \cos\varphi_0), \quad \text{(B19)}$$

$$\partial_k^2 x_s|_{\phi^*=\phi} = -A/2(\sin(2\phi_k + \varphi_0) - \sin\varphi_0). \quad \text{(B20)}$$

The consequence is an additional term D_{kl} to the second order derivative of the statistic $\partial_{kl}^2 \ell|_{\phi^*=\phi} = X_{kl} + D_{kl}$. With a direct calculation, we obtain its exact expression (no approximation needed):

$$D_{kl} = \frac{A^2}{2}(-1 + \hat{c}_k)\delta_{kl}. \quad \text{(B21)}$$

where the Kronecker symbol is $\delta_{kl} = 0$ for $k \neq l$ and 1 for $k = l$.

3. Approximated distance

From Eqs. (B16) and (B21), and assuming that $|\epsilon|, |\delta| \ll 1$, we have $\ell(s; \phi) \approx A^2 N/4$. The distance defined in Eq. (13) can thus be written as

$$\mathcal{L}(\phi, \phi^*) \approx \frac{1}{N}\sum_{k=0}^{N-1}(1 - \hat{c}_k)\Delta_k^2 - \left(\frac{1}{N}\sum_{k=0}^{N-1}(1 + \hat{c}_k)\Delta_k\right)^2 - \left(\frac{1}{N}\sum_{k=0}^{N-1}\hat{s}_k\Delta_k\right)^2. \quad \text{(B22)}$$

Considering that Δ_k and Δ_k^2 are slowly varying with respect to $\hat{c}_k$ and $\hat{s}_k$, we argue that, similarly to what is discussed in Appendix D, the positive and negative terms compensate when making the following sums $\sum_k \hat{c}_k \Delta_k$, $\sum_k \hat{s}_k \Delta_k$ and $\sum_k \hat{c}_k \Delta_k^2$. We neglect the small residual, which leads to the final approximation of the distance in Eq. (14).

APPENDIX C: CONSTRAINED MAXIMIZATION OF THE DISTANCE

We rewrite the constrained maximization problem described in Sec. IV C 3 of the distance in Eq. (14) under the constraint in Eq. (27) with simpler notations. We relate them to the initial problem at the end of this appendix.

Let $\{r_k\}$ a series of N real numbers. We want to maximize the empirical variance $V(r)$ expressed by

$$V(r) = \frac{1}{N}\sum_{k=0}^{N-1} r_k^2 - \left(\frac{1}{N}\sum_{k=0}^{N-1} r_k\right)^2, \quad \text{(C1)}$$

under the constraint that the increments $u_k \equiv r_k - r_{k-1}$ are

absolutely bounded by some constant $U > 0$ i.e., $|u_k| \leq U$ for $k > 0$.

The empirical variance $V(r)$ is invariant by the addition of an arbitrary constant C: let $r_k = y_k + C$, for all k, then $V(r) = V(y)$. We can thus assume with no loss of generality that $r_0 = 0$ (i.e., choose $C = -y_0$). Therefore, we have $r_k = \sum_{j=1}^{k} u_j$ for $k > 0$.

We want to maximize the convex function V in the set of feasible solution described by $\{r_k\}$ which is a polyhedron of $\mathbb{R}^N$. From a classical theorem of convex analysis (see [31], p. 187), we conclude that V reaches its maximum at one of the extreme points of this polyhedron. The extreme points are the points where the increments are either $u_k = +U$ or $u_k = -U$. There are 2^{N-1} extreme points and we need to identify the one which maximizes the convex function.

Let us rewrite the empirical variance $V(r)$ as a function of u_k. We leave the "autoterms" u_k^2 aside (for all extreme points, the autoterms are equal to U^2 independently of the sign of u_k. Their contribution is thus unimportant for the identification of the maximum) and concentrate on "cross terms" (i.e., terms in $u_j u_k$). A direct calculation leads to

$$V(r) = V_a + \sum_{j=1}^{N-2} \sum_{k=j+1}^{N-1} c_{jk} u_j u_k, \tag{C2}$$

where $c_{jk} = 2j(N-k)/N^2$ and V_a is the contribution due to the autoterms.

Since all $c_{jk} > 0$, the maximum of V is reached when all u_k have the same signs, that is when u_k are all identically $+U$ or $-U$. Therefore, the empirical variance is maximum when $r_k = \pm kU$ and in this case $V(r) = U^2(N^2-1)/12$.

We recall that the distance between the smooth chirps is well approximated by the empirical variance of the phase discrepancy [see Eq. (14)]. We apply this result to the original maximization problem by setting $r_k \triangleq \Delta_k$ and $U \triangleq 2\pi\Delta_f t_s$ as given in Eq. (27).

APPENDIX D: BOUNDING δ AND ϵ OF A CC

The simplification of the statistic in Sec. V B is closely related to the orthogonality and length difference of the vectors $\mathbf{c} \equiv \{\cos\phi_k, k = 0, \cdots, N-1\}$ and $\mathbf{s} \equiv \{\sin\phi_k, k = 0, \cdots, N-1\}$ of $\mathbb{R}^N$.

Noting that their norms and scalar-product are, respectively, given by $n_c = \langle \mathbf{c}, \mathbf{c} \rangle$, $n_s = \langle \mathbf{s}, \mathbf{s} \rangle$ and $n_x = \langle \mathbf{c}, \mathbf{s} \rangle$ as defined in Eq. (7), the departure from "orthonormality" of $\mathbf{c}$ and $\mathbf{s}$ can be quantified by the two parameters

$$\delta = \frac{n_c - n_s}{n_c + n_s} \qquad \epsilon = \frac{2n_x}{n_c + n_s}. \tag{D1}$$

The parameter δ measures the relative difference of the lengths of $\mathbf{c}$ and $\mathbf{s}$ while ϵ is related to the cosine of the angle between the two vectors.

When the vectors $\mathbf{c}$ and $\mathbf{s}$ are orthonormal i.e., orthogonal and of same lengths, both δ and ϵ are zero. By continuity, for nearly orthonormal vectors, δ and ϵ are then expected to be small. Intuitively, this should be true for vectors with oscillating components like $\mathbf{c}$ and $\mathbf{s}$. Indeed, ϵ and δ can be rewritten in the form of oscillating sums, namely

$$\delta = \frac{1}{N} \sum_{k=0}^{N-1} \cos 2\phi_k \qquad \epsilon = \frac{1}{N} \sum_{k=0}^{N-1} \sin 2\phi_k. \tag{D2}$$

The positive and negative contributions cancel in the summation, and thus leaves a small residual. In this appendix, we go beyond this intuitive rationale when the phase ϕ is a CC as defined in Eq. (11) and give a systematic investigation of the maximum value taken by δ and ϵ.

Equation (D2) motivates us to combine δ and ϵ is the following complex sum S

$$S \equiv \delta + i\epsilon = \frac{1}{N} \sum_{k=0}^{N-1} \exp i2\phi_k. \tag{D3}$$

Bounding the modulus of S is equivalent to bounding δ and ϵ. Analytic number theory provides a large number of results concerning exponential sums like S, for improving upon the trivial bound $|S| \leq 1$. We use one of these, namely, the Kuzmin-Landau lemma, see [32] p. 7. We present a proof of this lemma pertaining to the present case where the phase ϕ is a CC.

The proof can be summarized as follows. A change of variables is introduced which allows us to put a bound on the modulus of S by a sum of the finite difference of complex variables. These new variables appear to be collinear in the complex plane. The sum of the modulus of their difference is thus equal to the distance between the extremes. The final bound on $|S|$ is then obtained by combining this property with the explicit expression of the phase of the CC, provided a constraint on the lower and higher frequencies reached by the CC.

Let us define for $1 \leq k \leq N-1$, the following variables

$$d_k \equiv 2(\phi_k - \phi_{k-1}) \qquad \zeta_k \equiv \frac{1}{1 - \exp(id_k)}. \tag{D4}$$

We perform the above change of variables in the sum S using the relation

$$\exp(i2\phi_k) = [\exp(i2\phi_k) - \exp(i2\phi_{k+1})]\zeta_{k+1}, \tag{D5}$$

and we get

$$NS = \zeta_1 \exp(i2\phi_0) + \sum_{k=1}^{N-2} (\zeta_{k+1} - \zeta_k) \exp(i2\phi_k) + (1 - \zeta_{N-1}) \exp(i2\phi_{N-1}). \tag{D6}$$

By taking the modulus on both side, we obtain the following bound,

$$N|S| \leq |\zeta_1| + |1 - \zeta_{N-1}| + \sum_{j=0}^{Nt-1} \sum_{k=jb+1}^{(j+1)b-1} |\zeta_{k+1} - \zeta_k| + \sum_{j=1}^{N_t-2} |\zeta_{jb+1} - \zeta_{jb}|. \tag{D7}$$

where we split the sum in Eq. (D6) into smaller ones calculated over chirplet intervals i.e., $t_j \leq t_s k < t_{j+1}$ or equivalently $jb \leq k \leq (j+1)b - 1$ with $b = \delta_t/t_s$, the number of samples in a chirplet interval. In the last sum, we separate the terms corresponding to the transition between two consecutive chirplets.

We now obtain a bound on each term of the RHS of Eq. (D7), starting with the first sum. Equation (D4) can be rewritten as

$$\zeta_k = \frac{1}{2}[1 + i\cot(d_k/2)]. \tag{D8}$$

The variables ζ_k are all located on the line $\Re(\zeta) = 1/2$.

Within a chirplet interval, i.e. if $t_j \leq kt_s < t_{j+1}$, the phase difference is a linear function of k given by

$$d_k = 2\pi t_s[(2-r)f_{m_j} + rf_{m_{j+1}}], \tag{D9}$$

where $r = (2t_{j,k} - t_s)/\delta_t$.

We assume that the node frequencies of the CC are constrained in the following bandwidth:

$$f_l \leq f_{m_j} \leq f_s/2 - f_l, \tag{D10}$$

where $f_l = f_s c/2$ and $0 < c < 1/2$. In other words, the CC cannot approach arbitrarily close to neither DC nor the Nyquist frequency.

Since $0 < r < 2$, we have $4\pi t_s f_{m_j} \leq d_k \leq 4\pi t_s f_{m_{j+1}}$ if $f_{m_j} \leq f_{m_{j+1}}$ (and the opposite in the other case) which implies that

$$0 < 2\pi c \leq d_k \leq 2\pi(1-c) < 2\pi, \tag{D11}$$

for all k, hence $-\infty < \Im(\zeta_k) < +\infty$.

If $f_{m_j} \leq f_{m_{j+1}}$ (resp. $f_{m_j} \geq f_{m_{j+1}}$), the phase difference d_k and hence $\Im(\zeta_k)$, increases (resp. decreases) monotonically with k.

Since their imaginary parts are finite and monotonic, the variables ζ_k are associated to consecutive points on the line $\Re(\zeta) = 1/2$ of the complex plane. The sum of the lengths of the segments linking two nearby points is equal to the length between the extremes, thus

$$\sum_{k=jb+1}^{(j+1)b-1} |\zeta_{k+1} - \zeta_k| = |\zeta_{(j+1)b} - \zeta_{jb+1}|. \tag{D12}$$

Applying the mean value theorem to the function $g(x) = \cot(x/2)/2$, whose derivative is $\dot{g}(x) = 1/(4\sin^2(x/2))$ and using the constraint in Eq. (D11), we obtain the following bound

$$|\zeta_{(j+1)b} - \zeta_{jb+1}| \leq \frac{|d_{(j+1)b} - d_{jb+1}|}{4\sin^2(\pi c)}. \tag{D13}$$

We carry on by bounding the numerator

$$|d_{(j+1)b} - d_{jb+1}| = 4\pi t_s |f_{m_{j+1}} - f_{m_j}| \leq 4\pi N_r'/N, \tag{D14}$$

and denominator with $2c \leq \sin(\pi c)$ (this is valid for $0 \leq c \leq 1/2$) and by summing over all j to finally obtain the bound on first summation term in Eq. (D7),

$$\sum_{j=0}^{N_t-1} \sum_{k=jb}^{(j+1)b-1} |\zeta_{k+1} - \zeta_k| \leq \frac{\pi N_r' N_t}{4Nc^2}. \tag{D15}$$

The second summation coming from the boundary points of the chirplet intervals can be bounded in a similar way, considering that

$$|\zeta_{jb+1} - \zeta_{jb}| \leq \frac{|d_{jb+1} - d_{jb}|}{4\sin^2(\pi c)}, \tag{D16}$$

and combining with

$$|d_{jb+1} - d_{jb}| = 2\pi t_s^2 |f_{m_{j+1}} - f_{m_{j-1}}|/\delta_t \leq \frac{4\pi t_s N_r'}{N\delta_t}, \tag{D17}$$

we get the result

$$\sum_{j=1}^{N_t-2} |\zeta_{jb+1} - \zeta_{jb}| \leq \frac{\pi t_s N_r' N_t}{4Nc^2\delta_t}. \tag{D18}$$

Finally, from Eq. (D8), we have the following inequalities

$$|\zeta_k| = \frac{1}{2|\sin(d_k/2)|} \leq \frac{1}{2\sin(\pi c)} \leq \frac{1}{4c}, \tag{D19}$$

which, when applied with $k = 1$ and $k = N-1$, set an upper limit to the remaining terms in the RHS of Eq. (D7), noting that $|1 - \zeta_{N-1}| = |\zeta_{N-1}|$.

Combining this result with Eqs. (D15) and (D18), we get

$$|S| \leq \frac{1}{2Nc} + \frac{\pi N_r' N_t}{4c^2 N^2}(1 + 1/b). \tag{D20}$$

The number of samples in a chirplet interval being an integer $b \geq 1$, and selecting the dominating contribution, we conclude that $|S| \leq \eta$ with

$$\eta = \frac{\pi N_r' N_t}{2c^2 N^2}. \tag{D21}$$

This bound is obtained from a worst case estimate. Generally, δ and ϵ are smaller than this value. With the choice of a small c, a more realistic estimate rather than a strict bound can be obtained replacing the inequality $2c \leq \sin(\pi c)$ by the first order Taylor approximation $\pi c \sim$

$\sin(\pi c)$ in the proof above, yielding the following estimate

$$\eta = \frac{N_r' N_t}{\pi c^2 N^2}. \tag{D22}$$

Summarizing, we obtained an upper bound η on $|S|$ by restricting the frequency of the CC in a bandwidth defined by c. We rather use the reciprocal i.e., we get the limits of the frequency bandwidth from an acceptable value for η. If we assume that $N_r' \approx 4(N'/N_t)(N_f/(2N))$ as given by the regularity condition, the frequency bandwidth is $[f_l, f_s/2 - f_l]$ with

$$f_l = \frac{f_s c}{2} \approx 2.5\sqrt{N'}\delta_f \left(\frac{N_f}{N}\right)^{3/2} \left(\frac{0.1}{\eta}\right)^{1/2}, \tag{D23}$$

where the leading constant is obtained from $\sqrt{20/\pi} \approx 2.5$. We use this result in Sec. V B 1.

[1] (GEO600), www.geo600.uni-hannover.de; (LIGO), http://www.ligo.org; (Virgo), http://www.virgo.infn.it; (TAMA), http://tamago.mtk.nao.ac.jp.
[2] L. Blanchet, Living Rev. Relativity **5**, 3 (2002).
[3] K. D. Kokkotas and B. Schmidt, Living Rev. Relativity **2**, 2 (1999).
[4] B. Schutz, gr-qc/0410121.
[5] E. E. Flanagan and S. A. Hughes, Phys. Rev. D **57**, 4535 (1998).
[6] M. H. P. M. van Putten *et al.*, Phys. Rev. D **69**, 044007 (2004).
[7] V. Ferrari, G. Miniutti, and J. A. Pons, Classical Quantum Gravity **20**, S841 (2003).
[8] N. Arnaud *et al.*, Phys. Rev. D **67**, 062004 (2003).
[9] T. Pradier *et al.*, Phys. Rev. D **63**, 042002 (2001).
[10] E. Chassande-Mottin, Phys. Rev. D **67**, 102001 (2003).
[11] A. Vicerè, Phys. Rev. D **66**, 062002 (2002).
[12] W. Anderson, P. Brady, J. Creighton, and E. Flanagan, Phys. Rev. D **63**, 042003 (2001).
[13] W. Anderson and R. Balasubramanian, Phys. Rev. D **60**, 102001 (1999).
[14] J. Sylvestre, Phys. Rev. D **66**, 102004 (2002).
[15] S. Kay, *Fundamentals of Statistical Signal Processing: Detection theory* (Prentice Hall, Englewood Cliffs, NJ, 1998).
[16] B. J. Owen and B. S. Sathyaprakash, Phys. Rev. D **60**, 022002 (1999),.
[17] B. S. Sathyaprakash and S. V. Dhurandhar, Phys. Rev. D **44**, 3819 (1991).
[18] B. J. Owen, Phys. Rev. D **53**, 6749 (1996).
[19] I. S. Gradshteyn and I. M. Ryzhik, *Tables of Integrals, Series and Products* (Academic Press, New York, 1980).
[20] E. Arias-Castro, D. Donoho, and X. Huo, IEEE Trans. Inf. Theory **51**, 2402 (2005).
[21] E. Chassande-Mottin and A. Pai, IEEE Signal Process. Lett. **12**, 508 (2005).
[22] P. Flandrin, *Time-frequency/Time-scale Analysis* (Academic Press, New York, 1999).
[23] D. P. Bertsekas, *Dynamic Programming and Optimal Control* (Athena Scientific, Belmont, MA, 2000), 2nd ed., Vol. 1.
[24] LSC Algorithm Library, http://www.lsc-group.phys.uwm.edu/daswg/projects/lal.html.
[25] E. Chassande-Mottin and P. Flandrin, Applied and Computational Harmonic Analysis **6**, 252 (1999).
[26] M. Morvidone and B. Torrésani, International Journal on Wavelet and Multiresolution Information Processing **1**, 19 (2003).
[27] B. Krishnan, A. Sintes, M. A. Papa, B. F. Schutz, S. Frasca, and C. Palomba, Phys. Rev. D **70**, 082001 (2004).
[28] P. Brady and T. Creighton, Phys. Rev. D **61**, 082001 (2000).
[29] N. L. Johnson and S. Kotz, *Distribution in Statistics–Continuous Univariate Distributions* (John Wiley & Sons, New York, 1970).
[30] R. Balasubramanian, B. S. Sathyaprakash, and S. V. Dhurandhar, Phys. Rev. D **53**, 3033 (1996).
[31] D. P. Bertsekas, A. Nedić, and A. E. Ozdaglar, *Convex Analysis and Optimization* (Athena Scientific, Belmont, MA, 2003).
[32] S. W. Graham and G. Kolesnik, *Van der Corput's Method of Exponential Sums* (Cambridge Univ. Press, Cambridge, 1991).

Best network chirplet chain: Near-optimal coherent detection of unmodeled gravitational wave chirps with a network of detectors

Archana Pai*

Max-Planck Institut für Gravitationsphysik, Am Mühlenberg 1, 14476 Potsdam, Germany

Éric Chassande-Mottin†

CNRS, AstroParticule et Cosmologie, 10, rue Alice Domon et Léonie Duquet, 75205 Paris Cedex 13, France and Observatoire de la Côte d'Azur, Bd de l'Observatoire, BP 4229, 06304 Nice, France

Olivier Rabaste‡

CNRS, AstroParticule et Cosmologie, 10, rue Alice Domon et Léonie Duquet, 75205 Paris Cedex 13, France

(Received 29 August 2007; published 18 March 2008)

The searches of impulsive gravitational waves (GW) in the data of the ground-based interferometers focus essentially on two types of waveforms: short unmodeled bursts from supernova core collapses and frequency modulated signals (or chirps) from inspiralling compact binaries. There is room for other types of searches based on different models. Our objective is to fill this gap. More specifically, we are interested in GW chirps "in general," i.e., with an arbitrary phase/frequency vs time evolution. These unmodeled GW chirps may be considered as the generic signature of orbiting or spinning sources. We expect the quasiperiodic nature of the waveform to be preserved independently of the physics which governs the source motion. Several methods have been introduced to address the detection of unmodeled chirps using the data of a single detector. Those include the best chirplet chain (BCC) algorithm introduced by the authors. In the next years, several detectors will be in operation. Improvements can be expected from the joint observation of a GW by multiple detectors and the coherent analysis of their data, namely, a larger sight horizon and the more accurate estimation of the source location and the wave polarization angles. Here, we present an extension of the BCC search to the multiple detector case. This work is based on the coherent analysis scheme proposed in the detection of inspiralling binary chirps. We revisit the derivation of the optimal statistic with a new formalism which allows the adaptation to the detection of unmodeled chirps. The method amounts to searching for salient paths in the combined time-frequency representation of two *synthetic streams*. The latter are time series which combine the data from each detector linearly in such a way that all the GW signatures received are added constructively. We give a proof of principle for the full-sky blind search in a simplified situation which shows that the joint estimation of the source sky location and chirp frequency is possible.

DOI: 10.1103/PhysRevD.77.062005 PACS numbers: 04.80.Nn, 07.05.Kf, 95.55.Ym

I. SUMMARY

A large effort is underway to analyze the scientific data acquired jointly by the long-baseline interferometric gravitational wave (GW) detectors GEO 600, LIGO, TAMA, and Virgo [1]. In this paper, we contribute to the methodologies employed for this analysis, and, in particular, for the detection of impulsive GW signals.

The current GW data analysis effort is targeted on two types of impulsive GWs. A first target is poorly known short bursts of GWs with a duration in the hundredth of a millisecond range. The astrophysically known sources of such GW bursts are supernovae core collapses (or other similar cataclysmic phenomenon). The second target is frequency modulated signals or *chirps* radiated by inspiralling binaries of compact objects (either neutron stars (NS) or black holes (BH)). These chirp waveforms are well modeled and expected to last for a few seconds to a few minutes in the detector bandwidth. Our objective is to enlarge the signal range of impulsive GWs under consideration and to "fill the gap" between these two types. More specifically, we are interested in the detection of unmodeled GW chirps which last from a few tens of milliseconds to a few seconds in the detector bandwidth. We shall detail in the next section the astrophysical motivation for considering this kind of GWs.

Joint analysis of the data observed by different GW detectors has obvious benefits. First and foremost, a GW detection can get confirmed or vetoed out with such a joint observation. Further, the detector response depends on the position and orientation of the source and polarization of the wave. For this reason, the joint observation by multiple detectors gives access to physical parameters such as source location and polarization. The use of multiple detectors also allows to enlarge the observational horizon and sky coverage.

Built on the top of pioneering works [2–5], several methods have been proposed and implemented to detect unmodeled GW chirps which include the signal track search (STS) [6], the chirplet track search [7], and the best chirplet chain (BCC) search proposed by the authors [8]. However, none of the above addresses the multiple detector case. This requires the designing of specific algorithms which are able to combine the information received by the different detectors.

In practice, there are two approaches adopted to carry out network analysis from many detectors: the *coincidence* and *coherent* approaches. In the coincidence approach, the data from each detector is processed independently and only coincident trigger events (in the arrival time and the parameter values) are retained. On the other hand, in the coherent approach, the network as a whole is treated as a single "sensor": the data from various detectors is analyzed jointly and combined into a single *network statistic* which is tested for detection. In the literature, it has been shown that the coherent approach performs better than the coincidence approach for GW short bursts [9] as well as GW chirps from coalescing binaries [10]. Indeed, the signal phase information is preserved with the coherent approach, whereas it is not with the coincidence approach.

Another reason for this choice is that the coincidence method is not adequate for unmodeled chirps. A large number of parameters (of the same order as the number of signal samples) is needed to characterize their frequency evolution. A coincident detection occurs when the parameter estimates obtained from the analysis of the individual detector data match. Because of the noise perturbation, the occurrence of such a coincidence is very unlikely when the number of parameters is large, unless the incoming GW has very large amplitude. In this article, we adopt the coherent method and propose the *coherent extension of the BCC algorithm*.

Coherent schemes have been already developed for the detection of inspiralling binary chirps [11,12]. Here, we revisit the work presented in [11] with a new formalism. Comments in footnotes link the results presented here with the ones of [11]. We show that the new formalism presented here helps to understand the geometry of the problem and it is simple to establish connections with earlier works.

The outline of the paper goes as follows. In Sec. II, we present and motivate our model of an arbitrary GW chirp. In Sec. III, we describe the response of the detector network to an incoming GW chirp. Further, we show that the linear component of the signal model (parameters acting as scaling factors and phase shifts, so-called extrinsic parameters) can be factorized. This factorization evidences that the signal space can be represented as the direct product of two 2-dimensional spaces i.e., the GW polarization plane and the chirp plane. This representation forms the backbone of the coherent detection scheme that follows in the subsequent section.

In Sec. IV, based on a geometrical argument, we show that the above signal representation manifests the possible degeneracy of the response. This degeneracy has been already noticed and studied at length in the context of burst detection [13–15]. We investigate this question in the specific context of chirps and obtain similar results as were presented earlier in the literature.

In Sec. V, we obtain the expression of the network statistic. Following the principles of the generalized likelihood ratio test (GLRT), the statistic is obtained by maximizing the network likelihood ratio over the set of unknown parameters. We perform this maximization in two steps. We first treat the linear part of the parametrization and show that such a maximization is nothing but a *least-square* problem over the extrinsic parameters. The solution is obtained by projecting the data onto the signal space. We further study the effect of the response degeneracy on the resulting parameter estimates.

The projection onto the signal space is a combined projection onto the GW polarization and chirp planes. The projection onto the first plane generates two *synthetic streams* which can be viewed as the output of "virtual detectors." The network statistic maximized over the extrinsic parameters can be conveniently expressed in terms of the processing of those streams. In practice, the synthetic streams linearly combine the data from each detector in such a way that the GW signature received by each detector is added constructively. With this rephrasing, the source location angles can be searched over efficiently.

Along with the projection onto the GW polarization plane, we also examine the projection onto its complement which generates *null streams*. While synthetic streams concentrate the GW contents, the so-called null streams produced this way combine the data such that the GW signal is canceled out. The null streams are useful to veto false triggers due to instrumental artifacts (which do not obey this cancellation property). The null streams we obtained here are identical to the ones presented earlier in GW burst literature [16–18].

In Sec. VI, we perform the second and final step of the maximization of the network statistic over the chirp phase function. This step is the difficult part of the problem. For the one-detector case, we have proposed an efficient method, the BCC algorithm which addresses this question. We show that this scheme can be adapted to the multiple detector case in a straightforward manner, hence we refer to this as *best network CC* (BNCC).

Finally, Sec. VII presents a proof of principle of the proposed method with a full-sky blind search in a simplified situation.

II. GENERIC GW CHIRPS

A. Motivation

Known observable GW sources e.g., stellar binary systems, accreting stellar systems or rotating stars, commonly involve either orbiting or spinning objects. It is not unrea-

*Archana.Pai@aei.mpg.de
†Eric.Chassande-Mottin@apc.univ-paris7.fr
‡Olivier.Rabaste@apc.univ-paris7.fr

sonable to assume that the similar holds true even for the unknown sources.

The GW emission is essentially powered by the source dynamics which thus determines the shape of the emitted waveform. Under linearized gravity and slow motion (i.e., the characteristic velocity is smaller than the speed of light) approximation, the quadrupole formula [19] predicts that the amplitude of the emitted GW is proportional to the second derivative of the quadrupole moment of the physical system. When the dominant part of the bulk motion follows an orbital/rotational motion, the quadrupole moment varies quasiperiodically, and so is the GW.

The more information we have about the GW signal, the better the detection of its signature in the observations. Ideally, this requires precise knowledge of the waveform, and consequently requires precise knowledge of the dynamics. This is not always possible. In general, predicting the dynamics of GW sources in the nearly relativistic regime requires a large amount of effort. This task may get further complicated if mechanisms such as magnetic couplings, mass accretion, density-pressure-entropy gradients, or anisotropic angular momentum distribution are involved.

Here, we are interested in GW sources where the motion is orbital/rotational but the astrophysical dynamics is (totally or partially) unknown. While our primary target is the unforeseen sources (this is why we remain intentionally vague on the exact nature of the sources), several identified candidates enter this category because their dynamics is still not fully characterized. These include (see [8] for more details and references) binary mergers, quasinormal modes from young hot rotating NS, spinning BH accreting from an orbiting disk. As motivated before, following the argument of quadrupole approximation, the GW signature for such sources is not completely undetermined: it is expected to be a quasiperiodic, possibly frequency modulated GW; in brief, it is *a GW chirp*. This is the basic motivation for introducing a generic GW chirp model, as described in the next section.

B. Generic GW chirp model

In this section, we describe the salient features of the generic GW chirp model used in this paper. We motivate the nature of GW polarization, the regularity of its phase, and frequency evolution.

1. Relation between the polarizations

The GW tensor (in the transverse traceless (TT) gauge), associated to the GW emitted from slow-motion, weak gravity sources are mostly due to variations of the mass moments (in contrast to current moments) and can be expanded in terms of mass multipole moments as [20]

$$h^{\mathrm{TT}}(t) \propto \sum_{l=2}^{\infty} \sum_{m=-l}^{l} (\nabla\nabla Y^{lm})^{\mathrm{STF}} \frac{d^l}{dt^l} I^{lm}(t - r/c). \quad (1)$$

Here, STF means "symmetric transverse-tracefree," Y^{lm} are the spherical harmonics, and I^{lm} are the mass multipole moments.

We consider here isolated astrophysical systems with anisotropic mass distributions (e.g., binaries, accreting systems, bar/fragmentation instabilities) orbiting/rotating about a well-defined axis.[1] It can be shown that these systems emit GW predominantly in the $l = |m| = 2$ mode. Contributions from any other mass moments are negligibly small.[2] The pure-spin tensor harmonic $(\nabla\nabla Y^{lm})^{\mathrm{STF}}$ term provides the GW polarization. For $l = |m| = 2$, we have

$$(\nabla\nabla Y^{22})^{\mathrm{STF}} \propto (1 + \cos^2\epsilon)e_+ + 2i\cos\epsilon e_\times. \quad (2)$$

The tensors e_+ and $e_\times$ form a pair of independent and linear-polarization GW tensors ($e_\times$ is rotated by $\pi/4$ with respect to e_+). The orbital inclination angle ϵ is the angle between the line of sight to the source (in Earth's frame) and the angular momentum vector (or the rotation axis) of the physical system, see Fig. 1(a). This shows that the emitted GW in the considered case carries both GW polarizations.

The GW tensor is fully described as $h^{TT}(t) = h_+(t)e_+ + h_\times(t)e_\times$. The phase shift between the two polarizations h_+ and $h_\times$ arises from the I^{lm} term which is proportional to the moment of inertia tensor for $l = |m| = 2$. The quadratic nature of the moment of the inertia tensor introduces a phase shift of $\pi/2$ between the two polarizations h_+ and $h_\times$. This leads to the chirp model below

$$h_+(t) = A\frac{1 + \cos^2\epsilon}{2}\cos(\varphi(t - t_0) + \phi_0), \quad (3a)$$

$$h_\times(t) = A\cos\epsilon\sin(\varphi(t - t_0) + \phi_0), \quad (3b)$$

with $t_0 \le t < t_0 + T$ and $h_{+,\times}(t) = 0$ outside this interval. The phase ϕ_0 is the signal phase at $t = t_0$.

Here, we assume the GW amplitude A to be constant. This is clearly an oversimplified case since we indeed expect an amplitude modulation for real GW sources. However, we wish here to keep the model simple in order to focus the discussion on the aspects related to the coherent analysis of data from multiple detectors. We postpone the study of amplitude modulated GWs to future work.

The chirp model described in Eq. (3) clearly depends upon several unknown parameters (which need to be estimated from the data) which include the amplitude A, the initial phase ϕ_0, the arrival time t_0 of the chirp, and the inclination angle ϵ. As no precise assumption on the exact nature and dynamics of the GW source is made, we consider the phase evolution function $\varphi(\cdot)$ to be an unknown parameter of the model (3) as well. Clearly, it is a more complicated parameter than the others which are simply scalars. Just like any scalar parameter can be constrained to a range of values (e.g., $A > 0$), the phase function $\varphi(\cdot)$ has to satisfy conditions to be physically realistic which we describe in the next section.

[1] This condition can be relaxed to precessing systems provided that the precession is over time scales much longer than the observational time, typically of order of seconds.

[2] Recently, numerical relativity simulations [21] demonstrated that this is a fairly robust statement in the specific context of inspiralling BH binaries. The simulations show that BH binaries emit GW dominantly with $l = |m| = 2$. However, as the mass-ratio decreases, higher multipoles get excited. A similar claim was also made in the context of quasinormal modes produced in the ring-down after the merger of two BH, on the basis of a theoretical argument, see [22], page 4538.

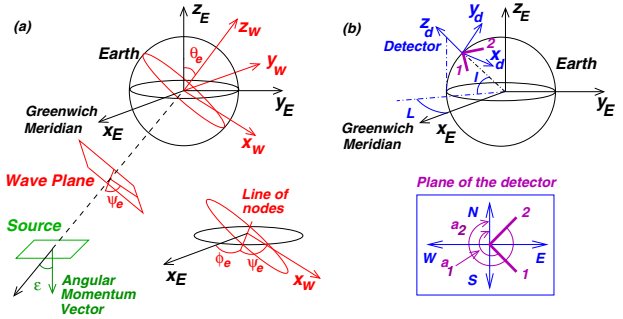

FIG. 1 (color online). *Coordinate transformations.*—(a) $\mathcal{O}(\phi_e, \theta_e, \psi_e)$: Earth frame $\mathbf{x}_E$: $(x_E, y_E, z_E) \rightarrow$ wave frame $\mathbf{x}_w$: (x_w, y_w, z_w), (b) $\mathcal{O}(\alpha, \beta, \gamma)$: Earth frame $\mathbf{x}_E$: $(x_E, y_E, z_E) \rightarrow$ detector frame $\mathbf{x}_d$: (x_d, y_d, z_d). The latitude l and longitude L of the detector are related to the Euler angles by Eqs. (8) and (9).

2. Smoothness of the phase evolution

As explained above, the chirp phase is directly related to the orbital phase of the source. The regularity of the orbital phase can be constrained by the physical arguments: the orbital phase and its derivatives are continuous. The same applies to the chirp phase and derivatives.

The detectors operate in a frequency window limited in the range from a few tenths of Hz to a kHz and they are essentially blind outside. This restricts our interest to sources emitting in this frequency range, which results in lower and upper limits on the chirp frequency $\nu(t) \equiv (2\pi)^{-1}d\varphi/dt$ and thus on the variations of the phase.

In addition, the variation of the frequency (the chirping rate) can be connected to the rate at which the source loses its energy. For isolated systems, this rate is clearly bounded. This argument motivates the following bounds on the higher-order derivatives of the phase:

$$\left|\frac{d\nu}{dt}\right| \le F', \qquad \left|\frac{d^2\nu}{dt^2}\right| \le F''. \quad (4)$$

Equation (4) determines and strengthens the smoothness of the phase/frequency evolution. This is the reason why we coined the term "smooth GW chirp" in [8]. The choice of the allowed upper bounds F' and F'' may be based on general considerations about the GW source of interest.

We give an example of how those bounds can be set in [8]. We fix F' and F'' according to the variation rate of the frequency of a typical inspiralling binary chirp at the last stable orbit. The resulting chirping rates (estimates obtained from the Newtonian model) can be viewed as a maximum for this kind of system and delimit a sensible range of values.

III. RESPONSE OF A NETWORK OF DETECTORS TO AN INCOMING GW

In this section we derive the response of a network of interferometric ground-based detectors with arbitrary locations and orientations to an incoming GW chirp. The first step is to identify the coordinate frames.

A. Coordinate frames

We follow the conventions of [11] and introduce three coordinate frames, namely, the wave frame, the Earth frame, and the detector frame as given below, see Fig. 1.

(i) the *wave* frame $\mathbf{x}_w \equiv (x_w, y_w, z_w)$ is the frame associated to the incoming GW with positive z_w-direction along the incoming direction and the $x_w - y_w$ plane corresponds to the plane of the polarization of the wave.

(ii) the *Earth* frame $\mathbf{x}_E \equiv (x_E, y_E, z_E)$ is the frame attached to the center of the Earth. The x_E axis is radially pointing outwards from the Earth's center and the equatorial point that lies on the meridian passing through Greenwich, England. The z_E axis points radially outwards from the center of Earth to the North Pole. The y_E axis is chosen to form a right-handed coordinate system with the x_E and z_E axes.

(iii) the *detector* frame $\mathbf{x}_d \equiv (x_d, y_d, z_d)$ is the frame attached to the individual detector. The $(x_d - y_d)$ plane contains the detector arms and is assumed to be tangent to the surface of the Earth. The x_d axis bisects the angle between the detector's arms. The z_d axis points towards the local zenith. The direction of the y_d axis is chosen so that we get a right-handed coordinate system.

A rotation transformation between the coordinate systems about the origin is specified by the rotation operator $\mathcal{O}$ which is characterized by three Euler angles. We define these angles using the "x-convention" (also known as $z - x - z$ convention) [23].

Let $(\phi_e, \theta_e, \psi_e)$ and (α, β, γ) be Euler angles of the rotation operator relating pairs of the above coordinate systems as follows:

$$\mathbf{x}_w = \mathcal{O}(\phi_e, \theta_e, \psi_e)\mathbf{x}_E, \tag{5}$$

$$\mathbf{x}_d = \mathcal{O}(\alpha, \beta, \gamma)\mathbf{x}_E. \tag{6}$$

All the angles in Eqs. (5) and (6) are related to physical/geometrical quantities described in Fig. 1. More specifically, we have

$$\phi_e = \phi - \pi/2, \qquad \theta_e = \pi - \theta, \qquad \psi_e = \psi, \tag{7}$$

where ϕ and θ are the spherical polar coordinates of the source in the Earth's frame and the angle ψ is the so-called polarization-ellipse angle which gives the orientation of the source plane. Throughout the paper, we shall use θ and ϕ to indicate the source location.

The detector Euler angles (α, β, γ) are directly related to the location and orientation of the detector as follows:

$$\alpha = L + \pi/2, \tag{8}$$

$$\beta = \pi/2 - l, \tag{9}$$

$$\gamma = \frac{a_1 + a_2}{2} + \frac{3\pi}{2} \quad \text{if } |a_1 - a_2| > \pi, \tag{10}$$

$$= \frac{a_1 + a_2}{2} + \frac{\pi}{2} \quad \text{if } |a_1 - a_2| \leq \pi, \tag{11}$$

where l and L are the latitude and longitude of the corner station. The angles a_1 and a_2 describe the orientation of the first and second arm, respectively. It is the angle through which one must rotate the arm clockwise (while viewing from top) to point the local north. In Table I, we tabulate the currently running interferometric detectors along with their Euler angles.

Combining Eqs. (5) and (6), we obtain the coordinate transformation from the wave frame to the detector frame as follows:

$$\mathbf{x}_s = \mathcal{O}(\phi'_e, \theta'_e, \psi'_e)\mathbf{x}_d, \tag{12}$$

where $\mathcal{O}(\phi'_e, \theta'_e, \psi'_e) \equiv \mathcal{O}(\phi_e, \theta_e, \psi_e)\mathcal{O}^{-1}(\alpha, \beta, \gamma)$.

B. Network response

The detector response to an incident GW is obtained by contracting the GW tensor with the detector tensor [see Appendix B], which can be reexpressed as a linear combination of the two polarizations h_+ and $h_\times$ i.e.

$$s = f_+ h_+ + f_\times h_\times \equiv \Re[f^* h]. \tag{13}$$

The linear coefficients $f_+(\phi'_e, \theta'_e, \psi'_e)$ and $f_\times(\phi'_e, \theta'_e, \psi'_e)$, commonly termed as the detector antenna pattern functions, represent the detector's directional response to the $+$ and $\times$ polarizations, respectively. For the compact expression provided by Eq. (13), we have defined the complex GW signal to be $h = h_+ + ih_\times$ and the complex antenna pattern function to be $f = f_+ + if_\times$.

The detector response s and the incident GW signal h are both times series. In a network where the various detectors are located at different locations on the Earth, for example, the LIGO-Virgo network, the GW arrives at the detector sites at different time instances. However, all the measurements at the various detectors need to be carried out with a reference time. Here, for our convenience, the time measured by an observer attached to the Earth's center as a reference is treated as a reference. Any other reference would be equally acceptable. We have

TABLE I. *Location and orientation of the GW detectors.*—We identify the detectors with two character label. Concerning the LIGO detectors, H1 and L1 refer to the Hanford (WA) and Livingstone (LA) detectors, respectively. The location of the corner station (vertex) of each detector is given in terms of the latitude and longitude. The longitudes with an East (respectively West) suffix receive a "+" sign (respectively "−" sign) when converted into radians in Eq. (8). The orientation of the arm is given by the angle through which one must rotate it clockwise (while viewing from top) to point the local north. The corresponding detector Euler angles (α, β, γ) are listed.

Detector	Vertex position		Arm orientation		Euler angles		
name & label	latitude (N)	longitude	a_1	a_2	α	β	γ
TAMA (T1)	35° 40′ 35.60″	139° 32′ 09.80″ E	90° 00′ 00.00″	179° 59′ 60.00″	229° 32′ 09.80″	54° 19′ 24.40″	225° 00′ 00.00″
GEO (G1)	52° 14′ 42.53″	9° 48′ 25.89″ E	291° 36′ 42.12″	25° 56′ 35.16″	99° 48′ 25.89″	37° 45′ 17.47″	68° 46′ 38.64″
Virgo (V1)	43° 37′ 53.09″	10° 30′ 16.19″ E	340° 34′ 02.03″	70° 34′ 02.03″	100° 30′ 16.19″	46° 22′ 06.91 ″	115° 34′ 02.03″
LIGO (H1)	46° 27′ 18.53″	119° 24′ 27.57″ W	35° 59′ 57.84″	125° 59′ 57.84″	−29°24′27.57″	43° 32′ 41.47″	170° 59′ 57.84″
LIGO (L1)	30° 33′ 46.42″	90° 46′ 27.27″ W	107° 42′ 59.40″	197° 42′ 59.40″	−0°46′27.27″	59° 26′ 13.58″	242° 42′ 59.40″

$$s(t) = \Re[f^* h(t - \tau(\phi, \theta))], \tag{14}$$

where $\tau(\phi, \theta) = (\mathbf{r}_d - \mathbf{r}_E) \cdot \mathbf{w}(\phi, \theta)/c$ denotes the difference in the arrival times of the GW (propagating with the unit wave vector $\mathbf{w}$) at the detector and at the center of the Earth located at $\mathbf{r}_d$ and $\mathbf{r}_E$, respectively. Note that this value can be positive or negative depending on the source location.

C. Vector formalism

In the following, we distinguish scalars by using roman letters, vectors are denoted by small bold letters, and matrices by bold capitals. We denote the k-th element of vector $\mathbf{a}$ by $a[k]$ and correspondingly, the element of matrix $\mathbf{A}$ at row k and column l by $A[k, l]$. The matrices $\mathbf{A}^T$ and $\mathbf{A}^H \equiv (\mathbf{A}^T)^*$ designate the real and Hermitian transposes of $\mathbf{A}$, respectively.

We consider now a GW detector network with d interferometers. Each detector and its associated quantities are labeled with an index $j = 1, \ldots, d$ which we also use as a subscript if required. We assume that the output response of each detector is sampled at the Nyquist rate $\nu_s \equiv 1/t_s$ where t_s is the sampling interval. We then divide the data in blocks of N consecutive samples. In this setup, the detector as well as the network response is then defined by forming vectors with these blocks of data.

Let us consider a given GW chirp source at sky location (ϕ, θ). Let the response of the j-th detector be $\mathbf{s}_j$ with entry $s_j[k] = s_j(t_k + \tau_j(\phi, \theta))$, where $t_k = t_0 + kt_s$, $k = 0, \ldots, N - 1$, and t_0 is the reference time i.e. the time of arrival of GW at the center of the Earth. Note that, with the above definition, we compensate for the time delay $\tau_j(\phi, \theta)$ between the detector j and the Earth's center. Thus, in this setup, the GW signal starts and ends in the same rows in the data vectors $\mathbf{s}_j$ of all the detectors.

For compactness, we stack the data from all the detectors in the network into a single vector $\mathbf{s}$ of size $Nd \times 1$, such that $\mathbf{s}^T = [\mathbf{s}_1^T \mathbf{s}_2^T \ldots \mathbf{s}_d^T]$ forms the *network response*. In this convention, the network response can be expressed compactly as the *Kronecker product* (see Appendix A for the definition) of the network complex beam pattern vector $\mathbf{f} = \{f_j, j = 1 \ldots d\} \in \mathbb{C}^{d \times 1}$ and the complex GW vector $\mathbf{h} = \{h(t_k), t_k = t_0 + t_s k \text{ with } k = 0 \ldots N - 1\} \in \mathbb{C}^{N \times 1}$ viz.,

$$\mathbf{s} = \Re[\mathbf{f}^* \otimes \mathbf{h}]. \tag{15}$$

The above expression is general enough to hold true for any type of incoming GW signal. The Kronecker product in this expression is the direct manifestation of the fact that the detector response is nothing but the tensor product between the detector and the wave tensors.

D. GW chirp as a linear model of the extrinsic parameters

In the previous section, we have obtained the network response to any type of incoming GW with two polarizations. In what follows, we wish to investigate how this response manifests in the case of a specific type of GW, namely, GW chirp described in Eq. (3). We also want to understand how various parameters explicitly appear in the network response.

It is insightful to distinguish the signal parameters based on their effect on the signal model. The parameters are separated into two distinct types traditionally referred to as the "*intrinsic*" and "*extrinsic*" parameters. The extrinsic parameters are those that introduce scaling factors or phase shifts but do not affect the shape of the signal model. Instead, intrinsic parameters significantly alter the shape of the signal and hence the underlying geometry.

The network response $\mathbf{s}$ mingles these two types of parameters. Our work is considerably simplified if we can "factorize" the extrinsic parameters from the rest. For the chirp model described in Eq. (3), we count four extrinsic parameters, namely $\{A, \phi_0, \boldsymbol{\epsilon}, \psi_e\}$ and perform this factorization in two steps.

1. Extended antenna pattern includes the inclination angle

We absorb the inclination angle $\boldsymbol{\epsilon}$ into the antenna pattern functions and rewrite the network signal as

$$\mathbf{s} = \Re[\tilde{\mathbf{f}}^* \otimes \tilde{\mathbf{h}}], \tag{16}$$

where $\tilde{\mathbf{h}} \equiv a\mathbf{e}$ is the GW vector. It only depends on the complex amplitude $a = A \exp i\phi_0$ and on the phase vector $\mathbf{e} = \{\exp(i\varphi[k]), \text{ with } \varphi[k] \equiv \varphi(kt_s), k = 0 \ldots N - 1\}$.

The *extended* antenna pattern $\tilde{\mathbf{f}}$ incorporates the inclination angle $\boldsymbol{\epsilon}$ as follows[3]

$$\tilde{\mathbf{f}} = \frac{1 + \cos^2 \boldsymbol{\epsilon}}{2} \mathbf{f}_+ + i \cos \boldsymbol{\epsilon} \mathbf{f}_\times. \tag{17}$$

2. Gel'fand functions factorize the polarization angles from source location angles

The second step is to separate the dependency of $\tilde{\mathbf{f}}$ on the polarization angles $\{\psi, \boldsymbol{\epsilon}\}$ from the source location angle and the detector orientation angles. The earlier work [11] shows that the Gel'fand functions (which are a representation of the rotation group $SO(3)$) provide an efficient tool to do the same. For the sake of completeness, Appendix B reproduces some of the calculations of [11]. The final result (see also Eqs. (3.14–3.16) of [11]) yields the following decomposition:

$$\tilde{\mathbf{f}} = t_+ \mathbf{d} + t_- \mathbf{d}^*, \tag{18}$$

where the vector $\mathbf{d} \in \mathbb{C}^{d \times 1}$ carries the information of the source location angles (ϕ, θ) via (ϕ_e, θ_e) and the detector Euler angles $\{\alpha_j, \beta_j, \gamma_j\}$. Its components are expressed as

[3]We remind the reader that a similar quantity was previously introduced in Eq. (3.19) of [11].

$$d[j] = -\sum_{n=-2}^{n=2} iT_{2n}(\phi_e, \theta_e, 0) \times [T_{2n}(\alpha_j, \beta_j \gamma_j) - T_{-2n}(\alpha_j, \beta_j, \gamma_j)]^*. \quad (19)$$

The tensor T_{mn} designates rank-2 Gel'fand functions. The coefficients t_+ and t_- depend only on the polarization angles $\{\psi, \epsilon\}$, viz.

$$t_\pm = T_{2\pm2}(\psi, \epsilon, 0) = \frac{(1 \pm \cos\epsilon)^2}{4} \exp(\mp 2i\psi). \quad (20)$$

Finally, we combine Eqs. (16) and (18) and obtain an expression of the network response where the extrinsic parameters are "factorized" as follows:

$$\mathbf{s} = \underbrace{\left([\mathbf{d} \quad \mathbf{d}^*]\right)}_{\mathbf{D}} \otimes \underbrace{\frac{1}{2}[\mathbf{e} \quad \mathbf{e}^*]}_{\mathbf{E}} \underbrace{\begin{pmatrix} at_-^* \\ a^* t_+ \\ at_+^* \\ a^* t_- \end{pmatrix}}_{\mathbf{p}} \equiv \mathbf{\Pi p}. \quad (21)$$

Equation (21) evidences the underlying linearity of the GW model with respect to the extrinsic parameters. The 4-dimensional complex vector $\mathbf{p}$ defines a one-to-one (nonlinear) mapping between its components and the four physical extrinsic parameters $\{A, \phi_0, \epsilon, \psi\}$ (we will detail this point later in Sec. V A 3). Note that the first and fourth components as well as the second and third components of $\mathbf{p}$ are complex conjugates. This symmetry comes from the fact that the data is real.

The *signal space* as defined by the network response is the range of $\mathbf{\Pi}$ and results from the Kronecker product of two linear spaces: the plane of $\mathbb{C}^d$ generated by the columns of $\mathbf{D}$ which we shall refer to as *GW polarization plane*[4] and the plane of $\mathbb{C}^N$ generated by the columns of $\mathbf{E}$ which we shall refer to as *chirp plane*. These two spaces embody two fundamental characteristics of the signal: the former characterizes gravitational waves while the latter characterizes chirping signals. The Kronecker product in the expression of $\mathbf{\Pi}$ shows explicitly that the network response is the result of the *projection* of incoming GW onto the detector network.

The norm of the network signal gives the "signal" (and not physical) energy delivered to the network, which is

$$\| \mathbf{s} \|^2 = \frac{NA^2}{2} \| \tilde{\mathbf{f}} \|^2 . \quad (22)$$

Clearly, the dependence on the number of samples N implies that the longer the signal duration, the larger the signal energy and is proportional to the length of the signal duration. The factor $\| \tilde{\mathbf{f}} \|$ is the modulus of the extended antenna pattern vector. It can be interpreted as the gain or attenuation depending on the direction of the source and on the polarization of the wave.

[4]In [11], this plane was referred to as "helicity plane" because it is formed by the network beam patterns for all possible polarizations.

IV. INTERPRETATION OF THE NETWORK RESPONSE

In this section, we focus on understanding the underlying geometry of the signal model described in Eq. (21). A useful tool to do so is the singular value decomposition (SVD) [24]. It provides an insight on the geometry by identifying the principal directions of linear transforms.

A. Principal directions of the signal space: Singular value decomposition

The SVD is a generalization of the eigen-decomposition for nonsquare matrices. The SVD factorizes a matrix $\mathbf{A} \in \mathbb{C}^{m\times n}$ into a product $\mathbf{A} = \mathbf{U}_A \mathbf{\Sigma}_A \mathbf{V}_A^H$ of three matrices $\mathbf{U}_A \in \mathbb{C}^{m\times r}$, $\mathbf{\Sigma}_A \in \mathbb{R}^{r\times r}$, and $\mathbf{V}_A \in \mathbb{C}^{n\times r}$ where $r \leq m, n$ is the rank of $\mathbf{A}$. The columns of $\mathbf{U}_A$ and $\mathbf{V}_A$ are orthonormal i.e., $\mathbf{U}_A^H \mathbf{U}_A = \mathbf{V}_A^H \mathbf{V}_A = \mathbf{I}_r$. The diagonal of $\mathbf{\Sigma}_A$ are the singular values (SV) of $\mathbf{A}$. We use here the so-called "compact" SVD (we retain the nonzero SV only in the decomposition), such that the matrix $\mathbf{\Sigma}_A$ is a positive definite diagonal matrix.

The SVD is compatible with the Kronecker product [25]: the SVD of a Kronecker product is the Kronecker product of the SVDs. Applying this property to $\mathbf{\Pi}$, we get

$$\mathbf{\Pi} = (\mathbf{U}_D \otimes \mathbf{U}_E)(\mathbf{\Sigma}_D \otimes \mathbf{\Sigma}_E)(\mathbf{V}_D \otimes \mathbf{V}_E)^H. \quad (23)$$

Therefore, the SVD of $\mathbf{\Pi}$ can be easily deduced from the one of $\mathbf{D}$ and $\mathbf{E}$. We note that $\mathbf{D}$ and $\mathbf{E}$ have similar structure (two complex conjugated columns), see Eq. (21). In Appendix C, we analytically obtain the SVD of a matrix with such a structure. Thus, applying this result, we can straightaway write down the SVDs for $\mathbf{D}$ and $\mathbf{E}$ as shown in the following sections.

1. GW polarization plane: SVD of D

Let us first introduce some variables

$$\mathcal{D} \equiv \mathbf{d}^H \mathbf{d} = \sum_{j=1}^{d} |d[j]|^2, \quad (24)$$

$$\Delta \equiv \mathbf{d}^T \mathbf{d} = \sum_{j=1}^{d} d[j]^2, \quad (25)$$

$$\delta \equiv \arg\Delta. \quad (26)$$

In the nominal case, the matrix $\mathbf{D}$ has rank 2, viz.

$$\mathbf{\Sigma}_D = \begin{bmatrix} \sigma_1 & 0 \\ 0 & \sigma_2 \end{bmatrix}, \quad (27)$$

with two nonzero SV $\sigma_1 = \sqrt{\mathcal{D} + |\Delta|}$ and $\sigma_2 = \sqrt{\mathcal{D} - |\Delta|}$ ($\sigma_1 \geq \sigma_2$) associated to a pair of left-singular vectors $\mathbf{V}_D = [\mathbf{v}_1, \mathbf{v}_2]$ with

$$\mathbf{v}_1 = \frac{1}{\sqrt{2}} \begin{bmatrix} \exp(-i\delta) \\ 1 \end{bmatrix}, \qquad \mathbf{v}_2 = \frac{1}{\sqrt{2}} \begin{bmatrix} \exp(-i\delta) \\ -1 \end{bmatrix}, \quad (28)$$

and of right-singular vectors $\mathbf{U}_D = [\mathbf{u}_1, \mathbf{u}_2]$ with

$$\mathbf{u}_1 = \frac{\exp(-i\delta)\mathbf{d} + \mathbf{d}^*}{\sqrt{2(\mathcal{D} + |\Delta|)}}, \quad (29)$$

$$\mathbf{u}_2 = \frac{\exp(-i\delta)\mathbf{d} - \mathbf{d}^*}{\sqrt{2(\mathcal{D} - |\Delta|)}}. \quad (30)$$

Note that the vector pair $\{\mathbf{u}_1, \mathbf{u}_2\}$ results from the Gram-Schmidt orthonormalization of $\{\mathbf{d}, \mathbf{d}^*\}$.

Barring the nominal case, for a typical network built with the existing detectors and for certain sky locations of the source, it is, however, possible for the smallest SV σ_2 to vanish. In such a situation, the rank of $\mathbf{D}$ reduces to 1. We then have $\mathbf{\Sigma}_D = \sigma_1$, $\mathbf{V}_D = \mathbf{v}_1$ and $\mathbf{U}_D = \mathbf{u}_1$. We give an interpretation of this degeneracy later in Sec. IV B.

2. Chirp plane: SVD of E

The results of the previous section essentially apply to SVD calculation of $\mathbf{E}$. However, there is an additional simplification due to the nature of the columns of $\mathbf{E}$. Indeed, the cross-product

$$\mathbf{e}^T \mathbf{e} = \sum_{k=0}^{N-1} \exp(2i\varphi[k]), \quad (31)$$

is an oscillating sum. This sum can be shown [8] to be of small amplitude under mild conditions compatible with the case of interest. We can thus consider[5] that $\mathbf{e}^T \mathbf{e} \approx 0$ and $\mathbf{e}^H \mathbf{e} = N$. Therefore, following Appendix C 2, the SVD of $\mathbf{E}$ is given by $\mathbf{\Sigma}_E = \sqrt{N}\mathbf{I}_2/2$, $\mathbf{V}_E = \mathbf{I}_2$, and $\mathbf{U}_E = 2\mathbf{E}/\sqrt{N}$.

3. Signal space: SVD of Π

We obtain the SVD for $\mathbf{\Pi}$ using the compatibility of the SVD with the Kronecker product stated in Eq. (23). In the nominal case where $\mathbf{D}$ has rank 2, we have

$$\mathbf{\Sigma}_\Pi = \frac{\sqrt{N}}{2} \begin{bmatrix} \sigma_1 \mathbf{I}_2 & \mathbf{0}_2 \\ \mathbf{0}_2 & \sigma_2 \mathbf{I}_2 \end{bmatrix}, \quad (32)$$

with four left-singular vectors

$$\mathbf{V}_\Pi = [\mathbf{v}_1 \otimes \mathbf{I}_2 \quad \mathbf{v}_2 \otimes \mathbf{I}_2], \quad (33)$$

and four right-singular vectors

$$\mathbf{U}_\Pi = \frac{2}{\sqrt{N}} [\mathbf{u}_1 \otimes \mathbf{e} \quad \mathbf{u}_1 \otimes \mathbf{e}^* \quad \mathbf{u}_2 \otimes \mathbf{e} \quad \mathbf{u}_2 \otimes \mathbf{e}^*]. \quad (34)$$

[5]This amounts to saying that the two GW polarizations (i.e., the real and imaginary parts of $\exp i\varphi[k]$) are orthogonal and of equal norm. Note that this approximation is not required and can be relaxed. This would lead to use a version of the polarization pair orthonormalized with a Gram-Schmidt procedure.

B. The signal model can be ill-posed

In the previous section, we obtained the SVD of $\mathbf{\Pi}$ in the nominal case where the matrix $\mathbf{D}$ has 2 nonzero SVs. As we have already mentioned, for a typical detector network, there might exist certain sky locations where the second SV σ_2 of $\mathbf{D}$ vanishes which implies that the rank of $\mathbf{D}$ degenerates to 1. In such cases, this degeneracy propagates to $\mathbf{\Pi}$ and subsequently its rank reduces from 4 to 2.

In order to realize the consequences of this degeneracy, we first consider a network of *ideal* GW detectors (with no instrumental noise). Let a GW chirp pass through such a network from a source in a sky location where $\sigma_2 = 0$. The detector output is *exactly* equal to $\mathbf{s}$. An estimate of the source parameters would then be obtained from the network data by inverting Eq. (21). However, in this case, this is impossible since it requires the inversion of an underdetermined linear system (there are 4 unknowns and only 2 equations).

This problem is identical to the one identified and discussed at length in a series of articles devoted to unmodeled GW bursts [13–15], where this problem is formulated as follows: at those sky locations where $\mathbf{D}$ is degenerated, the GW response is essentially made of only *one* linear combination of the *two* GW polarizations. It is thus impossible to separate the two individual polarizations (unless additional prior information is provided). We want to stress here that this problem is not restricted to unmodeled GW bursts but also affects the case of chirping signals (and extends to the chirps from inspiralling binaries of NS or BH[6]). This is mainly because the degeneracy arises from the geometry of the GW polarization plane which is the same for any type of source.

The degeneracy disappears at locations where $\sigma_2 > 0$ even if it is infinitesimally small. However, when σ_2 is small, the inversion of the linear equations in Eq. (21) is very sensitive to perturbations. With *real-world* GW detectors, instrumental noise affects the detector response i.e., perturbs the left-hand side of Eq. (21).

A useful tool to investigate this is the *condition number* [15]. It is a well-known measure of the sensitivity of linear systems. The condition number of a matrix $\mathbf{A}$ is defined as the ratio of its largest SV to the smallest. For unitary matrices, $\text{cond}(\mathbf{A}) = 1$. On the contrary, if $\mathbf{A}$ is rank deficient, $\text{cond}(\mathbf{A}) \to \infty$. For the matrix $\mathbf{\Pi}$, we have

[6]Contrary to the generic chirp model considered here, the phase and amplitude functions of inspiralling binary chirps follow a prescribed power-law time evolution. These differences affect only the geometry of the "chirp plane," but not that of the "GW polarization plane," hence the conclusion on the degeneracy remains the same.

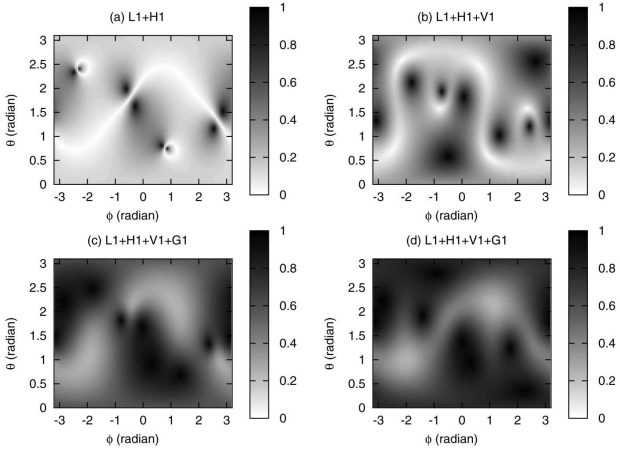

FIG. 2. *Degeneracy of the network response.*—We show here the inverse of cond($\mathbf{\Pi}$) for various detector networks (the abbreviated detector names are listed in Table I). The brighter regions of the sky correspond to the large conditioning number cond($\mathbf{\Pi}$). The fraction of the sky where $1/\text{cond}(\mathbf{\Pi}) > 0.1$ is (a) 27%, (b) 4.8%, (c) and (d) 0%. Since the LIGO detectors are almost aligned, this pair of detectors has the largest percentage of degeneracy.

$$\text{cond}\ (\mathbf{\Pi}) = \frac{\sigma_1}{\sigma_2} = \sqrt{\frac{\mathcal{D} + |\Delta|}{\mathcal{D} - |\Delta|}}. \tag{35}$$

In Fig. 2, we show full-sky plots of $1/\text{cond}(\mathbf{\Pi})$ for various configurations (these figures essentially reproduce the ones of [15]). We see that, even for networks of misaligned detectors, there are significantly large patches where cond($\mathbf{\Pi}$) takes large values. In those regions, the inversion of Eq. (21) is sensitive to the presence of noise and the estimate of the extrinsic parameters thus have a large variance.

a. Connection to the antenna pattern function—Interestingly, the SVs of $\mathbf{D}$ and $\mathbf{F} \equiv [\mathbf{f}\mathbf{f}^*]$ coincide. This can be seen from the following relationships we directly obtained from the definitions in Eqs. (17), (18), and (20)

$$\begin{bmatrix} \tilde{\mathbf{f}} & \tilde{\mathbf{f}}^* \end{bmatrix} = \mathbf{D}\begin{bmatrix} t_+ & t_-^* \\ t_- & t_+^* \end{bmatrix} = \mathbf{F}\begin{bmatrix} |t_+| & |t_-| \\ |t_-| & |t_+| \end{bmatrix}. \tag{36}$$

The matrix $\mathbf{F}$ can be obtained from $\mathbf{D}$ by a unitary transformation. Both matrices share the same singular spectrum. We can therefore write

$$\sigma_2^2 = \sum_{j=1}^{d} |f[j]|^2 - \left| \sum_{j=1}^{d} f[j] \right|^2. \tag{37}$$

When $\sigma_2 \sim 0$, we thus have $|\mathbf{f}_+ \times \mathbf{f}_\times|^2 \sim 0$ where $\mathbf{f}_+ \equiv \Re[\mathbf{f}]$ and $\mathbf{f}_\times \equiv \Im[\mathbf{f}]$ are the network antenna pattern vectors. This means that at such sky locations, the antenna pattern vectors get aligned even if the detectors in the network are misaligned. In other words, despite that the considered network is composed of misaligned detectors, it acts as a network of aligned detectors at those sky locations. (Of course, for perfectly coaligned detectors, $\mathbf{f}_+ \propto \mathbf{f}_\times$ at all sky locations.) Networks with many detectors having different orientations are less likely to be degenerate. This is confirmed in Fig. 2 where we see that the size of the degenerate sky patches reduces rapidly when the number of detector with varied orientations increases. The network formed by the four detectors L1-H1-V1-G1 (assuming they have the same noise spectrum) does not show any patches with significant degeneracy.

V. NETWORK LIKELIHOOD ANALYSIS: GW POLARIZATION PLANE AND SYNTHETIC STREAMS

Generally speaking, a signal detection problem amounts to testing the null hypothesis (H_0) (absence of signal in the data) vs the alternate hypothesis (H_1) (presence of signal in the data). Because of the presence of noise, two types of errors occur: false dismissals (decide H_0 when H_1 is present) and false alarms (decide H_1 when H_0 is present). There exist several objective criteria to determine the detection procedure (or statistic) which optimizes the occurrence of these errors. We choose the Neyman-Pearson (NP) approach which minimizes the number of false dismissals for a fixed false alarm rate. It is easily shown that for simple problems, the likelihood ratio (LR) is NP optimal. However, when the signal depends upon unknown

parameters, the NP optimal (uniformly overall allowed parameter values) statistic is not easy to obtain. Indeed for most real-world problems, it does not even exist. However, the generalized likelihood ratio test (GLRT) [26] has shown to give sensible results and hence is widely used. In the GLRT approach, the parameters are replaced by their maximum likelihood estimates. In other words, the GLRT approach uses the maximum likelihood ratio as the statistic. Here, we opt for such a solution.

As a first step, we consider the simplified situation where all detectors have independent and identical instrumental noises and this noise is white and Gaussian with unit variance. We will address the colored noise case later in Sec. V D.

In this case, the logarithm of the network likelihood ratio (LLR) is given by

$$\Lambda(\mathbf{x}) = -\parallel \mathbf{x} - \mathbf{s} \parallel^2 + \parallel \mathbf{x} \parallel^2, \tag{38}$$

where $\| \cdot \|^2$ is the Euclidean norm (here in $\mathbb{R}^{Nd}$) and we omitted an unimportant factor $1/2$. The network data vector $\mathbf{x}$ is constructed on similar lines as that of the network response $\mathbf{s}$, i.e. first, it stacks the data from all the detectors into $\mathbf{x}^T = [\mathbf{x}_1^T, \mathbf{x}_2^T, \ldots, \mathbf{x}_d^T]$ and then at each detector, the data is time-shifted to account for the delay in the arrival time $\mathbf{x}_j = \{x_j[k] = x_j(t_k + \tau_j), t_k = t_s k$ and $k = 0 \ldots N-1\}$.

A. Maximization over extrinsic parameters: scaling factors and phase shifts

Following the GLRT approach, we maximize the network LLR Λ with respect to the parameters of $\mathbf{s}$. We replace $\mathbf{s}$ by its model as given in Eq. (21) and consider at first the maximization with respect to the extrinsic parameters $\mathbf{p}$.

1. Least-square fit

The maximization of the network LLR over $\mathbf{p}$ amounts to fitting a linear signal model to the data in *least-square* (LS) sense, viz.

$$\text{minimize}\ -\Lambda(\mathbf{x}) + \parallel \mathbf{x} \parallel^2 = \parallel \mathbf{x} - \Pi\mathbf{p} \parallel^2 \text{ over } \mathbf{p}. \tag{39}$$

This LS problem is easily solved using the pseudoinverse $\mathbf{\Pi}^\#$ of $\mathbf{\Pi}$ [24]. The estimate of $\mathbf{p}$ is then given by

$$\hat{\mathbf{p}} = \mathbf{\Pi}^\# \mathbf{x}. \tag{40}$$

The pseudoinverse can be expressed using the SVD of $\mathbf{\Pi}$ as $\mathbf{\Pi}^\# = \mathbf{V}_\Pi \mathbf{\Sigma}_\Pi^{-1} \mathbf{U}_\Pi^H$ (note that $\mathbf{\Pi}^\#$ is always defined since we use the *compact* SVD restricted to nonzero SVs).

Substituting Eq. (40) in Eq. (39), we get the LS minimum to be

$$-\hat{\Lambda}(\mathbf{x}) + \parallel \mathbf{x} \parallel^2 = \parallel \mathbf{x} - \mathbf{U}_\Pi \mathbf{U}_\Pi^H \mathbf{x} \parallel^2, \tag{41}$$

where we used $\mathbf{V}_\Pi^H \mathbf{V}_\Pi = \mathbf{I}_r$. Equation (41) can be further simplified into[7]

$$\hat{\Lambda}(\mathbf{x}) = \parallel \mathbf{U}_\Pi^H \mathbf{x} \parallel^2. \tag{42}$$

It is interesting to note that the operator $\mathbf{U}_\Pi \mathbf{U}_\Pi^H$ is a (orthogonal) projection operator onto the signal space (over the range of $\mathbf{\Pi}$) i.e. $\mathbf{U}_\Pi \mathbf{U}_\Pi^H \mathbf{\Pi} = (\mathbf{\Pi}\mathbf{\Pi}^\#)\mathbf{\Pi} = \mathbf{\Pi}$.

2. Signal-to-noise ratio

The signal-to-noise ratio (SNR) measures the difficulty level for detecting a signal in the noise. In the present case, along with the amplitude and duration of the incoming GW, the network SNR also depends on the relative position, orientation of the source with respect to the network. Therefore, the SNR should incorporate all these aspects. A systematic way to define the SNR is to start from the statistic.

Let the SNR ρ of an injected GW chirp $\mathbf{s}_0 = \mathbf{\Pi}\mathbf{p}_0$ be[8]

$$\rho^2 \equiv \hat{\Lambda}(\mathbf{s}_0). \tag{43}$$

Note that in this expression, the matrix $\mathbf{\Pi}$ in the statistic and in $\mathbf{s}_0$ are the same. Using the SVD of $\mathbf{\Pi}$ and the property of the projection operator $\mathbf{U}_\Pi^H \mathbf{U}_\Pi = \mathbf{I}_r$, we get $\rho^2 = \parallel \mathbf{s}_0 \parallel^2$. The SNR is equal to the "signal energy" in the network data as defined in Eq. (22). Thus, the SNR ρ scales as $\sqrt{N}$ as expected and it depends on the source direction, polarization, and network configuration through the gain factor $\parallel \tilde{\mathbf{f}} \parallel$.[9] Figure 3 illustrates how this factor varies for the network formed by the two LIGO detectors and Virgo. Figure 3 displays the ratio ρ/ρ_{best} between the global SNR (obtained with a coherent analysis) and the largest individual SNR (obtained with the best detector of the network). The panels (a) and (b) are associated to the "worst" (minimum over all polarization angles ϵ and ψ) and "best" (maximum) cases, respectively. Ideally, when the detectors are aligned, the enhancement factor is expected to be $\sqrt{d}$ (≈ 1.73 in the present case). In the best case, the enhancement is $\gtrsim 1.7$ for more than half of the sky (94% of the sky when $\gtrsim 1.4$). In the worst case, the SNR enhancement is 1.28 at most and 8.5% of the sky gets a value $\gtrsim 1.1$.

3. From geometrical to physical parameter estimates

The components of $\mathbf{p}$ do not have a direct physical interpretation but as mentioned earlier, they are rather functions of the physical parameters. Following the above

[7] For the inspiral case, this expression is equivalent to Eq. (4.8) of [11].

[8] If the noise power is not unity, it would divide the signal energy in this expression. When we have only one detector, the SNR ρ^2 is consistent with the definition usually adopted in this case.

[9] The SNR ρ^2 is similar to b^2 defined in Eq. (3.17) of [11] in the case of inspiralling binary signal and colored noise.

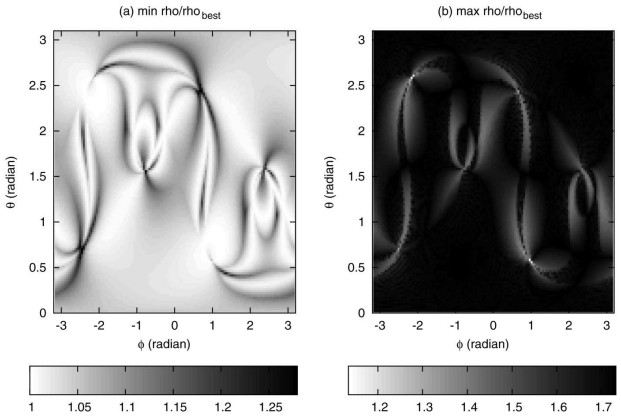

FIG. 3. *Benefits of a coherent network analysis (SNR enhancement).*—We display the polar maps of the following quantities for the L1-H1-V1 network (a) $\min_{\psi,\epsilon}\rho/\rho_{\rm best}$ and (b) $\max_{\psi,\epsilon}\rho/\rho_{\rm best}$. Here, $\rho_{\rm best}$ designates the best SNR of the detectors in the network. The maximum, minimum are taken over all the polarization angles $\{\psi, \epsilon\}$.

discussion, if we assume that we obtained parameter estimates $\hat{\mathbf{p}}$ from the data through Eq. (40), then one can retrieve the physical parameters A, ϕ_0, $\boldsymbol{\epsilon}$, and ψ by inverting the nonlinear map which links $\mathbf{p} = (at_-^* a^* t_+ at_+^* a^* t_-)^T$ to these parameters as given below

$$\hat{A} = (\sqrt{|\hat{p}[1]|} + \sqrt{|\hat{p}[2]|})^2, \tag{44}$$

$$\hat{\phi}_0 = \tfrac{1}{2}[\arg(\hat{p}[1]) - \arg(\hat{p}[2])], \tag{45}$$

$$\hat{\psi} = -\tfrac{1}{4}[\arg(\hat{p}[1]) + \arg(\hat{p}[2])], \tag{46}$$

$$\hat{\boldsymbol{\epsilon}} = \cos^{-1}\left[\frac{\sqrt{|\hat{p}[2]|} - \sqrt{|\hat{p}[1]|}}{\sqrt{|\hat{p}[2]|} + \sqrt{|\hat{p}[1]|}}\right]. \tag{47}$$

4. Degeneracy and sensitivity of the estimate to noise

Upper bounds for the estimation error can be obtained using a perturbative analysis of the LS problem in Eq. (39). A direct use of the result of [24], Sec. 5.3.8 yields

$$\frac{\| \hat{\mathbf{p}} - \mathbf{p} \|}{\| \mathbf{p} \|} \leq \frac{\sqrt{N}}{\rho} \mathrm{cond}\,(\boldsymbol{\Pi}). \tag{48}$$

This bound is a worst-case estimate obtained when the noise term which affects the data $\mathbf{x}$ is essentially concentrated along the directions associated to the smallest SV of $\boldsymbol{\Pi}$. The noise is random and it spans isotropically all Nd dimensions of the signal space. As described above, the space associated to the smallest SV has only 2 dimensions. Therefore, the worst case is very unlikely to occur and the above bound is largely overestimated on the average. However, it gives a general trend and shows that the estimation goes worst with the conditioning of $\boldsymbol{\Pi}$.

Regularization techniques seem to give promising results in the context of GW burst detection [13–15]. Following this idea, we may consider to "regularize" the LS problem in Eq. (39). To do so, additional information on the expected parameters is required to counterbalance the rank deficiency. Unfortunately, we do not expect $\mathbf{p}$ to follow a specific structure. The only sensible prior that can be assumed without reducing the generality of the search is that $\| \mathbf{p} \|$ is likely to be bound (since the GW have a limited amplitude A). It is known [27] that this type of prior is associated to the use of the so-called Tykhonov regulator and that we do not expect significant improvements upon the nonregularized solution.

One difference explains why regularization techniques do not work in the present case while it does work for burst detection. We recall that in the burst case, the parameter vector comparable to $\mathbf{p}$ are the samples of the waveform. This vector being a time series, it is expected to have some structure, in particular, it is expected to have some degree of smoothness. The use of this *a priori* information improves significantly the final estimation.

While regularization will not help for the *estimation* of the extrinsic parameters, they may be of use to improve the *detection* statistic. We consider this separate question later in Sec. VII B.

B. Implementation with synthetic streams

In the previous section, we maximize the network LLR with respect to the extrinsic parameters resulting in the statistic $\hat{\Lambda}$ in Eq. (42). Here, we obtain a more simple and practical expression for $\hat{\Lambda}$ which will be useful for maximization over the remaining intrinsic parameters.

From Eqs. (23) and (42), we have

$$\hat{\Lambda}(\mathbf{x}) = \| \, (\mathbf{U}_D \otimes \mathbf{U}_E)^H \mathbf{x} \, \|^2 \, . \tag{49}$$

It is useful to reshape the network data $\mathbf{x}$ into a $N \times d$ matrix $\mathbf{X} \equiv [\mathbf{x}_1 \mathbf{x}_2 \ldots \mathbf{x}_d]$. This operation is inverse to the *stack operator* vec() defined in Appendix A.

Using a property of the Kronecker product in Eq. (A2), we obtain the reformulation

$$\hat{\Lambda}(\mathbf{x}) = \| \, \mathrm{vec}(\mathbf{U}_E^H \mathbf{X} \mathbf{U}_D^*) \, \|^2 \, . \tag{50}$$

There are two possibilities to make this matrix product, each being associated to a different numerical implementation for the evaluation of $\hat{\Lambda}$.

We can first multiply $\mathbf{X}$ by $\mathbf{U}_E^H$ and then by $\mathbf{U}_D^*$. In practice, this means that we first compute the correlation of the data with a chirp template, then we combine the result using weights (related to the antenna pattern functions). This is the implementation proposed in [11]. It is probably the best for cases (like, searches of inspiralling binary chirps) where the number of chirp templates is large (i.e., larger than the number of source locations) and where the correlations with templates are computed once and stored.

The second choice is to first multiply $\mathbf{X}$ by $\mathbf{U}_D^*$ and then by $\mathbf{U}_E^H$ which we adopt here. This means that we first compute $\mathbf{Y} \equiv \mathbf{X}\mathbf{U}_D^*$ which transforms the network data into two N-dimensional complex data vectors $[\mathbf{y}_1, \mathbf{y}_2] \equiv \mathbf{Y}$ through an "instantaneous" linear combination. Then, we correlate these vectors with the chirp template. We can consider $\mathbf{y}_1$ and $\mathbf{y}_2$ as the output of two "virtual" detectors. For this reason, we refer to those as *synthetic streams* in connection to [28] who first coined the term for such combinations. Note that, irrespective of the number of detectors, one always gets at most two synthetic streams. We note that though the synthetic streams defined in [28] are *ad hoc* (i.e., they have no relation with the LR), the ones obtained here directly arise from the maximization of the network LLR.

We express the network LLR statistic in terms of the two synthetic streams as

$$\hat{\Lambda}(\mathbf{x}) = \frac{1}{N}(|\mathbf{e}^H \mathbf{y}_1|^2 + |\mathbf{e}^T \mathbf{y}_1|^2 + |\mathbf{e}^H \mathbf{y}_2|^2 + |\mathbf{e}^T \mathbf{y}_2|^2), \tag{51}$$

where $\mathbf{y}_l = \mathbf{X}\mathbf{u}_l^*$ for $l = 1, 2$. This expression can be further simplified by using the symmetry (easily seen from Eqs. (29) and (30)),

$$\mathbf{u}_1^* = \exp(i\delta)\mathbf{u}_1, \qquad \mathbf{u}_2^* = -\exp(i\delta)\mathbf{u}_2. \tag{52}$$

We finally obtain

$$\hat{\Lambda}(\mathbf{x}) = \frac{2}{N}(|\mathbf{e}^H \mathbf{y}_1|^2 + |\mathbf{e}^H \mathbf{y}_2|^2). \tag{53}$$

The linear combination in each stream is such that the signal contributions from each detector add up constructively. In this sense, synthetic streams are similar to beamformers used in array signal processing [29]. The GW chirp thus appears in the synthetic streams with an enhanced amplitude. The enhancement factor can be evaluated as follows. When the data is a noise free GW chirp, i.e., $\mathbf{x} = \mathbf{s}$, we then have

$$y_l[k] = \mathbf{p}^T(\mathbf{D} \otimes \mathbf{E}[k])^T \mathbf{u}_l^* = \mathbf{p}^T(\sigma_l \mathbf{v}_l^* \otimes \mathbf{E}[k]^T), \tag{54}$$

where $\mathbf{E}[k]$ represents the kth row of $\mathbf{E}$. Writing explicitly, we have

$$\mathbf{y}_1 = \frac{\sigma_1}{\sqrt{2}} \Re\{q_1 \tilde{\mathbf{h}}\} e^{i\delta/2}, \qquad \mathbf{y}_2 = \frac{i\sigma_2}{\sqrt{2}} \Im\{q_2 \tilde{\mathbf{h}}\} e^{i\delta/2}, \tag{55}$$

where we have $q_1 = t_-^* e^{i\delta/2} + t_+^* e^{-i\delta/2}$ and $q_2 = t_-^* e^{i\delta/2} - t_+^* e^{-i\delta/2}$. This shows that the synthetic streams $\mathbf{y}_l$ are rescaled and phase shifted copies of the initial GW chirp $\tilde{\mathbf{h}}$ as defined in Eq. (16).

SNR per synthetic streams

The network SNR can be split into the contributions from each synthetic stream i.e. using Eq. (43) we write $\rho^2 = \| \boldsymbol{\Sigma}_\Pi \mathbf{V}_\Pi^H \mathbf{p}_0 \|^2$, as

$$\rho^2 = \rho_1^2 + \rho_2^2, \tag{56}$$

where we define $\rho_l \equiv \sqrt{N}\sigma_l \| (\mathbf{v}_l \otimes \mathbf{I}_2)^H \mathbf{p}_0 \| /2$ for $l = 1, 2$. More explicitly, we have

$$\rho_l = \frac{\sqrt{N}}{2} \sigma_l |q_l| A. \tag{57}$$

The synthetic streams contribute differently depending on the polarization of the incoming wave. Figure 4 illustrates this with the network formed by the two LIGO detectors and Virgo.

Let us assume that $\mathbf{p}_0$ is randomly oriented. Since $\mathbf{v}_1$ and $\mathbf{v}_2$ have unit norms, we get the average value $0 < \langle \rho_2/\rho_1 \rangle_{\epsilon,\psi} \propto 1/\mathrm{cond}(\boldsymbol{\Pi}) \leq 1$ for most of the sky as indicated in Fig. 4(a). Note that this panel matches well with Fig. 2(b). Thus, on average, $\mathbf{y}_1$ contributes more to the SNR than $\mathbf{y}_2$. However, the situation may be different depending on the specific polarization state of the wave. Figure 4(b) shows the maximum of the ratio $\rho/\max_{l=1,2}\rho_l$ for all polarization angles $\boldsymbol{\epsilon}$ and ψ. For most sky locations, this quantity is $\approx \sqrt{2}$ which means that the two synthetic streams contribute equally. This holds true for all the sky locations, except at the degenerate ones where $\mathbf{y}_2$ does not contribute, hence the SNR ratio is 1. Inversely, one can

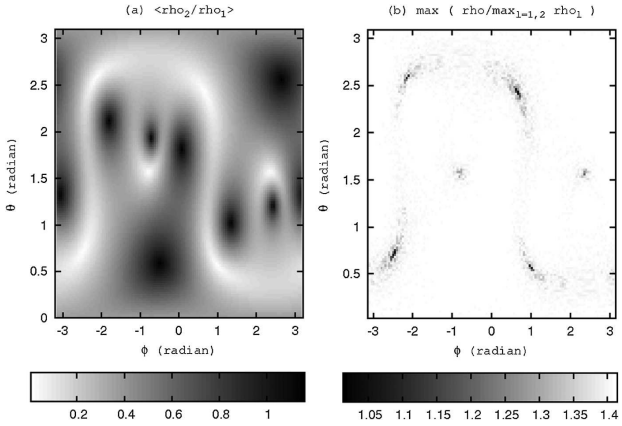

FIG. 4. *SNR per synthetic streams and benefits of a coherent network analysis (SNR enhancement).*—We display the polar maps of the following quantities for the L1-H1-V1 network: (a) $\langle \rho_2/\rho_1 \rangle_{\psi,\epsilon}$ and (b) $\max_{\psi,\epsilon}(\rho/\max_{l=1,2}\rho_l)$ where ρ_l denotes the SNR of synthetic stream $l = 1$ or 2, as defined in Eq. (57). The maximum and average are taken over all the polarization angles $\{\psi, \epsilon\}$.

always find a GW polarization such that one of the synthetic streams does not contribute to the SNR.

Another insight into this question is given by the following expression of the difference of the SNR in each synthetic stream

$$\rho_1^2 - \rho_2^2 = \frac{NA^2}{4}\left(\frac{|\Delta|}{2}\left[\left(\frac{1+\cos^2\epsilon}{2}\right)^2 + \cos^2\epsilon\right] + \frac{\| \mathbf{f}+ \|^4 - \| \mathbf{f}\times \|^4}{2|\Delta|}\frac{\sin^4\epsilon}{4}\right), \quad (58)$$

where we have[10] $|\Delta|^2 = (\| \mathbf{f}_+ \|^2 + \| \mathbf{f}_\times \|^2)^2 - 4 \| \mathbf{f}_+ \times \mathbf{f}_\times \|^2$.

For a face-on source, i.e. $\epsilon = 0$, and assuming $\mathbf{f}_\times$ is orthogonal to $\mathbf{f}_+$ with $\| \mathbf{f}_\times \| = \| \mathbf{f}_+ \|$, then both synthetic streams carry the same SNR $\rho_1 = \rho_2 = \sqrt{N/2}A \| \mathbf{f}_+ \|$.

C. Null streams

1. Review and relation to synthetic streams

The access to *noise only* data is crucial in the signal detection problem. Such data is not directly available in GW experiments, but the use of multiple detectors allows to access it indirectly using the *null streams*. The general idea behind the null stream is to construct a data stream from the individual detector streams which nullifies the signature of any incoming GW from a particular direction. Since this signal cancellation is specific to GWs, null streams naturally provide an extra tool to verify that a detected signal is indeed a GW or instead GW-like features mimicked by the detector noise whose detection thus has to be vetoed. This is a powerful check since it does not require detailed information about the potential GW signal under test, except an estimate of its source location. (Note that in practice, the implementation of the veto test may be complicated by the imprecision of the direction of arrival and of the errors of calibration [18]). The existence of null streams has been first identified in [31] in the case of three detector networks. At present, a handful of literature [17,18] exists on the use of null streams in GW data analysis.

Null streams are usually introduced as a general post-processing of the data independent of the detection of specific GWs. Below, we make this connection in the domain of our formalism. We recall that the network data at a given time (e.g., the first row of the matrix $\mathbf{X}$ introduced in Sec. V B) is a d-dimensional vector in $\mathbb{R}^d$. This space is a direct sum of the GW polarization plane and its orthogonal complementary space. We have shown that the GW polarization plane is a 2-dimensional space, spanned by a pair of orthonormal basis vectors which are associated to the two synthetic streams. The complementary space to the GW polarization plane is a $d-2$-dimensional space and it is spanned by $d-2$ "null vectors." Similar to the synthetic streams, the null streams can be constructed from these null vectors. Thus, the numbers of synthetic and null

[10]The synthetic streams (on the average sense) are also connected to the directional streams introduced in the context of LISA [30]. If we integrate ρ_l^2 over the inclination and polarization angles ϵ, ψ, we obtain $\langle(\rho_1^2 - \rho_2^2)/2\rangle_{\epsilon,\psi} = 2|\Delta|/5$ and $\langle \| \tilde{\mathbf{f}} \|^2 \rangle_{\epsilon,\psi} = 2\mathcal{D}/5$. Thus, the SNRs of the synthetic streams ρ_l^2 when averaged over the polarization angles are proportional to the SNRs obtained by v_+ and $v_\times$—the directional streams in the LISA data analysis, see Eqs. (25–28) of [30].

streams sum up to d. Nominally, we have $d-2$ null streams. However, when the GW polarization plane degenerates to a 1-dimensional space ($\sigma_2 \sim 0$) as explained in Sec. IV B, the number of null vectors becomes $d-1$. For a two detector network, in the nominal case, there is no null stream as $d-2=0$. However, for degenerate directions, one can construct a null stream. For an aligned pair of detectors (as is almost the case for the two LIGO L1 and H1), the fraction of the degenerate sky location is large, see Fig. 2. This null stream would turn out to be useful for vetoing in this case.

In the next section, we explain how the null streams can be obtained numerically in the nominal case. The extension to the degenerate case is straightforward.

2. Obtaining the null streams numerically

The numerical construction of the null streams can be achieved in various ways. One such approach could be to obtain the full SVD of $\mathbf{D}$ and construct the null streams from the eigenvectors corresponding to the zero SVs. This approach was taken in [18]. Here, we take an alternative approach. We construct the null streams by successive construction of orthonormal vectors via a multidimensional cross-product as described below.

Assuming some direction of arrival, we express any instantaneous linear combination of the time-shifted data (to compensate for different time of arrivals at the detectors' site with respect to the reference) as

$$\mathbf{y}(\mathbf{x}) \equiv \mathbf{X}\mathbf{u}, \quad (59)$$

where the vector $\mathbf{u} \in \mathbb{C}^{d\times 1}$ contains the tap coefficients.

Equation (58) can be rewritten as

$$\mathbf{y}(\mathbf{x}) = \mathrm{vec}(\mathbf{I}_N\mathbf{X}\mathbf{u}) = (\mathbf{u}^T \otimes \mathbf{I}_N)\mathbf{x}. \quad (60)$$

The vector $\mathbf{u}$ defines a null stream if $\mathbf{y}(\mathbf{x}) = \mathbf{0}_N$ whenever $\mathbf{x}$ is a GW. Let us assume that we indeed observe a GW chirp i.e., $\mathbf{x} = \mathbf{s}_0 \equiv \mathbf{\Pi}\mathbf{p}_0$. We thus have

$$\mathbf{y}(\mathbf{s}_0) = [(\mathbf{u}^T\mathbf{U}_D) \otimes \mathbf{U}_E]\mathbf{\Sigma}_\Pi \mathbf{V}_\Pi^H \mathbf{p}_0. \quad (61)$$

If $\mathbf{u}$ is in the null space of $\mathbf{U}_D$, the null-stream condition is satisfied for all $\mathbf{p}_0$. Since the null space of $\mathbf{U}_D$ is orthogonal to its range, an obvious choice for $\mathbf{u}$ is

$$\mathbf{u} = \mathbf{u}_1 \times \mathbf{u}_2 = \frac{\mathbf{d}^* \times \mathbf{d}}{\sqrt{\mathcal{D}^2 - \Delta^2}}. \quad (62)$$

Nominally, $\mathbf{U}_D$ is a 2-dimensional plane in $\mathbb{C}^d$. Its null space is therefore $d-2$ dimensional. An orthonormal basis of this space can be obtained recursively starting from $\mathbf{u}_3 = \mathbf{u}$ as defined above and applying the following generalized vector cross-product formula for $n > 3$:

$$\mathbf{u}_n[i] = \epsilon_{ijkl\ldots m}\mathbf{u}_1[j]\mathbf{u}_2[k]\mathbf{u}_3[l]\ldots\mathbf{u}_{n-1}[m]. \quad (63)$$

Here, $\epsilon_{ijkl\ldots m}$ is the Levi-Cività symbol.[11] The $\mathbf{u}_n$ denotes an orthonormal set of $d-2$ vectors, $\{\mathbf{u}_n$, for $3 \le n \le d\}$. The components of these vectors are the tap coefficients to compute the null streams. By construction, the resulting null streams are uncorrelated and have the same variance.

To summarize the main features of our formalism. The representation of a GW network response of unmodeled chirp as a Kronecker product between the GW polarization plane and the chirp plane forms the main ingredient of this formalism. Such a representation allows the signal to reveal the degeneracy in a natural manner in the network response. It also evidences the two facets of the coherent network detection problem, namely, the network signal detection via synthetic streams and vetoing via null streams. The coherent formalism developed in [11] for inspiralling binaries lacked this vetoing feature due to the difference in the signal representation.

In the rest of this paper, we do not discuss/demonstrate the null streams applied as a vetoing tool to the simulated data. This will be demonstrated in the subsequent work with the real data from the ongoing GW experiments.

D. Colored noise

The formalism developed till now was exclusively targeted for the white noise case. We assumed that the noise at each detector is white Gaussian. In this subsection, we extend our formalism to the colored noise case. We remind the reader that the main focus of this paper is to develop the coherent network strategy to detect unmodeled GW chirps with an interferometric detector network. Hence, we give more emphasis on the basic formalism and keep the colored noise case with basic minimal assumption: the noise from the different detectors is colored but with the same covariance. Based on this ground work, the work is in progress to extend this to the colored noise case with different noise covariances.

Let us therefore assume now that the noise components in each detector are independent and colored, with the same covariance matrix $\mathbf{R}_0$. Recall that the covariance matrix of a random vector $\mathbf{a}$ is defined as $\mathbb{E}[(\mathbf{a} - \mathbb{E}[\mathbf{a}]) \times (\mathbf{a} - \mathbb{E}[\mathbf{a}])^H]$ where $\mathbb{E}[.]$ denotes the expectation. From the independence of the noise components, the overall covariance matrix of the network noise vector is then a block-diagonal matrix, where all the blocks are identical and equal to $\mathbf{R}_0$: $\mathbf{R} = \mathrm{diag}(\mathbf{R}_0) \equiv \mathbf{I}_d \otimes \mathbf{R}_0$.

[11]The Levi-Cività symbol is defined as

$\epsilon_{ij\ldots} \equiv +1$ when $i, j, \ldots$ is an even permutation of $1, 2, \ldots$,

$\equiv -1$ when $i, j, \ldots$ is an odd permutation of $1, 2, \ldots$,

$\equiv 0$ when any two labels are equal.

In this case, the network LLR becomes

$$\Lambda(\mathbf{x}) = -\parallel \mathbf{x} - \mathbf{\Pi p} \parallel^2_{\mathbf{R}^{-1}} + \parallel \mathbf{x} \parallel^2_{\mathbf{R}^{-1}}, \quad (64)$$

where the notation $\| \cdot \|^2_{\mathbf{R}^{-1}}$ denotes the norm induced by the inner product associated to the covariance matrix $\mathbf{R}^{-1}$, i.e., $\| \mathbf{a} \|^2_{\mathbf{R}^{-1}} = \mathbf{a}^H \mathbf{R}^{-1} \mathbf{a}$.

Introducing the whitened version $\tilde{\mathbf{\Pi}} = \mathbf{R}^{-1/2}\mathbf{\Pi}$ and $\tilde{\mathbf{x}} = \mathbf{R}^{-1/2}\mathbf{x}$ of $\mathbf{\Pi}$ and $\mathbf{x}$, respectively, Eq. (65) can be rewritten as

$$\Lambda(\mathbf{x}) = -\parallel \tilde{\mathbf{x}} - \tilde{\mathbf{\Pi}}\mathbf{p} \parallel^2 + \parallel \tilde{\mathbf{x}} \parallel^2, \quad (65)$$

which is similar to Eq. (38) where all the quantities are replaced by their whitened version. Thus, the maximization of $\Lambda(\mathbf{x})$ with respect to the extrinsic parameters $\mathbf{p}$ will follow the same algebra as that derived in V. However, for the sake of completeness, we detail it below.

Following Sec. V, maximizing $\Lambda(\mathbf{x})$ with respect to the extrinsic parameters $\mathbf{p}$ leads to

$$\hat{\mathbf{p}} = \tilde{\mathbf{\Pi}}^{\#}\tilde{\mathbf{x}}, \quad (66)$$

where $\tilde{\mathbf{\Pi}}^{\#}$ is the pseudoinverse of $\tilde{\mathbf{\Pi}}$. Expressing this pseudoinverse by means of the SVD of $\tilde{\mathbf{\Pi}}$ as $\tilde{\mathbf{\Pi}}^{\#} = \mathbf{V}_{\tilde{\Pi}}\mathbf{\Sigma}^{-1}_{\tilde{\Pi}}\mathbf{U}^H_{\tilde{\Pi}}$ and introducing Eq. (67) into Eq. (66) provides the new statistic

$$\hat{\Lambda}(\mathbf{x}) = \parallel \mathbf{U}^H_{\tilde{\Pi}}\tilde{\mathbf{x}} \parallel^2 . \quad (67)$$

Now, from the definition of $\mathbf{\Pi}$ and the specific structure of $\mathbf{R}$, it is straightforward to see that

$$\tilde{\mathbf{\Pi}} = \mathbf{R}^{-1/2}(\mathbf{D} \otimes \mathbf{E}) = \mathbf{D} \otimes (\mathbf{R}_0^{-1/2}\mathbf{E}) = \mathbf{D} \otimes \tilde{\mathbf{E}}, \quad (68)$$

where we have introduced the whitened version $\tilde{\mathbf{e}} = \mathbf{R}_0^{-1/2}\mathbf{e}$ of the chirp signal and the corresponding matrix $\tilde{\mathbf{E}} = [\tilde{\mathbf{e}}\tilde{\mathbf{e}}^*]/2$.

For the white noise case, the statistic (68) can then be rewritten in terms of the SVD of the matrices $\mathbf{D}$ and $\tilde{\mathbf{E}}$:

$$\hat{\Lambda}(\mathbf{x}) = \parallel (\mathbf{U}_D \otimes \mathbf{U}_{\tilde{E}})^H \tilde{\mathbf{x}} \parallel^2 . \quad (69)$$

The computation of $\mathbf{U}_{\tilde{E}}$ is similar to the computation of $\mathbf{U}_{\tilde{E}}$. Furthermore, if we note that $\tilde{\mathbf{e}}^T\tilde{\mathbf{e}} \simeq 0$, and if we assume that $\tilde{\mathbf{e}}^H\tilde{\mathbf{e}} = N$, it turns out that $\mathbf{U}_{\tilde{E}} = 2\tilde{\mathbf{E}}/\sqrt{N} = 2\mathbf{R}_0^{-1/2}\mathbf{E}/\sqrt{N}$. Using the property of the Kronecker product in Eq. (A2), we then obtain

$$\hat{\Lambda}(\mathbf{x}) = \parallel \mathrm{vec}(\mathbf{E}^H\tilde{\tilde{\mathbf{X}}}\mathbf{U}_D^*) \parallel^2, \quad (70)$$

where the matrix $\tilde{\tilde{\mathbf{X}}} = [\tilde{\tilde{\mathbf{x}}}_1\tilde{\tilde{\mathbf{x}}}_2 \ldots \tilde{\tilde{\mathbf{x}}}_d]$ contains the data vector from each detector whitened twice: $\tilde{\tilde{\mathbf{x}}}_j = \mathbf{R}^{-1/2}\tilde{\mathbf{x}}_j = \mathbf{R}^{-1}\mathbf{x}_j$.

As this expression is similar to the white noise case, we can form two synthetic streams $[\tilde{\tilde{\mathbf{y}}}_1, \tilde{\tilde{\mathbf{y}}}_2] = \tilde{\tilde{\mathbf{X}}}\mathbf{U}_D^*$ and use them to express the LLR statistic as

$$\hat{\Lambda}(\mathbf{x}) = \frac{2}{N}(|\mathbf{e}^H\tilde{\tilde{\mathbf{y}}}_1|^2 + |\mathbf{e}^H\tilde{\tilde{\mathbf{y}}}_2|^2). \quad (71)$$

In this expression, the only difference with the white noise LLR of (53) comes from the computation of the synthetic streams $\tilde{\tilde{\mathbf{y}}}_1$ and $\tilde{\tilde{\mathbf{y}}}_2$ which are obtained after double-whitening the data.

VI. MAXIMIZATION OVER THE INTRINSIC PARAMETERS

In the previous section, we maximized the network LLR over the extrinsic parameters of the signal model, assuming that the remaining parameters (the source location angles ϕ and θ and the phase function $\varphi(\cdot)$) were known.

By definition, the intrinsic parameters modify the network LLR nonlinearly. For this reason, the maximization of $\hat{\Lambda}$ over these parameters is more difficult. It cannot be done analytically and must be performed numerically, for instance with an exhaustive search of the maximum by repeatedly computing $\hat{\Lambda}$ over the entire range of possibilities.

While the exhaustive search can be employed for the source location angles, it is not applicable to the chirp phase function, which requires a specific method. For the single detector case, we had addressed this issue in [8] with an original maximization scheme which is the cornerstone of the BCC algorithm. Here, we use and adapt the principles of BCC to the multiple detector case.

A. Chirp phase function

Let us examine first the case of the detection of inspiralling binary chirps. In this case, the chirp phase is a prescribed function of a small number of parameters i.e., the masses and spins of the binary stars. The maximization over those is performed by constructing a grid of reference or *template* waveforms which are used to search the data. This grid samples the range of the physical parameters. This sampling must be accurate (the template grid must be tight) to avoid missing any chirp.

A tight grid of templates can be obtained in the nonparametric case (large number of parameters) i.e., when the chirp is not completely known. We have shown in [8] how to construct a template grid which covers entirely the set of smooth chirps i.e., chirps whose frequency evolution has some regularity as described in Sec. II B 2. In the next section, we briefly describe this construction.

1. Chirplet chains: tight template bank for smooth chirps

We refer to the template forming this grid as *chirplet chain* (CC). These CCs are constructed on a simple geometrical idea: a broken line is a good approximation of a smooth curve. Since the frequency of a smooth chirp follows a smooth frequency vs time curve, we construct templates that are broken lines in the time-frequency (TF) plane.

More precisely, CC are defined as follows. We start by sampling the TF plane with a regular grid consisting of N_t time bins and N_f frequency bins. We build the template waveforms like a puzzle by assembling small chirp pieces which we refer to as *chirplets*. A chirplet is a signal with a frequency joining linearly two neighboring vertices of the grid. The result of this assembly is a *chirplet chain* i.e., a piecewise linear chirp. Since we are concerned with continuous frequency evolution with bounded variations, we only form continuous chains.

We control the variations of the CC frequency. The frequency of a single chirplet does not increase or decrease more than N'_t frequency bins over a time bin. Similarly, the difference of the frequency variations of two successive chirplets in a chain does not increase or decrease more than N''_t frequency bins.

The CC grid is defined by four parameters namely N_t, N_f, N'_t, and N''_t. Those are the available degrees of freedom we can tune to make the CC grid tight. A template grid is tight if the network ambiguity $\hat{\Lambda}(\mathbf{s}; \varphi') \propto |\mathbf{e}'^H\mathbf{y}_1(\mathbf{s})|^2 + |\mathbf{e}'^H\mathbf{y}_2(\mathbf{s})|^2$ which measures the similarity between an arbitrary chirp (of phase φ) and its closest template (of phase φ'), is large enough and relatively closed to the maximum (when $\varphi' = \varphi$).

As stated in Eq. (55), in the presence of a noise free GW chirp, the synthetic streams $\mathbf{y}_I(\mathbf{s})$ are rescaled and phase shifted copies of the initial GW chirp $\mathbf{s}$. Therefore, we treat the network ambiguity as a sum of ambiguities from two *virtual* detectors where each term in $\hat{\Lambda}(\mathbf{s}; \varphi')$ is the ambiguity computed in the single detector case. An estimate of the ambiguity has been obtained in [8] for this case. It can thus be directly reused to compute $\hat{\Lambda}(\mathbf{s}; \varphi')$.

The bottom line is that the ratio of the ambiguity to its maximum for the network case remains unaltered as compared to the single detector case and thus the same for the tight grid conditions. In conclusion, the rules (which we will not repeat here) established in [8] to set the search parameters can also be applied here.

2. Search through CCs in the time-frequency plane: best network CC algorithm

We have now to search through the CC grid to find the best matching template, i.e., which maximizes $\hat{\Lambda}(\mathbf{x}; \hat{\varphi}')$ over all CCs of phase φ'. Counting the number of possible CCs to be searched over is a combinatorial problem. This count grows exponentially with the number of time bins N_t. In the situation of interest, it reaches prohibitively large values. The family of CCs cannot be scanned exhaustively and the template based search is intractable.

In [8], we propose an alternative scheme yielding a close approximation of the maximum for the single detector statistic. When applied to the network, the scheme demands to reformulate the network statistic in the TF plane. The TF plane offers a natural and geometrically simple representation of chirp signals which simplifies the statistic. It turns out that the resulting statistic falls in a class of objective functions where efficient combinatorial optimization algorithms can be used. We now explain this result in more detail.

We use the TF representation given by the discrete Wigner-Ville (WV) distribution [32] defined for the time series $x[n]$ with $n = 0, \ldots, N-1$ as

$$w_x(n, m) \equiv \sum_{k=-k_n}^{+k_n} x[[n + k/2]]x^*[[n - k/2]]e^{-2\pi imk/(2N)}, \quad (72)$$

with $k_n \equiv \min\{2n, 2N - 1 - 2n\}$, where $[\cdot]$ gives the integer part. The arguments of w_x are the time index n and the frequency index m which correspond, in physical units, to the time $t_n = t_s n$ and the frequency $\nu_m = \nu_s m/(2N)$ for $0 \le m \le N$ and $\nu_m = \nu_s(N - m)/(2N)$ for $N + 1 \le m \le 2N - 1$.

The above WV distribution is a unitary representation. This means that the scalar products of two signals can be reexpressed as scalar products of their WV. Let $x_1[n]$ and $x_2[n]$ be two time series. The unitarity property of w_x is expressed by the Moyal's formula as stated below

$$\left| \sum_{n=0}^{N-1} x_1[n]x_2^*[n] \right|^2 = \frac{1}{2N} \sum_{n=0}^{N-1} \sum_{m=0}^{2N-1} w_{x_1}(n, m)w_{x_2}(n, m). \quad (73)$$

Applying this property to the network statistic in Eq. (53), we get

$$\hat{\Lambda}(\mathbf{x}) = \frac{1}{N^2} \sum_{n=0}^{N-1} \sum_{m=0}^{2N-1} w_y(n, m)w_e(n, m), \quad (74)$$

where $w_y = w_{y_1} + w_{y_2}$ combines the individual WVs of the two synthetic streams.

In order to compute $\hat{\Lambda}(\mathbf{x})$, we need to have a model for w_e. We know that the WV distribution of a linear chirp (whose frequency is a linear function of time) is essentially concentrated in the neighborhood of its instantaneous frequency [32]. We assume that it also holds true for an arbitrary (nonlinear) chirp. Applying this approximation to the WV w_e of the template CC in Eq. (75), we get

$$w_e(n, m) \approx 2N\delta(m - m_n), \quad (75)$$

where m_n denotes the nearest integer of $2T\nu(t_n)$ and ν is the instantaneous frequency of the CC.

Thus, substituting in Eq. (75), we obtain the following reformulation of the network statistic

$$\hat{\Lambda}(\mathbf{x}) = \frac{2}{N} \sum_{n=0}^{N-1} w_y(n, m_n). \quad (76)$$

The maximization of $\hat{\Lambda}(\mathbf{x})$ over the set of CC amounts to finding the TF path that maximizes the integral Eq. (77), which is equivalent to a *longest path problem* in the TF plane. This problem is structurally identical to the single detector case (the only change is the way we obtain the TF map). We can therefore essentially reuse the scheme proposed earlier for this latter case. The latter belongs to a class of combinatorial optimization problems where efficient (polynomial time) algorithms exist. We use one such algorithm, namely, the dynamic programming.

In conclusion, *the combination of the two ingredients, namely, the synthetic streams and the phase maximization scheme used in BCC allows us to coherently search the unmodeled GW chirps in the data of the GW detector network.* We refer to this procedure as the BNCC algorithm.

B. Source sky position

As we are performing maximization successively, till now we assume that we know the sky position of the source. Knowing the sky position, we construct the synthetic streams with appropriate direction dependent weight factors, time-delay shifts, and carry out the BNCC algorithm for chirp phase detection. In reality, the sky position is unknown. One needs to search through the entire sky by sampling the celestial sphere with a grid and repeating the above procedure for each point on this grid.

C. Time of arrival

Since we process the data streams sequentially and blockwise, the maximization over t_0 amounts to selecting that block where the statistic arrives at a local maximum (i.e., the maximum of the ''detection peak''). The epoch of this block yields an estimate of t_0. The resolution of the estimate may be improved by increasing the overlap between two consecutive blocks.

D. Estimation of computational cost

We estimate the computational cost of the BNCC search by counting the floating-point operations (flops) required by its various subparts. The algorithm consists essentially in repeating the one-detector search for all sky location angles. Let N_Ω be the number of bins of the sky grid. The total cost is therefore N_Ω times the cost of the one-detector search, which we give in [8] and summarize now. The computation of the WV of the two synthetic streams requires $10NN_f\log_2 N_f$ flops and the BCC search applied to the combined WV requires $[N + (2N_r'' + 1)N_t]N_c$ flops, where $N_c \approx (2N_r' + 1)N_f$ is the total number of chirplets. Since this last part of the algorithm dominates, the overall cost thus scales with

$$C \propto N_\Omega[N + (2N_r'' + 1)N_t](2N_r' + 1)N_f. \qquad (77)$$

This is the numerical cost for computing one data block of duration T. The computational power needed to process the data in real time is thus given by $C/(\mu T)$ where μ is the overlap between two successive blocks.

VII. RESULTS WITH SIMULATED DATA AND DISCUSSION

A. Proof of principle of a full blind search

We present here a proof of principle for the proposed detection method. For this case study, we consider a network of three detectors placed and oriented like the existing Virgo and the two four-kilometer LIGO detectors. The coordinates and orientation of these detectors can be found in Table I. We assume a simplified model for detector noise which we generate independently for each detector, using a white Gaussian noise. Figure 5 illustrates the possibility of a ''full blind'' search in this situation. This means that we perform the detection jointly with the estimation of the GW chirp frequency and the source sky location.

1. Description of the test signal

Because of computational limitation, we restrict this study to rather short chirps of $N = 256$ samples, i.e., a chirp duration $T = 250$ ms assuming a sampling rate of $\nu_s = 1024$ Hz. The chirp frequency follows a random time evolution which, however, satisfies chirping rate constraints. We make sure that the first and second derivatives of the chirp frequency are not larger than $F^{I} = 9.2$ kHz/s and $F^{II} = 1.57$ MHz/s^2, respectively. The chosen test signal has about 50 cycles. This is a larger number than what is considered typically for burst GWs (~ 10).

As a comparison with a well-known physical case, an inspiralling (equal mass) binary with total mass $M = 11M_\odot$ reaches the same maximum frequency variations at the last stable circular orbit. (Binary chirps with larger total mass also satisfy these chirping rate limits).

We set the SNR to $\rho = 20$. The chirp is injected at the sky position $\phi = 2.8$ rad and $\theta = 0.4$ rad where the contributions of the individual detectors are comparable, namely, the individual SNR are 10.4, 10.15, and 13.77 for Virgo, LIGO Hanford, and LIGO Livingstone, respectively.

2. Search parameters

We search through the set of CCs defined over a TF grid with $N_t = 128$ time intervals and $N = N_f = 256$ frequency bins (using $f_s = 2048$ Hz). We set the regularity parameters to $N_r' = 9$ and $N_r'' = 3$, consistent to the above chirping rate limits.

We select an *ad hoc* sky grid by dividing regularly the full range of the source localization angles θ and ϕ into 128 bins. The resulting grid has therefore a total of $N_\Omega = 16\,384$ bins. This is probably much finer than is required to perform the detection without missing candidate. However,

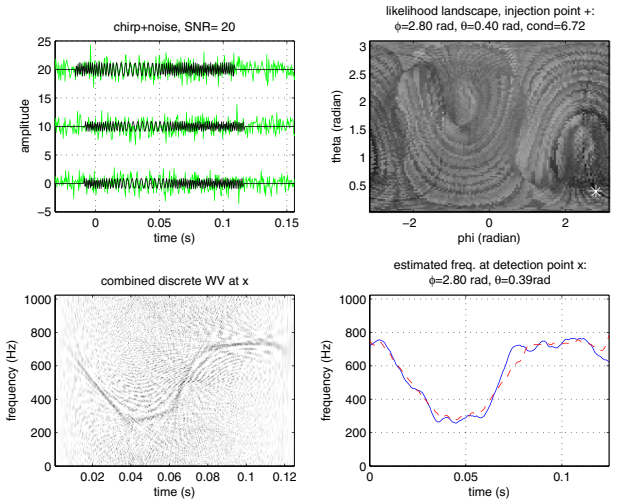

FIG. 5 (color online). *Coherent detection/estimation of a ''random'' chirp with network of three GW antennas.*—In the data of three GW antennas (the two LIGO and Virgo), we inject (a) a random GW chirp emitted from a source at the position marked with a ''+'' at $\phi = 2.8$ rad and $\theta = 0.4$ rad. We perform a full-sky search using the best network chirplet chain algorithm. It produces a likelihood landscape (b) where we select the maximum. This is the detection point and it is indicated with ''×''. In (c) we show the combined WV distribution of the synthetic streams at the detection point. In (d), we compare the exact frequency of the chirp (solid/blue line) with the estimation (dashed/red line) obtained at the detection point.

this oversampling leads to precise likelihood sky maps which helps to diagnose the method. With this parameter choice, the estimated computational power required to analyze the data in real time is of 2.8 TFlops, assuming an overlap of $\mu = 50\%$ between successive data blocks. Because of the crude choice for the sky grid, this requirement is probably overestimated.

The result of the search is displayed in Fig. 5 where we see that the injection is recovered both in sky position and frequency evolution. The source position is estimated at $\hat{\phi} = 2.8$ rad and $\hat{\theta} = 0.39$ rad.

B. Regularized variants

As shown in Sec. , the SNR carried by the synthetic stream is proportional to the corresponding SV. When the GW polarization plane is degenerate (i.e., when σ_2 is small), the second synthetic stream contains almost only noise. We thus do not lose information if we suppress its contribution from the statistic. This is the basic idea of Klimenko *et al.* in [13].

We have seen that the estimation of the extrinsic parameters is an ill-posed least-square problem in those cases. Suppressing the contribution of the second synthetic stream amounts to *regularizing* this problem [13]. In practice, this regularization can be done in various ways, corresponding to well-identified schemes.

A first possibility is to suppress the contribution of the second synthetic stream when the conditioning number of $\mathbf{\Pi}$ is too large (i.e., exceeds a given threshold). This scheme is referred to as *truncated SVD* [27]. A second possibility is to balance (divide) the contribution of the second synthetic stream by the conditioning number. This is referred to as the *Tykhonov* approach [27] and it was proposed for regularizing burst searches in [15].

In Fig. 6, we compare the likelihood landscape and frequency estimate obtained with the standard statistic and its regularized version using the Tykhonov approach. Visually, the regularization improves the contrast and concentration of the likelihood landscape around the injection point. This can be assessed more quantitatively with the contrast defined as the ratio of the likelihood landscape extremes. This contrast is improved by about 10% for the regularized statistic as compared to the standard version. It is also interesting to compare the ''width'' of the detection peak obtained with the two statistic. To do this, we measure the solid angle of the sky region where the statistic is larger than 90% of the maximum. This angle is reduced by a

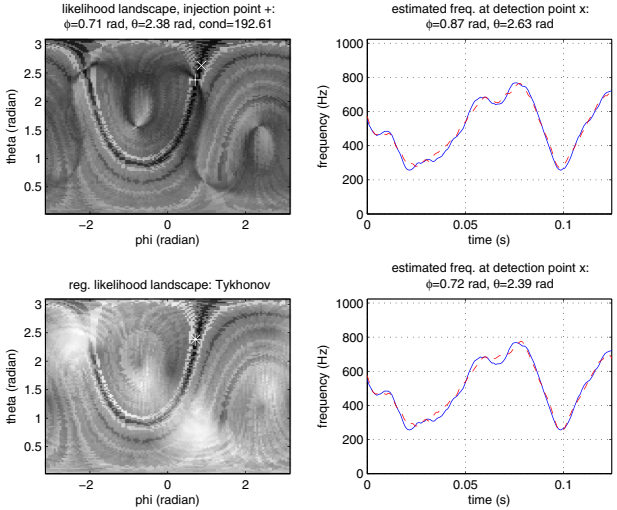

FIG. 6 (color online). *Coherent detection/estimation of a random chirp with network of three GW antennas. Standard and regularized statistic.*—We compare the likelihood landscape (left) and frequency estimation (right) obtained using the standard (top) and Tykhonov-regularized (bottom) versions of the network statistic. The test signal is a random GW chirp injected at the sky location marked with a "+". This location has been chosen because of the associated large value of the conditioning number, namely cond($\mathbf{\Pi}$) $\approx$ 192.

factor of $\sim$6 when computed with the regularized statistic. There is, however, no major improvement of the frequency estimate. More generally, it is unclear whether the regularized statistic performs better than the standard one.

VIII. CONCLUDING REMARKS

The coherent detection of unmodeled chirps with a network of GW have features and issues in common with the burst one. In particular, the same geometrical objects play a key role. While the noise spans the whole d-dimensional data space, GW signals (chirps or burst) only belong to a two-dimensional (one dimension per GW polarizations) subspace, the *GW polarization plane*. Detecting GWs amounts to checking whether the data has significant components in this plane or not. To do so, we compute the projections of the data onto a basis of the GW polarization plane. In practice, this defines two instantaneous linear mixtures of the individual detector data which we refer to as *synthetic streams*. Those may be considered as the output data of virtual detectors. This combination is such that the GW contributions from each real detector add constructively. The GW signature thus has a larger amplitude in the synthetic streams while the noise variance is kept at the same level.

The coherent detection amounts to looking for an excess in the signal energy in one or both synthetic streams (depending on the GW polarization model). This provides a generic and simple procedure to produce a coherent detection pipeline from a one-detector pipeline. In the one-detector case, the BCC search performs a path search in a time-frequency distribution of the data. In the multiple detector case, the BNCC search now uses the joint time-frequency map obtained by summing the time-frequency energy distributions of the two synthetic streams. The approach does not restrict to chirp detection and it can be applied to burst searches [18].

We demonstrated in a simplified situation that the full-sky blind detection of an unmodeled chirp is feasible. This means that the detection is performed jointly to estimate the source location and the frequency evolution. The application of this method to the real data, however, requires several improvements. First, the method has to be adapted to the case where the detectors have different sensitivities. In this respect, we already obtained first results [33].

We also have to refine the choice of the grid which samples the celestial sphere. In the present work, we select

an *ad hoc* grid. Clearly, the sky resolution and the bin shape depends on the geometry of the sphere and the location and orientation of the detectors in the considered network. A better grid choice (not too coarse to avoid SNR losses, and not too fine to avoid using useless computing resources) should incorporate this information keeping the search performance (detection probability and sky resolution) constant. In this respect, we may consider to other parametrizations of the sky location which makes the definition of the sky grid easier, for instance by choosing the time delays as investigated in [11]. We may also explore hierarchical schemes for the reduction of the computational cost.

The GW polarization plane depends on the detector antenna patterns functions. With the presently available networks, there are significantly large sky regions where the antenna patterns are almost collinear. In this case, the network observes essentially one polarization and is almost insensitive to the other: the GW polarization plane reduces to a one-dimensional space. The information carried by the missing polarization lacks and this makes the estimation of certain parameters ill-posed and hence very sensitive to noise. We can evaluate that the variance of the estimate scales with the condition number of the antenna pattern matrix. When this number (which quantifies in some sense the mutual alignment of the detectors) is large, the estimation is ill-posed and we expect poor results.

This is an important issue for burst detection since it affects significantly the shape of the estimated waveform (and, particularly the regularity of its time evolution). This has motivated the development of regularization schemes which penalize the estimation of nonphysical (i.e., irregular) waveforms. We have shown that this is, however, less of a problem for chirps because of their more constrained model. Ill-conditioning only affects global scaling factors in the chirp model. Unlike bursts, no additional prior is available for regularizing the estimation of these scaling factors.

The data space can be decomposed as the direct sum of the GW polarization plane and its complementary. While GWs have zero components in the latter null space, it is unlikely that instrumental noise (including its non-Gaussian and nonstationary part) will. This motivates the use of *null streams* (i.e., the projection of the data along a basis of the complementary space) to verify that a trigger is indeed a GW candidate and not an instrumental artifact. Since null streams are inexpensive to compute, we consider to use them to make preemptive cuts in order to avoid the analysis of bad data.

ACKNOWLEDGMENTS

A. P. is supported by the Alexander von Humboldt Foundation's Sofja Kovalevskaja Programme (funded by the German Ministry of Education and Research). O. R. is supported by the Virgo-EGO Scientific Forum. The authors would like to thank J.-F. Cardoso for an interesting exchange of ideas.

APPENDIX A: KRONECKER PRODUCT: DEFINITION AND PROPERTIES

The Kronecker product $\otimes$ transforms two matrices $\mathbf{A} \in \mathbb{C}^{m\times n}$ and $\mathbf{B} \in \mathbb{C}^{p\times q}$ into the following matrix of $\mathbb{C}^{mp\times nq}$ [25]

$$\mathbf{A} \otimes \mathbf{B} \equiv \begin{bmatrix} a_{11}\mathbf{B} & \dots & a_{1n}\mathbf{B} \\ \vdots & \ddots & \vdots \\ a_{m1}\mathbf{B} & \dots & a_{mn}\mathbf{B} \end{bmatrix}. \tag{A1}$$

The Kronecker product is a linear transform and can be considered as a special case of the tensor product. We define the operator vec() to be the stack operator which transforms the matrix into a vector by stacking its columns, i.e. $\mathbf{x} \equiv \mathrm{vec}(\mathbf{X})$. In the text, we use the following property:

$$(\mathbf{A} \otimes \mathbf{B})\mathrm{vec}(\mathbf{X}) = \mathrm{vec}(\mathbf{B}\mathbf{X}\mathbf{A}^T). \tag{A2}$$

The proof of this property is straightforward.

APPENDIX B: INTERFEROMETRIC DETECTOR RESPONSE IN TERMS OF GEL'FAND FUNCTIONS

The GW response of a detector to an incoming GW can be obtained by computing the interaction of the wave tensor W with the detector tensor D as follows[12]:

$$s = \sum_{i,j=1}^{3} W^{ij} D_{ij}. \tag{B1}$$

The wave tensor is related to the incoming GW tensor in the TT gauge by $h_{ij} = 2W_{ij}$. Both detector and wave tensors are rank 2 STF tensors. Any STF tensor can be expanded in the basis of spin-weighted spherical harmonics of rank 2 and the rank-2 Gel'fand functions provide the corresponding coefficients. Further, they are representation of rotation group SO(3) and provide compact representation for the detector response of any arbitrarily oriented and located detector on Earth which we present in this appendix [34].

a. Wave tensor—The incoming GW tensor in TT gauge is given by

$$h_{ij}^{TT} = (e_{xi}e_{xj} - e_{yi}e_{yj})h_+ + 2(e_{xi}e_{yj})h_\times, \tag{B2}$$

where $\mathbf{e_x}$ and $\mathbf{e_y}$ are unit vectors along the x_w and y_w axes in the wave frame; h_+ and $h_\times$ are the two GW polarizations. Let $\hat{m} = (\mathbf{e_x} + i\mathbf{e_y})/\sqrt{2}$ be a complex vector in the wave frame. Then, the wave tensor can be written down in terms of m as

$$W^{ij} = \Re[(m^i m^j)^* h], \tag{B3}$$

where we used the complex quantity $h = h_+ + ih_\times$ which combines both GW polarizations.

[12]Unless otherwise mentioned, the notations and symbols used in all appendices are confined to those appendices only.

The term $m_i m_j$ is a STF tensor of rank 2. We choose to work in the detector frame for convenience. Expanding $m_i m_j$ in terms of spin-weighted spherical harmonics of rank 2, namely $\mathcal{Y}^{ij}_{2n}$ and the rank-2 Gel'fand functions $T_{mn}(\phi'_e, \theta'_e, \psi'_e)$, we get

$$m^i m^j = \sqrt{\frac{8\pi}{15}} \sum_{n=-2}^{2} \mathcal{Y}^{ij}_{2n} T_{2n}(\phi'_e, \theta'_e, \psi'_e). \quad \text{(B4)}$$

The angles $(\phi'_e, \theta'_e, \psi'_e)$ are the Euler angles of the rotation operator which transforms the detector coordinates into the wave coordinates.

Substituting Eq. (B4) into Eq. (B3), we express the wave tensor in terms of the Gel'fand functions as

$$W^{ij} = \sqrt{\frac{8\pi}{15}} \sum_{n=-2}^{2} \Re[h \mathcal{Y}^{ij}_{2n} T_{-2n}]. \quad \text{(B5)}$$

b. Detector tensor—The detector tensor is

$$D_{ij} = n_{1i} n_{1j} - n_{2i} n_{2j}, \quad \text{(B6)}$$

where $\mathbf{n}_1$ and $\mathbf{n}_2$ are the unit vectors along the first and second arms of the interferometer. Recall that we choose the x_d-axis of the detector frame along the bisector of the two arms. The y_d-axis is chosen such that (x_d, y_d, z_d) is a right-handed coordinate system with z_d pointing towards the local zenith. With this choice, we have

$$D_{11} = D_{22} = 0, \qquad D_{12} = D_{21} = -1. \quad \text{(B7)}$$

From Eqs. (B6) and (B7), the detector response is

$$s = \Re[f^* h], \quad \text{(B8)}$$

where the complex antenna pattern function is given by

$$f = i[T_{-2-2}(\phi'_e, \theta'_e, \psi'_e) - T_{22}(\phi'_e, \theta'_e, \psi'_e)]. \quad \text{(B9)}$$

From the expansion of the above Eq. (B8) in terms of GW polarizations, it is consistent to define $f = f_+ + i f_\times$, which yields Eq. (13).

c. Extended complex antenna pattern for sources orbiting in a fixed plane—As discussed in Sec. III D 1, the extended antenna pattern functions incorporate the inclination angle ϵ and is given in Eq. (17) as

$$\tilde{f} = \frac{1 + \cos^2\epsilon}{2} f_+ + i \cos\epsilon f_\times, \quad \text{(B10)}$$

where $f_{+,\times}$ depend on the relative orientation of wave frame with respect to the detector frame. The detector to wave frame coordinate transformation can be split into two: detector to Earth's frame and Earth's frame to wave frame by the following rotation transformations as given in Eqs. (5) and (6)

$$\mathcal{O}(\phi'_e, \theta'_e, \psi'_e) = \mathcal{O}(\phi_e, \theta_e, \psi_e) \mathcal{O}^{-1}(\alpha, \beta, \gamma). \quad \text{(B11)}$$

The above successive rotation transformation can be translated into the addition theorem of Gel'fand functions [35] as given below

$$T_{mn}(\phi'_e, \theta'_e, \psi'_e) = \sum_{l=-2}^{2} T_{ml}(\phi_e, \theta_e, \psi_e) T^*_{nl}(\alpha, \beta, \gamma). \quad \text{(B12)}$$

We used the fact that the inverse rotation operator is associated to a complex conjugation.

Substituting in Eq. (B9), we rewrite the antenna pattern functions in terms of the Gel'fand functions as

$$f = -\sum_{s=-2}^{2} i T_{2s}(\phi_e, \theta_e, \psi_e) \times [T_{2s}(\alpha, \beta, \gamma) - T_{-2s}(\alpha, \beta, \gamma)]^*. \quad \text{(B13)}$$

Substituting in the extended beam pattern function given in Eq. (B10) and combining the dependencies upon $\psi = \psi_e$ and ϵ, we get

$$\tilde{f} = T_{22}(\psi, \epsilon, 0) d + T_{2-2}(\psi, \epsilon, 0) d^*, \quad \text{(B14)}$$

where

$$d = -\sum_{n=-2}^{2} i T_{2n}(\phi_e, \theta_e, 0)[T_{2n}(\alpha, \beta, \gamma) - T_{-2n}(\alpha, \beta, \gamma)]^*. \quad \text{(B15)}$$

There are various ways of expressing the antenna pattern functions. The main advantages of this one is that it is particularly compact and that the angles ψ and ϵ get factorized from the rest of the parameters. This helps in the maximization of the network LLR over the extrinsic parameters.

APPENDIX C: SVD OF A TWO-COLUMN COMPLEX MATRIX

In this appendix, we obtain the SVD of a complex matrix of the type $\mathbf{A} \equiv [\mathbf{a}, \mathbf{a}^*]$ where $\mathbf{a} \in \mathbb{C}^{N\times 1}$. The SVD decomposes $\mathbf{A}$ into the product $\mathbf{A} = \mathbf{U}_A \mathbf{\Sigma}_A \mathbf{V}_A^H$ where $\mathbf{U}_A$ and $\mathbf{V}_A$ are two orthogonal matrices and $\mathbf{\Sigma}_A$ is a positive definite diagonal matrix. To obtain it analytically, we first get the eigen-decomposition of

$$\mathbf{A}^H \mathbf{A} = \begin{bmatrix} \mathbf{a}^H\mathbf{a} & \mathbf{a}^H\mathbf{a}^* \\ \mathbf{a}^T\mathbf{a} & \mathbf{a}^T\mathbf{a}^* \end{bmatrix} \equiv \begin{bmatrix} a & b^* \\ b & a \end{bmatrix}. \quad \text{(C1)}$$

We distinguish two cases depending on the value of b.

1. For $|b| > 0$

The eigenvalues $\sigma_\pm$ and the eigenvectors $v_\pm$ of $\mathbf{A}^H\mathbf{A}$ are given below:

$$\sigma^2_\pm = a \pm |b|, \quad \text{(C2)}$$

$$\mathbf{v}_\pm = \frac{1}{\sqrt{2}} \begin{bmatrix} \exp(-i\varpi) \\ \pm 1 \end{bmatrix}, \quad \text{(C3)}$$

where $\varpi = \arg b = \arg[\mathbf{a}^T\mathbf{a}]$. The number of nonzero eigenvalues of $\mathbf{A}^H\mathbf{A}$ gives the rank of $\mathbf{A}$. The eigenvalues arranged in the descending order form the diagonal values of $\mathbf{\Sigma}_A^2$ as shown below. The eigenvectors $\mathbf{v}_\pm$ are the right-handed singular vectors of $\mathbf{A}$ and form $\mathbf{V}_A$ as given below:

$$\mathbf{\Sigma}_A = \begin{bmatrix} \sigma_+ & 0 \\ 0 & \sigma_- \end{bmatrix}, \quad \text{(C4)}$$

$$\mathbf{V}_A = [\mathbf{v}_+ \quad \mathbf{v}_-]. \quad \text{(C5)}$$

We then form the matrix $\mathbf{U}_A = \mathbf{A}\mathbf{V}_A\mathbf{\Sigma}_A^{-1} \equiv [\mathbf{u}_+, \mathbf{u}_-]$ containing the right-handed singular vectors, with

$$\mathbf{u}_\pm = \frac{\exp(-i\varpi)\mathbf{a} \pm \mathbf{a}^*}{\sqrt{2}\sigma_\pm}. \quad \text{(C6)}$$

The above expressions are valid only when the two SV are nonzero. It is possible that the smallest SV σ_- vanishes. In this case, the SVD collapses to $\mathbf{U}_A = \mathbf{u}_+$, $\mathbf{\Sigma}_A = \sigma_+$, and $\mathbf{V}_A = \mathbf{v}_+$.

2. For $|b| = 0$

In this case, the matrix $\mathbf{A}^H\mathbf{A} = a\mathbf{I}_2$ is diagonal. We thus have $\mathbf{\Sigma} = \sqrt{a}\mathbf{I}_2$, $\mathbf{V}_A = \mathbf{I}_2$, and $\mathbf{U}_A = \mathbf{A}/\sqrt{a}$.

[1] GEO600 Project, www.geo600.uni-hannover.de; LIGO Collaboration, http://www.ligo.org; Virgo Collaboration, http://www.virgo.infn.it.
[2] M. Feo *et al.*, in *Proceedings of the 7th Marcel Grossmann Meeting*, edited by R. T. Jantzen *et al.* (World Scientific, Singapore, 1996), p. 1086.
[3] J.-M. Innocent and B. Torrésani, Appl. Comput. Harmon. Anal. **4**, 113 (1997).
[4] E. Chassande-Mottin and P. Flandrin, Appl. Comput. Harmon. Anal. **6**, 252 (1999).
[5] F. A. Jenet and T. A. Prince, Phys. Rev. D **62**, 122001 (2000).
[6] W. Anderson and R. Balasubramanian, Phys. Rev. D **60**, 102001 (1999).
[7] E. Candès, P. Charlton, and H. Helgason, Appl. Comput. Harmon. Anal. **24**, 14 (2008).
[8] E. Chassande-Mottin and A. Pai, Phys. Rev. D **73**, 042003 (2006).
[9] N. Arnaud *et al.*, Phys. Rev. D **68**, 102001 (2003).
[10] H. Mukhopadhyay, N. Sago, H. Tagoshi, H. Takahashi, and N. Kanda, Phys. Rev. D **74**, 083005 (2006).
[11] A. Pai, S. Dhurandhar, and S. Bose, Phys. Rev. D **64**, 042004 (2001).
[12] L. S. Finn, Phys. Rev. D **63**, 102001 (2001).
[13] S. Klimenko, S. Mohanty, M. Rakhmanov, and G. Mitselmakher, Phys. Rev. D **72**, 122002 (2005).
[14] S. D. Mohanty, M. Rakhmanov, S. Klimenko, and G. Mitselmakher, Classical Quantum Gravity **23**, 4799 (2006).
[15] M. Rakhmanov, Classical Quantum Gravity **23**, S673 (2006).
[16] Y. Gürsel and M. Tinto, Phys. Rev. D **40**, 3884 (1989).
[17] L. Wen and B. F. Schutz, Classical Quantum Gravity **22**, S1321 (2005).
[18] S. Chatterji *et al.*, Phys. Rev. D **74**, 082005 (2006).
[19] E. E. Flanagan and S. A. Hughes, New J. Phys. **7**, 204 (2005).
[20] K. S. Thorne, Rev. Mod. Phys. **52**, 299 (1980).
[21] E. Berti *et al.*, Phys. Rev. D **76**, 064034 (2007).
[22] E. E. Flanagan and S. A. Hughes, Phys. Rev. D **57**, 4535 (1998).
[23] H. Goldstein, *Classical Mechanics* (Addison-Wesley, Redwood City, CA, 1980), 2nd ed.
[24] G. H. Golub and C. F. VanLoan, *Matrix Computations* (Johns Hopkins University Press, Baltimore, 1996), 3rd ed.
[25] R. A. Horn and C. R. Johnson, *Topics in Matrix Analysis* (Cambridge University Press, Cambridge, England, 1991).
[26] S. Kay, *Fundamentals of Statistical Signal Processing: Detection Theory* (Prentice-Hall, Englewood Cliffs, NJ, 1998).
[27] A. Neumaier, SIAM Rev. **40**, 636 (1998).
[28] J. Sylvestre, Phys. Rev. D **68**, 102005 (2003).
[29] H. L. Van Trees, *Optimum Array Processing* (Wiley, New York, 2002).
[30] K. R. Nayak, S. V. Dhurandhar, A. Pai, and J. Y. Vinet, Phys. Rev. D **68**, 122001 (2003).
[31] Y. Guersel and M. Tinto, in Proceedings of General Relativity and Gravitational Physics, Capri, 1990 (unpublished), p. 620.
[32] E. Chassande-Mottin and A. Pai, IEEE Signal Process. Lett. **12**, 508 (2005).
[33] O. Rabaste, E. Chassande-Mottin, and A. Pai, in *Actes du 21ème Colloque GRETSI* (Troyes, France, 2007), p. 741.
[34] S. V. Dhurandhar and M. Tinto, Mon. Not. R. Astron. Soc. **234**, 663 (1988).
[35] I. M. Gel'fand, R. A. Minlos, and Z. Y. Shapiro, *Representations of the Rotation and Lorentz Groups and their Applications* (Pergamon Press, New York, 1963).

Journal of Cosmology and Astroparticle Physics
An IOP and SISSA journal

A first search for coincident gravitational waves and high energy neutrinos using LIGO, Virgo and ANTARES data from 2007

The ANTARES collaboration, the LIGO scientific collaboration and the Virgo collaboration

E-mail: antares.spokesperson@in2p3.fr, lsc-spokesperson@ligo.org, virgo-spokesperson@ego-gw.it, Irene.DiPalma@aei.mpg.de, thierry.pradier@iphc.cnrs.fr

Received April 8, 2013
Accepted April 22, 2013
Published June 7, 2013

Abstract. We present the results of the first search for gravitational wave bursts associated with high energy neutrinos. Together, these messengers could reveal new, hidden sources that are not observed by conventional photon astronomy, particularly at high energy. Our search uses neutrinos detected by the underwater neutrino telescope ANTARES in its 5 line configuration during the period January - September 2007, which coincided with the fifth and first science runs of LIGO and Virgo, respectively. The LIGO-Virgo data were analysed for candidate gravitational-wave signals coincident in time and direction with the neutrino events. No significant coincident events were observed. We place limits on the density of joint high energy neutrino - gravitational wave emission events in the local universe, and compare them with densities of merger and core-collapse events.

Keywords: gravitational waves / experiments, neutrino astronomy

ArXiv ePrint: 1205.3018

doi:10.1088/1475-7516/2013/06/008

Contents

JCAP06(2013)008

1 Introduction

Multi-messenger astronomy is entering a stimulating period with the recent development of experimental techniques that will open new windows of cosmic radiation observation in all its components. In particular, both high-energy ($\gg$ GeV) neutrinos (HENs) and gravitational waves (GWs), neither of which have yet been directly observed from astrophysical sources, are becoming new tools for exploring the Universe.

While HENs are expected to be produced in interactions between relativistic protons and the external radiation field of the source (e.g., [85, 146]), GWs carry information on the intricate multi-dimensional dynamics in the source's central regions (e.g., [58]). HENs and GWs are thus complementary messengers.

Simultaneous emission of GWs and HENs has been proposed in a range of cataclysmic cosmic events including gamma-ray bursts (GRBs), core-collapse supernovae (CCSNe), soft-gamma repeater outbursts (SGRs), and, potentially, cosmic string cusps in the early universe.

Observational constraints on HEN and GW emission from some of these phenomena have already been obtained. The IceCube collaboration recently placed limits on the HEN emission in GRBs [8, 10, 11], SGRs and blazars [13], and jet-driven CCSNe [12] using data from the IceCube detector at various levels of completion. Similarly, the ANTARES Collaboration has placed limits on the HEN flux from gamma-ray flaring blazars [25] and GRBs [24], as well as a diffuse muon neutrino flux from extragalactic sources [33]. These limits, however, do not yet strongly constrain HEN emission and ultra-high-energy cosmic-ray production in relativistic outflows [80, 85, 99]. The LIGO Scientific Collaboration and Virgo placed limits on the GW emission in GRBs [1, 6, 20] and SGRs [4, 15, 19]. The exclusion distances of these searches were, however, not sufficiently large to expect a GW detection.

The above HEN and GW searches used timing and sky location information from observations of events in the electromagnetic spectrum. A potentially large subset of GW and HEN sources may be intrinsically electromagnetically faint, dust-obscured, or missed by telescopes, but sufficiently luminous in GWs and HEN to be detected. Such sources may include, but are not limited to, partially or completely choked GRBs with, perhaps, only mildly relativistic jets [38, 113, 130, 143], relativistic shock breakout in compact CCSN progenitor stars [147], and cosmic string cusps [45, 59, 134].

Searches for HENs and GWs from such events have thus far relied on blind (i.e., untriggered) all-sky searches. An all-sky search for point sources of HENs in IceCube data was performed [13] and a similar study was carried out with ANTARES data [26]. LIGO and Virgo have carried out a number of all-sky searches for GWs. The most recent and most sensitive such search for model-independent GW bursts was published in [5], whereas the most recent allsky search for binary inspiral-merger can be found in [7]. All-sky model-dependent constraints on cosmic string GW emission have been placed [17]. The sensitivity of such blind all-sky searches is limited by a much larger background compared to searches based on timing and sky locations from electromagnetic observations.

A search for *temporally and spatially coincident* HEN and GW signals is a strong alternative to electromagnetically triggered or blind all-sky analyses that search for GWs or HENs individually. Such a search is independent of bias from electromagnetic observations, but still enjoys a much reduced background thanks to timing and sky location constraints. A similar idea has been used in the follow-up of candidate GW events by the low-energy neutrino detector LVD [29]. A joint GW-HEN search was first proposed in [39] and [127], and constraints on joint GW-HEN signals based on the interpretation of independent GW and HEN observational results were derived in [43]. Here we present the first direct search for coincident GW-HEN events, using data taken by the ANTARES HEN telescope and by the LIGO and Virgo GW observatories from January to September 2007. At this time, ANTARES was still under construction and operating with only 5 active lines. At the same time, the fifth LIGO science run (S5) and the first Virgo science run (VSR1) were carried out. This was the first joint run of the LIGO-Virgo network with the detectors operating near their design sensitivities.

The basic principle of the analysis presented here is that of a "triggered" search: HEN candidates are identified in the ANTARES data, then the GW data around the time of the HEN event are analyzed for a GW incident from the HEN estimated arrival direction. This method has been applied previously in searches for GWs associated with GRB triggers [6, 20]. It has been shown to have a distance reach up to a factor of 2 larger [6] than a blind all-sky search of the GW data, due to the reduced background. The expected rate of detections depends also on the beaming of the trigger signal, since the triggered search is only sensitive to the subset of sources oriented towards Earth. The comparison of the analysis method used in this paper to the LIGO-Virgo blind all-sky search [5] has been done in [144], and predicts a detection rate for the triggered search of between 0.1 and 6 times that of the blind search for beaming angles in the range 5°–30°. These numbers are broadly consistent with estimates for the special case of dedicated matched-filter searches for compact binary coalescence signals associated with short GRBs [e.g., 54, 63, 89, 116] after rescaling for a smaller distance improvement factor (typically $\sim$1.3, due to the better inherent background rejection of these specialised searches). In either case, most of the GW events found by the triggered search will be new detections not found by the all-sky blind search, illustrating the value of the triggered search even when the relative detection rate is low [144].

We analyze a total of 158 HEN events detected at times when two or more of the LIGO-Virgo detectors were operating. ANTARES is sensitive to HENs with energies greater than ~ 100 GeV [27]. The LIGO-Virgo analysis targets model-independent burst GW signals with durations $\lesssim 1$ s and frequencies in the 60 Hz to 500 Hz band. The GW search is extended in frequency up to 2000 Hz only for a subset of the HEN events, because the computational cost of such a search with the current GW analysis pipeline is prohibitive.

Statistical analyses of the HEN sample show no sign of associated GW bursts.

This paper is organized as follows. In section 2 we discuss sources of coincident HEN and GW emission and expected prospects for their detection. In section 3 we describe the ANTARES, LIGO, and Virgo detectors and the joint data taking period. Section 4 describes how the HEN sample was selected. Section 5 describes the search for GWs coincident in time and direction with the HEN events. We present the results of the search in section 6. We discuss the astrophysical implications of the results in section 7 and conclude with considerations of the potential for future joint GW-HEN searches.

2 Candidate sources for high-energy neutrino and gravitational wave emission

HEN emission is expected from baryon-loaded relativistic astrophysical outflows. In the most common scenario (e.g., [146]), Fermi-accelerated relativistic protons interact with high-energy outflow photons in $p\gamma$ reactions leading to pions or kaons, whose decay results in neutrinos, e.g., $\pi^+ \to \mu^+ + \nu_\mu \to e^+ + \nu_e + \bar{\nu}_\mu + \nu_\mu$, which is the dominant process (see, e.g., [149]). This gives $(\nu_e + \bar{\nu}_e : \nu_\mu + \bar{\nu}_\mu : \nu_\tau + \bar{\nu}_\tau)$ production ratios of $(1:2:0)$, changing to approximately

(1 : 1 : 1) at Earth due to flavor oscillations (e.g., [40]). The HEN spectrum depends on the spectrum of the accelerated protons (e.g., [8, 76, 85]) and, thus, on the properties of the astrophysical source. In this section, we provide estimates of the sensitivity of the 5-line ANTARES detector for HENs from the various potential sources by estimating the probability $P = X\%$ that at least one HEN is detected for a source at a given distance d_X.

GW emission occurs, at lowest and generally dominant order, via accelerated quadrupolar mass-energy dynamics. The coupling constant in the standard quadrupole formula for GW emission (e.g., [140]) is $Gc^{-4} \approx 10^{-49}\,\mathrm{s^2\,g^{-1}\,cm^{-1}}$ and the directly detectable GW strain scales with (distance)$^{-1}$. For example, a source at 10 Mpc needs a quadrupole moment of $\sim 1\,M_\odot \times (100\,\mathrm{km})^2$ that is changing on a millisecond timescale to be detectable by a GW detector sensitive to a strain of 10^{-21}. Equivalently, the minimum GW energy emission detectable by the LIGO-Virgo network at this distance is approximately $E_{\rm GW} \simeq 10^{-2}\,M_\odot c^2$ to $10\,M_\odot c^2$ for frequencies between 100 Hz and 1000 Hz [5].

In the following, we discuss a number of astrophysical scenarios in which both HENs and GWs may be emitted at detectable levels.

2.1 Canonical long gamma-ray bursts from massive stars

Long-duration GRBs (LGRBs; $T_{90} \gtrsim 2\,\mathrm{s}$; T_{90} is the time over which 90% of the γ counts are detected) are observationally implicated to be related to the collapse of massive stars normally leading to core-collapse supernova explosions [83, 110]. Typical LGRBs are strongly beamed and most likely have jets with Lorentz factors $\Gamma \gtrsim 100$ and isotropic equivalent luminosities of $10^{51}\,\mathrm{erg\,s^{-1}}$ to $10^{53}\,\mathrm{erg\,s^{-1}}$ [68, 107, 123]. LGRBs are detected at a rate of order 1/(few days) by γ-ray monitors on satellite observatories such as Swift/BAT [42, 69] and Fermi/GBM [46, 105]. It is important to note, however, that Swift/BAT and Fermi/GBM miss ∼90% and ∼40% of the prompt emission of all GRBs, respectively. This is due to limited fields of view, technical downtime, and orbital passes through the South Atlantic Anomaly. A nearby (say ∼10 Mpc) LGRB will have a bright multi-wavelength afterglow and may be accompanied by a CCSN (see section 2.2), but a significant fraction of local CCSNe may have been missed by CCSN surveys based on galaxy catalogs [104].

The central engine of LGRBs is expected to either be a *collapsar* (a black hole with an accretion disk; [103, 150]) or a *millisecond magnetar* (an extremely rapidly spinning, extremely magnetized neutron star; e.g., [109]). In both scenarios, HEN emission may result from a relativistic expanding fireball. HENs may begin to be produced even before the jet breaks out of the stellar envelope [128] and may continue well into the afterglow phase [112].

HEN emission from canonical LGRBs is expected to have appreciable flux for energies in the range 100 GeV to 100 TeV. For a LGRB at ∼50 Mpc (∼10 Mpc) one would expect of order 1 (100) HEN events in a km^3-scale water- or ice-Cherenkov detector (e.g., [8, 76, 85, 146]). Based on the flux predictions of [76], the probability for detection in the 5-line ANTARES detector can be estimated to be ∼50% for a source at 10 Mpc, which decreases to ∼2% for a source at 50 Mpc. Note that these are most likely optimistic estimates, since more detailed analyses suggest lower HEN fluxes from GRBs [e.g., 85].

The most extreme scenario for GW emission in LGRBs is dynamical fragmentation of a collapsing extremely rapidly differentially spinning stellar core into a coalescing system of two protoneutron stars [61, 93]. Such a scenario may be unlikely given model predictions for the rotational configuration of GRB progenitor stars [e.g., 151]. Its GW emission, however, would be very strong, leading to emitted energies $E_{\rm GW} \sim 10^{-2}\,M_\odot c^2$ to $10^{-1}\,M_\odot c^2$ in the 50 Hz to 1000 Hz frequency band of highest sensitivity of the initial LIGO/Virgo detectors, which could observe such an event out to approximately 20 Mpc to 40 Mpc [6, 7].

In more moderate scenarios backed by computational models, GW emission from LGRBs is likely to proceed, at least initially, in a very similar fashion as in a rapidly spinning CCSN [67, 95, 118]. If a black hole with an accretion disk forms, a second phase of GW emission may come from various hydrodynamic instabilities in the accretion disk [e.g., 92, 124, 141].

In the initial collapse of the progenitor star's core, a rapidly rotating protoneutron star is formed. In this process, a linearly-polarized GW signal is emitted with typical GW strains $|h| \sim 10^{-21}$ to 10^{-20} at a source distance of 10 kpc and emitted energies $E_{\rm GW} \sim 10^{-8}\,M_\odot c^2$ to $10^{-7}\,M_\odot c^2$ between 100 Hz and 1000 Hz [64, 120]. This part of the GW signal will only be detectable for Galactic events and is thus not relevant here.

In its early evolution, the protoneutron star (or protomagnetar, depending on its magnetic field) may be spinning near breakup. This can induce various rotational instabilities that induce ellipsoidal deformations of the protoneutron star, leading to strong, quasi-periodic, elliptically-polarized GW emission [55, 66, 67, 118, 131]. A typical GW strain for a deformed protoneutron star of $1.4\,M_\odot$ and radius of 12 km, spinning with a period of 1 ms may be $h \sim \text{few} \times 10^{-22}$ at 10 Mpc. If the deformation lasted for 100 ms, $E_{\rm GW} \sim 10^{-1}\,M_\odot c^2$ would be emitted at 2000 Hz [66].

In the collapsar scenario, accretion onto the protoneutron star eventually leads to its collapse to a spinning black hole [117]. This and the subsequent ringdown of the newborn black hole leads to a GW burst at few $\times\,10^2$ Hz to few $\times\,10^3$ Hz with $h \sim 10^{-20}$ at 10 kpc and $E_{\rm GW} \sim 10^{-7}\,M_\odot c^2$. It is thus detectable only for a Galactic source [119].

More interesting are hydrodynamic instabilities in the accretion disk/torus that forms after seconds of hyperaccretion onto the newborn black hole. The inner parts of the disk are hot, efficiently neutrino cooled and thus thin [e.g., 126] while the outer regions are inefficiently cooled and form a thick accretion torus. Gravitational instability may lead to fragmentation of this torus into one or multiple overdense regions that may could condense to neutron-star-like objects and then inspiral into the central black hole [124]. For a source at 10 Mpc, a $1M_\odot$ fragment and a $8M_\odot$ central black hole, this would yield strains of $h \sim \text{few} \times 10^{-22}$ and emitted energies in the most sensitive band of $\sim 10^{-3}\,M_\odot c^2$ to $10^{-2}\,M_\odot c^2$.

The accretion torus may be unstable to the Papaloizou-Pringle instability or to co-rotation-type instabilities [121, 122]. $h \sim 10^{-21}$ to 10^{-20} was estimated in [92] for a source at 10 Mpc and GW frequencies of 100 Hz to 200 Hz for a $m = 1$ — dominated non-axisymmetric disk instability in a disk around a $10\,M_\odot$ black hole. This corresponds to $E_{\rm GW}$ of order $10^{-2}\,M_\odot c^2$ to $10^{-1}\,M_\odot c^2$.

In the speculative suspended accretion model for GRB accretion disks [141], low-order turbulence powered by black-hole spindown may emit strong GWs. In the frequency domain, this results in an anti-chirp behavior, since most of the emission is expected to occur near the innermost stable orbit, which moves out in radius as the black hole is spun down. Simple estimates suggest GW strains $h \sim 10^{-21}$ at 10 Mpc and frequencies in the 100 Hz to 1000 Hz band. Depending on the initial black hole spin, $E_{\rm GW}$ could be of order $1\,M_\odot c^2$.

2.2 Low-luminosity GRBs and engine-driven supernovae

Low-luminosity GRBs (LL-GRBs; also frequently referred to as X-ray flashes) form a subclass of long GRBs with low γ-ray flux (e.g., [57, 83, 110]). LL-GRBs are much more easily missed by observations than LGRBs (see section 2.1) and the small observable volume (due

to their low luminosity) suggests an event rate that may be significantly higher than the rate of canonical LGRBs [52, 97, 100, 135, 142]. Five of the seven GRBs that have been unambigously associated with a CCSN are LL-GRBs [83, 110, 152]. Moreover, all GRB-CCSNe are highly energetic and of the spectroscopic type Ic-bl subclass. Ic indicates a compact hydrogen/helium poor progenitor star and the postfix -bl stands for "broad line," because they have relativistically Doppler-broadened spectral features.

Type Ic-bl CCSNe occur also without LL-GRB or LGRB, but are frequently identified as *engine-driven CCSNe* that exhibit luminous radio emission [e.g., 135, 136].

Theory suggests (e.g., [50, 51, 90, 96]) that the transition between engine-driven CCSNe, LL-GRBs with CCSNe, and canonical LGRBs may be continuous. All are likely to be driven by a central engine that launches a collimated bipolar jet-like outflow and their variety may simply depend on the power output and duration of central engine operation [50, 96]. The power output of the engine determines the energy of the jet and its Lorentz factor. The duration of the central engine's operation determines if the jet can leave the progenitor star and make a normal LGRB. If it fails to emerge, the LGRB is "choked" and a more isotropic energetic CCSN explosion is likely to result. As suggested by [50], the relativistic shock breakout through the stellar surface could then be responsible for a LL-GRB.

The GW emission processes that may be active in LL-GRBs and engine-driven CCSNe are most likley very similar to the LGRB case discussed in section 2.1 and we shall not consider them further here. HEN emission is expected from the entire range of stellar collapse outcomes involving relativistic flows. Since LL-GRBs and engine-driven CCSNe are most likely much more frequent that canonical LGRBs, much effort has been devoted to understanding the HEN emission from such events [38, 84, 108, 112, 113, 128–130, 143, 147]. It is worthwhile to consider the probability of detection of HENs in the 5-line ANTARES detector from LL-GRBs and engine-driven CCSNe, in which mildly relativistic jets are likely to be involved. The detection probability depends strongly on the energy and the Lorentz factor of the jet. Using the reference parameters of [38], $\Gamma = 3$ and $E_{\rm jet} = E_0 \approx 3 \times 10^{51}$ erg, the detection probability is ∼50% at $d_{50} = 1\,$Mpc.

2.3 Mergers and short gamma-ray bursts

Short-duration GRBs (SGRBs; $T_{90} \lesssim 2\,$s) are rarer than LGRBs and expected to result from double neutron star (NS-NS) and/or neutron star - black hole (BH-NS) mergers [e.g., 68, 114]. The isotropic equivalent energy of SGRBs is 2 to 3 orders of magnitude smaller than the energy of LGRBs. Their jets have most likely lower Lorentz factors of $\Gamma \sim 10$ to 50 and wider opening angles. Due to their short duration and low isotropic equivalent energy, SGRBs are much easier to miss observationally than LGRBs and their observable volume is much smaller.

The efficiency of HEN emission in SGRBs depends on the efficiency of proton acceleration, the γ-ray flux, and the SGRB variability time scale [114]. For a simple estimate of the detection probability in the 5-line ANTARES detector, one may resort to the HEN flux estimates of [76] (but see [85] for refined results). Assuming a jet with $\Gamma = 300$, $E_{\rm jet} = 2 \times 10^{50}$ erg, one finds a distance $d_{10} \sim 10\,$Mpc at which the probability of HEN detection by the 5-line ANTARES detector is 10%. Hence, only the closest and/or the most powerful SGRBs may be detectable.

The GW emission from NS-NS and BH-NS mergers is well studied [see 65, 133, for reviews]. Most of the emission comes from the late inspiral and merger phase during which the binary sweeps through the 50 Hz to 1000 Hz band of highest sensitivity of LIGO/Virgo. The total emitted $E_{\rm GW}$ is of order $10^{-2}\,M_\odot c^2$ to $10^{-1}\,M_\odot c^2$. At the time of this analysis the LIGO/Virgo network had maximum sensitive distances of ∼30 Mpc for equal-mass NS-NS binaries and ∼50 Mpc for a BH-NS binary with a mass ratio of 4 : 1, and a dedicated merger search on this data did not find any evidence for GW candidates [2].

2.4 Bursting magnetars

Soft-gamma repeaters (SGRs) and anomalous X-ray pulsars are X-ray pulsars with quiescent soft ($2 - 10\,$keV) periodic X-ray emissions with periods ranging from 5 to 10 s. They exhibit repetitive outbursts lasting ∼0.1 s which reach peak luminosities of $\sim 10^{42}\,{\rm erg\,s^{-1}}$ in X-rays and γ-rays. There are a number of known SGRs and anomalous X-ray pulsars [86, 106], some of which have had rare hard spectrum giant flares with luminosities of up to $10^{47}\,{\rm erg\,s^{-1}}$. The favoured model for these objects is a magnetar, a neutron star with an extreme magnetic field of $B \sim 10^{15}\,$G. Giant flares are believed to be caused either by magnetic stresses fracturing the magnetar crust and leading to a large-scale rearrangement of the internal field [139] or by a large-scale rearrangement of the magnetospheric field due to magnetic reconnection [70, 102]. The sudden release of energy and magnetic field rearrangement lead to the creation and acceleration of pair plasma that may have some baryon loading, thus leading to the emission of HENs in $p\gamma$ reactions [78]. The detectability of the 2004 giant are of the Galactic SGR 1806-20 by HEN detectors was estimated in [88]: detectors such as IceCube and ANTARES should detect multiple HEN events from similar Galactic SGR eruptions, provided the baryon loading is sufficiently high. The AMANDA-II detector, which was operating during the giant flare of SGR 1806-20, did not detect HENs [23]. A search of IceCube data for HENs from regular (non-giant) Galactic SGR flares also found no significant coincident events [13]. Estimates based on [88] for the 5-line ANTARES detector show that, $d_{50} \approx 200\,$kpc for baryon-rich flares, suggesting that similar flares could be detected from anywhere within the Galaxy.

Significant emission of GWs in SGR giant flares may come from the potential excitation of nonradial pulsational modes with kHz-frequencies in the magnetar [62]. Theoretical upper limits on the possible strength of the GW emission were placed by [87] and [56], based on the the energy reservoir associated with a change in the magnetic potential energy of the magnetar. They found an upper limit for the emitted GW energy of $10^{-7}\,M_\odot c^2$ to $10^{-6}\,M_\odot c^2$, which can be probed by the LIGO/Virgo network for a Galactic source [4, 15]. However, studies that investigated the excitation of magnetar pulsational modes in more detail suggest much weaker emission that may not be detectable even with advanced-generation GW observatories [98, 153].

2.5 Cosmic string kinks and cusps

Cosmic strings are topological defects that may form in the early Universe and are predicted by grand unified theories and superstring theory [e.g., 91, 125]. Cosmic strings form initially as smooth loops, but through interactions and self-interactions may develop kinks and cusps [e.g., 125]. The kinks and cusps decay, which is expected to lead to ultra-high energy cosmic ray emission with energies in excess of $\sim 10^{11}\,$GeV and up to the Planck scale [47, 82], including ultra-high-energy neutrinos (UHENs; e.g., [37, 45, 101]) and GW bursts [e.g., 59, 60, 111, 134].

While not designed specifically for UHENs, HEN detectors like ANTARES and IceCube have some sensitivity to UHENs in the $\gtrsim 10^{11}\,$GeV energy range. Up to a few events per year for a km^3-scale detector are predicted in [35], depending on details of the underlying

emission model. Since Earth is opaque to UHENs, downgoing events must be selected. Since we are only considering ANTARES data for neutrinos that have passed through Earth (see section 3.1), the present data set does not contain any potential UHEN events.

The search for very energetic HENs performed with one year of IceCube-40 data did not reveal any neutrinos in the 10^6 GeV to 10^9 GeV energy range [9], but no limits on UHENs were reported. A number of dedicated UHEN experiments exist, including ANITA [71], NuMoon [132] and others, but have not yet constrained many emission scenarios from cosmic strings [e.g., 101].

The rate of GW bursts from a network of cosmic strings depends on the string tension and other network parameters, and individual bursts may be detectable with advanced detectors [60, 134]. The burst shape is expected to be generic, so that matched-filtering GW analysis approaches may be employed. A first search for GW bursts from cosmic string cusps in 15 days of LIGO data from early 2005 did not reveal any candidate events [17].

3 GW and HEN detectors

3.1 The ANTARES neutrino telescope

Since the Earth acts as a shield against all particles except neutrinos, a neutrino telescope mainly uses the detection of upgoing muons as a signature of muon-neutrino charged-current interactions in the matter around the detector. The ANTARES detector (Astronomy with a Neutrino Telescope and Abyss environmental RESearch) is currently the only deep sea high-energy-neutrino telescope and is operating in the Northern hemisphere [28]. The telescope covers an area of about 0.1 km^2 on the sea bed, at a depth of 2475 m, 40 km off the coast of Toulon, France. The detector is a three-dimensional array of photomultiplier tubes (PMTs) [30], hosted in pressure resistant glass spheres, called optical modules (OMs) [36]. In its full configuration, it is composed of 12 detection lines, each comprising up to 25 triplets of PMTs, storeys, regularly distributed along 350 m, the first storey being located 100 m above the sea bed. The first detection line was installed and connected in early 2006; the second line was put in operation in September 2006 and three more lines were connected in January 2007, so that a total of 5 lines were taking data in 2007. Five additional lines, together with an instrumentation line (containing an ensemble of oceanographic sensors dedicated to the measurement of environmental parameters), were connected by the end of 2007. The telescope reached its nominal configuration, with 12 lines immersed and taking data, in May 2008.

The three-dimensional grid of PMTs is used to measure the arrival time and position of Cherenkov photons induced by the passage of relativistic charged particles through the sea water. This information, together with the characteristic emission angle of the light (about 43 degrees), is used to determine the direction of the muon and hence infer that of the incident neutrino. The accuracy of the direction information allows to distinguish upgoing muons, produced by neutrinos, from the overwhelming background from downgoing muons, produced by cosmic ray interactions in the atmosphere above the detector [32]. Installing the detector at great depths serves to attenuate this background and also allows to operate the PMTs in a dark environment. At high energies the large muon range makes the sensitive volume of the detector significantly greater than the instrumented volume. By searching for upgoing muons, the total ANTARES sky coverage is 3.5π sr, with most of the Galactic plane being observable and the Galactic Center being visible 70% of the sidereal day.

3.2 Network of interferometers

3.2.1 LIGO

LIGO is a network of interferometric gravitational wave detectors consisting of three interferometers in the U.S.A.. These detectors are all kilometer-scale power-recycled Michelson laser interferometers with orthogonal Fabry-Perot arms [18] able to detect the quadrupolar strain in space produced by the GW. Multiple reflections between mirrors located at the end points of each arm extend the effective optical length of each arm, and enhance the sensitivity of the instrument.

There are two LIGO observatories: one located at Hanford, WA and the other at Livingston, LA. The Hanford site houses two interferometers: one with 4 km arms, denoted H1, and a second with 2 km arms, denoted H2. The Livingston observatory has one 4 km interferometer, L1. The observatories are separated by a distance of 3000 km, corresponding to a time-of-flight separation of 10 ms.

The LIGO instruments are designed to detect gravitational waves with frequencies ranging from ~ 40 Hz to several kHz, with a maximum sensitivity near 150 Hz (see figure 1). In fact, seismic noise dominates at lower frequencies and the sensitivity at intermediate frequencies is determined mainly by thermal noise, with contributions from other sources. Above ~ 200 Hz, laser shot noise corrected for the Fabry-Perot cavity response yields an effective strain noise that rises linearly with frequency. The average sensitivities of the H1 and L1 detectors during the second year of the S5 run were about 20% better than the first-year averages, while the H2 detector had about the same average sensitivity in both years.

3.2.2 Virgo

The Virgo detector, V1, is in Cascina near Pisa, Italy. It is a 3 km long power-recycled Michelson interferometer with orthogonal Fabry Perot arms [21]. The main instrumental difference with respect to LIGO is the seismic isolation system based on super-attenuators [48], chains of passive attenuators capable of filtering seismic disturbances. The benefit from super-attenuators is a significant reduction of the detector noise at very low frequency (<40 Hz) where Virgo surpasses the LIGO sensitivity. During 2007, above 300 Hz, the Virgo detector had sensitivity similar to the LIGO 4 km interferometers, while above 500 Hz it is dominated by shot noise, see figure 1.

The time-of-flight separation between the Virgo and Hanford observatories is 27 ms, and 25 ms between Virgo and Livingston. Due to the different orientation of its arms, the angular sensitivity of Virgo is complementary to that of the LIGO detectors, Virgo therefore enhances the sky coverage of the network. Moreover, simultaneous observations of multiple detectors are crucial to reject environmental and instrumental effects.

At the time of writing the LIGO and Virgo interferometers are undergoing upgrades to "advanced" configurations with distance sensitivity improved by approximately a factor of 10 [79]. The advanced instruments will commence operations around 2015.

3.3 Joint data taking periods

The fifth LIGO science run, S5 [14], was held from 2005 November 4 to 2007 October 1. Over one year of science-quality data were collected with all three LIGO interferometers in simultaneous operation at their design sensitivity, with duty factors of 75%, 76%, and 65% for H1, H2, and L1. The Virgo detector started its first science run, VSR1 [22], on 2007

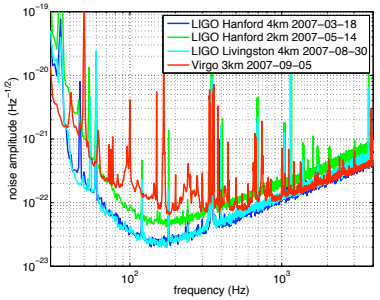

Figure 1. Noise amplitude spectral densities of the four LIGO and Virgo detectors during S5.

May 18. The Virgo duty factor over VSR1 was 78%. During this period, ANTARES was operating in its 5 line configuration. The concomitant set of ANTARES 5-line (5L), VSR1 and S5 data covers the period between January 27 and September 30, 2007; these data are the subject of the analysis presented here.

4 Selection of HEN candidates

4.1 HEN data sample

The ANTARES data sample used in the analysis is composed of runs from 2007 selected according to various quality criteria, based mainly on environmental parameters (e.g. sea current, counting rates), configuration and behaviour of the detector during the given run (e.g. duration of the run, alignment of the detector). Two basic quantities are used to characterise the counting rate of a given OM: the baseline rate (^{40}K activity and bioluminescence) and the burst fraction (flashes of light emitted by marine organisms). The baseline rate represents the most probable counting rate of a given OM computed from the rate distributions in each PMT over the whole run (typically a few hours). The burst fraction corresponds to the fraction of time during which the OM counting rates exceed by more than 20% the estimated baseline. The data selected for this search are required to have a baseline rate below 120 kHz and a burst fraction lower than 40%, with 80% of all OMs being active. With these quality criteria, the active time is 103.4 days out of the 244.8 days of the 5-line period. Finally, when restricting the data to the concomitant period with LIGO/Virgo, the remaining equivalent time of observation is $T_{\rm obs} = 91$ days.

4.2 Trigger levels

The ANTARES trigger system is multi-level [31]. The first level is applied *in situ*, while the remaining levels intervene after all data are sent to the shore station and before being written on disk. Trigger decisions are based on calculations done at three levels. The first trigger level, L0, is a simple threshold of about 0.3 photo-electron (pe) equivalent charge applied to the analog signal of the PMT. The second level trigger, L1, is based on two coincident L0 hits in the same storey within 20 ns or hits with large charge (≥ 3 pe or 10 pe depending on the configuration). The L2 trigger requires the presence of at least five L1 hits in a 2.2 μs time window (roughly the maximum muon transit time across the detector) and that each pair of

L1 hits are causally related according to the following condition: $\Delta t_{ij} \leq d_{ij} n/c + 20$ ns. Here Δt_{ij} and d_{ij} are the time difference and distance between hits i and j, c is the speed of light in vacuum and n is the index of refraction.

4.3 Reconstruction strategy

Hits selected according to the criteria described in section 4.2 are then combined to reconstruct tracks using their arrival time and charge as measured by the corresponding OM. Muons are assumed to cross the detector at the speed of light along a straight line from which the induced Cherenkov light originates. The time and charge information of the hits in the PMTs is used in a minimisation procedure to obtain the track parameters, namely, its direction (θ, ϕ) and the position (x_0, y_0, z_0) of one track point at a given time t_0. The reconstruction algorithm used for this analysis is a fast and robust method [34] which was primarily designed to be used on-line.

4.3.1 Description of the algorithm

The algorithm is based on a χ^2-minimisation approach. Its strict hit selection leads to a high purity up-down separation while keeping a good efficiency. The exact geometry of the detector is ignored: the detector lines are treated as straight and the 3 OMs of each storey are considered as a single OM centered on the line. Thus, the hit's altitude corresponds to the optical modules altitude. All hits at the same floor in coincidence within 20 ns are merged into one hit. The time of the merged hit is that of the earliest hit in the group and its charge is the sum of the charges. The algorithm uses the L1 hits as a seed for the hit selection. It requests a coincidence of 2 L1 hits in two adjacent floors within 80 ns or 160 ns in two next-to-adjacent floors. The quality of the reconstruction is measured by a χ^2-like variable with *NDF* degrees of freedom, based on the time differences between the hit times t_i and the expected arrival time t_i^γ of photons from the track or bright-point (see section 4.4). The quality function is then extended with a term that accounts for measured hit charges q_i and the calculated photon travel distances d_i^γ:

$$\chi^2 = \frac{1}{NDF} \sum_{i=1}^{N_{\rm hit}} \left[\frac{\Delta t_i^2}{\sigma_i^2} + \frac{Q(q_i)}{\bar{q}} \frac{D(d_i^\gamma)}{d_0} \right]. \tag{4.1}$$

In this expression, σ_i is the timing error, set to 10 ns for charges larger than 2.5 pe and to 20 ns otherwise. $\Delta t_i = t_i^\gamma - t_i$ is the time residuals between the hit time t_i and the expected arrival time of the photons t_i^γ from the muon track. In the second term, $\bar{q}$ is the average hit charge calculated from all hits which have been selected for the fit and $d_0 = 50$ m is the typical distance at which the signal in one PMT from a Cherenkov light front is of the order of 1 pe. The function $Q(q_i)$ accounts for the angular acceptance of the OMs, while $D(d_i^\gamma)$ penalises large amplitude hits originating from large distance tracks. A proper cut on the fit quality parameter allows the isolation of a high purity neutrino sample, which is crucial in the subsequent analysis.

4.3.2 Azimuthal degeneracy of the reconstruction

For a particle trajectory reconstructed from a Cherenkov cone giving hits on only two straight detector lines, there always exists an alternative trajectory having an identical χ^2 value, but a different direction. The degenerate trajectory is the mirror image of the original track in the plane formed by the two lines. As a consequence, each event reconstructed with only two

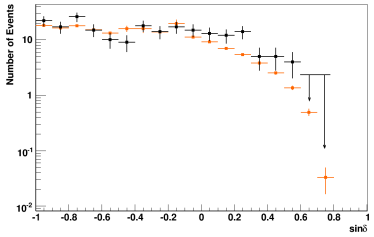

Figure 2. Distribution of the sine of the declination δ of selected events (black points), compared to Monte-Carlo expectations (sum of atmospheric muons and atmospheric neutrinos, orange (or grey) points).

lines will have two equiprobable arrival directions, which must be taken into account during the subsequent GW analysis.

4.4 Criteria for HEN event selection

The initial sample of reconstructed events contains both upgoing neutrino induced muons and downgoing muons from cosmic ray interactions in the atmosphere. Some of the atmospheric muons are misreconstructed as upgoing and the selection cuts, based on Monte-Carlo simulations, are devised to reduce this contamination so as to maximise the discovery potential. A minimum of 6 hits on at least 2 lines are required to reconstruct a track. Only upgoing tracks are kept for further analysis. Quality cuts are then applied based on two quantities computed according to equation (4.1). The first parameter used, χ^2_t, is the quality factor associated with the reconstructed particle track, whereas the second one, χ^2_b, is associated with a bright-point, light emitted from a point-like source inside the detector. This rejects events from large electromagnetic showers, likely to appear in downgoing muon bundles for instance.

A cut on χ^2_b reduces the number of such events and decreases the contribution of misreconstructed muons in the background. Further cuts are applied on χ^2_t depending on the arrival direction of the candidate - the muon contamination increases close to the horizon - which reduce the fraction of misreconstructed muons to less than 20% over the whole sample, while optimising the sensitivity (see section 4.6 and [77]).

Figure 2 shows the distribution of the sine of the declination of the events selected with the final cuts, which is globally consistent with background.

4.5 Angular error

The distribution of the space angle Ω between the true neutrino arrival direction and the reconstructed muon track can be described by a log-normal distribution:

$$P(\Omega) = \frac{1}{\sqrt{2\pi}} \frac{e^{-\frac{1}{2\sigma_0^2}\left(\ln\left(\frac{\Omega-\theta_0}{m_0}\right)\right)^2}}{(\Omega-\theta_0)\,\sigma_0}\,, \tag{4.2}$$

where θ_0 is a location parameter, σ_0 is related to the shape of the distribution and m_0 is a scaling parameter. In all cases for our study, the location parameter θ_0 is close to zero,

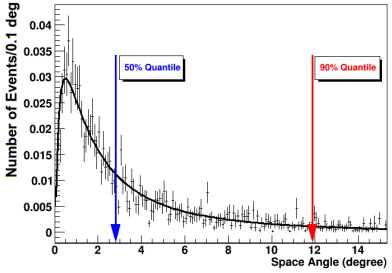

Figure 3. Example of space angle distribution with the associated fit to equation (4.2) obtained with a sample of Monte-Carlo HEN events, for a given declination and a given number of hits. The arrows indicate the 50^{th} (median) and the 90^{th} percentiles of the distribution. The distribution is normalised to unity.

and $(\Omega - \theta_0) > 0$ is always satisfied. This distribution depends on the energy associated to the track (estimated through the number of photons detected) and its declination. This parametrisation is used during the GW search to compute the significance of a hypothetical signal for the scanned directions inside the angular search window centred around the reconstructed neutrino arrival direction. Figure 3 shows an example of distribution of the space angle for a sample of Monte Carlo neutrinos with an E^{-2} spectrum, together with the best-fit parametrisation and the 50^{th} and 90^{th} percentiles of the distribution.

One of the main variables to describe the performance of a neutrino telescope is the angular resolution, defined as the median of the distribution of the angle between the true neutrino direction and the reconstructed track, also indicated in figure 3. This number is estimated from simulations.

For those events of our selected sample reconstructed with at least three lines the angular resolution is, assuming an E^{-2} energy spectrum, $\sim 2.5°$ at 100 GeV, improving to 1° around 100 TeV. For 2-line events, when selecting the reconstructed track closer to the true direction, the angular accuracy varies between 3° at low energy (100 GeV) and 2.5° at high energy (100 TeV).

We define the angular search window for the GW analysis as the 90^{th} percentile of the distribution, also indicated in figure 3; this window lies between 5° and 10° for 3-line events, depending on declination, and between 10° and 15° for 2-line events.

We note that the typical angular distance between galaxies within 10 Mpc is a few degrees [148], much smaller than the typical size of the 90^{th} percentile error region for our HEN events. This implies that we can associate a potential host galaxy to any of the HEN candidates if it turns out to be of cosmic origin.

4.6 Analysis sensitivity and selected HEN candidates

The limit-setting potential of the analysis, or sensitivity, has been quantified for the whole 5 line data period. Specifically, the sensitivity is defined as the median 90% upper limit obtained over an ensemble of simulated experiments with no true signal. The sensitivity depends on the declination of the potential source. For our sample and assuming an E^{-2}

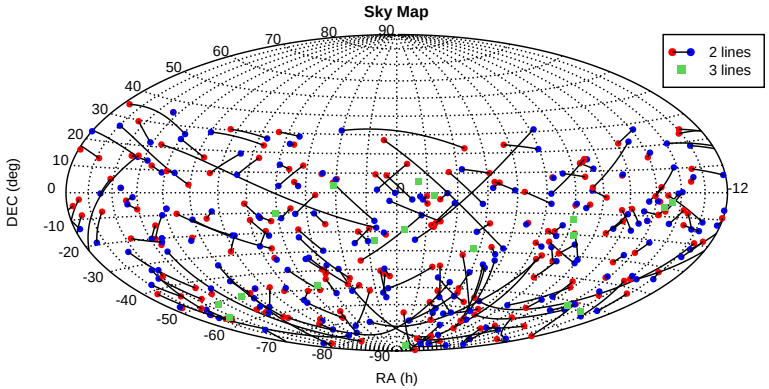

Figure 4. Skymap of the selected 216 HEN events in equatorial coordinates. A line connects the associated mirror solutions for events reconstructed with two lines as described in section 4.3.2.

steady flux, using the selection criteria described, the best sensitivity has been estimated to be $E^2 \frac{dN}{dE} \approx 10^{-6}\,\mathrm{GeV\,cm^{-2}\,s^{-1}}$. This best sensitivity is reached below $-47°$; i.e., at declinations which are always below the horizon at the latitude of ANTARES (43°N).

With the selection previously described, 181 runs corresponding to 104 days of live time were kept for the analysis. The selection has been divided into events reconstructed with 2 lines and events with at least 3 lines. Each of the mirror solutions for 2 line events will be searched for possible counterparts in the subsequent GW analysis. This results in 216 neutrinos to be analysed: 198 with two possible directions and 18 reconstructed with at least 3 lines. Figure 4 is a sky map of the candidate HEN events, where the degenerate solutions for 2 line events can be seen.

Of these HEN events, 158 occurred at times when at least two gravitational-wave detectors were operating. Since two or more detectors are required to discriminate GW signals from background noise (as described in section 5.2), in the following we consider only these remaining 158 HEN candidates: 144 2-line events and 14 3-line events.[1]

Finally, we note that IceCube operated in its 22-string configuration for part of 2007 [13]. However, this data was only used for time-dependent searches applied to source directions with observed X-ray or gamma-ray emission, such as GRBs; there were no untriggered, time-dependent searches over the sky. Furthermore, a comparison of ANTARES and IceCube sensitivities in 2007 indicates that the bulk of our HEN neutrino triggers come from declinations (the southern sky) such that it is unlikely that IceCube could have detected the source independently.

[1]Details of each of the HEN candidate events are given at https://dcc.ligo.org/cgi-bin/DocDB/ShowDocument?docid=p1200006.

5 GW search method

5.1 Search procedure

One of the simplest searches that may be performed combining GW and HEN data is a triggered analysis that scans GW data around the time of the putative neutrino event by cross-correlating data from pairs of detectors. This search exploits knowledge of the time and direction of the neutrino event to improve the GW search sensitivity. We use the X-Pipeline algorithm [137], which has been used in similar searches for GWs associated with GRBs [6, 20]. X-Pipeline performs a coherent analysis of data from arbitrary networks of gravitational wave detectors, while being robust against background noise fluctuations. Each trigger is analysed independently of the others, with the analysis parameters optimised based on background noise characteristics and detector performance at the time of that trigger, thereby maximising the search sensitivity.

5.2 GW event analysis

In our GW search, a neutrino candidate event is characterised by its arrival time, direction, and angular search window (and mirror-image window, for the 2-line events). Also important is the range of possible time delays (both positive and negative) between the neutrino emission and the associated gravitational-wave emission. This quantity is referred to as the *on-source* window for the neutrino; it is the time interval which is searched for GW signals. We use a symmetric on-source window of $\pm 496\,\mathrm{s}$ [41], which is conservative enough to encompass most theoretical models of GW and HEN emission. The maximum expected time delay between GWs and HENs due to a non-zero mass effect for either particle is much smaller than the coincidence windows used.

The basic search procedure follows that used in [20]. All detectors operating at the time of the trigger and which pass data-quality requirements are used for the GW search. The data from each detector are first whitened and time-delayed according to the sky location being analysed so that a GW signal from that direction would appear simultaneous in each data stream. The data are then Fourier transformed to produce time-frequency maps. The maps are summed coherently (using amplitude and phase) with weighting determined by each detector's frequency-dependent sensitivity and response to the sky location in question; the weightings are chosen to maximise the signal-to-noise ratio expected for a circularly polarized GW signal,[2] which is the expected polarisation for a GW source observed from near the rotational axis [94]. A threshold is placed on the map to retain the largest 1% of pixels by energy (squared amplitude). Surviving pixels are grouped using next-nearest-neighbours clustering; each cluster of pixels is considered as a candidate GW event. The event cluster is assigned a combined energy by summing the energy values of its constituent pixels; this combined energy is used as the ranking statistic for the events.

In addition to the marginalised circular polarization sum, a second ranking statistic is computed based on a maximum-likelihood analysis of the event assuming power-law distributed background noise with no assumption on the GW polarization. In practice this statistic is often found to provide signal-noise separation due to the non-Gaussian nature of the GW detector noise. Other combinations of the data are also constructed. Of particular importance are "null" combinations designed to cancel out the GW signal from the given

[2]Empirically it is found that the circular polarisation restriction also improves the overall detection probability for *linearly* polarised GWs, as the resulting background reduction outweighs the impact of rejecting some linearly polarised GWs.

JCAP06(2013)008

sky location; comparison to corresponding "incoherent" combinations provides powerful tests for identifying events due to background noise fluctuations [53], and are described in detail in [145]. Events are also characterised by their duration, central time, bandwidth, and central frequency.

The time-frequency analysis is repeated for Fourier transform lengths of 1/128, 1/64, 1/32, 1/16, 1/8, 1/4 s, to maximise the sensitivity to GW signals of different durations. It is also repeated over a grid of sky positions covering the 90% containment region of the HEN. This grid is designed such that the maximum relative timing error between any pair of GW detectors is less that 0.5 ms. When GW events from different Fourier transforms lengths or sky positions overlap in time-frequency, the highest-ranked event is kept and the others discarded. Finally, the events are decimated to a rate of 0.25 Hz before being written to disk.

This time-frequency analysis is performed for all of the data in the ± 496 s on-source window. To estimate the significance of the resulting GW candidates, the same analysis is repeated for all coincident data in the *off-source* window, defined as all data within ± 1.5 hours of the neutrino time, excluding the on-source interval. The same set of detectors and data-quality requirements as in the on-source analysis are used for the off-source data. These off-source data provide a sample of background that does not contain any signal associated with the neutrino event, but with statistical features similar to the data searched in association with the neutrino. To enlarge the background sample, we also repeat the off-source analysis after applying time shifts of multiples of 6 s to the data from one or more detectors; with such time slides we were able to produce $O(10^3)$ background trials for each HEN.

Finally, the analysis is repeated after "injecting" (adding) simulated GW signals to the on-source data. The amplitudes and morphologies tested are discussed in section 6.3.1. We use these simulations to optimise and assess the sensitivity of the search, as discussed below.

5.3 GW search optimisation

The sensitivity of searches for gravitational-wave bursts tends to be limited by the presence of non-Gaussian fluctuations of the background noise, known as glitches. To reduce this background, events that overlap in time within known instrumental and/or environmental disturbances are discarded. In addition to this "veto" step, GW consistency tests comparing the coherent and incoherent energies are applied to each event [145]. These tests are applied to the on-source, off-source and injection events; events failing one or more of these tests are discarded. The thresholds are optimised by testing a preset range of thresholds and selecting those which give the best overall detection efficiency at a fixed false alarm probability of 1% when applied to a random sample of background and injection events (the on-source events are *not* used; i.e., this is a blind analysis). These tests also determine which of the two ranking statistics discussed in section 5.2 (based on circularly polarized GW energy or powerlaw noise) gives the better detection efficiency; the winner is selected as the final ranking statistic.

Once the thresholds have been fixed, these consistency tests are applied to the on-source events and to the remaining off-source and injection events (those not used for tuning). The surviving on-source event with the largest significance (highest energy or powerlaw statistic) is taken to be the best candidate for a gravitational wave signal and is referred to as the loudest event [49]. All surviving on-source events are assigned a false alarm probability by comparison to the distribution of loudest events from the off-source trials. Any on-source event with probability $p < 0.01$ is subjected to additional checks to try to determine the origin of the event and additional background time slide trials are performed to improve the accuracy of the false alarm probability estimate.

After the p values have been determined for the loudest events associated with each of the 158 HEN events, the collective set of p values is tested for consistency with the null hypothesis (no GW signal) using the binomial test, discussed in section 6.2. We also set a frequentist upper limit on the strength of gravitational waves associated with each neutrino trigger, as discussed in section 6.3.

5.4 Low-frequency and high-frequency GW analyses

Given our knowledge of possible GW sources discussed in section 2, the most likely detectable signals at extra-galactic distances are in the low-frequency band ($f \lesssim 500$ Hz), where our detectors have maximum sensitivity, see figure 1. At the same time, the computational cost of the X-Pipeline analysis increases at high frequencies. This is due in part to the extra data to be analysed, but also to the need for finer-resolution sky grids to keep time delay errors much smaller than one GW period. We therefore split the gravitational wave band into two regions: 60 Hz to 500 Hz and 500 Hz to 2000 Hz. The low-frequency band is analysed for all HEN events — such a search is computationally feasible while covering the highest-sensitivity region of the GW detectors. However, compact objects such as neutron stars or collapsar cores have characteristic frequencies for GW emission above 500 Hz. Such emissions might be detectable from Galactic sources such as soft gamma repeater giant flares, or possibly from nearby galaxies. Since the computational cost of a high-frequency search for all HEN events is prohibitive with the current analysis pipeline, we perform the 500 Hz to 2000 Hz analysis on the 3-line HEN events only. The 3-line events are a small subset (∼10%) of the total trigger list and have the smallest sky position uncertainties, and therefore the smallest computational cost for processing. To reduce the computational cost further, we use the same sky grid for the high-frequency search as was used at low frequencies, after determining that the loss of sensitivity is acceptable. The high-frequency analysis is performed independently of the low-frequency analysis (independent tuning, background estimation, etc.) using the identical automated procedure. In the following sections we will present the results of the low- frequency and high-frequency searches separately.

6 Coincident search results

6.1 Per-HEN GW candidates

We analysed GW data in coincidence with 158 neutrino candidates for the low frequency search, and 14 neutrino events for the high frequency search. In the low frequency analysis, only one neutrino trigger had a corresponding GW event with false alarm probability below the threshold of $p = 0.01$ to become a candidate event. We found no candidates in the high frequency search. For the low-frequency candidate, additional time shifts totaling 18064 background trials yielded a refined false alarm probability of $p = 0.004$, which is not significant given a trials factor of 158 (this statement is quantified below). This event came from analysis of the H1, H2, and V1 data; follow-up checks were performed, including checks of detector performance at the time as indicated by monitoring programs and operator logs, and scans of data from detector and environmental monitoring equipment to look for anomalous behaviour. While these checks did not uncover a physical cause for the event, they did reveal that it occurred during a glitching period in V1. We conclude that we have no clear gravitational wave burst signal associated with any of our sample of 158 neutrino events.

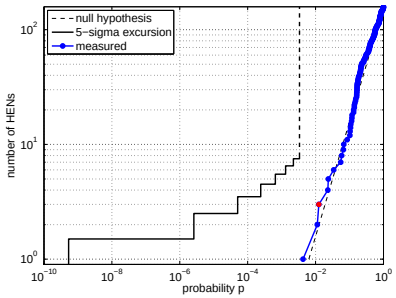

Figure 5. Distribution of observed p values for the loudest GW event associated with each neutrino analysed in the low frequency analysis. The red dot indicates the largest deviation of the low p tail from the uniform distribution null hypothesis; this occurs due to having the three loudest events below $p_3 \sim 0.013$. Deviations this large or larger occur in approximately 64% of experiments under the null hypothesis. The black line shows the threshold for a 5-sigma deviation from the null hypothesis.

6.2 Search for a cumulative excess: binomial test

A quantitative analysis of the significance of any candidate gravitational-wave event must take account of the trials factor due to the number of neutrino events analysed. We use the binomial test, which has been applied in previous GRB-triggered GW searches [16, 20]. Under the null hypothesis, the false alarm probabilities p for each HEN loudest event are expected to be uniformly distributed between 0 and 1. The binomial test compares the measured p values to the null distribution to determine if there is a statistically significant excess of (one or more) small p values which may be due to gravitational wave signals.

Briefly, the binomial test sorts the set of N measured loudest event probabilities in ascending order: $p_1 \leq p_2 \leq p_3 \leq \ldots \leq p_N$. For each $i \in [1, N_{\rm tail}]$ we compute the binomial probability $P_{\geq i}(p_i)$ of getting i or more events with p values $\leq p_i$:

$$P_{\geq i}(p_i) = \sum_{k=i}^{N} \frac{N!}{(N-k)!k!} p_i^k (1-p_i)^{N-k} \,. \tag{6.1}$$

Here N is the number of HEN events analysed (158 in the 60 Hz to 500 Hz band and 14 in the 500 Hz to 2000 Hz band), and $N_{\rm tail}$ is the number of the smallest p values we wish to test. We choose $N_{\rm tail}$ to be 5% of N; i.e., $N_{\rm tail} = 8$ for the low frequency band and $N_{\rm tail} = 1$ for the high frequency band.

The lowest $P_{\geq i}(p_i)$ for $i \in [1, N_{\rm tail}]$ is taken as the most significant deviation from the null hypothesis. To assess the significance of the deviation, we repeat the test using p values drawn from a uniform distribution and count the fraction of such trials which give a lowest $P_{\geq i}(p_i)$ smaller than that computed from the true measured p values.

Figures 5 and 6 show the cumulative distribution of p values measured in the low- and high-frequency analyses. In both cases the measured p values are consistent with the null hypothesis.

JCAP06(2013)008

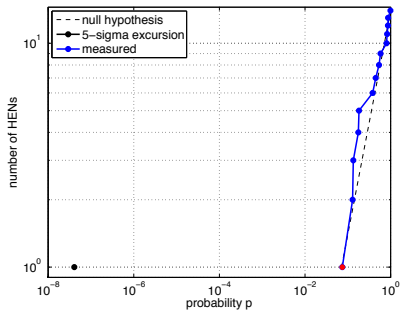

Figure 6. Distribution of observed p values for the loudest GW event associated with each neutrino analysed in the high frequency analysis. The red dot indicates the largest deviation of the low p tail from the uniform distribution null hypothesis; since $N_{\rm tail} = 1$, this is constrained to occur for p_1. Deviations this large or larger occur in approximately 66% of experiments under the null hypothesis. The black dot shows the threshold for a 5-sigma deviation from the null hypothesis.

6.3 GW upper limits

The sensitivity of the GW search is determined by a Monte-Carlo analysis. For each neutrino trigger, we add simulated GW signals to the on-source data and repeat the analysis described in section 5.2. We consider a simulated signal detected if it produces an event louder than the loudest on-source event after all event tests have been applied. We define a 90% confidence level lower limit on the distance to the source as the maximum distance $D_{90\%}$ such that for any distance $D \leq D_{90\%}$ the probability of detection is 0.9 or greater.

6.3.1 Injected waveforms

As in GRB-triggered searches, we use a mix of *ad hoc* and astrophysically motivated GW waveforms. The *ad hoc* waveforms are Gaussian-modulated sinusoids:

$$h_+ = \frac{(1+\cos^2\iota)}{2} \frac{h_{\rm rss}}{(2\pi\tau^2)^{\frac{1}{4}}} e^{-\frac{(t-t_0)^2}{4\tau^2}} \cos 2\pi f_0 (t-t_0) \,, \tag{6.2}$$

$$h_\times = \cos\iota \frac{h_{\rm rss}}{(2\pi\tau^2)^{\frac{1}{4}}} e^{-\frac{(t-t_0)^2}{4\tau^2}} \sin 2\pi f_0 (t-t_0) \,. \tag{6.3}$$

Here f_0 is the central frequency, t_0 is the central time, and τ is the duration parameter. This waveform is consistent with the GW emission from a rotating system viewed from an inclination angle ι to the rotational axis. We select the inclination uniformly in $\cos\iota$ with $\iota \in [0°, 5°]$. This corresponds to a nearly on-axis system, such as would be expected for association with an observed long GRB. We chose $\tau = 1/f_0$, and use central frequencies of 100 Hz, 150 Hz, and 300 Hz for the low-frequency analysis and 554 Hz and 1000 Hz for the high-frequency search. The quantity $h_{\rm rss}$ is the root-sum-square signal amplitude:

$$h_{\rm rss} \equiv \sqrt{\int \left(h_+^2(t) + h_\times^2(t)\right) dt} \,. \tag{6.4}$$

JCAP06(2013)008

For the small values of ι considered here ($\iota < 5°$) this amplitude is related to the total energy $E_{\rm GW}$ in a narrow-band gravitational-wave burst by

$$E_{\rm GW} \simeq \frac{2}{5}\frac{\pi^2 c^3}{G} h_{\rm rss}^2 f_0^2 D^2 \,. \tag{6.5}$$

For astrophysical injections we use the gravitational-wave emission of inspiraling neutron star and black hole binaries, which are widely thought to be the progenitors of short GRBs. Specifically, we use the post-Newtonian model for the inspiral of a double neutron star system with component masses $m_1 = m_2 = 1.35 M_\odot$, and the one for a black-hole - neutron-star system with $m_1 = 5 M_\odot$, $m_2 = 1.35 M_\odot$. We set the component spins to zero in each case. Motivated by estimates of the jet opening angle for short GRBs, we select the inclination uniformly in $\cos\iota$ with $\iota \in [0°, 30°]$.

For each HEN trigger, the injections are distributed uniformly in time over the on-source window. The injection sky positions are selected randomly following the estimated probability distribution (4.2) for the HEN trigger, to account for the uncertainty in the true HEN direction of incidence. The polarization angle (orientation of the rotational axis on the sky) is distributed uniformly. Finally, the amplitude and arrival time at each detector is perturbed randomly to simulate the effect of calibration errors in the LIGO and Virgo detectors.

6.3.2 Exclusion distances

For each waveform type we set a 90% confidence level lower limit on the distance to a GW source associated with a given HEN trigger.[3] This is defined as the maximum distance $D_{90\%}$ such that for any distance $D \leq D_{90\%}$ there is a probability of at least 0.9 that such a GW signal would have produced an event louder than the loudest on-source event actually measured. For inspirals, each distance corresponds to a well-defined amplitude. We can associate an amplitude to each distance for the sine-Gaussian waveforms as well, by assuming a fixed energy in gravitational waves. For concreteness, we select $E_{\rm GW} = 10^{-2} M_\odot c^2$. This corresponds to the optimistic limit of possible gravitational-wave emission by various processes in the collapsing cores of rapidly rotating massive stars ([66, 67, 93, 124], and discussion in section 2); more conservative estimates based on simulations have been made in [64, 118, 119, 131, 138].

For each type of gravitational wave simulated, the distributions of exclusion distances for our neutrino sample are shown in figures 7 and 8. For binary neutron star systems of $(1.35 - 1.35) M_\odot$ and black hole - neutron star systems of $(5 - 1.35) M_\odot$ typical distance limits are 5 Mpc and 10 Mpc respectively. For the sine-Gaussian waveforms with $E_{\rm GW} = 10^{-2} M_\odot c^2$ we find typical distance limits between 5 Mpc and 17 Mpc in the low-frequency band and of order 1 Mpc in the high-frequency band. For other $E_{\rm GW}$ the limits scale as $D_{90\%} \propto (E_{\rm GW}/10^{-2} M_\odot c^2)^{1/2}$. For example, for $E_{\rm GW} = 10^{-8} M_\odot c^2$ (typical of core-collapse supernovae) a signal would only be observable from a Galactic source.

7 Astrophysical implications

Observational constraints on joint sources of GW and HEN signals have been derived in [43]. However, they are based on the interpretation and the combination of previously published and independent GW and HEN observational results. The results presented in this section are the first derived from a joint GW-HEN analysis, using concomitant data obtained with LIGO/Virgo and ANTARES.

[3] Upper limits for each waveform and HEN trigger are available at https://dcc.ligo.org/cgi-bin/DocDB/ShowDocument?docid=p1200006.

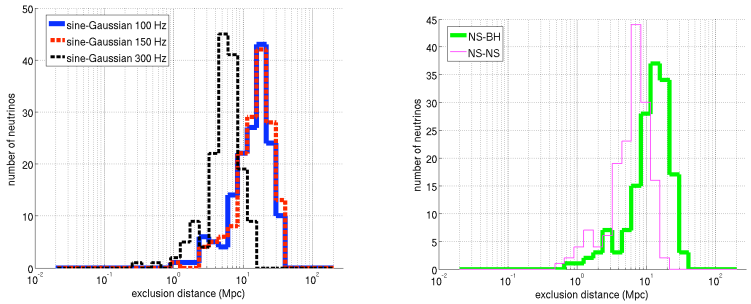

Figure 7. Low-frequency analysis: the top plot is the histogram for the sample of analysed neutrinos of the distance exclusions at the 90% confidence level for the 3 types of sine-Gaussian models considered: 100 Hz, 150 Hz and 300 Hz. A standard siren gravitational wave emission of $E_{GW} = 10^{-2}\, M_\odot\, c^2$ is assumed. The bottom plot shows the distance exclusions for the 2 families of binary inspiral models considered: NS-NS and BH-NS.

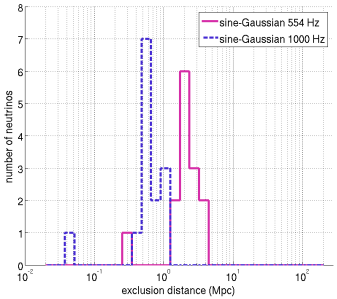

Figure 8. High-frequency analysis: the histogram for the sample of analysed neutrinos of the distance exclusions at the 90% confidence level for the 2 frequencies of circular sine-Gaussian models considered: 554 Hz and 1000 Hz.

7.1 Upper limits on GW-HEN populations

The present search for GW and HEN correlations in space and time revealed no evidence for coincident events. This implies a 90% confidence level upper limit on the rate of detectable coincidences of $2.3/T_{\rm obs}$, where $T_{\rm obs} \approx 90$ days is the duration of coincident observations. This can be expressed as a limit on the rate density (number per unit time per unit volume) $\rho_{\text{GW-HEN}}$ of joint GW-HEN sources:

$$\rho_{\text{GW-HEN}} \leq \frac{2.3 \mathcal{F}_b}{V T_{\rm obs}} \,. \tag{7.1}$$

Here $\mathcal{F}_b$ is the beaming factor (the ratio of the total number of sources to the number with jets oriented towards Earth[4]), and V is the volume of universe probed by the present analysis for typical GW-HEN sources.

We take as fiducial sources two classes of objects: the final merger phase of the coalescence of two compact objects (short GRB-like), or the collapse of a massive object (long GRB-like), both followed by the emission of a relativistic hadronic jet. We define the HEN horizon as the distance for which the probability to detect at least 1 HEN in ANTARES with 5 lines is 50%. In the case of short GRBs (SGRBs), the HEN horizon is estimated to be $d_{50} = 4\,\mathrm{Mpc}$ using [76], while the typical GW horizon from the inspiral model is 5 Mpc to 10 Mpc depending on the binary masses. For long GRBs (LGRB) the HEN horizon increases to $d_{50} = 12\,\mathrm{Mpc}$ using [76]. The GW emission associated with long GRBs is highly uncertain; our optimistic assumption of $E_{\mathrm{GW}} = 10^{-2} M_{\odot} c^2$ at low frequencies gives a typical horizon distance of 10 Mpc to 20 Mpc in GW. Using the lower of the GW and HEN distances in each case yields from equation (7.1) approximate limits on the population density. For SGRB-like sources, related to the merger of two compact objects, we find $\rho^{\mathrm{SGRB}}_{\text{GW-HEN}} \lesssim \mathcal{F}_b \times 10^{-2}\,\mathrm{Mpc}^{-3}\,\mathrm{yr}^{-1}$. For LGRB-like sources, related to the collapse of massive stars, we find $\rho^{\mathrm{LGRB}}_{\text{GW-HEN}} \lesssim \mathcal{F}_b E_{0.01}^{-3/2} \times 10^{-3}\,\mathrm{Mpc}^{-3}\,\mathrm{yr}^{-1}$, where $E_{0.01} \equiv E_{\mathrm{GW}}/10^{-2} M_{\odot} c^2$.

7.2 Comparison of limits with existing estimates

After correcting for beaming effects, a local rate density of SGRBs of $\rho_{\mathrm{SGRB}} \sim 10^{-7}\mathrm{Mpc}^{-3}\mathrm{yr}^{-1}$ to $10^{-6}\,\mathrm{Mpc}^{-3}\mathrm{yr}^{-1}$ is suggested in [72], [115], and [74]. This is similar to the abundance of binary neutron star mergers, their assumed progenitors, estimated to be $\rho_{\text{NS-NS}} \sim 10^{-8}$ $\mathrm{Mpc}^{-3}\,\mathrm{yr}^{-1}$ to $10^{-5}\,\mathrm{Mpc}^{-3}\,\mathrm{yr}^{-1}$ [see for example 3], and well below the reach of the present search ($\rho^{\mathrm{SGRB}}_{\text{GW-HEN}} \lesssim \mathcal{F}_b \times 10^{-2}\,\mathrm{Mpc}^{-3}\,\mathrm{yr}^{-1}$). With $T_{\mathrm{obs}} = 1\,\mathrm{yr}$, an improvement of a factor 10 on the detection distance is required in order to begin constraining the fraction of mergers producing coincident GW−HEN signals.

A total rate of long GRBs of $\rho_{\mathrm{LGRB}} \sim 3 \times 10^{-8}\,\mathrm{Mpc}^{-3}\,\mathrm{yr}^{-1}$ is estimated in [73], after correcting for beaming effects; these sources are closely related to Type II and Type Ibc core-collapse supernovae. The local rate of SNIbc is $\rho_{\mathrm{SNIbc}} \sim 2 \times 10^{-5}\,\mathrm{Mpc}^{-3}\,\mathrm{yr}^{-1}$ [75], whereas $\rho_{\mathrm{SNII}} \sim 2 \times 10^{-4}\,\mathrm{Mpc}^{-3}\,\mathrm{yr}^{-1}$ [44], relatively close to the obtained limit $\rho^{\mathrm{LGRB}}_{\text{GW-HEN}} \lesssim \mathcal{F}_b E_{0.01}^{-3/2} \times 10^{-3}\,\mathrm{Mpc}^{-3}\,\mathrm{yr}^{-1}$ under our optimistic assumptions of GW emission in this scenario. A factor 10 only is required in order to begin constraining the fraction of stellar collapse events producing coincident weakly beamed GW-HEN signals, which translates into a required improvement of 2 on the detection distance.

8 Conclusions

This first joint GW-HEN search using 2007 data, obtained with the ANTARES HEN telescope and the Virgo/LIGO GW interferometers, opens the way to a novel multi-messenger astronomy. Limits on the rate density $\rho_{\text{GW-HEN}}$ of joint GW-HEN emitting systems were extracted for the first time using the analysis of coincident GW-HEN data. We note that these limits are consistent with the ones obtained in [43] derived from independent GW-HEN observations. More stringent limits will be available by performing similar coincidence analyses using other data sets provided by the same instruments.

[4]For example, for a jet opening angle of 5° gives $\mathcal{F}_b \sim 300$, while 30° gives $\mathcal{F}_b \sim 10$.

For instance, the sixth LIGO science run S6 and second and third Virgo science runs VSR2,3 covered the period from 7 July 2009 to 21 October 2010. Meanwhile, the ANTARES telescope has taken data with first 10 then 12 active lines since the end of December 2007. Their enhanced sensitivities should permit a combined analysis to gain the factor required to obtain $\rho^{\mathrm{LGRB}}_{\text{GW-HEN}} \leq \rho_{\text{SNII/SNIbc}}$ and begin to constrain the fraction of stellar collapse events accompanied by the coincident emission of relativistic jets beamed towards Earth. The analysis of these data is underway, and a similar analysis using data from the LIGO/Virgo S5-VSR1 periods and the IceCube HEN telescope in its 22 string configuration is being finalized.

Future observing runs involving IceCube, KM3NeT [81], and the advanced LIGO and advanced Virgo projects [79], are likely to coincide as well. They will give other opportunities to look for potential coincident GW-HEN emissions.

Acknowledgments

The authors gratefully acknowledge the support of the United States National Science Foundation for the construction and operation of the LIGO Laboratory, the Science and Technology Facilities Council of the United Kingdom, the Max-Planck-Society, and the State of Niedersachsen/Germany for support of the construction and operation of the GEO600 detector, and the Italian Istituto Nazionale di Fisica Nucleare and the French Centre National de la Recherche Scientifique for the construction and operation of the Virgo detector. The authors also gratefully acknowledge the support of the research by these agencies and by the Australian Research Council, the International Science Linkages program of the Commonwealth of Australia, the Council of Scientific and Industrial Research of India, the Istituto Nazionale di Fisica Nucleare of Italy, the Spanish Ministerio de Educación y Ciencia, the Conselleria d'Economia Hisenda i Innovació of the Govern de les Illes Balears, the Foundation for Fundamental Research on Matter supported by the Netherlands Organisation for Scientific Research, the Polish Ministry of Science and Higher Education, the FOCUS Programme of Foundation for Polish Science, the Royal Society, the Scottish Funding Council, the Scottish Universities Physics Alliance, The National Aeronautics and Space Administration, the Carnegie Trust, the Leverhulme Trust, the David and Lucile Packard Foundation, the Research Corporation, and the Alfred P. Sloan Foundation.

The authors also acknowledge the financial support of the funding agencies for the construction and operation of the ANTARES neutrino telescope: Centre National de la Recherche Scientifique (CNRS), Commissariat à l'énergie atomique et aux énergies alternatives (CEA), Agence National de la Recherche (ANR), Commission Européenne (FEDER fund and Marie Curie Program), Région Alsace (contrat CPER), Région Provence-Alpes-Cote d'Azur, Département du Var and Ville de La Seyne-sur-Mer, France; Bundesministerium für Bildung und Forschung (BMBF), Germany; Istituto Nazionale di Fisica Nucleare (INFN), Italy; Stichting voor Fundamenteel Onderzoek der Materie (FOM), Nederlandse organisatie voor Wetenschappelijk Onderzoek (NWO), the Netherlands; Council of the President of the Russian Federation for young scientists and leading scientific schools supporting grants, Russia; National Authority for Scientific Research (ANCS), Romania; Ministerio de Ciencia e Innovacion (MICINN), Prometeo of Generalitat Valenciana (GVA) and Multi-Dark, Spain. They also acknowledge the technical support of Ifremer, AIM and Foselev Marine for the sea operation and the CC-IN2P3 for the computing facilities. This publication has been assigned LIGO Document Number LIGO-P1200006.

JCAP06(2013)008

References

[1] LIGO scientific collaboration, Virgo collaboration, J. Abadie et al., *Search for gravitational-wave inspiral signals associated with short Gamma-Ray Bursts during LIGO's fifth and Virgo's first science run*, *Astrophys. J.* **715** (2010) 1453 [arXiv:1001.0165] [INSPIRE].

[2] LIGO scientific collaboration, Virgo collaboration, J. Abadie et al., *Search for Gravitational Waves from Compact Binary Coalescence in LIGO and Virgo Data from S5 and VSR1*, *Phys. Rev.* **D 82** (2010) 102001 [arXiv:1005.4655] [INSPIRE].

[3] LIGO scientific collaboration, Virgo collaboration, J. Abadie et al., *Predictions for the Rates of Compact Binary Coalescences Observable by Ground-based Gravitational-wave Detectors*, *Class. Quant. Grav.* **27** (2010) 173001 [arXiv:1003.2480] [INSPIRE].

[4] Virgo collaboration, J. Abadie et al., *Search for Gravitational Wave Bursts from Six Magnetars*, *Astrophys. J.* **734** (2011) L35 [arXiv:1011.4079] [INSPIRE].

[5] LIGO scientific collaboration, Virgo collaboration, J. Abadie et al., *All-sky search for gravitational-wave bursts in the second joint LIGO-Virgo run*, *Phys. Rev.* **D 85** (2012) 122007 [arXiv:1202.2788] [INSPIRE].

[6] LIGO scientific collaboration, J. Abadie et al., *Search for gravitational waves associated with gamma-ray bursts during LIGO science run 6 and Virgo science runs 2 and 3*, *Astrophys. J.* **760** (2012) 12 [arXiv:1205.2216] [INSPIRE].

[7] LIGO scientific collaboration, Virgo collaboration, J. Abadie et al., *Search for Gravitational Waves from Low Mass Compact Binary Coalescence in LIGO's Sixth Science Run and Virgo's Science Runs 2 and 3*, *Phys. Rev.* **D 85** (2012) 082002 [arXiv:1111.7314] [INSPIRE].

[8] IceCube collaboration, R. Abbasi et al., *Search for muon neutrinos from Gamma-Ray Bursts with the IceCube neutrino telescope*, *Astrophys. J.* **710** (2010) 346 [arXiv:0907.2227] [INSPIRE].

[9] IceCube collaboration, R. Abbasi et al., *Constraints on the Extremely-high Energy Cosmic Neutrino Flux with the IceCube 2008-2009 Data*, *Phys. Rev.* **D 83** (2011) 092003 [*Erratum ibid.* **D 84** (2011) 079902] [arXiv:1103.4250] [INSPIRE].

[10] IceCube collaboration, R. Abbasi et al., *Limits on Neutrino Emission from Gamma-Ray Bursts with the 40 String IceCube Detector*, *Phys. Rev. Lett.* **106** (2011) 141101 [arXiv:1101.1448] [INSPIRE].

[11] IceCube collaboration, R. Abbasi et al., *An absence of neutrinos associated with cosmic-ray acceleration in γ-ray bursts*, *Nature* **484** (2012) 351 [arXiv:1204.4219] [INSPIRE].

[12] IceCube collaboration, ROTSE collaboration, R. Abbasi et al., *Searching for soft relativistic jets in Core-collapse Supernovae with the IceCube Optical Follow-up Program*, *Astron. Astrophys.* **539** (2012) A60 [arXiv:1111.7030] [INSPIRE].

[13] IceCube collaboration, R. Abbasi et al., *Time-Dependent Searches for Point Sources of Neutrinos with the 40-String and 22-String Configurations of IceCube*, *Astrophys. J.* **744** (2012) 1 [arXiv:1104.0075] [INSPIRE].

[14] LIGO scientific collaboration, B. Abbott et al., *Beating the spin-down limit on gravitational wave emission from the Crab pulsar*, *Astrophys. J.* **683** (2008) L45 [*Erratum ibid.* **706** (2009) L203-L204] [arXiv:0805.4758] [INSPIRE].

[15] LIGO scientific collaboration, B. Abbott et al., *Search for Gravitational Wave Bursts from Soft Gamma Repeaters*, *Phys. Rev. Lett.* **101** (2008) 211102 [arXiv:0808.2050] [INSPIRE].

[16] LIGO scientific collaboration, B. Abbott et al., *Search for gravitational waves associated with 39 gamma-ray bursts using data from the second, third and fourth LIGO runs*, *Phys. Rev.* **D 77** (2008) 062004 [arXiv:0709.0766] [INSPIRE].

[17] LIGO scientific collaboration, B. Abbott et al., *First LIGO search for gravitational wave bursts from cosmic (super)strings*, *Phys. Rev.* **D 80** (2009) 062002 [arXiv:0904.4718] [INSPIRE].

[18] LIGO scientific collaboration, B. Abbott et al., *LIGO: The Laser interferometer gravitational-wave observatory*, *Rept. Prog. Phys.* **72** (2009) 076901 [arXiv:0711.3041] [INSPIRE].

[19] LIGO scientific collaboration, B. Abbott et al., *Stacked Search for Gravitational Waves from the 2006 SGR 1900+14 Storm*, *Astrophys. J.* **701** (2009) L68 [arXiv:0905.0005] [INSPIRE].

[20] Virgo collaboration, B. Abbott et al., *Search for gravitational-wave bursts associated with gamma-ray bursts using data from LIGO Science Run 5 and Virgo Science Run 1*, *Astrophys. J.* **715** (2010) 1438 [arXiv:0908.3824] [INSPIRE].

[21] VIRGO collaboration, T. Accadia et al., *Virgo: a laser interferometer to detect gravitational waves*, 2012 *JINST* **7** P03012 [INSPIRE].

[22] F. Acernese et al., *Status of Virgo*, *Class. Quant. Grav.* **25** (2008) 114045.

[23] IceCube collaboration, A. Achterberg et al., *Limits on the high-energy gamma and neutrino fluxes from the SGR 1806-20 giant flare of December 27th, 2004 with the AMANDA-II detector*, *Phys. Rev. Lett.* **97** (2006) 221101 [astro-ph/0607233] [INSPIRE].

[24] ANTARES collaboration, S. Adrián-Martínez et al., *Contributions to the 32nd International Cosmic Ray Conference (ICRC 2011) by the ANTARES collaboration*, in *Proceedings of the 32th International Cosmic-Ray Conference*, arXiv:1112.0478 (2011).

[25] ANTARES collaboration, S. Adrián-Martínez et al., *Search for Neutrino Emission from Gamma-Ray Flaring Blazars with the ANTARES Telescope*, *Astropart. Phys.* **36** (2012) 204 [arXiv:1111.3473] [INSPIRE].

[26] ANTARES collaboration, S. Adrián-Martínez et al., *Search for Cosmic Neutrino Point Sources with Four Year Data of the ANTARES Telescope*, *Astrophys. J.* **760** (2012) 53 [arXiv:1207.3105] [INSPIRE].

[27] ANTARES collaboration, S. Adrián-Martínez et al., *Measurement of Atmospheric Neutrino Oscillations with the ANTARES Neutrino Telescope*, *Phys. Lett.* **B 714** (2012) 224 [arXiv:1206.0645] [INSPIRE].

[28] ANTARES collaboration, M. Ageron et al., *ANTARES: the first undersea neutrino telescope*, *Nucl. Instrum. Meth.* **A 656** (2011) 11 [arXiv:1104.1607] [INSPIRE].

[29] M. Aglietta, P. Antonioli, G. Bari, C. Castagnoli, W. Fulgione et al., *Search for low energy neutrino in correlation with the 8 events observed by the EXPLORER and NAUTILUS detectors in 2001*, *Astron. Astrophys.* **421** (2004) 399 [astro-ph/0403207] [INSPIRE].

[30] ANTARES collaboration, J. Aguilar et al., *Study of large hemispherical photomultiplier tubes for the antares neutrino telescope*, *Nucl. Instrum. Meth.* **A 555** (2005) 132 [physics/0510031] [INSPIRE].

[31] ANTARES collaboration, J. Aguilar et al., *The data acquisition system for the ANTARES Neutrino Telescope*, *Nucl. Instrum. Meth.* **A 570** (2007) 107 [astro-ph/0610029] [INSPIRE].

[32] ANTARES collaboration, J. Aguilar et al., *Zenith distribution and flux of atmospheric muons measured with the 5-line ANTARES detector*, *Astropart. Phys.* **34** (2010) 179 [arXiv:1007.1777] [INSPIRE].

[33] ANTARES collaboration, J. Aguilar et al., *Search for a diffuse flux of high-energy ν_μ with the ANTARES neutrino telescope*, *Phys. Lett.* **B 696** (2011) 16 [arXiv:1011.3772] [INSPIRE].

JCAP06(2013)008

JCAP06(2013)008

[34] ANTARES collaboration, J. Aguilar et al., *A fast algorithm for muon track reconstruction and its application to the ANTARES neutrino telescope*, *Astropart. Phys.* **34** (2011) 652 [arXiv:1105.4116] [INSPIRE].

[35] J. Alvarez-Muniz and F. Halzen, *10^{20} eV cosmic ray and particle physics with kilometer scale neutrino telescopes*, *Phys. Rev.* **D 63** (2001) 037302 [astro-ph/0007329] [INSPIRE].

[36] ANTARES collaboration, P. Amram et al., *Sedimentation and fouling of optical surfaces at the antares site*, *Astropart. Phys.* **19** (2003) 253 [astro-ph/0206454] [INSPIRE].

[37] L. Anchordoqui and F. Halzen, *IceHEP high energy physics at the south pole*, *Annals Phys.* **321** (2006) 2660 [hep-ph/0510389] [INSPIRE].

[38] S. Ando and J.F. Beacom, *Revealing the supernova-gamma-ray burst connection with TeV neutrinos*, *Phys. Rev. Lett.* **95** (2005) 061103 [astro-ph/0502521] [INSPIRE].

[39] Y. Aso, Z. Marka, C. Finley, J. Dwyer, K. Kotake et al., *Search method for coincident events from LIGO and IceCube detectors*, *Class. Quant. Grav.* **25** (2008) 114039 [arXiv:0711.0107] [INSPIRE].

[40] H. Athar, C. Kim and J. Lee, *The Intrinsic and oscillated astrophysical neutrino flavor ratios*, *Mod. Phys. Lett.* **A 21** (2006) 1049 [hep-ph/0505017] [INSPIRE].

[41] B. Baret, I. Bartos, B. Bouhou, A. Corsi, I. Di Palma et al., *Bounding the Time Delay between High-energy Neutrinos and Gravitational-wave Transients from Gamma-ray Bursts*, *Astropart. Phys.* **35** (2011) 1 [arXiv:1101.4669] [INSPIRE].

[42] S. Barthelmy, L. Barbier, J. Cummings, E. Fenimore, N. Gehrels et al., *The Burst Alert Telescope (BAT) on the Swift MIDEX mission*, *Space Sci. Rev.* **120** (2005) 143 [astro-ph/0507410] [INSPIRE].

[43] I. Bartos, C. Finley, A. Corsi and S. Marka, *Observational Constraints on Multi-messenger Sources of Gravitational Waves and High-energy Neutrinos*, *Phys. Rev. Lett.* **107** (2011) 251101 [arXiv:1108.3001] [INSPIRE].

[44] G. Bazin, N. Palanque-Delabrouille, J. Rich, V. Ruhlmann-Kleider, E. Aubourg et al., *The Core-collapse rate from the Supernova Legacy Survey*, *Astron. Astrophys.* **499** (2009) 653 [arXiv:0904.1066] [INSPIRE].

[45] V. Berezinsky, E. Sabancilar and A. Vilenkin, *Extremely High Energy Neutrinos from Cosmic Strings*, *Phys. Rev.* **D 84** (2011) 085006 [arXiv:1108.2509] [INSPIRE].

[46] P.N. Bhat et al., *The GLAST Burst Monitor*, in *AIP Conf. Ser., Vol. 727, Gamma-Ray Bursts: 30 Years of Discovery*, E. Fenimore and M. Galassi eds. (2004), pg. 684.

[47] P. Bhattacharjee, *Cosmic Strings and Ultrahigh-Energy Cosmic Rays*, *Phys. Rev.* **D 40** (1989) 3968 [INSPIRE].

[48] S. Braccini, L. Barsotti, C. Bradaschia, G. Cella, A. Di Virgilio et al., *Measurement of the seismic attenuation performance of the VIRGO superattenuator*, *Astropart. Phys.* **23** (2005) 557 [INSPIRE].

[49] P.R. Brady, J.D. Creighton and A.G. Wiseman, *Upper limits on gravitational-wave signals based on loudest events*, *Class. Quant. Grav.* **21** (2004) S1775 [gr-qc/0405044] [INSPIRE].

[50] O. Bromberg, E. Nakar and T. Piran, *Are low luminosity GRBs generated by relativistic jets?*, *Astrophys. J. Lett.* **739** (2011) L55 [arXiv:1107.1346] [INSPIRE].

[51] A. Burrows, L. Dessart, E. Livne, C.D. Ott and J. Murphy, *Simulations of Magnetically-Driven Supernova and Hypernova Explosions in the Context of Rapid Rotation*, *Astrophys. J.* **664** (2007) 416 [astro-ph/0702539] [INSPIRE].

[52] R. Chapman, N.R. Tanvir, R.S. Priddey and A.J. Levan, *How common are long Gamma-Ray Bursts in the Local Universe?*, *Mon. Not. Roy. Astron. Soc. Lett.* **382** (2007) L21 [arXiv:0708.2106] [INSPIRE].

[53] S. Chatterji, A. Lazzarini, L. Stein, P.J. Sutton, A. Searle et al., *Coherent network analysis technique for discriminating gravitational-wave bursts from instrumental noise*, *Phys. Rev.* **D 74** (2006) 082005 [gr-qc/0605002] [INSPIRE].

[54] H.-Y. Chen and D.E. Holz, *GRB beaming and gravitational-wave observations*, arXiv:1206.0703 [INSPIRE].

[55] A. Corsi and P. Mészáros, *GRB afterglow plateaus and Gravitational Waves: multi-messenger signature of a millisecond magnetar?*, *Astrophys. J.* **702** (2009) 1171 [arXiv:0907.2290] [INSPIRE].

[56] A. Corsi and B.J. Owen, *Maximum gravitational-wave energy emissible in magnetar flares*, *Phys. Rev.* **D 83** (2011) 104014 [arXiv:1102.3421] [INSPIRE].

[57] D.M. Coward, *Simulating a faint gamma-ray burst population*, *Mon. Not. Roy. Astron. Soc. Lett.* 360 (2005) L77 [astro-ph/0504493] [INSPIRE].

[58] J.D.E. Creighton and W.G. Anderson, *Gravitational-Wave Physics and Astronomy: An Introduction to Theory, Experiment and Data Analysis*, Wiley-VCH, Hoboken, NJ, U.S.A. (2011).

[59] T. Damour and A. Vilenkin, *Gravitational wave bursts from cosmic strings*, *Phys. Rev. Lett.* **85** (2000) 3761 [gr-qc/0004075] [INSPIRE].

[60] T. Damour and A. Vilenkin, *Gravitational wave bursts from cusps and kinks on cosmic strings*, *Phys. Rev.* **D 64** (2001) 064008 [gr-qc/0104026] [INSPIRE].

[61] M.B. Davies, A. King, S. Rosswog and G. Wynn, *Gamma-ray bursts, supernova kicks and gravitational radiation*, *Astrophys. J.* **579** (2002) L63 [astro-ph/0204358] [INSPIRE].

[62] J.A. de Freitas Pacheco, *Do soft gamma repeaters emit gravitational waves?* *Astron. Astrophys.* **336** (1998) 397.

[63] A. Dietz, N. Fotopoulos, L. Singer and C. Cutler, *Outlook for detection of GW inspirals by GRB-triggered searches in the advanced detector era*, arXiv:1210.3095 [INSPIRE].

[64] H. Dimmelmeier, C.D. Ott, A. Marek and H.-T. Janka, *The Gravitational Wave Burst Signal from Core Collapse of Rotating Stars*, *Phys. Rev.* **D 78** (2008) 064056 [arXiv:0806.4953] [INSPIRE].

[65] J.A. Faber and F.A. Rasio, *Binary Neutron Star Mergers*, *Living Rev. Rel.* **15** (2012) 8 [arXiv:1204.3858] [INSPIRE].

[66] C.L. Fryer, D.E. Holz and S.A. Hughes, *Gravitational wave emission from core collapse of massive stars*, *Astrophys. J.* **565** (2002) 430 [astro-ph/0106113] [INSPIRE].

[67] C.L. Fryer and K.C.B. New, *Gravitational waves from gravitational collapse*, *Living Rev. Rel.* **14** (2011) 1.

[68] N. Gehrels, E. Ramirez-Ruiz and D.B. Fox, *Gamma-Ray Bursts in the Swift Era*, *Ann. Rev. Astron. Astrophys.* **47** (2009) 567 [arXiv:0909.1531] [INSPIRE].

[69] SWIFT SCIENCE collaboration, N. Gehrels et al., *The Swift Gamma-Ray Burst Mission*, *AIP Conf. Proc.* **727** (2004) 637 [astro-ph/0405233] [INSPIRE].

[70] R. Gill and J.S. Heyl, *On the trigger mechanisms for SGR giant flares*, *Mon. Not. Roy. Astron. Soc.* **407** (2010) 1926 [arXiv:1002.3662] [INSPIRE].

[71] ANITA collaboration, P. Gorham et al., *Observational Constraints on the Ultra-high Energy Cosmic Neutrino Flux from the Second Flight of the ANITA Experiment*, *Phys. Rev.* **D 82** (2010) 022004 [arXiv:1003.2961], [*Erratum ibid.* **85** (2012) 049901 arXiv:1011.5004] [INSPIRE].

JCAP06(2013)008

[72] D. Guetta and T. Piran, *The batse-swift luminosity and redshift distributions of short-duration grbs*, *Astron. Astrophys.* **453** (2006) 823 [astro-ph/0511239] [INSPIRE].

[73] D. Guetta, T. Piran and E. Waxman, *The Luminosity and angular distributions of long GRBs*, *Astrophys. J.* **619** (2005) 412 [astro-ph/0311488] [INSPIRE].

[74] D. Guetta and L. Stella, *Short Gamma-Ray Bursts and Gravitational Waves from Dynamically Formed Merging Binaries*, *Astron. Astrophys.* **498** (2009) 329 [arXiv:0811.0684] [INSPIRE].

[75] D. Guetta and M.D. Valle, *On the Rates of Gamma-Ray Bursts and Type Ib/c Supernovae*, *Astrophys. J. Lett.* **657** (2007) L73.

[76] D. Guetta, D. Hooper, J. Alvarez-Muniz, F. Halzen and E. Reuveni, *Neutrinos from individual gamma-ray bursts in the BATSE catalog*, *Astropart. Phys.* **20** (2004) 429 [astro-ph/0302524] [INSPIRE].

[77] G. Halladjian, *Search for high energy neutrinos emitted by point-like sources with ANTARES*, Ph.D. thesis, Université de la Méditérranée–Aix Marseille II, Marseilles, France (2010).

[78] F. Halzen, H. Landsman and T. Montaruli, *TeV photons and neutrinos from giant soft-gamma repeaters flares*, astro-ph/0503348 [INSPIRE].

[79] LIGO scientific collaboration, G.M. Harry et al., *Advanced LIGO: The next generation of gravitational wave detectors*, *Class. Quant. Grav.* **27** (2010) 084006.

[80] H.-N. He, R.-Y. Liu, X.-Y. Wang, S. Nagataki, K. Murase et al., *IceCube non-detection of GRBs: Constraints on the fireball properties*, *Astrophys. J.* **752** (2012) 29 [arXiv:1204.0857] [INSPIRE].

[81] ANTARES collaboration, KM3NeT Consortium collaboration, J.J. Hernandez-Rey, *Neutrino Telescopes in the Mediterranean Sea*, *J. Phys. Conf. Ser.* **171** (2009) 012047 [arXiv:0904.4011] [INSPIRE].

[82] C.T. Hill, D.N. Schramm and T.P. Walker, *Ultrahigh-Energy Cosmic Rays from Superconducting Cosmic Strings*, *Phys. Rev.* **D 36** (1987) 1007 [INSPIRE].

[83] J. Hjorth and J.S. Bloom, *The GRB-supernova connection*, in *Gamma-Ray Bursts*, C. Kouveliotou et al. eds., Cambridge University Press Cambridge, U.K. (2011), pg. 169.

[84] S. Horiuchi and S. Ando, *High-energy neutrinos from reverse shocks in choked and successful relativistic jets*, *Phys. Rev.* **D 77** (2008) 063007 [arXiv:0711.2580] [INSPIRE].

[85] S. Hummer, P. Baerwald and W. Winter, *Neutrino Emission from Gamma-Ray Burst Fireballs, Revised*, *Phys. Rev. Lett.* **108** (2012) 231101 [arXiv:1112.1076] [INSPIRE].

[86] K. Hurkey, *Soft gamma repeaters*, *Adv. Space Res.* **47** (2011) 1326.

[87] K. Ioka, *Magnetic deformation of magnetars for the giant flares of the soft gamma-ray repeaters*, *Mon. Not. Roy. Astron. Soc.* **327** (2001) 639 [astro-ph/0009327] [INSPIRE].

[88] K. Ioka, S. Razzaque, S. Kobayashi and P. Mészáros, *TeV-PeV neutrinos from giant flares of magnetars and the case of SGR 1806-20*, *Astrophys. J.* **633** (2005) 1013 [astro-ph/0503279] [INSPIRE].

[89] L.Z. Kelley, I. Mandel and E. Ramirez-Ruiz, *Electromagnetic transients as triggers in searches for gravitational waves from compact binary mergers*, arXiv:1209.3027 [INSPIRE].

[90] A. Khokhlov, P. Hoeflich, E. Oran, J. Wheeler and L. Wang, *Jet-induced explosions of core collapse supernovae*, *Astrophys. J. Lett.* **524** (1999) L107 [astro-ph/9904419] [INSPIRE].

[91] T. Kibble, *Topology of Cosmic Domains and Strings*, *J. Phys.* **A 9** (1976) 1387 [INSPIRE].

[92] K. Kiuchi, M. Shibata, P.J. Montero and J.A. Font, *Gravitational waves from the Papaloizou-Pringle instability in black hole-torus systems*, *Phys. Rev. Lett.* **106** (2011) 251102 [arXiv:1105.5035] [INSPIRE].

[93] S. Kobayashi and P. Mészáros, *Gravitational radiation from gamma-ray burst progenitors*, *Astrophys. J.* **589** (2003) 861 [astro-ph/0210211] [INSPIRE].

[94] S. Kobayashi and P. Mészáros, *Polarized gravitational waves from gamma-ray bursts*, *Astrophys. J.* **585** (2003) L89 [astro-ph/0212539] [INSPIRE].

[95] K. Kotake, *Multiple physical elements to determine the gravitational-wave signatures of core-collapse supernovae*, *C. R. Physique* **14** (2013) 318 [arXiv:1110.5107] [INSPIRE].

[96] D. Lazzati, B.J. Morsony, C.H. Blackwell and M.C. Begelman, *Unifying the Zoo of Jet-Driven Stellar Explosions*, *Astrophys. J.* **750** (2012) 68 [arXiv:1111.0970] [INSPIRE].

[97] T. Le and C.D. Dermer, *On the Redshift Distribution of Gamma Ray Bursts in the Swift Era*, *Astrophys. J.* **661** (2007) 394 [astro-ph/0610043] [INSPIRE].

[98] Y. Levin and M. van Hoven, *On the excitation of f-modes and torsional modes by magnetar giant flares*, *Mon. Not. Roy. Astron. Soc.* **418** (2011) 659 [arXiv:1103.0880] [INSPIRE].

[99] Z. Li, *On the excitation of f modes and torsional modes by magnetar giant flares*, *Phys. Rev.* **D 85** (2012) 027301.

[100] E. Liang, B. Zhang and Z. Dai, *Low Luminosity Gamma-Ray Bursts as a Unique Population: Luminosity Function, Local Rate and Beaming Factor*, *Astrophys. J.* **662** (2007) 1111 [astro-ph/0605200] [INSPIRE].

[101] C. Lunardini and E. Sabancilar, *Cosmic Strings as Emitters of Extremely High Energy Neutrinos*, *Phys. Rev.* **D 86** (2012) 085008 [arXiv:1206.2924] [INSPIRE].

[102] M. Lyutikov, *Magnetar giant flares and afterglows as relativistic magnetized explosions*, *Mon. Not. Roy. Astron. Soc.* **367** (2006) 1594 [astro-ph/0511711] [INSPIRE].

[103] A. MacFadyen and S. Woosley, *Collapsars: Gamma-ray bursts and explosions in 'failed supernovae'*, *Astrophys. J.* **524** (1999) 262 [astro-ph/9810274] [INSPIRE].

[104] S. Mattila, T. Dahlen, A. Efstathiou, E. Kankare, J. Melinder et al., *Core-collapse supernovae missed by optical surveys*, *Astrophys. J.* **756** (2012) 111 [arXiv:1206.1314] [INSPIRE].

[105] C. Meegan, G. Lichti, P. Bhat, E. Bissaldi, M.S. Briggs et al., *The Fermi Gamma-Ray Burst Monitor*, *Astrophys. J.* **702** (2009) 791 [arXiv:0908.0450] [INSPIRE].

[106] S. Mereghetti, *The multi-wavelength properties of Anomalous X-ray Pulsars and Soft Gamma-ray Repeaters Adv. Space Res.* **47** (2011) 1317.

[107] P. Mészáros, *Gamma-Ray Bursts*, *Rept. Prog. Phys.* **69** (2006) 2259 [astro-ph/0605208] [INSPIRE].

[108] P. Mészáros and E. Waxman, *TeV neutrinos from successful and choked gamma-ray bursts*, *Phys. Rev. Lett.* **87** (2001) 171102 [astro-ph/0103275] [INSPIRE].

[109] B.D. Metzger et al., *The protomagnetar model for gamma-ray bursts*, *Mon. Not. Roy. Astron. Soc.* **413** (2011) 2031.

[110] M. Modjaz, *Tellar forensics with the supernova-GRB connection — Ludwig Biermann Award Lecture 2010*, *Astron. Nachr.* **332** (2011) 434.

[111] H.J. Mosquera Cuesta and D. Morejon Gonzalez, *Bursts of gravitational radiation from superconducting cosmic strings and the neutrino mass spectrum*, *Phys. Lett.* **B 500** (2001) 215 [astro-ph/0102454] [INSPIRE].

[112] K. Murase and S. Nagataki, *High Energy Neutrino Flash from Far-UV/X-ray Flares of Gamma-Ray Bursts*, *Phys. Rev. Lett.* **97** (2006) 051101 [astro-ph/0604437] [INSPIRE].

JCAP06(2013)008

[113] K. Murase, K. Ioka, S. Nagataki and T. Nakamura, *High Energy Neutrinos and Cosmic-Rays from Low-Luminosity Gamma-Ray Bursts?*, *Astrophys. J.* **651** (2006) L5 [astro-ph/0607104] [INSPIRE].

[114] E. Nakar, *Short-Hard Gamma-Ray Bursts*, *Phys. Rept.* **442** (2007) 166 [astro-ph/0701748] [INSPIRE].

[115] E. Nakar, A. Gal-Yam and D.B. Fox, *The Local Rate and the Progenitor Lifetimes of Short-Hard Gamma-Ray Bursts: Synthesis and Predictions for LIGO*, *Astrophys. J.* **650** (2006) 281 [astro-ph/0511254] [INSPIRE].

[116] S. Nissanke, M. Kasliwal and A. Georgieva, *Identifying Elusive Electromagnetic Counterparts to Gravitational Wave Mergers: an end-to-end simulation*, *Astrophys. J.* **767** (2013) 124 [arXiv:1210.6362] [INSPIRE].

[117] E. O'Connor and C.D. Ott, *Black Hole Formation in Failing Core-Collapse Supernovae*, *Astrophys. J.* **730** (2011) 70 [arXiv:1010.5550] [INSPIRE].

[118] C.D. Ott, *The Gravitational Wave Signature of Core-Collapse Supernovae*, *Class. Quant. Grav.* **26** (2009) 063001 [arXiv:0809.0695] [INSPIRE].

[119] C. Ott, C. Reisswig, E. Schnetter, E. O'Connor, U. Sperhake et al., *Dynamics and Gravitational Wave Signature of Collapsar Formation*, *Phys. Rev. Lett.* **106** (2011) 161103 [arXiv:1012.1853] [INSPIRE].

[120] C. Ott, E. Abdikamalov, E. O'Connor, C. Reisswig, R. Haas et al., *Correlated Gravitational Wave and Neutrino Signals from General-Relativistic Rapidly Rotating Iron Core Collapse*, *Phys. Rev.* **D 86** (2012) 024026 [arXiv:1204.0512] [INSPIRE].

[121] J.C. Papaloizou and G.J. Savonije, *Instabilities in self-gravitating gaseous discs*, *Mon. Not. Roy. Astron. Soc.* **248** (1991) 353.

[122] J.C.B. Papaloizou and J.E. Pringle, *The dynamical stability of differentially rotating discs with constant specific angular momentum*, *Mon. Not. Roy. Astron. Soc.* **208** (1984) 721.

[123] T. Piran, *The physics of gamma-ray bursts*, *Rev. Mod. Phys.* **76** (2004) 1143 [astro-ph/0405503] [INSPIRE].

[124] A.L. Piro and E. Pfahl, *Fragmentation of Collapsar Disks and the Production of Gravitational Waves*, *Astrophys. J.* **658** (2007) 1173 [astro-ph/0610696] [INSPIRE].

[125] J. Polchinski, *Introduction to cosmic F- and D-strings*, hep-th/0412244 [INSPIRE].

[126] R. Popham, S. Woosley and C. Fryer, *Hyperaccreting black holes and gamma-ray bursts*, *Astrophys. J.* **518** (1999) 356 [astro-ph/9807028] [INSPIRE].

[127] T. Pradier, *Coincidences between Gravitational Wave Interferometers and High Energy Neutrino Telescopes*, *Nucl. Instrum. Meth.* **A 602** (2009) 268 [arXiv:0807.2562] [INSPIRE].

[128] S. Razzaque, P. Mészáros and E. Waxman, *Neutrino tomography of gamma-ray bursts and massive stellar collapses*, *Phys. Rev.* **D 68** (2003) 083001 [astro-ph/0303505] [INSPIRE].

[129] S. Razzaque, P. Mészáros and E. Waxman, *TeV neutrinos from core collapse supernovae and hypernovae*, *Phys. Rev. Lett.* **93** (2004) 181101 [*Erratum ibid.* **94** (2005) 109903] [astro-ph/0407064] [INSPIRE].

[130] S. Razzaque, P. Mészáros and E. Waxman, *High energy neutrinos from a slow jet model of core collapse supernovae*, *Mod. Phys. Lett.* **A 20** (2005) 2351 [astro-ph/0509729] [INSPIRE].

[131] S. Scheidegger, R. Kaeppeli, S. Whitehouse, T. Fischer and M. Liebendoerfer, *The Influence of Model Parameters on the Prediction of Gravitational wave Signals from Stellar Core Collapse*, *Astron. Astrophys.* **514** (2010) A51 [arXiv:1001.1570] [INSPIRE].

[132] O. Scholten, S. Buitink, J. Bacelar, R. Braun, A. de Bruyn et al., *First results of the NuMoon experiment*, *Nucl. Instrum. Meth.* **A 604** (2009) S102 [INSPIRE].

[133] M. Shibata and K. Taniguchi, *Coalescence of Black Hole-Neutron Star Binaries*, *Living Rev. Relat.* **14** (2011) 6.

[134] X. Siemens, J. Creighton, I. Maor, S. Ray Majumder, K. Cannon et al., *Gravitational wave bursts from cosmic (super)strings: Quantitative analysis and constraints*, *Phys. Rev.* **D 73** (2006) 105001 [gr-qc/0603115] [INSPIRE].

[135] A.M. Soderberg, S. Kulkarni, E. Nakar, E. Berger, D.B. Fox et al., *Relativistic ejecta from X-ray flash XRF 060218 and the rate of cosmic explosions*, *Nature* **442** (2006) 1014 [astro-ph/0604389] [INSPIRE].

[136] A.M. Soderberg et al., *A relativistic type Ibc supernova without a detected γ-ray burst*, *Nature* **463** (2010) 513.

[137] P.J. Sutton, G. Jones, S. Chatterji, P.M. Kalmus, I. Leonor et al., *X-Pipeline: An Analysis package for autonomous gravitational-wave burst searches*, *New J. Phys.* **12** (2010) 053034 [arXiv:0908.3665] [INSPIRE].

[138] T. Takiwaki and K. Kotake, *Gravitational Wave Signatures of Magnetohydrodynamically-Driven Core-Collapse Supernova Explosions*, *Astrophys. J.* **743** (2011) 30 [arXiv:1004.2896] [INSPIRE].

[139] C. Thompson and R.C. Duncan, *The Soft gamma repeaters as very strongly magnetized neutron stars - 1. Radiative mechanism for outbursts*, *Mon. Not. Roy. Astron. Soc.* **275** (1995) 255 [INSPIRE].

[140] K.S. Thorne, *Gravitational radiation*, in *300 Years of Gravitation*, S.W. Hawking and W. Israel eds., Cambridge University Press Cambridge, U.K. (1987).

[141] M.H.M. van Putten, A. Levinson, H.K. Lee, T. Regimbau, M. Punturo et al., *Gravitational radiation from gamma-ray bursts as observational opportunities for LIGO and VIRGO*, *Phys. Rev.* **D 69** (2004) 044007 [gr-qc/0308016] [INSPIRE].

[142] F.J. Virgili, E.W. Liang and B. Zhang, *Low-luminosity gamma-ray bursts as a distinct GRB population: a firmer case from multiple criteria constraints*, *Mon. Not. Roy. Astron. Soc.* **392** (2009) 91.

[143] X.-Y. Wang, S. Razzaque, P. Mészáros and Z.-G. Dai, *High-energy Cosmic Rays and Neutrinos from Semi-relativistic Hypernovae*, *Phys. Rev.* **D 76** (2007) 083009 [arXiv:0705.0027] [INSPIRE].

[144] M. Was, *Searching for gravitational waves associated with gamma-ray bursts in 2009-2010 LIGO-Virgo data*, Ph.D. thesis, Université Paris Sud, LAL 11-119 (2011).

[145] M. Was, P.J. Sutton, G. Jones and I. Leonor, *Performance of an externally triggered gravitational-wave burst search*, *Phys. Rev.* **D 86** (2012) 022003 [arXiv:1201.5599] [INSPIRE].

[146] E. Waxman and J.N. Bahcall, *High-energy neutrinos from cosmological gamma-ray burst fireballs*, *Phys. Rev. Lett.* **78** (1997) 2292 [astro-ph/9701231] [INSPIRE].

[147] E. Waxman and A. Loeb, *TeV neutrinos and GeV photons from shock breakout in supernovae*, *Phys. Rev. Lett.* **87** (2001) 071101 [astro-ph/0102317] [INSPIRE].

[148] D.J. White, E.J. Daw and V.S. Dhillon, *Low-luminosity gamma-ray bursts as a distinct GRB population a firmer case from multiple criteria constraints*, *Class. Quant. Grav.* **28** (2011) 085016.

[149] W. Winter, *Neutrinos from Cosmic Accelerators Including Magnetic Field and Flavor Effects*, *Adv. High Energy Phys.* **2012** (2012) 586413 [arXiv:1201.5462] [INSPIRE].

[150] S.E. Woosley, *Gamma-ray bursts from stellar mass accretion disks around black holes*, *Astrophys. J.* **405** (1993) 273 [INSPIRE].

JCAP06(2013)008

[151] S. Woosley and A. Heger, *The Progenitor stars of gamma-ray bursts*, *Astrophys. J.* **637** (2006) 914 [astro-ph/0508175] [INSPIRE].

[152] B.-B. Zhang, Y.-Z. Fan, R.-F. Shen, D. Xu, F.-W. Zhang et al., *GRB 120422A: A Low-luminosity Gamma-ray Burst Driven by Central Engine*, *Astrophys. J.* **756** (2012) 190 [arXiv:1206.0298] [INSPIRE].

[153] B. Zink, P.D. Lasky and K.D. Kokkotas, *Are gravitational waves from giant magnetar flares observable?*, *Phys. Rev.* **D 85** (2012) 024030 [arXiv:1107.1689] [INSPIRE].

The ANTARES collaboration

S. Adrián-Martínez[1], I. Al Samarai[2], A. Albert[3], M. André[4], M. Anghinolfi[5], G. Anton[6], S. Anvar[7], M. Ardid[1], T. Astraatmadja[8,39], J-J. Aubert[2], B. Baret[9], S. Basa[10], V. Bertin[2], S. Biagi[11,12], C. Bigongiari[13], C. Bogazzi[8], M. Bou-Cabo[1], B. Bouhou[9], M.C. Bouwhuis[8], J. Brunner[2], J. Busto[2], A. Capone[14,15], C. Cârloganu[16], J. Carr[2], S. Cecchini[11], Z. Charif[2], Ph. Charvis[17], T. Chiarusi[11], M. Circella[18], R. Coniglione[19], L. Core[2], H. Costantini[2], P. Coyle[2], A. Creusot[9], C. Curtil[2], G. De Bonis[14,15], M.P. Decowski[8], I. Dekeyser[20], A. Deschamps[17], C. Distefano[19], C. Donzaud[9,21], D. Dornic[13,2], Q. Dorosti[22], D. Drouhin[3], T. Eberl[6], U. Emanuele[13], A. Enzenhöfer[6], J-P. Ernenwein[2], S. Escoffier[2], K. Fehn [6], P. Fermani[14,15], M. Ferri[1], S. Ferry[23], V. Flaminio[24,25], F. Folger[6], U. Fritsch[6], J-L. Fuda[20], S. Galatà[2], P. Gay[16], K. Geyer[6], G. Giacomelli[11,12], V. Giordano[19], J.P. Gómez-González[13], K. Graf[6], G. Guillard[16], G. Hallewell[2], M. Hamal[26], H. van Haren[27], A.J. Heijboer[8], Y. Hello[17], J.J. Hernández-Rey[13], B. Herold[6], J. Hößl[6], C.C. Hsu[8], M. de Jong[8,39], M. Kadler[28], O. Kalekin[6], A. Kappes[6,40], U. Katz[6], O. Kavatsyuk[22], P. Kooijman[8,29,30], C. Kopper[8,6], A. Kouchner[9], I. Kreykenbohm[28], V. Kulikovskiy[31,5], R. Lahmann[6], G. Lambard[13], G. Larosa[1], D. Lattuada[19], D. Lefèvre[20], G. Lim[8,30], D. Lo Presti[32,33], H. Loehner[22], S. Loucatos[23], F. Louis[7], S. Mangano[13], M. Marcelin[10], A. Margiotta[11,12], J.A. Martínez-Mora[1], S. Martini[20], A. Meli[6], T. Montaruli[18,34], M. Morganti[24,41], L. Moscoso[9,23,†], H. Motz[6], M. Neff[6], E. Nezri[10], D. Palioselitis[8], G.E. Păvălaş[35], K. Payet[23], J. Petrovic[8], P. Piattelli[19], V. Popa[35], T. Pradier[36], E. Presani[8], C. Racca[3], C. Reed[8], G. Riccobene[19], C. Richardt[6], R. Richter[6], C. Rivière[2], A. Robert[20], K. Roensch[6], A. Rostovtsev[37], J. Ruiz-Rivas[13], M. Rujoiu[35], G.V. Russo[32,33], D.F.E. Samtleben[8], A. Sánchez-Losa[13], P. Sapienza[19], J. Schmid[6], J. Schnabel[6], F. Schöck[6], J-P. Schuller[23], F. Schüssler[23], T. Seitz [6], R. Shanidze[6], F. Simeone[14,15], A. Spies[6], M. Spurio[11,12], J.J.M. Steijger[8], Th. Stolarczyk[23], M. Taiuti[5,38], C. Tamburini[20], A. Trovato[32], B. Vallage[23], C. Vallée[2], V. Van Elewyck[9], M. Vecchi[2], P. Vernin[23], E. Visser[8], S. Wagner[6], G. Wijnker[8], J. Wilms[28], E. de Wolf[8,30], H. Yepes[13], D. Zaborov[37], J.D. Zornoza[13], J. Zúñiga[13]

The LIGO and the Virgo collaboration

J. Aasi[42], J. Abadie[42], B. P. Abbott[42], R. Abbott[42], T. D. Abbott[43], M. Abernathy[44], T. Accadia[45], F. Acernese[46,48], C. Adams[49], T. Adams[50], P. Addesso[48], R. Adhikari[42], C. Affeldt[52,53], M. Agathos[8], K. Agatsuma[55], P. Ajith[42], B. Allen[52,56,53], A. Allocca[24,57], E. Amador Ceron[56], D. Amariutei[58], S. B. Anderson[42], W. G. Anderson[56], K. Arai[42], M. C. Araya[42], S. Ast[52,53], S. M. Aston[49], P. Astone[14], D. Atkinson[59], P. Aufmuth[53,52], C. Aulbert[52,53], B. E. Aylott[60], S. Babak[61], P. Baker[62], G. Ballardin[63], S. Ballmer[64], Y. Bao[58], J. C. B. Barayoga[42], D. Barker[59], F. Barone[46,48], B. Barr[44], L. Barsotti[65], M. Barsuglia[9], M. A. Barton[59], I. Bartos[66], R. Bassiri[44,67], M. Bastarrika[44], A. Basti[24,25], J. Batch[59], J. Bauchrowitz[52,53], Th. S. Bauer[8], M. Bebronne[45], D. Beck[67], B. Behnke[61], M. Bejger[70], M.G. Beker[8], A. S. Bell[44], C. Bell[44], I. Belopolski[66], M. Benacquista[74], J. M. Berliner[59], A. Bertolini[52,53], J. Betzwieser[49], N. Beveridge[44], P. T. Beyersdorf[75], T. Bhadbade[67], I. A. Bilenko[76], G. Billingsley[42], J. Birch[49], R. Biswas[74], M. Bitossi[24], M. A. Bizouard[77], E. Black[42], J. K. Blackburn[42], L. Blackburn[79], D. Blair[80], B. Bland[59], M. Blom[8], O. Bock[52,53], T. P. Bodiya[65], C. Bogan[52,53], C. Bond[60], R. Bondarescu[81], F. Bondu[83], L. Bonelli[24,25], R. Bonnand[84], R. Bork[42], M. Born[52,53], V. Boschi[24], S. Bose[85], L. Bosi[86], S. Braccini[24,†], C. Bradaschia[24], P. R. Brady[56], V. B. Braginsky[76], M. Branchesi[88,89], J. E. Brau[90], J. Breyer[52,53], T. Briant[91], D. O. Bridges[49], A. Brillet[82], M. Brinkmann[52,53], V. Brisson[77], M. Britzger[52,53], A. F. Brooks[42], D. A. Brown[64], T. Bulik[69], H. J. Bulten[8,54], A. Buonanno[92], J. Burguet–Castell[93], D. Buskulic[45], C. Buy[9], R. L. Byer[67], L. Cadonati[94], G. Cagnoli[74,84], E. Calloni[46,47], J. B. Camp[79], P. Campsie[44], K. Cannon[95], B. Canuel[63], J. Cao[96], C. D. Capano[92], F. Carbognani[63], L. Carbone[60], S. Caride[97], S. Caudill[98], M. Cavaglià[99], F. Cavalier[77], R. Cavalieri[63], G. Cella[24], C. Cepeda[42], E. Cesarini[89], T. Chalermsongsak[42], P. Charlton[100], E. Chassande-Mottin[9], W. Chen[96], X. Chen[80], Y. Chen[101], A. Chincarini[5], A. Chiummo[63], H. S. Cho[102], J. Chow[103], N. Christensen[104], S. S. Y. Chua[103], C. T. Y. Chung[105], S. Chung[80], G. Ciani[58], F. Clara[59], D. E. Clark[67], J. A. Clark[94], J. H. Clayton[56], F. Cleva[82],

JCAP06(2013)008

E. Coccia[106,107], P.-F. Cohadon[91], C. N. Colacino[24,25], A. Colla[14,15], M. Colombini[15], A. Conte[14,15], R. Conte[48], D. Cook[59], T. R. Corbitt[65], M. Cordier[75], N. Cornish[62], A. Corsi[42], C. A. Costa[98,109], M. Coughlin[104], J.-P. Coulon[82], P. Couvares[64], D. M. Coward[80], M. Cowart[49], D. C. Coyne[42], J. D. E. Creighton[56], T. D. Creighton[74], A. M. Cruise[60], A. Cumming[44], L. Cunningham[44], E. Cuoco[63], R. M. Cutler[60], K. Dahl[52,53], M. Damjanic[52,53], S. L. Danilishin[80], S. D'Antonio[106], K. Danzmann[52,53], V. Dattilo[63], B. Daudert[42], H. Daveloza[74], M. Davier[77], E. J. Daw[110], R. Day[63], T. Dayanga[85], R. De Rosa[46,47], D. DeBra[67], G. Debreczeni[111], J. Degallaix[84], W. Del Pozzo[8], T. Dent[50], V. Dergachev[42], R. DeRosa[98], S. Dhurandhar[112], L. Di Fiore[46], A. Di Lieto[24,25], I. Di Palma[52,53], M. Di Paolo Emilio[106,108], A. Di Virgilio[24], M. Díaz[74], A. Dietz[45,99], F. Donovan[65], K. L. Dooley[52,53], S. Doravari[42], S. Dorsher[113], M. Drago[114,115], R. W. P. Drever[118], J. C. Driggers[42], Z. Du[96], J.-C. Dumas[80], S. Dwyer[65], T. Eberle[52,53], M. Edgar[44], M. Edwards[50], A. Effler[98], P. Ehrens[42], G. Endrőczi[111], R. Engel[42], T. Etzel[42], K. Evans[44], M. Evans[65], T. Evans[49], M. Factourovich[66], V. Fafone[106,107], S. Fairhurst[50], B. F. Farr[119], M. Favata[56], D. Fazi[119], H. Fehrmann[52,53], D. Feldbaum[58], I. Ferrante[24,25], F. Ferrini[63], F. Fidecaro[24,25], L. S. Finn[81], I. Fiori[63], R. P. Fisher[64], R. Flaminio[84], S. Foley[65], E. Forsi[49], L. A. Forte[46], N. Fotopoulos[42], J.-D. Fournier[82], J. Franc[84], S. Franco[77], S. Frasca[14,15], F. Frasconi[24], M. Frede[52,53], M. A. Frei[120], Z. Frei[121], A. Freise[60], R. Frey[90], T. T. Fricke[52,53], D. Friedrich[52,53], P. Fritschel[65], V. V. Frolov[49], M.-K. Fujimoto[55], P. J. Fulda[60], M. Fyffe[49], J. Gair[122], M. Galimberti[84], L. Gammaitoni[86,87], J. Garcia[59], F. Garufi[46,47], M. E. Gáspár[111], G. Gelencser[121], G. Gemme[5], E. Genin[63], A. Gennai[24], L. Á. Gergely[123], S. Ghosh[85], J. A. Giaime[98,49], S. Giampanis[56], K. D. Giardina[49], A. Giazotto[24], S. Gil-Casanova[93], C. Gill[44], J. Gleason[58], E. Goetz[52,53], G. González[98], M. L. Gorodetsky[76], S. Goßler[52,53], R. Gouaty[45], C. Graef[52,53], P. B. Graff[122], M. Granata[84], A. Grant[44], C. Gray[59], R. J. S. Greenhalgh[124], A. M. Gretarsson[125], C. Griffo[43], H. Grote[52,53], K. Grover[60], S. Grunewald[61], G. M. Guidi[88,89], C. Guido[49], R. Gupta[112], E. K. Gustafson[42], R. Gustafson[97], J. M. Hallam[60], D. Hammer[56], G. Hammond[44], J. Hanks[59], C. Hanna[42,126], J. Hanson[49], J. Harms[118], G. M. Harry[127], I. W. Harry[64], E. D. Harstad[90], M. T. Hartman[58], K. Haughian[44], K. Hayama[55], J.-F. Hayau[83], J. Heefner[42,†], A. Heidmann[91], M. C. Heintze[49], H. Heitmann[82], P. Hello[77], G. Hemming[63], M. A. Hendry[44], I. S. Heng[44], A. W. Heptonstall[42], V. Herrera[67], M. Heurs[52,53], M. Hewitson[52,53], S. Hild[44], D. Hoak[94], K. A. Hodge[42], K. Holt[49], M. Holtrop[128], T. Hong[101], S. Hooper[80], J. Hough[44], E. J. Howell[80], B. Hughey[56], S. Husa[93], S. H. Huttner[44], T. Huynh-Dinh[49], D. R. Ingram[59], R. Inta[103], T. Isogai[104], A. Ivanov[42], K. Izumi[55], M. Jacobson[42], E. James[42], Y. J. Jang[119], P. Jaranowski[71], E. Jesse[125], W. W. Johnson[98], D. I. Jones[129], R. Jones[44], R.J.G. Jonker[8], L. Ju[80], P. Kalmus[42], V. Kalogera[119], S. Kandhasamy[113], G. Kang[130], J. B. Kanner[92,79], M. Kasprzack[63,77], R. Kasturi[131], E. Katsavounidis[65], W. Katzman[49], H. Kaufer[52,53], K. Kaufman[101], K. Kawabe[59], S. Kawamura[55], F. Kawazoe[52,53], D. Keitel[52,53], D. Kelley[64], W. Kells[42], D. G. Keppel[42], Z. Keresztes[123], A. Khalaidovski[52,53], F. Y. Khalili[76], E. A. Khazanov[132], B. K. Kim[130], C. Kim[133], H. Kim[52,53], K. Kim[134], N. Kim[67], Y. M. Kim[102], P. J. King[42], D. L. Kinzel[49], J. S. Kissel[65], S. Klimenko[58], J. Kline[56], K. Kokeyama[98], V. Kondrashov[42], S. Koranda[56], W. Z. Korth[42], I. Kowalska[69], D. Kozak[42], V. Kringel[52,53], B. Krishnan[61], A. Królak[68,72], G. Kuehn[52,53], P. Kumar[64], R. Kumar[44], R. Kurdyumov[67], P. Kwee[65], P. K. Lam[103], M. Landry[59], A. Langley[118], B. Lantz[67], N. Lastzka[52,53], C. Lawrie[44], A. Lazzarini[42], A. Le Roux[49], P. Leaci[61], C. H. Lee[102], H. K. Lee[134], H. M. Lee[135], J. R. Leong[52,53], I. Leonor[90], N. Leroy[77], N. Letendre[45], V. Lhuillier[59], J. Li[96], T. G. F. Li[8], P. E. Lindquist[42], V. Litvine[42], Y. Liu[96], Z. Liu[58], N. A. Lockerbie[136], D. Lodhia[60], J. Logue[44], M. Lorenzini[88], V. Loriette[78], M. Lormand[49], G. Losurdo[88], J. Lough[64], M. Lubinski[59], H. Lück[52,53], A. P. Lundgren[52,53], J. Macarthur[44], E. Macdonald[44], B. Machenschalk[52,53], M. MacInnis[65], D. M. Macleod[50], M. Mageswaran[42], K. Mailand[42], E. Majorana[14], I. Maksimovic[78], V. Malvezzi[106], N. Man[82], I. Mandel[60], V. Mandic[113], M. Mantovani[24], F. Marchesoni[86], F. Marion[45], S. Márka[66], Z. Márka[66], A. Markosyan[67], E. Maros[42], J. Marque[63], F. Martelli[88,89], I. W. Martin[44], R. M. Martin[58], J. N. Marx[42], K. Mason[65], A. Masserot[45], F. Matichard[65], L. Matone[66], R. A. Matzner[137], N. Mavalvala[65], G. Mazzolo[52,53], R. McCarthy[59], D. E. McClelland[103], S. C. McGuire[138], G. McIntyre[42], J. McIver[94], G. D. Meadors[97], M. Mehmet[52,53], T. Meier[53,52], A. Melatos[105], A. C. Melissinos[139], G. Mendell[59], D. F. Menéndez[81], R. A. Mercer[56], S. Meshkov[42], C. Messenger[50], M. S. Meyer[49], H. Miao[101], C. Michel[84], L. Milano[46,47], J. Miller[103], Y. Minenkov[106], C. M. F. Mingarelli[60], V. P. Mitrofanov[76], G. Mitselmakher[58], R. Mittleman[65], B. Moe[56], M. Mohan[63], S. R. P. Mohapatra[94], D. Moraru[59], G. Moreno[59], N. Morgado[84], A. Morgia[106,107], T. Mori[55], S. R. Morriss[74], S. Mosca[46,47], K. Mossavi[52,53], B. Mours[45], C. M. Mow–Lowry[103], C. L. Mueller[58], G. Mueller[58], S. Mukherjee[74], A. Mullavey[98,103], H. Müller-Ebhardt[52,53], J. Munch[140], D. Murphy[66], P. G. Murray[44], A. Mytidis[58], T. Nash[42], L. Naticchioni[14,15], V. Necula[58], J. Nelson[44], I. Neri[86,87], G. Newton[44], T. Nguyen[103], A. Nishizawa[55], A. Nitz[64], F. Nocera[63], D. Nolting[49], M. E. Normandin[74], L. Nuttall[50], E. Ochsner[56], J. O'Dell[124], E. Oelker[65], G. H. Ogin[42], J. J. Oh[141], S. H. Oh[141], R. G. Oldenberg[56], B. O'Reilly[49], R. O'Shaughnessy[56], C. Osthelder[42], C. D. Ott[101], D. J. Ottaway[140], R. S. Ottens[58], H. Overmier[49], B. J. Owen[81], A. Page[60], L. Palladino[106,108], C. Palomba[14], Y. Pan[92], C. Pankow[56], F. Paoletti[24,63], R. Paoletti[24,57], M. A. Papa[61,56], M. Parisi[46,47], A. Pasqualetti[63], R. Passaquieti[24,25], D. Passuello[24], M. Pedraza[42], S. Penn[131], A. Perreca[64], G. Persichetti[46,47], M. Phelps[42], M. Pichot[82], M. Pickenpack[52,53], F. Piergiovanni[88,89], V. Pierro[51], M. Pihlaja[113], L. Pinard[84], I. M. Pinto[51], M. Pitkin[44], H. J. Pletsch[52,53], M. V. Plissi[44], R. Poggiani[24,25], J. Pöld[52,53], F. Postiglione[48], C. Poux[42], M. Prato[5], V. Predoi[50], T. Prestegard[113], L. R. Price[42], M. Prijatelj[52,53], M. Principe[51], S. Privitera[42], R. Prix[52,53], G. A. Prodi[114,115], L. G. Prokhorov[76], O. Puncken[52,53], M. Punturo[86], P. Puppo[14], V. Quetschke[74], R. Quitzow-James[90], F. J. Raab[59], D. S. Rabeling[8,54], I. Rácz[111], H. Radkins[59], P. Raffai[66,121], M. Rakhmanov[74], C. Ramet[49], B. Rankins[99], P. Rapagnani[14,15], V. Raymond[119], V. Re[106,107], C. M. Reed[59], T. Reed[142], T. Regimbau[82], S. Reid[44], D. H. Reitze[42], F. Ricci[14,15], R. Riesen[49], K. Riles[97], M. Roberts[67], N. A. Robertson[42,44], F. Robinet[77], C. Robinson[50], E. L. Robinson[61], A. Rocchi[106], S. Roddy[49], C. Rodriguez[119], M. Rodruck[59], L. Rolland[45], J. G. Rollins[42], J. D. Romano[74], R. Romano[46,48], J. H. Romie[49], D. Rosińska[70,73], C. Röver[52,53], S. Rowan[44], A. Rüdiger[52,53], P. Ruggi[63], K. Ryan[59], F. Salemi[52,53], L. Sammut[105], V. Sandberg[59], S. Sankar[65], V. Sannibale[42], L. Santamaría[42], I. Santiago-Prieto[44], G. Santostasi[143], E. Saracco[84], B. Sassolas[84], B. S. Sathyaprakash[50], P. R. Saulson[64], R. L. Savage[59], R. Schilling[52,53], R. Schnabel[52,53], R. M. S. Schofield[90], B. Schulz[52,53], B. F. Schutz[61,50], P. Schwinberg[59], J. Scott[44], S. M. Scott[103], F. Seifert[42], D. Sellers[49], D. Sentenac[63], A. Sergeev[132], D. A. Shaddock[103], M. Shaltev[52,53], B. Shapiro[65], P. Shawhan[92], D. H. Shoemaker[65], T. L Sidery[60], X. Siemens[56], D. Sigg[59], D. Simakov[52,53], A. Singer[42], L. Singer[42], A. M. Sintes[93], G. R. Skelton[56], B. J. J. Slagmolen[103], J. Slutsky[98], J. R. Smith[43], M. R. Smith[42], R. J. E. Smith[60], N. D. Smith-Lefebvre[65], K. Somiya[101], B. Sorazu[44], F. C. Speirits[44], L. Sperandio[106,107], M. Stefszky[103], E. Steinert[59], J. Steinlechner[52,53], S. Steinlechner[52,53], S. Steplewski[85], A. Stochino[42], R. Stone[74], K. A. Strain[44], S. E. Strigin[76], A. S. Stroeer[74], R. Sturani[88,89], A. L. Stuver[49], T. Z. Summerscales[144], M. Sung[98], S. Susmithan[80], P. J. Sutton[50], B. Swinkels[63], G. Szeifert[121], M. Tacca[63], L. Taffarello[116], D. Talukder[85], D. B. Tanner[58], S. P. Tarabrin[52,53], R. Taylor[42], A. P. M. ter Braack[8], P. Thomas[59], K. A. Thorne[49], K. S. Thorne[101], E. Thrane[113], A. Thüring[53,52], C. Titsler[81], K. V. Tokmakov[136], C. Tomlinson[110], A. Toncelli[24,25], M. Tonelli[24,25], O. Torre[24,57], C. V. Torres[74], C. I. Torrie[42,44], E. Tournefier[45], F. Travasso[86,87], G. Traylor[49], M. Tse[66], D. Ugolini[145], H. Vahlbruch[53,52], G. Vajente[24,25], J. F. J. van den Brand[8,54], C. Van Den Broeck[8], S. van der Putten[8], A. A. van Veggel[44], S. Vass[42], M. Vasuth[111], R. Vaulin[65], M. Vavoulidis[77], A. Vecchio[60], G. Vedovato[116], J. Veitch[50], P. J. Veitch[140], K. Venkateswara[146], D. Verkindt[45], F. Vetrano[88,89], A. Viceré[88,89], A. E. Villar[42], J.-Y. Vinet[82], S. Vitale[8], H. Vocca[86], C. Vorvick[59], S. P. Vyatchanin[76], A. Wade[103], L. Wade[56], M. Wade[56], S. J. Waldman[65], L. Wallace[42], Y. Wan[96], M. Wang[60], X. Wang[96], A. Wanner[52,53], R. L. Ward[9], M. Was[77], M. Weinert[52,53], A. J. Weinstein[42], R. Weiss[65], T. Welborn[49], L. Wen[101,80], P. Wessels[52,53], M. West[64], T. Westphal[52,53], K. Wette[52,53], J. T. Whelan[120], S. E. Whitcomb[42,80], D. J. White[110], B. F. Whiting[58], K. Wiesner[52,53], C. Wilkinson[59], P. A. Willems[42], L. Williams[58], R. Williams[42], B. Willke[52,53], M. Wimmer[52,53], L. Winkelmann[52,53], W. Winkler[52,53], C. C. Wipf[65], A. G. Wiseman[56], H. Wittel[52,53], G. Woan[44], R. Wooley[49], J. Worden[59], J. Yablon[119], I. Yakushin[49], H. Yamamoto[42], K. Yamamoto[115,117], C. C. Yancey[92], H. Yang[101], D. Yeaton-Massey[42], S. Yoshida[147], M. Yvert[45], A. Zadrożny[72], M. Zanolin[125], J.-P. Zendri[116], F. Zhang[96], L. Zhang[42], C. Zhao[80], N. Zotov[142,†], M. E. Zucker[65], J. Zweizig[42]

JCAP06(2013)008

[1]Institut d'Investigació per a la Gestió Integrada de les Zones Costaneres (IGIC) - Universitat Politècnica de València. C/ Paranimf 1 , 46730 Gandia, Spain.
[2]CPPM, Aix-Marseille Université, CNRS/IN2P3, Marseille, France
[3]GRPHE - Institut universitaire de technologie de Colmar, 34 rue du Grillenbreit BP 50568 - 68008 Colmar, France
[4]Technical University of Catalonia, Laboratory of Applied Bioacoustics, Rambla Exposició, 08800 Vilanova i la Geltrú, Barcelona, Spain
[5]INFN - Sezione di Genova, Via Dodecaneso 33, 16146 Genova, Italy
[6]Friedrich-Alexander-Universität Erlangen-Nürnberg, Erlangen Centre for Astroparticle Physics, Erwin-Rommel-Str. 1, 91058 Erlangen, Germany
[7]Direction des Sciences de la Matière - Institut de recherche sur les lois fondamentales de l'Univers - Service d'Electronique des Détecteurs et d'Informatique, CEA Saclay, 91191 Gif-sur-Yvette Cedex, France
[8]Nikhef, Science Park, Amsterdam, The Netherlands
[9]APC, Université Paris Diderot, CNRS/IN2P3, CEA/IRFU, Observatoire de Paris, Sorbonne Paris Cité, 75205 Paris, France
[10]LAM - Laboratoire d'Astrophysique de Marseille, Pôle de l'Étoile Site de Château-Gombert, rue Frédéric Joliot-Curie 38, 13388 Marseille Cedex 13, France
[11]INFN - Sezione di Bologna, Viale C. Berti-Pichat 6/2, 40127 Bologna, Italy
[12]Dipartimento di Fisica dell'Università, Viale Berti Pichat 6/2, 40127 Bologna, Italy
[13]IFIC - Instituto de Física Corpuscular, Edificios Investigación de Paterna, CSIC - Universitat de València, Apdo. de Correos 22085, 46071 Valencia, Spain
[14]INFN -Sezione di Roma, P.le Aldo Moro 2, 00185 Roma, Italy
[15]Dipartimento di Fisica dell'Università La Sapienza, P.le Aldo Moro 2, 00185 Roma, Italy
[16]Clermont Université, Université Blaise Pascal, CNRS/IN2P3, Laboratoire de Physique Corpusculaire, BP 10448, 63000 Clermont-Ferrand, France
[17]Géoazur - Université de Nice Sophia-Antipolis, CNRS/INSU, IRD, Observatoire de la Côte d'Azur and Université Pierre et Marie Curie, BP 48, 06235 Villefranche-sur-mer, France
[18]INFN - Sezione di Bari, Via E. Orabona 4, 70126 Bari, Italy
[19]INFN - Laboratori Nazionali del Sud (LNS), Via S. Sofia 62, 95123 Catania, Italy
[20]MIO, Mediterranean Institute of Oceanography, Aix-Marseille University, 13288, Marseille, Cedex 9, France; Université du Sud Toulon-Var, 83957, La Garde Cedex, France CNRS-INSU/IRD UM 110
[21]Univ Paris-Sud , 91405 Orsay Cedex, France
[22]Kernfysisch Versneller Instituut (KVI), University of Groningen, Zernikelaan 25, 9747 AA Groningen, The Netherlands
[23]Direction des Sciences de la Matière - Institut de recherche sur les lois fondamentales de l'Univers - Service de Physique des Particules, CEA Saclay, 91191 Gif-sur-Yvette Cedex, France
[24]INFN - Sezione di Pisa, Largo B. Pontecorvo 3, 56127 Pisa, Italy
[25]Dipartimento di Fisica dell'Università di Pisa, Largo B. Pontecorvo 3, 56127 Pisa, Italy
[26]University Mohammed I, Laboratory of Physics of Matter and Radiations, B.P.717, Oujda 6000, Morocco
[27]Royal Netherlands Institute for Sea Research (NIOZ), Landsdiep 4,1797 SZ 't Horntje (Texel), The Netherlands
[28]Dr. Remeis-Sternwarte and ECAP, Universität Erlangen-Nürnberg, Sternwartstr. 7, 96049 Bamberg, Germany
[29]Universiteit Utrecht, Faculteit Betawetenschappen, Princetonplein 5, 3584 CC Utrecht, The Netherlands
[30]Universiteit van Amsterdam, Instituut voor Hoge-Energie Fysica, Science Park 105, 1098 XG Amsterdam, The Netherlands
[31]Moscow State University, Skobeltsyn Institute of Nuclear Physics, Leninskie gory, 119991 Moscow, Russia
[32]INFN - Sezione di Catania, Viale Andrea Doria 6, 95125 Catania, Italy
[33]Dipartimento di Fisica ed Astronomia dell'Università, Viale Andrea Doria 6, 95125 Catania, Italy

JCAP06(2013)008

[34]Département de Physique Nucléaire et Corpusculaire, Université de Genève, 1211, Geneva, Switzerland
[35]Institute for Space Sciences, R-77125 Bucharest, Măgurele, Romania
[36]IPHC-Institut Pluridisciplinaire Hubert Curien - Université de Strasbourg et CNRS/IN2P3 23 rue du Loess, BP 28, 67037 Strasbourg Cedex 2, France
[37]ITEP - Institute for Theoretical and Experimental Physics, B. Cheremushkinskaya 25, 117218 Moscow, Russia
[38]Dipartimento di Fisica dell'Università, Via Dodecaneso 33, 16146 Genova, Italy
[39] Also at University of Leiden, the Netherlands
[40] On leave of absence at the Humboldt-Universität zu Berlin
[41] Also at Accademia Navale di Livorno, Livorno, Italy
[42]LIGO - California Institute of Technology, Pasadena, CA 91125, U.S.A.
[43]California State University Fullerton, Fullerton CA 92831 U.S.A.
[44]SUPA, University of Glasgow, Glasgow, G12 8QQ, United Kingdom
[45]Laboratoire d'Annecy-le-Vieux de Physique des Particules (LAPP), Université de Savoie, CNRS/IN2P3, F-74941 Annecy-Le-Vieux, France
[46]INFN, Sezione di Napoli, Complesso Universitario di Monte S.Angelo, I-80126 Napoli, Italy
[47]Università di Napoli 'Federico II', Complesso Universitario di Monte S.Angelo, I-80126 Napoli, Italy
[48]Università di Salerno, I-84084 Fisciano (Salerno), Italy
[49]LIGO - Livingston Observatory, Livingston, LA 70754, U.S.A.
[50]Cardiff University, Cardiff, CF24 3AA, United Kingdom
[51]University of Sannio at Benevento, I-82100 Benevento, Italy and INFN (Sezione di Napoli), Italy
[52]Albert-Einstein-Institut, Max-Planck-Institut für Gravitationsphysik, D-30167 Hannover, Germany
[53]Leibniz Universität Hannover, D-30167 Hannover, Germany
[54]VU University Amsterdam, De Boelelaan 1081, 1081 HV Amsterdam, the Netherlands
[55]National Astronomical Observatory of Japan, Tokyo 181-8588, Japan
[56]University of Wisconsin–Milwaukee, Milwaukee, WI 53201, U.S.A.
[57]Università di Siena, I-53100 Siena, Italy
[58]University of Florida, Gainesville, FL 32611, U.S.A.
[59]LIGO - Hanford Observatory, Richland, WA 99352, U.S.A.
[60]University of Birmingham, Birmingham, B15 2TT, United Kingdom
[61]Albert-Einstein-Institut, Max-Planck-Institut für Gravitationsphysik, D-14476 Golm, Germany
[62]Montana State University, Bozeman, MT 59717, U.S.A.
[63]European Gravitational Observatory (EGO), I-56021 Cascina (PI), Italy
[64]Syracuse University, Syracuse, NY 13244, U.S.A.
[65]LIGO - Massachusetts Institute of Technology, Cambridge, MA 02139, U.S.A.
[66]Columbia University, New York, NY 10027, U.S.A.
[67]Stanford University, Stanford, CA 94305, U.S.A.
[68]IM-PAN 00-956 Warsaw, Poland
[69]Astronomical Observatory Warsaw University 00-478 Warsaw, Poland
[70]CAMK-PAN 00-716 Warsaw, Poland
[71]Białystok University 15-424 Białystok, Poland
[72]NCBJ 05-400 Świerk-Otwock, Poland
[73]Institute of Astronomy 65-265 Zielona Góra, Poland
[74]The University of Texas at Brownsville, Brownsville, TX 78520, U.S.A.
[75]San Jose State University, San Jose, CA 95192, U.S.A.
[76]Moscow State University, Moscow, 119992, Russia
[77]LAL, Université Paris-Sud, IN2P3/CNRS, F-91898 Orsay, France
[78]ESPCI, CNRS, F-75005 Paris, France
[79]NASA/Goddard Space Flight Center, Greenbelt, MD 20771, U.S.A.
[80]University of Western Australia, Crawley, WA 6009, Australia
[81]The Pennsylvania State University, University Park, PA 16802, U.S.A.
[82]Université Nice-Sophia-Antipolis, CNRS, Observatoire de la Côte d'Azur, F-06304 Nice, France

JCAP06(2013)008

[83]Institut de Physique de Rennes, CNRS, Université de Rennes 1, 35042 Rennes, France
[84]Laboratoire des Matériaux Avancés (LMA), IN2P3/CNRS, F-69622 Villeurbanne, Lyon, France
[85]Washington State University, Pullman, WA 99164, U.S.A.
[86]INFN, Sezione di Perugia, I-06123 Perugia, Italy
[87]Università di Perugia, I-06123 Perugia, Italy
[88]INFN, Sezione di Firenze, I-50019 Sesto Fiorentino, Italy
[89]Università degli Studi di Urbino 'Carlo Bo', I-61029 Urbino, Italy
[90]University of Oregon, Eugene, OR 97403, U.S.A.
[91]Laboratoire Kastler Brossel, ENS, CNRS, UPMC, Université Pierre et Marie Curie, 4 Place Jussieu, F-75005 Paris, France
[92]University of Maryland, College Park, MD 20742 U.S.A.
[93]Universitat de les Illes Balears, E-07122 Palma de Mallorca, Spain
[94]University of Massachusetts - Amherst, Amherst, MA 01003, U.S.A.
[95]Canadian Institute for Theoretical Astrophysics, University of Toronto, Toronto, Ontario, M5S 3H8, Canada
[96]Tsinghua University, Beijing 100084 China
[97]University of Michigan, Ann Arbor, MI 48109, U.S.A.
[98]Louisiana State University, Baton Rouge, LA 70803, U.S.A.
[99]The University of Mississippi, University, MS 38677, U.S.A.
[100]Charles Sturt University, Wagga Wagga, NSW 2678, Australia
[101]Caltech-CaRT, Pasadena, CA 91125, U.S.A.
[102]Pusan National University, Busan 609-735, Korea
[103]Australian National University, Canberra, ACT 0200, Australia
[104]Carleton College, Northfield, MN 55057, U.S.A.
[105]The University of Melbourne, Parkville, VIC 3010, Australia
[106]INFN, Sezione di Roma Tor Vergata, I-00133 Roma, Italy
[107]Università di Roma Tor Vergata, I-00133 Roma, Italy
[108]Università dell'Aquila, I-67100 L'Aquila, Italy
[109]Instituto Nacional de Pesquisas Espaciais, 12227-010 - São José dos Campos, SP, Brazil
[110]The University of Sheffield, Sheffield S10 2TN, United Kingdom
[111]Wigner RCP, RMKI, H-1121 Budapest, Konkoly Thege Miklós út 29-33, Hungary
[112]Inter-University Centre for Astronomy and Astrophysics, Pune - 411007, India
[113]University of Minnesota, Minneapolis, MN 55455, U.S.A.
[114]INFN, Gruppo Collegato di Trento, I-38050 Povo, Trento, Italy
[115]Università di Trento, I-38050 Povo, Trento, Italy
[116]INFN, Sezione di Padova, I-35131 Padova, Italy
[117]Università di Padova, I-35131 Padova, Italy
[118]California Institute of Technology, Pasadena, CA 91125, U.S.A.
[119]Northwestern University, Evanston, IL 60208, U.S.A.
[120]Rochester Institute of Technology, Rochester, NY 14623, U.S.A.
[121]Eötvös Loránd University, Budapest, 1117 Hungary
[122]University of Cambridge, Cambridge, CB2 1TN, United Kingdom
[123]University of Szeged, 6720 Szeged, Dóm tér 9, Hungary
[124]Rutherford Appleton Laboratory, HSIC, Chilton, Didcot, Oxon OX11 0QX United Kingdom
[125]Embry-Riddle Aeronautical University, Prescott, AZ 86301 U.S.A.
[126]Perimeter Institute for Theoretical Physics, Ontario, N2L 2Y5, Canada
[127]American University, Washington, DC 20016, U.S.A.
[128]University of New Hampshire, Durham, NH 03824, U.S.A.
[129]University of Southampton, Southampton, SO17 1BJ, United Kingdom
[130]Korea Institute of Science and Technology Information, Daejeon 305-806, Korea
[131]Hobart and William Smith Colleges, Geneva, NY 14456, U.S.A.
[132]Institute of Applied Physics, Nizhny Novgorod, 603950, Russia
[133]Lund Observatory, Box 43, SE-221 00, Lund, Sweden

JCAP06(2013)008

[134]Hanyang University, Seoul 133-791, Korea
[135]Seoul National University, Seoul 151-742, Korea
[136]University of Strathclyde, Glasgow, G1 1XQ, United Kingdom
[137]The University of Texas at Austin, Austin, TX 78712, U.S.A.
[138]Southern University and A&M College, Baton Rouge, LA 70813, U.S.A.
[139]University of Rochester, Rochester, NY 14627, U.S.A.
[140]University of Adelaide, Adelaide, SA 5005, Australia
[141]National Institute for Mathematical Sciences, Daejeon 305-390, Korea
[142]Louisiana Tech University, Ruston, LA 71272, U.S.A.
[143]McNeese State University, Lake Charles, LA 70609 U.S.A.
[144]Andrews University, Berrien Springs, MI 49104 U.S.A.
[145]Trinity University, San Antonio, TX 78212, U.S.A.
[146]University of Washington, Seattle, WA, 98195-4290, U.S.A.
[147]Southeastern Louisiana University, Hammond, LA 70402, U.S.A.
[†]Deceased

JCAP06(2013)008

doi:10.1088/0067-0049/211/1/7

FIRST SEARCHES FOR OPTICAL COUNTERPARTS TO GRAVITATIONAL-WAVE CANDIDATE EVENTS

J. Aasi[1], J. Abadie[1], B. P. Abbott[1], R. Abbott[1], T. Abbott[2], M. R. Abernathy[1], T. Accadia[3], F. Acernese[4,5], C. Adams[6], T. Adams[7], R. X. Adhikari[1], C. Affeldt[8], M. Agathos[9], N. Aggarwal[10], O. D. Aguiar[11], P. Ajith[1], B. Allen[8,12,13], A. Allocca[14,15], E. Amador Ceron[12], D. Amariutei[16], R. A. Anderson[1], S. B. Anderson[1], W. G. Anderson[12], K. Arai[1], M. C. Araya[1], C. Arceneaux[17], J. Areeda[18], S. Ast[13], S. M. Aston[6], P. Astone[19], P. Aufmuth[13], C. Aulbert[8], L. Austin[1], B. E. Aylott[20], S. Babak[21], P. T. Baker[22], G. Ballardin[23], S. W. Ballmer[24], J. C. Barayoga[1], D. Barker[25], S. H. Barnum[10], F. Barone[4,5], B. Barr[26], L. Barsotti[10], M. Barsuglia[27], M. A. Barton[25], I. Bartos[28], R. Bassiri[26,29], A. Basti[14,30], J. Batch[25], J. Bauchrowitz[8], Th. S. Bauer[9], M. Bebronne[3], B. Behnke[21], M. Bejger[31], M. G. Beker[9], A. S. Bell[26], C. Bell[26], I. Belopolski[28], G. Bergmann[8], J. M. Berliner[25], A. Bertolini[9], D. Bessis[32], J. Betzwieser[6], P. T. Beyersdorf[33], T. Bhadbhade[29], I. A. Bilenko[34], G. Billingsley[1], J. Birch[6], M. Bitossi[14], M. A. Bizouard[35], E. Black[1], J. K. Blackburn[1], L. Blackburn[36], D. Blair[37], M. Blom[9], O. Bock[8], T. P. Bodiya[10], M. Boer[38,39], C. Bogan[8], C. Bond[20], F. Bondu[40], L. Bonelli[14,30], R. Bonnand[41], R. Bork[1], M. Born[8], S. Bose[42], L. Bosi[43], J. Bowers[2], C. Bradaschia[14], P. R. Brady[12], V. B. Braginsky[34], M. Branchesi[44,45], C. A. Brannen[42], J. E. Brau[46], J. Breyer[8], T. Briant[47], D. O. Bridges[6], A. Brillet[38], M. Brinkmann[8], V. Brisson[35], M. Britzger[8], A. F. Brooks[1], D. A. Brown[24], D. D. Brown[20], F. Brückner[20], T. Bulik[48], H. J. Bulten[9,49], A. Buonanno[50], D. Buskulic[3], C. Buy[27], R. L. Byer[29], L. Cadonati[51], G. Cagnoli[41], J. Calderón Bustillo[52], E. Calloni[4,53], J. B. Camp[36], P. Campsie[26], K. C. Cannon[54], B. Canuel[23], J. Cao[55], C. D. Capano[50], F. Carbognani[23], L. Carbone[20], S. Caride[56], A. Castiglia[57], S. Caudill[12], M. Cavaglià[17], F. Cavalier[35], R. Cavalieri[23], G. Cella[14], C. Cepeda[1], E. Cesarini[58], R. Chakraborty[1], T. Chalermsongsak[1], S. Chao[59], P. Charlton[60], E. Chassande-Mottin[27], X. Chen[37], Y. Chen[61], A. Chincarini[62], A. Chiummo[23], H. S. Cho[63], J. Chow[64], N. Christensen[65], Q. Chu[37], S. S. Y. Chua[64], S. Chung[37], G. Ciani[16], F. Clara[25], D. E. Clark[29], J. A. Clark[51], F. Cleva[38], E. Coccia[58,66], P.-F. Cohadon[47], A. Colla[19,67], M. Colombini[43], M. Constancio, Jr.[11], A. Conte[19,67], R. Conte[68,69], D. Cook[25], T. R. Corbitt[2], M. Cordier[33], N. Cornish[22], A. Corsi[70], C. A. Costa[11], M. W. Coughlin[71], J.-P. Coulon[38], S. Countryman[28], P. Couvares[24], D. M. Coward[37], M. Cowart[6], D. C. Coyne[1], K. Craig[26], J. D. E. Creighton[12], T. D. Creighton[32], S. G. Crowder[72], A. Cumming[26], L. Cunningham[26], E. Cuoco[23], K. Dahl[8], T. Dal Canton[8], M. Damjanic[8], S. L. Danilishin[37], S. D'Antonio[58], K. Danzmann[8,13], V. Dattilo[23], B. Daudert[1], H. Daveloza[32], M. Davier[35], G. S. Davies[26], E. J. Daw[73], R. Day[23], T. Dayanga[42], R. De Rosa[4,53], G. Debreczeni[74], J. Degallaix[41], W. Del Pozzo[9], E. Deleeuw[16], S. Deléglise[47], T. Denker[8], H. Dereli[38], V. Dergachev[1], R. DeRosa[2], R. DeSalvo[68,69], S. Dhurandhar[75], L. Di Fiore[4], A. Di Lieto[14,30], I. Di Palma[8], A. Di Virgilio[14], M. Díaz[32], A. Dietz[17], K. Dmitry[34], F. Donovan[10], K. L. Dooley[8], S. Doravari[6], M. Drago[76,77], R. W. P. Drever[78], J. C. Driggers[1], Z. Du[55], J.-C. Dumas[37], S. Dwyer[25], T. Eberle[8], M. Edwards[7], A. Effler[2], P. Ehrens[1], J. Eichholz[16], S. S. Eikenberry[16], G. Endrőczi[74], R. Essick[10], T. Etzel[1], K. Evans[26], M. Evans[10], T. Evans[6], M. Factourovich[28], V. Fafone[58,66], S. Fairhurst[7], Q. Fang[37], B. Farr[79], W. Farr[79], M. Favata[80], D. Fazi[79], H. Fehrmann[8], D. Feldbaum[6,16], I. Ferrante[14,30], F. Ferrini[23], F. Fidecaro[14,30], L. S. Finn[81], I. Fiori[23], R. Fisher[24], R. Flaminio[41], E. Foley[18], S. Foley[10], E. Forsi[6], L. A. Forte[4], N. Fotopoulos[1], J.-D. Fournier[38], S. Franco[35], S. Frasca[19,67], F. Frasconi[14], M. Frede[8], M. Frei[57], Z. Frei[82], A. Freise[20], R. Frey[46], T. T. Fricke[8], P. Fritschel[10], V. V. Frolov[6], M.-K. Fujimoto[83], P. Fulda[16], M. Fyffe[6], J. Gair[71], L. Gammaitoni[43,84], J. Garcia[25], F. Garufi[4,53], N. Gehrels[36], G. Gemme[62], E. Genin[23], A. Gennai[14], L. Gergely[82], S. Ghosh[42], J. A. Giaime[2,6], S. Giampanis[12], K. D. Giardina[6], A. Giazotto[14], S. Gil-Casanova[52], C. Gill[26], J. Gleason[16], E. Goetz[8], R. Goetz[16], L. Gondan[82], G. González[2], N. Gordon[26], M. L. Gorodetsky[34], S. Gossan[61], S. Goßler[8], R. Gouaty[3], C. Graef[8], P. B. Graff[36], M. Granata[41], A. Grant[26], S. Gras[10], C. Gray[25], R. J. S. Greenhalgh[85], A. M. Gretarsson[86], C. Griffo[18], H. Grote[8], K. Grover[20], S. Grunewald[21], G. M. Guidi[44,45], C. Guido[6], K. E. Gushwa[1], E. K. Gustafson[1], R. Gustafson[56], B. Hall[42], E. Hall[1], D. Hammer[12], G. Hammond[26], M. Hanke[8], J. Hanks[25], C. Hanna[87], J. Hanson[6], J. Harms[1], G. M. Harry[88], I. W. Harry[24], E. D. Harstad[46], M. T. Hartman[16], K. Haughian[26], K. Hayama[83], J. Heefner[1,144], A. Heidmann[47], M. Heintze[6,16], H. Heitmann[38], P. Hello[35], G. Hemming[23], M. Hendry[26], I. S. Heng[26], A. W. Heptonstall[1], M. Heurs[8], S. Hild[26], D. Hoak[51], K. A. Hodge[1], K. Holt[6], M. Holtrop[89], T. Hong[61], S. Hooper[37], T. Horrom[90], D. J. Hosken[91], J. Hough[26], E. J. Howell[37], Y. Hu[26], Z. Hua[55], V. Huang[59], E. A. Huerta[24], B. Hughey[86], S. Husa[52], S. H. Huttner[26], M. Huynh[12], T. Huynh-Dinh[6], J. Iafrate[2], D. R. Ingram[25], R. Inta[64], T. Isogai[10], A. Ivanov[1], B. R. Iyer[92], K. Izumi[25], M. Jacobson[1], E. James[1], H. Jang[93], Y. J. Jang[79], P. Jaranowski[94], F. Jiménez-Forteza[52], W. W. Johnson[2], D. Jones[25], D. I. Jones[95], R. Jones[26], R. J. G. Jonker[9], L. Ju[37], Haris K[96], P. Kalmus[1], V. Kalogera[79], S. Kandhasamy[72], G. Kang[93], J. B. Kanner[36], M. Kasprzack[23,35], R. Kasturi[97], E. Katsavounidis[10], W. Katzman[6], H. Kaufer[13], K. Kaufman[61], K. Kawabe[25], S. Kawamura[83], F. Kawazoe[8], F. Kéfélian[38], D. Keitel[8], D. B. Kelley[24], W. Kells[1], D. G. Keppel[8], A. Khalaidovski[8], F. Y. Khalili[34], E. A. Khazanov[98], B. K. Kim[93], C. Kim[93,99], K. Kim[100], N. Kim[29], W. Kim[91], Y.-M. Kim[63], E. J. King[91], P. J. King[1], D. L. Kinzel[6], J. S. Kissel[10], S. Klimenko[16], J. Kline[12], S. Koehlenbeck[8], K. Kokeyama[2], V. Kondrashov[1], S. Koranda[12], W. Z. Korth[1], I. Kowalska[48], D. Kozak[1], A. Kremin[72], V. Kringel[8], B. Krishnan[8], A. Królak[101,102], C. Kucharczyk[29], S. Kudla[2], G. Kuehn[8], A. Kumar[103], P. Kumar[24], R. Kumar[26], R. Kurdyumov[29], P. Kwee[10], M. Landry[25], B. Lantz[29], S. Larson[104], P. D. Lasky[105], C. Lawrie[26], A. Lazzarini[1],

A. Le Roux[6], P. Leaci[21], E. O. Lebigot[55], C.-H. Lee[63], H. K. Lee[100], H. M. Lee[99], J. Lee[10], J. Lee[18], M. Leonardi[76,77], J. R. Leong[8], N. Leroy[35], N. Letendre[3], B. Levine[25], J. B. Lewis[1], V. Lhuillier[25], T. G. F. Li[9], A. C. Lin[29], T. B. Littenberg[79], V. Litvine[1], F. Liu[106], H. Liu[7], Y. Liu[55], Z. Liu[16], D. Lloyd[1], N. A. Lockerbie[107], V. Lockett[18], D. Lodhia[20], K. Loew[86], J. Logue[26], A. L. Lombardi[51], M. Lorenzini[58], V. Loriette[108], M. Lormand[6], G. Losurdo[44], J. Lough[24], J. Luan[61], M. J. Lubinski[25], H. Lück[8,13], A. P. Lundgren[8], J. Macarthur[26], E. Macdonald[7], B. Machenschalk[8], M. MacInnis[10], D. M. Macleod[7], F. Magana-Sandoval[18], M. Mageswaran[1], K. Mailand[1], E. Majorana[19], I. Maksimovic[108], V. Malvezzi[58], N. Man[38], G. M. Manca[8], I. Mandel[20], V. Mandic[72], V. Mangano[19,67], M. Mantovani[14], F. Marchesoni[43,109], F. Marion[3], S. Márka[28], Z. Márka[28], A. Markosyan[29], E. Maros[1], J. Marque[23], F. Martelli[44,45], I. W. Martin[26], R. M. Martin[16], L. Martinelli[38], D. Martynov[1], J. N. Marx[1], K. Mason[10], A. Masserot[3], T. J. Massinger[24], F. Matichard[10], L. Matone[28], R. A. Matzner[110], N. Mavalvala[10], G. May[2], N. Mazumder[96], G. Mazzolo[8], R. McCarthy[25], D. E. McClelland[64], S. C. McGuire[111], G. McIntyre[1], J. McIver[51], D. Meacher[38], G. D. Meadors[56], M. Mehmet[8], J. Meidam[9], T. Meier[13], A. Melatos[105], G. Mendell[25], R. A. Mercer[12], S. Meshkov[1], C. Messenger[26], M. S. Meyer[6], H. Miao[61], C. Michel[41], E. E. Mikhailov[90], L. Milano[4,53], J. Miller[64], Y. Minenkov[58], C. M. F. Mingarelli[20], S. Mitra[75], V. P. Mitrofanov[34], G. Mitselmakher[16], R. Mittleman[10], B. Moe[12], M. Mohan[23], S. R. P. Mohapatra[24,57], F. Mokler[8], D. Moraru[25], G. Moreno[25], N. Morgado[41], T. Mori[83], S. R. Morriss[32], K. Mossavi[8], B. Mours[3], C. M. Mow-Lowry[8], C. L. Mueller[16], G. Mueller[16], S. Mukherjee[32], A. Mullavey[2], J. Munch[91], D. Murphy[28], P. G. Murray[26], A. Mytidis[16], M. F. Nagy[74], D. Nanda Kumar[16], I. Nardecchia[19,67], T. Nash[1], L. Naticchioni[19,67], R. Nayak[112], V. Necula[16], I. Neri[43,84], G. Newton[26], T. Nguyen[64], E. Nishida[83], A. Nishizawa[83], A. Nitz[24], F. Nocera[23], D. Nolting[6], M. E. Normandin[32], L. K. Nuttall[7], E. Ochsner[12], J. O'Dell[85], E. Oelker[10], G. H. Ogin[1], J. J. Oh[113], S. H. Oh[113], F. Ohme[7], P. Oppermann[8], B. O'Reilly[6], W. Ortega Larcher[32], R. O'Shaughnessy[12], C. Osthelder[1], D. J. Ottaway[91], R. S. Ottens[16], J. Ou[59], H. Overmier[6], B. J. Owen[81], C. Padilla[18], A. Pai[96], C. Palomba[19], Y. Pan[50], C. Pankow[12], F. Paoletti[14,23], R. Paoletti[14,15], M. A. Papa[12,21], H. Paris[25], A. Pasqualetti[23], R. Passaquieti[14,30], D. Passuello[14], M. Pedraza[1], P. Peiris[57], S. Penn[97], A. Perreca[24], M. Phelps[1], M. Pichot[38], M. Pickenpack[8], F. Piergiovanni[44,45], V. Pierro[68,69], L. Pinard[41], B. Pindor[105], I. M. Pinto[68,69], M. Pitkin[26], J. Poeld[8], R. Poggiani[14,30], V. Poole[42], C. Poux[1], V. Predoi[7], T. Prestegard[72], L. R. Price[1], M. Prijatelj[8], M. Principe[68,69], S. Privitera[1], R. Prix[8], G. A. Prodi[76,77], L. Prokhorov[34], O. Puncken[32], M. Punturo[43], P. Puppo[19], V. Quetschke[32], E. Quintero[1], R. Quitzow-James[46], F. J. Raab[25], D. S. Rabeling[9,49], I. Rácz[74], H. Radkins[25], P. Raffai[28,82], S. Raja[114], G. Rajalakshmi[115], M. Rakhmanov[32], C. Ramet[6], P. Rapagnani[19,67], V. Raymond[1], V. Re[58,66], C. M. Reed[25], T. Reed[116], T. Regimbau[38], S. Reid[117], D. H. Reitze[1,16], F. Ricci[19,67], R. Riesen[6], K. Riles[56], N. A. Robertson[1,26], F. Robinet[35], A. Rocchi[58], S. Roddy[6], C. Rodriguez[79], M. Rodruck[25], C. Roever[8], L. Rolland[3], J. G. Rollins[1], J. D. Romano[32], R. Romano[4,5], G. Romanov[90], J. H. Romie[6], D. Rosińska[31,118], S. Rowan[26], A. Rüdiger[8], P. Ruggi[23], K. Ryan[25], F. Salemi[8], L. Sammut[105], V. Sandberg[25], J. Sanders[56], V. Sannibale[1], I. Santiago-Prieto[26], E. Saracco[41], B. Sassolas[41], B. S. Sathyaprakash[7], P. R. Saulson[24], R. Savage[25], R. Schilling[8], R. Schnabel[8,13], R. M. S. Schofield[46], E. Schreiber[8], D. Schuette[8], B. Schulz[8], B. F. Schutz[7,21], P. Schwinberg[25], J. Scott[26], S. M. Scott[64], F. Seifert[1], D. Sellers[6], A. S. Sengupta[119], D. Sentenac[23], A. Sergeev[98], D. Shaddock[64], S. Shah[9,120], M. S. Shahriar[79], M. Shaltev[8], B. Shapiro[29], P. Shawhan[50], D. H. Shoemaker[10], T. L. Sidery[20], K. Siellez[38], X. Siemens[12], D. Sigg[25], D. Simakov[8], A. Singer[1], L. Singer[1], A. M. Sintes[52], G. R. Skelton[12], B. J. J. Slagmolen[64], J. Slutsky[8], J. R. Smith[18], M. R. Smith[1], R. J. E. Smith[20], N. D. Smith-Lefebvre[1], K. Soden[12], E. J. Son[113], B. Sorazu[26], T. Souradeep[75], L. Sperandio[58,66], A. Staley[28], E. Steinert[25], J. Steinlechner[8], S. Steinlechner[8], S. Steplewski[42], D. Stevens[79], A. Stochino[64], R. Stone[32], K. A. Strain[26], S. Strigin[34], A. S. Stroeer[32], R. Sturani[44,45], A. L. Stuver[6], T. Z. Summerscales[121], S. Susmithan[37], P. J. Sutton[7], B. Swinkels[23], G. Szeifert[82], M. Tacca[27], D. Talukder[46], L. Tang[32], D. B. Tanner[16], S. P. Tarabrin[8], R. Taylor[1], A. P. M. ter Braack[9], M. P. Thirugnanasambandam[1], M. Thomas[6], P. Thomas[25], K. A. Thorne[6], K. S. Thorne[61], E. Thrane[1], V. Tiwari[16], K. V. Tokmakov[107], C. Tomlinson[73], A. Toncelli[14,30], M. Tonelli[14,30], O. Torre[14,15], C. V. Torres[32], C. I. Torrie[1,26], F. Travasso[43,84], G. Traylor[6], M. Tse[28], D. Ugolini[122], C. S. Unnikrishnan[115], H. Vahlbruch[13], G. Vajente[14,30], M. Vallisneri[61], J. F. J. van den Brand[9,49], C. Van Den Broeck[9], S. van der Putten[9], M. V. van der Sluys[79], J. van Heijningen[9], A. A. van Veggel[26], S. Vass[1], M. Vasúth[74], R. Vaulin[10], A. Vecchio[20], G. Vedovato[123], J. Veitch[9], P. J. Veitch[91], K. Venkateswara[124], D. Verkindt[3], S. Verma[37], F. Vetrano[44,45], A. Viceré[44,45], R. Vincent-Finley[111], J.-Y. Vinet[38], S. Vitale[9,10], B. Vlcek[12], T. Vo[25], H. Vocca[43,84], C. Vorvick[25], W. D. Vousden[20], D. Vrinceanu[32], S. P. Vyachanin[34], A. Wade[64], L. Wade[12], M. Wade[12], S. J. Waldman[10], M. Walker[2], L. Wallace[1], Y. Wan[55], J. Wang[59], M. Wang[20], X. Wang[55], A. Wanner[8], R. L. Ward[64], M. Was[8], B. Weaver[25], L.-W. Wei[38], M. Weinert[8], A. J. Weinstein[1], R. Weiss[10], T. Welborn[6], L. Wen[37], P. Wessels[8], M. West[24], T. Westphal[8], K. Wette[8], J. T. Whelan[57], S. E. Whitcomb[1,37], D. J. White[73], B. F. Whiting[16], S. Wibowo[12], K. Wiesner[8], C. Wilkinson[25], L. Williams[16], R. Williams[1], T. Williams[125], J. L. Willis[126], B. Willke[8,13], M. Wimmer[8], L. Winkelmann[8], W. Winkler[8], C. C. Wipf[10], H. Wittel[8], G. Woan[26], J. Worden[25], J. Yablon[79], I. Yakushin[6], H. Yamamoto[1], C. C. Yancey[50], H. Yang[61], D. Yeaton-Massey[1], S. Yoshida[125], H. Yum[79], M. Yvert[3], A. Zadrożny[102], M. Zanolin[86], J.-P. Zendri[123], F. Zhang[10], L. Zhang[1], C. Zhao[37], H. Zhu[81], X. J. Zhu[37], N. Zotov[116,145], M. E. Zucker[10], and J. Zweizig[1]

(The LIGO Scientific Collaboration and the Virgo Collaboration)

and

C. Akerlof[56], C. Baltay[127], J. S. Bloom[128], Y. Cao[78], S. B. Cenko[36], A. Ćwiek[102], M. Ćwiok[129], V. Dhillon[73], D. B. Fox[81], A. Gal-Yam[130], M. M. Kasliwal[131,146], A. Klotz[132], M. Laas-Bourez[37,39], R. R. Laher[78], N. M. Law[133], A. Majcher[102], K. Małek[134,135], L. Mankiewicz[135], K. Nawrocki[102], S. Nissanke[78], P. E. Nugent[128,136], E. O. Ofek[130], R. Opiela[135], L. Piotrowski[129,137], D. Poznanski[138], D. Rabinowitz[127], S. Rapoport[64], J. W. Richards[128], B. Schmidt[139], M. Siudek[135], M. Sokołowski[102,140,141], I. A. Steele[142], M. Sullivan[143], A. F. Żarnecki[129], and W. Zheng[128]

[1] LIGO - California Institute of Technology, Pasadena, CA 91125, USA
[2] Louisiana State University, Baton Rouge, LA 70803, USA
[3] Laboratoire d'Annecy-le-Vieux de Physique des Particules (LAPP), Université de Savoie, CNRS/IN2P3, F-74941 Annecy-le-Vieux, France
[4] INFN, Sezione di Napoli, Complesso Universitario di Monte S. Angelo, I-80126 Napoli, Italy
[5] Università di Salerno, Fisciano, I-84084 Salerno, Italy
[6] LIGO - Livingston Observatory, Livingston, LA 70754, USA
[7] Cardiff University, Cardiff, CF24 3AA, UK
[8] Albert-Einstein-Institut, Max-Planck-Institut für Gravitationsphysik, D-30167 Hannover, Germany
[9] Nikhef, Science Park, 1098 XG Amsterdam, The Netherlands
[10] LIGO - Massachusetts Institute of Technology, Cambridge, MA 02139, USA
[11] Instituto Nacional de Pesquisas Espaciais, 12227-010 - São José dos Campos, SP, Brazil
[12] University of Wisconsin–Milwaukee, Milwaukee, WI 53201, USA
[13] Leibniz Universität Hannover, D-30167 Hannover, Germany
[14] INFN, Sezione di Pisa, I-56127 Pisa, Italy
[15] Università di Siena, I-53100 Siena, Italy
[16] University of Florida, Gainesville, FL 32611, USA
[17] The University of Mississippi, University, MS 38677, USA
[18] California State University Fullerton, Fullerton, CA 92831, USA
[19] INFN, Sezione di Roma, I-00185 Roma, Italy
[20] University of Birmingham, Birmingham, B15 2TT, UK
[21] Albert-Einstein-Institut, Max-Planck-Institut für Gravitationsphysik, D-14476 Golm, Germany
[22] Montana State University, Bozeman, MT 59717, USA
[23] European Gravitational Observatory (EGO), I-56021 Cascina, Pisa, Italy
[24] Syracuse University, Syracuse, NY 13244, USA
[25] LIGO - Hanford Observatory, Richland, WA 99352, USA
[26] SUPA, University of Glasgow, Glasgow, G12 8QQ, UK
[27] APC, AstroParticule et Cosmologie, Université Paris Diderot, CNRS/IN2P3, CEA/Irfu, Observatoire de Paris, Sorbonne Paris Cité, 10, rue Alice Domon et Léonie Duquet, F-75205 Paris Cedex 13, France
[28] Columbia University, New York, NY 10027, USA
[29] Stanford University, Stanford, CA 94305, USA
[30] Università di Pisa, I-56127 Pisa, Italy
[31] CAMK-PAN, 00-716 Warsaw, Poland
[32] The University of Texas at Brownsville, Brownsville, TX 78520, USA
[33] San Jose State University, San Jose, CA 95192, USA
[34] Moscow State University, Moscow 119992, Russia
[35] LAL, Université Paris-Sud, IN2P3/CNRS, F-91898 Orsay, France
[36] NASA/Goddard Space Flight Center, Greenbelt, MD 20771, USA
[37] University of Western Australia, Crawley, WA 6009, Australia
[38] ARTEMIS UMR 7250, Université Nice-Sophia-Antipolis, CNRS, Observatoire de la Côte d'Azur, F-06304 Nice, France
[39] Observatoire de Haute-Provence, CNRS, F-04870 Saint Michel l'Observatoire, France
[40] Institut de Physique de Rennes, CNRS, Université de Rennes 1, F-35042 Rennes, France
[41] Laboratoire des Matériaux Avancés (LMA), IN2P3/CNRS, Université de Lyon, F-69622 Villeurbanne, Lyon, France
[42] Washington State University, Pullman, WA 99164, USA
[43] INFN, Sezione di Perugia, I-06123 Perugia, Italy
[44] INFN, Sezione di Firenze, I-50019 Sesto Fiorentino, Firenze, Italy
[45] Università degli Studi di Urbino "Carlo Bo," I-61029 Urbino, Italy
[46] University of Oregon, Eugene, OR 97403, USA
[47] Laboratoire Kastler Brossel, ENS, CNRS, UPMC, Université Pierre et Marie Curie, F-75005 Paris, France
[48] Astronomical Observatory Warsaw University, 00-478 Warsaw, Poland
[49] VU University Amsterdam, 1081 HV Amsterdam, The Netherlands
[50] University of Maryland, College Park, MD 20742, USA
[51] University of Massachusetts–Amherst, Amherst, MA 01003, USA
[52] Universitat de les Illes Balears, E-07122 Palma de Mallorca, Spain
[53] Università di Napoli "Federico II," Complesso Universitario di Monte S. Angelo, I-80126 Napoli, Italy
[54] Canadian Institute for Theoretical Astrophysics, University of Toronto, Toronto, Ontario, M5S 3H8, Canada
[55] Tsinghua University, Beijing 100084, China
[56] University of Michigan, Ann Arbor, MI 48109, USA
[57] Rochester Institute of Technology, Rochester, NY 14623, USA
[58] INFN, Sezione di Roma Tor Vergata, I-00133 Roma, Italy
[59] National Tsing Hua University, Hsinchu 300, Taiwan
[60] Charles Sturt University, Wagga Wagga, NSW 2678, Australia
[61] Caltech-CaRT, Pasadena, CA 91125, USA
[62] INFN, Sezione di Genova, I-16146 Genova, Italy
[63] Pusan National University, Busan 609-735, Korea
[64] Australian National University, Canberra, ACT 0200, Australia
[65] Carleton College, Northfield, MN 55057, USA
[66] Università di Roma Tor Vergata, I-00133 Roma, Italy
[67] Università di Roma "La Sapienza," I-00185 Roma, Italy

[68] University of Sannio at Benevento, I-82100 Benevento, Italy
[69] INFN (Sezione di Napoli), Italy
[70] The George Washington University, Washington, DC 20052, USA
[71] University of Cambridge, Cambridge, CB2 1TN, UK
[72] University of Minnesota, Minneapolis, MN 55455, USA
[73] The University of Sheffield, Sheffield S10 2TN, UK
[74] Wigner RCP, RMKI, H-1121 Budapest, Konkoly Thege Miklós út 29-33, Hungary
[75] Inter-University Centre for Astronomy and Astrophysics, Pune-411007, India
[76] INFN, Gruppo Collegato di Trento, I-38050 Povo, Trento, Italy
[77] Università di Trento, I-38050 Povo, Trento, Italy
[78] California Institute of Technology, Pasadena, CA 91125, USA
[79] Northwestern University, Evanston, IL 60208, USA
[80] Montclair State University, Montclair, NJ 07043, USA
[81] The Pennsylvania State University, University Park, PA 16802, USA
[82] MTA-Eotvos University, "Lendulet" A. R. G., Budapest 1117, Hungary
[83] National Astronomical Observatory of Japan, Tokyo 181-8588, Japan
[84] Università di Perugia, I-06123 Perugia, Italy
[85] Rutherford Appleton Laboratory, HSIC, Chilton, Didcot, Oxon, OX11 0QX, UK
[86] Embry-Riddle Aeronautical University, Prescott, AZ 86301, USA
[87] Perimeter Institute for Theoretical Physics, Ontario, N2L 2Y5, Canada
[88] American University, Washington, DC 20016, USA
[89] University of New Hampshire, Durham, NH 03824, USA
[90] College of William and Mary, Williamsburg, VA 23187, USA
[91] University of Adelaide, Adelaide, SA 5005, Australia
[92] Raman Research Institute, Bangalore, Karnataka 560080, India
[93] Korea Institute of Science and Technology Information, Daejeon 305-806, Korea
[94] Białystok University, 15-424 Białystok, Poland
[95] University of Southampton, Southampton, SO17 1BJ, UK
[96] IISER-TVM, CET Campus, Trivandrum Kerala 695016, India
[97] Hobart and William Smith Colleges, Geneva, NY 14456, USA
[98] Institute of Applied Physics, Nizhny Novgorod 603950, Russia
[99] Seoul National University, Seoul 151-742, Korea
[100] Hanyang University, Seoul 133-791, Korea
[101] IM-PAN, 00-956 Warsaw, Poland
[102] NCBJ, 05-400 Świerk-Otwock, Poland
[103] Institute for Plasma Research, Bhat, Gandhinagar 382428, India
[104] Utah State University, Logan, UT 84322, USA
[105] The University of Melbourne, Parkville, VIC 3010, Australia
[106] University of Brussels, Brussels 1050, Belgium
[107] SUPA, University of Strathclyde, Glasgow, G1 1XQ, UK
[108] ESPCI, CNRS, F-75005 Paris, France
[109] Dipartimento di Fisica, Università di Camerino, I-62032 Camerino, Italy
[110] The University of Texas at Austin, Austin, TX 78712, USA
[111] Southern University and A&M College, Baton Rouge, LA 70813, USA
[112] IISER-Kolkata, Mohanpur, West Bengal 741252, India
[113] National Institute for Mathematical Sciences, Daejeon 305-390, Korea
[114] RRCAT, Indore, MP 452013, India
[115] Tata Institute for Fundamental Research, Mumbai 400005, India
[116] Louisiana Tech University, Ruston, LA 71272, USA
[117] SUPA, University of the West of Scotland, Paisley, PA1 2BE, UK
[118] Institute of Astronomy, 65-265 Zielona Góra, Poland
[119] Indian Institute of Technology, Gandhinagar, Ahmedabad, Gujarat 382424, India
[120] Department of Astrophysics/IMAPP, Radboud University Nijmegen, P.O. Box 9010, 6500 GL Nijmegen, The Netherlands
[121] Andrews University, Berrien Springs, MI 49104, USA
[122] Trinity University, San Antonio, TX 78212, USA
[123] INFN, Sezione di Padova, I-35131 Padova, Italy
[124] University of Washington, Seattle, WA 98195, USA
[125] Southeastern Louisiana University, Hammond, LA 70402, USA
[126] Abilene Christian University, Abilene, TX 79699, USA
[127] Yale University, New Haven, CT 06520, USA
[128] University of California Berkeley, Berkeley, CA 94720, USA
[129] Faculty of Physics, University of Warsaw, Hoza 69, 00-681 Warsaw, Poland
[130] Weizmann Institute of Science, 76100 Rehovot, Israel
[131] Observatories of the Carnegie Institution for Science, Pasadena, CA 91101, USA
[132] Institut de Recherche en Astrophysique et Planetologie (IRAP), F-31400 Toulouse, France
[133] Department of Physics and Astronomy, University of North Carolina at Chapel Hill, Chapel Hill, NC 27599-3255, USA
[134] Division of Particles and Astrophysical Science, Nagoya University, Furo-cho, Chikusa-ku, 464-8601 Nagoya, Japan
[135] Centre for Theoretical Physics of Polish Academy of Sciences, Al. Lotnikow 32/46, 02-668 Warsaw, Poland
[136] Lawrence Berkeley National Laboratory, Berkeley, CA 94720, USA
[137] RIKEN, 2-1 Hirosawa, Wako, 351-0198, Saitama, Japan
[138] School of Physics and Astronomy, Tel Aviv University, Tel Aviv 69978, Israel
[139] The Research School of Astronomy and Astrophysics, The Australian National University, via Cotter Rd, Weston Creek, ACT 2611, Australia
[140] International Centre for Radio Astronomy Research-Curtin University, GPO Box U1987, Perth, WA 6845, Australia
[141] ARC Centre of Excellence for All-sky Astrophysics (CAASTRO)
[142] Astrophysics Research Institute, Liverpool John Moores University, L3 5RF, UK
[143] School of Physics and Astronomy, University of Southampton, Highfield, Southampton, SO17 1BJ, UK

Received 2013 October 30; accepted 2014 January 18; published 2014 February 11

ABSTRACT

During the Laser Interferometer Gravitational-wave Observatory and Virgo joint science runs in 2009–2010, gravitational wave (GW) data from three interferometer detectors were analyzed within minutes to select GW candidate events and infer their apparent sky positions. Target coordinates were transmitted to several telescopes for follow-up observations aimed at the detection of an associated optical transient. Images were obtained for eight such GW candidates. We present the methods used to analyze the image data as well as the transient search results. No optical transient was identified with a convincing association with any of these candidates, and none of the GW triggers showed strong evidence for being astrophysical in nature. We compare the sensitivities of these observations to several model light curves from possible sources of interest, and discuss prospects for future joint GW-optical observations of this type.

Key words: binaries: close – catalogs – gravitational waves – stars: neutron – surveys

Online-only material: color figures

1. INTRODUCTION

Transient gravitational-wave (GW) emission is expected from highly energetic astrophysical events such as stellar-core collapses and mergers of binary neutron stars (NSs). The Laser Interferometer Gravitational-wave Observatory (LIGO; Abbott et al. 2009; Harry et al. 2010) includes detectors located in the United States near Hanford, Washington (H1) and Livingston, LA (L1). A similarly designed Virgo (V1; Accadia et al. 2012; Virgo Collaboration 2009) detector is located in Italy near the city of Cascina. Each interferometer contains a pair of perpendicular arms, 4 km long in the LIGO detectors and 3 km in Virgo, whose effective optical path length is slightly altered by passing GW signals. Since 2007, LIGO and Virgo have coordinated operations and shared data, so the three sites operate as a single network of detectors seeking direct measurements of GW signals. A fourth site, GEO600 in Hannover, Germany (Grote et al. 2008), also shares data with LIGO and Virgo.

During the 2009–2010 science run of the LIGO/Virgo network (Abadie et al. 2012e) we implemented low-latency searches for GW transients. The analysis software identified GW event candidates ("triggers"), estimated their statistical significance, and reconstructed likely source positions in approximately 10 minutes. Alert messages were transmitted to a network of electromagnetic observatories after the manual validation of the GW triggers with a total latency of ∼30 minutes. The collection of optical telescopes, as well as the *Swift* satellite, LOFAR, and the Expanded Very Large Array (Lazio et al. 2012), provided target of opportunity follow-up observations to the GW triggers. In earlier publications, we described the search method and likely sources of both GW and emission measure (EM) transients (Abadie et al. 2012c, 2012d), as well as the results of the follow-up observations performed with the *Swift* satellite (Evans et al. 2012).

In this paper, we describe the data set collected with optical telescopes, detail the methods used to search the data for transients consistent with expected optical counterparts to GWs, and report the results of this analysis. In this first effort to use optical instruments to search for transients based on data from GW detectors, none of the GW triggers showed strong evidence for being astrophysical in nature. However, searching for transients in a large sky area is a challenging problem, and uncertainty in the expected light curve and spectrum of the sought optical counterpart makes the problem harder still. For this reason, we emphasize the methodologies used to identify transient phenomena in our data set and to separate objects consistent with our target models from those that are not. In addition, we discuss the results of Monte Carlo simulations used to test the efficiency of our pipelines in recovering various types of transients, and the implications for future searches of optical counterparts of GW events discovered with next generation observatories.

A variety of astrophysical processes are likely to be associated with both GW and EM emission. Among these, gamma-ray bursts (GRBs) are promising sources for joint GW and EM studies (e.g., Kochanek & Piran 1993; Kobayashi & Mészáros 2003; Abadie et al. 2012b). GRBs are traditionally divided in two main classes, long and short bursts (Kouveliotou et al. 1993), which are thought to be associated with different progenitors (e.g., Gehrels et al. 2007; Mészáros 2006, and references therein). Long GRBs are associated with "collapsars," the gravitational collapse of cores of massive stars (Woosley 1993; MacFadyen & Woosley 1999), while short GRBs may be produced by mergers of binary systems of compact objects (NS/NS or black-hole/NS; e.g., Eichler et al. 1989; Paczynski 1991; Narayan et al. 1992). A compact binary merger results from gravitational radiation, producing a characteristic "inspiral" of the binary orbit and a corresponding strong GW signal (e.g., Thorne 1987; Shibata & Taniguchi 2011). GW emission from a collapsar depends on non-spherically-symmetric flow of material during the collapse, which may be enhanced by centrifugal effects if the progenitor is rotating rapidly (Davies et al. 2002; Fryer et al. 2002; Shibata et al. 2003; Piro & Pfahl 2007; Corsi & Mészáros 2009; Ott 2009; Romero et al. 2010).

High-energy emission from GRBs is thought to escape as narrow relativistic jets (e.g., Sari et al. 1999; Harrison et al. 1999; Frail et al. 2001; Racusin et al. 2009), though at least in the case of the short GRBs, there is uncertainty regarding the angular extent of typical beams (Fong et al. 2012), as well as how the beaming angle depends on wavelength (van Eerten & MacFadyen 2011). Afterglows of both classes of GRBs have been observed over a wide range of wavelengths (Costa et al. 1997; Frail et al. 1997; van Paradijs et al. 1997; Gehrels et al. 2005; Hjorth et al. 2005; Abdo et al. 2009), from times nearly concurrent with the prompt emission to days later (e.g., Nousek et al. 2006; Molinari et al. 2007; Racusin et al. 2011, and references therein). Generally, the observed optical afterglows fade with a temporal power-law decay, with typical indices between 1 and 1.5 (e.g., Sari et al. 1998; Nakar 2007). A wide range of luminosities have been observed, with the afterglows of short bursts tending to be less energetic than the afterglows of long bursts (Kann et al. 2011).

[144] Deceased, 2012 April.
[145] Deceased, 2012 May.
[146] Hubble Fellow and Carnegie-Princeton Fellow.

Table 1
R-band Light Curve Models Used for Simulated Injections

Source	Light Curve Model		Normalization Condition
Short GRB	$L \propto t^{-1.1}$		23–31 mag at 1 day from $z = 1$
Long GRB	$L \propto t^{-1.1}$		16–24 mag at 1 day from $z = 1$
Kilonova	$L = (1.2 \times 10^{42}) t^{0.43}$ erg s^{-1}	$t < 0.7$ days	
	$L = (6.7 \times 10^{41}) t^{-1.29}$ erg s^{-1}	$t > 0.7$ days	

Notes. Normalizations used for the on-axis short GRB and long GRB models correspond to the full range of observed on-axis GRB afterglows in each class in the observer frame, assuming $z = 1$, from Kann et al. (2010, 2011). The kilonova model is intended to mimic the light curves shown in Metzger et al. (2010) and Piran et al. (2013).

The merger of two NSs or a NS with a black hole may lead to a supernova-like transient, as described by Li & Paczyński (1998). In their model, heavy radioactive elements are formed in the merger ejecta through rapid neutron capture nucleosynthesis. As the newly formed isotopes decay toward stability, they release energy and heat the ejecta. Thermal emission becomes visible after the ejecta has expanded enough to allow photons to escape. The expected transient, referred to as a kilonova throughout this paper, is roughly isotropic, and the associated light curve is expected to peak about a day after the merger time (Metzger et al. 2010; Piran et al. 2013). The model has been supported by a variety of computational work (Faber & Rasio 2012; Roberts et al. 2011), though some details of the model are still uncertain, including the amount of mass ejected from the merger and the physics of the radiative transport. These unknowns lead to uncertainties in the peak luminosity, time-scale, and color evolution of the model. For example, Barnes & Kasen (2013) found that the ejected NS material may have a high opacity, leading to light curves that peak in infrared rather than optical wavelengths; this prediction seems consistent with one recent observation (Tanvir et al. 2013; Berger et al. 2013). For testing purposes, we adopted a simple model which was intended to mimic the main features of the light curves in Metzger et al. (2010) and Piran et al. (2013) (see Table 1).

Core-collapse supernovae are expected to emit enough GW energy to be observable with current detectors within some fraction of the Milky Way, to distances of perhaps a few kpc (Ott 2009). A rare class of core-collapse supernovae is also known to be linked to long GRBs (Galama et al. 1998; Woosley & Bloom 2006; Soderberg et al. 2006). Indeed, optical follow-ups of GW triggers could catch optical supernovae harboring off-axis GRBs, whose gamma-ray emission would be missed because the relativistic GRB jet is not pointed toward earth (Granot et al. 2002; Rhoads 2003; van Eerten et al. 2010). However, unlike the models discussed above, tracking a supernova light curve requires several days or weeks of observations after the GW trigger (Doggett & Branch 1985). Slow light curves are also expected from off-axis GRBs, whose emission is expected to peak on timescales of weeks to months (e.g., van Eerten & MacFadyen 2011). Taking into account that the LIGO and Virgo detectors are expected to detect more merger events than core-collapse events, the cadence of our optical follow-up observations was chosen mainly for shorter optical transients, but with some observations extending to later times to possibly catch a slower transient.

The paper is organized as follows: Section 2 first gives a description of the ground-based telescopes involved in the follow-up program. In Section 3, we present the set of GW triggers that were selected and sent as alerts to the telescopes and we describe their associated follow-up observations. Section 4 details the methods employed to search for optical transients in the collected series of images and Section 5 reports the results of the searches. Finally, estimates of the search sensitivity are presented in Section 6.

2. TELESCOPES INVOLVED IN THE FOLLOW-UP PROGRAM

The optical follow-up program took place during times when the LIGO and Virgo observatories were operating in coincidence during 2009 and 2010. This time was divided into two segments: the "winter" run, between 2009 December and 2010 January, and the "autumn" run spanning most of 2010 September and October. The program was executed as a joint study between the LIGO and Virgo collaborations, and about 10 teams which operated automated and remotely controlled telescopes.

During the winter run, triggers from the LIGO/Virgo network were passed to the TAROT (Klotz et al. 2009) and QUEST (Baltay et al. 2007) telescopes. For the autumn run, the optical network was expanded to include Palomar Transient Factory (PTF; Rahmer et al. 2008; Law et al. 2009; Rau et al. 2009), Pi of the Sky (POTS; Malek et al. 2009), ROTSE III (Akerlof et al. 2003), SkyMapper (Keller et al. 2007), the Zadko Telescope (Coward et al. 2010), and the Liverpool Telescope (Steele et al. 2004). The large number (12) of telescopes participating in the autumn run allowed for better sky coverage. The main characteristics of these observatories are listed in Table 2. With the exception of the Liverpool RATCam and Zadko, they are all equipped with wide field cameras. A wide field of view (FOV) was considered an important feature for this study, due to the imprecise source localization of the GW instruments. We expected localizations of a few tens of square degrees up to 200 deg^2, and so instruments without a wide FOV would be unable to image a significant fraction of the uncertainty region (Cavalier et al. 2004; Nissanke et al. 2011; Fairhurst 2011; Klimenko et al. 2011). However, with the limited sensitive range to an optimally aligned source (horizon distance) of initial LIGO and Virgo, it was also possible for an instrument to observe only the most likely host galaxies for a compact object merger (Abadie et al. 2012d; Kanner et al. 2008; Nuttall & Sutton 2010).

Separate observing plans were constructed for each observatory. Some of the instruments targeted only the single most likely field for a given GW trigger, while others observed multiple fields in an effort to cover an area comparable to the GW position uncertainty (see Table 2). Planned cadences were also different for each observatory. Generally, the goal was to observe at least once as quickly as possible to image a potential rapidly fading counterpart. Where possible, attempts were made to image each field over several nights following the GW trigger, in order to trace the light curves of potential transients. The details of the observations are described in Section 5.

Table 2
Characteristics of Instruments Involved in the Search

Name	Locations	FOV (deg^2)	Aperture (m)	Exposure Time (s)	Limiting Magnitude	Tiles
Palomar Transient Factory	1	7.3	1.2	60	20.5	10
Pi of the Sky	1	400	0.072	10	11.5	1
QUEST	1	9.4	1	60	20.5	3
ROTSE III	4	3.4	0.45	20	17.5	1
SkyMapper	1	5.7	1.35	110	21.5	8
TAROT	2	3.4	0.25	180	17.5	1
Zadko Telescope	1	0.15	1	120	20.5	5
Liverpool Telescope - RATCam	1	0.0058	2	300	21	1
Liverpool Telescope - SkyCamZ	1	1	0.2	10	18	1

Notes. The column labeled "Tiles" indicates the maximum number of different field positions that the telescope searched in response to a trigger. The shown limiting magnitudes are estimates, under ideal observing conditions. They are listed in r' band for RATCam, r band for SkyMapper, and R band for all other instruments. Palomar Transient Factory, SkyMapper and RATCam are calibrated to the SDSS/AB photometric system; the others are expressed in the Vega photometric system.

3. GRAVITATIONAL-WAVE TRIGGERS SELECTED FOR FOLLOW-UP OBSERVATIONS

3.1. Trigger Selection

Triggers for this search were identified with a collection of low-latency pipelines designed to find transient GW events in data from the three site LIGO/Virgo network. Here, we provide a brief summary of the trigger production and selection, while a more detailed description is described in Abadie et al. (2012c, 2012d). During the winter run, two pipelines were used to identify generic short-duration transients of significant signal power, or "bursts," and estimate their source positions: the Omega (Ω) Pipeline (Searle et al. 2008; Abadie et al. 2010a) and the coherent WaveBurst (cWB) pipeline (Klimenko et al. 2011). For the autumn run, a third trigger pipeline was added: the Multi-Band Template Analysis (MBTA; Beauville et al. 2008; Abadie et al. 2012c), which sought inspiral waveforms from coalescing compact objects. The autumn run also added a second instance of cWB, configured to target linearly polarized GW signals, as might be expected from supernovae.

To compare triggers from different pipelines and identify the ones suitable for observation, follow-up software made event candidate selections based on the estimated false alarm rate (FAR) of each trigger. The rate of background false alarms was estimated by forming a distribution of artificial triggers from data with one or more data streams shifted by at least several seconds. Time-shifting data removes correlations of possible GW signals between detectors, so this distribution was considered to be free from any putative signals and represented the rate of triggers not due to transient GWs (Abadie et al. 2012a, 2012e). During the winter run, a FAR threshold of 1 trigger day^{-1} was applied to triggers, and a less significant FAR was accepted in the last week to exercise the system. For the autumn run, the FAR threshold was set to 0.25 day^{-1}. Triggers which passed the automated threshold received attention from an on-call follow-up team. The on-call team checked that the trigger occurred in high quality data in each interferometer. In addition, the criteria for manual validation in the winter run included demands that the three suggested (see below) QUEST fields covered a sky area corresponding to a greater than 50% probability of containing the GW source and that follow-up requests were sent at a rate of less than one per 24 hr.

The trigger pipelines reported the estimated position of each candidate GW event as a *skymap*, a list of probability densities assigned to pixels in a grid covering the sky. The grid used pixels approximately 0.4 on a side, selected to be similar to the degree-scale resolving power of the GW network (for example, Fairhurst 2011; Klimenko et al. 2011; Vitale et al. 2012; Nissanke et al. 2011). The large angular size of the skymaps required a choice of where within the uncertainty region to observe. To observe the regions most likely to contain an observable GW source, we used a catalog of galaxies within 50 Mpc and Milky Way globular clusters (GWGC; White et al. 2011), thought to be around 70% complete to 50 Mpc by B-band luminosity. Each pixel in the skymap was given a weight P according to the formula

$$P \propto L\left(\frac{M}{D}\right), \quad (1)$$

where L is the probability of the pixel derived from the GW data alone; M is the blue light luminosity of the galaxy or galaxies contained in the pixel, which is used as a proxy for the star formation rate; and D is the distance to the galaxy (Nuttall & Sutton 2010). For MBTA triggers, a slightly modified version of this approach was applied, using the maximum distance consistent with the apparent inspiral signal (Abadie et al. 2012c). The suggested fields for each telescope were those that maximized the sum of P within the respective FOV. Unless unobservable due to daylight or geometrical constraints, the suggested fields were passed to each optical telescope for every GW event candidate that passed manual validation. However, a more stringent selection was applied for PTF, and only one GW trigger was sent to PTF.

3.2. Data Set

In the winter run, the on-call team was alerted a total of nine times. Three of these triggers were vetoed by the on-call team. Six triggers were approved by the on-call team and sent to the QUEST and TAROT telescopes with roughly 30 minutes of latency. Of the six requests, four were rejected as unobservable by the scheduling software of both telescopes and two triggers were followed-up with the QUEST telescope. In addition, two triggers that did not pass the automated FAR threshold were selected by the on-call team and passed to the partner observatories in an effort to expand the winter run data set (see Table 3).

In the autumn run, only one trigger was manually rejected due to data quality concerns. Six triggers resulted in alerts

Table 3
Gravitational Wave Triggers in the Winter Run

ID	Date	UTC	Pipeline	FAR (day^{-1})	Follow-up
G3821	2009 Dec 29	15:16:33	Ω	0.66	QUEST collected 12 images
CWB1	2010 Jan 3	20:37:22	cWB	1.3	Alert sent Jan 7; TAROT collected 6 images
G4202	2010 Jan 6	06:49:45	Ω	4.5	QUEST collected 9 images
CWB2	2010 Jan 7	08:46:37	cWB	1.6	QUEST collected 12 images

Table 4
Gravitational Wave Triggers in the Autumn Run

ID	Date	UTC	Pipeline	FAR (day^{-1})	Follow-up
G19377	2010 Sep 16	06:42:23	cWB (unmodeled)	<0.01	ROTSE collected 117 images, TAROT collected 20, Zadko 129, and SkyMapper 21. Blind injection
G20190	2010 Sep 19	12:02:25	MBTA	0.16	ROTSE collected 257 images, QUEST 23, Zadko 159, and TAROT 3
G21852	2010 Sep 26	20:24:32	cWB (linear)	0.02	ROTSE collected 130 images, PTF 149, CAT 3 DQ
G23004	2010 Oct 3	16:48:23	Ω	0.21	ROTSE collected 153 images, QUEST 40, Liverpool - RATCam 22, Liverpool - SkyCamZ 121, and POTS 444

to the observing partners, four of which resulted in follow-up observations[147] (see Table 4). Two of the triggers are worth special note. The September 16 trigger was recognized by the on-call team as having a special significance: in addition to a small estimated FAR, spectrograms of the GW data revealed frequency evolution characteristic of the late inspiral and merger of two compact objects. This event was later revealed to be a blind hardware injection, a simulated signal secretly added to the data to test the end-to-end system. The September 26 event candidate was also discovered with a low FAR estimate. In subsequent GW data analysis, this trigger was found to be the most significant cWB trigger above 200 Hz in the time period where H1, L1, and V1 were running in coincidence in this science run, though was removed from the analysis based on data quality concerns. The FAR was measured to be 0.023 events per day, or one such trigger expected for every 44 days of network livetime. Since these detectors ran in coincidence for a total of 52.2 days throughout the Virgo science run, this trigger was consistent with expectations for detector noise.

4. SEARCHES FOR OPTICAL TRANSIENTS

A search for optical transients essentially consists of searching for fading optical point sources in a sequence of astronomical images. A few characteristics make the search for GW counterparts unique. First, there is a significant uncertainty regarding the expected light curve from a GW source; we targeted short duration (hours to days) transients consistent with GRB afterglows and kilonovae light curves. Second, the poor localization of the GW error box required searching through a large portion of the sky. This significantly differed from the arcminute-scale error box used to find optical afterglows of GRBs discovered by *Swift*. Finally, we designed automated pipelines with Monte-Carlo simulations to evaluate the statistical significance of any apparent counterpart.

The telescopes involved in the program included very different instruments ranging from shallow, very wide-field cameras to meter-class telescopes (Table 2). They collected images with different cadences and follow-up strategies, leading to a heterogeneous data set. This has led us to develop a similarly heterogeneous analysis approach, with techniques tailored to match the requirements of each observational data set. Where possible, we leveraged existing software already in use by the various astronomical teams. The list of techniques which were applied in some, but not all, of the developed searches included image subtraction, identification of host galaxies, cuts on shape parameters, automated transient classifiers, volunteer work by citizen scientists, and consistency checks on light curve properties.

In future searches for optical counterparts to GW sources, a critical component will be rapidly down-selecting candidate lists to allocate follow-up resources such as large aperture photometry and spectroscopy. In this work, we attempted to unify results from disparate analyses by developing two common search statistics, which were applied in multiple analyses. The first statistic was used to quantify the ability to reject false positives, and labeled the "false-alarm probability" (FAP). The FAP was defined as the probability that a set of optical images taken with a given telescope in response to a single GW trigger, and analyzed with a given pipeline, would lead to a false positive. The FAP could encompass both false positives arising from technical noise, such as procedure artifacts, and astrophysical transients not related to the GW sources, such as M dwarf flares, Galactic variable stars, and extragalactic active galactic nuclei (AGNs) and supernovae. For most data sets, we set a FAP target of 10%. This FAP level was chosen to reduce the number of false positives to a manageable level, so that each object passing the selection criteria could, in principle, be further studied with sensitive photometric and/or spectroscopic observations. The second statistic used to characterize an analysis was the detection efficiency, defined as the recovery rate for simulated optical transients added to representative images. We measured detection efficiencies for a few different model light curves, using data and analysis procedures from several different telescopes. The FAP measurements and the Monte Carlo simulations allowed us to find a good compromise between rejection of false positives and reduction of interesting EM candidates. For example, in a study with the QUEST and TAROT data, we found that increasing the FAP to 0.20 would produce less than a 30% improvement in the sensitive distance range of the search, and so would increase the sensitive search volume by roughly a factor

[147] Of the two triggers not observed, one was the first alert generated during the autumn run and ROTSE imaged the wrong location due to a software bug, while the other was too close to the Sun to be observable by any of the telescopes.

of two, while also doubling the number of false positives. This section describes the different methods that were used to identify potential transients consistent with our models, and reduce false positives.

4.1. Catalog-based Search for TAROT, Zadko, and QUEST Observations

This section describes the image analysis pipeline developed specifically for the TAROT, Zadko Telescope, and QUEST observations. Unlike other approaches presented in this work, the pipeline did not use image subtraction but it extracted a source catalog from each image, and sought transients by comparing the set of catalogs to a reference. For this reason, we refer to this pipeline as the "catalog-based search."

4.1.1. Analysis Pipeline

The search consisted of three main steps applied to the image set (after dark, flat and sky background level corrections): data photometric calibration, reconstruction of object light curves, and transient selection to identify possible electromagnetic counterparts.

TAROT, the Zadko Telescope, and QUEST observed with a clear filter. The magnitude zero-point calibration was performed using the USNO-A2.0 catalog (Monet et al. 1998) as reference and resulted in red equivalent magnitudes. For the QUEST camera, which is composed of 112 individual CCDs, calibration was performed separately on each CCD. The different response, data quality, and sensitivity of each CCD prevented managing them as a single mosaic, and the data analysis was performed CCD by CCD.

The source catalog of each image was extracted using `SExtractor` (Bertin & Arnouts 1996). Each list of sources was spatially cross-correlated with the star catalog USNO-A2.0 using the tool `match` (Droege et al. 2006). The radius used to search for common sources was set to 10″ for TAROT, 2″ for Zadko, and 3″ for QUEST. These values took into account the positional uncertainties in the images and in the USNO-A2.0 catalog. Sources found to coincide in position and luminosity with objects listed in the reference catalog were excluded from the search. The lists of remaining sources were then mutually cross-correlated in position to link sources observed at different times to common astrophysical objects. This resulted in a light curve for each identified object.

At this point, two types of analyses were conducted to select GW associated transients and reject background objects. The *on-source analysis* was restricted to objects lying in the image regions associated with galaxies within 50 Mpc[148] and Galactic globular clusters. For each galaxy a circular region with a radius five times the galaxy's semi-major axis (as provided by the GWGC; White et al. 2011) was analyzed. This region (which corresponds to an average radius of about 20 kpc) accounted for the typical projected physical offsets observed between GRB afterglows and their host galaxy centers (e.g., Berger 2010). The *whole-field analysis* covered the entire FOV but was limited to bright objects. For the QUEST telescope, large variations in the sensitivity and image quality between different CCDs made setting a whole-field magnitude threshold unfeasible to search the expected counterparts. For this reason, we performed only the on-source analysis on the QUEST data, which allowed us to search for faint transients while limiting the number of false positives (see Section 4.1.2).

For both types of analysis, rapid contaminating transients, including cosmic rays, asteroids, and CCD noise, were rejected by requiring the presence of the object in a minimum number of consecutive images. Further selection of transient objects (and hence rejection of background) was performed by applying thresholds to the initial (first observation) magnitude and light curve variability of each source. Variability was characterized by assuming power-law luminosity dimming with time, $\mathcal{L} \propto t^{-\beta}$, corresponding to a linear magnitude variation $m = 2.5\beta \log_{10}(t) + C$. The slope index 2.5β was evaluated for each object. The expected slope indices for GRB afterglows and kilonova light curves are around 2.5–4 (see Table 1). To seek these transients, we applied a cut which selected slope indices greater than 0.5. Because of the small number of repeated observations with QUEST (maximum of eight for each galaxy), a different variability measurement was used for this instrument's analysis. A threshold on the flux variation between the first and the following nights of observation was set by requiring a dimming larger than +0.5 mag (while we expected >+1 based on the light curve models and the QUEST observational cadence).

Studies of the background events (Section 4.1.2) and the ability to detect simulated on-axis GRBs and kilonovae (Section 6) were used to design selection criteria yielding a FAP of under 10% (prior probability that a background event passes all the selection criteria), while also accepting a wide range of astrophysical models. The thresholds applied to the variability measure (slope index or flux variation) were designed to detect fading transients while leaving the possibility of detecting light curves showing flaring within short time-scales (hours). However, recent re-evaluations of kilonova emission by Barnes & Kasen (2013) and others have indicated that more realistic values for the opacities of the heavy radioactive elements lead to dimmer and broader light curves. These would be difficult to detect with the depth and cadence of our data set.

4.1.2. Background Estimation

The background was estimated by running the analysis over a series of images obtained from random time permutations of the real observation images. The first night observations were excluded from being selected as the first image in each permuted sequence to remove any astrophysical electromagnetic counterparts from the data set. The background simulation was repeated 100 times for TAROT and the Zadko Telescope and for all the permutations allowed by the observations for QUEST.

Genuine optical transients would have lost their regularly fading light curve in the scrambled image set. Random sequencing thus erased them while artifacts such as CCD noise, pixel saturation, bad pixels, errors in the de-blending and source association, etc., were just as likely to pass the pipeline's selection cuts as with the true sequencing. This procedure allowed a measurement of the rate of false positives due to "technical" noise. However, this procedure did not permit a valuable estimate of the "astrophysical" background since the randomization reduced the number of identified astrophysical transients that actually dimmed over time. A statistically significant estimate of the astrophysical background would require the study of survey data not associated with GW triggers, which was not available at this time.

An example of the distribution of technical background events (after the removal of rapid transients) detected in the FOV of TAROT for trigger G19377 is shown in Figure 1. The cumulative distribution of their initial magnitude is shown in the left plot, and the FAP as a function of the slope index is in the central plot. The on-source analysis showed a greatly reduced background level compared to the whole-field analysis, since only objects near a local galaxy were included. In this example, the nominal slope index threshold of 0.5 reduced the FAP to less than 1% in the on-source analysis. For the whole-field analysis, in addition to the same cut on slope index, a requirement that objects showed an initial flux brighter than magnitude 14 was needed to reduce the FAP below the 10% objective.

The "technical background" rate varied significantly between different instruments due to different fields of view, limiting magnitudes, image quality, and star crowding. For TAROT and Zadko, the number per square degree of "technical false positives" brighter than a reference magnitude of 14.5 mag for TAROT and 15.5 mag for Zadko was evaluated to be less than 1 deg^{-2} using a slope index threshold of 0.5. For QUEST, the background study was performed CCD by CCD to account for the different density of false positives on each CCD. Compared to TAROT and Zadko, the deeper sensitivity observations of QUEST led to a higher number of false positives: an average value of 6 deg^{-2} brighter than 18 mag and with magnitude variation larger than 0.5. Reducing the analysis to the on-source regions allowed us to lower the density of background transients to less than 1 deg^{-2}.

4.1.3. Analysis Tuning

For TAROT and Zadko the two types of analysis were tuned to achieve 10% FAP using the on-source and whole-field backgrounds, respectively. The nominal slope index threshold (<0.5) resulted in the target FAP (<10%) for half of the on-source analyses. For the other half, a threshold on the initial magnitude (in the range 12–13 mag) was also required. For the whole-field analyses, an initial magnitude threshold of 14 mag was demanded for the TAROT follow-up of G19377 and a threshold of 10 mag for the Zadko follow-up of G19377, and the Zadko and TAROT follow-up of G20190. For these last three follow-ups the presence of observations taken months after the GW trigger allowed the additional requirement of the object's presence in the early observations and its absence in the reference ones.

For the QUEST on-source analysis, two methods were used to estimate the false positives. First, the background was evaluated directly in each on-source area. Due to the low statistics in these areas, a second estimate was also produced by rescaling the background event counts in the entire CCD to the on-source area. The target FAP (evaluated by both methods) was achieved for the majority of galaxies by demanding a magnitude variation larger than 0.5 between the first night and follow-up night observations, and an initial magnitude brighter than 17.5 for G20190, and 18.5 for G23004. For eight galaxies associated with G23004, stronger thresholds on the initial magnitude (between 15 and 18.2) were required.

Simulations have been performed for each set of images by using the exact thresholds applied for the analysis of the data associated with the GW trigger to prove the ability to detect likely EM counterparts (GRBs and kilonovae), and to evaluate the search sensitivity for the analysis procedure described above (see Section 6).

4.2. ROTSE Search

The ROTSE-III network consists of four robotic telescopes at various locations around the world. For each GW trigger in the autumn run, the telescopes repeatedly observed a single field. Each field was observed in a series of 30 exposures on the first night after the trigger time. Follow-up images were collected over the next 30 nights, with observations spaced an

[148] Except for trigger G20190, for which we selected galaxies within 30 Mpc in accordance with the gravitational wave horizon estimated for this event candidate.

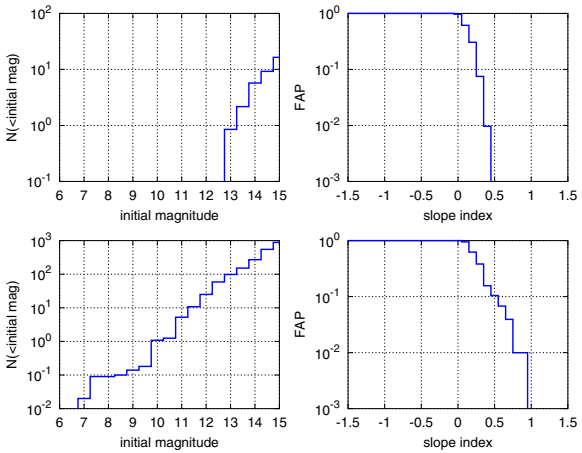

Figure 1. Background plots for TAROT data associated with trigger G19377 obtained by performing the *on-source analysis* (top plots) and *whole-field analysis* (bottom plots). In the left plots, *N* gives the cumulative number of technical background events found in a permuted set of images above the magnitude threshold shown on the *X*-axis, averaged over 100 permutations. The right plots show the FAP as a function of the slope index (in the case of *whole-field analysis* the requirement of an initial magnitude brighter than 14 was applied).

(A color version of this figure is available in the online journal.)

average of every 2 nights. Each follow-up observation included 8 exposures, each 20 or 60 s.

We used the existing ROTSE pipeline to analyze the images taken with the network. Based on the ISIS package,[149] which uses a single convolution algorithm described in Alard & Lupton (1998) and Alard (2000), the ROTSE pipeline was adapted to use cross correlation to improve image subtraction results. The details of this method can be found in Yuan & Akerlof (2008). The pipeline was implemented for our analysis to require minimal user interaction and for large scale processing which enabled characterization of the background, as described in Nuttall et al. (2013).

The pipeline began by stacking images from the same night on top of one another to form a coadded image. `SExtractor` was used to produce a list of objects and their coordinates for each coadded image. These images were then subtracted from the coadded reference image, and several criteria were imposed on any objects found in the subtracted image. Selection criteria included requiring a full width at half-maximum consistent with a point source, seeking a minimum fractional flux variation between images and a signal-to-noise ratio (S/N) greater than some amount. The specific criteria depended on the location of the source in an image. For example, if a source matched a star or an unknown object a flux change of 60% was required, whereas if a source was within 20% of the semi-major axis length from the center of a galaxy, but not consistent with a core, only a 3% flux change was required. The result was several lists of candidates (one from each night), which we combined to produce a single list of unique candidates which appeared in the images, and generated light curves for all candidates.

The vast majority of these candidates were due to poor subtraction, with a fraction of real but uninteresting transients (such as variable stars or asteroids). In order to remove contaminants from the list of candidate transients, each object was subjected to a series of cuts. In order to be of interest, the transient must have appeared on more than one night, shown a sufficiently decaying light curve 48 hr after the trigger, and not have been coincident with a known variable source (from the SIMBAD catalog[150]) or with a minor planet (Minor Planet Checker[151]). These cuts proved efficient at rejecting the majority of the background. Candidates were then highlighted if they overlapped with known galaxies or if their light curves were consistent with a target theoretical light curve (Metzger et al. 2010; Kann et al. 2011, 2010). They were also assigned an ad hoc ranking statistic, R, defined as:

$$R \equiv \sum_i (18 - m_i)\Theta(18 - m_i) \times w_i \,. \quad (2)$$

Here $\Theta(x)$ is the step function, m_i is the background-subtracted magnitude of the transient in image i, and w_i is a weight factor defined by

$$w_i = \begin{cases} 1 & t_i - t_{\rm GW} < 1\ {\rm day} \\ \left(1 + \log_{10} \frac{t_i - t_{\rm GW}}{1\ {\rm day}}\right)^{-3} & t_i - t_{\rm GW} \geqslant 1\ {\rm day} \end{cases} \quad (3)$$

where $t_{\rm GW}$ is the time of the GW trigger, t_i is the time of image i. The ranking statistic was designed to prefer events which were bright within a day of the trigger time and which appear in multiple images.

[149] http://www2.iap.fr/users/alard/package.html
[150] http://simbad.u-strasbg.fr/simbad/
[151] http://scully.cfa.harvard.edu/cgi-bin/checkmp.cgi

The ROTSE FAR was investigated by processing sets of images for each of 100 random field locations selected from the ROTSE archive. Each set contained ∼240 images of the field from a month of nominally nightly observing. The FAP for each GW candidate was estimated by counting the number of transient objects visible in archived images with a similar cadence as the images collected for that GW candidate. The ranking statistic for each such transient object was calculated using Equation (2). These studies allowed us to set thresholds on the ranking statistic to keep the target light curves, while rejecting contaminants.

4.3. Catalog-based Search for Pi of the Sky

POTS has an unusually wide FOV of $20^\circ \times 20^\circ$, with a typical limiting magnitude of 11.5 for a 10 s exposure. This allowed the telescope to image a large part of the sky in response to one LIGO/Virgo trigger, over $40^\circ \times 40^\circ$ on most nights. We used the standard *POTS* pipeline to analyze the images taken by the telescope. A detailed description may be found in Malek et al. (2009) and Sokolowski (2008). The full analysis was carried out in two steps. First, in each image taken by the telescope, the Guide Star Catalog (Jenkner et al. 1990) was used to identify previously unknown sources. Second, POTS's nova recognition algorithm was applied to the list of unknown sources. To separate optical transients from contaminating sources, the algorithm utilized several types of vetoes, including checks on background saturation, nearby bright objects, satellite databases, and the Guided Star Catalog. Objects that passed the cuts were then visually inspected.

During the human inspection stage, every candidate that was not identified as a satellite or background fluctuation was checked against lists of known sources. First, we queried the POTS, INTA (Spain) site for observations made in 2011. Due to the long time (∼1 yr) between the autumn science run and observations from the INTA site, any objects observed by INTA were likely unrelated to the GW trigger.[152] Finally, objects were cross-correlated with the SIMBAD catalog, and sources that appeared nearer than 150″ to the position of any known star or infrared source were rejected.

4.4. SkyMapper Search

SkyMapper obtained two epochs of an eight image mosaic covering a total of ∼42 deg^2 in response to the 2010 September 16 trigger. An image subtraction technique was applied to identify possible transients. The SkyMapper images were reduced via the normal bias subtraction, overscan correction and flat fielding using a custom made Python-based pipeline. Thereafter, frames from the two epochs were aligned with the `WCSREMAP`[153] routine and subtracted with `HOTPANTS`[154] to create residuals images. `SExtractor` was used to identify sources with S/N greater than three. Then, a series of cuts was applied to the `SExtractor` output parameters to identify noise and bad subtractions. These included using the ellipticity parameter, photometry from different size apertures, and catalog matching of variable stars. In addition, a study of the point-spread function (PSF) of each object was performed on the subtracted images by fitting the detection with a two-dimensional Gaussian and comparing the fit parameters to the expected, known, PSF. The

[152] All Pi of the Sky telescopes have the same cameras, so data gathered is easily comparable.
[153] http://www.astro.washington.edu/users/becker/v2.0/c_software.html
[154] http://www.astro.washington.edu/users/becker/hotpants.html

remaining objects were then examined manually to verify they correspond to an object which was visible in the first epoch and not detectable/fainter in the second. The light curves were then measured using differential photometry with nearby stars.

4.5. PTF Search

The PTF accepted the trigger of 2010 September 26. Nine PTF fields, each covering 7.26 deg^2, were schedule automatically for observations, and they were observed beginning ≈6 hr after the trigger time (since the trigger occurred during day-time on the Pacific Coast). PTF then repeated the observations on several subsequent nights. The number of follow-up observations was mainly limited by full moon constraints.

The imaged fields were searched for candidate transients using the image subtraction pipeline hosted at LBNL (P. E. Nugent et al. 2014, in preparation; Gal-Yam et al. 2011). Only three of the fields imaged by PTF had previously constructed reference images. For the rest of the fields, image subtraction was performed using a reference image constructed by co-adding several images taken during the first night of observations. Image differencing inherently produces a large number of spurious candidates, and only a small fraction (less than few percent) of these are real events. As described in Bloom et al. (2012), in a typical PTF night of order 10^5 residual sources are found per 100–200 deg^2 of imaging, after performing subtraction of the reference image.

To distinguish between astrophysical objects and "bogus" image subtraction residuals, we made use of a classification parameter named the "realbogus" parameter (*RB*; Bloom et al. 2012), which was assigned by a machine-learned (ML) classifier so as to reasonably mimic the human scanning decision of real or bogus. The *RB* parameter ranged from 0 (definitely bogus) to 1 (definitely real), and was constructed from 28 `SExtractor` output parameters, including magnitude, ellipticity of the source, and distance from the candidate to reference source.

To maximize the chances of identifying a potential optical counterpart to G21852, the images collected by PTF were analyzed using two different procedures for transient identification, both based on the *RB* parameter as a starting point (P. E. Nugent et al. 2014, in preparation). While the first procedure (hereafter, the "automated" approach) was largely based on automated ML techniques and optimized for fast transients, the second (hereafter, the "citizen-based" approach) was largely based on a citizen project (Smith et al. 2011) and optimized for supernova searches. In what follows, we describe these two approaches in more detail.

4.5.1. Automated Approach

We identified the most promising fast transient candidates (i.e., transients with a variability on a timescale of a week or less) obtained in an image subtraction by applying the following selection criteria:

1. $RB \geqslant 0.17$ in at least one detection;
2. matching of the candidate with at least one other detection with $RB \geqslant 0.07$;
3. the second detection should be coincident with the candidate position within 2″ on the sky;
4. the second detection should be at least 45 minutes (and no more than 6 days) before or after the original candidate.

Candidates satisfying the above criteria were further passed through the so-called "Oarical classification routine" which, as part of the standard PTF operations, was designed to distinguish between two main classes of events, namely "transients" and "variable stars." The classifier used both time-domain features, such as light-curve evolution, and context features, including the location of the source relative to known stars and galaxies (see Bloom et al. 2012 for details).

Candidates with high *RB* and high classification confidence were saved automatically in the so-called "PTF Marshal" web archive, and thus assigned an official "PTF name" and a tentative object type. Further spectroscopic follow-up was pursued only for sources that looked particularly promising in relation with the main science objectives of the PTF survey.

The main challenge of our study was to identify, among the list of candidates retrieved using the criteria described here (and in the absence of spectral classification for most of them), the ones more likely to be of interest for LIGO and Virgo, in the sense of having properties consistent with "explosive" events such as binary mergers or stellar collapses, that our search was targeting.

4.5.2. Citizen-based Approach

In addition to the list of candidates described in the previous section, we also considered candidates passing selection criteria optimized for the identification of young supernovae:

1. candidate *RB* parameter value >0.07;
2. detected at least twice;
3. flat or rising light curve;
4. not seen prior to 10 days before the earliest day.

As part of normal PTF operations during 2010, candidates passing the above criteria were further examined by citizen scientists through the Galaxy Zoo Supernovae project (Smith et al. 2011). The Galaxy Zoo scanners were presented with a series of detection "triplets" for each candidate. Each triplet contained three images: the current image of the field containing the candidate; the historical or reference image of the same field; and the image of the difference between the previous two (which should contain only the candidate light). Each examiner was asked a series of questions to determine if the candidate appeared consistent with a supernova, and the answers were converted into a score. The arithmetic mean of the scores from many scanners was calculated, and candidates with strong (supernova-like) scores were counted in our final list of candidates.

4.5.3. Selection for LIGO/Virgo Event Candidates

All of the candidates from both the automated approach and citizen-based approach were vetted by human scanners to judge which candidates deserved to be kept for further investigation as "LIGO/Virgo interesting." To do so, we took advantage of two new parameters recently developed by the PTF team, to improve confidence in transient identification. The first parameter is the so-called "realbogus 2" (*RB2*; Brink et al. 2013). The *RB2* parameter is similar to the *RB* parameter, but it was defined by using a much larger training sample (78,000 objects). The *RB2* also utilized some additional features that the original *RB* parameter did not use, including correlations in different PTF filters. By using a sample of spectroscopically confirmed sources discovered by PTF, it has been found that selecting candidates with $RB2 > 0.3$ yields a false positive rate of ≈3%, and a missed detection rate of ≈3.2% (Brink et al. 2013).

The second parameter is known as the *Supernova Zoo predictor*, a ML classifier that was trained using the Supernova Zoo mark up of tens of thousands of candidate transients, so as to construct a classifier capable of efficiently discovering

supernovae. The Supernova Zoo predictor assigns a score (hereafter, SN_{zoo}) to each of the candidates, which is higher for more promising candidates (i.e., the ones that are most likely to be real supernovae). By using a sample of spectroscopically confirmed supernovae discovered by PTF, it has been found that selecting candidates with $SN_{zoo} > 0.025$ yields a false positive rate of ≈14%, and a missed detection rate of ≈10%.

For our final selection cuts, we applied the following criteria:

1. Was the transient classified spectroscopically as a variable star, an AGN, or a SN of type Ia? If yes, discard.
2. Was the candidate detected for the first time before the GW trigger time? If yes, discard.
3. Does the transient appear to have subtracted correctly? If not, discard after double checking that this is consistent with a low value of the *RB2* ($RB2 < 0.3$) *and* of the supernova zoo predictor parameter ($SN_{zoo} < 0.025$).
4. Is the candidate classified as a STAR in Sloan Digital Sky Survey (SDSS), and/or is it spatially coincident with a known stellar or AGN source in SIMBAD? If yes, discard.
5. If the analyzed field is not in the SDSS footprint and nothing is found in SIMBAD (see above), can the candidate be securely associated with a point-like host in the PTF reference image (or in an image taken a year after the LIGO/Virgo trigger in case a previous reference image was not available)? If yes, is the Oarical classification (see Section 4.5) consistent with a "variable star" and/or is there enough photometry to confirm a long-term variable origin from the light curve? If yes, discard.
6. If the analyzed field is not in the SDSS footprint, nothing is found in SIMBAD, and a point-like host cannot be identified in the reference image (see above), then: Does the candidate have *both RB2* and SN_{zoo} below threshold? Or, is it classified by the Oarical classifier (Section 4.5) as variable star or AGN, and is there enough photometry to confirm a long-term variable origin from the light curve? If yes, discard.

4.6. Liverpool Telescope Search

The Liverpool Telescope observed the G23004 trigger using both the 4.6 arcmin FOV RATCam instrument and the 1° FOV SkyCamZ camera. This produced a total of 22 SDSS r'-band RATCam images and 121 "clear" filter SkyCamZ images from two nights 29 days apart. In addition, 3 RATCam and 17 SkyCamZ images were taken in early 2012 to serve as reference images for image subtraction. The analysis made use of several freely available software packages, and was split into several sections written in Python.

First, we combined the images from 2012 to create our reference images. This was done by aligning the images using the `WCSRemap`[155] package and combining them using the `SWarp`[156] package. We also combined sets of five SkyCamZ images on each night to improve image quality and provide a similar cadence to the RATCam images. We removed one RATCam image and two SkyCamZ images due to quality issues.

Second, as the SkyCamZ images used a non-standard filter,[157] they were calibrated using the USNO-B catalog of stars to determine the zero point offset required to calculate correct magnitudes, in the same way ROTSE and TAROT images were calibrated (see Section 4.1). This was done by comparing the USNO-B *R*-band magnitude of stars in the combined SkyCamZ fields with those same stars found using `SExtractor`.

The images were then aligned individually to the reference images, again using `WCSRemap`, and the reference image was subtracted using the `HOTPANTS`[158] image subtraction package. `SExtractor` was then used to detect potential candidates in each individual field with a minimum of 4 pixels each with a flux greater than 4σ above the background noise of the image. This reduced the frequency of detecting uninteresting objects, such as cosmic rays, extremely faint stars and noise from the image subtraction process while allowing us to achieve a sensitivity around 20th magnitude in the narrow-field RATCam images.

Using the output of `SExtractor` from each of the subtracted images, a Python script combined the objects found into a master list containing every unique candidate found in those images, along with useful parameters from `SExtractor`. From this data, a series of cuts were made to find candidates interesting to this analysis. First, candidates found to be near an image edge (or a bad pixel strip in the case of RATCam images) were rejected. Second, a cut was made to remove artifacts due to bad subtraction. This was achieved by examining the region in the subtracted image around the candidate and calculating the total flux more than 4σ below the median noise of the image. Since bad subtractions are usually caused by poor alignment or convolution, they typically produce a large amount of "negative" flux in the residual image. If the total amount of flux below this threshold was the equivalent required for detection of candidates (4 pixels above 4σ) then the candidate was rejected. The next cut removed candidates not seen in at least half of the images available on the first night, to ensure candidates were visible long enough to be used in our analysis. We also rejected candidates that appeared close to known variable stars and minor planets. Finally, we required that a candidate must decrease in brightness by more than 5σ of the median error on the magnitude measurements from `SExtractor`, from the first night to the second night 29 days later. Since the pipeline is designed to work with images from two telescopes for this analysis which may have different magnitude errors for the same trigger, we used a threshold based on the noise in the image rather than a fixed magnitude variation in the same way as ROTSE and TAROT.

Any objects that remained after these cuts were considered likely candidates, and looked at in more detail. This was done by plotting the light curves of each object across both nights and inspecting images of the candidates in both the original and subtracted images. This allowed us to gauge whether any transients warranted further investigation.

5. OPTICAL TRANSIENT SEARCH RESULTS

In this section we present the details of the associated optical images for each GW trigger. The center location of each observed field is shown in Table 5. We also present the results of the transient analysis for each data set. Data from the two periods of our search were handled differently. The winter run triggers were not observed with sufficient cadence to reconstruct light curves, so only a limited analysis was performed on those triggers. Section 5.1 describes the results of the analysis along with figures showing the position reconstruction and image locations for each winter run GW trigger (Figures 2 and 3).

[155] http://www.astro.washington.edu/users/becker/v2.0/c_software.html
[156] http://www.astromatic.net/software/swarp
[157] http://telescope.livjm.ac.uk/Info/TelInst/Inst/SkyCam/
[158] http://www.astro.washington.edu/users/becker/hotpants.html

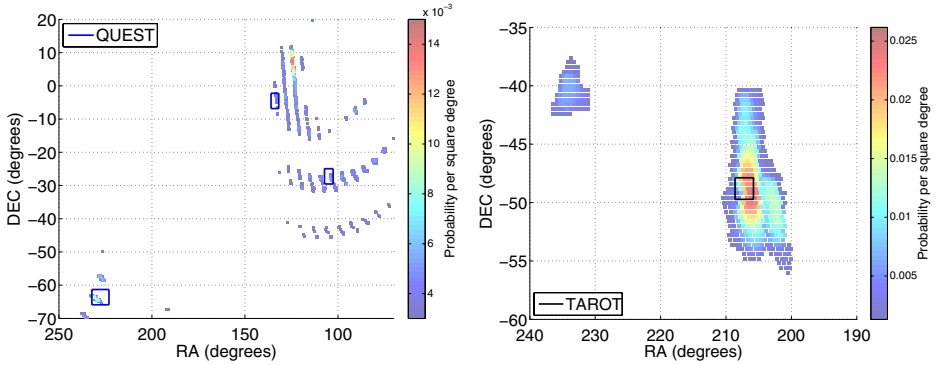

Figure 2. GW skymaps for triggers G3821 (left) and CWB1 (right). The colored regions show the estimated probability per square degree that each location is the true source direction before applying the galaxy weighting. The locations of the observed fields (selected using galaxy weighting) for telescopes that observed the trigger are also marked.

(A color version of this figure is available in the online journal.)

Table 5
Center Locations of All Fields Observed

GW Trigger	Telescope	R.A.	Decl.	R.A.	Decl.	R.A.	Decl.
G3821	QUEST	104.89	−27.94	133.88	−5.24	227.61	−64.26
CWB1	TAROT	207.21	−48.80				
G4202	QUEST	89.34	−0.70	86.33	−9.78	89.34	−5.24
CWB2	QUEST	81.00	−32.49	75.63	−50.65	91.23	−41.57
G19377	ROTSE-c	115.56	−30.00				
	SkyMapper	115.43	−30.03	120.01	−29.91	110.78	−29.92
		115.40	−34.00	115.39	−25.99	110.94	−25.93
		110.58	−33.91	120.22	−33.90		
	TAROT	115.40	−30.00				
	Zadko	110.98	−27.53	114.75	−22.05	115.25	−32.07
		115.80	−29.98	115.85	−29.22		
G20190	ROTSE-abcd	333.25	18.03				
	TAROT	333.33	18.00				
	Zadko	322.49	12.17	323.37	−0.82	329.77	18.18
		330.17	17.74	333.96	19.23		
	QUEST	336.29	8.50	334.49	10.63	331.61	17.57
G21852	ROTSE-b	11.04	41.61				
	PTF	11.39	41.62	55.80	−19.12	52.20	−19.12
		56.93	−21.37	39.42	−7.87	52.25	−28.12
		55.24	−16.87	51.15	−25.87	34.38	−32.62
G23004	ROTSE-bcd	61.97	−20.91				
	Liverpool	61.11	−2.20				
	Pi of the Sky	Various					

Note. All coordinates are in degrees using the J2000 equinox.

The methods described in Section 4 were applied to the data collected in response to each GW trigger in the autumn run. To display the sky coverage and depth of each response, two panels are presented for each autumn run trigger (Figures 4–7). The left panel shows the GW skymap (without the use of galaxy weighting) along with the positions and approximate field sizes of each observed tile. The right panel shows a timeline of the observations by each observatory. The *y*-axes of the timeline plots display the limiting magnitudes of the observations. In these plots, for TAROT, POTS, and Zadko, each arrow represents one observation. For QUEST, each arrow is a median of limiting magnitudes over the CCDs covering the on-source galaxy regions observed at a given time. For PTF, the arrows give the limiting magnitudes reached in a central CCD of the camera, for the field containing the M31 galaxy (which was observed with highest cadence).

The right panel of each figure also shows several models for possible EM counterparts. The off-axis long GRB model (L-GRB; solid dark green line) is from van Eerten et al. (2010), and assumes a total energy in the jets of 2×10^{51} erg, jet half opening angle of 0.2 rad, off-axis observer's angle of 0.3 rad, interstellar medium number density of 1 cm^{-3}, and distance of 30 Mpc. We note that within this model, the associated optical transient peaks at ≈1 day since trigger. The off-axis

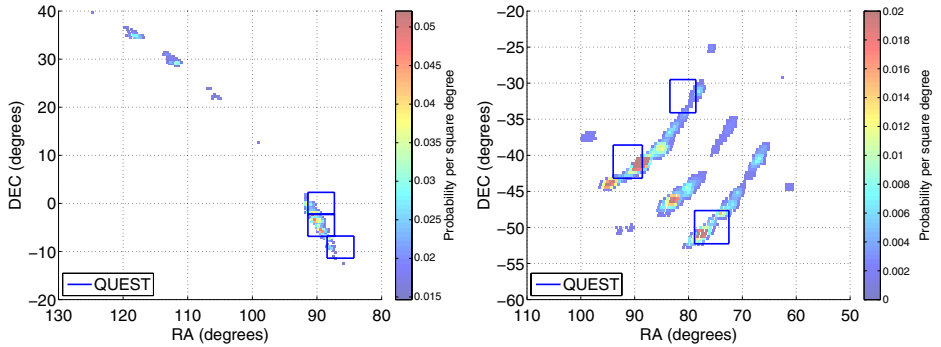

Figure 3. GW skymaps for triggers G4202 (left) and CWB2 (right). See Figure 2 caption for explanation.
(A color version of this figure is available in the online journal.)

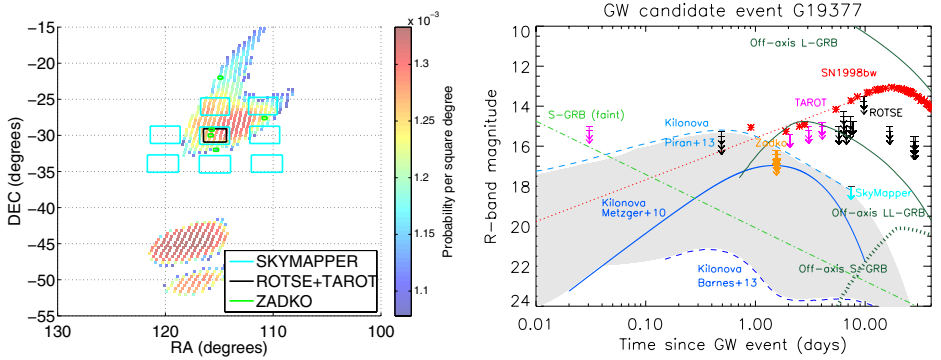

Figure 4. On the left, the GW skymap for G19377, which was later revealed to be a blind injection. The skymap shows the probability per square degree that each location is the true source direction before applying the galaxy weighting. The locations of the observed fields (selected using galaxy weighting) for telescopes that observed the trigger are also marked. On the right, a timeline showing when each telescope observed the requested fields, with time zero corresponding to the GW trigger time. Model light curves for several sources, scaled to 30 Mpc, are shown for comparison (see Section 5 for details).
(A color version of this figure is available in the online journal.)

low-luminosity GRB model (LL-GRB; dash-dot-dot-dotted dark green line) is from van Eerten & MacFadyen (2011), and assumes a total energy in the jets of 10^{50} erg, jet half opening angle of 0.2 rad, off-axis observer's angle of 0.4 rad, and interstellar medium density of 1 cm^{-3}. The off-axis short GRB model (S-GRB; dashed dark green line) also refers to a total energy in the jets of 10^{50} erg (and similar jet and observer's angles), but the interstellar medium density is set to 10^{-3} cm^{-3}. The light green line represents the case of a faint short GRB observed on-axis (see Table 1 and Kann et al. 2010, 2011). The emission from typical short GRBs and long GRBs observed on-axis lies above this line. In particular, on-axis long GRBs at 30 Mpc would appear as very bright optical transients.

The kilonova models are courtesy of Barnes & Kasen (dashed dark blue), B. Metzger (dark blue), and E. Nakar (light blue). Specifically, the light blue line represents one of the kilonova bolometric light curves from Piran et al. (2013) (BH–NS merger with BH mass of 10 $M_\odot$). This light curve assumes that all of the bolometric luminosity is emitted in the R-band, and it represents an upper-limit to the true R-band luminosity of the kilonova event. The solid dark blue line is one of the kilonova light curves from Metzger et al. (2010), and is calculated for an ejecta mass 10^{-2} $M_\odot$ assuming a blackbody emission. Finally, the dashed dark blue line is one of the kilonova models from Barnes & Kasen (2013), for the case of low-velocity ($0.1c$) low-mass ($M = 10^{-3}$ $M_\odot$) ejecta. Since the kilonova models are subject to large uncertainties, we selected these three light curves to give an indication of the possible scatter in the model predictions.

Finally, the prototype emission from a GRB-associated SN is plotted with a red dotted line: this is a tentative extrapolation to early times of the R-band light curve observed for SN 1998bw (red asterisks; Clocchiatti et al. 2011), associated with GRB 980425 (Galama et al. 1998). The light curve assumes that SN 1998bw exploded at the same time at which GRB 980425 was triggered.

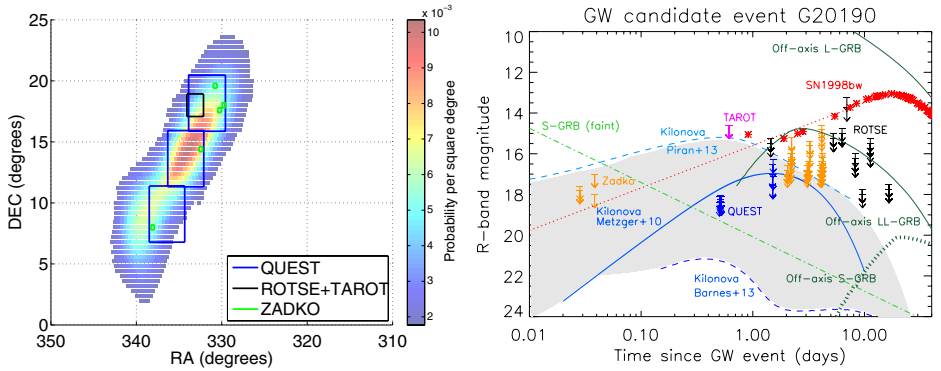

Figure 5. GW skymap and observations of trigger G20190. See Figure 4 caption for explanation.
(A color version of this figure is available in the online journal.)

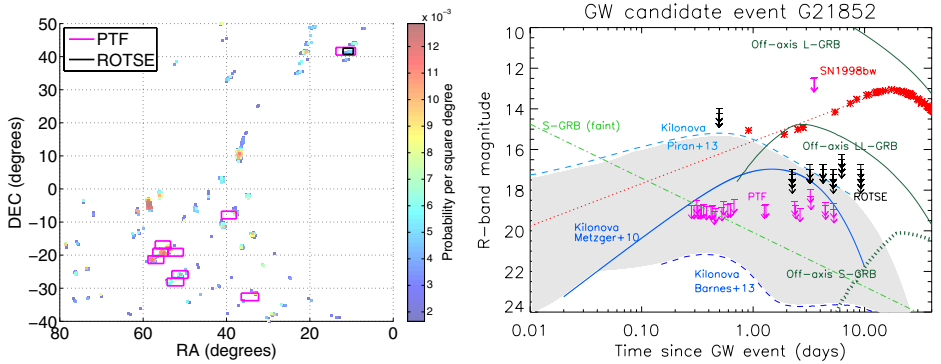

Figure 6. GW skymap and observations of trigger G21852. See Figure 4 caption for explanation.
(A color version of this figure is available in the online journal.)

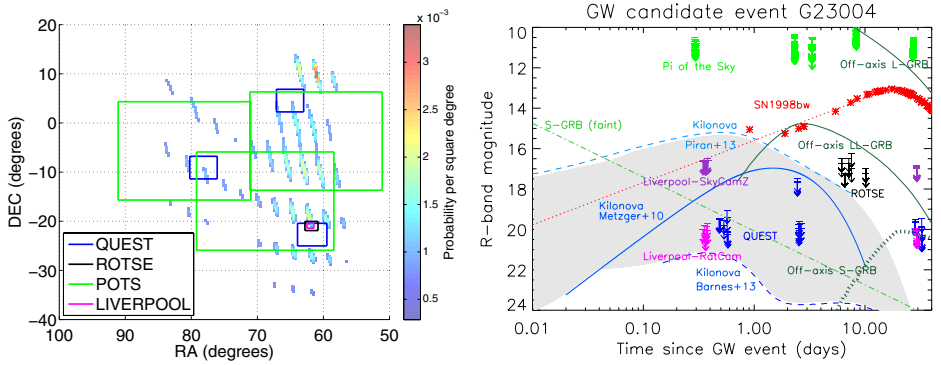

Figure 7. GW skymap and observations of trigger G23004. See Figure 4 caption for explanation. The shown Pi of the Sky (POTS) fields are a subset of the 10 overlapping pointing positions used to observe the GW uncertainty region.
(A color version of this figure is available in the online journal.)

5.1. Winter Run Triggers

For each winter run trigger, images were collected only during one night. The absence of a second night's observations prevented the construction of variability measures and limited the analyses to only identify "unknown objects," i.e., those not listed in the USNO catalog or with a magnitude significantly different from USNO, but visible in all the collected images. For both the TAROT and QUEST image analysis procedure, at least one observation on another night would have been required to identify a unique electromagnetic counterpart.

In the winter run, TAROT responded to one trigger, CWB1, and collected six images starting the single night observation at T+3d11h. The QUEST camera responded to three triggers, G3821, G4202, CWB2, starting the observations at T+9h46m, T+24m, and T+16h12m, respectively. For each trigger it collected images corresponding to three fields. Each field was observed twice within 20 minutes during the same night.

The TAROT observation associated with CWB1 reached a sensitivity of 15.8 mag. Fifteen galaxies with a distance smaller than 50 Mpc were in the FOV. The analysis found 9 unknown objects in the on-source region and 46 in the entire FOV up to the limiting magnitude. No unknown objects were found with magnitude brighter than 11.8 in the on-source region and brighter than 10.7 mag in the entire FOV.

The three QUEST fields associated with G3821 included a total of 34 galaxies with a distance smaller than 50 Mpc. Only 14 of the galaxies were analyzed due to the exclusion of galaxies observed only one time or lying in CCDs that did not work or had calibration problems. The average limiting magnitude was about 18.6 mag.

For trigger G4202 the three fields included a total of 17 galaxies with a distance smaller than 50 Mpc. Ten galaxies were removed from the analysis because they were observed only one time or associated with poor image quality (impacted by bad lines and pixels or by background subtraction artifacts) or calibration problems of the CCDs (astrometric calibration or flat-field problems). An average limiting magnitude of 19.2 mag was reached during the observations.

For trigger CWB2 the three fields included a total of 12 galaxies with a distance smaller than 50 Mpc. Two of the galaxies were not analyzed due to poor image quality or CCD calibration problems. An average limiting magnitude of 19.8 mag was reached during the observations.

The QUEST analysis found 9, 1 and 1 unknown objects in the on-source region with a magnitude brighter than 14 mag for the triggers G3821, G4202 and CWB2, respectively. The number of unknown objects increased to 140, 35, 6 for magnitudes brighter than 18 mag. The number of unknown objects showed a stronger dependence on the density of image artifacts and stars in the FOV than on the on-source area. No "unknown objects" were found for magnitude brighter than 9, 12, 7 mag for G3821, G4202 and CWB2, respectively.

5.2. G19377

Event G19377 was a simulated signal added to the GW detector data in order to test our data analysis pipelines. The ROTSE-IIIc telescope responded at T+∼12 hr when 30, 20 s exposure images were taken within ∼15 minutes. On subsequent follow-up nights (6–29) both ROTSE-IIIa and c telescopes gathered 80, 20 s exposure images. The images from the two scopes varied vastly in terms of image quality, which posed difficulties for injection studies. We discarded the lower quality images from the 3c telescope, leaving just the 3a images, with an average limiting magnitude of 15.1. Two galaxies at ∼24 Mpc (PGC 078144 and PGC 078133) were visible within the FOV. The ROTSE image processing pipeline revealed 68 unique objects, one of which passed the candidate validation. Further tests found this candidate was consistent with background, with a FAP of 7%. This left no significant candidates. At the location of this background transient there is a known star (red magnitude of 13.1 from the USNO catalog), which shows no significant magnitude variation in the TAROT images associated with the same GW trigger. This location was not covered by the *Swift* observations taken for G19377. We also tried analyzing images from both the 3a and 3c telescopes together, and found no additional candidates.

SkyMapper observed an eight tile mosaic, 7 days after the initial alert. An analysis was performed, but no plausible transients were discovered.

TAROT took images starting at T+43m and repeated the observations at T+2d, T+3d and T+4d. Observations from the four nights displayed an average limiting magnitude of 15.1. The on-source analysis was performed on the two same galaxies observed by ROTSE and identified no transient counterpart. The whole-field analysis was performed with an initial magnitude threshold of 14 mag, and identified one transient candidate with a slope index of 0.6. A deeper analysis showed that this candidate resulted from an artifact of the de-blending in crowded images.

The Zadko telescope observed the regions around the five galaxies evaluated to be the most likely hosts of the G19377 trigger: NGC 2380, ESO 560-004, ESO 429-012, PGC 078133, and PGC 078144; the last two being in common with ROTSE and TAROT. The observations started at T+1d12.6h and were repeated 5 months later for reference. The average limiting magnitude for both the early and reference images was 16.5 mag. No electromagnetic counterparts were identified by either the on-source on whole-field analysis.

5.3. G20190

All four ROTSE-III telescopes responded to this GW trigger, taking images spanning T+34h38m to T+29d, centered on the region around the galaxy UGC 11944. However, all images taken with the ROTSE-IIIa, b and d telescopes were discarded because of defocusing factors in addition to weather conditions at those sites being less than optimal. This resulted in 56 images being used for the analysis, with an average limiting magnitude of 15.5. The ROTSE image subtraction pipeline found 77 potential candidates, none of which passed the candidate validation procedure.

The TAROT telescope collected three images in association with G20190. Due to the full moon only an average limiting magnitude of 14.6 mag was reached. Nine months later 18 images were taken by TAROT in the same region of the sky as reference. A mean limiting magnitude of 17 mag was reached during this second observation. No counterpart with a FAP less than 10% was identified by the on-source analysis. The whole-field analysis was performed with a threshold of 10 mag on the initial magnitude and the required presence in the first three images and absence in the reference images. It resulted in four identified candidates. The candidates were seen to be image artifacts linked to the spikes of saturated stars.

The Zadko telescope was pointed toward two Galactic globular clusters: NGC 7078 and NGC 7089, and three galaxies UGC 11868, NGC 7177, and NGC 7241, evaluated to be the most likely hosts of the GW source. Observations of galaxies UGC 11868 and NGC 7241 were taken about 50 minutes after the GW trigger. All five fields were observed subsequently during at least two nights between T+1d and T+4d. The observations were repeated 11 months later for reference. The average limiting magnitudes were 16.4 mag and 17.3 mag for the very first and reference observations, respectively. The on-source analysis identified three transient candidates associated with NGC 7078 and 15 associated with the center of NGC 7089. The candidates were found to be due to problematic de-blending in the central region of globular clusters. No transient was identified by the on-source analysis associated with the three galaxies. The whole-field analysis required a magnitude brighter than 10 and the presence during the first nights and absence in the reference images. This resulted in no detected transient.

The QUEST observations started at T+12h3m. Each field was observed twice within 15 minutes as pairs of images dithered to fill the gaps between rows of CCDs. The entire observation sequence was repeated at T+1.5d. A total of 10 galaxies with a distance smaller than 30 Mpc were identified in the three fields. Three of the galaxies were not analyzed due to poor image quality CCDs or calibration problems. The observation was taken during a full moon night that allowed an average limiting magnitude of 17.6 mag. The on-source analysis[159] identified one possible transient with a FAP less than 10% (see Section 6) associated with the galaxy UGC 11916. A deeper analysis of the candidate showed this to be artificial. The analysis pipeline identified the possible GW host galaxy itself as a transient due to variations in the estimate of its surface photometry over the two nights. An estimate using fixed photometry apertures indicated magnitudes in agreement within the errors with no flux decrease.

5.4. G21852

ROTSE-IIIb took images spanning T+11h53m to T+29d centered on a region containing both M31 and M110. One follow-up night had to be ignored due to defocusing issues. The average limiting magnitude of the images was 16.6, with 81% of them having an exposure times of 60s. The subtraction pipeline found 187 objects, which resulted in four candidates after candidate validation. All four candidates overlapped with one of the galaxies mentioned, however all were consistent with background. The highest ranked candidate had a FAP of 9%. Consequently, we found no significant candidates. Within the 2 arcsec positional accuracy of PTF, the ROTSE background events are all coincident with known stars, and according to the PTF analysis criteria applied, these sources are not considered candidates.

PTF observed nine different fields on five nights, beginning at T+6h37m. The median limiting magnitude reached in the observed fields over the observation time (and over the 11 CCDs that make the core of the PTF imager) was in the range $R \approx 20.2$–19.2. The images collected by PTF were analyzed using two different procedures for transient identification, one entirely based on automated selection criteria for fast transients, and the other largely based on a citizen project targeting supernovae (see Section 4.5 for more details). These procedures for transient identification were routinely used by the PTF survey (P. E. Nugent et al. 2014, in preparation). By applying the selection criteria for fast transients (automated approach; see Section 4.5.1) on the images that were taken for follow-up of trigger G21852, we obtained a list of 172 candidates, none of which passed the vetting for "LIGO/Virgo interesting" transients performed according to the criteria described in Section 4.5.3. We also applied these last criteria to the candidates obtained via the citizen-based approach (optimized for supernova searches—see Section 4.5.2). Of the 218 candidates selected according to criteria (1)–(4) in Section 4.5.2 and sent out to the citizens for scanning, 28 were saved by the citizens and assigned an official PTF name. However, none of these 28 candidates passed the additional vetting described in Section 4.5.3. We also took a closer look at 55 other candidates that were not saved by the citizens, but that had a SN_{zoo} predictor score >0.025 *or* a $RB2 > 0.3$ (see Section 4.5.3). We vetted these candidates according to criteria (1)–(5) in Section 4.5.3, and none of them passed our screening.

[159] The 7% of the total on-source area within the gaps between the CCDs does not have data and was not analyzed.

5.5. G23004

The ROTSE-IIIb, c and d telescopes responded to G23004 at T+6h25m and collected data up to T+29d. These images contained one galaxy (NGC 1518) at 11.5 Mpc within the FOV. Around 75% of the data was of poor quality; many of the images were out of focus and cloud cover was also a factor. This resulted in the analysis of 30 images with an average limiting magnitude of 16.7. The ROTSE subtraction pipeline found 124 potential candidates of which none survived the candidate validation tests.

The Liverpool Telescope observed a single field centered on the location of the galaxy NGC 1507, with one hour of observations taken at T+9h and a further one hour at T+30d. The limiting magnitude of the RATCam images was $r' \approx 20.5$, averaged over all images, with the calibrated limiting magnitude of the SkyCamZ images averaging $R \approx 17.5$. We found 406 unique objects in the RATCam images and 163 unique objects in the SkyCamZ images. After applying cuts described in Section 4 we found no candidates in either the RATCam or SkyCamZ images that met our criteria.

The POTS telescope responded at T+6h56m after the alert. On the first night the telescope used 10 different pointing locations to cover an area containing 40% of the G23004 probability map. Each location was imaged twice. The limiting magnitudes for the first night's observations spanned 10.5–11.0 mag. On the first night there were over 700 cases that were recognized by the pipeline as possible optical transients, but all of them were either already included in the database of weak stars or were noise due to ice crystals on the camera. There were no real optical transients found. The same fields were followed up on the nights of October 5, 6, 7, 11, and 30. Each follow-up night's observed area was covered by nine pointing locations, with each location imaged at least three times. Images from the first four nights were searched by the pipeline for optical transients, and 40 objects were identified as existing in images over multiple nights and have been present on all frames that were taken of that field. Each of these was manually investigated, and none were found to be linked to the GW trigger. Most of the 40 objects were traced to variable stars or were caused by ice crystals on the camera.

The QUEST follow-up for this GW trigger consisted of three nights of observations over three different fields. The first observation began at T+11h32m and then observations were repeated at T+2.4d and T+32.4d. Each night's observations included two visits to each of two dithered positions for each of the three field locations. A total of 32 galaxies with a distance smaller than 50 Mpc were identified in the three fields. Due to inoperative CCDs or CCD calibration problems the regions occupied by four galaxies were not analyzed. The average limiting

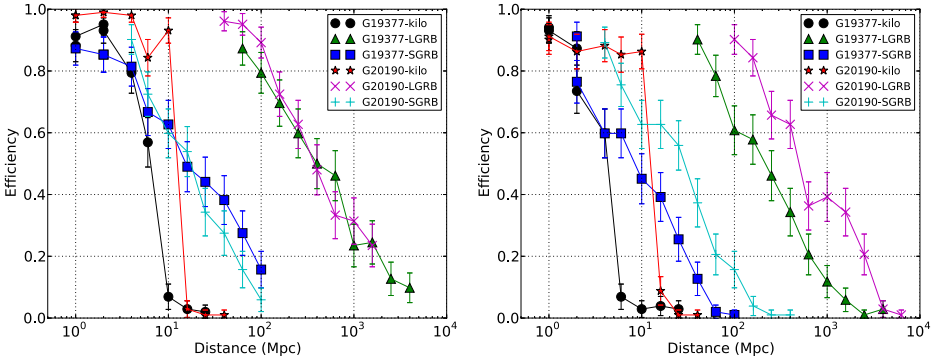

Figure 8. Efficiency in recovering simulated optical transients in the TAROT data (left) and Zadko data (right). The figure reflects the success rate in recovering transients added to the observed fields, and does not include efficiency lost due to observing only a fraction of the possible source locations. The signals have been simulated based on the models shown in Table 1, with the power law flux of each GRB randomly scaled within the shown range of normalization conditions.

(A color version of this figure is available in the online journal.)

magnitude for the three night observations was 19.7 mag. The *on-source*[160] analysis identified one possible transient with an "on source" FAP of less than 10% (see Section 6). The candidate transient overlaid the extended emission of the galaxy IC0402. A deeper analysis indicated no flux change for the object: the point source immersed in the fainter galaxy edge emission has a similar neighboring object that biased its photometry. Using a suitable fixed photometry aperture the magnitudes of the object agree within the errors in all the images. The object could be a foreground star not listed in the USNO catalog or a bright knot of one of the galaxy's arms.

6. EFFICIENCIES FOR RECOVERING SIMULATED OPTICAL TRANSIENTS

Simulated transients were added to each set of images to measure the efficiency in recovering optical counterparts located at different distances from earth. The different telescope pipelines were run over the simulated data with the same analysis tuning used in the real data. For TAROT, Zadko, QUEST, ROTSE, and the Liverpool Telescope the simulated transients reproduced the observed light curves (see, e.g., Figures 5 and 4 of Kann et al. 2011, 2010) of on-axis GRB afterglows and a modeled light curve for the kilonovae (Metzger et al. 2010; Piran et al. 2013). Table 1 summarizes the features of injected models. These models were scaled on the basis of the observation time from the GW trigger and the source distance. We emphasize here that while the simulated GRB afterglows cover the range of observed luminosities, kilonovae have not been observed yet and so our efficiency results are dependent on the assumed model.

6.1. TAROT and Zadko Telescope

For each set of images collected by TAROT and the Zadko telescopes, 100 simulated transients were added to the data for each counterpart model and distance. To model PSF variations in the wide-field images, reference model stars were identified in each image, and the PSF of the reference star closest to the injection position was used for each simulated object. For the GRB afterglows, we used a range of magnitudes uniformly distributed between the brightest and faintest GRBs (see normalization in Table 1). The results are presented in Figure 8. Long GRB afterglows/short GRB afterglows/kilonovae were recovered with 50% efficiency in TAROT observations to distances of 400 Mpc/18 Mpc/6.5 Mpc respectively for trigger G19377 and 355 Mpc/16 Mpc/13 Mpc for trigger G20190. For Zadko Telescope observations, we obtained 195 Mpc/8 Mpc/4 Mpc for G19377, and 505 Mpc/ 25 Mpc 13 Mpc for G20190. As expected, the results showed some dependence on the depth of the observations, the observation time after the GW trigger, and the density of stars in the field.

6.2. QUEST

The QUEST pipeline's recovery efficiency was evaluated separately for each on-source galaxy region. As for TAROT and Zadko, 100 simulated transients were added to the images for each model (kilonova, short and long GRBs) and distance. Randomly distributed magnitudes between the brightest and faintest GRBs (see normalization in Table 1) were used. Figures 9–11 show some representative examples of the achieved recovery efficiencies. The wide range in the recovery efficiencies reflects variations in CCD sensitivity and rates of contaminating artifacts. In addition, bright galaxy extended emission prevented the recovery of some injections, even at close distances. A similar efficiency loss was found when a large part of the on-source region was occupied by foreground stars or image problems like bad pixels and bad lines. The results for the QUEST observations can be characterized by the mean and the standard deviation of the distances corresponding to 50% efficiency to recover injections. For trigger G20190, we found mean distances of 33 Mpc ($\sigma = 7$ Mpc) for kilonovae, 30 Mpc ($\sigma = 6$ Mpc) for short GRBs, and 820 Mpc ($\sigma \approx 180$ Mpc) for long GRBs. For G23004, a mean distance of 64 Mpc ($\sigma = 25$ Mpc) for kilonovae, 63 Mpc ($\sigma = 30$ Mpc) for short GRBs, and 1530 Mpc ($\sigma \approx 700$ Mpc) for long GRBs were found.[161] The larger spreads for

[160] The 10% of the total on-source area within the gaps between the CCDs does not have data and was not analyzed.

[161] Taking into account the galaxy regions lying in the CCD gaps, the 50% efficiency distances for G20190 (G23004) reduce to 32 (61) Mpc for kilonovae, 26 (53) Mpc for short GRBs, and 700 (1260) Mpc for long GRBs.

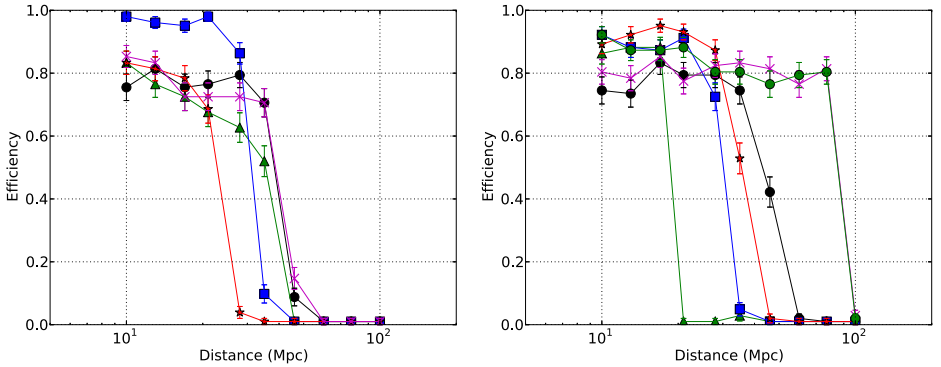

Figure 9. Some representative success rates in recovering simulated kilonovae lightcurves with the QUEST data for triggers G20190 (left) and G23004 (right). Each curve represents the efficiency from individual on-source galaxy regions, and so does not include efficiency lost due to observing only a fraction of the possible source locations.

(A color version of this figure is available in the online journal.)

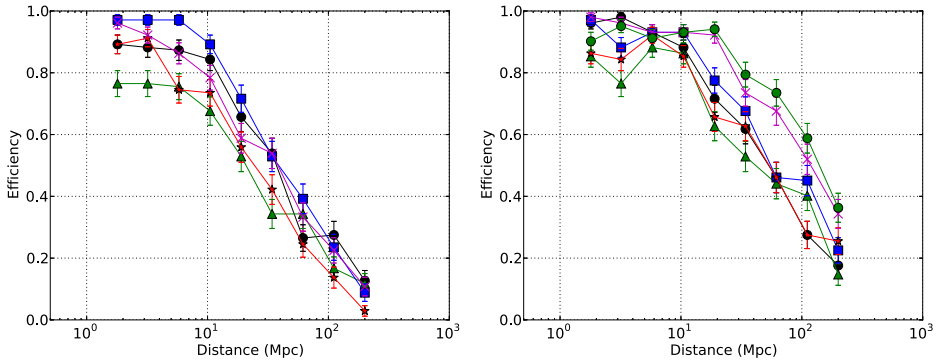

Figure 10. Some representative success rates in recovering simulated short GRB afterglow light curves with the QUEST data for triggers G20190 (left) and G23004 (right). Each curve represents the results from individual on-source galaxy regions, and so does not include efficiency lost due to observing only a fraction of the possible source locations. Each simulated afterglow lightcurve was randomly scaled within the range of normalization conditions showed in Table 1.

(A color version of this figure is available in the online journal.)

QUEST reflect CCD-to-CCD variations. For both GW triggers, the 50% efficiency distances for long GRB afterglows were well beyond the maximum distance that the LIGO and Virgo detectors could have detected signals coming from NS binary coalescences, while the kilonova and short GRB distances were comparable. However, the result obtained for the kilonova transients is dependent on the adopted model and relies on the fact that the QUEST observations were made around the peak time of the light curve model used for this study.

6.3. ROTSE

For each set of images collected by ROTSE, 140 simulated transients were added to the data for each counterpart model for 10 different distances. The PSFs for the injected transients were modeled on "good" objects PSFs within each image, as described in White et al. (2012). The GRB models used the brightest normalizations shown in Table 1; i.e., assuming magnitude 16 (23) at 1 day from $z = 1$ for LGRB (SGRB) afterglows. The results are presented in Figure 13. For each GW trigger, the efficiencies for the different counterpart models are very similar as functions of the injection magnitude. The efficiencies peak at ∼70%–80% for triggers G19377 and G20190, and at ∼55% for G21852. Trigger G23004 (not shown) contained images of very poor quality and the injection efficiency only reached a maximum of ∼20%. Long GRB afterglows/short GRB afterglows/kilonovae were recovered with 50% detection efficiency to distances of 400 Mpc/16 Mpc/2 Mpc for trigger G19377, 1000 Mpc/40 Mpc/5 Mpc for trigger G20190, and 1000 Mpc/90 Mpc/5 Mpc for trigger G21852. The maximum sensitive distances correspond to transient magnitudes of approximately 15 on the second night. This was typical of the

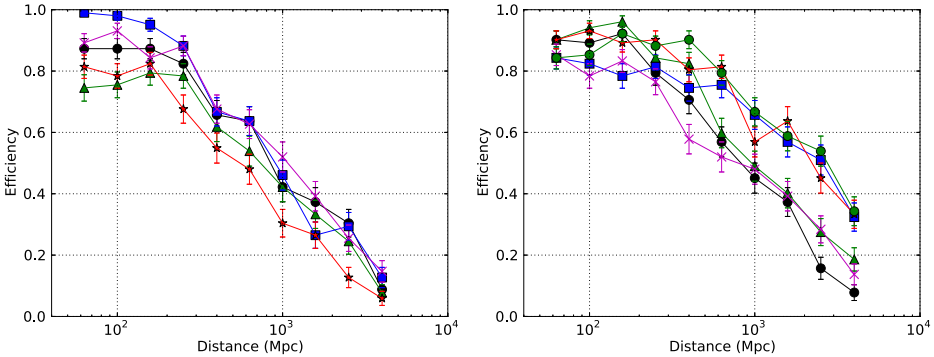

Figure 11. Some representative success rates recovering simulated long GRB light curves with the QUEST data for triggers G20190 (left) and G23004 (right). Each curve shows the results from individual on-source galaxy regions, and so does not include efficiency lost due to observing only a fraction of the possible source locations. Each simulated afterglow lightcurve was randomly scaled within the range of normalization conditions showed in Table 1.

(A color version of this figure is available in the online journal.)

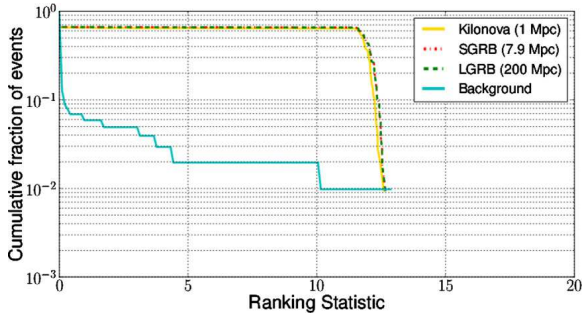

Figure 12. Distribution of ROTSE background (time-shifted) triggers and recovered injections for event G19377. This plot shows the distribution ranking statistic for kilonova injections simulated from 1 Mpc, short GRBs from 7.9 Mpc, and long GRBs from 200 Mpc. The GRB models correspond to the brightest observed GRB afterglows.

(A color version of this figure is available in the online journal.)

average limiting magnitude of ROTSE over the FOV. Since the pipeline required transients to be seen on at least two nights, the magnitude on the second night was the primary factor determining the sensitivity to each model. Transients at much smaller distances tended to suffer from saturation and were discarded in the image subtraction. The maximum detection efficiency was less than 100% because the pipeline was not always able to produce the background-subtracted lightcurve for a transient; this depended on the position in the image and on the image quality, as 16 reference stars were needed in the region around the transient for accurate image subtraction. Variations in efficiency between triggers were due mainly to differences in image quality and also differences in CCD performance between the different telescopes in the ROTSE network.

An example of the distribution of injections against the background can be seen in Figure 12. This figure shows that of all the injections that produced a nonzero ranking statistic with the specific distance scales shown, more than 60% of the injections were recovered with a rank comparable to the most highly ranked background event. However, none of the injections were found with a ranking statistic higher than loudest background event. As the injection distances increased, the injections fell more and more within the background.

6.4. Liverpool Telescope

The efficiency of the Liverpool Telescope pipeline was measured with the same methods used for ROTSE. A Python script was written to inject 100 transient objects per 10 Mpc bin per model, with light curves following the three models described in Table 1, assuming the brightest normalization for the GRB models. These images were then analyzed using the pipeline, and a script used to find and flag injections found in the pipeline output. Figure 14 shows that we obtained efficiencies around 90% for injections brighter than the limiting magnitude, including saturated objects normally discarded in other image subtraction methods. For RATCam, any of the tested models would have been observable out to 100 Mpc or more—well beyond the initial LIGO/Virgo horizon distance for NS mergers.

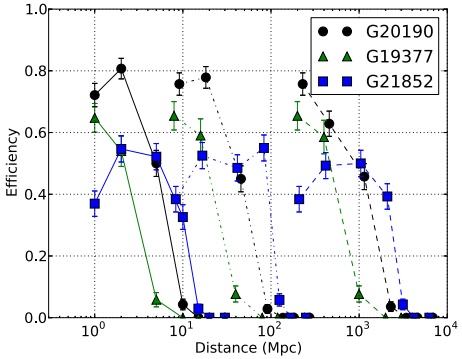

Figure 13. Efficiency of the ROTSE pipeline in recovering simulated kilonovae transients (left, solid), short GRBs (middle, dash-dotted), and long GRBs (right, dashed). The figure reflects the success rate in recovering transients added to the observed fields, and does not include efficiency lost due to observing only a fraction of the possible source locations. The efficiencies shown for the GRB afterglow models are based on the brightest models shown in Table 1. At very close distances, the simulated objects became so bright that they caused saturations in the data, and were missed by the pipeline. The images associated with trigger G23004 were of poor quality, so the efficiencies with this data are not shown.

(A color version of this figure is available in the online journal.)

For SkyCamZ, we found similar efficiencies, over smaller distance ranges.

6.5. Pi of the Sky

The efficiency of the POTS transient search was investigated by adding simulated stars to existing images and reprocessing them. The objects that were injected had different magnitudes and were chosen from real observed stars during the autumn science run. Unlike the other simulations described in this paper, objects added to POTS data did not follow model light curves, but instead measured the ability of the pipeline to recover a transient of a given magnitude using data from a single night. Stars injected in one image were also injected in subsequent images of that field taken during the same night. Only injections that were made to the inner part of the CCD chip, at least 150 pixels from CCD borders, were considered to estimate transient detection efficiency. The border part of the CCD was rejected by the off-line optical transient recognition algorithm due to the possibility of CCD anomalies that might be mistaken as short optical transients. Also, only injections starting on a good quality image were considered in efficiency estimation. This means that the effective FOV for optical transient recognition corresponds to $15^\circ \times 15^\circ$. At each stage of the processing it was determined how many of the injected objects were detected.

Figure 15 shows two curves demonstrating the efficiency of the POTS pipeline. The first one describes how many of the injected objects were detected in at least one image and the second curve shows how many of the injections were detected in five or more images. The first case corresponds to the minimal criterion that was required for the candidate to be classified as an optical transient and be inspected by a human. The second case reflects the criteria used for an optical transient to have been automatically classified as a nearly certain real event. On both curves we see that the maximal efficiency did not reach near 100%, even for very bright sources. This can be attributed to several causes. An important loss of efficiency came from areas excluded from the search due to the presence of previously discovered stars. Objects injected within a radius of 150″ of stars listed in the POTS star catalogue were not recognized as optical transients and discarded by the pipeline, resulting in a 12%–15% impact to the injection recovery rate. Additional sources were lost to structure in the CCD: 10%–15% of the CCD area consisted of wire guiding electric charge. A significant part of the losses also came from quality checks in the algorithm preprocessing. At this stage transients that were fainter than 11th magnitude, or observed on multiple low quality frames, were discarded. This impacted the efficiency by 10% for bright transients, and up to 30% for faint transients injected with brightness around magnitude 11. Other cuts in the data processing pipeline resulted in an additional 3%–10% loss of efficiency.

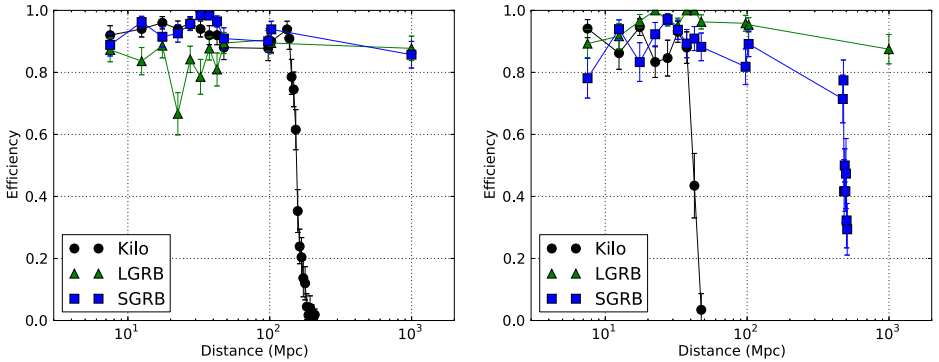

Figure 14. Success rates recovering simulated short GRB afterglows, long GRB afterglows and kilonova light curves for the Liverpool Telescope, using the RATCam (left) and SkyCamZ (right). The figure reflects the success rate in recovering transients added to the observed fields, and does not include efficiency lost due to observing only a fraction of the possible source locations. The shown results for GRB afterglows are based on the brightest models that we considered.

(A color version of this figure is available in the online journal.)

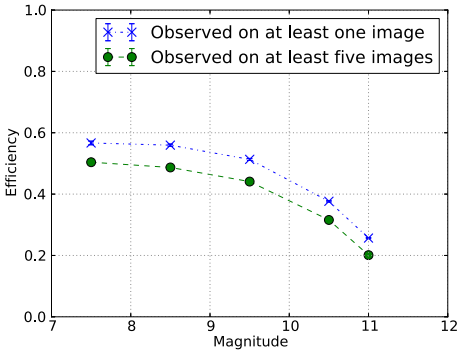

Figure 15. Success rate of the Pi of the Sky pipeline in recovering simulated transients of various magnitudes. The figure reflects the success rate in recovering transients added to the observed fields, and does not include efficiency lost due to observing only a fraction of the possible source locations. (A color version of this figure is available in the online journal.)

7. DISCUSSION AND SUMMARY

This paper describes the first end-to-end searches for optical transients associated with GW candidate events. Unfortunately, no convincing transient counterpart was found. This effort included a range of different types of telescopes, as well as a range of different analysis strategies. While the variety of analysis strategies employed presents a challenge for interpretating the results, we believe that this approach is forward-looking. The LIGO and Virgo collaborations have recently made an open call for partners to search for EM counterparts to GW events discovered with the next generation of GW detectors.[162] It is likely that partners will use a variety of facilities and instruments, and each apply their own data analysis techniques. Both the successes and lessons of this work should serve as useful guideposts to investigators pursuing similar searches with the up-coming "advanced" generation of GW detectors. Strategies are also being discussed in the literature (Metzger & Berger 2012; Nissanke et al. 2013; Singer et al. 2013).

Rapidly down-selecting candidates for follow-up observations, integrating results for astrophysical interpretation, and communicating findings will require a common framework to describe transients discovered with disparate techniques. In this work, we presented two complementary statistics for characterizing the results of a transient classification pipeline, the FAP and the detection efficiency. These statistics were calculated for several different analyses, so that objects discovered in the searches could be quantitatively evaluated and compared. This paradigm, where results from transient searches with different selection criteria must be discussed in a common language, is likely to be a theme that becomes more common as survey instruments evolve.

Because GW event candidates are poorly localized, searches for counterparts need to consider the large population of optically variable sources that could produce false positive coincidences (Kulkarni & Kasliwal 2009). Classification based on light curves, spectroscopy and other properties can help, but these strategies are complicated by the fact that the light curves associated with compact object mergers and other potential GW sources are largely uncertain. However, we were able to demonstrate several automated strategies that reduced false positives, while selecting for a wide range of models. These techniques included demands on the rate of dimming in objects, spatial coincidence with galaxies within the GW observable distance, anti-coincidence with cataloged stars and asteroids, and shapes consistent with point objects. For a variety of data sets over wide areas, we showed how these cuts could be applied to reduce the rate of false positives to less than 10%, meaning that a single telescope taking a series of images in response to a GW trigger would have less than a 10% chance of reporting a false positive. Monte Carlo simulations of model light curves were used to show that this false-positive rejection was possible while still maintaining sensitivity to models of both GRB afterglow light curves and kilonova light curves.

Follow-up observations of the type presented in this paper will probably be just the first stage in efforts to find Advanced LIGO/Virgo counterparts. While essential to identify candidate counterparts, wide field imaging is unlikely to be sufficient to make definitive associations with a GW trigger. Further observations, including sensitive photometry and spectroscopy, will be needed to confirm possible associations and characterize the source. The level of false-positive rejection achieved by software in this work, if promptly applied to collected optical image data, would reduce candidate objects associated with a LIGO/Virgo trigger to a manageable level, such that they could be pursued with further follow-up observations. The challenge presented by false positives is likely to increase with the advent of Advanced LIGO/Virgo, when a larger horizon distance will require imaging to fainter magnitudes, and so increase the number of potential contaminants.

The Monte Carlo studies we performed demonstrated that we typically recovered a range of light curve models to a depth consistent with the limiting flux of the observations, proving the validity of our selection criteria. During the observing periods, typical position averaged sensitive ranges for NS–NS mergers was 18 Mpc, or 35 Mpc for NS–BH mergers (Abadie et al. 2012e). The efficiency curves shown in Figures 9 through 15 show that the data sets with better limiting magnitudes (QUEST, Liverpool Telescope) were successful in recovering all the considered models at these distance scales. The less sensitive data sets (ROTSE, TAROT, Zadko) would have missed a kilonova at these distances, but were potentially sensitive to GRB afterglows. Looking toward the future, the simulation results show that short exposures (∼1 minute) with small aperture telescopes, with observations to depths of less than 18th magnitude, failed to recover short GRB or kilonova light curves at distances comparable to the expected 200 Mpc range of advanced GW detectors to NS–NS mergers (Abadie et al. 2010b; Aasi et al. 2013). This means that, while smaller telescopes may be valuable in searching for counterparts to galactic GW sources, they may require long total exposures, and/or a hierarchical observing strategy with larger telescopes, to be able to detect the expected optical signature of distant compact object mergers. Another factor that is likely to impact transient recovery in the advanced detector era is the incompleteness of available galaxy catalogs (Nissanke et al. 2013). Currently, catalogs are missing a significant fraction of the extragalactic starlight within 200 Mpc, however, planned surveys can help address this problem (Nissanke et al. 2013).

This study has been a valuable exercise that will help the preparation of the data analysis and observing strategies for the up-coming second generation GW detectors, which are anticipated to begin operating in 2015 and to improve in sensitivity over the following few years (Aasi et al. 2013). Searches for optical and other transient counterparts will become even more compelling as the range of the detectors increases. Moreover, the rapid growth of large area survey instruments, including plans for the Large Synoptic Survey Telescope (Ivezic et al. 2011), means that the problem of choosing among rapidly fading candidates selected with different criteria is likely to become a theme that extends beyond GW related searches. The LIGO and Virgo collaborations are committed to providing prompt triggers for astronomers to follow up, with a more open model to allow broader participation (LIGO Scientific Collaboration & Virgo Collaboration 2012). We can therefore hope that future searches will yield multi-messenger transient events that reveal the astrophysical sources and processes that produce them.

[162] http://www.ligo.org/science/GWEMalerts.php

We thank J. Barnes, D. Kasen, B. Metzger, and E. Nakar for providing the kilonova model light curves that we have used in our Figures 4–7.

The authors gratefully acknowledge the support of the United States National Science Foundation for the construction and operation of the LIGO Laboratory, the Science and Technology Facilities Council of the United Kingdom, the Max-Planck-Society, and the State of Niedersachsen/Germany for support of the construction and operation of the GEO600 detector, and the Italian Istituto Nazionale di Fisica Nucleare and the French Centre National de la Recherche Scientifique for the construction and operation of the Virgo detector. The authors also gratefully acknowledge the support of the research by these agencies and by the Australian Research Council, the International Science Linkages program of the Commonwealth of Australia, the Council of Scientific and Industrial Research of India, the Istituto Nazionale di Fisica Nucleare of Italy, the Spanish Ministerio de Economia y Competitividad, the Conselleria d'Economia Hisenda i Innovacio of the Govern de les Illes Balears, the Foundation for Fundamental Research on Matter supported by the Netherlands Organisation for Scientific Research, the Polish Ministry of Science and Higher Education, the FOCUS Programme of Foundation for Polish Science, the Royal Society, the Scottish Funding Council, the Scottish Universities Physics Alliance, The National Aeronautics and Space Administration, OTKA of Hungary, the Lyon Institute of Origins (LIO), the National Research Foundation of Korea, Industry Canada and the Province of Ontario through the Ministry of Economic Development and Innovation, the National Science and Engineering Research Council Canada, the Carnegie Trust, the Leverhulme Trust, the David and Lucile Packard Foundation, the Research Corporation, FIRB 2012 Project RBFR12PM1F (Italian Ministry of Education, University and Research), and the Alfred P. Sloan Foundation. This work is based on results partially obtained at the ESO observatory, La Silla. The Liverpool Telescope is operated on the island of La Palma by Liverpool John Moores University in the Spanish Observatorio del Roque de los Muchachos of the Instituto de Astrofisica de Canarias with financial support from the UK Science and Technology Facilities Council. This document has been assigned the identifier LIGO-P1200171-v19.

REFERENCES

Aasi, J., Abadie, J., Abbott, B. P., et al. 2013, arXiv:1304.0670
Abadie, J., Abbott, B. P., Abbott, R., et al. 2012a, PhRvD, 85, 122007
Abadie, J., Abbott, B. P., Abbott, R., et al. 2012b, ApJ, 760, 12
Abadie, J., Abbott, B. P., Abbott, R., et al. 2012c, A&A, 541, A155
Abadie, J., Abbott, B. P., Abbott, R., et al. 2012d, A&A, 539, A124
Abadie, J., Abbott, B. P., Abbott, R., et al. 2012e, PhRvD, 85, 082002
Abadie, J., Abbott, B. P., Abbott, R., et al. 2010a, PhRvD, 81, 102001
Abadie, J., Abbott, B. P., Abbott, R., et al. 2010b, CQGra, 27, 173001
Abbott, B. P., Abbott, R., Adhikari, R., et al. 2009, RPPh, 72, 076901
Abdo, A. A., Ackermann, M., Arimoto, M., et al. 2009, Sci, 323, 1688
Accadia, T., Acernese, F., Alshourbagy, M., et al. 2012, JINST, 7, P03012
Akerlof, C. W., Kehoe, R. L., McKay, T. A., et al. 2003, PASP, 115, 132
Alard, C. 2000, A&AS, 144, 363
Alard, C., & Lupton, R. 1998, ApJ, 503, 325
Baltay, C., Rabinowitz, D., Andrews, P., et al. 2007, PASP, 119, 1278
Barnes, J., & Kasen, D. 2013, ApJ, 775, 18
Beauville, F., Bizouard, M.-A., Blackburn, L., et al. 2008, CQGra, 25, 045001
Berger, E. 2010, ApJ, 722, 1946
Berger, E., Fong, W., & Chornock, R. 2013, ApJL, 774, L23
Bertin, E., & Arnouts, S. 1996, A&AS, 117, 393
Bloom, J. S., Richards, J. W., Nugent, P. E., et al. 2012, PASP, 124, 1175
Brink, H., Richards, J. W., Poznanski, D., et al. 2013, MNRAS, 435, 1047
Cavalier, F., Barsuglia, M., Bizouard, M.-A., et al. 2004, PhRvD, 74, 082004
Clocchiatti, A., Suntzeff, N. B., Covarrubias, R., & Candia, P. 2011, AJ, 141, 163
Corsi, A., & Mészáros, P. 2009, ApJ, 702, 1171
Costa, E., Frontera, F., Heise, J., et al. 1997, Natur, 387, 783
Coward, D. M., Todd, M., Vaalsta, T. P., et al. 2010, PASA, 27, 331
Davies, M. B., King, A., Rosswog, S., & Wynn, G. 2002, ApJL, 579, L63
Doggett, J. B., & Branch, D. 1985, AJ, 90, 2303
Droege, T. F., Richmond, M. W., Sallman, M. P., & Creager, R. P. 2006, PASP, 118, 1666
Eichler, D., Livio, M., Piran, T., & Schramm, D. N. 1989, Natur, 340, 126
Evans, P. A., Fridriksson, J. K., Gehrels, N., et al. 2012, ApJS, 203, 28
Faber, J. A., & Rasio, F. A. 2012, LRR, 15, 8
Fairhurst, S. 2011, CQGra, 28, 105021
Fong, W., Berger, E., Margutti, R., et al. 2012, ApJ, 756, 189
Frail, D. A., Kulkarni, S. R., Nicastro, L., Feroci, M., & Taylor, G. B. 1997, Natur, 389, 261
Frail, D. A., Kulkarni, S. R., Sari, R., et al. 2001, ApJL, 562, L55
Fryer, C. L., Holz, D. E., & Hughes, S. A. 2002, ApJ, 565, 430
Gal-Yam, A., Kasliwal, M. M., Arcavi, I., et al. 2011, ApJ, 736, 159
Galama, T. J., Vreeswijk, P. M., van Paradijs, J., et al. 1998, Natur, 395, 670
Gehrels, N., Cannizzo, J. K., & Norris, J. P. 2007, NJPh, 9, 37
Gehrels, N., Sarazin, C. L., O'Brien, P. T., et al. 2005, Natur, 437, 851
Granot, J., Panaitescu, A., Kumar, P., & Woosley, S. E. 2002, ApJL, 570, L61
Grote, H., & LIGO Scientific Collaboration, 2008, CQGra, 25, 114043
Harrison, F. A., Bloom, J. S., Frail, D. A., et al. 1999, ApJL, 523, L121
Harry, G. M., & LIGO Scientific Collaboration 2010, CQGra, 27, 084006
Hjorth, J., Watson, D., Fynbo, J. P. U., et al. 2005, Natur, 437, 859
Ivezic, Z., Tyson, J. A., Acosta, E., et al. 2011, LSST: From Science Drivers to Reference Design and Anticipated Data Products (arXiv:0805.2366v2)
Jenkner, H., Lasker, B. M., Sturch, C. R., et al. 1990, AJ, 99, 2082
Kann, D. A., Klose, S., Zhang, B., et al. 2010, ApJ, 720, 1513
Kann, D. A., Klose, S., Zhang, B., et al. 2011, ApJ, 734, 96
Kanner, J., Huard, T. L., Marka, S., et al. 2008, CQGra, 25, 184034
Keller, S. C., Schmidt, B. P., Bessell, M. S., et al. 2007, PASA, 24, 1
Klimenko, S., Vedovato, G., Drago, M., et al. 2011, PhRvD, 83, 102001
Klotz, A., Boer, M., Atteia, J. L., & Gendre, B. 2009, AJ, 137, 4100
Kobayashi, S., & Mészáros, P. 2003, ApJ, 589, 861
Kochanek, C. S., & Piran, T. 1993, ApJL, 417, L17
Kouveliotou, C., Meegan, C. A., Fishman, G. J., et al. 1993, ApJL, 413, L101
Kulkarni, S. R., & Kasliwal, M. M. 2009, Astrophysics with All-Sky X-Ray Observations (Saitama: RIKEN, and JAXA Suzuki Umetaro Hall, RIKEN Wako), 312
Law, N. M., Kulkarni, S. R., Dekany, R. G., et al. 2009, PASP, 121, 1395
Lazio, J., Keating, K., Jenet, F. A., et al. 2012, in IAU Symp. 285, New Horizons in Time-Domain Astronomy, ed. R. E. M. Griffin, R. J. Hanisch, & R. Seaman (Cambridge: Cambridge Univ. Press), 67
Li, L., & Paczyński, B. 1998, ApJL, 507, L59
LIGO Scientific Collaboration, & Virgo Collaboration 2012, LIGO DCC, M1200055, https://dcc.ligo.org/LIGO-M1200055-v2/public
MacFadyen, A. I., & Woosley, S. E. 1999, ApJ, 524, 262
Malek, K., Batsch, T., Cwiok, M., et al. 2009, Proc. SPIE, 7502, 75020D
Mészáros, P. 2006, RPPh, 69, 2259
Metzger, B. D., & Berger, E. 2012, ApJ, 746, 48
Metzger, B. D., Martínez-Pinedo, G., Darbha, S., et al. 2010, MNRAS, 406, 2650
Molinari, E., Vergani, S. D., Malesani, D., et al. 2007, A&A, 469, L13

Monet, D., Bird, A., Canzian, B., Dahn, C., et al. 1998, The USNO-A2.0 Catalogue (Washington, DC: U.S. Naval Observatory)
Nakar, E. 2007, PhR, 442, 166
Narayan, R., Paczynski, B., & Piran, T. 1992, ApJL, 395, L83
Nissanke, S., Kasliwal, M., & Georgieva, A. 2013, ApJ, 767, 124
Nissanke, S., Sievers, J., Dalal, N., & Holz, D. 2011, ApJ, 739, 99
Nousek, J. A., Kouveliotou, C., Grupe, D., et al. 2006, ApJ, 642, 389
Nuttall, L. K., & Sutton, P. J. 2010, PhRvD, 82, 102002
Nuttall, L. K., White, D. J., Sutton, P. J., et al. 2013, ApJS, 209, 24
Ott, C. D. 2009, CQGra, 26, 063001
Paczynski, B. 1991, AcA, 41, 257
Piran, T., Nakar, E., & Rosswog, S. 2013, MNRAS, 430, 2121
Piro, A. L., & Pfahl, E. 2007, ApJ, 658, 1173
Racusin, J. L., Liang, E. W., Burrows, D. N., et al. 2009, ApJ, 698, 43
Racusin, J. L., Oates, S. R., Schady, P., et al. 2011, ApJ, 738, 138
Rahmer, G., Smith, R., Velur, V., et al. 2008, Proc. SPIE, 7014, 70144Y
Rau, A., Kulkarni, S. R., Law, N. M., et al. 2009, PASP, 121, 1334
Rhoads, J. E. 2003, ApJ, 591, 1097
Roberts, L. F., Kasen, D., Lee, W. H., & Ramirez-Ruiz, E. 2011, ApJL, 736, L21
Romero, G. E., Reynoso, M. M., & Christiansen, H. R. 2010, A&A, 524, A4
Sari, R., Piran, T., & Halpern, J. P. 1999, ApJL, 519, L17
Sari, R., Piran, T., & Narayan, R. 1998, ApJL, 497, L17
Searle, A. C., Sutton, P. J., Tinto, M., & Woan, G. 2008, CQGra, 25, 114038
Shibata, M., Karino, S., & Eriguchi, Y. 2003, MNRAS, 343, 619
Shibata, M., & Taniguchi, K. 2011, LRR, 14, 6
Singer, L. P., Cenko, S. B., Kasliwal, M. M., et al. 2013, ApJL, 776, L34
Smith, A. M., Lynn, S., Sullivan, M., et al. 2011, MNRAS, 412, 1309
Soderberg, A. M., Nakar, E., Berger, E., & Kulkarni, S. R. 2006, ApJ, 638, 930
Sokolowski, M. 2008, PhD thesis, Andrzej Soltan Institute for Nuclear Studies (arXiv:0810.1179)
Steele, I. A., Smith, R. J., Rees, P. C., et al. 2004, Proc. SPIE, 5489, 679
Tanvir, N. R., Levan, A. J., Fruchter, A. S., et al. 2013, Natur, 500, 547
Thorne, K. S. 1987, in Gravitational Radiation, ed. S. W. Hawking & W. Israel (Cambridge: Cambridge Univ. Press), 330
van Eerten, H., Zhang, W., & MacFadyen, A. 2010, ApJ, 722, 235
van Eerten, H. J., & MacFadyen, A. I. 2011, ApJL, 733, L37
van Paradijs, J., Groot, P. J., Galama, T., et al. 1997, Natur, 386, 686
Virgo Collaboration 2009, Advanced Virgo Baseline Design, Tech. Rep., VIR-0027A-09, https://tds.ego-gw.it/ql/?c=6589
Vitale, S., Del Pozzo, W., Li, T. G. F., et al. 2012, PhRvD, 85, 064034
White, D. J., Daw, E. J., & Dhillon, V. S. 2011, CQGra, 28, 085016
White, D. J., LIGO Scientific Collaboration, & Virgo Collaboration 2012, JPhCS, 363, 012036
Woosley, S. E. 1993, ApJ, 405, 273
Woosley, S. E., & Bloom, J. S. 2006, ARA&A, 44, 507
Yuan, F., & Akerlof, C. W. 2008, ApJ, 677, 808

Contributions à la détection directe des ondes gravitationnelles avec Virgo : caractérisation du détecteur, analyse de données et astrophysique multi-messager

La théorie de la Relativité Générale prédit l'existence des ondes gravitationnelles qui sont des solutions radiatives aux équations d'Einstein régissant la dynamique de l'espace-temps. Grâce aux détecteurs interférométriques tels que Virgo, nous sommes vraisemblablement proche de la première détection directe des ondes gravitationnelles qui viendra confirmer les preuves indirectes recueillies jusqu'ici. Ces détecteurs permettent l'observation des ondes gravitationnelles provenant de phénomènes cosmiques violents comme les coalescences de binaires d'étoiles à neutrons ou de trous noirs. Au cours de mes recherches, j'ai contribué, à différents niveaux, au développement et à l'exploitation scientifique de ces détecteurs. J'ai d'abord participé à la phase de mise en service de l'instrument, et plus spécifiquement au développement d'un ensemble d'outils de pré-analyse pour la caractérisation du bruit instrumental. J'ai ensuite proposé de nouvelles méthodes de recherche de signaux gravitationnels quasi-périodiques suivant une approche alternative à la méthode de référence basée sur le filtrage adapté. L'introduction d'un modèle markovien s'appuyant sur un graphe temps-fréquence permet de reformuler le problème de la détection optimale de ces signaux comme un problème d'optimisation combinatoire pour lequel il existe un algorithme de recherche efficace dont nous montrons les bonnes performances. Cette nouvelle méthode est particulièrement utile lorsque la complexité du signal visé est grande rendant prohibitif le coût calculatoire du filtrage adapté. Finalement, j'ai réalisé plusieurs projets de recherche "multi-messager" couplant les observations en ondes gravitationnelles avec celles qui proviennent d'autres canaux. J'ai contribué au premier programme de suivi électromagnétique effectué en collaboration avec un réseau global de télescopes optiques robotisés. J'ai également conduit la recherche d'un signal conjoint avec les neutrinos de haute énergie observés par ANTARES.

Contributions to the direct detection of gravitational waves with Virgo : detector characterization, data analysis and multimessenger astronomy

The theory of General Relativity predicts the existence of gravitational waves which are radiative solutions of the Einstein's equations that govern space-time dynamics. Thanks to interferometric detectors such as Virgo, we are probably close to the first direct detection of gravitational waves, that will confirm the indirect evidences collected so far. These detectors allows the observations of gravitational waves from violent cosmic phenomena such as the merger of neutron star and/or black hole binary. In the course of my researches, I contributed, at various levels, to the development and scientific exploitation of these detectors. First, I participated in the instrument starting phase, specifically to the development of a set of pre-analysis tools for the instrumental noise characterization. I also proposed a new method to search for quasi-periodic gravitational signals following an alternative approach to the reference method using matched filtering. The introduction of a Markovian model based on a time-frequency graph allows to reformulate the problem of optimally detecting such signals in a combinatorial optimization problem, for which an efficient search algorithm exists. This new method proves to be particularly useful when the complexity of the targeted signal is large and prohibits the use of matched filtering techniques. Finally, I realized several "multi-messengers" search projects that couple gravitational wave observations to that from other channels. I contributed to the first electromagnetic follow-up program performed in jointly with a global network of autonomous robotic telescopes. I also conducted the search for a joint signal with the high-energy neutrinos by ANTARES.